Progress in Colloid and Polymer Science
Volume 136

# Progress in Colloid and Polymer Science

Recently published and Forthcoming Volume

**Gels: Structures, Properties, and Functions**
Volume Editors: Masayuki Tokita, Katsuyoshi Nishinari
Vol. 136, 2009

**Colloids for Nano- and Biotechnology**
Volume Editors: Hórvölgyi, Z.D., Kiss, É.
Vol. 135, 2008

**Surface and Interfacial Forces From Fnndamentals to Applications**
Volume Editors: Auernhammer, G.K., Butt, H.-J , Vollmer, D.
Vol. 134, 2008

**Smart Colloidal Materials**
Volume Editors: Richtering, W.
Vol. 133, 2006

**Characterization of Polymer Surfaces and Thin Films**
Volume Editors: Grundke, K., Stanun, M., Adler, H.-J.
Vol. 132, 2006

**Analytical Ultracentrifugation VIII**
Volume Editors: Wandrey, C., Cölfen, H.
Vol. 131, 2006

**Scattering Methods and the Properties of Polymer Materials**
Volume Editors: Stribeck, N., Smarsly, B.
Vol. 130, 2005

**Mesophases, Polymers, and Particles**
Volume Editors: Lagaly, G., Richtering, W.
Vol. 129, 2004

**Surface and Colloid Science**
Volume Editors: Galembeck, F.
Vol. 128, 2004

**Analytical Ultracentrifugation VII**
Volume Editors: Lechner, M.D., Börger, L.
Vol. 127, 2004

**Trends in Colloid and Interface Science XVII**
Volume Editors: Cabuil, V., Levitz, P., Treiner, C.
Vol. 126, 2004

**From Colloids to Nanotechnology**
Volume Editors: Zrinyi, M., Horvolgyi, Z.D.
Vol. 125, 2004

**Aqueous Polymer Dispersions**
Volume Editor: Tauer, K.
Vol. 124, 2004

**Trends in Colloid and Interface Science XVI**
Volume Editors: Miguel, M., Burrows, H.D.
Vol. 123, 2004

**Aqueous Polymer – Cosolute Systems**
Volume Editors: Anghel, D.F.
Vol. 122, 2002

**Molecular Organisation on Interfaces**
Volume Editors: Lagaly, G.
Vol. 121, 2002

**Lipid and Polymer–Lipid Systems**
Volume Editor: Nylander, T.
Vol. 120, 2002

Masayuki Tokita and Katsuyoshi Nishinari
Editors

# Gels: Structures, Properties, and Functions

## Fundamentals and Applications

Springer

*Editors*
Prof. Dr. Masayuki Tokita
Kyushu University
Graduate School of Sciences
Dept. Physics
6-10-1 Hakozaki
Fukuoka
812-8581 Japan
tokita@phys.kyushu-u.ac.jp

Prof. Dr. Katsuyoshi Nishinari
Osaka City University
Graduate School of Human Life Sciences
Dept. Food and Human Health Sciences
3-3-138 Sugimoto
Osaka
558-5858 Japan
nishinari@life.osaka-cu.ac.jp

ISSN: 0340-255X e-ISSN: 1437-8027
ISBN: 978-3-642-00864-1 e-ISBN: 978-3-642-00865-8
DOI 10.1007/978-3-642-00865-8
Springer Dordrecht Heidelberg London New York

Library of Congress Control Number: 2009928099



*Cover design:* eStudioCalamar Figueres/Berlin

Printed on acid-free paper

Springer is part of Springer Science+Business Media (www.springer.com)

# Preface

It is a great pleasure for us to present a collection of papers read at the Toyoichi Tanaka Memorial Symposium on Gels held on 10-12 September 2008 in Tokyo. Professor Toyoichi Tanaka of MIT has developed gel science after the discovery of volume phase transition, but unfortunately he passed away so early in 2000. His friends and co-workers decided to organize a symposium commemorating the 30th anniversary for the discovery of the volume phase transition in 1978.

The symposium was held in a style of Faraday Discussions. Full papers written in Japanese were sent beforehand to all the participants, and discussions were active after a short (5min) presentation of each paper. Since Japanese language is very different from European languages, we Japanese could speak freely without any hesitation. Although all the participants are good at English as proved by their publication of many papers in English, yet the discussion of delicate nuances could be done better in Japanese than in English.

After the successful symposium, papers written in English taking into account the discussions during the symposium were reviewed by expert scientists, and the papers were revised accordingly. We hope that this collection of papers is interesting and useful for all the scientists and engineers working in the area of gels both in academia and industry. Finally, we thank all the contributors and reviewers for their enthusiastic efforts.

Summer 2009

Masayuki Tokita
Katsuyoshi Nishinari

# Contents

Progr Colloid Polym Sci (2009) 136:1–8
DOI: 10.1007/2882_2009_1

# Competitive Hydrogen Bonds and Cononsolvency of Poly(*N*-isopropylacrylamide)s in Mixed Solvents of Water/Methanol

Fumihiko Tanaka[1], Tsuyoshi Koga[1], and Françoise M. Winnik[2]

**Abstract** Collapse of a poly(*N*-isopropylacrylamide) (PNIPAM) chain upon heating in aqueous solutions is theoretically studied on the basis of cooperative dehydration (simultaneous dissociation of bound water molecules in a group of correlated sequence), and compared with the experimental observation of temperature-induced coil-globule transition by light scattering methods. The transition becomes sharper with the cooperativity parameter σ of hydration. Phase diagrams with very flat LCST phase separation line for aqueous poly(*N*-isopropylacrylamide) (PNIPAM) solutions are theoretically derived on the basis of sequential hydrogen bond formation between polymer chains and water molecules (*cooperative hydration*), and compared with experimental spinodal curves. The two-phase region systematically changes its shape with the cooperativity parameter σ, and the spinodals turned out to be almost independent of the polymer molecular weight for strongly cooperative hydration (small σ) as observed in PNIPAM solutions. Reentrant coil-globule-coil transition in mixed solvent of water and methanol is also studied from the viewpoint of competitive hydrogen bonds between polymer-water and polymer-methanol. The downward shift of the cloud-point curves (LCST cononsolvency) with the mol fraction of methanol due to the competition is calculated and compared with the experimental data.

**Keywords** Consolvency • Competitive hydrogen bond • Reentrant coil-globule-coil transition

**PACS** 82.70.Gg,64.60.-i, 64.70.-p, 64.75.+g

F. Tanaka (✉)
[1]Department of Polymer Chemistry
Graduate School of Engineering, Kyoto University
e-mail: ftanaka@phys.polym.kyoto-u.ac.jp
[2]Department of Chemistry and Faculty of Pharmacy
University of Montréal

## Introduction

Aqueous solutions of temperature-sensitive poly(*N*-isopropylacrylamide) (PNIPAM) exhibit flat LCST cloud-point curves at around 32°C, which are almost independent both of the concentration up to 20 %wt and of the polymer molecular weight [1–5]. The transmittance of light sharply diminishes in a very narrow temperature region where coil-globule transition of the polymer chain takes place [6]. Sudden change in polymer conformation leads to the temperature sensitivity. Although the origin of temperature-sensitivity had long been a mistery, we recently pointed out that it is caused by the cooperative dehydration of the bound water molecules upon heating [7]. On the basis of this idea, we constructed a theoretical model of cooperative hydration, and succeeded in explaining the peculiar LCST phase separation [7]. It was experimentally reported that the spinodal curves are also flat in a similar way to the cloud-point curve except in a very dilute regime [3]. The solution doesn't phase separate even if it is brought to the unstable region above the spinodal, but particles of hundred nanometer scale consisting of the aggregates of PNIPAM chains are formed [8,9]. They are called mesoglobules. Mesoglobules are glassy and highly concentrated, as high as 80 %wt. They persist for a long time.

If methanol is mixed to such aqueous PNIPAM solutions, polymer chain collapses [10], cross-linked gels undergo volume phase transition [11,12], and polymer solutions phase separate [13–15], although methanol is a good solvent for PNIPAM. If two good solvents become poor when mixed, they are called cononsolvents. In water/methanol mixture, cononsolvency is most evident at around 0.35 mol fraction of methanol. The mixture recovers good solvency at high concentration of methanol. We show here that such a peculiar reentrant behavior of the solutions is caused by the competitive hydrogen bonding of water and methanol onto the polymer chain [16]. The effect becomes strongest where the competition is highest, where the total number of bound molecules shows a minimum. In this paper, after reviewing

the temperature-induced coil-globule transition in pure water, we study the reentrant coil-globule-coil transition and lower shift of LCST curves in the mixed solvents.

## Temperature-Induced Coil-Globule Transition of PNIPAM chains and their Phase Separation in Pure Water

The cooperativity in hydration is caused by the positive correlation between neighboring bound water molecules due to the existence of large hydrophobic isopropyl side groups. If a water molecule succeeds in forming a hydrogen bond with an amido group on a chain, a second water molecule can form a bond more easily than the first one because the first molecule causes some displacement of the isopropyl group, which creates more access space for the next molecule. As a result, consecutive sequences of bound water appear along the chain, which leads to a pearl-necklace type chain conformation. When the chain is heated, each sequence is dehydrated in a group, resulting in the sharp collapse of the chain.

Figure 1 shows a pearl-necklace conformation of PNIPAM chain consisting of collapsed globules connected by the hydrated swollen partial chains [7,16,17]. We study the thermodynamic nature of the coil-globule transition and average end-to-end distance by starting with the single chain partition function $Z(T)$, and then move to thermodynamics of phase separation in mixed solvents.

Let us first specify the polymer conformation by the index $\mathbf{j} \equiv \{j_1, j_2, \cdots\}$, which indicates that the chain with total number $n$ of repeat units carries the number $\mathbf{j}_\zeta$ of the hydrated sequences of length $\zeta$ (in terms of the number of repeat units). The statistical properties of the chain is described by the standard partition function

$$Z(T) = \sum_{\mathbf{j}} \omega(\mathbf{j}) \prod_{\zeta} (\eta_\zeta)^{j_\zeta}, \tag{1}$$

where $\omega(\mathbf{j}) \equiv (n - \sum \zeta j_\zeta)! / \prod j_\zeta! [n - \sum(\zeta + 1) j_\zeta]!$ is the number of different ways to place the hydrated coils and globules alternatively along the chain and is related to the entropy of hydration[18]. The weight $\eta_\zeta$ gives the statistical weight for the appearance of the sequence of length $\sigma$. To describe cooperativity, let $-\varepsilon$ be the binding free energy of a water molecule, and let $-\Delta\varepsilon$ be the interaction energy between the nearest neghboring bound water molecules. Then, the statistical weight of one contiguous sequence ofthe length $\sigma$ is given by the Zimm-Bragg form[19]

$$\eta_\zeta = \sigma \eta(T)^\zeta, \tag{2}$$

where $\sigma \equiv \exp(-\beta\Delta\varepsilon)$ is the coopearativity parameter, $\eta(T) \equiv \exp[(\varepsilon + \Delta\varepsilon)/k_B T]$ is the association constant of the hydrogen bonding. When hydration is random, as seen in aqueous solutions of poly(ethylene oxide)s, we have $\sigma = 1$. Smaller $\sigma$ gives stronger cooperativity.

Instead of summing up all possible types $\mathbf{j}$, we find the most probable distribution function $\mathbf{j}$ by minimizing the free energy, and calculate the degree of hydration

$$\theta(\mathbf{j}) \equiv \sum_{\zeta=1}^{n} \zeta j_\zeta \, / n \tag{3}$$

and the mean end-to-end distance $\langle R^2 \rangle$. Results are plotted in Figure 3. The latter is normalized by the reference value at 20°C, and is plotted in terms of the expansion factor $\alpha_R \equiv [\langle R^2 \rangle / \langle R^2 \rangle (T = 20)]^{1/2}$. With stronger cooperativity, the transition becomes sharper. Figure 4 compares our calculation with the experimental data[6] of the mean radius of gyration measured by light scattering method. Calculation assumes $\sigma = 10^{-4}$ to fit the data.

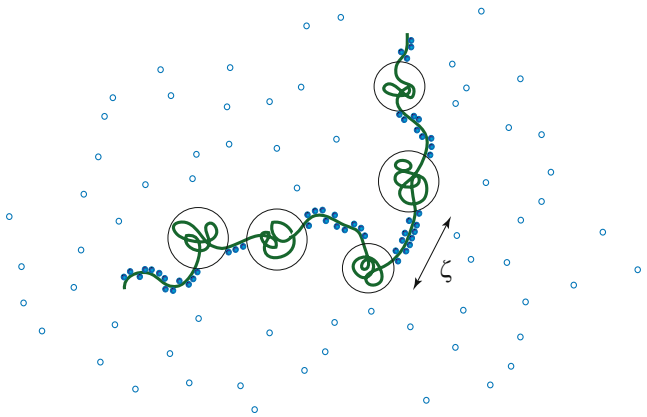


**Fig. 1** Sequential hydrogen bonds formed along the polymer chain due to the cooperative interaction between the nearest-neghboring bound water molecules. The type of polymer-water associated complex is specified by the index $\mathbf{j} \equiv \{j_1, j_2, \cdots\}$, where $j_\zeta$ is the number of sequences that consist of a run of hydrogen-bonded $\zeta$ consecutive water molecules. The average length of sequences sharply reduces as temeprature approaches LCST from below. The globule parts (thin circles) are collapsed near LCST

## LCST Phase Separation of Aqueous PNIPAM Solutions

We next consider a model solution in which the number $N_1$ of polymer chains with $n$ repeat units are mixed with the number $N_0$ of water molecules. We are based on the lattice-theoretical picture of polymer solutions, and divide the system volume $V$ into cells of size $a$, each of which can

accommodate either a water molecule or a statistical repeat unit of the polymer. We assume incompressibility of the solution, so that we have $\Omega = N_0 + nN_1$, where $\Omega \equiv V/a^3$ is the total number of cells. To describe adsorption of water, let $N(\mathbf{j})$ be the number of polymer-water (p-w) complexes whose type is specified by the index $\mathbf{j}$(see Figure 1). The total DP of a complex is given by $n(\mathbf{j}) \equiv n[1 + \theta(\mathbf{j})]$.

Then, the free energy of mixing is given by

$$\beta\Delta F = N_{\rm fw}\ln\phi_{\rm fw} + \sum_{\mathbf{j}} N(\mathbf{j})\ln\phi(\mathbf{j}) + \beta\sum_{\mathbf{j}} \Delta A(\mathbf{j})N(\mathbf{j}) + \chi(T)\phi(1-\phi)\Omega, \tag{4}$$

where $\phi(\mathbf{j}) \equiv n(\mathbf{j})N(\mathbf{j})/\Omega$ is the volume fraction of the complex $\mathbf{j}$, $N_{\rm fw}$ the number of free water molecules in the solution, and $\phi_{\rm fw} \equiv N_{\rm fw}/\Omega$ their volume fraction. $\Delta A(\mathbf{j})$ the conformational free energy to form a complex of the type $\mathbf{j}$ measured relative to the reference conformation $\mathbf{j}_0 \equiv \{0, 0, \cdots\}$ where no water molecule is adsorbed. It is related to the statistical weight (1) as

$$\beta\Delta A(\mathbf{j}) = -\ln\left[\omega(\mathbf{j})\prod_{\zeta}(\eta_\zeta)^{j_\zeta}\right]. \tag{5}$$

The total volume of the solution is now written as $\Omega = \sum_{\mathbf{j}} n(\mathbf{j})N(\mathbf{j}) + N_{\rm fw}$. The number density of the complexes specified by $\mathbf{j}$ is given by $v(\mathbf{j}) = N(\mathbf{j})/\Omega$.

By finding the chemical potentials for the hydrated polymer and water from the free energy, and imposing the hydration equilibrium condition

$$\Delta\mu(\mathbf{j}) = \Delta\mu(\mathbf{j}_0) + n\theta(\mathbf{j})\Delta\mu_{\rm fw} \tag{6}$$

we can study solution properties such as hydration, phase separation, spinodals. Figure 5 draws the spinodal curves for different cooperative parameter σ with fixed other parameters. It theoretically demonstrates how the bottom part of the miscibility loops become flatter with decrease in σ. In the calculation, usual miscibility domes with UCST appear at low temperature, but these are not observable in the experiments because of the freezing of water. For the polymer concentration higher than $\phi = 0.5$, our theoretical description becomes poor because of the depletion of water molecules, i.e., the number of water molecules becomes insufficient to cover the polymers.

Figure 6 compares theoretical calculation with experimental data[3] on the spinodal points. In the experiments, the upper part of the miscibility square is impossible to observe because temperature is too high. Also, UCST phase separation seen in the theoretical calculation is not observable because of the freezing of water. The polymer molecular weight used in the experiment is $M_{\rm w} = 615,500$, so that the nominal number of monomers is roughly given by $n = 5,400$. Although polymers used in the experiment are polydisperse with the index $M_{\rm w}/M_{\rm n} = 2.04$, we expect that this may not cause any serious problems because the dependence of binodals as well as spinodals on the polymer molecular weight becomes weaker with increase in cooperativity in hydration. Since the statistical unit used in the lattice theory must be regarded as a group of monomers, we have tried to fit the data by $n = 100$ and 1000. (Theoretical calculation does not depend so much upon the number $n$ if it is larger than 500.) We have seen a good agreement by fixing the cooperative parameter at $\sigma = 0.3$. There is, however, a slight descripancy in the dilute regime; theoretical curve predicts a sharper upward bend. Closer examination on the very dilute regime from both experimental and theoretical viewpoint is therefore neccessary.

## Reentrant Coil-Globule-Coil Transition in Mixed Solvent of Water/Methanol

Because methanol is also hydrogen-bonding solvent, we assume pearl-necklace conformation with globules connected by the two kinds of swollen hydrogen-bonded subchains (Figure 2). Let $\theta^{(\rm w)}$ and $\theta^{(\rm m)}$ be the number of p-w and p-m hydrogen-bonds relative to $n$ for a given mol fraction $x_{\rm m}$ of methanol in the bulk solution. The cooperativity parameter for methanol is assumed to be given by $\sigma_{\rm m}$. The total degree of hydrogen bonding is given by $\theta = \theta^{(\rm w)} + p\theta^{(\rm m)}$, where we

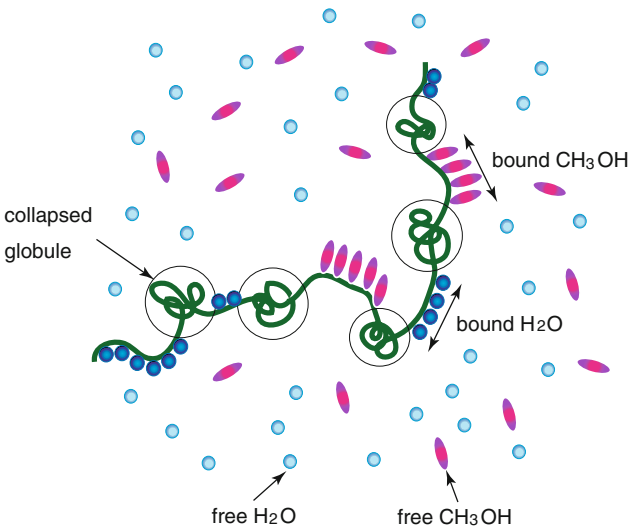


**Fig. 2** Competitition between PNIPAM-water and PNIPAM-methanol hydrogen bonding. When there is strong cooperativity, continuous sequences of each species are exclusively formed along the chain. As a result, the chain takes a pearl-necklace conformation

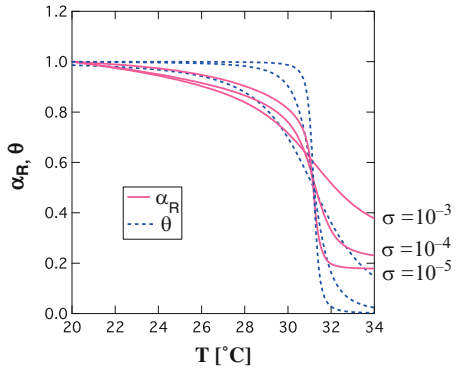


**Fig. 3** Theoretical calculation of the expansion factor $\alpha_R$ (solid lines) and the degree of hydration $\theta$ (broken lines) are plotted against temperature for three different cooperativity parameters. With increase in cooperativity, the coil-globule transition becomes sharper

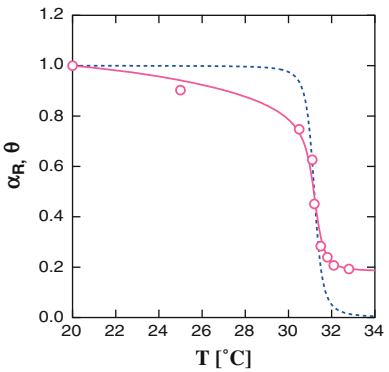


**Fig. 4** Comaprison of the experimental data obtained by Fujishige et al [6] by the theoretical curve. The fitting parameters are: $n = 7.0\times 10^4, \lambda_{w0} = 0.001, \gamma_w = 3.788, \Theta = 555, \sigma_w = 2\times 10^{-5}, \kappa_w = 0.31$

have assumed that molecular volume of methanol relative to water is $p$. Since the solution is a particle reservoir, we introduce the activity $\lambda_\alpha(\alpha = \mathrm{w}, \mathrm{m})$ of each type of solvent as independent variables (functions of the solvent composition), and move to the grand partition function

$$\Xi(\{\lambda\}) \equiv \sum_{n^{(\mathrm{w})},n^{(\mathrm{m})}=0}^{n} {\lambda_\mathrm{w}}^{n^{(\mathrm{w})}}\, {\lambda_\mathrm{m}}^{n^{(\mathrm{m})}}\, Z(n^{(\mathrm{w})}, n^{(\mathrm{m})}), \qquad (7)$$

where $n^{(\alpha)}$ is the number of bound molecules of the species $\alpha$. The most probable distribution function of sequences that maximizes this grand partition function (equivalent to minimizing the free energy) is then found by variational calculation to be

$$j_\zeta{}^{(\mathrm{w})}/n = (1-\theta)\eta_\zeta^{(\mathrm{w})} t(\lambda_\mathrm{w} t)^\zeta \qquad (8a)$$

$$j_\zeta{}^{(\mathrm{m})}/n = (1-\theta)\eta_\zeta^{(\mathrm{m})} t(\lambda_\mathrm{m} t^p)^\zeta \qquad (8b)$$

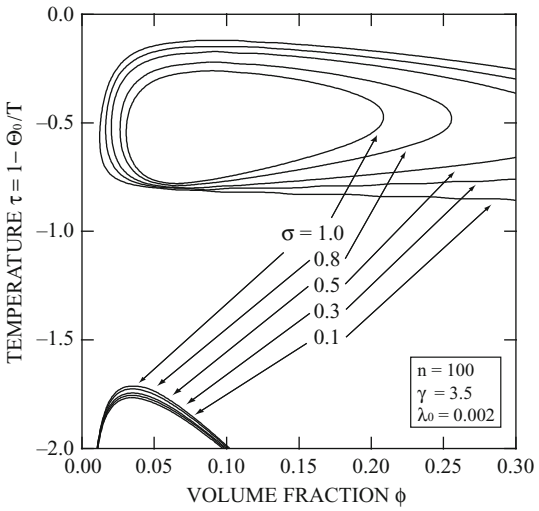


**Fig. 5** Spinodal lines drawn on the (reduced) temperature and concentration plane for different cooperative parameter σ. Other parameters are fixed at $n = 100, \psi = 1.0, \lambda_0 = 0.002, \gamma = 3.5$. The bottom part of the miscibility square becomes flatter with decrease in the cooperative factor σ

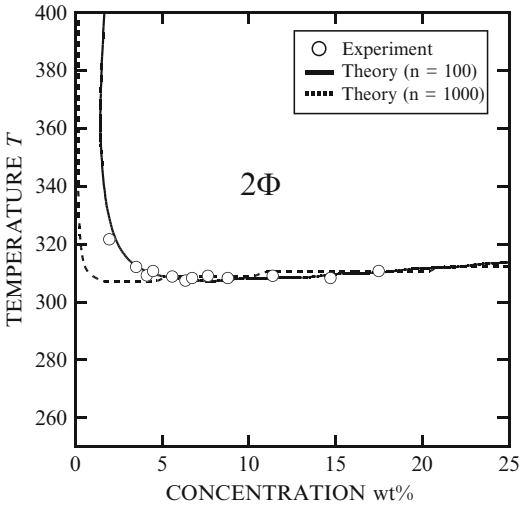


**Fig. 6** Phase diagrams of aqueous PNIPAM solution. Experimental data ( ◯ ) of the spinodal curve is compared with theoretical calculation. The DP of the polymer is $n = 100$(solid line) and $n = 1000$(broken line). Theoretical parameters used are $\Theta_0 = 555$ and $\lambda_0 = 0.002$ for $n = 100$, and $\Theta_0 = 565$ and $\lambda_0 = 0.003$ for $n = 1000$. Other parameters are fixed at $\gamma = 3.5, \sigma = 0.3$

Here $\theta = \theta^{(\mathrm{w})} + p\theta^{(\mathrm{m})}$ is the total coverage (number of monomers covered by bound molecules relative to the total DP) with $\theta^{(\alpha)} \equiv \sum_{\zeta\geq 1} \zeta j_\zeta{}^{(\alpha)}/n$ being the coverage by each solvent. Similarly, $\nu = \nu^{(\mathrm{w})} + \nu^{(\mathrm{m})}$ is the total number of sequences (relative to the total DP) with $\nu^{(\alpha)} \equiv \sum_{\zeta\geq 1} j_\zeta{}^{(\alpha)}/n$ being the number of sequences of each solvent. The parameter $t$ is defined by $t \equiv 1 - \nu/(1-\theta)$, and has a physical meaning of the probability such that an

arbitralily chosen monomer belongs to the free part. The grand partition function is given by $\Xi(\{\lambda\}) = t^{-n}$.

To find $t$ as a function of the activities, we now substitute the equilibrium distribution $j_\zeta{}^{(\mathrm{w})}$ and $j_\zeta{}^{(\mathrm{m})}$ into the definitions of $\theta$ and $v$, and find

$$\theta^{(\mathrm{w})} = (1-\theta)tV_1^{(\mathrm{w})}(\lambda_\mathrm{w} t), \tag{9a}$$

$$v^{(\mathrm{w})} = (1-\theta)tV_0^{(\mathrm{w})}(\lambda_\mathrm{w} t) \tag{9b}$$

for water, and

$$\theta^{(m)} = (1-\theta)tV_1^{(\mathrm{m})}(\lambda_\mathrm{m} t^p), \tag{10a}$$

$$v^{(\mathrm{m})} = (1-\theta)tV_0^{(\mathrm{m})}(\lambda_\mathrm{m} t^p) \tag{10b}$$

for methanol. Here, the functions $\mathrm{V}_k$ are defined by $V_k^{(\alpha)}(x) \equiv \sum_{\zeta=1}^{n^*} \zeta^k \eta_\zeta{}^{(\alpha)} x^\zeta$. The upper limit of the sum is $n^* = n$ for water, and $n^* = [n/p]$ for methanol, where $[k]$ means the maximum integer smaller than, or equal to, $k$.

By the definition of $t$, we find that it should satisfy the condition

$$\frac{t}{1-t}\left\{V_0^{(\mathrm{w})}(\lambda_\mathrm{w} t) + V_0^{(\mathrm{m})}(\lambda_\mathrm{m} t^p)\right\} = 1. \tag{11}$$

This is basically the same as the equation found by ZB, but here it is properly extended to describe competiton in p-w and p-m hydrogen bonding. Upon substitution of the solution for $t$ into $\theta$, we find that the total coverage $\theta$ is given by

$$\theta = 1 - 1/\left\{1 + t\left[V_1^{(\mathrm{w})}(\lambda_\mathrm{w} t) + pV_1^{(\mathrm{m})}(\lambda_\mathrm{m} t^p)\right]\right\}. \tag{12}$$

The mean end-to-end distance is calculated by

$$\begin{aligned}\langle R^2\rangle = {} & (an^{\nu_G})^2[1-\theta^{(\mathrm{w})}(\lambda_\mathrm{w} t) - \theta^{(\mathrm{m})}(\lambda_\mathrm{m} t)] \\ & + [\kappa_\mathrm{w}^2 \overline{\zeta_\mathrm{w}^{2\nu_F-1}}(\lambda_\mathrm{w} t)]\theta_\mathrm{w}(\lambda_\mathrm{w} t) \\ & + p[\kappa_\mathrm{m}^2 \overline{\zeta_\mathrm{m}^{2\nu_F-1}}(\lambda_\mathrm{m} t^p)]\theta_\mathrm{m}(\lambda_\mathrm{m} t^p),\end{aligned} \tag{13a}$$

where $\langle R^2\rangle_c^{1/2} \equiv an^{\nu_G}$ is that of the globular state, and $\overline{\zeta^{2\nu_F-1}}(x) \equiv V_{2\nu_F}(x)/V_1(x)$is the average length of the hydrated coils. $\kappa$ is the ratio of the fundamental step length of hydrated sequences to that of the globules. The index $\nu_F = 3/5$ is Flory's exponent, $\nu_G = 1/3$ is the exponent of a globule.

If we employ the ZB form for the statistical weight $\eta_\zeta$, the arguments of the $V$ functions become the combined variable $\lambda_\mathrm{w} s_\mathrm{w} t$ for water, and $\lambda_\mathrm{m} s_\mathrm{m} t^p$ for methanol. We assume that the solvent-solvent interaction is weak, compared to the solvent-polymer interaction, and neglect it. The mixed solvent is regarded as an ideal mixture. Then the activity is proportional to the molar fraction of each component. We can write $\lambda_w s_\mathrm{w} = \tilde{\lambda}_\mathrm{w}(T)(1-x_\mathrm{m})$ and $\lambda_\mathrm{m} s_\mathrm{m} = \tilde{\lambda}_\mathrm{m}(T)x_\mathrm{m}$, where $\tilde{\lambda}$s are functions of the temperature only. In the following study, we fix the temperature, and hence $\tilde{\lambda}$s are constants depending upon the strength of the hydrogen bonds.

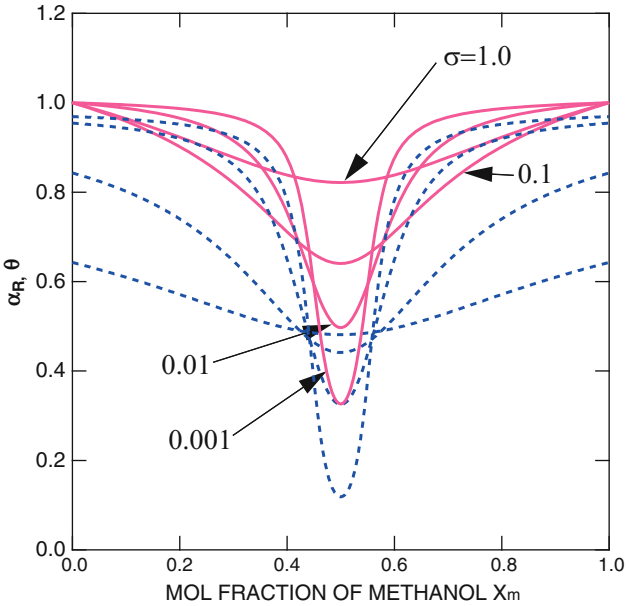


**Fig. 7** The normalized end-to-end distance (solid lines) and the total coverage by bound molecules (broken lines) are plotted against the molar fraction of methanol. The DP of the polymer chain is fixed at $n = 100$. The volume ratio of the solvents is fixed at $p$=1. The cooperativity parameter $\sigma_\mathrm{w} = \sigma_\mathrm{m}$ is varied from curve to curve. The association constants are fixed at $\tilde{\lambda}_\mathrm{w} = \tilde{\lambda}_\mathrm{m} = 1.8$. The monomer expansion factors are fixed at $\kappa_\mathrm{w} = \kappa_\mathrm{m} = 2.0$

Figure 7 shows the expansion factor for the end-to-end distance $\alpha_R \equiv [\langle R^2\rangle/\langle R^2\rangle_0]^{1/2}$ (solid lines) and the total coverage $\theta$ (broken lines) plotted against the molar fraction $x_m$ of methanol. Here, $\langle R^2\rangle_0$ is the value in pure water. The calculation was done by assuming that all parameters are symmetric and with $p = 1$. The cooperativity parameter $\sigma$ varies from curve to curve. We can clearly see that the coverage takes a minimum value at $x_\mathrm{m} = 0.5$ (stoichiometric concentration) as a result of the competition, so that the end-to-end distance also takes minimum at $x_\mathrm{m} = 0.5$. A slight deviation from stoichiometry is nonlinearly magnified on the chain by cooperativity (nonlinear amplification). As cooperativity becomes stronger, the depression of the end-to-end distance becomes narrower and deeper. In a real mixture, the association constant and cooperativity parameter are different for water and methanol, so that we expect asymmetric behavior with respect to the molar fraction.

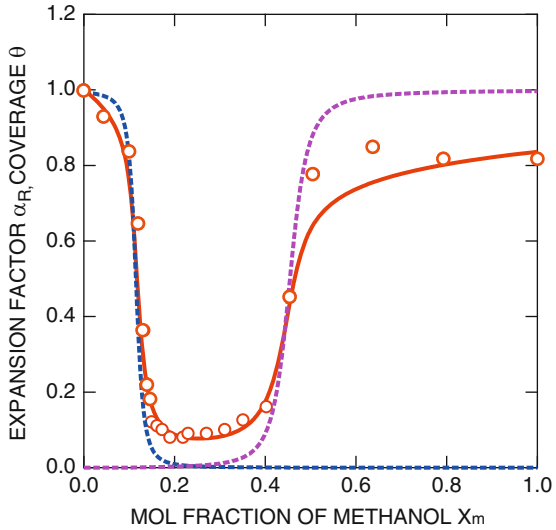


**Fig. 8** Comparison between the present calculation (line) of the expansion factor for the mean square end-to-end distance for $n = 10^5$ and $p = 2$ and the experimental data of the radius of gyration by Zhang and Wu (circles)[10]. The total coverage is also plotted (broken line). The fitting parameters are $\tilde{\lambda}_w = 1.13, \tilde{\lambda}_m = 2.20, \kappa_w = 1.15, \kappa_m = 1.06$

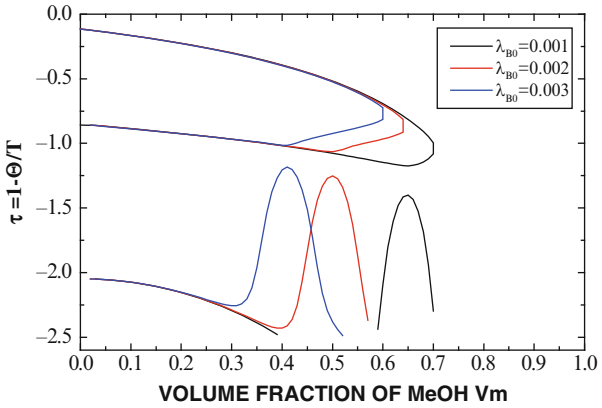


**Fig. 9** The phase separation region plotted on the reduced temperature-solvent composition plane. The UCST miscibility dome expands sharply in a very narrow region of the volume fraction of methanol. The miscibility loop shifts downward with themethanol volume fraction

Figure 8 shows a comparison between the experimental mean radii of gyration (circles) obtained by laser light scattering measurements [10] and mean end-to-end distances obtained by theoretical calculations (solid line). Both are normalized by the reference value in pure water, so that they correspond to the expansion factor $\alpha_S$ for the radius of gyration and $\alpha_R$ for the end-to-end distance. They need not be identical, but are proportional to each other. Because the calculation of the radius of gyration of pearl-necklace conformation is not easy, we made such a comparison. The total coverage $\theta$ including bound water and bound methanol is also plotted (broken line). The molecular weight of the polymer used in the experiment is $M_w = 2.63 \times 10^7$ g mol$^{-1}$, and hence we fixed $n = 10^5$. The volume ratio is set to be $p = 2$ from the molecular structure of methanol. For larger $p$, it turned out that the recovery of the expansion factor at high methanol composition was not sufficient. In order to have a sharp collapse at around $x_m \simeq 0.17$ we had to fix the cooperativity as high as $\sigma_w = 10^{-4}$. Similarly, to produce the gradual recovery at around $x_m \simeq 0.4$, we used $\sigma_m = 10^{-3}$. The existence of p-w and p-m competition may be detectable experimentally by techniques such as Fourier-transformed infrared spectroscopy.

## Cononsolvency of Mixed Solvent as evidenced by Enhanced Tendency to Phase Separation

Theoretical modelling of PNIPAM solutions in mixed solvent of water/methanol was attempted by using three interaction parameters of Flory type [13], but analysis was incomplete; no definite conclusion was drawn due to the unbiguity of their temperature dependence. We start from the concept of competitive hydrogen bonds as shown in Figure 2. Similarly to (4), we find

$$\begin{aligned}\beta\Delta F = {} & N_{fw}\ln\phi_{fm} + N_{fw}\ln\phi_{fm} + \sum_{\mathbf{j}w} N(\mathbf{j}_w)\ln\phi(\mathbf{j}_w) \\ & + \sum_{\mathbf{j}m} N(\mathbf{j}_w)\ln\phi(\mathbf{j}_m) + \beta\sum_{\mathbf{j}w,\mathbf{j}m} \Delta A(\mathbf{j}_w,\mathbf{j}_m)N(\mathbf{j}_w,\mathbf{j}_m) \\ & + \left[\chi_{pw}\phi_p\phi_w + \chi_{pm}\phi_p\phi_m + \chi_{wm}\phi_w\phi_m\right]\Omega,\end{aligned}$$

for the free energy in the presence of two hydrogen-bonding components. Because water and methanol are mixed well to each other, we have $\chi_{wm} = 0$. Also, methanol dissolves PNIPAM at all temperature, we assume $\chi_{pm} = 0$.

Let $\phi_p \equiv \phi, \phi_w \equiv (1-\phi)(1-v_m), \phi_m \equiv (1-\phi)v_m$ be the volume fraction of PNIPAM, water and methanol, and let

$$G = \begin{pmatrix} \partial\Delta\mu_m/\partial\phi_m, \partial\Delta\mu_m/\partial\phi_w \\ \partial\Delta\mu_w/\partial\phi_m, \partial\Delta\mu_w/\partial\phi_w \end{pmatrix} \qquad (15)$$

be the Gibbs determinant for the ternary mixture, where derivatives of the chemical potentials have been taken. Figure 9 shows the spinodal lines obtained from the condition for stability limit $|G| = 0$ plotted on the plane of reduced temperature $\tau \equiv 1 - \Theta/T$ and mol fraction of methanol $v_m$. The volume fraction of the polymer is fixed at $\phi = 0.1$. The parameters concerning water are fixed at the values we found by fitting theoretical calculation in pure water used in Figure 5.

We need experimental data in pure methanol to fix the parameters pertaining to methanol, but here we fix cooperativity parameter at $\sigma_m = 0.3$, and change the amplitude $\lambda_{m0}$ (entropy contribution) in the association constant $\lambda_m(T) = \lambda_{m0}\ \exp[\gamma_m(1-\tau)]$. From the miscibility loop in

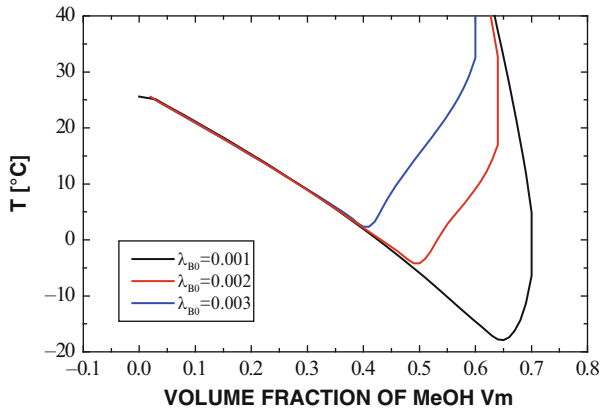


**Fig. 10** The LCST cononsolvency region is magnified on the temperature-volume fraction plane. The initial slope of the LCST downward shift remains the same for 3 different strength of the methanol hydrogen bonds

pure water, we have two boundaries (UCST and LCST) which shift downwards with the mol fraction of methanol. The downward shift of the lower boundary from LCST is called LCST cononsolvency. Also we have other phase boundary starting from the miscibility dome in pure water (called UCST cononsolvency). Figure 10 magnifies LCST cononsolvency and plot by the real temperature, which corresponds to the observed downward shift of the cloud point curves. The minimum of the cloud-point curve depends upon the strength of p-m hydrogen bond, but the initial slopes of the curves are independent of it. In the experiment[15], the temperature drop is the largest, from 31.5°C down to −7°C, for specific molar fraction $x_m = 0.35$ of methanol. Hence, we can estimate $\lambda_{m0}$ to be as small as 0.001.

**Acknowledgements** We wish to acknowledge the partial support of this work by a Grant-in-Aid for Scientific Research (B) from the Japan Society for the Promotion of Science under grant number 19350057.

## References

1. Schild HG (1992) Prog. Polym. Sci. 17: 163
2. Afroze F, Nies E, Berghmans, H (2000) J. Mol. Structure 554: 55
3. de Azevedo RG, Rebelo LPN, Ramos AM, Szydlowski J, de Sousa HC, Klein J (2001) Fluid Phase Eq. 185: 189
4. Rebelo LPN, Visak ZP, de Sousa HC, Szydlowski J, de Azevedo RG, Ramos AM, Najdanovic-Visak V, da Ponte MN, Klein J (2002) Macromolecules 35: 1887
5. Milewska A, Szydlowski J, Rebelo LPN (2003) J. Polym. Sci., Polym. Phys. Ed. 41: 1219
6. Fujishige S, Kubota K, Ando I (1989) J. Phys. Chem. 93: 3311
7. Okada Y, Tanaka F (2005) Macromolecules 38: 4465
8. Kujawa P, Aseyev V, Tenhu H, Winnik FM (2006) Macromolecules 39: 7686
9. Balu C, Delsanti M, Guenoun P (2007) Langmuir 23: 2404
10. Zhang G, Wu C (2001) Macromolecules 123: 1376
11. Hirotsu S (1987) J. Phys. Soc. Jpn 56: 233
12. Hirotsu S (1988) J. Chem. Phys. 88: 427
13. Schild HG, Muthukumar M, Tirrel DA (1991) Macromolecules 24: 948
14. Winnik FM, Ottaviani MF, Bossmann SH, Garcia-Garibay M, Turro NJ (1992) Macromolecules 25: 6007
15. Winnik FM, Ottaviani MF, Bossmann SH, Pan W, Carcia-Gaibay M, Turro NJ (1993) Macromolecules 26: 4577
16. Tanaka F, Koga T, Winnik FM (2008) Phys. Rev. Lett. 101: 028302[1–4]
17. Ye X, Lu Y, Ding Y, Liu S, Zhang G, Wu C (2007) Macromolecules 40: 4750
18. Tanaka F (2003) Macromolecules 36: 5392
19. Zimm BH, Bragg JK (1959) J. Chem. Phys. 31: 526

Progr Colloid Polym Sci (2009) 136:9–14
DOI: 10.1007/2882_2009_2

# Rheological Properties of Solutions of a Polyampholytic Block Copolymer

Tomomitsu Sekitani[1], Kenji Urayama[1], Manabu Tsuruta[2], Masahiko Mitsuzuka[2], and Toshikazu Takigawa[1]

**Abstract** Steady shear flow behavior as well as dynamic viscoelsticicity was investigated for solutions of a polyampholytic block copolymer. Benzyl alcohol solutions of the polymer show behavior common to usual polymer solutions, whereas the aqueous solutions form transient networks at short times. Shear thickening and shear thinning emerge on the flow curves of the aqueous solutions at high shear rates. Curves of dynamic loss modulus ($G$") for the aqueous solutions move to the long time side by the application of steady shear. The increase in relaxation intensity also occurs by shear. The shift of the $G$" curves to the long time side disappears but a long time is required for the recovery. The origin of the shear thickening is related not only to the shift of the curves but also to the increase in relaxation intensity. These changes on the $G$" curves are originated from a developed microphase separation under shear flow.

**Keywords** Associative polymer • Shear thickening • Shift of relaxation time • Increased relaxation intensity • Shear-induced development of microphase separation

## Introduction

Polymer solutions forming transient networks show unique rheological properties. Specifically, most of the systems undergo shear thickening at high shear rates [1–7]. The transient network systems might be divided into two categories. One is the systems composed of polymer chains and small-sized crosslinkers, and the other is so-called associative polymer systems. Aqueous solutions of poly(vinyl alcohol) (PVA) and sodium borate [1–3] belong to the former, and hydrophobic ethoxylated urethanes (HEURs) are typical of the latter [4–7], both of which show shear thickening. Until now much work, in experimental [1–7] and theoretical [8–11] approaches, has been made to clarify the origin of the shear thickening in a microscopic level. The results provide several possibilities for the shear thickening (for example, non-Gaussian elasticity of polymer chains [9–11]), but they are still in controversy. The origin of the shear thickening in the microscopic level may be different if the category differs, but causes in phenomenological rheology must be common for both categories.

The aim of this study is to examine the origin of the shear thickening of an associative polymer system belonging to the latter category: more directly, to survey experimental evidences for long time relaxations causing the shear thickening under flow.

## Experimental

The polymer sample used in this study is a commercial polymer sample-coded as VSR-50K (Mitsui Chemicals Polyurethanes Inc., Japan). Figure 1 shows the chemical structure of VSR-50K: the polymer is polyampholytic, composed of poly(ethylene glycol) (PEG), hexyldiisocyanate and comb-shaped diol units, the ratio $n$ / $m$ being 6. Number and weight average molecular weights ($M_n$ and $M_w$, respectively), reduced to the molecular weight of the equivalent size of PEG, are reported to be $M_n = 1.5 \times 10^5$ and $M_w = 4.1 \times 10^5$. The powdery sample was dissolved in pure water at 80°C to obtain aqueous solutions. The concentration for aqueous solutions was fixed to be 1 %. Benzyl alcohol solutions at various concentrations were also prepared in the similar way. According to the supplier's data sheet, benzyl alcohol is one of good solvents for the polymer VSR-50K. In calculating the polymer

T. Takigawa (✉)
[1]Department of Material Chemistry
Kyoto University
Nishikyo-ku, Kyoto 615-8510, Japan
e-mail: takigawa@rheogate.polym.kyoto-u.ac.jp
[2]R&D Center
Mitsui Chemicals Polyurethanes Inc.,
Sodegaura, Chiba 299-0265, Japan

**Fig. 1** Chemical structure of VSR-50K

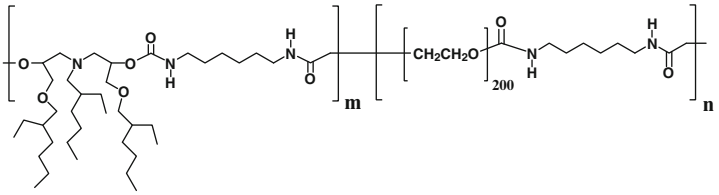


concentration ($c$) in kg m$^{-3}$, the density 1.046 g cm$^{-3}$ was employed for benzyl alcohol and the density 1.0 g cm$^{-3}$ was assumed for VSR-50K.

Rheological measurements were performed with a strain-controlled type rheometer (ARES; Rheometric Scientific, USA) or a stress-controlled type (DAR-100; Reologica, Sweden) at 10 and 20°C. ARES was chiefly used to examine the effect of the strain amplitude on dynamic viscoelastic functions of the aqueous solutions with a cone-plate geometry (diameter, 50 mm; cone angle, 0.04 rad). The strain amplitude ranged from 0.1 to 0.5. The rheometer DAR-100 was used for steady shear and dynamic viscoelasticity measurements. A bob-cup geometry was used for these measurements. The diameters of the bob and the cup were 25.0 mm and 26.7 mm, respectively. In angular frequency ($\omega$) and shear rate ($\dot{\gamma}$) sweeps the scans were made in the low-to-high direction.

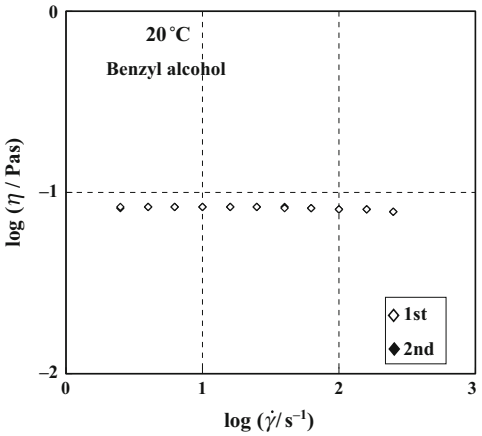


**Fig. 2** Plot of viscosity ($\eta$) plotted against shear rate ($\dot{\gamma}$) for VSR-50K in benzyl alcohol at 20°C

## Results and discussion

Figure 2 shows steady shear viscosity ($\eta$) plotted against $\dot{\gamma}$ for the 1 % solution of VSR-50K in benzyl alcohol at 20°C. Here, the 2nd run measurement was made immediately after the 1st run was completed. The two curves are well coincided and are almost independent of $\dot{\gamma}$ over the range of $\dot{\gamma}$ examined. Similar behavior was observed for solutions at other concentrations. The leveling-off value of $\eta$ corresponds to the zero-shear viscosity ($\eta_0$) of the solution. Figure 3 shows the $c$ dependence of $\eta_0$ for VSR-50K in benzyl alcohol at 20°C. The $c$ dependence becomes strong with increasing $c$. By applying a two-line approximation to the dependence curve, a concentration at the intersection ($c_c$; a critical concentration dividing the dilute and the semi-dilute regimes by the viscosity profile) can be estimated to be ca. 15 kg m$^{-3}$ (ca. 1.5 %).

In Fig. 4 $\omega$ dependence curves of the dynamic storage and loss moduli ($G$' and $G$", respectively) of the 1% aqueous solution, measured with an ARES rheometer at 20°C, are shown. The applied strain amplitude here was 0.3, but almost the same curves were obtained for the other strain amplitudes up to 0.5. A tail of plateau on the $G$' curve and a broad peak on the $G$" curve are observed in the high $\omega$ region. Typical flow behavior is observed in the intermediate

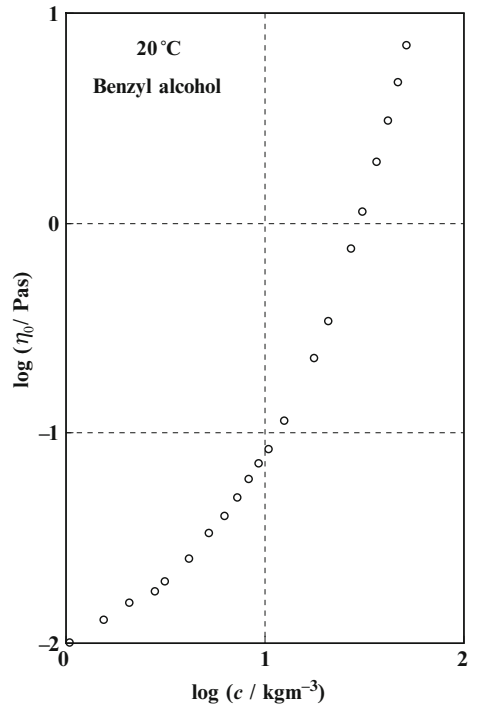


**Fig. 3** Concentration ($c$) dependence of the zero-shear viscosity ($\eta_0$) for VSR-50K in benzyl alcohol at 20°C

and low $\omega$ region: the slope of the $G$" curve is identical to unity, but that of the $G$' curve is slightly smaller than 2. These suggest that a network structure is formed in the

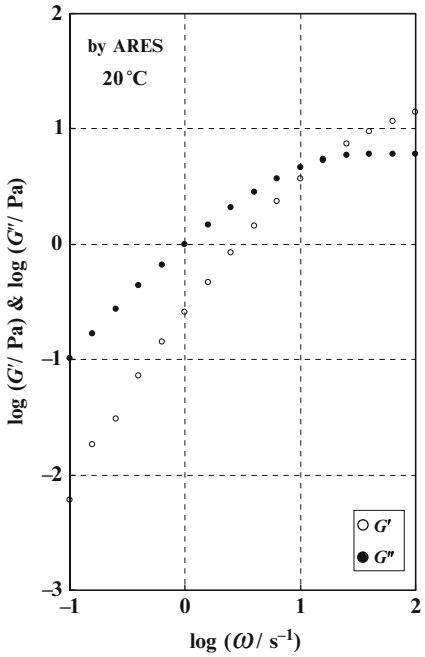


**Fig. 4** Dynamic storage modulus (G') and loss modulus (G") plotted against angular frequency ($\omega$) for 1 % aqueous solution of VSR-50K at 20°C

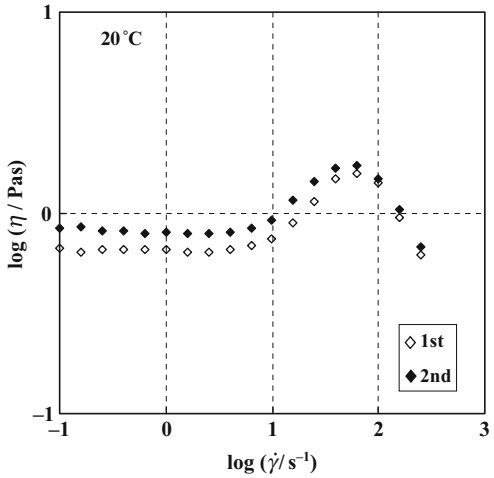


**Fig. 5** Viscosity ($\eta$) plotted against shear rate ($\dot{\gamma}$) for 1 % aqueous solution of VSR-50K at 20°C

aqueous solution at short times. Because the polymer sample VSR-50K is a multi-block copolymer composed of hydrophobic and hydrophilic blocks, a microphase-separated structure works as a network: hydrophobic domains, i.e., aggregates of hydrophobic blocks, act as physical crosslinks and hydrophilic blocks interconnect the crosslinks. Since the fact that the slope of the $G$' versus $\omega$ curve is smaller than 2 means that the relaxation times have a distribution, we define an average relaxation time ($\tau_p$) for the dynamic viscoelasticity as a reciprocal of $\omega$ where the $G$' and $G$" curves intersect. This relaxation time corresponds to pulling-out of hydrophobic block chains from the crosslink domains. At 20°C, $\tau_p$ is estimated to be 0.06 s.

Figure 5 shows $\dot{\gamma}$ dependence curves of $\eta$ obtained from $\dot{\gamma}$ sweep tests for the 1 % aqueous solution at 20°C. For both of the 1st and 2nd runs, $\eta$ in the low $\dot{\gamma}$ region is almost independent of $\dot{\gamma}$, giving $\eta_0$ of the solution. However, the values are different: the value for the 2nd run is higher than that for the 1st run. It should be noted here that even $\eta_0$ for the 1st run is about 10 times higher than that for the benzyl alcohol solution because of the formation of the transient network. In the intermediate region of $\dot{\gamma}$, shear-thickening is observed on the both curves, and the 2nd run is still located in the upper side compared with the 1st run. In the high $\dot{\gamma}$ region, shear thinning occurs with increasing $\dot{\gamma}$, but the 1st and 2nd runs coincide well with each other. Figure 6 shows double-logarithmic plots of shear stress ($\sigma$) versus $\dot{\gamma}$ obtained from the $\dot{\gamma}$ sweep tests shown in Fig. 5. In the low $\dot{\gamma}$ region, the 2nd run is shifted upwards compared with the 1st run, but both are linear with a slope of unity. In the intermediate region of $\dot{\gamma}$, shear-thickening emerges as a steep rise on each curve. As is the case of Fig. 5, the both curves coincide with each other at high $\dot{\gamma}$, where a plateau ("yielding" region) is clearly observed. The $G$"($\omega$) curves before and after steady shear measurements with a DAR-100 rheometer are also included in this figure. In the low $\dot{\gamma}$ ($\omega$) region, the $G$" curve before shear traces out the 1st run of $\sigma$; an empirical relation that the $G$"– $\omega$ curve becomes identical to the $\sigma - \dot{\gamma}$ curve if $\omega$ is equated with $\dot{\gamma}$ holds for the VSR-50K solution. The $G$" curve after shear is shifted upwards compared with that before shear and is close to the 2nd run of $\sigma$ in position. Comparing the peak position of the two $G$" curves a very small shift to the long time side as well as an increase in $G$" due to the application of shear flow is observed. To clarify the peak shift on the $G$" curves by high shear flow, $\omega$ sweep tests were conducted again for $G$" at 10°C. A lower temperature (10°C) was chosen because the $G$" curve was expected to move to the low $\omega$ side by lowering temperature. The results are shown in Fig. 7: the curve after steady shear flow (at $\dot{\gamma} = 2.5 \times 10^2$ s$^{-1}$ for 600 s) exhibits a peak shift to the long time side as well as an increase in $G$" value. The peak shift corresponds to the increase of $\tau_p$. About 16 h after shear, the $G$" curve recovers the original position before shear.

It was confirmed that the application of flow did change neither shape nor position of the 2nd runs (for $\eta$ and $\sigma$) or the $\omega$ dispersion curve of $G$" after shear, as long as the value of $\dot{\gamma}$ did not exceed 10 s$^{-1}$, which corresponds to the position of $\dot{\gamma}$ ($\omega$) where the dynamic and steady flow data branch out (Fig. 6), at 20°C. This means that if we monitor a $G$" value after the 2nd run no reduction in $G$" value occurs for this region of $\dot{\gamma}$. We observed that the reduction of $G$" really occurred for $\dot{\gamma}$ larger than 10 s$^{-1}$. The degree of reduction in $G$" and a characteristic time for the reduction ($\tau_s$: a recovery

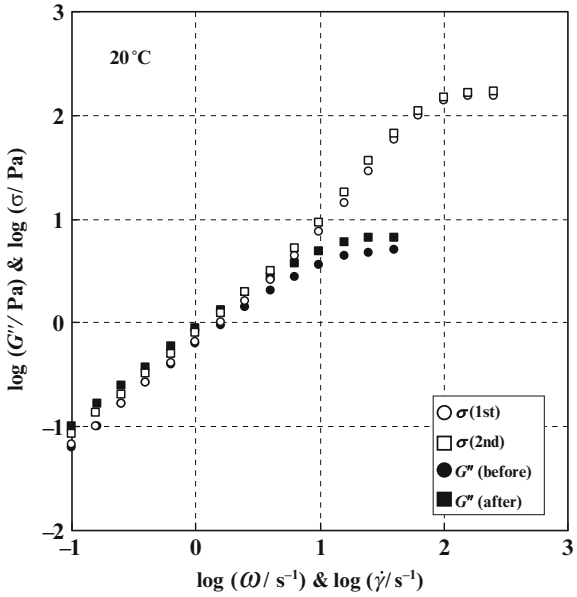


**Fig. 6** Shear stress ($\sigma$) plotted against shear rate ($\dot{\gamma}$) for 1 % aqueous solutions of VSR-50K at 20°C. The $\omega$ dependence of dynamic loss modulus ($G$") is also plotted

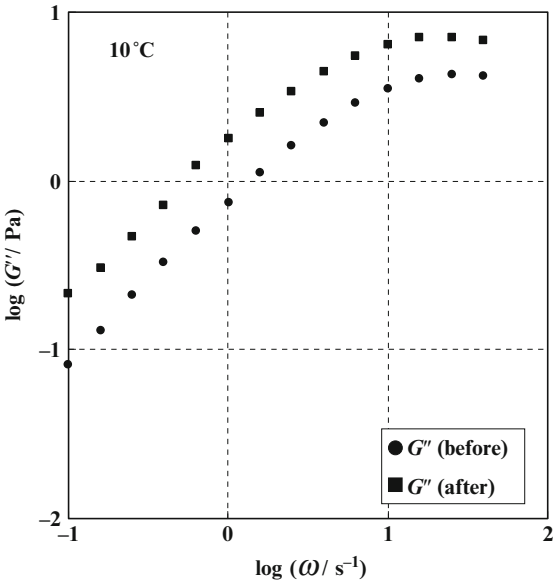


**Fig. 7** Loss modulus ($G$") plotted against angular frequency ($\omega$) before and after shear at 10°C

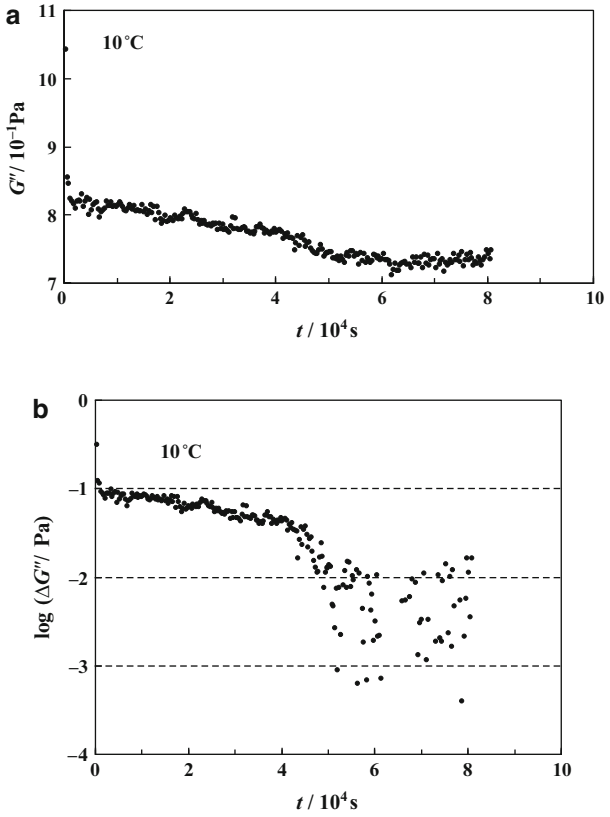


**Fig. 8** (a) Time ($t$) dependence of $G$" at $\omega = 1$ s$^{-1}$ after shear; (b) Semi-logarithmic plot of $\Delta G$" against time ($t$). For the definition of $\Delta G$", see text

time to the original structure) was rather short when $\dot{\gamma}$ lay in the region of 10 s$^{-1}$ < $\dot{\gamma}$ < 70 s$^{-1}$: for example, $\tau_s$ at $\dot{\gamma} = 20$ s$^{-1}$ for 600 s$^{-1}$ was estimated to be the order of magnitude of 10 s. For $\dot{\gamma} > 70$ s$^{-1}$, the degree of reduction increased and $\tau_s$ also became very long. An example is shown in Fig. 8. Figure 8(a) shows a $t$ dependence curve of $G$" measured at $\omega = 1$ s$^{-1}$ after the cessation of the shear flow as an example. The value of $\dot{\gamma}$ applied here is beyond the value at which the $\eta_0$ curve shows a peak. After a steep decrease of $G$" at very short times the value gradually decreases with increasing $t$ but levels off at long times. To evaluate $\tau_s$, we define $\Delta G$"($t$) by $\Delta G$"($t$) = $G$"($t$) − $G$"$_\infty$ with $G$"$_\infty$ being an average of $G$" in the leveling-off region. Then, we assume the functional form $\Delta G$"($t$) = $A$exp(− $t$ / $\tau_s$) at long times, where $A$ is a constant. In Figure 8(b) a semi-logarithmic plot of $\Delta G$"($t$) versus $t$ is shown. The data points over a fairly wide range of $t$ can be approximated by a single line, giving $\tau_s$ of ca. 5 × 10$^4$ s. Beyond the $\dot{\gamma}$ value where the peak emerges on the $\eta_0$ curves, the shear thinning was observed. This thinning occurs because very high shear flow causes a large scale change in structure such as a breakdown of the microphase-separated structure. In this case, a very long time (large value of $\tau_s$) is required for recovery.

At 20°C, the shear thickening occurred in the region of 10 s$^{-1}$ < $\dot{\gamma}$ < 70 s$^{-1}$. Why the shear-thickening occurs by the application of high shear flow can be understood in terms of the linear viscoelasticity theory. Since the $G$" curve becomes a crude approximation to the relaxation spectrum $H$ if we set $\omega = 1 / \tau$ [15], we have

$$H(\tau) \cong \frac{2}{\pi}[G''(\omega)]_{\omega=1/\tau} \quad (1)$$

Defining a relaxation spectrum under shear flow at $\dot{\gamma}$ $H(\tau, \dot{\gamma})$ by

$$H(\tau, \dot{\gamma}) \cong \frac{2}{\pi}[G''(\omega, \dot{\gamma})]_{\omega=1/\tau} \quad (2)$$

the steady shear viscosity at $\dot{\gamma}$ can be calculated by

$$\eta(\dot{\gamma}) = \int_{-\infty}^{\infty} \tau H(\tau, \dot{\gamma}) d\ln\tau \cong \frac{2}{\pi}\int_{-\infty}^{\infty} \tau G''(\omega, \dot{\gamma})_{\omega=1/\tau} d\ln\tau \quad (3)$$

Here, $G''(\omega, \dot{\gamma})$ stands for the loss modulus under the flow at $\dot{\gamma}$, and thus this is a virtual quantity. Equation (3) states that the shift and increase of $G''$ in the flow field enhance the viscosity, giving an explanation for the shear thickening for the aqueous solutions. The increased value of $\eta_0$ at the 2nd run results from the similar origin; the enhancement is due to the aftereffect of flows at the 1st run and is thus only transient.

The origin of the shift and increase of $G''$ under flow is not clear at present. One possible reason for the changes is the development of the microphase separation by flow. The aqueous solutions of VSR-50K show the shear thickening at low temperatures (10 and 20°C), but at an elevated temperature (60°C), no shear thickening was observed for the aqueous solutions. This suggests that the VSR-50/water system has a phase diagram with an upper critical solution temperature (UCST). In addition, the system is highly viscoelastic due to the existence of the microphase separated structure, i.e., transient network structure. This kind of system has a possibility of a marked shear-induced phase separation if the system stays just above the coexistence curve [12, 13]. If the system is located in the two-phase region, the application of shear increases a quench depth; namely, the shear flow develops the microphase separation. An increase in the number of crosslink domains and also an increase in the dimension as well as rigidity of the domains must originate from the development of the microphase separation by shear flow. The degree of development is expected to increase with increasing $\dot{\gamma}$. The developed structure can move back to the original one after the cessation of shear flow. The recovery proceeds rather fast (small value of $\tau_s$) when the applied$\dot{\gamma}$ is not so high ($\dot{\gamma} < 70\ s^{-1}$ at 20°C), because the recovery is attained only by partial dissolution. At high $\dot{\gamma}$, however, the recovery process is composed of the partial dissolution and the large scale change in microphase separated structure. Thus, this recovery process becomes very slow because the latter takes long time.

**Acknowledgements** This work was partly supported by a Grant-in-Aid for Scientific Research on Priority Area "Soft Matter Physics" (No. 19031014) from the Ministry of Education, Culture, Sports, Science and Technology of Japan.

## References

1. Savins JG (1968) Rheol Acta 7: 87
2. Maerker JM, Sinton SW (1986) J Rheol 30: 77
3. Inoue T, Osaki K (1993) Rheol Acta 32: 550
4. Annable T, Buscall R, Ettelaie R, Whittlestone D (1993) J Rheol 37: 695
5. Yekta A, Xu B, Duhamel J, Adiwidjaja H, Winnik MA (1995) Macromolecules 29: 2229
6. Tam KC, Jenkins RD, Winnik MA, Bassett DR (1998) Macromolecules 31: 4149
7. Berert J-F, Serero Y, Whinkelman B, Calvet D, Collet A, Viguier M (2001) J Rheol 45: 477
8. Witten TA, Cohen MH (1985) Macromolecules 18: 1915
9. Vrahopoulou EP, McHugh AJ (1987) J Rheol 31 :371
10. Marrucci G, Bhargava S, Cooper SL (1993) Macromolecules 26: 6483
11. Indei T, Koga T, Tanaka F (2005) Macromol Rapid Commun 26: 701
12. Hashimoto T, Fujioka K (1991) J Phys Soc Jpn 60: 356
13. Imaeda T, Furukawa A, Onuki A (2004) Phys Rev E 70: 051503

Progr Colloid Polym Sci (2009) 136:15–22
DOI: 10.1007/2882_2009_3

# Helix-Coil Transition and Association Behavior of Water-Soluble Polypeptides Having Hydrophobic Alkyl Side Chains

Katsuhiro Inomata, Tomokazu Takai, Noriyoshi Ohno, Yoshiaki Yamaji, Erina Yamada, Hideki Sugimoto, and Eiji Nakanishi

**Abstract** Water soluble polypeptide, poly[$N^5$-(2-hydroxyethyl) L-glutamine] (PHEG), was hydrophobiocally modified partially along the main chain by long alkyl groups -$(CH_2)_{n-1}CH_3$ (C$n$) as side chains. Association and viscoelastic behavior of solutions of these self-assembling polymers (PHEG-g-C$n$, $n = 12$, 16 and 18) were investigated by means of steady-flow viscosity and linear dynamic viscoelasticity measurements. In the mixed solvent of water/ethylene glycol (EG), the main chain of PHEG-g-C$n$ changed its conformation from flexible random coil to rodlike α-helix with the increase in EG content of the solvent. When the solvent was pure water, existence of the associative alkyl chains induced a drastic increase in shear flow viscosity ($\eta$) than PHEG homopolymer, probably because of formation of self-assembled large aggregates via intermolecular association. When EG was used as solvent, $\eta$ and the elastic storage modulus ($G'$) of the solution revealed a unique concentration dependence, i.e., $\eta$ and $G'$ of PHEG-g-C18 solution at 20 wt% were smaller than those at 15 wt%. These viscoelastic behaviors may be described by the α-helical rodlike conformation of PHEG main chain, which is suitable to form an ordered anisotropic phase like lyotropic liquid crystal, with destruction of a physically crosslinked network structure.

**Keywords** Polypeptides • Association • Viscoelastisity • Associative polymers • Helix-coil transition

## Introduction

In amphiphilic polymers such as a water-soluble hydrophilic polymer modified by some hydrophobic groups, the hydrophobic groups have a tendency to associate each other by intra- and inter-molecular manner in aqueous solution. As the results, various types of associates such as an isolated small micelle and an intermolecularlly associated physical network are possibly formed [1–11].

In our previous study [12], we have prepared a telechelic-type associative polymer consisting of water-soluble nonionic polypeptide, poly[$N^5$-(2-hydroxyethyl) L-glutamine] (PHEG), both ends of which were hydrophobically modified by dodecyl chains (C12-PHEG-C12). Such kind of telechelic polymers dissolved in selective solvent forms various associates by association of the badly soluble end groups [1,13]. It has been reported that PHEG is in random coil state when dissolved in water, and takes α-helical rodlike conformation in alcoholic solvent [14,15]. It may be possible that the both-ends hydrophobes are incorporated in the same associated domain if the middle PHEG chain is in random coil state to take a loop conformation. On the other hand, if the PHEG chain is in α-helical state, it may not be able to take the loop conformation and a bridge conformation, in which the hydrophobes at the chain-ends are incorporated in different hydrophobic domains, may be permitted. In this case, an isolated associate such as a flower-like micelle cannot be formed, and a microgel-like network structure, consisting of many hydrophobic domains acting as crosslinking points is most plausible. The light scattering experiments for dilute solutions of C12-PHEG-C12 in water/ethylene glycol (EG) mixed solvents supported the above prediction. When weight fraction of EG in the mixed solvent ($W_{EG}$) were lower than 0.5, circular dichloism (CD) measurements revealed that helix content ($f^H$) of PHEG was lower than 30 %, and the light scattering measurements suggested the existence of small micelles with its hydrodynamic radius ($R_h$) ∼10 nm. With the increase in $W_{EG}$ as well as $f^H$, the observed particle size became much larger such as $R_h > 100$ nm [12].

In this study, we have prepared amphiphilic polymer PHEG-g-C$n$, in which the water soluble PHEG was randomly modified by hydrophobic alkyl group (C$n$ with $n = 12$, 16 and 18, where $n$ is the number of carbon atom of the alkyl group) as side chains, as shown in Fig. 1. Viscoelastic and association behavior of PHEG-g-C$n$, as well as the helix-coil transition in water/EG mixed solvent, have been investi-

K. Inomata (✉)
Department of Materials Science and Engineering
Nagoya Institute of Technology
Gokiso-cho, Showa-ku, Nagoya 466-8555, Japan
e-mail: inomata.katsuhiro@nitech.ac.jp

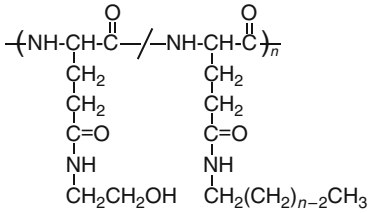


**Fig. 1** Chemical structure of PHEG-*g*-C*n*. As shown in the chemical structure, PHEG-g-Cn corresponds to a random copolymer of $N^5$-(2-hydroxyethyl) L-glutamine and $N^5$-alkyl L-glutamine units

gated. Conformational change of the main chain is expected by the change in $W_{EG}$, and the association strength of the hydrophobic C*n* will be influenced by the side chain length *n* and hydrophobicity of solvent ($W_{EG}$). Effects of these parameters on the viscoelasticity and association behavior of PHEG-g-C*n* solutions will be discussed.

## Experimental

### *Synthesis of PHEG-g-Cn*

Poly($\gamma$-benzyl L-glutamate) (PBLG), 2-hydroxypyridine (5-fold molar) as catalyst, and primary aliphatic amine (C*n*-$NH_2$, 20-fold molar) were dissolved in dry *N*,*N*-dimethylformamide, and heated at 37°C. To this solution, 30-fold amount of 2-aminoethanol was added, and the reaction was continued for 48 hours. The reacted solution was poured into ethanol/diethyl ether (1/5 v/v), and the collected precipitate was dissolved in water in order to dialyze against water by using cellulose membrane with nominal fractional molecular weight of 8,000. Finally, PHEG-g-C*n* was obtained after freeze-drying of aqueous polymer solution.

### *Measurements*

$^1$H-NMR spectrum of PHEG-g-C*n* was recorded with using DMSO-$d_6$ as solvent. Size exclusion chromatography (SEC) was performed with using DMF/LiBr (1 wt%) as eluent, and standard polystyrene was used for molecular weight calibration. Intrinsic viscosity of PBLG/dichloroacetic acid solution at 25°C was measured by using an Ubbelohde type viscometer, and Mark-Howink-Sakurada parameters [16] were used to evaluate the viscosity-averaged molecular weight ($M_v$). Circular dichroism (CD) measurements were conducted for solution with ca. $5 \times 10^{-4}$ g/ml, and solution temperature was maintained at 30°C. Fluorescence spectrum was measured at room temperature in order to investigate a formation of hydrophobic domains by association of PHEG-g-C*n*. 1-Anilino-8-naphthalen sulfonic acid magnesium salt (ANS-Mg, concentration: $6.4 \times 10^{-6}$ mol/l) was used as fluorescence probe. An excitation wavelength of 350 nm was employed for the measurements. Steady-flow viscosity and linear dynamic viscoelasticity measurements were performed on an ARES (Rheometrics), with cone-plate fixture having diameter of 25 mm and cone angle of 0.04 rad. The sample temperature was maintained at 25°C. The sample solution was loaded between the rotators, and maintained for 30 minutes before measurements. In the steady-flow viscosity measurements, shear rate was increased from the lowest shear rate (0.1 $sec^{-1}$) by stepwise manner, and the viscosity was measured at each shear rate. An Olympus BX50-F was used to take polarized optical micrographs under a crossed polarizer. Static and dynamic light scattering (SLS and DLS, respectively) was measured by a laboratory-made apparatus equipped with an ALV/SO-SIPD detector and an ALV-5000 correlator using He-Ne laser (wavelength $\lambda_0 = 633$nm) as a light source. Solution temperature was maintained at 30°C. Measurements were performed at finite concentration, and apparent values of weight-averaged molecular weight ($M_w$) and hydrodynamic radius ($R_h$) were evaluated. Refractive index increment was measured by a differential refractometer. Values of solvent viscosity for the water/EG mixed solvents were derived from the data reported by Tsierkezos et al. [17]. Experimental and analytical details for all the measurements have been described in the previous paper [12,18].

Sample solutions were prepared by dissolving the polymer in water/EG mixed solvent, which was prepared at desired $W_{EG}$ in advance, at room temperature.

## Results and Discussion

### *Sample characterization*

Molecular weights for the prepared PHEG homopolymer and hydrophobically modified PHEG-g-C*n* were evaluated from SEC measurements, and the results are listed in Table 1. In our previous paper [18], one-end hydrophobically modified PEHG samples were prepared, and their $M_w$ from SEC and $M_n$ from $^1$H-NMR revealed reasonable agreement. In Table 1, $M_v$ values for the starting PBLG are also indicated. As shown in the table, $M_v$ for PBLG and $M_w$ for its derivative PHEG-g-C*n* are consistent. Hereafter, we use the values of $M_w$ evaluated from the SEC measurements as the molecular weight for PHEG-g-C*n* and PHEG homopolymer (PHEG-H).

Because of the different molecular weight of the starting PBLG, PHEG-g-C18 had larger $M_w$ than other PHEG-g-C*n* or PHEG-H. For PHEG-g-C18, -C16, and C12-A, the fraction of the hydrophobic C*n* group ($f_{alkyl}$) were in the range of 2.6–3.7 mol%. In order to investigate an effect of

**Table 1** Characterstics of Polymers

| Sample code | $M_v$ of PBLG[a] | $M_w$ | $M_w/M_n$ | $f_{alkyl}$ (mol%) | inter-side-chain molecular weight |
|---|---|---|---|---|---|
| PHEG-g-C18 | 134,000 | 128,000 | 1.76 | 2.6 | 6,500 |
| PHEG-g-C16 | 51,000 | 69,000 | 1.59 | 3.7 | 4,500 |
| PHEG-g-C12-A | 51,000 | 64,000 | 1.49 | 3.5 | 4,800 |
| PHEG-g-C12-B | 60,000 | 87,000 | 1.51 | 1.1 | 16,000 |
| PHEG-H[b] | 51,000 | 65,000 | 1.49 | 0 | – |

[a]Mv of the starting PBLG sample
[b]Homopolymer of PHEG

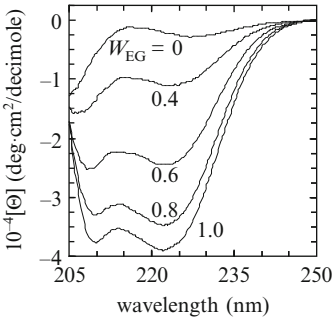


**Fig. 2** CD spectra for PHEG-g-C16 in water/EG mixed solvent. EG weight fraction, $W_{EG}$, is also indicated

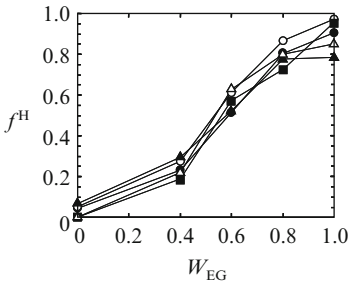


**Fig. 3** Plots of α-helix content $f^H$ against $W_{EG}$ for PHEG-g-C18 (●), -C16 (○), -C12-A (▲), -C12-B (△), and PHEG-H (■) solutions evaluated from CD spectra

$f_{alkyl}$, PHEG-g-C12-B in which the the hydrophobic alkyl chain was introduced only $f_{alkyl} = 1.1$ mol%, was prepared. In Table 1, averaged molecular weight for the PHEG main chain between adjacent alkyl chains, i.e., inter-alkyl-chain molecular weight for PHEG, is also indicated.

## Conformation of PHEG main chain

CD spectra for PHEG-g-C16 in water/EG mixed solvent with various weight fraction of EG ($W_{EG}$) are shown in Fig. 2. A double-minima spectrum was clearly observed with increase in $W_{EG}$, which suggests that the α-helical conformation was increased with $W_{EG}$. From the observed mean residual ellipticity [Θ] at the wavelength of 222 nm, α-helix content $f^H$ for the PHEG main chain was evaluated, and plotted against $W_{EG}$ in Fig. 3. In all samples investigated in this work, $f^H$ values similarly increased with $W_{EG}$. The plots in Fig. 3 were almost identical with the results for one-end or both-ends hydrophobically-modified PHEG [12,18].

## Fluorescence spectroscopy

Fluorescence spectra for PHEG-g-C*n* solutions were measured with using ANS-Mg as fluorescence probe. Typical examples are shown in Fig. 4. As described in the previous paper [18], fluorescence peak of ANS shifted to shorter

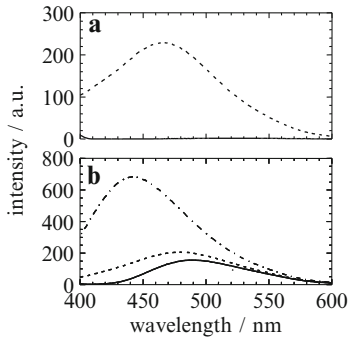


**Fig. 4** Fluorescence spectra for PHEG-g-C16 solutions with (a) $W_{EG} = 0$ and (b) $W_{EG} = 1.0$. Solid line: pure solvent; broken line: $C = 0.1$ wt%; a dot-and-dash line: $C = 1.0$ wt%

wavelength with increasing its intensity when ANS molecule located in hydrophobic environment. As shown in Fig. 4a for PHEG-g-C16/water solution ($W_{EG} = 0$) with polymer concentration $C = 0.1$ wt%, an intense peak at ~460 nm was observed, which suggests that the alkyl chains were associated to form hydrophobic domains in this solution. With increase in $W_{EG}$, the spectrum for ANS solution without polymer slightly increased in intensity because of an increase in hydrophobicity with $W_{EG}$. Even in these mixed solvents, the fluorescence peak intensity was increased with shifting to the shorter wavelength, by the increase in $C$ from 0 to 0.1 wt% ($W_{EG} = 0$ and 0.4) and from 0.1 to 1 wt% ($W_{EG} = 0.6$ and 1.0). From these results, we can point out that the alkyl chains of PHEG-g-C16 in water/EG mixed

solvent were associated self-assembly to form hydrophobic domains in 1 wt% solutions.

According to these procedures, formation of the hydrophobic domains was evaluated for 1wt% solutions, and the results are summarized in Table 2. In this table, the symbol ○ are marked if the hydrophobic domains were recognized by the fluorescence spectrum, on the other hand, symbol × indicate that the polymers were dissolved without association even in 1 wt% solution. This table clearly indicates that the association strength of the alkyl chains was enhanced with (1) decrease in $W_{EG}$, (2) increase in the alkyl chain length $n$, and (3) increase in the fraction of the alkyl chains $f_{alkyl}$.

## Light scattering measurements

For 1 wt% solutions of PHEG-g-C16 with various $W_{EG}$, in which the formation of the associated domains was confirmed in the previous section, light scattering measurements were performed at 30°C.

Distribution of $R_h$ was calculated by using decay rate distribution, which was evaluated from autocorrelation function of the scattered light intensity by DLS measurements. Thus obtained results for various $W_{EG}$ solutions at scattering angle $\theta = 90°$ are indicated in Fig. 5. For these solutions, SLS measurements were performed to obtain apparent $M_w$ at the finite concentration, and aggregation number $N = M_w/(M_w$ of PHEG-g-C16) was evaluated. As shown in the distribution curves in Fig. 5, main peak was located around $R_h = 10$ nm in the solutions of $W_{EG} = 0 \sim 0.6$. The values of $N$ suggested that several polymers were associated to form a micelle with associated alkyl chain as core and PHEG as shell.

On the other hand, in $W_{EG} = 1.0$ solution, the main peak was located around 100 nm, however, the evaluated $N$ was smaller than the other solutions. In the previous section, however, the hydrophobic domains were suggested to exist in this solution, although the association strength should be weak. These experimental data may indicate that only limited number of C16 side chains was associated weakly to form large aggregate, but most of the polymers were in unimer state in EG solution. (Note: In our pervious paper [18], similar distribution curves with a peak at larger $R_h$ region were also observed in water/EG solutions of PHEG having butyl group at the chain end. This polymer should be dissolved molecularly as judged by the weak intensity of scattered light and short hydrophobic group. We postulated that only a little amount of aggregates existed in the solution, but it was not clear why such aggregates were formed [18]. About the present results of light scattering for PHEG-g-C16/EG solution, therefore, we refrain from further discussion about its association structure.)

**Table 2** Results of Fluorescence Measurements

| Sample code | $W_{EG}$ | | | |
|---|---|---|---|---|
| | 0 | 0.4 | 0.6 | 1.0 |
| PHEG-g-C18 | ○ | ○ | ○ | × |
| PHEG-g-C16 | ○ | ○ | ○ | ○ |
| PHEG-g-C12-A | ○ | ○ | × | × |
| PHEG-g-C12-B | ○ | × | × | × |
| PHEG-H | × | × | × | × |

## Steady shear-flow viscosity

Steady-state shear viscosity ($\eta$) measurements for solutions of PHEG-g-C$n$ dissolved in water/EG mixed solvents with their concentration range of $C = 1$–20 wt% were investigated with shear-rate ($\dot{\gamma}$) range of $0.1 - 100\ sec^{-1}$. In Fig. 6, $\dot{\gamma}$ and $C$ dependences of $\eta$ for PHEG-g-C18 solutions with (a) $W_{EG} = 0$ and (b) $W_{EG} = 1.0$ are shown by filled symbols. Because of the limitation of measurable torque range, the lower $\dot{\gamma}$ region for low $\eta$ solutions and higher $\dot{\gamma}$ region for viscous solutions

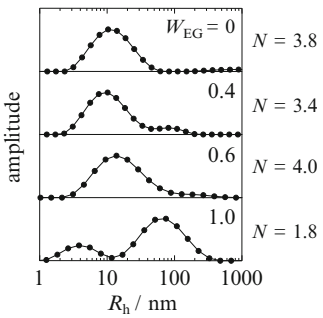


**Fig. 5** $R_h$ distribution curves for 1 wt% PHEG-g-C16 solutions in various mixed solvents, obtained from DLS measured at θ = 90°. Aggregation number $N$ evaluated from SLS measurements are also indicated

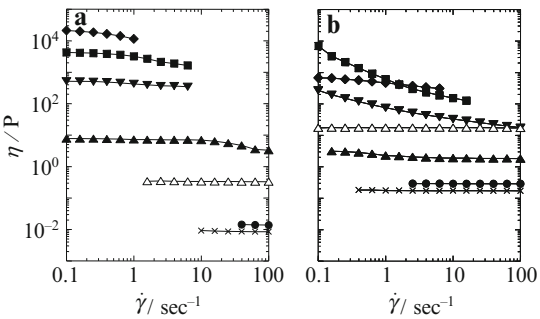


**Fig. 6** Shear-rate ($\dot{\gamma}$) dependences of steady-state shear-flow viscosity of PHEG-g-C18 solutions with $W_{EG} = 0$ (a) and 1.0 (b). Polymer concentrations are (◆) 20, (■) 15, (▼) 10, (▲) 5, (●) 1, and (×) 0 wt %. Results for PHEG-H at 20 wt% are also plotted (△) for comparison

were not plotted. For comparison, results for pure solvents and PHEG-H solutions with $C = 20$ wt% are also plotted by using X and Δ, respectively. The viscosity for PHEG-H solution was independent of $\dot{\gamma}$, indicating that the solution was a Newtonian fluid. On the other hand, PHEG-g-C18 solutions exhibited high $\eta$ even at low $C$, and shear thinning behavior at high $\dot{\gamma}$ region, especially in $W_{EG} = 1.0$ solutions.

For each solution, the obtained $\eta$ value at the lowest $\dot{\gamma}$ was divided by the solvent viscosity ($\eta_0$), and plots of $\eta/\eta_0$ against the polymer concentration are shown in Fig. 7. Results for PHEG-H and PHEG-g-C12-B were almost identical, suggesting that the attached C12 side chain groups with $f_{alkyl} = 1.1$ mol% had little influence on the solution viscosity. Viscosity of concentrated solution of PHEG-g-C12-A/water was obviously larger than that for PHEG-g-C12-B, instead of the lower molecular weight of PHEG-g-C12-A than -B. With increase in $W_{EG}$, the viscosity difference between these samples became small, and $\eta$ for PHEG-g-C12-A/EG solution were almost identical with that for PHEG-H solution as shown in Fig. 7b. These results are consistent with the change in segregation strength of C12 with $W_{EG}$ evaluated by the fluorescence measurements.

In the case of PHEG-g-C18 solutions with $W_{EG} = 0$, the viscosity at 1 wt% was almost identical with the homopolymer solution, however, it exhibited a drastic increase with the increase in polymer concentration as shown in Fig. 7a. Further increase in $\eta/\eta_0$ was observed with the increase in $C$, and at 20 wt%, $\eta/\eta_0$ value was about $10^5$ times larger than the PHEG-H solution. This large difference in $\eta$ between PHEG-g-C18 and PHEG-H clearly indicate that the high $\eta$ value was owing to the existence of the strongly associated C18 side chains. Similar concentration dependence of $\eta/\eta_0$ was also observed in PHEG-g-C16.

Such drastic increase in $\eta$ with $C$ for PHEG-g-C18 and -C16 became less obvious with the increase in $W_{EG}$. In PHEG-g-C16/EG solution, as shown in Fig. 7b, $\eta/\eta_0$ value was almost identical with the PHEG-H solution when $C \leq 10$ wt%. Fig. 6b revealed the marked non-Newtonian behavior in PHEG-g-C18/EG, which can be compared with PHEG-H/EG 20 wt% solution (△ in Fig. 6b), and suggests the association of the C18 chains even though its strength was weak as mentioned above. Interestingly, in PHEG-g-C18/EG solution, the non-Newtonian characteristics was most remarkable when $C = 15$ wt%, and less significant in 20 wt% solution. As the result, the $\eta/\eta_0$ value at $\dot{\gamma} = 0.1$ $sec^{-1}$ had a maximum at $C = 15$ wt% as plotted in Fig. 7b. This unique behavior has a good resemblance to concentration dependence of steady-shear viscosity for lyotropic liquid crystalline solution around isotropic-anisotropic transition region, in which rigid rodlike polymers are dissolved with high concentration [19–21]. This concentration dependence of rheological behavior will be discussed in the later section.

## Linear dynamic viscoelasticity

For concentrated solutions (20 wt%) of PHEG-g-C12-A, -C16, and -C18 in various mixed solvents, linear dynamic viscoelastisity measurements with oscillatory shear were performed at 25°C, and storage ($G'$) and loss ($G''$) moduli at various angular frequency ($\omega$) were evaluated. The obtained $G'$ and $G''$ were plotted against $\omega$, and shown in Fig. 8. Both in PHEG-g-C12-A solutions with $W_{EG} = 0$ and 1.0, the obtained moduli were almost scaled as $G' \sim \omega^2$ and $G'' \sim \omega^1$ as shown in Fig. 8a. In these solutions, the association strength of C12 was not so strong and the solution behaved as a simple liquid, even though the $\eta$ value for $W_{EG} = 0$ solution was larger than the homopolymer solution.

In PHEG-g-C16 solutions with $W_{EG} = 0$ (open and filled circles in Fig. 8b), crossover of $G'$ and $G''$ was observed and $G'$ were larger than $G''$ in high $\omega$ region. Comparison with the results for PHEG-g-C12-A/water in Fig. 8a suggests that the existence of the more hydrophobic group contributed to the viscoelasticity of the solution. In low $\omega$ region, $G'$ and $G''$ obeyed the power law of $\omega^2$ and $\omega^1$, respectively, and the same terminal flow was clearly observed in $W_{EG} = 0.4$

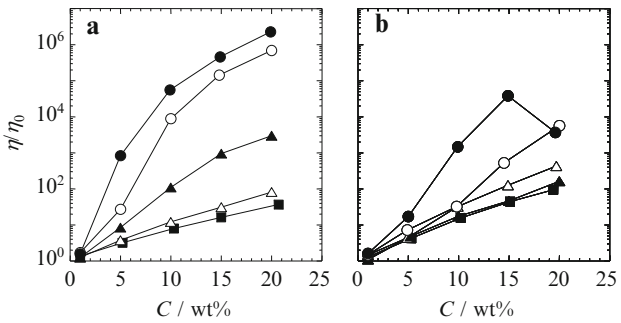


**Fig. 7** Plots of the relative viscosity $\eta/\eta_0$ against polymer concentration $C$ for solutions of PHEG-g-C18 (●), -C16 (○), -C12-A (▲), -C12-B (△), and PHEG-H (■) with $W_{EG} = 0$ (a) and 1.0 (b)

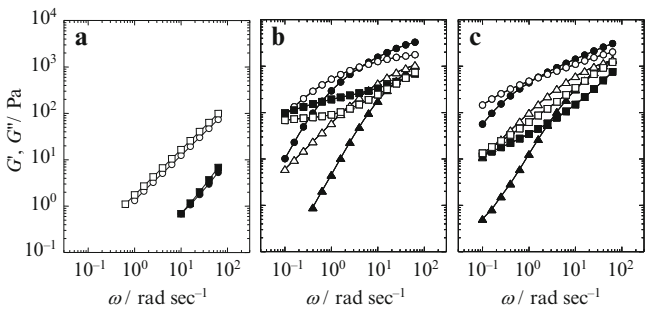


**Fig. 8** Plots of storage ($G'$, filled) and loss ($G''$, open) moduli against angular frequency $\omega$ for solutions of PHEG-g-C12-A (a), -C16 (b), and -C18 (c) at 20 wt%. $W_{EG} = 0$ (●, ○), 0.4 (▲, △) and 1.0 (■, □)

solution. This result was consistent with the decrease in the association strength of C16 with the increase in $W_{EG}$. In contrast to these solutions, in $W_{EG} = 1.0$, such a terminal flow behavior was not observed, instead, $G'$ and $G''$ values in the lower frequency region were much larger than $W_{EG} = 0.4$ solution. In this $\omega$ region, relationship of $G' > G''$ was revealed, which means that the solution was rather elastic. This result is in contrast to the solution of PHEG-g-C12-A/EG in Fig. 8a, therefore, we can also point out that the C16 side chains play an important role for the elastic behavior of PHEG-g-C16/EG solution.

Similar viscoelastic curves were also obtained in PHEG-g-C18 solutions with $W_{EG} = 0$ and 0.4, as shown in Fig. 8c. However, in $W_{EG} = 1.0$ solution, the relationship of $G' > G''$ was not recognized within the measured $\omega$ region.

In Fig. 9, concentration dependence of the viscoelastic curves for $W_{EG} = 1.0$ solutions is indicated. In PHEG-g-C16 solutions (Fig. 9a), both of $G'$ and $G''$ shifted to lower position by the dilution from 20 to 15 wt%. For PHEG-g-C18 solutions, the plots of 20 and 15 wt% solutions are shown in Fig. 9b, c respectively, in order to avoid overlapping. As represented by the filled symbols, the elastic $G'$ term in the low $\omega$ region at 15 wt% was larger than at 20 wt%. As the results, in this $\omega$ region for 15 wt% solution, $G'$ was larger than $G''$, i.e., this solution was more elastic than the more concentrated solution. This trend in concentration dependency of viscoelasticity for PHEG-g-C18/EG solution has a similarity with the steady shear viscosity, i.e., $\eta$ value for 15 wt% was larger than that for 20 wt% as shown in Fig. 7b.

## Plausible association structure

Above experimental results indicate that the existence of the hydrophobic C16 or C18 side group influences the viscoelastic behavior of solutions of water/EG mixed solvents.

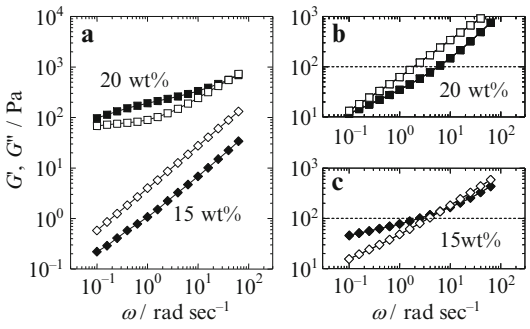


**Fig. 9** Plots of $G'$ (filled) and $G''$ (open) against ω for EG solutions ($W_{EG} = 1.0$) of PHEG-g-C16 (a) and -C18 (b and c) at 20 or 15 wt% as indicated

In the concentrated solutions with $W_{EG} = 0$, the steady shear viscosity was $\sim 10^5$ times larger than the homopolymer solution as shown in Fig. 6a. The viscoelastic curves in Fig. 8b, c revealed the crossover of $G'$ and $G''$, however, distinct plateau could not be recognized in $G'$ and $G''$ and these values increased continuously with $\omega$. In transient network, in which the polymer chains are crosslinked by physically associated crosslinking points having finite life time, the Maxwell-type viscoelasticity with single relaxation time corresponding to the life time of the crosslinks is expected [1,13,22]. In this sense, the experimental viscoelastic curves for aqueous solutions of PHEG-g-C16 and -C18 are hard to be described by the transient network, instead, have a resemblance to a concentrated solution of high molecular weight polymers [2,23]. Therefore, it may be plausible that PHEG-g-C16 or -C18 forms large aggregates via the multiple association of the hydrophobic groups attached randomly along the PHEG chain, and entanglement of these large aggregates may be the origin of the elastic behavior of solution. Rearrangement of the network structure like the transient network should be restricted because of the strong association power of C16 and C18 chains. Similar structure model was also proposed by Aubry et al. for hydrophobically modified (hydroxypropyl)guar [2], and schematically represented in Fig. 10.

In PHEG-g-C16/EG solution, the viscosity of 10 wt% solution was almost identical with that for homopolymer (Fig. 7b). By the further increase in concentration, $\eta$ became larger than that for PHEG-H, and at 20 wt%, the solution was rather elastic ($G' > G''$) in low $\omega$ region (Fig. 8b). It should be noted that, in these solutions, the polymer chain was close to a rodlike shape as judged by the value of the α-helix content (Fig. 3). As mentioned in Introduction, the rodlike conformation is suitable for forming the network structure because the rodlike PHEG is appropriate to connect the

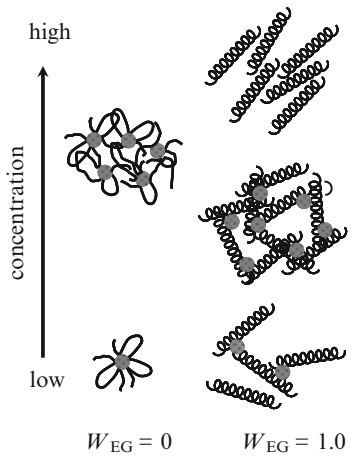


**Fig. 10** Schematic models for the plausible association structure of PHEG-g-C18 solutions with $W_{EG} =$ (left) and 1.0 (right)

associated hydrophobic domains as bridging chain. Therefore, the viscoelastic behavior should be related to the intermolecular association and forming the network structure like the large aggregate.

In PHEG-g-C18/EG systems, even at 10 wt%, the solution was enough viscous than the homopolymer solution probably because of the stronger association power of C18 than C16. The 15 wt% solution exhibited $G' > G''$ relationship in the low $\omega$ region (Fig. 9c). However, the elastic $G'$ term and shear viscosity $\eta$ decreased by the increase in concentration to 20 wt%. As pointed out above, similar concentration dependence in viscoelasticity was reported in the lyotropic liquid crystalline solution of rodlike solute around isotropic-anisotropic biphasic region [19–21]. Therefore, a possible association model for PHEG-g-C18/EG may be described as follows: When the concentration was lower than 15 wt%, the network structure by the multiple association of the rodlike PHEG-g-C18 induced the increase in elasticity. However, by the increase in concentration, the formation of the anisotropic order phase might be preferred, which destruct the network structure and decrease viscoelasticity. These are schematically imaged in the right part of Fig. 10. It should be noted that the molecular weight of PHEG-g-C18 was larger than PHEG-g-C16, as shown in Table 1. If the α-helical PHEG-g-C18 is fully rodlike with $f^{\mathrm{H}} = 100\%$, length of the rod will be 112 nm with using the helical pitch as 1.5 nm per repeating unit [24]. Reported crystal structure of PHEG was orthorhombic unit cell with $a = b = 1.21$ nm [24]. With assuming that the diameter of the rod be 1.21 nm, its axial ratio can be evaluated as 92. Lattice theory for the rodlike solute by Flory-Ronca [25] predicts that the polymer volume fraction at the isotropic-anisotropic-phase boundary will be 0.08. By the same procedure, calculated phase boundary for PHEG-g-C16 will be 0.16. These calculations suggest that the longer PHEG-g-C18 chain had a strong tendency to form the anisotropic phase with destruction of the existing network structure. On the other hand, in the shorter PHEG-g-C16, the driving force to form the anisotropic phase is weaker, and the isotropic network structure was still maintained even at 20 wt%.

In the polarized optical microscopic image for 20 wt% PHEG-g-C18 solution, however, any distinct birefringence could not be recognized as shown in Fig. 11a. This solution was concentrated by evaporating the solvent in vacuum, as the result, optically anisotropic domains were confirmed as shown in Fig. 10b. Therefore, although any evidences for the anisotropic phase formation except for the rheological results were not obtained, it was found that PHEG-g-C18 in EG had an ability to form the anisotropic phase, and 20 wt% was close to the isotropic-anisotropic transition concentration.

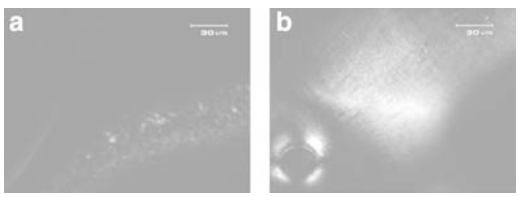


**Fig. 11** Polarized optical microscopic images for PHEG-g-C18/EG with $C = 20$ wt% (a) and more concentrated solutions (b)

## Conclusion

Association and viscoelastic behavior of solutions of amphiphilic polymers PHEG-g-C*n*, in which the water-soluble PHEG was partially modified by hydrophobic groups, have been investigated. With the increase of the hydrophobicity of water/EG mixed solvent ($W_{\mathrm{EG}}$), the main chain conformation changed from flexible random coil to rodlike α-helix, and the association strength of the alkyl group became weaker. When the solvent was pure water ($W_{\mathrm{EG}} = 0$), existence of the associative alkyl chains induced a drastic increase in shear flow viscosity $\eta$ than PHEG homopolymer, probably because of the formation of large aggregates via intermolecular multiple association and their entanglement in concentrated solution. In solutions of PHEG-g-C18/EG ($W_{\mathrm{EG}} = 1.0$), steady shear-flow viscosity $\eta$ and storage modulus $G'$ at 15 wt% were larger than those at 20 wt%. This experimental result was described by the change of association structure. At 15 wt%, because the rodlike conformation of PHEG-g-C18 is suitable as the bridging chain, physically crosslinked network by the association of C18 side groups may be formed. In more concentrated solution, the rodlike PHEG-g-C18 preferred to be aligned to form the ordered anisotropic phase, with the destruction of the isotropic network structure. In conclusion, we can point out that the association strength and chain conformation of the associative amphiphilic polymers have great influence on the association and viscoelastic behavior.

**Acknowledgement** We would like to acknowledge the financial support by Grant-in-Aid for Scientific Research from the Japan Society for the Promotion of Science (No. 15550105 and No. 18550193).

## References

1. Annable T, Buscall R, Ettelaie R, Whittlestone D (1993) J Rheol 37:695
2. Aubry T, Moan M (1994) J Rheol 38:1681
3. Klucker R, Schosseler F (1997) Macromolecules 30:4927
4. Itakura M, Inomata K, Nose T (2001) Polymer 42:9261
5. Noda T, Hashidzume A, Morishima Y (2001) Macromolecules 34:1308
6. Rogovina LZ, Vasil'ev VG, Churochkina NA, Pryakhina TI (2001) Macromol Symp 171:225

7. Borzacchiello A, Ambrosio L (2001) J Biomater Sci Polymer Edn 12:307
8. Aubry T, Bossard F, Moan M (2002) Polymer 43:3375
9. Kujawa P, Audibert-Hayet A, Selb J, Candau F (2004) J Polym Sci Part B Polym Phys 42:1640
10. Hashidzume A, Kawaguchi A, Tagawa A, Hyoda K, Sato T (2006) Macromolecules 39:1135
11. Kawata T, Hashidzume A, Sato T (2007) Macromolecules 40:1174
12. Inomata K, Kasuya M, Sugimoto H, Nakanishi E (2005) Polymer 46:10035
13. Inomata K, Nakanishi D, Banno A, Nakanishi E, Abe Y, Kurihara R, Fujimoto K, Nose T (2003) Polymer 44:5303
14. Lotan N, Yaron A, Berger A (1966) Biopolymers 4:365
15. Miyake M, Akita S, Teramoto A, Norisuye T, Fujita H (1974) Biopolymers 13:1173
16. Doty P, Bradbury JH, Holtzer AM (1956) J Am Chem Soc 78:947
17. Tsierkezos NG, Molinou IE (1998) J Chem Eng Data 43:989
18. Inomata K, Doi R, Yamada E, Sugimoto H, Nakanishi E (2007) Colloid Polym Sci 285:1129
19. Kiss G, Porter RS (1980) J Polym Sci Polym Phys Ed 18:361
20. Doi M, Edwards SF (1986) The Theory of Polymer Dynamics. Oxford University Press, New York
21. Oertel R, Kulicke WM (1991) Rheol Acta 30:140
22. Tanaka F, Edwards SF (1992) J Non-Newtonian Fluid Mech 43:247
23. Holmes LA, Kusamizu S, Osaki K, Ferry JD (1971) J Polym Sci Part A-2 9:2009
24. Spadon P, Verdini AS, Del Pra A (1978) Biopolymers 17:2029
25. Flory PJ, Ronca G (1979) Mol Cryst Liq Cryst 54:289

Progr Colloid Polym Sci (2009) 136:23–30
DOI: 10.1007/2882_2009_4

# Effects of Surfactants on the Linear Rheology of Telechelic Associating Polymers

Tsutomu Indei

**Abstract** The influence of low-molecular-weight surfactants on the linear rheology of telechelic associating polymers is studied on the basis of the transient network theory. It is shown that dynamic shear moduli are well described in terms of a Maxwell model characterized by a plateau modulus $G_\infty$ and a single relaxation time $\tau$. As reported experimentally, a peak appears in $G_\infty$ and $\tau$ (and therefore in the zero-shear viscosity) with an increase in the surfactant concentration under the conditions that the junction multiplicity has upper and lower bounds and that the formation of the pairwise junctions is allowed. As the surfactant concentration increases, a contraction occurs followed by the extension of the concatenated chain comprising several polymers connected in series. The peak of the relaxation time is attributed to this contraction and extension. On the other hand, the peak of the plateau modulus is attributed to the upper and lower bounds on the multiplicity, as suggested by Tanaka [Macromolecules (1998) 31: 384].

**Keywords** Telechelic polymers • Surfactants • Mixed micelles • Transient networks • Linear rheology

## Introduction

Aqueous solutions of hydrophobically-modified water-soluble amphiphilic polymers, or associating polymers, have attracted widespread interest in recent years mainly due to their interesting rheological behavior [1, 2]. The simplest classes of associating polymers are telechelic polymers that have a hydrophobic group only at each of their two ends. The linear rheology of aqueous solutions of telechelic polymers, such as telechelic poly(ethylene oxide) (PEO) shows the Maxwellian behavior with a plateau modulus $G_\infty$ and a single relaxation time $\tau$ [3–9]. $G_\infty$ and $\tau$ (and the zero-shear viscosity $\eta_0$) are changed dramatically by the addition of surfactants such as sodium dodecyl sulfate (SDS) into the polymer solution; they exhibit a peak with an change in the surfactant concentration [10–12].

In this paper, effects of added surfactants on the linear rheology of telechelic polymer solutions is studied on the basis of the transient network theory that explicitly takes account of the correlation among associative groups [13]. In this theoretical framework, elastically effective chains are defined only locally, i.e., chains whose both ends are connected with other chains are assumed to be responsible for the elasticity of the network.

Effects of added surfactants on the equilibrium properties of associating polymers has been theoretically studied by Tanaka [14]. He has shown that a peak appears in the number of elastically effective chains (corresponding to the plateau modulus) if an upper and a lower bound exist in the multiplicity (or aggregation number) of the micellar junctions. In this paper, we also consider the pairwise junctions in order to take account of the effect of *superbridge*. In the present level of a description of the elastically effective chain, a superbridge is represented as a concatenated chain formed by several polymers connected in series through pairwise junctions. We have shown in ref.[13] that with increasing the polymer concentration, a fraction of the pairwise junction decreases (corresponding to the contraction of concatenated chains), and as a result, the relaxation time increases [13]. This partially explains the dependence of the relaxation time of the pure polymer network on the polymer concentration. Here this idea is applied to the case that surfactants are mixed with the polymers in the solution. Annable *et al*. have discussed the effect of surfactants on the rheological properties of telechelic polymers from the viewpoint of superbridges and a transition in the ratio of looped chains to bridged chains within the network [11]. In this paper, we consider a simpler situation where superbridges are present but looped chains are absent within the framework of ref.[14] in order to seek an essential origin of the

Fukui Institute for Fundamental Chemistry, Kyoto University, Kyoto 606-8103, Japan (Present Address: Faculty of Engineering, Department of Polymer Science and Engineering, Yamagata University
4-3-16 Jonan, Yonezawa 992-8510, Japan
e-mail: indei@yz.yamagata-u.ac.jp

influence of added surfactant. Additional effects of looped chains will be reported elsewhere.

## Theoretical Model of the Mixed System of Telechelic Polymers and Surfactants

We deal with aqueous solutions of $n^e$ telechelic polymers mixed with $n^s$ surfactants per unit volume. A polymer chain is assumed to be the Gaussian comprising $N$ statistical units whose length is $a$. A hydrophobe (on both the polymer and the surfactant) is assumed to have the same characteristic length $a$ as that of the statistical unit of the polymer. The volume fraction of the hydrophobe on the polymer and on the surfactant are then $\psi^{\mathrm{e}}= 2n^e a^3$ and $\psi^s= n^s a^3$, respectively. $\psi^e + \psi^s (\equiv \psi)$ is the total volume fraction of the hydrophobe. In the solution, telechelic polymers and surfactants are temporarily connected with each other through their hydrophobic moieties, and, in a certain thermodynamic condition, a transient network whose backbone is supported by middle chains of the polymer is constructed. Interactions between the hydrophilic middle part of the polymer and the surfactant are not considered here, and looped chains are assumed to be absent.

Let $\chi^e_{k,l}$ and $\chi^s_{k,l}$ be the number density of the polymer and the surfactant, respectively, belonging to the micelle comprising $k$ polymer ends and $l$ surfactants (called ($k$,$l$)-micelle in the following). The probability $q^e_{k,l}$ that a randomly chosen polymer end is incorporated into the ($k$,$l$)-micelle is written as $q^e_{k,l} = \chi^e_{k,l}/n^e$, and the probability for an arbitrary selected surfactant to belong to the ($k$,$l$)-micelle is expressed as $q^s_{k,l} = \chi^s_{k,l}/n^s$. The probability for an arbitrary chosen hydrophobe irrespective of whether it is on the polymer or on the surfactant is incorporated into the ($k$,$l$)-micelle is then given by $q_{k,l} = (2\chi^e_{k,l} + \chi^s_{k,l})/(2n^e + n^s)$. These three probabilities are related with each other through the following equations

$$\psi^e q^e_{k,l} = \frac{k}{k+l}\,\psi q_{k,l} \quad \text{and} \quad \psi^s q^s_{k,l} = \frac{l}{k+l}\psi q_{k,l}. \tag{1}$$

Here, $\psi^e q^e_{k,l}$ (or $\psi^s q^s_{k,l}$) is the volume fraction of the hydrophobe on the polymer (or on the surfactant) belonging to the ($k$,$l$)-micelle, and $\psi q_{k,l}$ is the volume fraction of the ($k$, $l$)-micelle.

### *Dissociation/connection rates of hydrophobes*

We consider the case that each hydrophobe is associated with/dissociated from the micelle in a stepwise manner as in refs. [13, 15]. The probability $\beta^e_{k+1,l}$ that a polymer end is dissociated from the ($k$+1,$l$)-micelle per unit time (referred to as dissociation rate) is $\beta^e_{k+1,l} = \omega_0 \exp\left[-\varepsilon^e_{k,l}/k_BT\right]$ where $\varepsilon^e_{k,l}$ is the binding energy between the polymer end and the ($k$, $l$)-micelle, $\omega_0$ is a reciprocal of a microscopic time, $k_B$ is the Boltzmann constant and $T$ is the temperature. The binding energy is derived from the potential energy $U_{k,l}$ of the ($k$,$l$)-micelle, i.e., $\varepsilon^e_{k,l} = U_{k,l} - U_{k+1,l}$ (see Figure 1 (a)). Since only linear viscoelasticities are studied in this article, we assume that the dissociation rate does not depend on $r$. It is reasonable to expect that the larger the number of ($k$,$l$)-micelles in the solution, the larger the connection rate $p^e_{k,l}$ of a free polymer end to be combined with the ($k$,$l$)-micelle. To take this effect into account, we assume that $p^e_{k,l}$ is simply proportional to the volume fraction of ($k$,$l$)-micelles, that is,

$$p^e_{k,l} = h_{k+l}\omega_0 \psi q_{k,l} \tag{2}$$

where a prefactor $h_{k+l}$ depends on the multiplicity of the micelle (see below). Similarly, the dissociation rate of a surfactant from the ($k$,$l$+1)-micelle is given by $\beta^s_{k,l+1} = \omega_0 \exp\left[-\varepsilon^s_{k,l}/k_BT\right]$ where $\varepsilon^s_{k,l} = U_{k,l} - U_{k,l+1}$ is the binding energy between the surfactant and the ($k$,$l$)-micelle (see Figure 1 (b)), and the connection rate of a free surfactant with the ($k$,$l$)-micelle is supposed to be

$$p^s_{k,l} = h_{k+l}\omega_0 \psi q_{k,l} (= p^e_{k,l}). \tag{3}$$

According to ref. [14], a peak appears in the number of active chains when surfactants are added to the telechelic polymer solution under the assumption that a lower and an upper bounds exist in the junction multiplicity. We also adopt this natural assumption. However, it seems that this assumption is somewhat strong in a sense that a spectrum of the multiplicity is not continuous at $m(=k+l) = 1$. In order to narrow

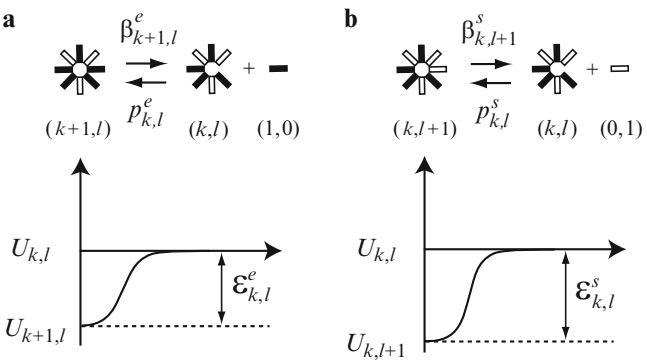


**Fig. 1** Interaction between a polymer end (black rectangle) and a ($k$,$l$)-micelle (a), and interaction between a surfactant (white rectangle) and a ($k$,$l$)-micelle (b)

the gap at $m = 1$, we also allow the pairwise micelle whose multiplicity is $m = 2$ to exist in the system[1]. Pairwise micelles together with micelles with the multiplicity between $s_0$ and $s$ can be (approximately) generated by putting $h_{m(=k+l)} = 1$ (for $m = 1, s_0 \le m \le s-1$), $\delta$ (for $2 \le m \le s_0 - 2$), $\delta^{-(s_0-3)}$ (for $m = s_0 - 1$), 0 (for $m \ge s$) with $\delta$ being a small positive value.

It has been shown in ref.[13] for pure polymeric systems that the dissociation rate of the polymer from a pairwise junction is double of that from a junction comprising larger amount of polymer hydrophobes. A polymer whose both ends are connected with the pairwise junction can be an ingredient of the so-called superbridge [4].[2] It is expected that the longer the superbridge the larger the breakage rate because the number of breakable junctions inside the longer superbridge is larger [4, 15]. Although it is difficult to directly incorporate this important effect into the present model in which the global structure of the network is not properly dealt with, the effect of the superbridge is approximately considered by taking account of the pairwise junction whose lifetime is short,

## Equilibrium distribution of the micelle

In an equilibrium state, detailed balance between the association and the dissociation among hydrophobes should hold. Under the present condition that only stepwise reactions are allowed to occur, the detailed balance condition is expressed as [16]

$$\beta^e_{k,l} q^e_{k,l} = p^e_{k-1,l} q^e_{1,0} \quad \text{and} \quad \beta^s_{k,l} q^s_{k,l} = p^s_{k,l-1} q^s_{0,1}. \tag{4}$$

Substituting $\beta^e_{k,l}, p^e_{k,l}$ and $\beta^s_{k,l}, p^s_{k,l}$ introduced above into eq. (4), we obtain the volume fraction of the $(k,l)$-micelle having the following form [16]:

$$\psi q_{k,l} = \gamma_{k+l} \frac{(k+l)!}{k!l!} e^{-U_{k,l}/k_BT} (\psi^e q^e_{1,0})^k (\psi^s q^s_{0,1})^l, \tag{5}$$

where we have put $U_{1,0} = U_{0,1} = 0$, and $\gamma_m \equiv \prod_{n=1}^{m-1} h_n$. Substitution of eq. (1) with eq. (5) into the normalization conditions $\sum_{k\ge1,l\ge0} q^e_{k,l} = \sum_{k\ge0,l\ge1} q^s_{k,l} = 1$ gives us a simultaneous equation for $q^e_{1,0}$ and $q^s_{0,1}$ that is usually solved numerically for given $\psi^e, \psi^s, U_{k,l}$ and $h_{k+l}$. By putting thus obtained $q^e_{1,0}$ and $q^s_{0,1}$ into eq. (5), we finally get $q_{k,l}$.

In this article, we consider the simplest case that the mixed micelle formation is ideal, in other words, there is no change in the interaction on mixing. In this case, the potential energy of a micelle is approximately expressed as $U_{k,l} = -(k + l - 1)\varepsilon$ where $\varepsilon$ is associated with the binding energy between neighboring hydrophobes in the micelle ($\varepsilon$ is roughly estimated from the relaxation time $\sim \exp(\varepsilon/k_BT)$ determined from the dynamic shear modulus [4]). Then eq. (5) reduces to

$$cq_{k,l} = \gamma_{k+l} \frac{(k+l)!}{k!l!} (c^e q^e_{1,0})^k (c^s q^s_{0,1})^l, \tag{6}$$

where $c^e \equiv \lambda\psi^e$, $c^s \equiv \lambda\psi^s$ and $c \equiv c^e + c^s = \lambda\psi$ are referred to as reduced concentration ($\lambda \equiv \exp[\varepsilon/k_BT]$ is the association constant). Note that the probability $q_m \equiv \sum_{n=0}^{m} q_{n,m-n}$ that an arbitrary chosen hydrophobe belongs to the micelle with multiplicity $m$ is $\lambda\psi q_m = \gamma_m (\lambda\psi q_1)^m$. This expression for $q_m$ was used in ref. [14].

## Dynamic shear modulus

We assume that polymer chains whose both ends are connected with other polymers are elastically effective (called active chain), that is, elasticity of the system is attributed to active chains, and assume that the active chains deform affinely to the macroscopic deformation applied to the network. Other than the active chain, two types of the chain exist in the system; dangling chain and isolated chain. The dangling chain is connected with the other polymers only through its one end, whereas isolated chains are not incorporated into other polymers. Since the time constant of a polymer (represented by the Rouse relaxation time) is rather smaller than the characteristic time of the macroscopic deformation applied to the system in many cases, we can reasonably assume that dangling and isolated chains are always in an equilibrium state and the distribution function for the chain end-to-end length $r$ is given by $f_0(r) = [3/(2\pi Na^2)]^{3/2} \exp[-3r^2/(2Na^2)]$ at all times. These two types of polymer do not contribute to the stress of the system.

Let $F_{k,l;k',l'}(\mathbf{r}, t)d\mathbf{r}$ be the number density of the polymer chains at time $t$ having the end-to-end vector $\mathbf{r} \sim \mathbf{r} + d\mathbf{r}$ whose one end is belonging to the $(k,l)$-micelle while the other end is incorporated into the $(k', l')$-micelle (called $(k, l;\ k', l')$-chain in the following). The time development of the active $(k, l;\ k', l')$-chain is governed by the following equation

[1] A pairwise micelle is a micelle comprising any two associative groups (i.e., two surfactants, a single polymer end and a single surfactant, or two polymer ends), whereas a pairwise junction is a micellar junction in which two polymer ends exist.

[2] In a real system, a junction inside the superbridge includes hydrophobes from the dangling chain (or dangling end) and the looped chain.

$$\frac{\partial F_{k,l;k',l'}(\mathbf{r},t)}{\partial t} + \nabla\cdot(\boldsymbol{\kappa}(t)\cdot\mathbf{r}F_{k,l;k',l'}(\mathbf{r},t)) = W_{k,l;k',l'}(\mathbf{r},t) \text{ (for } k,k'\geq 2, l,l'\geq 0) \quad (7)$$

where $\boldsymbol{\kappa}(t)$ is the rate of deformation tensor applied to the system. A small oscillatory shear deformation is represented by $\kappa_{xy} = \tilde{\varepsilon}\omega\cos\omega t$ where $\tilde{\varepsilon}$ is the dimensionless infinitesimal amplitude and $\omega$ is the frequency of the oscillation (other components of $\boldsymbol{\kappa}$ are 0). A right-hand-side $W_{k,l;k',l'}$ in eq. (7) describes the net increase in $F_{k,l;k',l'}(\mathbf{r},t)$ per unit time due to the association/dissociation reactions of the hydrophobes related to the $(k,l;k',l')$-chain (having the end-to-end vector $\mathbf{r}$). This term can be derived by considering all reactions with respect to the $(k,l;k',l')$-chain (not shown here). See refs. [13, 16] for details.

Since the amplitude $\tilde{\varepsilon}$ of the oscillation is small, $F_{k,l;k',l'}(\mathbf{r},t)$ can be expanded with respect to the powers of $\tilde{\varepsilon}$ up to the first order (the higher order terms can be negligible): $F_{k,l;k',l'}(\mathbf{r},t) = v_{k,l;k',l'}f_0(r) + \tilde{\varepsilon}F^{(1)}_{k,l;k',l'}(\mathbf{r},t)$ where $v_{k,l;k',l'} = n^e q^e_{k,l}q^e_{k',l'} = n^e(\psi/\psi^e)^2 kk'/((k+l)(k'+l'))\ q_{k,l}q_{k',l'}$ is the equilibrium number density of the $(k,l;k',l')$-chain with $q_{k,l}$ given by eq. (5). The number density of the active chain is obtained by summing $v_{k,l;k',l'}$ over $k\geq 2$, $l\geq 0$ and $k'\geq 2$, $l'\geq 2$. After the long-time limit, the first order term is expressed as [13]

$$F^{(1)}_{k,l;k',l'}(\mathbf{r},t) = \left[g'_{k,l;k',l'}(\omega)\sin\omega t + g''_{k,l;k',l'}(\omega)\cos\omega t\right] \times \frac{3xy}{Na^2}n^e f_0(r). \quad (8)$$

In-phase $g'_{k,l;k',l'}(\omega)$ and out-of-phase $g''_{k,l;k',l'}(\omega)$ components of $F^{(1)}_{k,l;k',l'}$ can be obtained by solving a simultaneous equation derived by substituting eq. (8) into eq. (7). The shear stress originated from the $(k,l;k',l')$-chain is obtained from the relation: $\sigma_{k,l;k',l'}(t) = (3k_BT)/(Na^2)\int d\mathbf{r}xyF_{k,l;k'l'}(\mathbf{r},t)$ that holds for the Gaussian chain, and then the total shear stress is derived from the equation: $\sigma_{xy}(t) = \sum_{k\geq 2,l\geq 0}\sum_{k'\geq 2,l'\geq 0}\sigma_{k,l;k'l'}(t) = \tilde{\varepsilon}(G'(\omega)\sin\omega t + G''(\omega)\cos\omega t)$ where the storage and loss moduli are given by

$$G'(\omega) = n^e k_BT\sum_{k\geq 2,l\geq 0}\sum_{k'\geq 2,l'\geq 0}g'_{k,l;k'l'}(\omega) \text{ and } G''(\omega) = n^e k_BT\sum_{k\geq 2,l\geq 0}\sum_{k'\geq 2,l'\geq 0}g''_{k,l;k'l'}(\omega), \quad (9)$$

respectively. The plateau modulus $G_\infty \equiv G'(\omega\to\infty)$ is found to be [16]

$$\frac{G_\infty}{n^e k_BT} = \left(\sum_{k\geq 2,1\geq 0}q^e_{k,1}\right)^2. \quad (10)$$

## Results and Discussion

Figure 2 shows the dynamic shear moduli $G', G''$ calculated from eq. (9) as a function of $\omega$ scaled by $\beta_0 \equiv \omega_0\exp(-\varepsilon/k_BT)$. It is seen that they are well described in terms of the single-mode Maxwell model. The high-frequency plateau modulus $G_\infty$ is obtained from eq. (10), whereas the relaxation time is well approximated by $\tau = (\tau_1+\tau_2)/2$ [16] where

$$\tau_1 = \frac{1}{2}\frac{\sum_{k=2}^{s}w_k\sum_{l=0}^{s-k}q^e_{k,l}/\ \beta^e_{k,l}}{\sum_{k=2}^{s}\sum_{l=0}^{s-k}q^e_{k,l}} \quad (11)$$

and $\tau_2 \equiv 1/\langle\beta\rangle$ with

$$\langle\beta\rangle = 2\frac{\sum_{k=2}^{s}1/w_k\sum_{1=0}^{s-k}\beta^e_{k,1}q^e_{k,1}}{\sum_{k=2}^{s}\sum_{l=0}^{s-k}q^e_{k,1}} \quad (12)$$

A weight $w_k \equiv 1/2(\text{for } k=2),\ 1(\text{for } k>2)$ reflects the fact that the dissociation rate of a polymer end from the junction including only two polymer ends ($k=2$) is a double of the one from the junction comprising more polymer ends ($k>2$).

Figure 3 (a) shows the plateau modulus plotted against the reduced surfactant-hydrophobe concentration $c^s$ (divided by the reduced polymer-hydrophobe concentration $c^e$) for a fixed $c^e$. We see that a peak appears in $G_\infty$ if there is a lower bound in the multiplicity. This is explained as follows [14]. With increasing the surfactant concentration, a possibility that the number of free end of the polymer and free surfactants around an arbitrary chosen free end of a polymer exceeds $s_0$ is increased, and hence mixed micelles whose

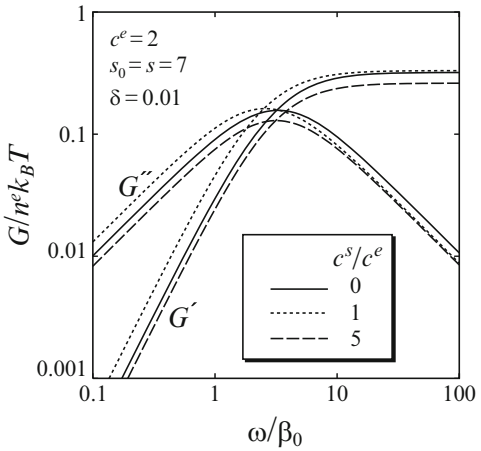


**Fig. 2** Dynamic shear moduli plotted against the frequency for several different surfactant concentrations with $c^e = 2$ and $s_0 = s = 7$

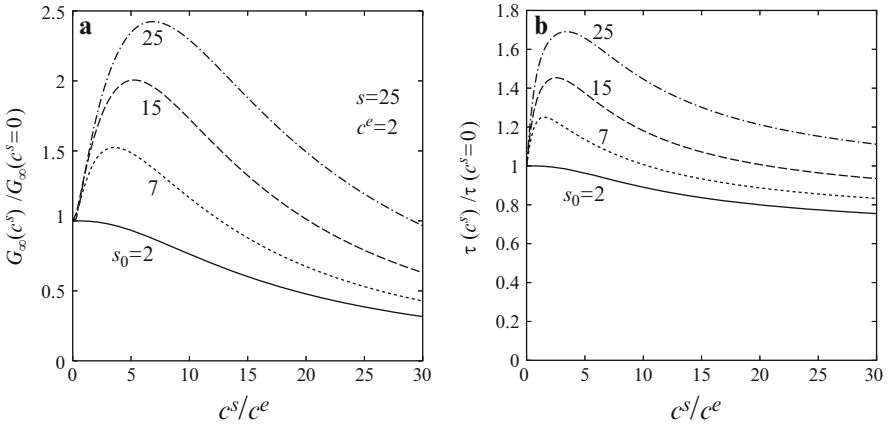


**Fig. 3** The plateau modulus (a) and the mean relaxation time (b) as a function of the ratio between the reduced surfactant-hydrophobe concentration $c^s$ and the reduced polymer-hydrophobe concentration $c^e$ for a fixed $c^e(=2)$. Both are divided by the value at $c^s = 0$. The lower bound of the multiplicity $s_0$ is different for each curve with a fixed upper bound $s = 25$

multiplicity is between $s_0$ and $s$ may be newly created (see Figure 4(b)). The creation of the mixed micelle including more than or equal to two polymer ends causes the increase in the number of active chain (and $G_\infty$). On the other hand, the more the surfactants in the polymer solution, the more the dangling ends formed by a single polymer end and several surfactants due to the existence of an upper bound in the multiplicity. This leads to a decrease in the number of active chains in the higher surfactant concentration regime. If there is no lower bound in the multiplicity, surfactants added into the solution simply connect with the existing micellar junctions, and hence they do not play a role as a trigger to create new micelles. Therefore, no peak appears in the plateau modulus.

The (normalized) plateau modulus (eq. (10)) is a square of the probability $\sum_{k\geq 2}^{s}\sum_{l\geq 0}^{s-k} q^e_{k,l} \equiv G_1$ that an arbitrary chosen polymer end belongs to the micellar junction containing more than or equal to two polymer ends. This quantity is divided into two parts: $G_1 = \alpha^e(1 - p_d)$ where $\alpha^e \equiv 1 - q^e_{1,0} - q^e_{1,1}$ is the "association rate" of the polymer end (in order to exclude the minor effect originating from the pairwise micelle, $q^e_{1,1}$ is subtracted from the original association rate $1 - q^e_{1,0}$) and $p_d \equiv \sum_{l=2}^{s-1} q^e_{1,l}/\alpha^e$ is the probability that an arbitrary selected associated polymer end (except for the (1,1)-micelle) belongs to the dangling end. The appearance of a peak in $G_1$ (and $G_\infty$) is determined from the balance between $\alpha^e$ and $p_d$ because an increase in $\alpha^e$ causes the growth of $G_1$ while the increase in $p_d$ leads to the decrease in $G_1$ (see Figure 4 (a)).

A peak also appears in the relaxation time $\tau = (\tau_1 + \tau_2)/2$ when a lower bound exists in the multiplicity (Figure 3(b)). This is explained as follows. When there are no surfactants in the solution, polymer ends are comprising micellar junctions by themselves. Some of them are pairwise junctions and the others are junctions formed by more than two polymer ends. When a small amount of surfactants are added to the solution, pairwise junctions

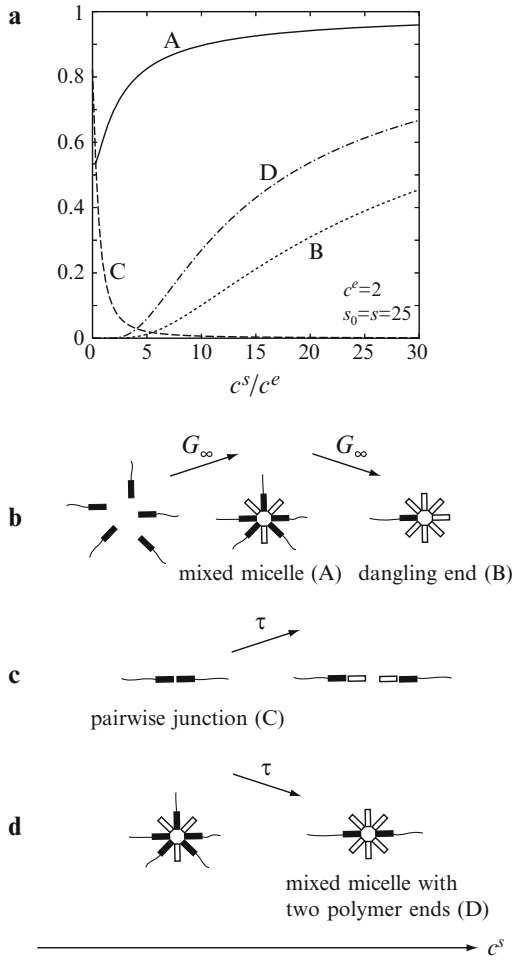


**Fig. 4** (a) A: Association rate $\alpha^e$ of the polymer end (see text). B: Probability $p_d$ for an associated polymer end to belong to the dangling end. C: Probability for a polymer end (except for the one belonging to the dangling end) to be incorporated into the pairwise junction comprising two polymer ends. D: Probability for a polymer end to belong to the mixed micelle including two polymer ends. All curves correspond to Figure 3 ($s = 25$). (b, c, d) Schematic explanation of the peak appeared in the plateau modulus and the relaxation time. See text for details

tend to break and pairwise micelles formed by a polymer end and a surfactant can be created instead (see Figure 4(c)). A curve C in Figure 4(a) shows the probability $q^e_{2,0}/\sum_{k=2}^{s}\sum_{l=0}^{s-k} q^e_{k,l}$ that an arbitrary chosen polymer end (except for the one incorporated into the dangling end) belongs to the pairwise junction. We see that it decreases with increasing the surfactant concentration. A decrease in this probability, representing the contraction of the superbridge, enhances the relaxation time of the network since the dissociation of a polymer from the pairwise junction occurs two times as often as that from the junction formed by more than two polymer ends [13]. When a relatively large amount of surfactants are added to the solution, a fraction of the mixed micelle formed by two polymer ends and several surfactants increases because of the presence of an upper bound in the multiplicity (see Figure 4(d)). A curve D in Figure 4(a) shows the probability $\sum_{l=1}^{s-2} q^e_{2,l} / \sum_{k=2}^{s}\sum_{l=0}^{s-k} q^e_{k,l}$ that an arbitrary selected polymer end (except for the one belonging to the dangling end) is incorporated into the micelle including two polymer ends. We see that it monotonically increases with increasing $c^s$. An increase in this probability, indicating the elongation of the superbridge, causes a decrease in the relaxation time. When there is no lower bound in the multiplicity, pairwise junctions comprising two polymer ends cannot break by the addition of surfactants on the junction. Thus the relaxation time does not increase with the surfactant concentration and it decreases monotonically.

Figure 5(a) shows the plateau modulus plotted for several different polymer concentrations. A peak height in $G_\infty$ decreases with an increase in the polymer concentration and finally it disappears. This is because many of polymer ends are forming micelles in the solution of higher polymer concentration before adding surfactants, and these existing micelles tend to become dangling ends with increasing the surfactant concentration [14]. Figure 5(b) shows the relaxation time corresponding to Figure 5(a). We see that $\tau$ increases with increasing the polymer concentration. This is because the fraction of pairwise junction is smaller for a higher polymer concentration. However, the dependence of $\tau$ on the polymer concentration is weak and the relative peak height becomes low with increasing the polymer concentration. These results are different from experimental facts observed for aqueous solutions of telechelic PEO/SDS mixture [11], and are probably due to the lack of global information of the network in the present model [15] and the assumption of the ideality in the mixed micelle formation.

## Summary and Conclusions

The influence of added surfactants on the linear rheology of telechelic associating polymer networks under small oscillatory shear deformation was studied on the basis of the transient network theory that takes account of the correlation among polymer ends and surfactants. The dynamic shear modulus is well described in terms of the single-mode Maxwell model and the modulus changes as the surfactant concentration varies. A peak in the plateau modulus as a function of the surfactant concentration can be ascribed to the existence of an upper and a lower bounds in the multiplicity of the micellar junction as suggested by Tanaka [14]. On the other hand, a peak in the relaxation time is caused by the dissociation followed by the creation of pairwise junctions connecting two polymers with an increase in the surfactant concentration. This indicates that the contraction and extension of the superbridge (or concatenated chain comprising several polymers connected in series) by an addition of surfactants in the network play a important role to determine the relaxation behavior of the mixed system of associating polymers and surfactants.

In the present article, only an ideal case that the hydrophobe on a polymer and that on a surfactant are exactly the same and hence there is no change in the interaction on mixing was studied to reveal essential reasons of a peak appeared in the

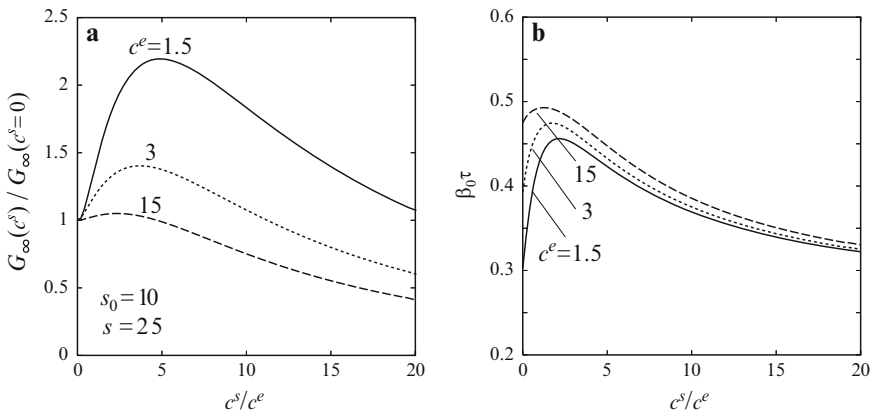


**Fig. 5** The plateau modulus (a) and the mean relaxation time (b) plotted against the ratio between the reduced surfactant-hydrophobe concentration $c^s$ and the reduced polymer-hydrophobe concentration $c^e$ for several $c^e$. The plateau modulus is divided by the value at $c^s = 0$. The lower bound in the multiplicity is set to $s_0 = 10$ while the upper bound is $s = 25$

plateau modulus and the relaxation time. Effects of the non-ideality in the mixed micelle formation on the linear rheology will be reported in the forthcoming paper [16].

**Acknowledgements** This research was partially supported by the Ministry of Education, Culture, Sports, Science and Technology of Japan, Grant-in-Aid for Young Scientists (B) 19740259.

## References

1. Winnik MA, Yekta A (1997) Curr Opin Colloid Interface Sci 2: 424
2. Piculell I, Thuresson K, Lindman B (2001) Polym Adv Technol 12: 44
3. Jenkins RD, Silebi CA, El-Aasser MS (1991) ACS Symp Ser 462: 222
4. Annable T, Buscall R, Ettelaie R, Whittlestone D (1993) J Rheol 37: 695
5. Xu B, Yekta A, Li L, Masoumi Z, Winnik MA (1996) Colloids Surf A 112: 239
6. Pham QT, Russel WB, Thibeault JC, Lau W (1999) Macromolecules 32: 5139
7. Ng WK, Tam KC, Jenkins RD (2000) J Rheol 44: 137
8. Ma SX, Cooper SL (2002) Macromolecules 35: 2024
9. Bagger-Jörgensen H, Coppola L, Thuresson K, Olsson U, Mortensen K (1997) Langmuir 13: 4204
10. Binana-Limbele W, Clouet F, François J (1993) Colloid Polym Sci 271: 748
11. Annable T, Buscall R, Ettelaie R, Shepherd P, Whittlestone D (1994) Langmuir 10: 1060
12. Zhang KW, Xu B, Winnik MA, Macdonald PM (1996) J Phys Chem 100: 9834
13. Indei T (2007) J Chem Phys 127: 144904
14. Tanaka F (1998) Macromolecules 31: 384
15. Indei T (2007) J Chem Phys 127: 144905
16. Indei T (2008) in preparation for publication

Progr Colloid Polym Sci (2009) 136:31–38
DOI: 10.1007/2882_2009_5

# Time-Dependent Flow Properties of Transient Hydrogels with Temporal Network Junctions

Isamu Kaneda[1], Tsuyoshi Koga[2], and Fumihiko Tanaka[2]

**Abstract** The nonlinear rheological behavior under startup shear flows in aqueous solutions of telechelic hydrophobically ethoxylated urethane carrying branched alkyl end-chains, 2-decyl-tetradecyl, (referred to as C24-HEUR) was studied by strain-controlled rheomery. Unusual stress upturn (known as strain hardening), followed by the stress overshoot, was observed for 3 wt% aqueous solution above a critical shear rate. The phenomenon is explained by our recent transient network theory in terms of nonlinear chain stretching occurring during the stress build-up. Upon addition of glycerol, the relaxation time was shortened, while the equilibrium modulus increased with the concentration of glycerol. The stress upturn disappeared above a certain value of the glycerol concentration, strongly suggesting that glycerol affects the dynamics of the transient network through the interaction with the micellar junctions.

**Keywords** HEUR • Strain hardening • Glycerol • Transient network • Stress growth

## Introduction

A physical gel consisted with weak interaction is applied to foods, personal care products and cosmetics, since these products are fractured during the usage. In particular, reversible gel is quite interesting in the industrial and academic viewpoint. Hydrophobically ethoxylated urethane (HEUR) is a kind of telechelic polymer. HEUR makes a reversible gel in aqueous solution. Since the rheological property of HEUR is quite unique and interesting, several studies on the material have reported [1–4]. The molecular dynamics of the polymer is one of the most important topics. Tanaka and Edwards constructed the transient network theory [5–8], and recently, the theory has been refined to explain the dynamic phenomenon in nonlinear region [9]. On the other hand, recently a new type HEUR type viscosity thickener for cosmetics has been developed and applied to many kinds of cosmetic products [10,11]. The polymer has designed to achieve the required performance that is, for example, high thickening effect and unexpected usage texture as a novel viscosity thickener for cosmetics. In particular, the unexpected usage texture is the most important feature of the novel ingredient.

In general, nonlinear rheological properties are quite important for food and cosmetics. Recently, some studies on such large deformation behavior of HEUR have reported [12–14]. We focused in such nonlinear rheological properties for a HEUR aqueous solution in this paper. It is well known that the mechanical property of HEUR aqueous solution can be explained using a single mode Maxwellian model [3], namely it is considered a viscoelastic fluid. When we apply such a viscoelastic fluid to food or cosmetics, we should consider the rheological behavior under large deformation, since food or cosmetics must be largely deformed during the usage of them. As one of such nonlinear deformation, the stress growth behavior under the step shear flow was taken up in this study. The experimental data was interpreted by using the theory mentioned above [9]. Moreover, the effect of glycerol on the various rheological properties of the HEUR aqueous solution also investigated. Since glycerol is quite popular additive ingredient for food and cosmetics, it is useful to study systematically the effect of glycerol on such mechanical properties for food or cosmetics ingredient.

## Experimental sections

### *Materials*

A hydrophobically ethoxylated urethane carrying branched alkyl end-chains, 2-decyl-tetradecan, (referred to as C24-HEUR) was synthesized according to the method

I. Kaneda (✉)
[1]Department of Food Science
Rakuno Gakuen University
e-mail: kaneda-i@rakuno.ac.jp
[2]Graduate school of Technology, Kyoto University

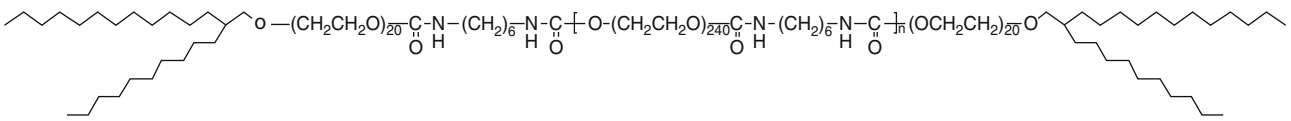

**Fig. 1** The chemical structure of C24-HEUR

reported elsewhere [10, 11]. The used sample of C24-HEUR was kindly gifted from Shiseido Co., Ltd. The chemical structure of C24-HEUR is shown in Fig. 1. Remarkable feature of the polymer is the size of the hydrophobic moiety. A branched hydrophobic chains, 2-decyl-tetradecan, are attached to the main chain through urethane. The polymer was used as receive without further purification. The weight average molecular weight ($M_w$) of the polymer was 27000 and the molecular weight distribution, $M_w$ / $M_n$, was 2.5 [11]. Since the polymer was synthesized via condensation reaction using polyethylene oxide (PEO) chains ($M_w$ = ca. 10000), the value indicated the sample contains several PEO chains (1-3 chains) in the polymer. All the sample solutions contain 3 wt% C24-HEUR and various concentration of glycerol. The sample code AG0, AG10, AG20, and AG30 denote the sample containing 0%, 10%, 20% and 30% of glycerol in its solvent, respectively. Glycerol was purchased from Wako Pure Chemical (Osaka, Japan) and distilled water was used.

### *Rheology measurement*

A strain controlled rheometer, RDA II (TA instruments, USA) was used for rheology measurement. Parallel plate geometry was employed (25 mm in diameter and 1.5 mm gap). The measurement was conducted at room temperature (22± 1°C).

## Results and discussion

### *Dynamic modulus and Steady state viscosity*

As reported results for a HEUR aqueous solution, C24-HEUR aqueous solution also showed a typical rheological character as an associated thickening polymer, namely, the dynamic modulus of C24-HEUR aqueous solution at various frequencies followed a single relaxation Maxwell model. Fig. 2 (A, B, C. and D) shows the frequency dependency of the dynamic modulus for AG0, AG10, AG20, and AG30, respectively. A Maxwell model comprises an elastic component connected in series with a viscous component. In this model G'(ω) and G"(ω) are described by the following equations.

$$G'(\omega) = G_0 \frac{\omega^2\tau^2}{1+\omega^2\tau^2} \quad (1)$$

$$G(\omega) = G_0 \frac{\omega\tau}{1+\omega^2\tau^2} \quad (2)$$

Here $G_0$, ω, and τ are the equilibrium modulus, the angular velocity, and the relaxation time, respectively. The experimental data of G"(ω) at around its peak area were used to estimate $G_0$ and τ using the Maxwell model. The lines in Fig. 2 denote the estimated values using (1) and (2). The samples almost exhibited a Mawxwell type mechanical spectrum. However, we can see that there is slight difference between the experimental data and estimated value at low frequency, namely the experimental data of G'(ω) seems slightly higher than the estimated value for all the samples. It is well known that associated polymers make micelles consisting with the hydrophobic chains due to hydrophobic interaction. We can treat such polymer solution as condensed colloid system. If the colloid particles (micelles, in this case) are close packed, a slow relaxation mode would appear in its mechanical spectrum as so called second plateau [15, 16]. Although there is no precise evidence of such a slow relaxation mode in Fig. 2, the deviation of the fitting result at the low frequency region exhibits its possibility. The parameters of all the samples were estimated in the same procedure. Fig. 3 shows the glycerol concentration dependency of the mechanical characteristics. Upon addition of glycerol, the relaxation time was shortened with the glycerol concentration. On the other hand, $G_0$ slightly increased with the glycerol concentration.

The steady state viscosity for the samples was measured at various shear rates ranging from $10^{-2}$ to $10^{2}$ $s^{-1}$. The shear rate dependency of the steady state viscosity and also the complex viscosity from the dynamic measurement for AG0, AG10, AG20, and AG30 are shown in Fig. 4 (A, B, C, and D). Although the Cox-Mertz rule failure for the entire sample, the Newtonian plateau level at low shear rate almost agree with the steady state viscosity and the complex viscosity for the entire sample.

These results suggest that glycerol affects the structure of the polymer network at high concentration. The effect of glycerol on the micellar structure of a non-ionic surfactant [17]

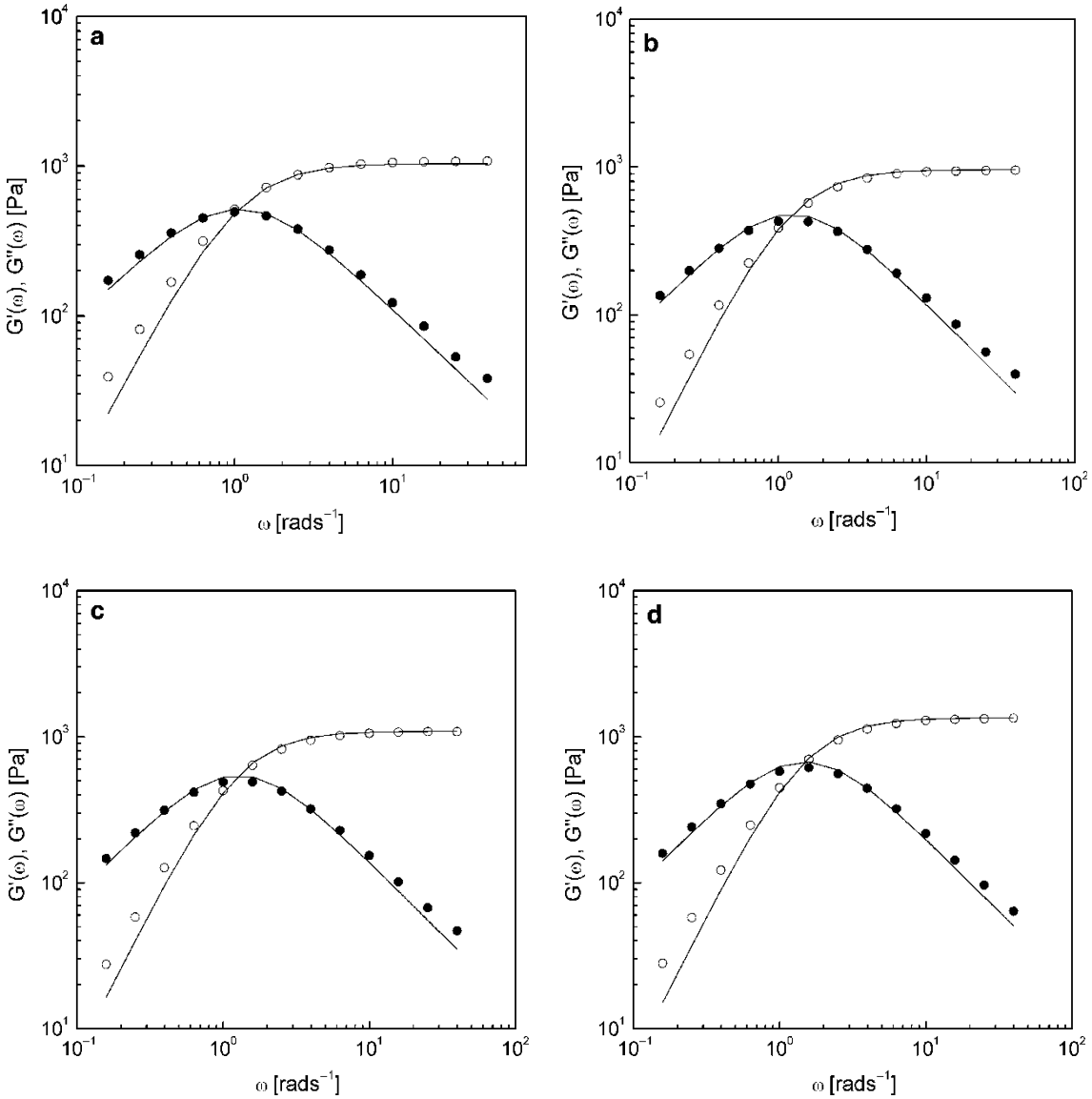


**Fig. 2** The frequency dependency of the dynamic modulus for AG0 (A), AG10 (B), AG20 (C), and AG30 (D). The open and closed circles denote the storage modulus and the loss modulus, respectively. Lines denote the estimated value obtained by fitting with a single mode Maxwell model

and polyethylene oxide – polypropylene oxide – polyethylene oxide (PEO-PPO-PEO) block copolymers [18] are reported. In general, upon addition glycerol, PEO chains shrink as a result of dehydration. From the dynamic modulus, glycerol seems to change the crosslink points of the transient network. As shown in Fig. 3, shorter the relaxation time means the reduction of the duration time of the hydrophobic end chains of C24-HEUR to stay in micellar junctions. On the other hand, such a change would affect to the total number of the crosslink points per unit volume. The aggregation number may increase due to the change of the hydrophilic-hydrophobic balance of the polymer. The increase of the aggregation number drives the decrease of the micellar number, and consequently, the number of the crosslink points decrease. Such a change may decrease the equilibrium modulus. However, as shown Fig. 3, the equilibrium modulus slightly increased with the concentration of glycerol. It is difficult to explain the reason of this phenomenon at the present time. Since the phenomenon is quite interesting, further study on the problem is planning.

## *Viscosity growth behavior in the start up shear flow*

The dynamics of the transient network for an associated thickener such as HEUR is quite interesting in the viewpoint of the texture for food or cosmetics, since the mechanical

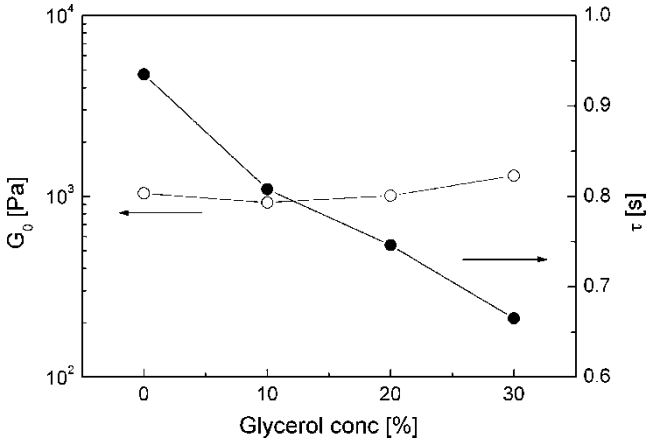


**Fig. 3** The effect of glycerol on the equilibrium modulus and the zero-shear viscosity that were estimated by using the result of the dynamic modulus

properties under large deformation dominates the texture of food or cosmetics. The theory for a detailed molecular picture for the Maxwellian behavior has been established by Tanaka and Edwards [5–8]. Recently, the theory refined to account for the observed shear rate dependency of the non-linear viscosity and the molecular dynamics calculation using the theory was conducted [9]. In this paper, we try to apply the refined and expanded theory to the experimental data for the viscosity growth behavior under the start up shear flow for C24-HEUR aqueous solution. In general, the stress under certain strain is defined by the balance of the strength of tension between the end of the active chain and the life time, dissociation rate of the transient crosslink point. If we can estimate the tension and the dissociation rate for the system, the mechanical properties can be estimated precisely. In particular, the behavior in the non-linear region is quite interesting. The details of the theory and the results of numerical calculation are elsewhere in this special issue [19].

The shear stress growth behavior can be explained as (3)

$$\eta^{+}(t) = \eta^{(1)}t + \eta^{(2)}\frac{t^2}{2!} + \eta^{(3)}\frac{t^3}{3!} + \cdots \tag{3}$$

Here $\eta^{(1)}$, $\eta^{(2)}$, and $\eta^{(3)}$ are given as follows;

$$\eta^{(1)} = G'(\omega \to \infty) \tag{4}$$

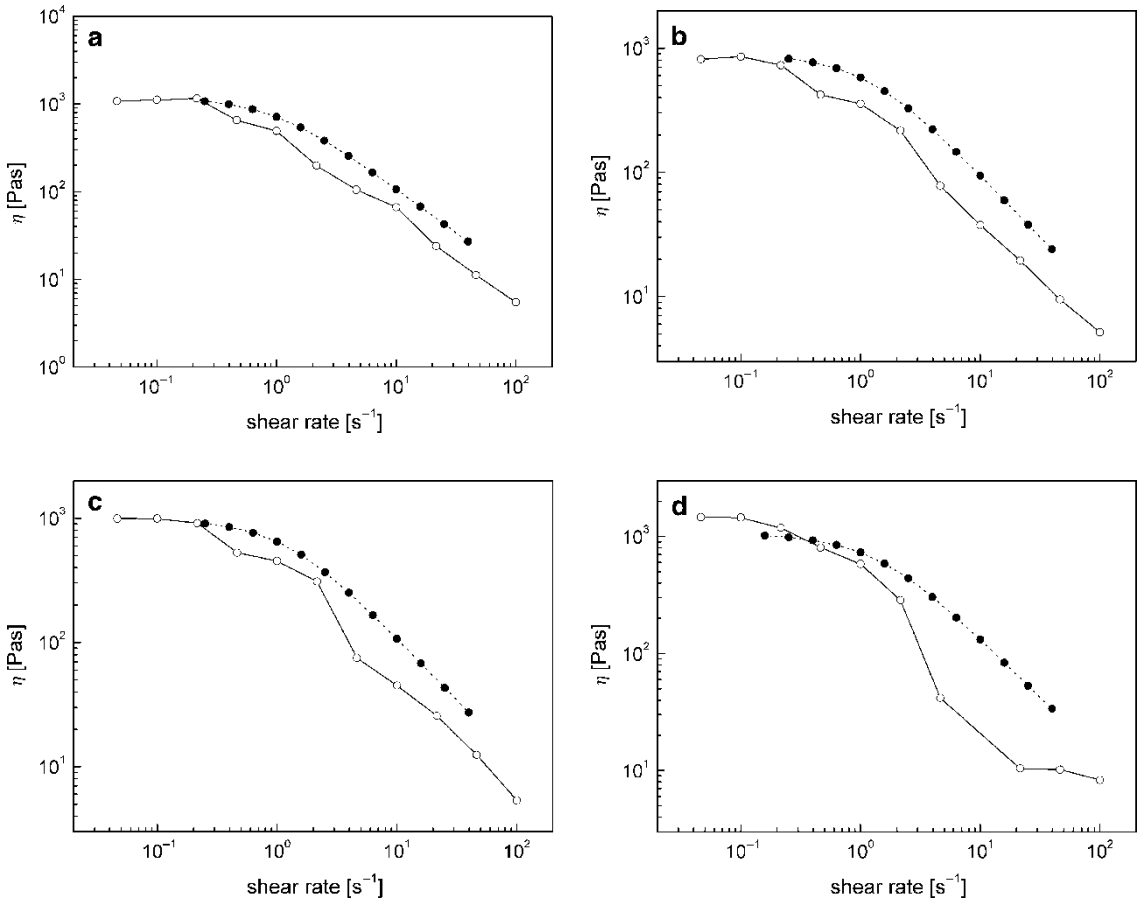


**Fig. 4** The dependency of the shear rate on the steady state viscosity for AG0 (A), AG10 (B), AG20 (C), and AG30 (D). The closed circles and open circles denote the complex viscosity (dynamic) and the steady state viscosity (static), respectively

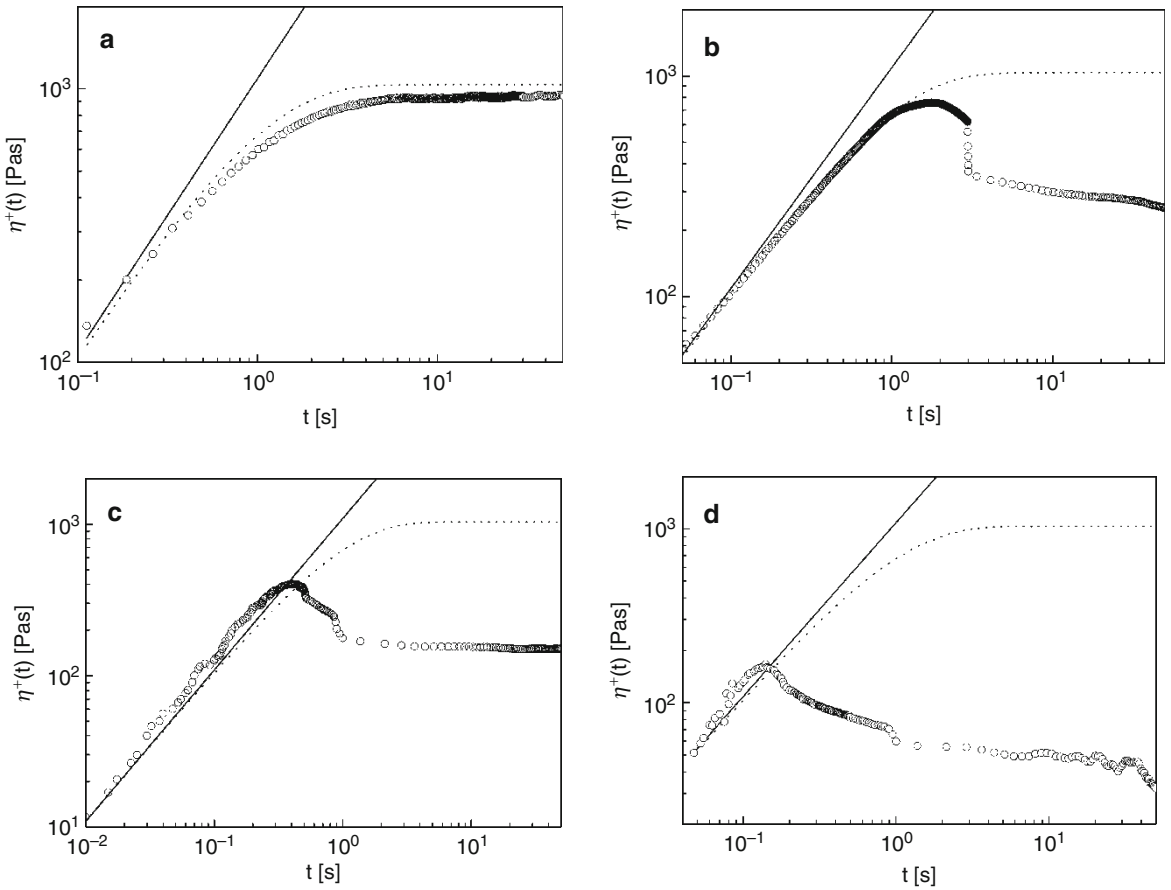


**Fig. 5** The viscosity growth curves under the step shear flow at various shear rates for AG0. A, B, C, and D show the result of the shear rate was 0.1, 1, 3, and 10 $s^{-1}$, respectively. The line and dotted line denote the elastic response at very short time period (G't) and the expected viscosity growth curve estimated with a single mode Maxwell model, respectively

$$\eta^{(2)} = -\lim_{\omega\to\infty} \omega G''(\omega) \tag{5}$$

$$\eta^{(3)} = -\left(Q_0 + Q_2\dot{\gamma}^2\right) \tag{6}$$

The first and second terms are independent of the shear rate. The coefficient $\eta^{(3)}$ of the third – order term depends on the shear rate. The coefficient $Q_0$ is positive and $Q_2$ depends on the nonlinearity under deformation. If the middle chains are deforms as the Gaussian chain, $Q_2$ is zero. On the other hand, in the case of nonlinear chains, $Q_2$ should be non-zero value and increases with the shear rate, so that the rapid increase in the shear stress is expected to observe in the short time region [19].

Fig. 5 (A, B, C, and D) shows the viscosity growth behavior at various shear rates for AG0 containing no glycerol. The lines denote G't that is the first term of (3). The dotted lines denote the expected viscosity growth curve according to (7)

$$\eta^+(t) = \eta_0\left\{1 - \exp\left(-\frac{t}{\tau}\right)\right\} \tag{7}$$

Here $\eta_0$ and $\tau$ are the estimated value from the dynamic modulus measurement for each sample. The measured values agreed with the Maxwellian viscosity growth curve at the low shear rate (Fig. 5 A), however, unexpected strain hardening, the viscosity upturn over the line of G't in very early stage of the observation, appeared above 3 $s^{-1}$. Such a stress upturn appearing depended on the shear rate. This result means that the unusual stress upturn would be occurred as a result of nonlinear stretching mentioned above for C24-HEUR aqueous solution.

The effect of glycerol on the viscosity growth behavior is shown in Fig. 6, 7, and 8. The stress upturn was appeared similar to AG0 (Fig. 5 C) in Fig. 6 and 7. However, the highest glycerol concentration sample AG30 never showed the stress upturn (Fig. 8). The result revealed that glycerol affected to the dynamics of the network, particularly the mechanical response of the active chains of the networks.

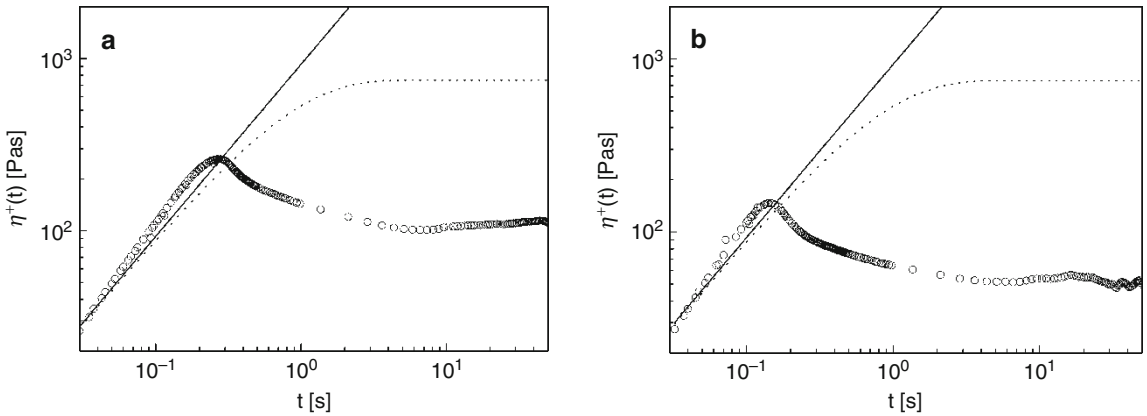


**Fig. 6** The viscosity growth curves under the step shear flow at various shear rates for AG10. A, and B show the result of the shear rate was 5 and

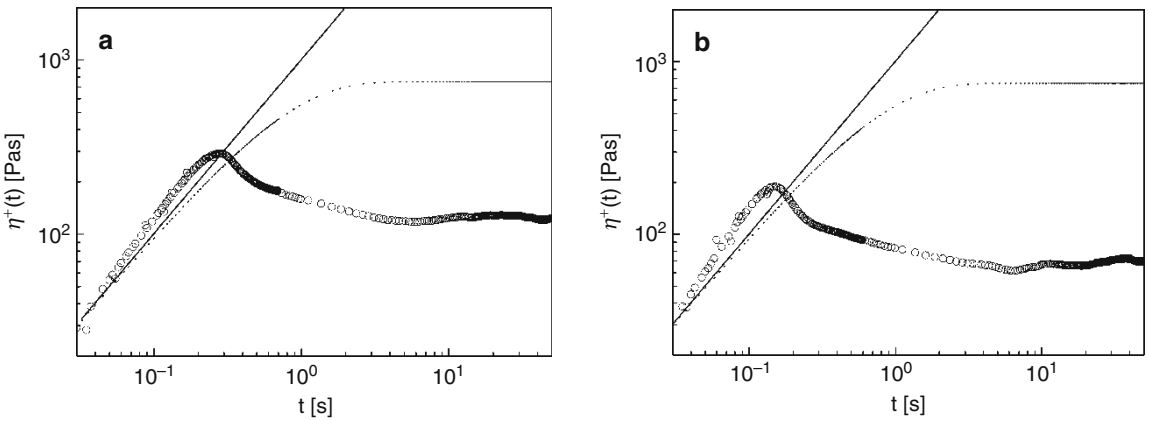


**Fig. 7** The viscosity growth curves under the step shear flow at various shear rates for AG20. A, and B show the result of the shear rate was 5 and 10 $s^{-1}$, respectively. The line and dotted line denote the elastic response at very short time period (G't) and the expected viscosity growth curve estimated with a single mode Maxwell model, respectively

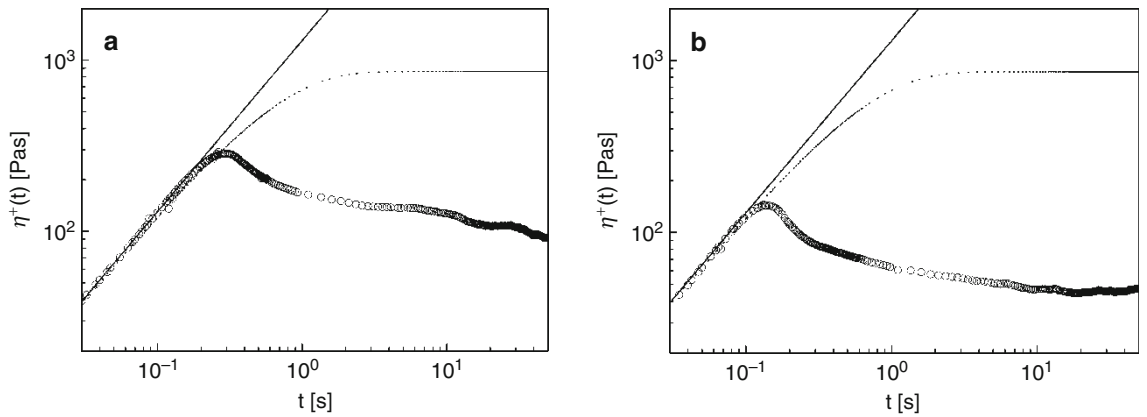


**Fig. 8** The viscosity growth curves under the step shear flow at various shear rates for AG30. A, and B show the result of the shear rate was 5 and 10 $s^{-1}$, respectively. The line and dotted line denote the elastic response at very short time period (G't) and the expected viscosity growth curve estimated with a single mode Maxwell model, respectively

Disappear of the unusual stress upturn means that AG30 containing 30% glycerol in its solvent never occurs a nonlinear stretching. The phenomenon can be considered with the result discussed in the section 3.1. As mentioned above, glycerol made shorter the relaxation time and higher the equilibrium modulus. It is considered that glycerol obviously affected to the structure of the crosslink point of the transient network for the system. Moreover, glycerol also affected to the nonlinear deformation manner. A possible hypothesis is described as follows; since glycerol is a water soluble solvent and having 3 hydroxyl groups in the molecular, it may affect the hydration behavior for the hydrophilic chains of C24-HEUR, namely PEO chains. It is reported that a small amount of water-miscible solvent occurs a cononsolvency effect [20–23]. A polymer would be shrunk its spatial size as a result of the dehydration. If the active chains connected both ends to the crosslink point are shrunk, the active chains would be collapsed between the crosslink points. When applied shear flow to the system, the collapsed chains would be reeled out from there. Since the polymer chains are reeled out, they would never be stretched. Therefore, the sample containing high concentration glycerol never showed unusual stress upturn.

The effect of glycerol on the dynamics for HEUR aqueous solution is quite complicated problem. Since we never get enough information to describe the experimental result mentioned above without contradiction, a possible speculation is discussed in this paper. We think that further study on the influence of a water-miscible solvent on the rheological properties for an associated polymer, which is applied to consumer products as a texture modifier is needed for supporting the development a novel ingredient in the filed.

## Conclusion

We have reported new observations on the time-development of the stress after a step shear flow is started in the transient network of C24 HEUR. The start-up flow experiment using a strain-controlled rheometry revealed that C24 HEUR aqueous solutions exhibited unusual stress upturn within a very short time that depends on the applied shear rate. The critical shear rate for strain hardening, and for overshoot were found for 3% solution. Recent transient network theory was employed to study the molecular origin of such nonlinear rheological properties. From a numerical calculation, it is highly probable that such phenomena are caused by the nonlinear stretching of the bridge chains connecting the micellar junction under shear before their chain ends are dissociated from the junctions.

The effect of added water-miscible solvent on the rheological properties of C24 HEUR aqueous solutions was also studied by the rheometry. We found that Glycerol, which is widely used as food additive or cosmetic moisturizer, strongly affected the rheological properties. In particular, it changed nonlinear rheological properties such as unusual stress upturn during the start up flow. The effect is very important from the industrial viewpoint, because the texture of food or cosmetics is strongly related to the nonlinear rheological properties [24]. Consumers may detect the unusual stress upturn as unusual usage feeling (texture) when they use them. Therefore, the systematic studies on the rheological properties in both experimental and theoretical viewpoints are quite important for such applications. More detailed experimental and theoretical studies of the time-development of stresses, shear as well as normal, will be reported in our forthcoming papers.

**Acknowledgment** This work is partially supported by a Grant-in-Aid for Scientific Research (B)19350057 from the Ministry of Education, Culture, Sports, Science and Technology of Japan.

## References

1. Jenkins RD (1990) Ph.D. dissertation, Lehigh University
2. Lundberg DJ, Glass JE, and Eley RR (1991) Rheol. Acta 7, 1255
3. Annable T, Buscall R, Ettelaie R, and Whittlestone D (1993) J. Rheol.,37, 695
4. Annable T, Buscall R, Ettelaie R, Shepherd P, and Whittlestone D (1994) Langmuir, 10, 1060
5. Tanaka F and Edward SF (1991) Macromolecules, 25, 147
6. Tanaka F and Edwards SF (1992) J. Non-Newtonean Fluid Mech., 43, 247
7. Tanaka F and Edwards SF (1992) J. Non-Newtonean Fluid Mech., 43, 273
8. Tanaka F and Edwards SF (1992) J. Non-Newtonean Fluid Mech., 43, 289
9. Tanaka F and Koga T (2006) Macromolecules, 39, 5913
10. Patent WO 02051939
11. Yoshida K, Nakamura A, Nakajima Y, Fukuhara T, Inoue H, and Kaneda I (2007) IFSCC magazine, 10, 2
12. Barmar M, Barikani M, and Kaffashi (2005) Colloids and Surfaces A, 253, 77
13. Kaffashi B, Barmar M, and Eyvani J (2005) Colloids and Surfaces A, 254, 125
14. Tripathi A, Tam KC, and McKinley GH (2006) Macromolecules, 39, 1981
15. Onogi S, Masuda T, and Matsumoto T (1970) Trans. Soc. Rheol., 14, 275
16. Matsumoto T, Tamamoto O, Onogi S (1980) J. Rheol., 24 (4), 379
17. Penfold J, Staples E, Tucker I, and Cummins P (1997) J. Colloid Inter. Sci., 185, 424
18. Alexandridis P and Yang L (2000) Macromolecules, 33, 5587
19. Koga T, Tanaka F, and Kaneda I (2009) Progr Colloid Polym Sci., 136, Chapter 6
20. Winnik FM, Ringsdorf H, Venzmer J (1990) Macromolecules 23, 2415
21. Winnik FM, Ottaviani M F, Bossmann, Garcia-Garibay M, and Turro NJ (1992) Macromolecules 25, 6007
22. Kaneda I and Vincent B (2004) J. Colloid Interface Sci., 274, 49
23. Tanaka F, Koga T, and Winnik FM (2008) Physical Review Letters, 101, 028302
24. Nishinari K (2004) J. Texture Studies, 35, 113

Progr Colloid Polym Sci (2009) 136:39–46
DOI: 10.1007/2882_2009_6

# Stress Growth in Transient Polymer Networks under Startup Shear Flow

Tsuyoshi Koga, Fumihiko Tanaka, and Isamu Kaneda

**Abstract** We study the stress growth in transient networks of telechelic associating polymers under the startup shear flow within the framework of our recent nonaffine transient network theory. We show that a transient strain hardening takes place due to the nonlinearity in the tension-elongation relation of the main chain. We calculate the critical shear rate $\dot{\gamma}_c$ for the strain hardening as a function of the chain nonlinearity, and the overshoot time $t_{max}$ as a function of the shear rate $\dot{\gamma}$. The theoretical results are compared with experimental data on aqueous solutions of a hydrophobically modified ethoxylated urethane (HEUR). The experimental results are consistent with the theoretical prediction. By detailed comparisons, we find that the effect of the polydispersity in the chain length significantly affects the transient stress because the nonlinear stretching effect of shorter polymer chains appears at smaller strains.

**Keywords** Startup flow • Stress overshoot • Strain hardening • Transient network • Associating polymer

## Introduction

Rheological properties of associating polymer solutions have attracted much experimental and theoretical interest in recent years. The characteristic rheological properties are attributed to the formation of transient networks where association and dissociation of junctions are possible by thermal motion of molecules and by external forces. Typical examples are networks in aqueous solutions of polymers with short hydrophobic chains attached at both chain ends (telechelic polymers) such as hydrophobic ethoxylated urethane (called HEUR) [1–4], hydrophobic poly(*N*-isopropylacrylamide) [5, 6] etc. The rheological properties of the associating polymers are commonly studied by dynamic mechanical measurements.

From theoretical viewpoints, such rheological properties have been studied on the basis of the transient network theory developed by Tanaka and Edwards [7, 8] (hereafter referred to as TE). Recently, we have refined the transient network theory by taking into account the effect of the nonaffine displacement of network junctions and the effect of nonlinearity in the tension-elongation relation of bridge chains [9]. The nonaffine transient network theory was developed to eliminate the assumption of the affine deformation of network junctions assumed in the TE theory (the end-to-end vector of a bridge chain connecting the neighboring junctions deforms affinely to the macroscopic deformation tensor). We considered the diffusive movement of the network junctions because the junctions can diffuse from one place to another due to the breakage and recombination of bridge chains. We showed that diffusive motion around the mean position of the junction gives rise to the high-frequency shoulder and low-frequency softening in the loss modulus. Also, we found that the nonlinear stretching effect is essential to study nonlinear rheological properties. For example, we have succeeded to explain the molecular origin of shear thickening, i.e., the steady shear viscosity increases with the shear rate, by taking the nonlinear stretching effect into consideration [10]. This fact has been also confirmed by recent molecular dynamics simulations [11].

Despite a large amount of experimental [1–6] and theoretical studies [7–14] on linear dynamic response and stationary viscoelasticity, no systematic theoretical studies on transient phenomena such as stress overshoot under the startup shear flow has been reported so far. We therefore study here the stress evolution of transient networks under startup shear flow. We also compare theoretical results with experiments of aqueous solutions of a kind of HEUR (C24-HEUR [15])in detail [16].

T. Koga (✉)
Department of Polymer Chemistry
Graduate School of Engineering, Kyoto University
Kyoto 615-8510, Japan
e-mail: tkoga@phys.polym.kyoto-u.ac.jp

## Theory

### *Nonaffine Transient Network Theory*

We consider transient networks made up of telechelic polymers carrying short hydrophobic groups at their chain ends (Fig. 1). Let $v$ be the number of chains in a unit volume, $n$ the number of statistical units on a middle chain, and $a$ the size of the statistical repeat unit. The total length of the middle chain is given by $L \equiv na$.

There are fundamentally three kinds of chains in such networks: bridge chain (elastically effective chain), dangling chain, and loop chain. A bridge chain connects two different junctions, while a dangling chain has one free end. There may be many loops attached to the junctions, but we neglect them in this study for simplicity because their effect is only to reduce the number of chains in the network from the total number given by the polymer concentration to the effective number governed by the thermodynamic equilibrium condition.

We consider the network subjected under a time-dependent deformation described by the tensor $\hat{\lambda}(t)$. Let $\psi(\mathbf{r}, t)$ be the number of bridge chains per unit volume at time $t$ whose end-to-end vector is given by $\mathbf{r}$, and let $\phi(\mathbf{r},t)$ be that of the dangling chain (see Fig. 1). Time evolution of the distribution functions of bridge chains, $\psi(\mathbf{r},t)$, and that of dangling chains, $\phi(\mathbf{r},t)$ can be written as [9]

$$\frac{\partial \psi(\mathbf{r},t)}{\partial t} + \nabla \cdot [\bar{\mathbf{v}}\psi(\mathbf{r},t)] = D\nabla \cdot [\nabla + \mathbf{f}/k_{\mathrm{B}}T + \nabla \ln\ K(\mathbf{r})]\psi(\mathbf{r},t) - \beta(\mathbf{r})\psi(\mathbf{r},t) + \alpha(\mathbf{r})\phi(\mathbf{r},t) \quad (1)$$

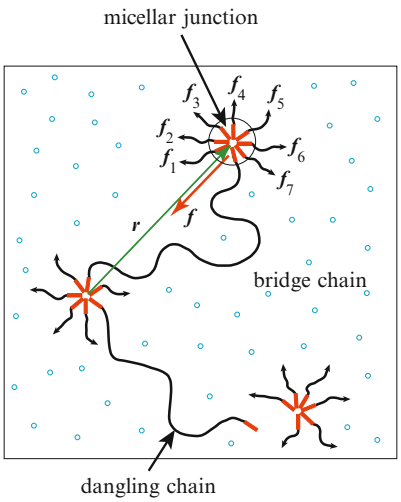


**Fig. 1** Bridge chain with the end-to-end vector $\mathbf{r}$, a dangling chain with one free end, and micellar junctions in the transient network made up of telechelic polymers

$$\frac{\partial \phi(\mathbf{r},t)}{\partial t} = D_1 \nabla \cdot [\nabla + \mathbf{f}/k_{\mathrm{B}}T]\phi(\mathbf{r},t) + \beta(\mathbf{r})\psi(\mathbf{r},t) - \alpha(\mathbf{r})\phi(\mathbf{r},t) \quad (2)$$

where $\beta(\mathbf{r})$ is the chain dissociation rate of bridge chain, i.e., the probability per unit time for an end chain to dissociate from the junction it is attached to, and $\alpha(\mathbf{r})$ is the recombination rate from a dangling chain to a bridge chain, i.e., the probability per unit time for a free end to catch a junction in the neighborhood at the position specified by the chain vector $\mathbf{r}$. $\mathbf{f}(\mathbf{r})$ is the tension acting on the chain ends. The average velocity $\bar{\mathbf{v}} = d\hat{\lambda}(t)/dt \cdot \hat{\lambda}(t)^{-1}\mathbf{r}(t)$ is given by $\bar{\mathbf{v}} = \dot{\gamma} r_y \mathbf{e}_x$ in the case of the steady shear flow with the shear rate $\dot{\gamma}$. The first term on the right hand side of Eq. (1) represents the effect of diffusion of cross-linking points with the diffusion constant $D$. $K(\mathbf{r}) = \beta(\mathbf{r})/\alpha(\mathbf{r})$ is the equilibrium constant of the conversion between a bridge chain and a dangling chain. $D_1$ in Eq. (2) is the diffusion constant for an end chain. Hereafter, we assume, as in TE, that all the dangling chains instantaneously relax to equilibrium conformation because the relaxation time of the dangling chains is much shorter than that of the bridge chains under ordinary experimental conditions of associating polymers.

The chain dissociation rate is assumed to be

$$\beta(\mathbf{r}) = \beta_0(T)\left[1 + g\tilde{f}(\tilde{r})^2\right] \quad (3)$$

where $\beta_0(T)$ is the thermal dissociation rate, and $g$ the coupling constant between the dissociation rate and the chain tension. The dimensionless tension $\tilde{f} \equiv fa/k_{\mathrm{B}}T$ is assumed to be

$$\tilde{f}(\tilde{r}) = 3\tilde{r}\left(1 + \frac{2}{3}A\frac{\tilde{r}^2}{1-\tilde{r}^2}\right) \quad (4)$$

where $\tilde{r} = r/L$ (Fig. 2). The numerical amplitude $A$ shows the effect of nonlinear stretching. If $A = 0$, the chain reduces to Gaussian. If $A = 1$, this profile agrees with that of a Langevin chain within a very high accuracy. The nonlinearity increases with the amplitude $A$. Hence, we can see the effect of nonlinear elongation of the bridge chains on the rheological properties of the networks by changing $A$.

The linear viscoelasticity of the nonaffine transient network model including the nonlinear stretching effect has been studied in ref. [9].

#### *Stress Growth*

We calculate the stress growth function $\eta^+(t)$ from Eq. (1) in the short time region by using the series expansion in powers of time. We then find that the stress growth function $\eta^+(t) \equiv \sigma_{xy}(t)/\dot{\gamma}$ is written as

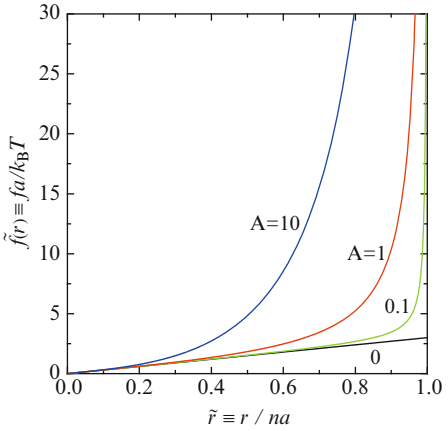


**Fig. 2** Force-elongation relation of a polymer chain, Eq. (4). The parameter $A$ characterizing the nonlinearity in the force-elongation relation is changed from curve to curve

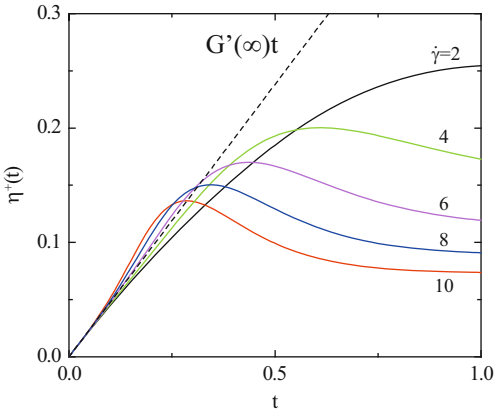


**Fig. 3** Stress growth function obtained by the transient network theory. The broken line represents the expected initial slope $G'(\infty)$ of the stress growth function. The parameters are $n = 20$, $A = 10$, $g = 0.2$, and $D = 0$

$$\eta^+(t) = \eta^{(1)}t + \eta^{(2)}t^2/2! + \eta^{(3)}t^3/3! + \cdots \tag{5}$$

where the coefficients $\eta^{(1)}$ and $\eta^{(2)}$ satisfy the following relation

$$\eta^{(1)} = G'(\omega \to \infty) \tag{6}$$

$$\eta^{(2)} = -\lim_{\omega\to\infty} \omega G''(\omega) \tag{7}$$

where $G'(\omega)$ and $G''(\omega)$ are storage and loss moduli. The first and sencond terms are independent of the shear rate $\dot{\gamma}$. The coefficient $\eta^{(3)}$ of the third-order term depends on the shear viscosity as

$$\eta^{(3)} = Q_0 + Q_2\dot{\gamma}^2 \tag{8}$$

The coefficient $Q_0$ is positive and $Q_1$ is zero for the Gaussian chain. Therefore, if the third-order term depends on the shear rate, that is considered to be due to the effect of nonlinearity in the chain tension. In the case of nonlinear chains ($A > 0$), the third-order term increases with the shear rate, so that the rapid increase (upturn) in the shear stress is expected to be observed in the short time region. This can be regarded as a transient strain hardening. We define the critical shear rate $\dot{\gamma}_c$ for this upturn in the shear stress by

$$\eta^{(2)} = \frac{1}{3}(Q_0 + Q_2\dot{\gamma}_c^2)t = 0 \tag{9}$$

The results by numerical calculation for the stress growth function are presented in Fig. 3. The shear stress shows such strain hardening (upturn) for $\dot{\gamma} > 6$. In the numerical calculation, the elastic modulus and the time is scaled by $\nu k_BT$ and $\beta_0^{-1}$, respectively. The dependence of the critical shear rate on the parameter $A$ calculated on the basis of the power expansion method Eq. (9) with $t=0.1$ is shown in Fig. 4. For $A = 10$, we have $\dot{\gamma}_c = 6.3$, which agrees well with the result in Fig. 3.

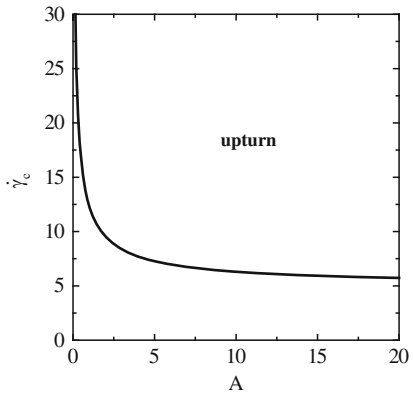


**Fig. 4** Critical shear rate $\dot{\gamma}_c$ for the stress upturn as a function of $A$. The parameters except for $A$ are the same as those in Fig. 3

In order to calculate the overshoot time $t_{max}$, at which the shear stress takes a maximum, we need higher order terms in the series expansion. By numerical calculation, it is found that the stress takes a maximum at which the total strain $\gamma = \dot{\gamma}t$ takes a certain value $\gamma_{max}$ independent of $\dot{\gamma}$.

## Experiment

In order to examine the validity of the theoretical prediction presented above, we have experimentally studied the rheological properties of HEUR aqueous solutions. We used C24-HEUR [15], which consists of a poly(ethylene

oxide) (PEO) main chain end-capped with 2-decyl-tetradecan through urethane (Fig. 5). The polymer was synthesized by condensation reaction using PEO chains ($M_w \simeq 11,000$). The weight average molecular weight ($M_w$) of the polymer was 27,000 and the molecular weight distribution, $M_w/M_n$, was 2.5 [15]. According to GPC measurements, the sample used in this study contains polymers consisting of several primary PEO chains (1–3 chains). The effect of the polydispersity in the degree of polymerization will be discussed in Sec. 4.3.

Rheological measurements were conducted with a rheometer(RDA II, Rheometrics) in the parallel-plate geometry. The plate radius was 25 mm, and the gap between the plates was 1.5 mm. The storage and loss moduli, $G'(\omega)$ and $G''(\omega)$, were measured as a function of angular frequency, ω. In the startup experiments, a constant shear rate ranged from 1 $s^{-1}$ to 100 $s^{-1}$ was applied to the solution and the stress was recorded as a function of time. Measurements were carried out at 22 ± 1°C with 2∼3 % C24-HEUR aqueous solutions. The concentration range covered in this study is well beyond the gelation threshold concentration (≃0.4% [15]). Therefore, transient networks are expected to be formed in C24-HEUR solutions under the condition in this study.

The storage and loss moduli, $G'(\omega)$ and $G''(\omega)$, for a C24-HEUR solution of 2wt% are shown in Fig. 6. The complex moduli of the solution are similar to those of Maxwell model with a single relaxation time τ as previously reported for HEUR aqueous solutions [1–4]:

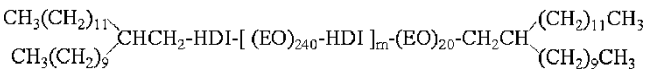


**Fig. 5** The chemical structure of C24-HEUR. (HDI:Hexamethylene diisocyanate)

$$G'(\omega) = G'_\infty \frac{\omega^2\tau^2}{1+\omega^2\tau^2} \tag{10}$$

$$G''(\omega) = G'_\infty \frac{\omega\tau}{1+\omega^2\tau^2} \tag{11}$$

where $G'_\infty$ and τ are the high-frequency modulus and relaxation time, respectively. By the fitting to the experimental results, we obtain the modulus $G'_\infty = 358$ Pa and the relaxation time $\tau = 0.739$s.

Figure 7 shows the time dependence of the shear stress obtained by startup experiments. At small shear rates $\dot{\gamma} < 1s^{-1}$, which correspond to the Newtonian regime, the stress first increases linearly with time obeying the first term in Eq. (5) with Eq. (6), and then saturates at its stationary value. The solid line in Figure 7 is the stress growth function for the Maxwell model with a single relaxation time τ (Eqs. (10) and (11)):

$$\eta^+(t) = G'_\infty \tau\left(1 - e^{-t/\tau}\right) \tag{12}$$

The experimental stress growth function in the Newtonian regime is well described by the Maxwell model.

For large shear rates $\dot{\gamma} \geq 1s^{-1}$, which correspond to the shear-thinning regime, the stress growth function deviates from that of the Maxwell model. At short times, $t < 5$s, the stress increases linearly. The stress takes a maximum, then drops towards the stationary value. For larger shear rates $\dot{\gamma} \geq 7s^{-1}$, the increase in the stress is steeper than the linear growth. This corresponds to a stress upturn predicted by the theory. Therefore, the experimental results are consistent with the theoretical prediction.

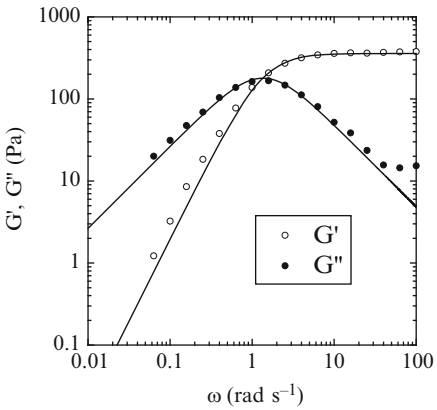


**Fig. 6** Complex moduli for a C24-HEUR aqueous solution of 2 wt%. The solid lines are obtained by fitting the data to the Maxwell model

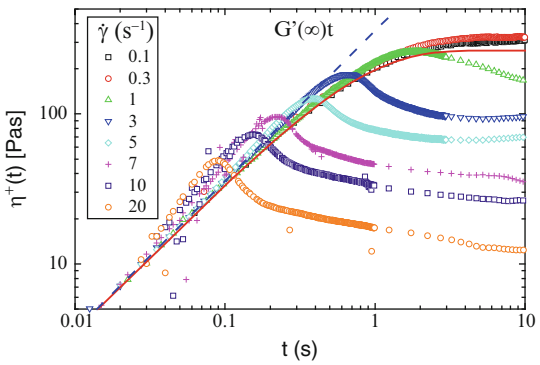


**Fig. 7** Stress growth function for a C24-HEUR aqueous solution of 2 wt%. The broken line represents the expected initial slope $G'(\infty)$ of the stress growth function

## Comparison between Theory and Experiment

### Estimation of Parameters

In this section, we make quantitative comparisons between theory and experiment. For this purpose, we first estimate the parameters in the theory from the molecular parameters and the experimental conditions.

The number of segments of the PEO main chain is estimated as $n = 160$ based on the literature value of the Kuhn length $a = 1.38$nm [17] and the length of a monomeric unit $a_0 = 0.36$ nm. From the polymer concentration $c = 2$wt% and the molecular weight, the number density $\nu$ of polymers is

$$\nu = \frac{cN_A}{M_w} = 4.46 \times 10^{23}(\mathrm{m}^{-3}) \tag{13}$$

In the case of $T = 293$K, we have

$$\nu k_B T = 1803(\mathrm{Pa}) \tag{14}$$

For the parameter $A$ characterizing the nonlinearity in the chain tension, we use $A = 2.2$ estimated from the tension-elongation curve obtained by AFM measurement [18, 19].

### Comparison of Linear Viscoelasticity and Steady Shear Viscosity

We next determine the parameters $\beta_0$, $g$, and $\alpha$ by the fitting of the linear viscoelasticity and the steady shear viscosity between theory and experiment. The obtained values are

$$\beta_0 = 0.46(\mathrm{s}^{-1}) \tag{15}$$

$$g = 20 \tag{16}$$

$$\alpha = 0.32(\mathrm{s}^{-1}) \tag{17}$$

The fitting results are shown in Figs. 8 and 9. In both cases, the experimental results are well described by the theory. From the fitting in Fig. 8, we obtain the relaxation time $\tau = 0.79$s from the peak position of $G''$ and the modulus $G'_\infty = 363$ (Pa). These values are almost the same as those by the fitting using the Maxwell model. By this analysis, we also obtain the number of elastically effective chains $\nu_e/\nu = 0.25$. This means that a quarter of the total polymer chains act as bridge chains.

### Stress Growth

We calculate the stress as a function of time by using the parameters obtained above. Figure 10 shows a comparison

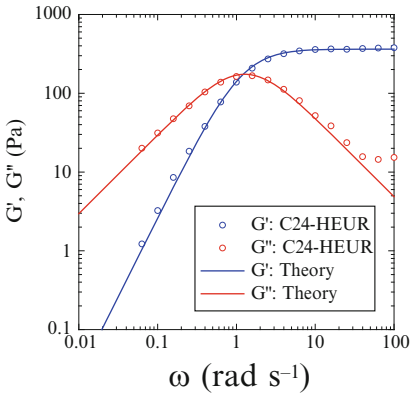


**Fig. 8** Comparison of the complex moduli between theory and experiment for a C24-HEUR aqueous solution of 2wt%

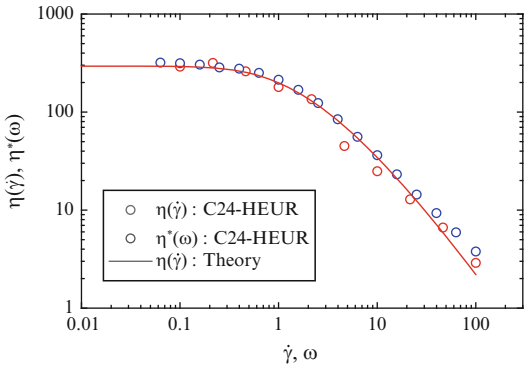


**Fig. 9** Comparison of the steady shear viscosity $\eta(\dot{\gamma})$ between theory and experiment for a C24-HEUR aqueous solution of 2wt%. Experimental data of the complex viscosity $\eta^*(\omega)$ is also shown

between the numerical and experimental results. At small shear rate $\dot{\gamma} = 1\mathrm{s}^{-1}$, the theoretical result agrees with the experimental one as shown in Figure 10(a). At large shear rates, however, the time evolution of the stress by the theory becomes slower than that of the experiment as shown in Figure 10(b). For example, the overshoot time by the theory is about twice as long as that of the experiment. In addition, the stress upturn is less pronounced in the theoretical results.

We found that this discrepancy is reduced by increasing the value of $A$. However, in order to fit the theory to the experiment, we need to use extremely large values of $A$, such as more than 1,000. Such large value of $A$ is not realistic because the tension-elongation relation Eq. (4) with such large $A$ is completely different from that measured by AFM experiment.

To explain this discrepancy, we consider the effect of the polydispersity in the degree of polymerization. According to GPC measurements, the sample used in this study consists of polymers with $m = 1,2,3$ in the chemical structural formula in Fig. 5. This is because the polymer was synthesized by condensation reaction using PEO chains ($M_w \simeq 11,000$). Since the average molecular weight $M_w = 27,000$ is close

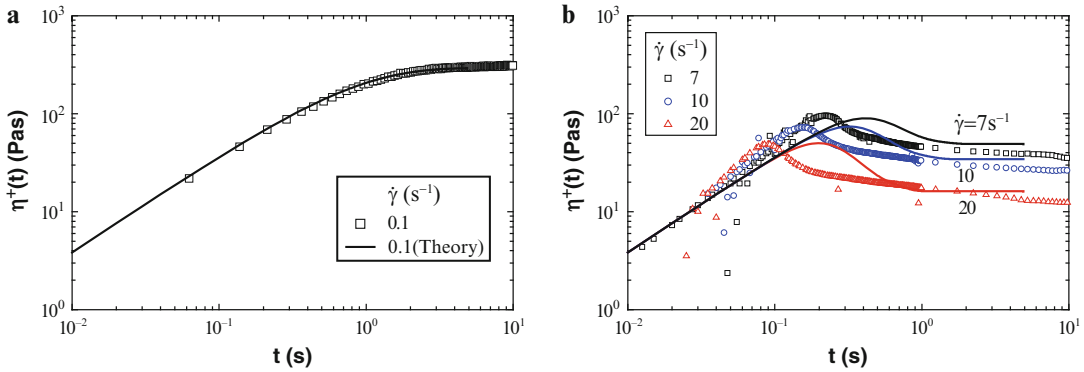


**Fig. 10** Comparison of the stress growth function between theory and experiment for a C24-HEUR aqueous solution of 2wt%

to that of polymers with $m = 2$, there are many short chains with $M_w/2$ in the system.

Since short chains are stretched to the nonlinear regime in the tension-elongation relation by small strain, phenomena related to the nonlinearity in the chain tension, such as the nonlinear viscoelasticity, are strongly affected by the presence of the short chains.

In the case of the startup flow, the stress upturn occurs due to the nonlinear stretching of bridge chains. The stress overshoot is also affected by the chain stretching effect because the chain dissociation is enhanced by the force acting on the chain ends. Therefore, if there are short chains in the system, the upturn time and the overshoot time are expected to become short.

For quantitative discussion, we estimate the time $t_L$ required for a polymer chain with $n$ to be stretched to its total length $L = na$. Let the end-to-end distance of the polymer chain at a quiescent state $\dot{\gamma} = 0$ be $R_0$. The strain $\gamma_L \equiv \dot{\gamma} t_L$ required for the chain to be stretched from $R_0$ to $L$ under shear deformation is given by

$$\gamma_L^2 = \frac{L^2}{R_0^2} - 1 \simeq \frac{L^2}{R_0^2} \tag{18}$$

The ratio of for $\gamma_L$ polymer chains with $n_1$ and $n_2$ is, therefore, given by

$$\frac{\gamma_{L2}}{\gamma_{L1}} \simeq \frac{L_2}{L_1} \tag{19}$$

This gives the ratio of the time $t_L$ as

$$\frac{t_{L2}}{t_{L1}} \simeq \frac{L_2}{L_1} = \frac{n_2}{n_1} \tag{20}$$

If, $n_2 = n_1/2$, $t_{L2} = t_{L1}/2$. Since the overshoot time is considered to be estimated by the elongation time $t_L$, the discrepancy between the theory and experiment shown in Fig. 10(b) can be explained by the effect of short chains.

## Conclusion

In this paper, we studied the stress growth in transient networks of telechelic associating polymers under the startup shear flow by using the nonaffine transient network theory. It is found that the transient strain hardening takes place due to the nonlinearity in the chain tension before the stress shows a maximum. Since the critical shear rate for the hardening is written in terms of the nonlinear parameter $A$, it gives a measure of the nonlinearity in the chain tension. The overshoot phenomena of the stress were also studied by numerical calculation.

The theoretical results were compared with our recent experimental data of HEUR aqueous solutions. The experimental data are consistent with the theoretical prediction. For detailed comparisons, we determined the parameters in the theory by the fitting of the linear viscoelasticity and the steady shear viscosity between theory and experiment. We found that the presence of short polymer chains in solutions significantly affects the transient strain hardening and the stress overshoot in associating polymer solutions because the nonlinear stretching effect of short polymers appears at small strains.

## References

1. Jenkins RD, Silebi CA, El-Asser MS (1991) p 222, Polymers as Rheology Modifiers, ACS Symposium Series 462, American Chemical Society, Washington DC
2. Annable T, Buscall R, Ettelaie R, Whittlestone D, (1993) J. Rheol. 37: 695
3. Annable T, Buscall R, Ettelaie R, Shepherd P, Whittlestone D (1994) Langmuir 10: 1060
4. Yekta A, Xu B, Duhamel J, Adiwidjaja H, Winnik MA (1995) Macromolecules 28: 956
5. Kujawa P, Watanabe H, Tanaka F, Winnik FM (2005) Eur. Phys. J. E 17: 129
6. Kujawa P, Segui F, Shaban S, Diab C, Okada Y, Tanaka F, Winnik FM (2006) Macromolecules 39: 341

7. Tanaka F, Edwards SF (1992) Macromolecules 25: 1516
8. Tanaka F, Edwards SF (1992) J. Non-Newtonian Fluid Mech. 43: 247, 272, 289
9. Tanaka F, Koga T (2006) Macromolecules 39: 5913
10. Indei T, Koga T, Tanaka F (2005) Macromol. Rapid Commun. 26: 701
11. Koga T, Tanaka F (2005) Eur Phys J E 17:115
12. Wang SQ, (1992) Macromolecules 25: 7003
13. Marrucci G, Bhargava S, Cooper SL (1993) Macromolecules 26: 6483
14. Vaccaro A, Marrucci G (2000) J. Non-Newtonian Fluid Mech. 92: 261
15. Yoshida K, Nakamura A, Nakajima Y, Fukuhara T, Inoue H, Kaneda I (2007) IFSCC magazine 10: 2
16. Kaneda I, Koga T, Tanaka F (2008) in this issue
17. Pellens L, Ahn KH, Lee SJ, Mewis J (2004) J. Non-Newtonian Fluid Mechanics 121:87
18. Oesterhelt F, Rief M, Gaub HE (1999) New Journal of Physics 1:6.1
19. There are two problems in the estimation of $A$. One is that it is difficult to fit Eq. (4) to the tension-elongation curve by AFM over the whole $r$ range. This is because there is a plateau region in the tension-elongation curve due to loose helical conformation of PEO in aqueous solutions. We estimate $A = 2.2$ in the range $0 \leq r/na < 0.8$. The other is that the value of $A$ depends on the Kuhn length $a$ used to obtain the dimensionless force from the experimental one. We use $a = 0.36$nm in this study, which corresponds to the size of a monomeric unit. These problems will be discussed in detail in our future publication. Since the conclusion of this study are not affected by small changes in $A$, we use $A = 2.2$ as a typical value.

Progr Colloid Polym Sci (2009) 136:47–54
DOI: 10.1007/2882_2009_7

# Self-assembling Structures and Sol-Gel Transition of Optically Active and Racemic 12-Hydroxystearic Acids in Organic Solvents

Hiroyuki Takeno, Tomomitsu Mochizuki, Kazuto Yoshiba, Shingo Kondo, and Toshiaki Dobashi

**Abstract** Self-assembling structures and sol-gel transition in solution of optically active and racemic 12-Hydroxystearic acids (HSA) have been investigated by means of small-angle X-ray scattering (SAXS), differential scanning calorimetry and rheological measurements. Apparently two kinds of gel, transparent gel and turbid gel were obtained in different solvents or by changing concentrations in the same solvent. The melting temperature of the turbid gel is higher than that of the transparent gel. The difference can be qualitatively explained by the dissolution of the crystals (melting point depression) in non-ideal solutions. The SAXS profiles of the transparent gel composed of fibrillar structures have a similar shape at different concentrations, although the intensity is larger for the gels with higher concentrations of 12-HSA. The SAXS analysis reveals that the cross-section of fibrils have square or circular shape (no anisotropic shape) with the radius of gyration 83 Å. On the other hand, for the turbid gel structural inhomnogeneity becomes significant with concentration. The gelation properties and the structures are found to be similar in the racemic HSA gel and the optically active (D-HSA) gel.

**Keywords** Self-assembling structures • Sol-gel transition • Low-molecular weight gelator • Small-angle X-ray scattering

## Introduction

In recent years a large number of studies have been made on the gelation of low-molecular weight molecules (the substances are referred as low-molecular weight gelators) in organic solvents [1]. The organogels exhibit thermally reversible sol-gel transition and the gelators spontaneously aggregate into fibers below the gelation temperature peculiar to the system. The fibers form three-dimensional network structures in the organic solvents, so that the solutions are solidified. It has been so far shown that the fibrillar network is composed of microcrystallites by comparing X-ray diffraction of the powdery low-molecular weight gelators with that of the gel.

12-Hydroxystearic acid (12-HSA) is well known as the low-molecular weight gelator with the chiral center on the position of the 12th carbon. Tachibana and Kambara showed by the electron microscope observation that twisted fibers were produced by evaporating the solvent in the gel of optically active 12-HSA [2,3], e.g D-12-HSA gel forms left-handed helical structures, while L-12-HSA gel forms right-handed helical structures.

In this study we investigate structures and gelation properties of three types of gels, (i) transparent gel, (ii) turbid gel (iii) gel transformed from turbid gel into transparent gel or vice versa, by changing the concentrations or temperatures. Moreover, we compare the structures of D-12-HSA gel and D,L-12-HSA gel.

## Experimental

### *Sample and sample preparation*

D,L-12-HSA (racemic HSA) was purchased from Aldrich Co. (purity 99 %) and used without further purification. D-12-HSA purchased from Wako Pure Chemical Ind. was recrystalized several times with ethanol for the sample purification. All the solutions were put into a glass tube by known amounts of sample and solvent, and the weight fraction of the mixture was determined. After the mixtures were heated, the homogeneous solutions prepared were cooled at room temperature. Three solvents (reagent grade), toluene,

H. Takeno (✉)
Department of Chemistry and Chemical Biology
Faculty of Engineering, Gunma University
Kiryu, Gunma 376-8515, Japan
e-mail: takeno@chem-bio.gunma-u.ac.jp

dodecane and polybutadiene (PB) oligomer {molecular weight of 3000 (commercial value)} were used as solvents. The PB oligomer in a toluene solution was precipitated with a large amount of warmed ethanol. The precipitated PB oligomer was dried in *vacuo* at room temperature for one week.

### Differential scanning calorimetry (DSC)

The melting temperatures and enthalpy of fusion of HSA powders (D,L-12-HSA and D-12-HSA) and the gels were determined by a differential scanning calorimeter, DSC-7 (Perkin-Elmer) with the intracooler system at a heating rate of 3 °C/min. The temperature scale of the calorimeter was calibrated at the melting temperature of indium and cyclohexane as two reference temperatures. All the samples were sealed with an aluminum cell. The peak point of the DSC trace was taken as the melting temperature.

### Small-angle and wide-angle X-ray scattering

X-ray scattering measurements were conducted at temperature of 25 °C at beam line 15A of the Photon Factory at the High Energy Acceleration Research Organization in Tsukuba, Japan. X-ray with wavelength of $\lambda = 1.5$ Å was used for the measurements. The scattering experiments were carried out at two sample-to-detector distances of 2260 mm (small-angle X-ray scattering) and 524 mm (wide-angle X-ray scattering). The scattered intensity was detected with an image intensifier coupled to a CCD camera. The two dimensional scattered images were circularly averaged in order to obtain the scattering profiles as a function of the scattering vector $q$ defined by $q = 4\pi \sin(\theta/2)/\lambda$, where θ is the scattering angle. The background scattering intensity was subtracted from the scattering intensity of the sample. The subtracted data were normalized by the intensity of the incident beam and the exposure time of the measurement. The sample was sandwiched between Kapton films with a thickness of 7.5 μm (DuPont Company) for the HSA gel in PB oligomer (sample thickness of 1mm) or put into a capillary quartz tube with a diameter of 1.5 mm for the HSA gel in toluene or dodecane in the SAXS measurements. In the WAXS measurements, it was put between polyethyrene telephtalate (PET) films with a thickness of 12 μm.

### Viscoelastic measurement

Rheological measurements were performed during the gelation process with a freely damping oscillation apparatus (Rhesca Model RD-1100 AD coaxial cylinder-type torsional viscoelastometer). The mixture of HSA and PB oligomer was poured between an outer cylinder (Pyrex tube with 13.9 mm i.d.) and an inner cylinder (stainless rod covered with Pyrex tube with 8 mm o.d.) supported by a piano wire. A freely damping oscillation was induced by rotating the inner cylinder. The shear modulus of the mixture was obtained from the damping oscillation curve. We measured it as a function of time after we quenched the sample from sol phase into gel phase by pouring liquid nitrogen into the sample jacket.

## Results and Discussion

### DSC result

Figure 1 presents the DSC traces of (a) D,L-12-HSA and D-12-HSA powders, (b) D,L-12-HSA gels in PB oligomer and (c) D-12-HSA gels in dodecane. The endothermic peaks around 80 °C in Figure 1(a) are due to the fusion of the sample; 80.6 °C for D,L-12-HSA and 80.5 °C for D-12-HSA. As shown in Figure 1, the melting temperature of D-12-HSA crystalline powder is almost the same as that of D,L-12-HSA crystalline powder. On the other hand, the endothermic peak of the gels is broader than that of the crystalline powder. As the HSA concentration of the solution gets higher, the peak area grows larger and the peak temperature becomes higher. These features are seen frequently in the melting point depression of solutions, if the difference between the eutectic temperature and their melting temperature is large.

### Phase diagram

Figure 2 shows the concentration dependence of the melting temperatures of gels of D,L-12-HSA or D-12-HSA in PB oligomer, dodecane and toluene. Furthermore, we added the cloud points above the melting temperature of the gels in Figure 2. In the temperature range higher than the melting temperature of the gel, only the liquid mixtures of HSA and PB with high concentrations of HSA were turbid. With further increase of temperature, they became transparent. Thus, the liquid mixtures of HSA and PB oligomer have an upper critical solution temperature (UCST) type of the phase diagram. The melting temperatures of the gels in toluene are sufficiently lower than those of the gels in PB oligomer or dodecane. Here, note that all the melting temperatures of the gels are lower than that of the HSA crystalline powder, which suggests that the melting of the gel may be related to the melting point depression for the HSA solution.

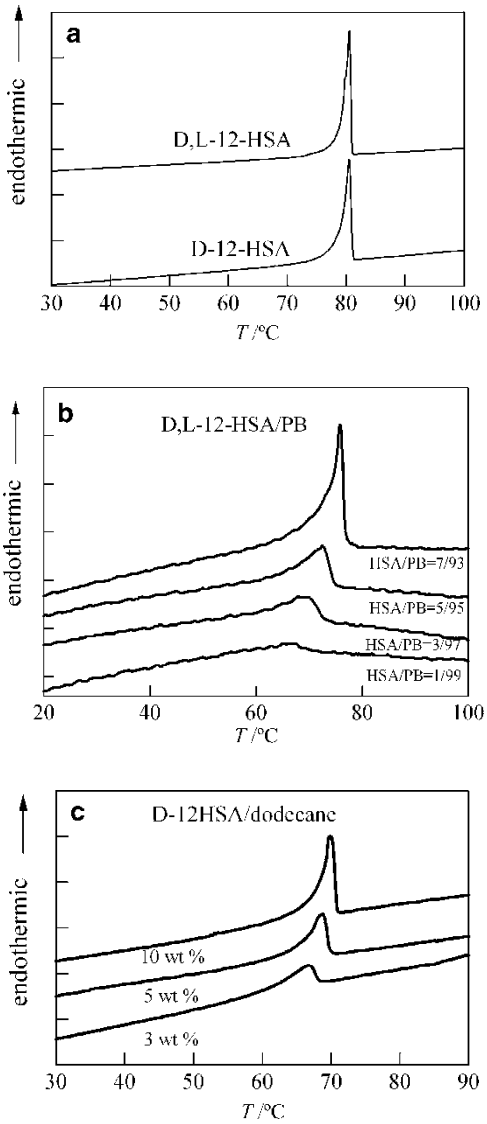


**Fig. 1** DSC traces of (a) D,L- and D-12-HSA powders, (b) D,L-12-HSA gels in PB oligomer and (c) D-12-HSA gels in dodecane. For visual clarity the traces were vertically shifted

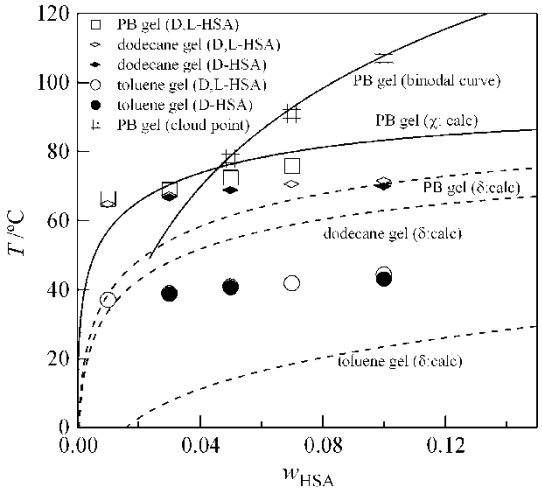


**Fig. 2** Phase diagram of D,L-12-HSA and D-12-HSA gels in PB oligomer, toluene and dodecane. The upper solid line represents the one obtained by equating the chemical potentials of two components in the two coexisting phases. The lower solid line represents the one calculated by substituting the χ parameter obtained in the above fit into eq. (1). Broken lines represent the melting curves calculated by substituting the solubility parameter of each component into eq. (1)

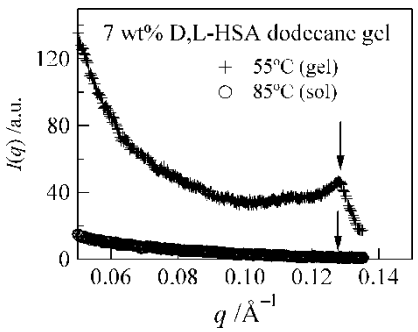


**Fig. 3** SAXS profiles of 7 wt% D,L-12-HSA gels in dodecane at 55 °C (gel state) and 85 °C (sol state)

Here let us discuss the melting temperature of the gels. So far, many studies have been made on the melting temperature of thermally reversible polymer gels composed of crystallites. Takahashi et al. showed [4] that the melting temperature was represented not by the theory of melting point depression for polymer solutions but by the Eldridge-Ferry theory [5]. Doty et al. [6] and Newman et al. [7] discussed the reason for the result and showed that many crystallites were present even above the melting temperature of the gels. In the case of low-molecular weight organo gels, whether such crystallites are present or not above the melting temperature of the gels seems to be open at the present stage. Here we show comparison of the SAXS profiles at a gel state (55 °C) and at a sol state (85 °C) for 7 wt% D,L-12-HSA gels in dodecane in Figure 3. A peak at $q = 0.13$ Å$^{-1}$ was observed at the gel state, while it disappeared at the sol state. As detailed later, the peak is attributed to (001) Bragg reflection of the crystalline structures of HSA. Thus, at least at 15°C higher temperature than the melting temperature, crystallites are not expected to be present. The finding is also supproted by the fact that no further endothermic peaks in the DSC traces were observed above the melting temperature. Therefore, assuming that the melting temperature of the gels corresponds to that of the crystals, we carry out analysis of the melting temparature of the gels.

In the framework of the Flory-Huggins theory, the melting point depression for polymer solutions is described by [8–10]

$$\frac{1}{T_{m,1}} - \frac{1}{T^*_{m,1}} = -\frac{R}{\Delta_f h}\left[\ln\phi_1 + \phi_2\left(1 - \frac{V_1}{N_2 V_2}\right) + \frac{\chi}{V_r} V_1 \phi_2^2\right] \quad (1)$$

where $T_{m,1}$ and $T^*_{m,1}$ are the melting temperature of the component 1 for the solution and that of the pure component, respectively. $N_2$ is the number of the segment of the constituent polymer (component 2). $\Delta_f h$ and $R$ are the heat of fusion for pure component and the gas constant, respectively. $\phi_i$ represents the volume fraction of $i$ th component ($i = 1$ or 2) with the molar volume $V_i$. $\chi$ is the Flory-Huggins interaction parameter and $V_r$ is the reference volume. In fact, crystals in the gel state are dispersed. Therefore, the increase of the surface energy and the increase of the entropy due to the dispersion of crystals should be considered, because eq. (1) does not include such factors. Here we neglect these effects of the dispersion, assuming that it is small [11]. The $\chi$ parameter can be divided into two terms: the enthalpic part $\chi_H$ and the entropic part $\chi_S$ ($\chi = \chi_H + \chi_S$). The enthalpic part $\chi_H$ is related to the solubility parameter.

$$\chi_H = \frac{V_1(\delta_1 - \delta_2)^2}{RT} \tag{2}$$

On the other hand, the phenomenological $\chi$ parameter is often represented by the following experimental form:

$$\chi/V_r = A + B/T \tag{3}$$

where $A$ and $B$ are constants. Here we obtained the binodal curve for the mixture of HSA and PB oligomer by the best fit of the Flory-Huggins theory to the cloud point data by using eq. (3). The condition of the fitting is obtained by equating the chemical potentials of two components in the two coexisting phases, where $A$ and $B$ are treated as the fitting parameters. We added the fitting curve calculated in the above manner in Figure 2. By using the same values of $A$ and $B$, we calculated the melting curve from the eq. (1) with the heat of fusion $\Delta_f h$ = 53200 J/mol estimated from the DSC result for the D,L-12-HSA powder. The calculated curve (PB gel ($\chi$: calc)) quite agrees to the melting data for gels. For the gels prepared in toluene, dodecane and PB oligomer, we also calculated the melting curves by using the values of the solubility parameters, where the following values for $\delta$ are used: 16.2 $(MPa)^{1/2}$ for dodecane, 18.2 $(MPa)^{1/2}$ for toluene and 17.2 $(MPa)^{1/2}$ for PB [12]. The $\delta$ value of 12-HSA was calculated according to the group contribution method, so that it is 20.5 $(MPa)^{1/2}$ [13]. The broken curves in Figure 2 represent the ones calculated in the above manner. As a consequence, we obtained the experimental inequalities of $T_{m,PB} > T_{m,dodecane} >> T_{m,toluene}$, though the calculated curves are quantitatively inconsistent with the data because factors other than the solubility parameters, e.g., $\chi_S$ and the excess volume of the solution, are neglected. Thus, the result of the melting temperature of the gels can be qualitatively explained by using the meting point depression of the crystals.

Figure 4(a) shows WAXS profiles of D,L-12-HSA powder and 7 wt% D,L-12-HSA gels in PB oligomer, dodecane and toluene. The scattering profiles of the powder and the gels have two peaks at $q$ = 0.13 $Å^{-1}$ and 0.41 $Å^{-1}$. These peaks were attributed to (001) and (003) Bragg reflections, respectively, by other researchers [14,15]. Thus, the self-assembling structures of the gels are considered to be composed of crystalline structures of HSA. When we take a careful look at the WAXS profiles in Figure 4(a), the scattering peak for the gel in toluene slightly shifts toward smaller $q$ and is broader in comparison with those of other gels. The latter result suggests that the crystalline size of the gel in toluene is smaller than those of other gels. Figure 4(b) shows a comparison of WAXS profiles for D,L-12-HSA gels in PB oligomer at various concentrations. The peak position does not change with HSA concentration, indicating that the crystalline structure in the gel does not change with HSA concentration.

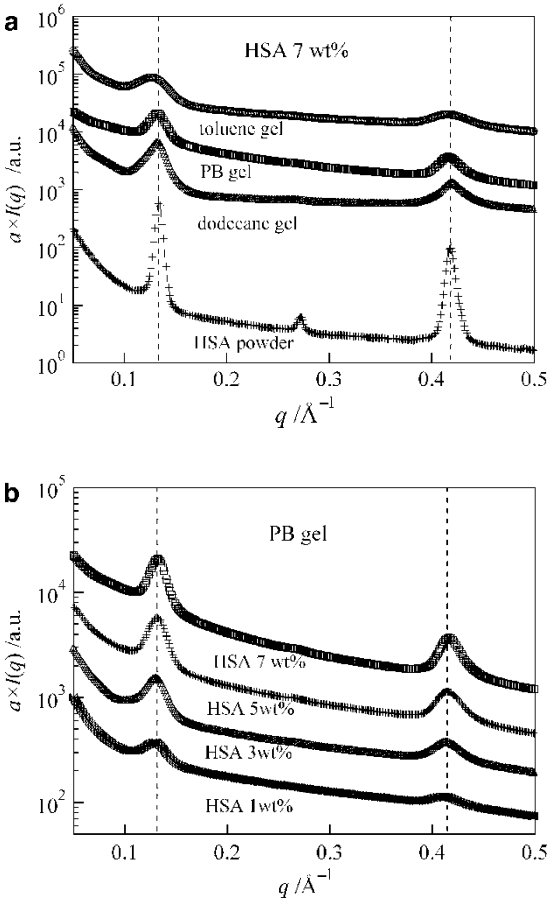


**Fig. 4** WAXS profiles of (a) D,L-12-HSA powder and the 7 wt% D,L-12-HSA gels in PB oligomer, toluene and dodecane and (b) D,L-12-HSA gels in PB oligomer with various concentrations of HSA. Dashed lines at $q$ = 0.13 Å and $q$ = 0.41 Å denote (001) and (003) Bragg reflections, respectively

## Viscoelastic measurement

Time course of shear modulus $G$ after quench from a sol state into a gel state is presented in Figure 5. After the quench, $G$ increases with time and levels off in a while. At low temperatures, we could not measure appropriate G value in the long time region due to separation between the gel sample and the inner cylinder associated with increase of solidity. As temperature decreases, G becomes larger, indicating that a stiffer gel is formed at lower temperatures. The behavior is consistent with the result of our preliminary SAXS experiments that the scattering intensity is larger at lower temperatures. The result may reflect that as the temperature lowers, the fibrils becomes denser.

## SAXS studies

Figure 6 shows SAXS profiles for the gels in toluene at various concentrations. The scattering profiles have the Bragg peak at $q = 0.13$ Å$^{-1}$, which corresponds to the (001) Bragg reflection as mentioned above. Moreover, they have a broad peak around $q \sim 0.046$ Å$^{-1}$. The scattering profiles show almost the same shape for the gels with various concentrations, though the larger scattering intensity is obtained for the gel with the higher concentrations of HSA. The former result suggests that the geometry of the fibers is not influenced by the concentration of HSA. We try to analyze the data with the scattering function from rod-like particles. The form factor $P(q)$ from the rod particles is described by [18]

$$P(q) = \frac{L\pi}{q} I_c(q) \tag{4}$$

for $2\pi/L << q$ where $I_c(q)$ is related to the scattering intensity from the structure of the particle in the cross section. For $2\pi/L << q << 2\pi/R_c$, $I_c(q)$ can be represented by the Guinier-type scattering behavior

$$I_c(q) = A^2 \exp\left(-\frac{R_c^2 q^2}{2}\right) \tag{5}$$

where $A$ is the area of the cross-section. Thus, linear relation between $\ln(Iq)$ vs $q^2$ is obtained from eqs. (4) and (5). We show a plot of $\ln(Iq)$ vs $q^2$ for the D,L-12-HSA gels in toluene in Figure 7. We estimated the value of $R_c$ from the slope of the figure, which is listed in Table 1. As shown in Table 1, the value of $R_c$ has almost the same value (82 – 85 Å) and is not almost affected by the HSA concentration. Next, we analyze the geometry of the cross-section of the rods. From eq. (4), multiplying the scattering intensity by $q$ represents information on the geometry of the cross-section of the particles. Therefore, we show the double logarithmic plot of $q\,I(q)$ vs $q$ in Figure 8. We tried to fit the cross-sectional function with rectangular shape by

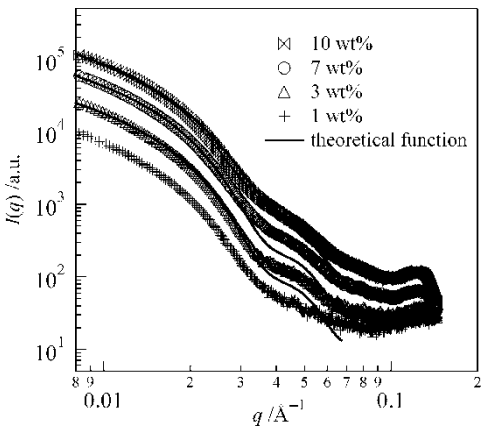


**Fig. 6** SAXS profiles for D,L-12-HSA gel in toluene. The solid curves represent the fitted curves using theoretical function of eq. (7)

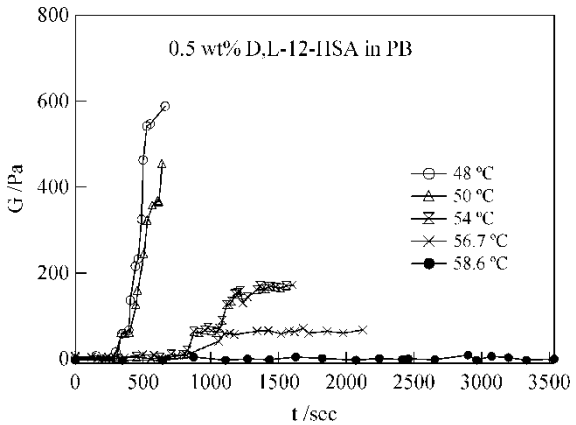


**Fig. 5** Time course of shear modulus $G$ for 0.5 wt% D,L-12-HSA gel in PB oligomer after the quench into a given gel state

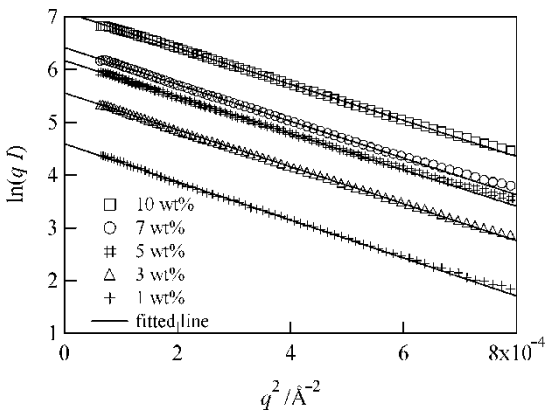


**Fig. 7** Plot of $\ln(Iq)$ vs $q^2$ for the D,L-12-HSA gel in toluene. Solid lines are the fitted ones to eq. (5)

**Table 1** The values of the radii of gyration of the cross-section of fibrils estimated by SAXS measurements for D,L-12-HSA / D-12-HSA mixture in toluene. $w_{HSA}$ represents the percent of the total amount of D,L-12-HSA and D-12-HSA in toluene

| | $R_c$ of D,L-12-HSA/ D-12-HSA gel in toluene (Å) | | | | |
|---|---|---|---|---|---|
| $w_{HSA}$ (wt%) | 100/0 | 80/20 | 50/50 | 20/80 | 0/100 |
| 1 | 85.0 | - | - | - | - |
| 3 | 83.7 | - | - | - | |
| 5 | 83.1 | - | - | - | |
| 7 | 83.6 | 81.2 | 82.1 | 81.7 | 80.6 |
| 10 | 82.7 | - | - | - | - |

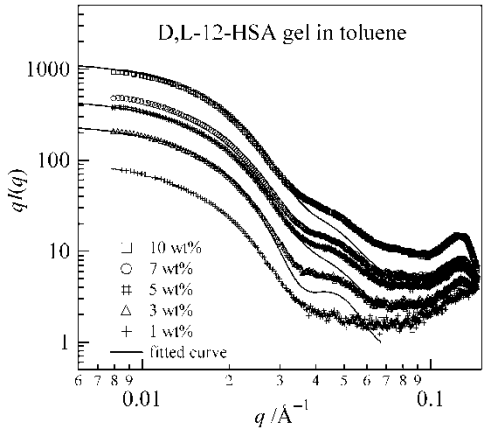


**Fig. 8** Double logarithmic plot of $Iq$ vs $q$ for D,L-12-HSA gel in toluene. Solid curves are the fitted ones to eq. (6)

changing the anisometry (the ratio of the values of $a$ and $b$) to the data with keeping $R_c$ constant. The cross-sectional scattering intensity of the particles with rectangular shape is described by [19]

$$I_c = \frac{2}{\pi}\int_0^{\pi/2}\left[\frac{\sin(qa\sin\beta/2)}{qa\sin\beta/2}\right]^2\left[\frac{\sin(qb\cos\beta/2)}{qb\cos\beta/2}\right]^2 d\beta \quad (6)$$

where $a$ and $b$ are the lengths of the sides of the rectangular cross-section, respectively. $\beta$ is the angle between the scattering vector $q$ and the axis of the rod. Otherwise, the scattering function from the circular cross-section (i.e., cylinder) with the height $2H$ ($2H = L$) and the diameter $2R$ was taken into consideration.

$$P(q) = 4\int_0^{\pi/2}\left[\frac{\sin^2(qH\cos\beta)}{(qH\cos\beta)^2}\right]\left[\frac{J_1^2(qR\sin\beta)}{(qR\sin\beta)^2}\right]\sin\beta d\beta \quad (7)$$

In the fits, the inhomogeneity of the length with Gaussian distribution was taken into consideration. The result of the fit with eq. (6) is shown in Figure 8 (The solid curve represents the fitted one). The scattering curve of rods with equal length of the sides (i.e., square) fits the data well. The fitted curve

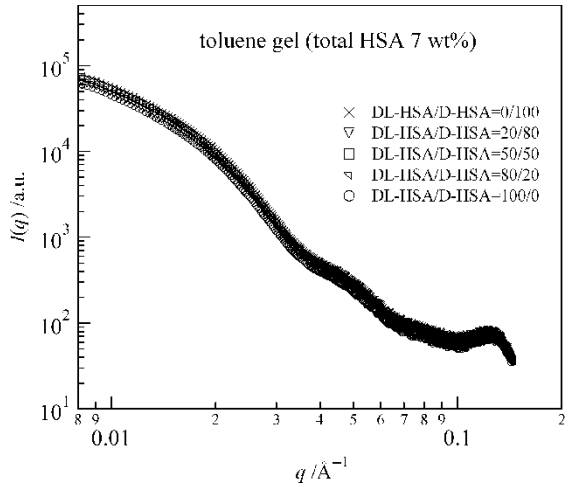


**Fig. 9** Comparison between the scattering profiles of DL-12-HSA gel, D-12-HSA gel and the mixture in toluene

well describes the scattering behavior in small $q$ and the position of the broad peak around $q \approx 0.046$ Å$^{-1}$. However, the peak intensity in the fit is smaller than that of the data in high $q$. The value of the side length (mean value $2a = 204$ Å, the standard deviation 15 Å) obtained thus is very consistent with the value reported using SANS by Terech et al [16,17]. On the other hand, in the fit using eq. (7) the values of $R$= 117 Å and the standard deviation 20 Å were obtained. However, it turned out to be difficult to determine that the cross-section is circular or square from our data, because the peak of the high order could not be clearly observed. Figure 9 represents a comparison between the scattering profiles of DL-12-HSA gel, D-12-HSA gel and the gel composed of the mixture in toluene. The result indicates that all the scattering profiles have almost the same shape, indicating that the cross-section of the fiber has the same geometry and almost the same size. The result is consistent with that of Terech et al [16]. Using eq. (5) we estimated the value of $R_c$ for D-12-HSA gel and DL-12-HSA/ D-12-HSA gel. The result is also added in Table 1. The values of $R_c$ for D-12-HSA gel and DL-12-HSA/ D-12-HSA gel are slightly smaller than that of DL-12-HSA gel. Thus, apart from slight difference in size, it turned out to be difficult to distinguish the difference between their self-assembling structures in terms of SAXS measurement. Figure 10 shows the double logarithmic plots of $q$ $I(q)$ vs $q$ for D,L-12-HSA gels in dodecane. The scattering profiles have a broad peak around $q \approx 0.045$ Å$^{-1}$, near that of the gel in toluene. However, the scattering behavior in small $q$ depends upon the HSA concentration unlike the gel in toluene. The power in small $q$ $\{I(q) \sim q^{-m}\}$, i.e., the value of $m$ changes from 1.7 to 2.9, as the concentration of HSA increases. The increase of the scattering intensity in small $q$ may be related to inhomogeneity of the gel, i.e., nonuniform spatial distribution of network. Thus, the concentration dependence of the self-assembling

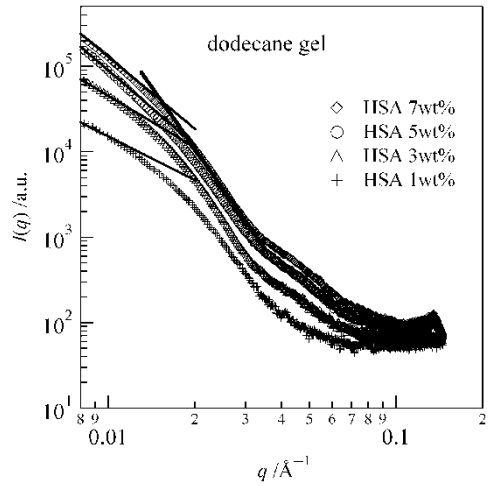


**Fig. 10** Small-angle X-ray scattering profiles for the gel in dodecane with various concentrations

structures is found to be largely different between the transparent gel and the turbid gel.

## Conclusion

We studied the self-assembling structures and the melting temperatures of 12-HSA gel in different solvents by means of small-angle X-ray scattering and differential scanning calorimetry. The melting curve of the gels obtained can be quite explained by the melting point depression of the micorcrystallite. It turned out to be difficult to distinguish between the structure of the racemic gel and that of the optically active gel from SAXS measurements.

**Acknowledgment** H. T. acknowledges Prof. T. Hashimoto for his valuable comments.

## References and Notes

1. Terech P, Weiss RG (1997) Chem. Rev. 97:3133
2. Tachibana T, Kambara H (1969) Bull. Chem. Soc. Jpn, 42:3422
3. Tachibana T, Kambara H (1968) J. Colloid Sci., 28:173
4. Takahashi A, Nakamura T, Kagawa I (1972) Polymer J. 3:207
5. Eldridge JE, Ferry JD (1954) J. Chem. Phys. 58:992
6. Doty P, Wagner H, Singer S, (1947) J. Phys. Chem. 51:32
7. Newman S, Krigbaum WR, Carpenter KK (1956) J. Phys. Chem. 58:968
8. Hildebrand JH, Scott RL (1950): The solubility of Nonelectrolytes 3rd ed Dover Publications, New York
9. Flory PJ (1941) J Chem Phys, 9:660
10. Huggins ML (1941) J Chem Phys, 9:440
11. In order to experimentally estimate the effect of dispersion of the crystals, we measured the melting temperature of the sample prepared by freeze-drying of 7wt% D,L-12-HSA gel in benzene, i.e., the structures are expected to be frozen in the dispersed state. As a consequence, the melting temperature was 79.4 °C, which is by 1.2 °C lower than that of the bulk crystal. Therefore, the effect of the dispersion of the crystal in the gel state is expected to be small
12. Polymer HandBook, third ed
13. Van Kreveren (1972): Properties of Polymers, Elsevier Publishing Company, Amsterdam
14. Tachibana T, Mori T, Hori K (1980) Bull. Chem. Soc. Jpn, 54:1714
15. Terech P (1991) Colloid Polym. Sci., 269: 490
16. Terech P, Rodriguez V, Barnes JD, McKenna GB (1994) Langmuir, 10:3406
17. Terech P, Pasquier D, Bordas V, Rossat C (2000) Langmuir, 16:4485
18. Feigin LA, Svergun DI (1987): Structure Analysis by Small-Angle X-ray and Neutron Scattering. Plenum Press, New York
19. Mittelbach, Porod G (1961) Acta Phys Austriaca, 14:185

Progr Colloid Polym Sci (2009) 136:55–62
DOI: 10.1007/2882_2009_8

# The Gel Point and Network Formation in the Polymerisation of an Epoxy-Amine System Including Ring Formation

Yutaka Tanaka[1], John L. Stanford[2], and Robert. F. T. Stepto[2]

**Abstract** The molecular scheme, accounting for intramolecular reaction, was constructed to predict the gel point in the $RA_4$+$R'B_2$ type polymerisation. The scheme is intended to be applied for the cure of a polyoxypropylene (POP) diamine and the diglycidyl ether of bisphenol A, and based on the classification of the reaction state of the POP diamine unit. The linear sequence of structural units for the chain growth in the cure was given to define the gelation following Ahmed-Rolfes-Stepto theory, where a ring-forming parameter ($\lambda_a$) and internal concentration ($P_{ab}$) of the reactive groups can be applied to characterise the competition between intermolecular and intramolecular reaction. The chain growth was expressed by the fractional concentration of the reacted hydrogen atoms that belong to reactive amino groups, which corresponds to the extent of reaction determined experimentally. From the result of the calculation, the delay of gel point from Flory – Stockmayer criterion is shown to increase with the increase in the internal concentration.

**Keywords** Gel Points • Network • Ring Formation • Epoxy – Amine • Polycondensation

## Introduction

Polymerisation of multifunctional monomers that generate branched polymers leads to progressively larger molecules. They are often expressed as $RA_{fa} + R'B_{fb}$ polymerisation where $f_a$ and $f_b$ are the functionalities for monomers of RA and R'B respectively. At a critical extent of reaction or density of bonds, the size of the largest molecules formed spans the reaction volume and this is termed the gel point. Classical theories of gelation consider ideal reactions, which are defined using two assumptions; all like groups are equally reactive, and there is no intramolecular reaction [1]. Many authors have considered such ideal reactions [1–9]. In many real systems, neither assumption is valid. When more realistic models are attempted, in general, only one of the assumptions is removed. In contrast, the present paper treats the gel points of an epoxy-amine system including the effects of unequal reactivity and intramolecular reaction.

To quantify the numbers and types of ring structures formed is important, because intramolecular reaction, leading to ring structures, delays the gel point[10–20]. In the previous work, the gel points determined experimentally in the polymerisation of a polyoxypropylene (POP) diamine and the diglycidyl ether of bisphenol A (DGEBA) were presented [21]. The polymerisations are of the type $RA_4 + R'B_2$. The present paper, describes the reaction scheme, gel-point condition and the results of the calculation of the relation between the gel point and the ring-forming parameter.

The competition between intermolecular and intramolecular reaction in the course of a $RA_{fa} + R'B_{fb}$ polymerisation can be characterised by the mutual, internal concentration of reactive groups, which is denoted by $P_{ab}$. In order to find the relationship between $P_{ab}$ and the delay in gelation for the DGEBA and POP diamine polymerisations, a molecular reaction scheme was constructed. The scheme describes the irreversible reaction of a tetrafunctional monomer ($RA_4$) with a bifunctional monomer ($R'B_2$) and intramolecular reaction incorporated into the gel-point condition by means of a development of Ahmed-Rolfes-Stepto (ARS) theory [15,19].

## Reaction Scheme

The scheme considered is for the reaction between a POP diamine with four reactive hydrogen atoms, and DGEBA, having two epoxy groups. In the course of network formation,

Y. Tanaka (✉)
[1]Department of Materials Science and Engineering, Faculty of Engineering, University of Fukui
Fukui, 910-8507, Japan
e-mail: tanaka@matse.u-fukui.ac.jp
[2]Polymer Science and Technology Group, School of Materials, The University of Manchester
Grosvenor Street, Manchester, M1 7HS, U.K

the primary amine and an epoxy group react with a rate constant $k_1$; hydrogen atoms are categorised as being in states H1, H2 and HR according to the reactions. That is, the hydrogen atoms that belong to unreacted amino groups are defined as H1, the unreacted hydrogen atoms that belong to the semi-reacted amino groups are defined as H2, and reacted hydrogen atoms are defined as HR. In the reaction with rate constant $k_1$, two H1 atoms are lost, and one H2 atom and one HR atom are formed. The hydrogen atom H2 on the secondary amine group and an epoxy group react to form the tertiary amine group with rate constant $k_2$. In the reaction with $k_2$, one H2 atom is lost and one HR atom is formed.

The concentrations of H1, H2, HR atoms and epoxy groups, are written as $C_{H1}$, $C_{H2}$, $C_{HR}$ and $C_{EP}$ respectively. Let the concentration of H1 and epoxy groups before the reaction(i.e. $t = 0$ ) be $C^0_{H1}$, $C^0_{EP}$, then $p_{HR}$, the extent of reaction of hydrogen atoms is;

$$p_{HR} = \frac{C_{HR}}{C^0_{H1}}. \tag{1}$$

It should be remarked that the value of $p_{HR}$ is directly measurable by the FT-IR spectroscopy[21, 22]. Further, $p_{HR}$ can easily be incorporated into the equation of chain growth expressed in terms of the probability of paths shown below. The fractional concentrations of H1 and H2 atoms and reacted epoxy groups can be defined as; $p_{H1} = (C_{H1}/C^0_{H1})$, $p_{H2} = (C_{H2}/C^0_{H1})$, $p_{EP} = (C_{EPR}/C^0_{EP})$. The reactive-group ratio for the reaction mixture, $r_{EP}$, can be written as, $r_{EP} = (C^0_{EP}/C^0_{H1})$. Solving the rate equations with other experimental conditions gives, in terms of $p_{H1}$, $p_{H2}$ and $p_{HR}$ , with the rate-constant ratio of $\rho$ $(= k_2/k_1)$

$$p_{H2} = \frac{1}{2-\rho}\left(p_{H1}^{(\rho/2)} - p_{H1}\right) \tag{2}$$

$$p_{HR} = 1 - \frac{1-\rho}{2-\rho}p_{H1} - \frac{1}{2-\rho}p_{H1}^{(\rho 12)}. \tag{3}$$

The results of calculations of the relationship between $p_{H1}$, $p_{H2}$ and $p_{HR}$ are displayed in Figure 1 as the curves of $p_{H1}$*vs.* $p_{HR}$ and $p_{H2}$ *vs.* $p_{HR}$ , for different values of $\rho$. The increase in $p_{HR}$ from 0 to 1 shows the progress of the polymerisation to completion. After the H2 atom is produced in the $k_1$-reaction, the consumption of H2 follows in the $k_2$-reaction, these two reactions produce the maxima in the $p_{H2}$*vs.* $p_{HR}$ curves.

Six states of the diamine unit can be defined as shown schematically in Figure 2. The classification of the diamine unit shown here is similar to that of Dušek et al [11]. However, its use to define the gel point is different. The gel point in the study of Dušek et al is defined as the point of divergence of the mass-average molar mass. Whereas the gel point is derived in terms of the probabilities of continuing paths in this work so as to incorporate experimentally measurable value of $p_{HR}$. The divergence of molecular mass has widely been used to estimate the gel point. Also the relationship with the gel point derived from the probability of paths has been discussed.[23]

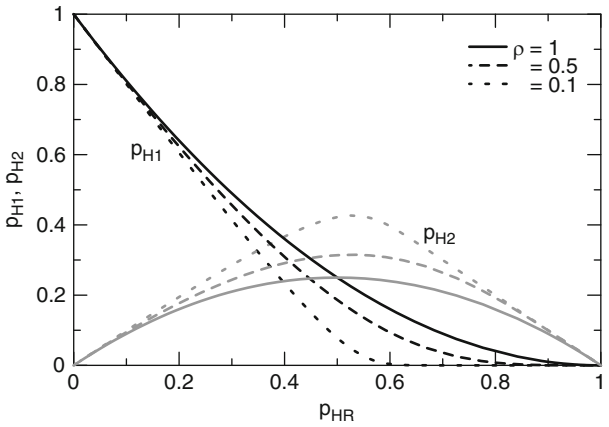


**Fig. 1** The relations of $p_{H1}$ *vs.* $p_{HR}$ and $p_{H2}$ *vs.* $p_{HR}$ with different values of $\rho$ $(=k_2 / k_1)$

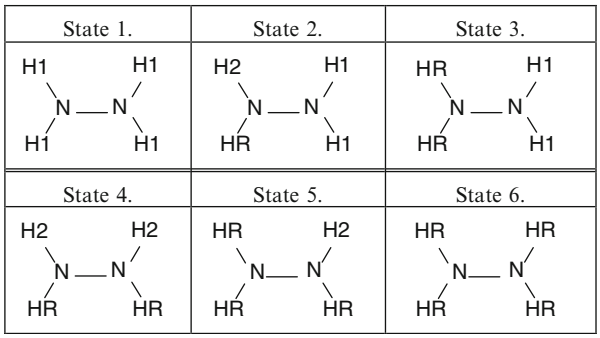


**Fig. 2** Classification of the state of reaction for POP diamine unit in the progress of polymerisation. Numbers are placed as State $i$, $i$ = 1–6

If the mole fractions of the six states are written as $X_i$, $i$=1–6, they can be expressed as functions of $p_{H1}$, $p_{H2}$ and $p_{HR}$. Hence, the $X_i$ are functions of $p_{HR}$ which is experimentally measurable. Figure 3 shows the results of calculation of $\rho$=1 on the relation between $X_i$, $i$=1–6, and $p_{HR}$. As expected from the result of $\rho$=1 in Figure 1, symmetrical curves have been obtained for $X_i$*vs.* $p_{HR}$.

## Gel Point

To define the gel point, the probability of path continuation is introduced. The assumed linear sequence of structural units used to define gelation in the reaction of DGEBA and

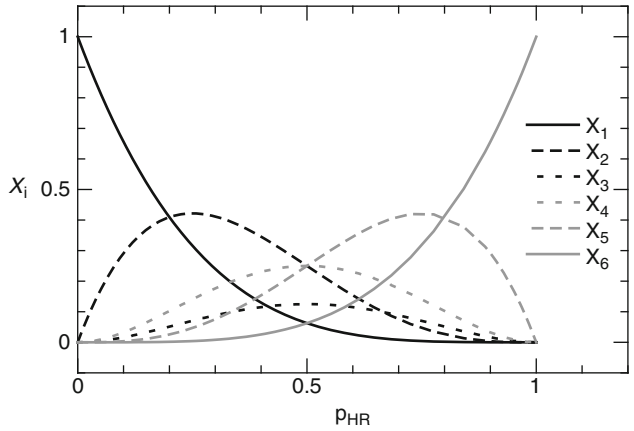


**Fig. 3** Results of calculation on mole fractions of POP diamine units, $X_i$, $i$=1–6, corresponding with State $i$ shown in Figure 2

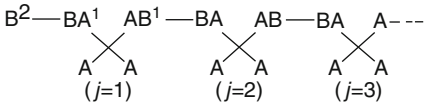


**Fig. 4** Linear sequence of reactive units used to show chain growth and to define the size of the ring structure, $j$. The reactive group A corresponds to an H atom of the amino group and the group B to an epoxy group

**Table 1** Probability of Choosing and Number of Paths for Each H Atom of Amino Group in the Chain Growth

| | State 2 | | State 3 | | State 4 | | State 5 | | State 6 |
|---|---|---|---|---|---|---|---|---|---|
| H Atom Chosen | H1, H2 | HR | H1 | HR | H2 | HR | H2 | HR | HR |
| Probability of Choosing | $\frac{3}{4}$ | $\frac{1}{4}$ | $\frac{1}{2}$ | $\frac{1}{2}$ | $\frac{1}{2}$ | $\frac{1}{2}$ | $\frac{1}{4}$ | $\frac{3}{4}$ | 1 |
| Number of Paths | 1 | 0 | 2 | 1 | 2 | 1 | 3 | 2 | 3 |

POP diamine is shown in Figure 4, following ARS theory [15]. The reactive group A corresponds to an H atom of the amino group and the group B to an epoxy group. The variable $j$ gives the size of the ring written below. Suppose that the chain in Figure 4 grows from right to left, then $\gamma_a$ is defined as the probability of a continuing path from a diamine unit attached to a randomly chosen H atom to the next diamine unit. Likewise, $\gamma_b$ is defined.

In order to obtain the expression of network formation, we need to consider the probability of continuing paths from a randomly chosen group to a statistically equivalent group; for example, a path from $B^1$ to $B^2$ in Figure 4. Let the fractions of A and B groups be $X_a$ and $X_b$ respectively, then the probability of continuing path, $\gamma$ can be given as below;

$$\gamma = X_a\gamma_a + X_b\gamma_b \tag{4}$$

In order to derive the expression of $\gamma_a$, the probability of chain growth from a diamine unit to next diepoxy unit is considered in terms of the states of diamine unit and the count of the number of continuing paths. If a diamine unit of State 2 is chosen, more specifically, an HR atom in State 2 is chosen, then it gives no paths out. If it is either an H1 or H2 atom, it gives one path out, which is HR in State 2. Because the probability that either an H1 or H2 atom is chosen in State 2 is 3/4 (see Figure 2), the contribution from State 2 to the chain growth is $3X_2/4$; it is given by the product of the number of paths and the probability. The probabilities that individual H atom is chosen and the number of paths out in each state of POP diamine unit are summarised in Table 1. The probability of chain growth from diepoxy to next diamine unit is $p_{EP}$. Hence, $\gamma_a$ can be expressed by $p_{EP}$ and the total of the contributions from the respective state of diamine unit.

$$\gamma_a = \left(\frac{3}{4}X_2 + \frac{3}{2}X_3 + \frac{3}{2}X_4 + \frac{9}{4}X_5 + 3X_6\right) \times p_{EP} \tag{5}$$

Similarly, $\gamma_b$ can be expressed by $p_{EP}$ and the total of the contribution from the respective state of diamine unit.

$$\gamma_b = p_{EP} \times (Q_{HR,3} + Q_{HR,4} + 2Q_{HR,5} + 3Q_{HR,6}) \tag{6}$$

Following relations are obtained taking account of the number of HR atoms in the respective state.

$$Q_{HR,1} = 0, \quad Q_{HR,2} = \frac{X_2}{X_2 + 2X_3 + 2X_4 + 3X_5 + 4X_6},$$
$$Q_{HR,3} = \frac{2X_3}{X_2 + 2X_3 + 2X_4 + 3X_5 + 4X_6},$$
$$Q_{HR,4} = \frac{2X_4}{X_2 + 2X_3 + 2X_4 + 3X_5 + 4X_6},$$
$$Q_{HR,5} = \frac{3X_5}{X_2 + 2X_3 + 2X_4 + 3X_5 + 4X_6},$$
$$Q_{HR,6} = \frac{4X_6}{X_2 + 2X_3 + 2X_4 + 3X_5 + 4X_6}.$$

The calculation results of $\gamma$ as a functions of $p_{HR}$ with $r_{EP} = 1$ are shown in Figure 5. $r_{EP} = 1$, namely $X_a = X_b = 1/2$, is the value used in the polymerisation of POP diamine and DGEBA[21]. $\rho$ values used for the calculations are 1, 0.5, 0.1. The $\gamma$ value increases from 0 to 3 as $p_{HR}$ increases from 0 to 1. The result that $\gamma$=3 as $p_{HR}$=1 comes from the fact that functionalities of POP diamine and DGEBA are 4 and 2 respectively; when all the groups are reacted POP diamine units are all in State 6 which has 3 paths of continuation from a randomly chosen reacted amino group.

Curves of $\gamma$ *vs.* $p_{HR}$ depend on $\rho$, as can be seen in the inset figure; $p_c$, the value of $p_{HR}$ corresponding to $\gamma$=1 is

$p_c$=0.577 for $\rho$=1 which agrees with the value calculated from Flory-Stockmayer theory [1]. As $\rho$ decreases $p_c$ shifts to a higher value, which is confirmed to come from the dependence of the $\gamma_b$*vs.* $p_{HR}$ curve on $\rho$ as shown in Figure 6. The $\gamma_a$*vs.* $p_{HR}$ curve, which is calculated from eq. (5), does not depend on $\rho$, and thus $p_{HR}$ value corresponding to $\gamma$=1 is constant. Whereas, it shifts to a higher $p_{HR}$ value as the decrease in $\rho$ in the curve of $\gamma_b$*vs.* $p_{HR}$ calculated from eq. (6). The shift of $p_c$ corresponds to the delay of gel point. The decrease in $\rho$ means less reactions of $k_2$; that is, formation of State 3, 5 and 6 is delayed. State 5 and 6 brings about bifurcation that leads to the gelation. It can be considered that the delay of gel point with the decrease in $\rho$ is caused by the delay of formation of State 5 and 6.

## Ring–Forming Parameter

For an $RA_4 + R'B_2$ type polymerisation, competition always occurs between intermolecular and intramolecular reaction[9]. In the competition between intermolecular and intramolecular reaction, let $C_{b,int}$ be the internal concentration of B groups from the same molecule around an A group being on the point of reacting, and let $C_{b,ext}$ be the concentration of B groups from other molecules. Then, the ring-forming parameter $\lambda_b$ can be given concerning B group as;

$$\lambda_b = C_{b,int}/\left(C_{b,ext} + C_{b,int}\right) \tag{7}$$

$C_{a,int}$, and $C_{a,ext}$ can be similarly defined when a B group is about to react with an A group. The definition of $\lambda_a$ is as follows.

$$\lambda_a = C_{a,int}/\left(C_{a,ext} + C_{a,int}\right) \tag{8}$$

The size of the ring structure can be given by $j$ as shown in Figure 4. For example, the smallest ring structure is comprised of a pair of POP diamine and DGEBA units. This structure is regarded as that of $j = 1$. The second smallest ring consists of two of each unit and is regarded as the structure of $j = 2$. In consequence, $C_{b,int}$ is the total of the concentration of each size.

$$C_{b,int} = \sum_{j=1}^{\infty} C_{b,int,j} \tag{9}$$

$C_{b,int,\,j}$ , $j = 1, 2$ – is the concentration of the B groups to form each size of the ring structure around an A group. Likewise, $C_{a,int}$ can be written by the total of the concentration of the A groups to form each size of the ring structure around the B group.

$$C_{a,int} = \sum_{j=1}^{\infty} C_{a,int,j} \tag{10}$$

In counting the concentration $C_{b,int,\,j}$, it is necessary to consider a specific feature of the ring structure; that is, it can be thought of as a chain which end-to-end distance is equal to zero[24]. It is assumed that the distribution of end-to-end distance can be written by independent Gaussian sub-chain statistics of eq. (11).

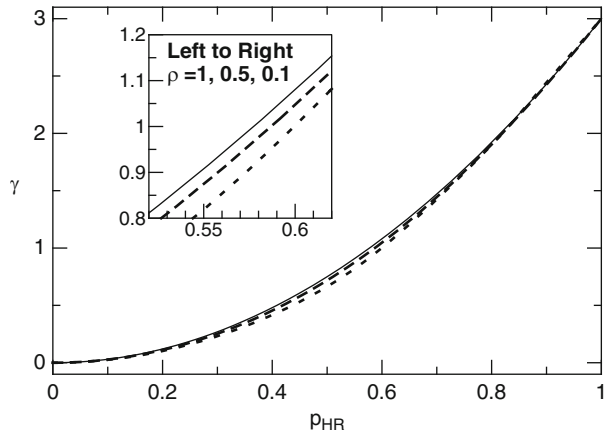


**Fig. 5** The results of calculations for $\gamma$ as functions of $p_{HR}$ with different $\rho$ values. The inset figure magnifies near $\gamma = 1$. $\rho$ =1: solid thin line, $\rho = 0.5$: dashed line, $\rho$=0.1: dotted line

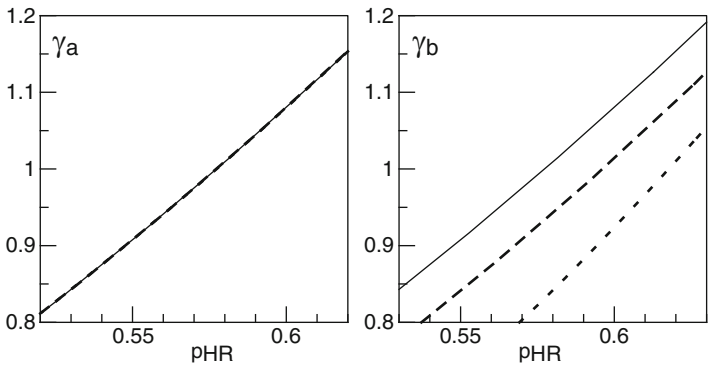


**Fig. 6** The curves of$\gamma_a$ *vs.* $p_{HR}$ (left) and $\gamma_b$ *vs.* $p_{HR}$ (right) are shown with different $\rho$ values near $\gamma_a$=$\gamma_b$=1. $\rho$=1: solid thin line, $\rho$=0.5: dashed line, $\rho$=0.1: dotted line. It should be remarked that $\gamma_a$ *vs.* $p_{HR}$ does not depend on $\rho$, whereas $\gamma_b$ *vs.* $p_{HR}$ depends on $\rho$

$$P(r) = \left(\frac{3}{2\pi v b^2}\right)^{3/2} \exp\left(-\frac{3r^2}{2vb^2}\right) \tag{11}$$

$$\langle r^2 \rangle = vb^2 \tag{12}$$

$r$ is end-to-end vector. $b$ is the effective bond length of the chain of n bonds. Although Gaussian statistics was applied in this work for polymer chain including POP diamine unit and DGEBA unit, it requires further investigation for this assumption. In particular, DGEBA can be thought of as a relatively rigid unit, thus it is likely to be inapplicable in Gaussian statistics. If a definition is given on $P_{ab}$ with substituting $r$=0 and dividing by $N_{av}$ , Avogadro's number, then it becomes a useful parameter in counting the concentration of $C_{a,int,\,j}$ and $C_{b,int,\,j}$ [15].

$$P_{ab} = \frac{1}{N_{AV}} \left(\frac{3}{2\pi\langle r^2\rangle}\right)^{3/2} \tag{13}$$

Similar approach to describe intramolecular reaction has been reported for $RA_3$ + $R'B_2$ type polymerisation[25]. $P_{ab}$ means the concentration of intramolecular B groups of $j$=1 around an A group; it can also be said that it means the concentration of intramolecular A groups of $j = 1$ around a B group.

Consequently, eq. (9) can be calculated as shown below.

$$C_{b,int} = \sum_{j=1}^{\infty} \frac{1}{N_{AV}} \left(\frac{3}{2\pi\langle r^2\rangle}\right)^{3/2} = P_{ab} \sum_{j=1}^{\infty} \left(\frac{1}{j}\right)^{3/2} = 2.61 P_{ab} \tag{14}$$

In the above calculation Truesdell function was taken into account [26]. Similarly, $C_{a,int}$ =2.61$P_{ab}$ can be given and an expression of $\lambda_a$ is derived;

$$\lambda_a = P_{ab}/C_a^0 \tag{15}$$

where $C^0{}_a$ is the concentration of A group before the reaction and $C^0{}_a$=$C^0{}_{H1}$ in this work.

## The Path Continuation and Ring–Forming Parameter

*Continuation From Diamine to Diamine Units.*

In order to obtain an expression for $\gamma$ into which the ring-forming parameter was incorporated, both the path continuation and the count of the concentration of intramolecular reactive groups are considered simultaneously. Suppose that the randomly chosen group is the H atom in the amino group, that is A group. Then, the contribution to the probability of continuing path, $\gamma_a$, is considered taking account of the internal concentration according to the states of diamine unit.

If the randomly chosen A group is in POP diamine unit of State 2, then there must be a B group continuing from the State 2. The reaction of this B group with the next A group is considered. Let the ring-forming parameter of A group be $\lambda_{a2}$; the second subscript is the state of POP diamine unit.

$$\lambda_{a2} = \frac{C_{a,int,2}}{C_{a,int,2} + C_{a,ext}} \tag{16}$$

$C_{a,int,2}$ is the concentration of intramolecular A group when a B group continuing from POP diamine unit in State2 is about to react. $C_{a,ext}$ can be given as,

$$C_{a,ext} = C^0_{H1}(1 - p_{HR}) \tag{17}$$

$B^2$ can form a ring structure of $j = 1$ with A groups (see Figure 4) in the diamine unit of State 2 in three ways.

$$C_{a,int,2} = 3P_{ab} \tag{18}$$

If there is no ring formation, the diamine unit of State 2 contributes (3/4)$X_2$×$p_{EP}$ to the path continuation. The formation of the ring reduces the contribution by a factor of $\lambda_{a2}$; that is, the contribution of the diamine unit of State 2 to $\gamma_a$ can be expressed as (3/4)$X_2$×$p_{EP}$(1−$\lambda_{a2}$).

If the randomly chosen A group is in POP diamine unit of State 3, then the ring-forming parameter of B group, $\lambda_{b3}$, can be defined for A groups in this diamine unit. In addition, that of A group, $\lambda_{a3}$, can also be defined for the B group continuing from the diamine unit.

$$\lambda_{b3} = \frac{C_{b,int,3}}{C_{b,int,3} + C_{b,ext}} \tag{19}$$

$$\lambda_{a3} = \frac{C_{a,int,3}}{C_{a,int,3} + C_{a,ext}} \tag{20}$$

$C_{b,int,3}$ is the concentration of intramolecular B group when an unreacted A group in the diamine unit of State 3 is about to react. $C_{a,int,3}$ is defined similarly. $C_{b,ext}$ can be given as,

$$C_{b,ext} = C^0_{EP}(1 - p_{EP}). \tag{21}$$

To count $C_{b,int,3}$, the reaction of A group in State 3 is considered. The probability of choosing an unreacted H atom is (1/2), and there are two paths from the unreacted H atom. If the B group paired with $B^1$ is unreacted, which probability is (1-$p_{EP}$), then the unreacted H atom in State 3 can form a ring structure of $j$=1 (see Figure 4). That is, the

concentration of $j$=1 is (1-$p_{EP}$)$P_{ab}$. Note that $B^2$ is excluded because the ring structure is always formed by the backward reaction. The reaction between $B^2$ and the unreacted H atom appears later in counting $C_{a,int,3}$. If the B group paired with $B^1$ is reacted, which probability is $p_{EP}$, two alternative side chains can be assumed, which branch from each of the diamine unit in the linear sequence. The concentrations of B groups branching from the diamine unit of $j = 2, 3$ — are $2p_{EP}\times p_{HR}$ $(1-p_{EP})P_{ab}$. Consequently, the expression of $C_{b,int,3}$ can be written as follows,

$$C_{b,int,3} = (1-p_{EP})P_{ab} + \sum_{j=2}^{\infty} 2p_{EP}\times p_{HR}(1-p_{EP})P_{ab} = P_{ab}\{(1-p_{EP}) + 3.22p_{EP}\times p_{HR}(1-p_{EP})\}. \quad (22)$$

On the other hand, in order to count $C_{a,int,3}$ the reaction of B group continuing from State 3, that is $B^2$, is considered. $B^2$ can form a ring structure of $j$=1 with A groups of State 3 in two ways. There is a linear sequence in State 3. The concentrations of A groups are $2p_{EP}$ $(1-p_{HR})P_{ab}$ for the diamine unit of $j$=2, 3, — on the linear sequence. Then, the side chains branching from the linear sequence are ignored. $C_{a,int,3}$ is the total of these concentrations.

$$C_{a,int,3} = 2P_{ab} + \sum_{j=2}^{\infty} 2p_{EP}\times(1-p_{HR})P_{ab} = 2P_{ab} + 3.22p_{EP}(1-p_{HR})P_{ab} \quad (23)$$

If there is no ring formation, the diamine unit of State 3 contributes (3/2)$X_3\times p_{EP}$ to the path continuation. When the path from the A group chosen to the B group is counted, the formation of the ring reduces the contribution by a factor of $\lambda_{b3}$. Likewise, $\lambda_{a3}$ reduces the path. As a result, the contribution of the diamine unit of State 3 to $\gamma_a$ can be expressed as (3/2)$X_3(1-\lambda_{b3})\times p_{EP}(1-\lambda_{a3})$.

The same argument as shown for State 3 can be applied to other states for POP diamine unit. The total of contributions of states $i$, $i$ = 2–6, to the path continuation shown above give $\gamma_a$ incorporating the ring-forming parameters.

$$\gamma_a = \{\frac{3}{4}X_2(1-\lambda_{a2}) + (\frac{3}{2})X_3(1-\lambda_{b3})(1-\lambda_{a3}) + (\frac{3}{2})X_4(1-\lambda_{b4})(1-\lambda_{a4}) + (\frac{9}{4})X_5(1-\lambda_{b5}) \times(1-\lambda_{a5}) + 3X_6(1-\lambda_{b6})(1-\lambda_{a6})\}\times p_{EP} \quad (24)$$

*Continuation From Diepoxy to Diepoxy Units.*

Next, suppose that the randomly chosen group is an epoxy group, for example it is $B^2$ in Figure 4, in order to determine the expression of $\gamma_b$ which incorporated the ring-forming parameters. The ring-forming parameter $\lambda_{(a)}$ can be defined as follows for the reaction between $B^2$ and an intramolecular A group.

$$\lambda_{(a)} = \frac{C_{(a),int}}{C_{(a),int} + C_{a,ext}} \quad (25)$$

$C_{a,ext}$ can be given by eq. (17). $C_{(a),int}$ is the internal concentration of A group around the B group.

$$C_{(a),int} = \sum_{j=1}^{\infty} 2p_{EP}\times(1-p_{HR})P_{ab} = 5.22p_{EP}(1-p_{HR})P_{ab} \quad (26)$$

If the A group reacted with $B^2$ is in State 3, there is one other continuing path out from State 3. For this path, the ring forming parameter $\lambda_{b3}$ can be defined in the same way as eq. (19). $C_{b,int,3}$, can be given by the same equation as eq. (22). The probability that the diamine unit next to $B^2$ is in State 3 is given by $Q_{HR,3}$. Therefore, the path continuation from $B^2$ to the next B group through the diamine unit of State 3 is given by $p_{EP}(1-\lambda_{(a)})Q_{HR,3}(1-\lambda_{b3})$ .

Similarly, the path continuation through the diamine unit of State 4 is given by $p_{EP}(1-\lambda_{(a)})Q_{HR,4}(1-\lambda_{b4})$. As for the diamine unit of State 5 and 6, the same consideration can be given. Then, $\gamma_b$ can be given by totaling contributions shown above.

$$\gamma_b = p_{EP}(1-\lambda_{(a)})\times\{Q_{HR,3}(1-\lambda_{b3}) + Q_{HR,4}(1-\lambda_{b4}) + 2Q_{HR,5}(1-\lambda_{b5}) + 3Q_{HR,6}(1-\lambda_{b6})\} \quad (27)$$

## Calculational Results and Discussion

Although the relationship of the equations appeared above looks complicated at a first glance, almost all the equations are to be substituted into eq. (4) of the equation of the number of continuing paths. As a result, at $r_{EP}$=1 we see $\gamma$ is a function of $p_{HR}$, $\rho$, $C^0_{H1}$ and $P_{ab}$. Further, the relation of $p_{HR}$ and ($P_{ab}/C^0_{H1}$) is obtained by solving the equation of $\gamma$=1, which corresponds with the gel point, given that $\rho$ is a fixed value. The results of calculation with different $\rho$ values were shown in Figure 7. Note that $P_{ab}$ stands for the internal concentration of the reactive groups and $C^0_{H1}$ is the initial concentration of A group, and hence it is equivalent to that of B group as $r_{EP}$=1, in the polymerisation. Because $P_{ab}$ is a function of $\langle r^2\rangle$ (see eq. (13)), the molar masses and the chemical structure of monomer reactants determine the

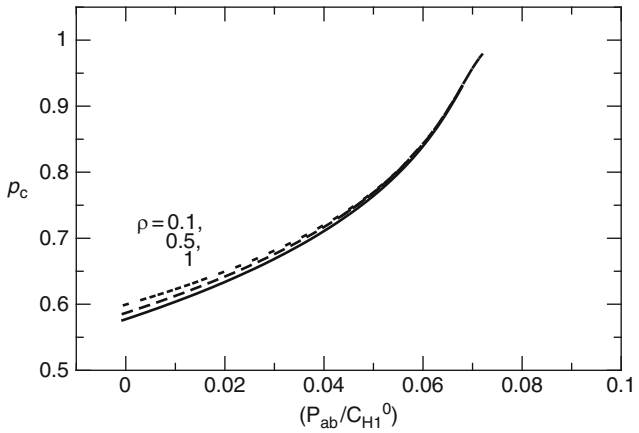


**Fig. 7.** The relation between $p_c$ and $(P_{ab}/C_{H1}{}^0)$ calculated for different $\rho$ values. $\rho = 0.1, 0.5, 1$ are used

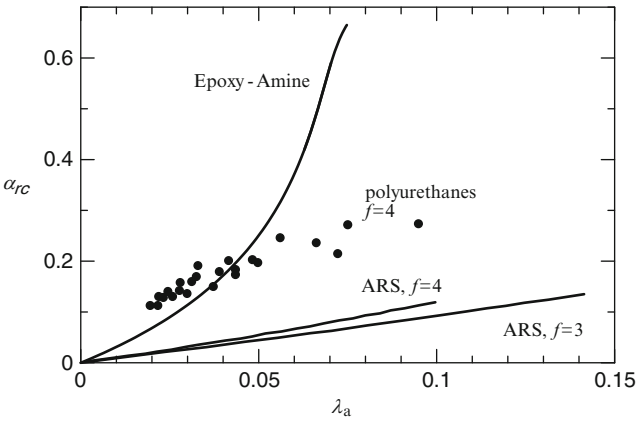


**Fig. 8.** Comparison between ARS theory of $f = 3, 4$ and the result of calculation in the present work(indicated as Epoxy-Amine) and the experimental result of $f = 4$ on polyurethane reaction systems(filled circles). Universal representation of $\alpha_{rc}$ *vs.* $\lambda_a$ is used

value of $P_{ab}$. In addition, $P_{ab}$ determines how likely the growing polymer chain forms a ring structure.

For $\rho$=1, Figure 7 shows $p_c = 0.577$ at $(P_{ab}/C^0{}_{H1}) = 0$, i.e. the internal concentration is equivalent with zero and no ring structure forms, which corresponds with the gel point of Flory-Stockmayer theory. As $P_{ab}$ increases, i.e. more ring structures are formed, or $C^0{}_{H1}$ decreases, $p_c$ increases, which implies that the more intramolecular reactions cause the delay of gel point.

It can be seen that the curves of $p_c$*vs.* $(P_{ab}/C^0{}_{H1})$ have less dependence on $\rho$ than expected, which reason was considered as follows. Concerning the value of $\rho$ since a primary amine has two reactive hydrogen atoms and a secondary amine has one, the ideal ratio for the rate constants $k_1$ and $k_2$ is 0.5[27]. As for the transition of state of POP diamine unit, State 2 → State 3 → State 5, these two transitions always occur with $k_2$ and $k_1$ respectively; similarly, State 2 → State 4 → State 5 occur with $k_1$ and $k_2$ respectively. The transition of State 3 → State 4 cannot happen. Further, State 3 and 4 have an equivalent role as a unit in a sequence of DGEBAs and POP diamines. Therefore, the effect of the variation of $\rho$ on $(P_{ab}/C^0{}_{H1})$ may be almost cancelled out while transitions from State 2 to State 5.

As mentioned above, the curves in Figure 7 are hardly dependent on $\rho$, in particular, it is indistinguishable for $(P_{ab}/C^0{}_{H1})$ larger than 0.05. The curve of $\rho$=1 was used here for further discussion as a representative of calculation result.

The relation shown in Figure 7 can be compared with the previous results on the basis of universal ARS plots of $\alpha_{rc}$*vs.* $\lambda_a$ with a valuable of $f$, where $f$ stands for the functionality of reactive A group, i.e. $f = f_a \cdot \lambda_a$ is equal to $(P_{ab}/C^0{}_{H1})$. $\alpha_{rc}$ is determined by eq. (28) written below and means the excess of the product of the extent of reaction at gel point over the value predicted by Flory-Stockmayer theory[20].

$$\alpha_{rc} = p_c^2 - 1/(f-1) \tag{28}$$

$\lambda_a$ shown in eq. (8) is the ratio of concentration for intramolecular A group, which characterise the competition between intermolecular and intramolecular reaction. The increase in $\lambda_a$ means that more intramolecular reaction occurs during the network formation. ARS plots reduce the combined effects of dilution, molar mass and chain structure between different chemical species. $\alpha_{rc} = 0$ means no delay from Flory-Stockmayer gel point.

The result of calculation for $\rho = 1$ shown in Figure 7 was converted to the plot of $\alpha_{rc}$*vs.* $\lambda_a$ using $f = 4$ for the reactant of POP diamine and shown in Figure 8. Figure 8 also shows previous results of theoretical prediction obtained by the general form of ARS of $f = 3$ and 4, and the experiments for the reaction systems forming polyurethanes of $f = 4$[20]. The general form of ARS theory does not contain the scheme of unequal reactivity. As a result, the theoretical prediction shows linear relations between $\alpha_{rc}$ and $\lambda_a$, whereas the curve of Epoxy-Amine has a sharp upturn. That is, the gel point shifts higher if the unequal reactivity is taken into consideration in the polymerisation. For $\lambda_a$ lower than 0.05 the calculation curve obtained in the present work roughly agrees with the gel point of poly(urethane) reaction systems; showing an improvement concerning the molecular scheme of network formation of $f = 4$.

## Concluding Remarks

The equation for the chain growth in the course of polymerisation of DGEBA and POP diamine can be expressed as a function of $p_{HR}$, the extent of reaction of H atom in amino group. The classification of the state of reaction for POP diamine unit is effective in deriving the equation.

The ring-forming parameter can be incorporated into the equation of the chain growth. $P_{ab}$ and other related parameters can be obtained using the curve of $p_c$*vs*. ($P_{ab}$/ $C^0_{H1}$). The results of this work showed higher values of the gel point in comparison with the result of the general form of ARS theory which assumes the equal reactivity for functional groups.

**Acknowledgements** One of the authors, YT, acknowledges the financial support by Grant-in-Aid for Overseas Advanced Research Practice Support Program from the Ministry of Education, Culture, Sports, and Science and Technology of Japan.

## References

1. P.J. Flory "Principles of Polymer Chemistry", Chap.9., Cornell University Press (1953)
2. Stockmayer WH (1952) J Polym Sci 9:69
3. Stockmayer WH (1953) J Polym Sci 11:424
4. Gordon M (1962) Proc R Soc London SerA 268:240
5. Macosko CW, Miller DR (1976) Macromolecules 9:199
6. Miller DR, Macosko CW(1978) Macromolecules 11:656
7. Kumar A, Wahal S, Sastri S, Gupta SK (1986) Polymer 27:583
8. Matsumoto A, Kohama Y, Oiwa M (1990) Polymer 31:2141
9. R. F. T. Stepto, in : *Polymer Networks – Principles of their Formation Structure and Properties*, ed. R. F. T. Stepto, Blackie Academic & Professional, London, Chapter 2(1998)
10. Kilb RW (1958) J Phys Chem 62:969
11. Dušek K, Ilavský M, Luňák S (1975) J Polym Sci 53:29
12. Ilavský M, Dušek K (1986) Macromolecules 19:2139
13. Lee KJ, Eichinger BE (1990) Polymer 31:406
14. Smith RS, Stepto RFT (1974) Makromolekulare Chemie 175:2365
15. Ahmad Z, Stepto RFT (1980) Coll Polym Sci 258:663
16. Stanford JL, Stepto RFT (1982) ACS symp Ser 193:377
17. Rolfes H, Stepto RFT (1990) Makromol Chem Macromol Symp 40:61
18. Rolfes H, Stepto RFT (1993) Makromol Chem Macromol Symp 65:233
19. Rolfes H, Stepto RFT (1993) Makromol Chem Macromol Symp 76:1
20. Stepto RFT and Taylor DJR (1996) Polym Gels Networks 4:405
21. Tanaka Y, Stanford JL, Stepto RFT (2006) Abstract Booklet:Polymer Networks Group Conference T27
22. Mijovic J, Andjelic S (1995) Macromolecules 28:2787
23. Zhu S, Hamielec AE (1992) Macromolecules 25:5457
24. Jacobson H, Stockmayer WH (1950) J Chem Phys 18:1600
25. Pereda S, Brandolin A, Valles EM, Sarmoria C (2001) Macromolecules 34:4390
26. Truesdell C (1945) An. Math 46:144
27. In: Allen G, Bevington JC(ed) Comprehensive Polymer Science, The synthesis, Characterization, Reactions & Applications of Polymers vol. 5 (1989) Hodd K, Epoxy Resins 667

Progr Colloid Polym Sci (2009) 136:63–68
DOI: 10.1007/2882_2009_9

# The Effective Surface Roughness Scaling of the Gelation Surface Pattern Formation

T. Mizoue[1], M. Tokita[2], H. Honjo[1], H. J. Barraza[3], and H. Katsuragi[1]

**Abstract** The surface pattern formation on a gelation surface is analyzed using an effective surface roughness. The spontaneous surface deformation on DiMethylAcrylAmide (DMAA) gelation surface is controlled by temperature, initiator concentration, and ambient oxygen. The effective surface roughness is defined using 2-dimensional photo data to characterize the surface deformation. Parameter dependence of the effective surface roughness is systematically investigated. We find that decrease of ambient oxygen, increase of initiator concentration, and high temperature tend to suppress the surface deformation in almost similar manner. That trend allows us to collapse all the data to a unified master curve. As a result, we finally obtain an empirical scaling form of the effective surface roughness. This scaling is useful to control the degree of surface patterning. However, the actual dynamics of this pattern formation is not still uncovered.

**Keywords** Surface pattern formation • Gel • Radical polymerization • Effective surface roughness

## Introduction

Pattern formation of soft materials is one of the most ubiquitous phenomena in nature [1]. Our body is certainly an example of soft pattern formation. And many dissipative structures appear in soft materials. However, we don't know any general method to characterize/analyze these fascinating pattern formation phenomena properly. Natural patterns have very wide range of diversity. The pattern formation of gel is a typical example of such soft pattern formation.

Since Tanaka et al., have discovered the beautiful surface pattern formation on polymer gels during volume phase transition [2,3], it has been extensively studied both by experiments [4,5] and theories [6,7,8]. In this pattern formation, mechanical instability due to the abrupt volume change is crucial to understand it. Obviously, complex polymer network resulting in intriguing viscoelastic behavior of polymer gel is a main reason of this pattern formation.

On the other hand, recent studies have shown a novel kind of pattern formation which appears during polymer gelation. The one entity is 1-dimesional (1D) pattern formation. Narita and Tokita have found a Liesegang pattern formation on 1D k-karageenan gel [9]. The diffusion of potassium chloride in k-karageenan solution is an essential process in this pattern formation. The other entity is a quasi-2-dimesional (2D) one. The Acrylamide (AA) gelation on a Petri-dish has shown a spontaneous surface deformation [10]. The competition between the positive feedback of radical polymerization and the inhibition by oxygen is thought a main reason of this pattern formation. This surface deformation is actually 3-dimenstional (3D) phenomena, while the gelation occurs in quasi 2D space, i.e., the situation is not very simple. The observed pattern looks like wrinkles on brains or surface pattern on reptiles. This similarity reminds us that nature might be using this kind of spontaneous surface deformation. The study of this pattern formation is thus important both by means of gelation dynamics itself, and pattern formation dynamics in bio soft matter. In Ref.[10], the reaction diffusion dynamics is presented to understand this pattern formation. However, some difficulties remain to explain pattern formation using simple reaction diffusion dynamics. More detail experiments and a universality check are necessary to model this pattern formation correctly.

In this paper, we will focus on this quasi 2D pattern formation with radical polymerization. First, we check the universality of this pattern formation using some kinds of monomer that undergo radical polymerization gelation. In addition, we will characterize the degree of surface pattern using the Effective Surface Roughness (ESR) of 2D pictures. The

H. Katsuragi (✉)
[1]Department of Applied Science for Electronics and Materials
Kyushu University
Kasuga, Fukuoka 816-8580, Japan
e-mail: katsurag@asem.kyushu-u.ac.jp
[2]Department of Physics
Kyushu University
Hakozaki, Fukuoka 812-8581, Japan
[3]Unilever R&D, Quarry Road East, Bebington
CH63 9HW, United Kingdom

experimental conditions are systematically varied and resultant surface deformation is characterized by the ESR. Finally, we find an empirical unified scaling of the ESR.

## Experimental

The experimental system is simple. Pre-gel solution is poured onto a Petri-dish, and it is left undisturbed for about 2 hours. Then, spontaneous surface deformation occurs depending on the experimental condition. If Ref.[10], only AA gel is used as a monomer. Thus, herein we try some monomers that are able to undergo radical polymerization. Concretely, Sodium acrylate (SA, $M_w = 94.05$), N-Isopropylacrylamide (NIPA, $M_w = 113.16$), and Dimethylacrylamide (DMAA, $M_w = 99.13$) are used as monomers. In all cases, Methylenbisacrylamide (BIS) constitutes cross-link. And, Ammonium persulfate (APS) and Tetramethylethlyenediamine (TEMD) are used as an initiator, and an accelerator of the radical polymerization, respectively.

We mainly controlled the concentration of initiator, temperature, and ambient oxygen. Sample preparation and temperature control method are same as in Ref.[10]. Here, we additionally control the ambient oxygen concentration using an airtight chamber and $O_2$, $N_2$ gas cylinders. After 2 hours polymerization, resulting surface patterns are taken by a CCD camera, and the photos are processed by a PC.

In Fig. 1, typical patterns observed with each monomer are shown. It is hard to see the clear surface deformation with SA and NIPA gel. They seem to have very weak surface deformation instability. This is due to that the lower critical solution temperature (LCST) in NIPA being close to the experimental temperature (30 degree Celsius); and the remaining inhibitor in commercial SA. The NIPA gel is very sensitive to temperature. The detailed temperature dependence of NIPA gel pattern formation is still open for future work. Since the DMAA doesn't have such difficulties, it shows a relatively clear surface pattern. The observed pattern is more or less similar to the AA one. Thus, we decided to focus on DMAA surface deformation pattern formation in this study.

## Phase Diagram

As a next step, we systematically make DMAA gel slabs under various experimental conditions and compose the phase diagram as shown in Fig. 2. The specific experimental conditions are shown in Table 1. Qualitative structure of this phase diagram is very similar to the AA case [10]. The surface deformation pattern appears in between the completely flat gelation ("Flat") and the incomplete gelation ("Not-gelation"). This means that the inhibition of polymerization is a crucial process to produce surface instability. In addition, the large scale buckling can be observed in the marginal region between the "Surface deformation" and "Not-gelation". In the surface deformation pattern, the bottom plane of the gel slab is flat (i.e., the deformation is limited on the top surface); while the buckling includes bottom deformation. The origin of this large scale buckling has not been clarified yet, since it is more difficult than the surface deformation pattern. Here, we focus on surface deformation pattern again, because we don't know the details of this even easier case. A noticeable feature of Fig. 2 phase diagram is the wider patterning region in relatively low temperature regime. It is a characteristic feature of DMAA pattern formation different from the AA. Moreover, the clear stripe patterns cannot be observed in DMAA surface pattern formation.

## Effective surface roughness analysis

In order to quantify the degree of surface deformation, we employ the standard deviation of 2D photos. We can recognize the surface deformation through the contrast of 2D photos (like Fig. 3). This suggests that the standard deviation

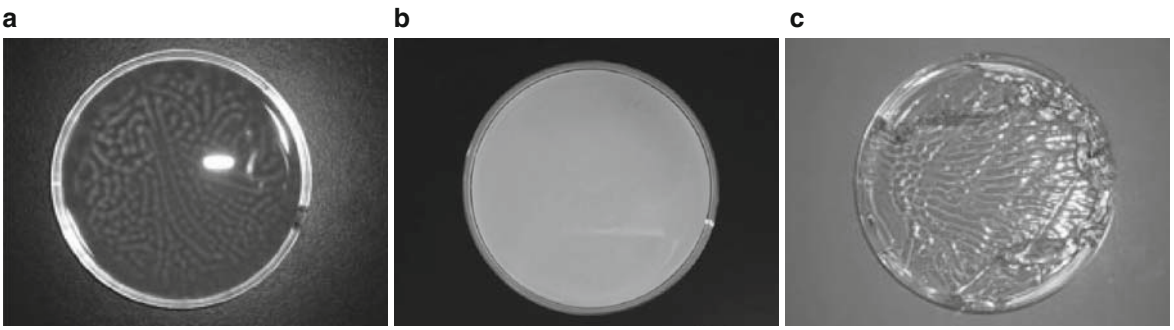


**Fig. 1** Gel patterns with **a** SA (=2 mg), **b** NIPA (=1.9 mg), and **c** DMAA (=2.4 mg) monomers. In all cases, 6 mg BIS, 70 μl TEMD, and 10 mg APS are dissolved to 12 ml deionized water under the room temperature. SA and NIPA gel show very marginal patterns, while DMAA gel shows clear pattern

of 2D photos can be used as an indicator of the surface deformation degree. In Fig. 3, typical 2D pictures with varying initiator concentration are presented. As can be seen in Fig. 3, increasing initiator concentration tends to suppress the surface deformation. Moreover, buckling can be observed in very low initiator cases. We don't use such buckling regime. To characterize these photos, the central part (1,000 pix.* 1,000 pix.) of raw data (3,072 pix. * 2,304 pix.) is extracted for each photo. Then, the data are translated to 8 bit gray scale, and finally the standard deviation and average of the photo intensity values are computed. We define this standard deviation as the effective surface roughness (ESR).

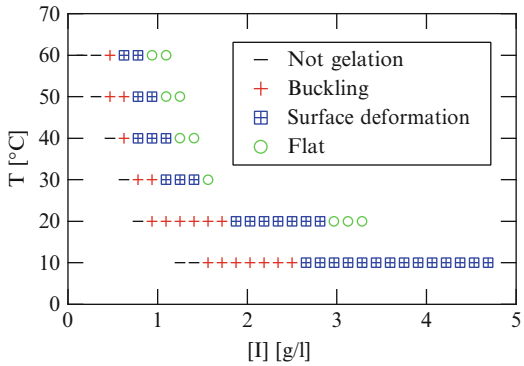


**Fig. 2** Phase diagram of DMAA gel slabs. [*I*] is the initiator concentration. In low temperature regime, pattern appearing range is wider than AA gel case. No clear stripe patterns are observed. Other features are similar to the phase diagram of AA gel surface pattern [10]

**Table 1** Experimental conditions

| | |
|---|---|
| DMAA [ml] | 1.8 |
| BIS [mg] | 4 |
| TEMD [μl] | 70 |
| water [ml] | 11 |
| APS [mg] | 0–60 |
| Temperature [°C] | 10–60 |

First, we vary the initiator concentration and temperature under atmospheric condition (ambient oxygen concentration is about 21 %). Since the surface deformation regime is limited as shown in Fig. 2 phase diagram, the completely independent change of initiator concentration and temperature is difficult. We have to adjust both of them simultaneously to create surface deformation pattern. We show the computed average intensity and ESR values in Fig. 4. While almost the constant average intensity is confirmed in Fig. 4 (a), increasing ESR is observed for decreasing initiator concentration (Fig. 4(b)). This trend is consistent with pictures in Fig. 3. The almost constant average indicates the reproducible lighting and/or other external noise factors. The negative correlation between the ESR and initiator concentration implies that the more initiator present, the more stable the polymerization is. As a result, a uniform flat slab is created in the case with sufficient amount of initiator.

Next, the ambient oxygen and temperature are maintained to create surface deformed slabs. We have to vary the initiator concentration as well to create clear surface deformation, owing to the narrow patterning regime (same reason as previous Fig. 4 case). The measured average intensity and ESR are shown in Fig. 5. Constant average intensity is the same trend as Fig. 4 case. However, the ESR and oxygen concentration shows a positive correlation. This trend is consistent with the inhibition effect of oxygen

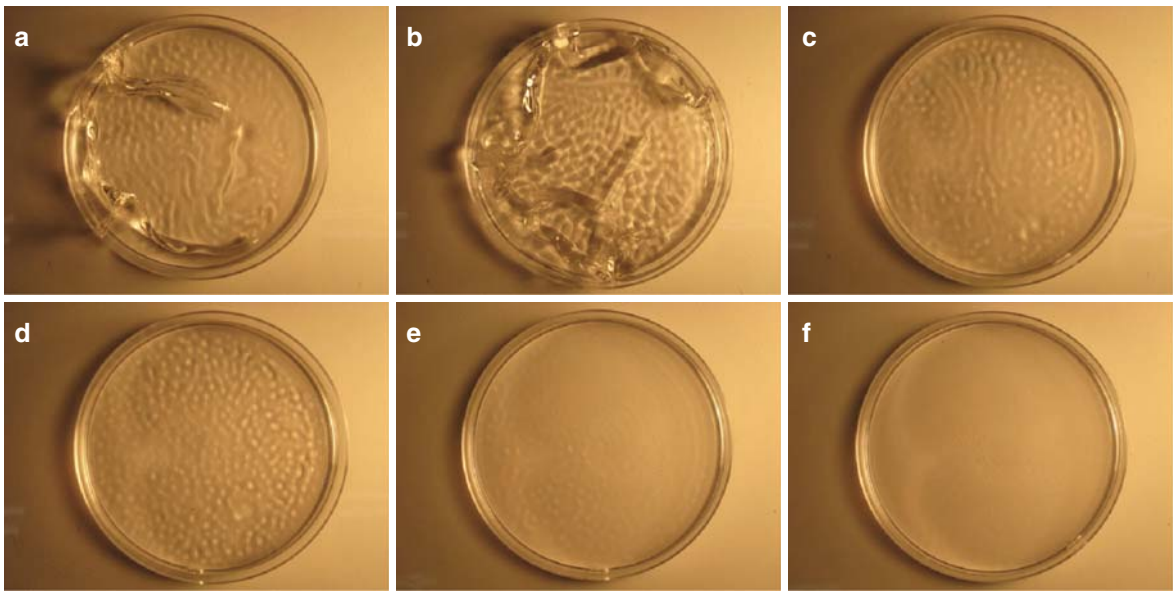


**Fig. 3** Examples of DMAA surface deformation and buckling. 1.8 ml DMAA, 4 mg BIS, 70 ml TEMD, and 11 ml deionized water are used. Enviromental temperature is controlled as 30 degree Celsius. The amount of initiator (APS) is varied as **a** 10, **b** 12, **c** 14, **d** 16, **e** 18, **f** 20 mg, respectively

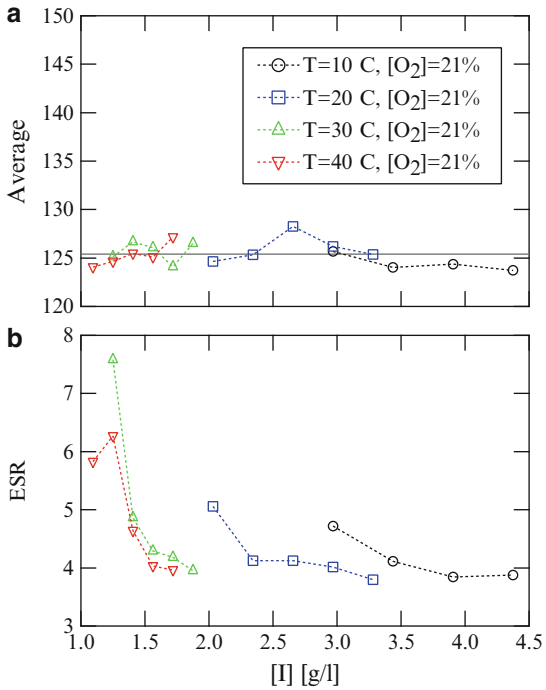


**Fig. 4** **a** Average and **b** Effective Surface Roughness (ESR) of varying initiator concentration $[I]$ and temperature $T$. Constant average and varying ESR can be observed as a function of $[I]$

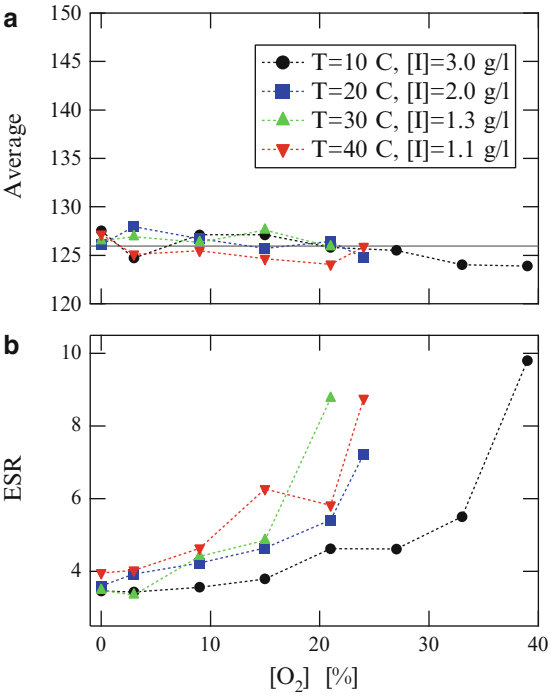


**Fig. 5** **a** Average and **b** ESR of varying oxygen concentration and temperature. Where $[O_2]$ is the oxygen concentration. Qualitative behavior of average and ESR is similar to Fig. 4 case, except that the effect of $[I]$ and $[O_2]$ is opposed each other

in radical polymerization. The oxygen scavenges and stops the radical polymerization, so that the flat surface becomes inhomogeneous and unstable. This is presumably the principal origin of surface instability.

This oxygen inhibitor effect corresponds to the counter against the initiator stabilizing effect. And, the concave structure of ESR is similar in Figs. 4 and 5. From these reasons, one can expect that all ESR curves can be unified to a single master curve. To unify all ESR data, here we use a cubic function as a fitting form,

$$[ESR] = \alpha + \left(\frac{1}{\sigma_T} \cdot \frac{[O_2]}{[I]}\right)^3 \tag{1}$$

where $\sigma_T$ is a parameter depending on the temperature $T$ (degree Celesius), and $\alpha$ denotes the background noise level from camera, lighting, etc. The $[I]$ and $[O_2]$ correspond to initiator concentration (g/l) and ambient oxygen concentration (%), respectively. The reason we choose the cubic function is that the exponential form is too fast and the quadratic form is too slow to fit and unify the ESR data. In principle, the exponent of the fitting function can be assumed as a free fitting parameter. However, that would not improve the data collapse so well, in spite of adding one more free fitting parameter. One of the reasons to use the cubic function is to reduce free fitting parameters. The form of Eq. (1) is a completely empirical form. It is found in a heuristic way as mentioned above.

We fitted all ESR data to Eq. (1) and obtained the following scaling,

$$\frac{1}{\sigma_T} = 0.38 T^{-0.41}. \tag{2}$$

The actual relation between $\sigma_T$ and $T$ is shown in Fig. 6(a). The data scatters a little, but they agree with a trend described by Eq. (2) (gray curve in Fig. 6(a)). The scaling form Eq. (2) means that the following scaling variable $f([O_2], [I], T)$ is useful to unify the data,

$$f([O_2], [I], T) \sim \frac{[O_2]}{[I] \cdot T^{0.41}}. \tag{3}$$

The final data collapse using this scaling variable is displayed in Fig. 6(b). The data show a little scattering again, but the scaling function captures the trend of the ESR data. The concrete function form of the final scaling (gray curve in Fig. 6(b)) is as following,

$$[ESR] = 3.7 = 6.6\left(\frac{[O_2]}{[I] \cdot T^{0.41}}\right)^3. \tag{4}$$

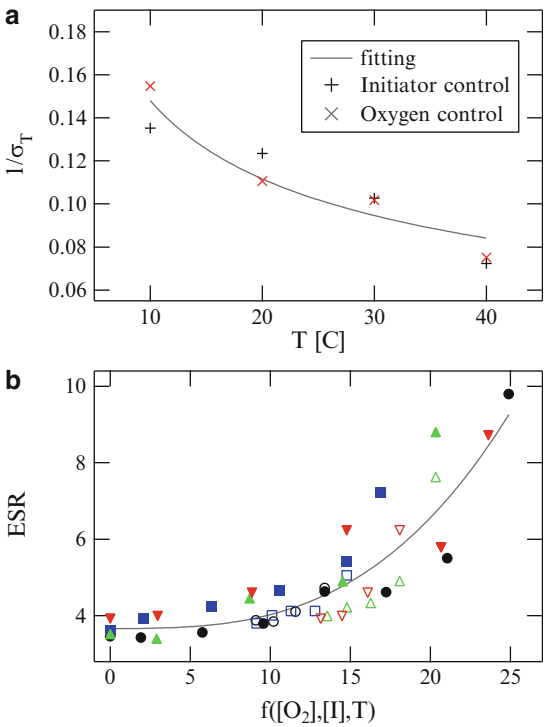


**Fig. 6** **a** Scaling of temperature factor and **b** data collapse of ESR by scaling form Eq. (4). All different conditions data are roughly collapsed to the master curve

This scaling form enables us to approximately predict the degree of surface deformation, while it is only an empirical law. The relation between this empirical scaling form and physical mechanism of surface deformation is a future problem.

## Discussion

There are theoretical studies for the gel surface deformation [6,7,8,11]. Most of them were focusing on the volume phase transition. However, the present surface deformation clearly occurs at the gelation (polymerization) stage. In that stage, polymer blobs diffusion and polymerization reaction are basic processes. When the polymerization is inhibited at the gel-solution interface by oxygen, the swelling of polymer network might cause deformation locally. Thus, the diffusion, reaction, and network swelling, all factors might have to be coupled to explain this surface deformation pattern formation. As long as we see the gelation process by eyes, the gelation seems to grow from the bottom to the surface. More direct observation of gelation surface is necessary to understand the pattern formation properly.

In this study, we use a cubic function to fit the ESR data. The cubic function is concave, and it means that abrupt growth of ESR occurs at a certain $f([O_2], [I], T)$. Such concave growth inevitably leads the divergent ESR. Then the large scale buckling happens to avoid the divergence. In fact, the gel slab with $f([O_2], [I], T) > 25$ tends to show buckling. The detailed investigation of buckling instability is also an open problem. Besides, the characteristic length scale study like Ref. [10] might be helpful to discuss the pattern formation dynamics.

Self-organizing pattern formation is a frontier in materials science. Most of all self-organized patterns show nano or micro meter order structures [12,13]. Such micro structures are of course practical to design functional materials. Contrastively, the pattern we report here has macro (millimeter order) structure. Although the benefit of such macro structure is still unclear in terms of functionality, it is visible by naked eye and easy to control. We believe that macro structures in soft matter also have a great potential innovative applications.

## Conclusions

We systematically performed experiments on surface deformation occurring on free gelation surfaces. We define the ESR (Effective Surface Roughness) of the gel slabs utilizing 2D digital photo data, in a very simple way. We varied the initiator concentration, ambient oxygen concentration, and temperature as control parameters of gelation, and measured the ESR for each slab. As a result, we obtained the simple empirical scaling form Eq. (4) to characterize the degree of surface deformation. While we can estimate the surface deformation amount owing to this empirical scaling, the detailed relation between this form and surface deformation dynamics is still unsolved.

## References

1. Cross MC, Hohenberg PC (1993) Rev Mod Phys 65:851
2. Tanaka T, Sun ST, Hirokawa Y, Katayama S, Kucera J, Hirose Y, Amiya T (1987) Nature 325:796
3. Matsuo ES, Tanaka T (1992) Nature 358:482
4. Tanaka H, Tomita H, Takasu A, Hayashi T, Nishi T (1992) Phys Rev Lett 68:2794
5. Tokita M, Miyamoto M, Komai T (2000) J Chem Phys 113:1647
6. Sekimoto K, Kawasaki K (1987) J Phys Sco Jpn 56:2997
7. Onuki A (1988) J Phys Soc Jpn 57:703
8. Hwa T, Karder M (1988) Phys Rev Lett 61:106
9. Narita T, Tokita M (2006) Langmuir 22:349
10. Katsuragi H (2006) Europhys Lett 73:793
11. Onuki A (2002) Phase transition dynamics, Cambridge University Press
12. Bowden N, Brittain S, Evans AG, Huchinson JW, Whitesides GM (1998) Nature 393:146
13. Takahashi M, Maeda T, Uemura K, Yao J, Tokuda Y, Yoko T, Kaji H, Marcelli A, Innocenzi P (2007) Adv Mater 19:4343

Progr Colloid Polym Sci (2009) 136:69–76
DOI: 10.1007/2882_2009_10

# Discontinuous Growth of Onion Structure under Shear

Shuji Fujii

**Abstract** Discontinuous growth process of the Multilamellar vesicle (so called Onion) driven by shear quench was investigated by viscometry and microscopy in detail. Discontinuous Onion growth was observed when the final shear rate corresponded to the intermediate shear rate domain where the shear-thickening and shear-thinning viscosity appeared. In this process, large Onion transformed back into the lamellae and then formed large Onion. Small Onion to lamellae degradation process might be achieved by two modes, first the disruption of the configurational order of densely packed Onions followed by the rupture of Onion as second process. The second process would be characterized by the shear-banding flow pattern composed of the Onion-$L_\alpha$ coexisting state. We suggest that the appearance of the shear-band structure and the Onion reformation developed from the shear-band might be scaled by considering the mechanical energy balance with the bending elastic energy of bilayers.

**Keywords** Surfactant • Lamellar Phase • Onion Phase • Growth Mechanism • Vesicle

## Introduction

Shear-induced non-equilibrium phenomena frequently observed for soft matter systems have attracted many researchers [1]. Especially, dynamic coupling phenomena between shear flow field and structural transition and phase transition yields unique structure and pattern formation, which is never observed at quiescent state, such as an Isotropic-to-Nematic transition coupled with concentration fluctuation and diffusion for surfactant systems or a shear-band formation reported for many polymer, colloid and surfactant systems [1,2]. One of the interesting shear-induced phenomena is a shear-induced Lamellae-to-Onion (multilamellar vesicles) structural transformation for the surfactant systems [3,4,5,6]. Onion has a quite fascinating structure organized by amphiphilic bilayer membranes, in which smaller vesicles are enveloped in larger one (schematic diagram of the onion structure is shown in the inset of figure 1). The shear-induced Onion formation has been observed for many different surfactant systems [3–22]. Many researchers have tried to understand the physics underlying the shear-induced non-equilibrium phase transition experimentally and theoretically, respectively. Characteristic feature of the Onion phase is a reversibility of the radius, $R_{Onion}$, against the shear rate [10,11,12]. Most of Onion phase follow the scaling law proposed by Roux et al., $R_{Onion} \propto \dot{\gamma}^{-0.5}$, i.e., the Onion radius is determined by the shear rate [3,4]. According to their unique structure, a decrease in the onion radius might be considered to be a serial event induced by peeling off the outer shell. However, it is not well known how onion grows up, when a shear rate is changed.

So far, Panizza et al., Courbin et al., Medronho et al., and Koschoreck et al. reported the size growth mechanism by a shear quench method, a shear step from higher to lower shear rates [10,11,12,16,22]. Panizza et al., and Courbin et al. observed a continuous and discontinuous growth mechanism with large and small shear quench gaps, respectively. In the case of discontinuous growth, the initial Onion structure first disappeared completely and a new Onion appears. Medronho et al. also observed the discontinuous growth process after the shear quench and they also observed the $L_\alpha$-Onion coexisting region in the discontinuous growth process. Recently, we have also observed $L_\alpha$-Onion coexisting region during the discontinuous process by a viscometry [15]. However, it is not known why $L_\alpha$-Onion coexisting region appears in the discontinuous growth process and its physical origin causing the discontinuous growth behavior. As far as we know, no detailed investigation has been done on the discontinuous growth mechanism of the Onion size, in spite of that most of Onion size change process seems to be driven by the discontinuous mechanism [10,11,12,15,22].

S. Fujii
Nagaoka University of Technology
940-2188, Niigata, Nagaoka, Kamitomioka, 1603-1, Japan
e-mail: sfujii@mst.nagaokaut.ac.jp

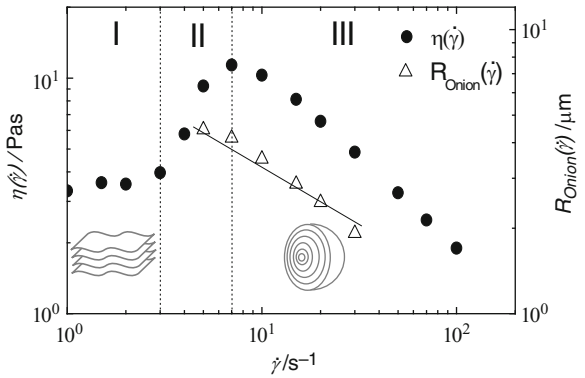


**Fig. 1** Shear rate dependence of the steady state viscosity and Onion radius estimated by polarized microscopy images. Onion radius reduces with increase in the shear rate. Inset indicates the schematic structure of the planar lamellae and the Onions, respectively. Solid line indicates the power law relation with a slope of −0.5, which corresponds to the scaling law, $R_{Onion} \propto \dot{\gamma}^{-0.5}$, proposed by Roux et al

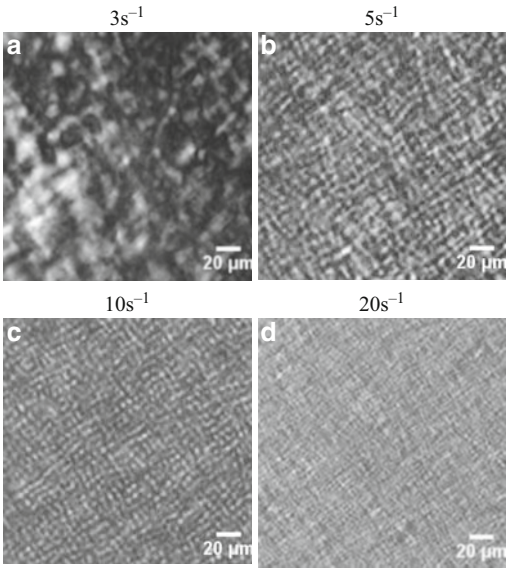


**Fig. 2** Polarized microscopy images in the steady state at the shear rate of (a) 3s$^{-1}$, (b) 5s$^{-1}$, (c) 10s$^{-1}$ and (d) 20s$^{-1}$, which correspond to different shear rate domains shown in figure 1. (a) the Newtonian domain, (b) the shear-thickening, (c) and (d) the shear-thinning domains

In the present study, we investigated to understand the Onion growth mechanism, especially the discontinuous process.

## Experimental

In this study, we used non-ionic surfactant, tri-ethylene glycol mono-decylether ($C_{10}E_3$) purchased from Nikko Chemicals Co. Ltd. The surfactant was used without further purification. De-ionized distilled water was used as solvent. Surfactant lamellar phase was prepared by dissolving non-ionic surfactant, $C_{10}E_3$, into $H_2O$ with the concentration of 40wt.%. Solution was gently stirred by a magnetic stirrer for 2 days. Stirring gently causes the onion structure formation. From previous reports, we know that thermal treatment makes sure to erase any memory of the Onion and create well-controlled initial state, and the Onion radius can be controlled by the shear rate.[0,0,0] In order to prepare well defined Onions, surfactant solution was always sheared with a shear rate of 10s$^{-1}$ at 42°C until the Onions formed during the sample preparation disappeared. After Onions disappeared, the temperature was cooled down at 25°C, and the aligned-$L_\alpha$ phase was obtained. Homogeneous Onion phase was prepared by pre-shearing.

Viscoelastic measurements were performed using an ARES-LS strain-controlled rheometer of TA Insturument Co., Ltd., with a couette shear geometry (radius of inner bob; 16.5 mm, gap size; 250 μm). Microscopy under shear was performed by using the Linkam shear cell, CSS450, which has a plate-plate shear geometry. The shear cell was attached onto the polarized microscope (Olympus BX-50) and positioned between two polarizers. Sample thickness between upper and lower plates was always fixed at 250 μm to fit the experimental condition with that of the rheometer. By using the same sample thickness, we can study the size change process of the Onion texture without any spatial confinement effects. All measurements were performed at 25°C.

## Results and Discussion

### *Steady state viscosity and Onion radius*

Figure 1 shows a shear rate dependence of the steady state viscosity. Each data points were obtained from plateau value of the time dependent measurements of the viscosity. In figure 1, the Onion radius obtained at the steady state is also shown. The Onion radius was estimated by a polarized microscopy observation. Figure 2 shows the microscopy images of the lamellar morphology in the steady state obtained at different shear rates.

We can clearly see that the flow curve is classified into three shear rate domains. First, the Newtonian behavior was observed in the low shear rate region (domain I), 1−3 s$^{-1}$, indicating no structural transition from the planar lamellae to the Onion texture. Microscopy images presented in figure 2(a) actually showed a typical mosaic pattern for the planar lamellae instead of the Onion. In the intermediate shear rate region (domain II), the viscosity was remarkably increased

with the shear rate, referred as a shear-thickening viscosity. Previous study showed that inhomogeneous Onion formation was observed in this shear rate domain [6]. Our microscopy obervation also showed inhomogeneously packed Onion texture (figure 2(b)). Further increase in the shear rate caused a drastic change in the viscoelastic properties from the shear-thickening to the shear-thinning viscosity (domain III), where the viscosity decreased as a function of the shear rate. Densely and homogeneously packed Onions are formed in the domain (figure 2(c) and (d)). Shear rate dependence of the Onion radius was well described by a power law relation proposed by Roux et al., $R_{Onion} \propto \dot{\gamma}^{-0.5}$ [3,4]. In spite of the different viscoelastic property in the shear rate domains II and III, the Onion radius was a monotonically decreasing function of the shear rate. Steady state properties observed in the shear rate domains II and III well agree with the observations previously done for many variety of surfactant lamellar systems [3–16, 21].

## *Shear quench-induced Onion size change*

On the basis of the flow curve at the steady state, shear quench tests were preformed by changing the shear rate from fixed initial shear rate to different final one with step like function at time $t = 0$. As a typical example of the shear quench tests, figure 3 shows decay curves of transient viscosity as a function of elapsed time after shear quench. Here, the initial shear rate was fixed at $\dot{\gamma}_i = 100\text{s}^{-1}$ and the final shear rate was varied. Shear quench behavior was classified into three groups in figure 3 on the basis of the time development of the transient viscosity.

### Quenching into the domain I

The final shear rates in figure 3(a) belong to the Newtonian domain where the lamellar structure only exists but no Onions. After the shear quench, the shear viscosity showed a decay with a single exponential *like* function form [22]. The decay curves of the transient viscosity could not be fitted by an exponential function with a single decay time. Thus, the single decay curve would be composed of multiple relaxation modes. The curves seem to be a stretched exponential like function form. Note that the transient viscosity approaches to the same value as that of the Newtonian region. The same viscosity as the Newtonian region suggests that the onion was collapsed and transformed back into a planar lamellae structure when the shear rate was reduced. Since the Onion structure is not formed at low shear rate domain ($\dot{\gamma}_f = 1 - 3\text{s}^{-1}$), the single exponential like decay indicates the Onion to planar lamellae degradation process.

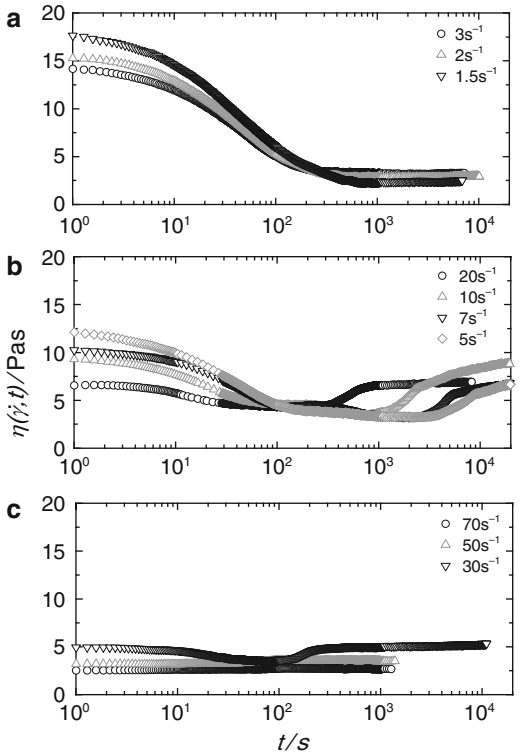


**Fig. 3** Time dependence of the transient viscosity after shear quench from $\dot{\gamma}_i = 100\text{s}^{-1}$ (initial shear rate) to different final shear rates $\dot{\gamma}_f$. Shear quench behavior was classified into three regimes, (a), (b) and (c)

Recently, Medronho et al. have found that planar lamellar fraction increases with a single exponential function form in the Onion-to-lamellae when the shear rate is quenched by means of rheo-NMR spectroscopy [13]. Thus, our observation might also show the time development of the planar lamellae fraction.

### Quenching into the domain II and III

Different behavior from domain I was observed when the shear rate was quenched into domains II and III. The time dependence of the transient viscosity showed double decay modes (fast and slow decay modes) followed by increase in the viscosity through the minimum (figure 3(b)). From our previous study, the increase in the viscosity was attributed to the Onion reformation after degradation into the lamellar structure [22]. Since the Onion formation accompanies with the increase in the viscosity, the growth mechanism of the Onion in this shear rate domain can be regarded as "a discontinuous pathway" kinetically, i.e., small Onion cannot grow up continuously but reset the structure via planar lamellae once, and then lamellae transforms into large Onions. The elapsed time at the viscosity minimum would be considered to be an induction time for the Onion reformation.

Note again that the minimum viscosity does not depend on the final shear rate, but the induction time showed the final shear rate dependence. The induction time shifts to long time region as the final shear rate is reduced. Therefore the characteristic time of the Onion to $L_\alpha$ degradation would also depend on the final shear rate. This means that the growth of the Onion size might be dominated by the final shear rate. When the final shear rate was increased further close enough to the initial one, the transient viscosity did not show the exponential like decay anymore (figure 3(c)). Observation in the third shear rate group suggests an existence of another Onion growth mechanism but not the discontinuous one as observed in figure 3(b).

### Onion to $L_\alpha$ degaradation dynamics

Double decay modes observed in figure 3(b) would be induced by the rupture of the Onion structure. In order to characterize the decay time of the Onion degradation, the decay curves were analyzed by applying the inverse Laplace transformation [25]. The inverse Laplace transformation is a useful method to obtain a decay time distribution by analyzing a decay curve with multi-relaxation modes, which can never represented by the exponential function with a single relaxation time. Figure 4 shows the distribution function of the decay time obtained by the inverse Laplace transformation. Distribution function clearly depends on the final shear rate. At large final shear rates ($\dot{\gamma} = 20 - 15\mathrm{s}^{-1}$), only one decay mode (fast mode) was observed. As the final shear rate was reduced, however, extra slow mode appeared and remarkably developed at the intermediate shear rate regimes ($\dot{\gamma} = 10 - 4\mathrm{s}^{-1}$). The characteristic times of these dynamics range were 10 – 20s and 100 – 1000s for the fast and slow mode, respectively. Eventually the slow mode combined with the fast mode at low final shear rate region corresponding to the Newtonian domain ($\dot{\gamma} = 3 - 1.5\mathrm{s}^{-1}$). The peak of the fast mode in the distribution function, i.e., the average fast decay time, did not show significant final shear rate dependence. It seems that the time range of the fast mode is too short to rupture the Onion structure.[0,0] Thus, the slow mode may play an important role for the Onion degradation process.

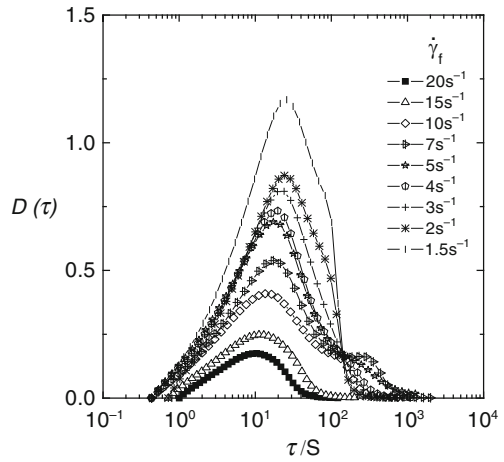


**Fig. 4** Distribution function of the decay time obtained by the inverse Laplace transformation analyze of the transient viscosity curves in figure 3

Medronho et al. have found the Onion and $L_\alpha$ coexistence region in the course of the degradation process. We have performed polarized microscopy observation under shear with the same experimental conditions except for the shear geometry in order to confirm what structure exists in the slow mode.

## *Shear-banding flow in the degradation process*

Figure 5 shows a time-space chart for the Onion-to-$L_\alpha$ degradation process when the shear rate is quenched from 100 to $10\mathrm{s}^{-1}$ as a representative result. Onion degradation process was recorded for 500s corresponding to the time scale where the fast mode shifts to slow one (see figure 3(b)). Since microscopy observation was performed under crossed polarizers, brightness in the photographs is proportional to the birefringence intensity. Therefore bright and dark birefringent region on the chart coincide with $L_\alpha$ and the Onion structure, respectively. The Onions prepared at $100\mathrm{s}^{-1}$ have rather isotropic orientation of bilayers and are packed homogeneously with high configurational order. Chart indicates that the birefringence intensity gradually increases in the time region corresponding to the fast decay mode. However, the birefringence intensity decreased again when the slow decay mode was initiated and showed strong fluctuation with time. The same behavior as the polarized microscopy observation was also confirmed by a flow birefringence measurement in lower panel of figure 5. Flow birefringence also showed decay, which was almost the same time scale as that in the transient viscosity measurement. In the time range where the slow mode was observed, the flow birefringence showed strong fluctuation. Interesting is that the appearance of stripe-like flow pattern with weak and bright birefringence along the neutral direction in addition to the birefringence intensity fluctuation. This stripe flow pattern is referred as a shear-band structure, which is often observed for viscoelastic inhomogeneous complex fluids systems [20,21,26]. For imposed shear rate, inhomogeneous state of the complex fluids will lead a coexistence phase of different apparent viscosities flowing at the same shear rate. In figure 5(b), a typical snap shot of the shear-band structure observed during the Onion degradation process is shown. We can see coexistence of weak and bright birefringence intensities

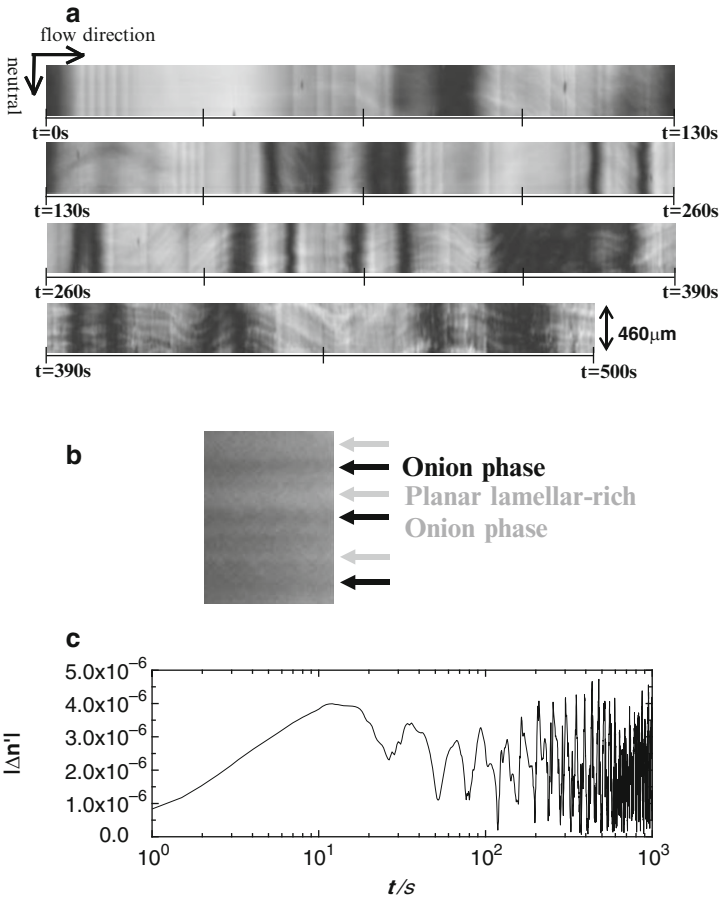


**Fig. 5 (a)** Time-Space chart for representing the Onion degradation process after shear quench from 100 to $10s^{-1}$. Length of ordinate is 460μm corresponding to the field of view under the polarized microscope and abscissa is elapsed time. Shear rate was quenched at $t = 0$. (b) A typical snap shot of the shear-band structure appeared during the Onion degradation process. Black and gray arrows show the Onion and planar lamellar-rich Onion phase, respectively. (c) Lower diagram shows the time development of the flow birefringence

along the neutral direction. Since the Onion phase have the isotropic orientation of the bilayer membranes, dark region corresponds to the Onion phase. On the other hand, the bright region corresponds to the planar lamellae-rich Onion phase in which the Onion transforms back into the lamellae actively. The shear-band like structure showed a meander in the slow mode region.

Increase in the birefringence intensity will indicate the rupture of the Onion in the fast mode. However, time range in the fast mode is too short to collapse the Onion. Salmon et al. found that the shear-band flow can be induced by a shear-induced layering transition of the Onion texture [20]. Thus, the fast mode and strong fluctuation of birefringence might be caused by a disruption of the high configurational order of densely packed Onions. Appearance of the slow decay mode seems to be attributed to the coexistence of the Onion and $L_\alpha$, which also forms the shear-band structure because of the difference in the viscoelastic properties [2]. Wilkins et al. found the shear-band structure in the shear-induced Onion transition process [21]. The discontinuous behavior in the Onion degradation process might consist of two mechanisms. In the fast mode, configurational order of the densely packed Onion would be disturbed and causes highly strained Onions which yield the bright birefringent. Then, as the second mechanism, the strained Onions would be ruptured and form the planar lamellae.

The same flow behavior was also observed for other shear quench tests except for high shear rate region in figure 3(c). In the high shear rate region where transient viscosity did not show the exponential like decay, no shear-band like flow was observed. Onion texture seems to change continuously [15].

## Kinetic state diagram

We made a kinetic state diagram for the Onion size change process by summarizing the transient viscosity curves in figure 3. Diagram was represented in a gray scale in order to express the viscosity by dark level in figure 6. On the same diagram, the induction time for the Onion reformation and an initiation time of the slow mode were also plotted. Different symbols in the induction time correspond to different initial shear rate for the shear quench. The initiation time in the Newtonian regime was not shown because of difficulty in the estimation. Kinetic states after shear quench can be seen on the viscosity map. The induction time for the Onion reformation and the initiation time for the slow mode in

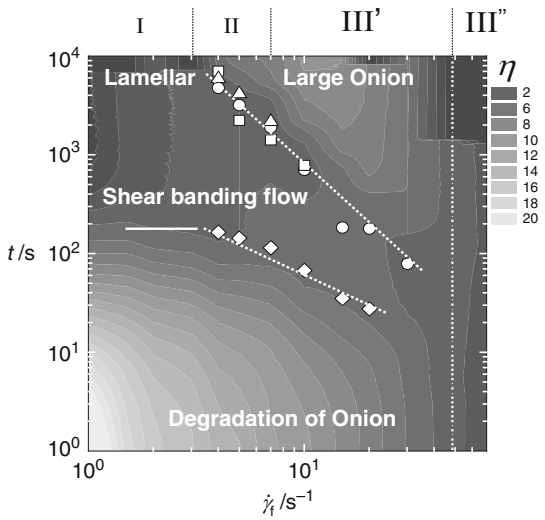


**Fig. 6** Gray scale representation of the transient viscosity in the Onion-to-$L_\alpha$ degradation and $L_\alpha$-to-Onion reformation processes after shear quench from $\dot{\gamma}_i = 100\text{s}^{-1}$ to difference final shear rates. White shows a high viscosity, black lower. Symbols indicate the induction time for the Onion reformation ($\bigcirc\dot{\gamma}_i = 100\text{s}^{-1}\square{:}30\text{s}^{-1}\triangle{:}15\text{s}^{-1}$) and the initiation time of the slow mode ($\diamond$: $\dot{\gamma}_i = 100\text{s}^{-1}$), respectively. Dotted lines on the induction time and on the initiation time show a power law relation with a slope of $-2$ and $-1$, respectively

the shear rate domain II and III' were described by power law relations with the slope of $-2$ and $-1$, respectively. The power law relation in the initiation time, $t_{slow} \propto \dot{\gamma}_f^{-1}$, indicates that the slow decay mode can be scaled by strain, $t\,\dot{\gamma}_f$. Thus, the shear-band structure in the slow mode would be also caused by mechanical deformation of the Onion phase. Since the Onion structure seems to degrade into the planar lamellae in the slow mode, degradation of the Onion would be also triggered by a mechanical process. Scaling the kinetic state diagram by strain unit modifies the power law relation of the induction time $t_{ind} \propto \dot{\gamma}_f^{-2}$ into $\gamma_{ind}(= t_{ind}\dot{\gamma}_f) \propto \dot{\gamma}_f^{-1}$. Here, $\gamma_{ind}$ is an induction strain, which is necessary for causing the Onion reformation. At the induction time, the viscosity minimum was independent of the final shear rate. Thus, the final shear rate at the induction time is proportional to the shear stress, $\dot{\gamma}_f \approx \sigma_{ind}/\eta_{\min}$. Therefore the induction strain will be further rescaled by the stress at the induction time as $\gamma_{ind}\sigma_{ind} \propto \dot{\gamma}^{-2}$. The product of strain and stress yields a mechanical energy. The induction of the Onion reformation might be also appeared when the mechanical energy of the Onion is dissipated and relaxed [17, 24]. Thus the slow decay mode might be driven by a mechanical energy dissipation rate, $\dot{W} \propto \eta\dot{\gamma}^2$, here $\dot{W}$ is the dissipation rate. The degradation of the Onion seems to be caused by unbalance of the mechanical energy between the elastic bending energy of bilayer membrane and the applied external stress. Reduction of externally applied shear stress will be proportional to the shear quench depth. When the shear rate is quenched, thus, the onions prepared at high shear rate will be instable because the mechanical energy of the applied shear stress is not high enough compared to the bending energy of the bilayer membranes of the onion. This excess energy of the bilayer membranes will drives the rupture of the Onion. Thus, the slow decay mode depends on the final shear rate. Shear-banding flow in the slow decay mode of the discontinuous process might be a result of the rearrangement of the Onion configuration for compensating the excess elastic bending energy.

## Summaries

In this study, we investigated the discontinuous growth mechanism of the Onion sturucture induced by shear quench in detail. Discontinuous growth behavior induced by quenching shear rate was observed in an intermediate shear rate domain. In the anomalous Onion-$L_\alpha$-Onion transformation process, Onion-$L_\alpha$ degradation is scaled by shear strain. In the Onion-$L_\alpha$ degradation process, the shear-band structure appeared which might appear because of the rupture of the Onions. The induction time of the Onion reformation will be attributed to the energy dissipation rate. Rupture of the Onion structure might be attributed to excess elastic bending energy of bilayer membrane. At high shear rate regions, viscous stress applied by shear flow is balanced with elastic bending energy. However, unbalance between the viscous stress and excess elastic bending energy caused by shear quench may drive the instability of membrane. This instability will cause the degradation of membrane resulting in rupture of onion structure.

**Acknowledgement** This research was supported by the Ministry of Education, Science, Sports and Culture, Grant-in-Aid for Young Scientists (B) No.19740258 and Scientific Research on Priority Area "Soft Matter Physics" No.19031008. S.F. thanks to Prof. T. Takahashi at Nagaoka University of Technology, Japan, for use the rheometer ARES-LS and the Linkam shear cell CSS450.

## References

1. Larson RG, (1999) The Structure and Rheology of Complex Fluids, Oxford Univ.Press
2. Olmsted PD, (1999) Europhys Lett 48:339
3. Diat O, Nallet F, Roux D, (1993) J Phys II 3: 1427
4. Diat O, Roux D, (1993) J Phys II 3: 9
5. Schmidt G, Mueller S, Schmidt C, Richtering W. (1999) Rheol Acta 38: 486
6. Nettesheim F, Zipfel J, Olsson U, Renth F, Lindner P, Richtering W. (2003) Langmuir 19: 3603
7. Le TD, Olsson U, Mortensen K, Zipfel J, Richtering, W. (2001) Langmuir 17: 999

8. Oliviero C, Coppola L, Gianferri R, Nicotera I, Olsson U, (2003) Colloids Surf A 228: 85
9. Medronho B, Miguel M. G, Olsson U, (2007) Langmuir 23: 5270
10. Medronho B, Fujii S, Richtering W, Olsson U (2005) Colloid Polym Sci 284: 317
11. Panizza P, Cloin A, Coulon C, Roux D (1998) Eur Phys J B 4: 65
12. Courbin L, Engl W, Panizza P, (2004) Phys Rev E 69: 061508
13. Medronho B, Shafaei S, Szopko R, Miguel M. G, Olsson U, Schmidt C. (2008) Langmuir 24: 6480
14. Fujii S, Richtering W, (2006) Eur Phys J E 19: 139
15. Fujii S, Konno M, Isono Y, (2008) Trans-MRS. Jpn 33: 425
16. Koschoreck S, Fujii S, Richtering W, (2008) Progress of Theoretical Physics. in press
17. Helfrich W, (1978) Zeitschrift Fur Naturforschung Section a-a Journal of Physical Sciences 33: 305
18. Auernhammer G K, Brand H R, Pleiner H, (2000) Rheol. Acta 39: 215
19. Zilman AG, Granek R, (1999) Euro Phys J B 11: 593
20. Salmon JB, Manneville S, Colin A, (2003) Phy Rev E 68: 051504
21. Wilkins GMH, Olmsted PD, (2006) Eur Phys J E 21: 133
22. Koschoreck S, Fujii S, Lindner P, Richtering W. (2008) submitted to Rheol Acta
23. Olsson U, Wennerstroem H, (2002) J Phys Chem B 106: 5135
24. Kleman M, Lavrentovich OD (2001) Soft Matter Physics: An Introduction. Springer, Berlin Heidelberg New York
25. Press WH, Vetterling WT (2002) Numerical Recipes in C: Chapter 18, Cambridge University Press
26. Olmsted PD, (2008) Rheol Acta 47: 283

Progr Colloid Polym Sci (2009) 136:77–86
DOI: 10.1007/2882_2009_11

# Study on Self-Assembly of Telechelic Hydrophobically Modified Poly(*N*-isopropylacrylamide) in Water

Taisuke Fujimoto, Emi Yoshimoto, and Masahiko Annaka

**Abstract** The microscopic structures of aqueous dispersions of hydrophobically modified poly(*N*-isopropylacrylamides) (HM-PNIPAM) and hydrophobically modified poly(ethylene oxide) (HM-PEO), which carry an octadecyl group at each chain end and have an average molecular weight of 20,000 g/mol, were investigated by small-angle neutron scattering (SANS). When the polymer concentration exceeds the overlap concentration, connectivity through bridging chains takes place, resulting in the formation of a network in which flower micelles act as junctions. The temperature dependence of the micelle structure is significant in the case of the HM-PNIPAM system but not significant in the case of the HM-PEO system, indicating the importance of hydrophobic interactions in the structural stability of flower micelles. Two different parameters relating to the micelle size are defined depending on the polymer concentration. One is the total micelle radius in the dilute regime and the other is the "non-overlapping radius" of the micelles in the semi-dilute regime. These two parameters exhibit qualitatively different trends with respect to temperature.

**Keywords** Poly(*N*-isopropylacrylamides) • Poly(ethylene oxide) • Telechelic Hydrophobically Modified Polymer • Inter-Micellar Network • Small-Angle Neutron Scattering

## Introduction

Among the various families of hydrophobically modified water-soluble polymers, telechelic derivatives bearing hydrophobic end-groups have attracted attention over the decades, primarily because of their ability to form flower-like micellar aggregates which associate above a given polymer concentration, giving rise to highly viscoelastic fluids. Winnik and coworkers [1–3] reported recently the preparation and solution properties of well defined telechelic hydrophobically modified poly(*N*-isopropylacrylamides) (HM-PNIPAM), which carry an octadecyl group at each chain end and range in size from $M_n$ = 12,000 to 49,000 g/mol with narrow molecular weight distribution. Structurally, the HM-PNIPAM samples bear close resemblance to the important class of polymeric additives known as hydrophobic-ethylene oxide-urethane (HEUR) copolymers which are key components of numerous water-borne fluids, primarily because of their ability to induce viscoelastic properties in aqueous solutions. The characteristic feature of HEUR polymers in water is their ability to form flower micelles via attraction of the end groups [4 5]. When the polymer concentration exceeds the overlap concentration, connectivity through bridging chains takes place, resulting in the formation of a network in which flower micelles act as junctions. This scenario described for the PEO-based systems, turned out to be applicable also to the case of HM-PNIPAMs. In cold aqueous solutions (0.1 to 11 g/L), HM-PNIPAM samples were shown to associate in the form of flower-like micelles ($R_G/R_H \approx 1.3 - 1.5$). Significant viscosity enhancement was observed upon increasing the concentration of HM-PNIPAMs above a threshold value, leading to the formation of a gel phase at even higher concentrations.

Both PEO and PNIPAM possess a lower critical solution temperature (LCST) in water. An increase in the solution temperature induces dehydration of the polymer chains, triggering the collapse of hydrated polymer coils into globules which associate to form mesoglobules. Several studies have shown that the LCST of aqueous telechelic HM-PEO solutions is much lower than those of solutions of PEO samples of comparable molecular weight. The magnitude of the shift can be as large as 100 °C. In contrast, in the case of aqueous telechelic HM-PNIPAMs solutions, the end group-induced decrease of the LCST is much weaker, on the order of 5 to 10 °C. This significant difference between telechelic HM-PEOs and HM-PNIPAMs can be traced to

M. Annaka (✉)
Department of Chemistry
Kyushu University
Fukuoka 812-8581, Japan
e-mail: annaka@chem.kyushu-univ.jp

differences in the interactions of water molecules with the main chain. Hydration of the main chain tends to prevent close contacts between chains and hinders polymer self-assembly. In the case of telechelic HM-polymers, the competition between hydration and chain association affects primarily the sections of polymer closest to the hydrophobic tails, since a large fraction of the polymer chains remain exposed to water even when association takes place. Nonetheless, as described in a theoretical treatment by Tanaka and coworkers [6], the differences in the hydration mechanisms of PEO and PNIPAM are significant and affect the macroscopic properties of their hydrophobically-modified derivatives.

We report here the results of a small-angle neutron scattering (SANS) study of aqueous solutions of telechelic HM-PNIPAM and telechelic HM-PEO aimed at obtaining and comparing detailed structural information on the micellar network structure of the gel phase and their changes as a function of temperature and concentration.

## Experimental

**Materials.** *N*-isopropylacrylamide (NIPAM) was kindly supplied by KOHJIN. It was recrystallized from a toluene/hexane mixture and dried in vacuo. 2, 2'-azobisiso- butyronitrile (AIBN, Wako Pure Chemicals) was recrystallized from methanol. 1, 4-Dioxane, hexane and toluene (Wako Pure Chemical) were distilled over lithium aluminum hydride under $N_2$ atmosphere prior to use. S-*n*-tetradecyl-S'-(α,α'-dimethyl-α"-N-*n*-octadecylacetamide)-trithiocarbonate was prepared according to the literature by Winnik and coworkers [2]. PEO ($M_w$ = 20,000, Polyscience) was purified by chromatography on activated alumina and lyophilized. Heavy water ($D_2O$, Cambridge Isotope) was used as received. Water was deionized with a Millipore Milli-Q system.

**Instrumentation.** $^1$H NMR spectra were recorded on a JEOL AX-270 (270 MHz) with solutions in $CDCl_3$. The chemical shifts are referenced to trimethylsilane (TMS). Gel permeation chromatography (GPC) was performed with a TOSOH HLC-8220GPC apparatus with TSK gel Super HM-M x 2 columns, in HPLC grade DMF with 10mM LiBr used as the mobile phase at a flow rate 0.4 mL/min at 40°C. Calibration was carried out with PEO standards purchased from TOSOH Corp.

**Preparation of HM-PNIPAM.** $C_{18}$-PNIPAM-$C_{18}$ samples were prepared by reversible addition-fragmentation chain transfer (RAFT) polymerization using S-*n*-tetradecyl-S'- (α,α'-dimethyl-α"-N-*n*-octadecylacetamide)-trithiocarbonate as chain transfer agent (CTA), according to the procedure reported by Winnik and coworkers (Scheme 1) [2]. NIPAM, CTA and AIBN as initiator were dissolved in 1,4-dioxane/hexane (5/1 v/v). The solution was deoxygenated by three freeze-pump-thaw cycles, and polymerization was carried out at 65°C under $N_2$ atmosphere. The polymer was isolated by precipitation in an excess of diethyl ether, and purified by repeated precipitations, followed by drying in

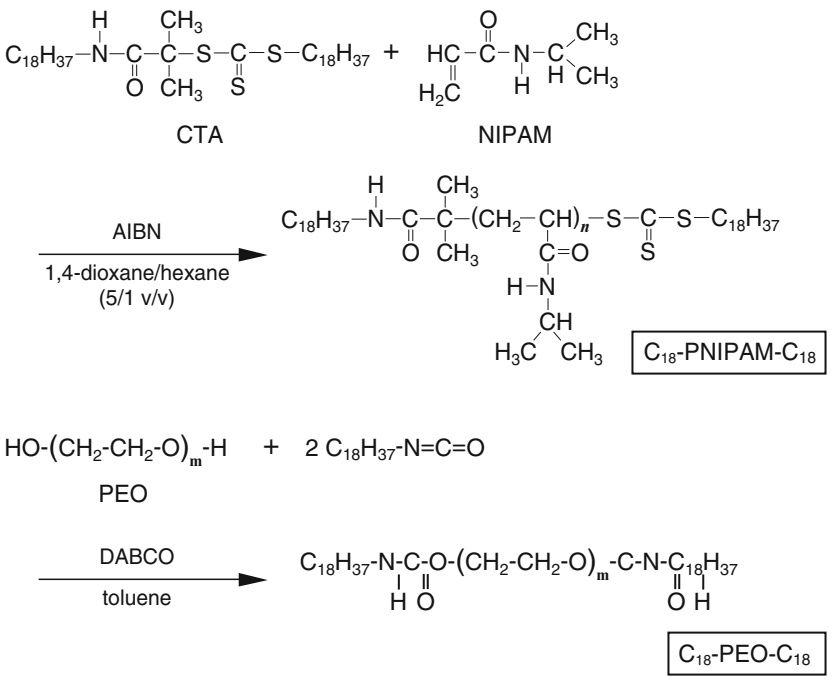


**Scheme 1** Preparation of telechelic hydrophobically modified poly(*N*-isopropylacrylamide), $C_{18}$-PNIPAM-$C_{18}$ and telechelic hydrophobically modified poly (ethylene oxide), $C_{18}$-PEO-$C_{18}$

vacuo. Number-average molecular weight, $M_n$, was determined by $^1$H NMR with using the signal at δ 0.88 ppm attributed to the resonance of the protons of the terminal methyl group of the *n*-octadecyl chains and the signal at δ 4.01 ppm ascribed to the isopropyl methine group. The molecular weight distribution (PDI, $M_w/M_n$) of $C_{18}$-PNIPAM-$C_{18}$ was estimated by GPC (Fig. 1). Specific conditions employed in each polymerization are given in Table 1, together with the molecular characteristics of the corresponding polymers.

**Preparation of HM-PEO.** $C_{18}$-PEO-$C_{18}$ samples (Scheme 1) were prepared by reacting *n*-octadecyl isocyanate with hydroxyl chain ends of poly(ethylene oxide) in the presence of diazabicyclo[2, 2, 2]octane (DABCO) [7]. PEO was dissolved in toluene at 60°C. DABCO (1% w/w with respect to PEO) and an excess of *n*-octadecyl isocyanate (300 mol% with respect to the PEO chain ends) were introduced and the reaction medium was maintained at 60°C for 7 days under $N_2$ atmosphere to obtain complete functionalization. The polymer was isolated by precipitation in an excess of petroleum ether, and purified by repeated precipitations, followed by drying in vacuo. The degree of functionalization was determined by $^1$H NMR, using the signal at δ 0.88 ppm attributed to the resonance of the protons of the terminal methyl group of the *n*-otadecyl chains and the signal at δ 3.65 ppm ascribed to the methylene protons of the main chain of PEO and found to be 100%. The molecular weight distribution (PDI, $M_w/M_n$) of $C_{18}$-PEO-$C_{18}$ was estimated by GPC (Fig. 1). The reaction condition and the molecular characteristics of polymer are given in Table 1.

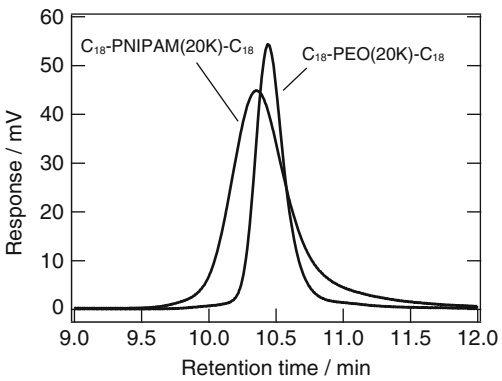


**Fig. 1** GPC traces of $C_{18}$-PNIPAM(20K)-$C_{18}$ and $C_{18}$-PEO(20K)-$C_{18}$

**Determination of Phase Diagrams.** The gelation and gel dissolution were examined by the inversion tube method as the temperature was increased and decreased between 5°C and 40°C. Glass tubes (1 mL) containing polymer solution samples of varying polymer concentrations were kept in a thermostated water bath for 1 h prior to their inversion. The gelation temperature was determined visually when the polymer solutions did not flow by inverting the vials. Generally, after the sample has equilibrated for 1 h, one can easily distinguish several states: transparent sol, opaque sol, transparent gel, opaque gel, and syneresis.

**Small-Angle Neutron Scattering.** The small-angle neutron scattering (SANS) experiments for $C_{18}$-PNIPAM(20K)-$C_{18}$ were carried out at the SANS-U, Institute for Solid State Physics, the University of Tokyo, installed at the research reactor JRR-3 at JAEA, Tokai, Japan. Cold neutrons from the reactor, monochromatized with a velocity selector to a flux of neutrons with the wavelength of $\lambda = 7$ Å and a distribution of $\Delta\lambda/\lambda = 0.1$, were used as the incident beam. Each sample was put into a quartz cell with an optical length of 2 mm. The observed scattered intensity was corrected for cell and solvent scattering, incoherent scattering, and transmission and then rescaled to the absolute intensity, and azimuthally averaged. The incoherent scattering from a polyethylene standard sample was used for the absolute intensity calibration.

SANS experiments for $C_{18}$-PEO(20K)-$C_{18}$ were performed by using the Small/Wide-Angle Neutron Scattering Instrument (SWAN) spectrometer located at C1 in the Neutron Science Laboratory (KENS) of the High Energy Accelerator Research Organization (KEK). Samples were prepared in $D_2O$ and placed in quartz cells of a path length of 1 mm. For isothermal conditions, the temperature of the sample was controlled within an accuracy of 0.1°C by circulating water. The raw spectra were corrected for backgrounds from the solvent, sample cell, and other sources by conventional procedures. The two-dimensional isotropic scattering spectra were azimuthally averaged, and corrected for detector efficiency by dividing by the incoherent scattering spectrum of solvent.

**Table 1** Preparation and Characterization of telechelic HM-PNIPAM and telechelic HM-PEO

| Code | Feed[a] | Reaction time | $M_n$[b] | Monomer units[c] | PDI[d] |
|---|---|---|---|---|---|
| | [M]/[CTA]/[I] | | | NIPAM | |
| $C_{18}$-PNIPAM(20K)-$C_{18}$ | 4360/10/1 | 3.5 h | 20000 | ~180 | 1.19 |
| | [PEO]/[Isocyanate] | | | EO | |
| $C_{18}$-PEO(20K)-$C_{18}$ | 1/600 | 7 days | 20000 | ~450 | 1.03 |

[a]Concentrations of monomer [M], CTA [CTA], initiator [I], poly(ethylene oxide) [PEO], and *n*-octadecylisocyanate [Isocyanate]. [b]Number-averaged molecular weight $M_n$ estimated by $^1$H NMR. [c]Estimated by $^1$H NMR. [d]Polydispersity index determined by GPC in DMF with 10mM LiBr with PEG calibration

## Results and Discussion

**Phase Diagram.** The phase diagram of the $C_{18}$-PNIPAM (20K)-$C_{18}$/water system, established by the tube inversion method is shown in Fig 2. As seen in Fig. 2a, we can distinguish macroscopically five regions in the phase diagram of $C_{18}$-PNIPAM(20K)-$C_{18}$ with increasing concentration or temperature: transparent sol, opaque sol, transparent gel, opaque gel, and syneresis. These changes occur reversibly, without hysteresis, when the temperature is decreased. The threshold concentration for gel formation is $\sim$ 200 g/L and the temperature of transition from clear gel to opaque gel is $\sim$ 30 °C, independently of the polymer concentration. Fig. 2b shows the phase diagram of the aqueous solution of $C_{18}$-PEO(20K)-$C_{18}$. With low polymer concentrations, the sample remains below the gelation threshold. A sol-gel transition is observed for a polymer concentration C $\geq$ 100 g $L^{-1}$ at 25°C.

**Small-angle Neutron Scattering. (i) Dilute regime** Fig. 3 shows the temperature dependence of the SANS profiles for aqueous solutions of $C_{18}$-PEG(20K)-$C_{18}$ and $C_{18}$-PNIPAM(20K)-$C_{18}$ having concentrations of 30 g/L and 52 g/L, respectively. A scattering peak is observed in both systems as indicated by arrows. The peaks correspond to the intermicellar interference. With increasing temperature, the upturn in the lowest $q$ region ($q < 0.02$ Å$^{-1}$) increases while no significant variation is observed in the high $q$ region ($q > 0.07$ Å$^{-1}$). In order to quantify the difference between the $C_{18}$-PNIPAM(20K)-$C_{18}$ and $C_{18}$-PEO(20K)-$C_{18}$ systems, we carried out a fitting analysis by employing the star-like micelle model following the expressions developed by Beaudoin et al. [7]. The model used to calculate the form factor of the micellar corona in dilute regime, $P_{\text{dilute}}(q)$, is represented in Fig. 4 [8−10]. As long as the radius of the core is negligible in comparison to that of the corona, the latter can be assimilated to a star-like polymer and can be presented as an array of concentric shell of close-packed blobs.

$$I(q) = I_{\text{P}}(0)P_{\text{dilute}}(q)S(2qR_{\text{hs}}, \Phi) + \frac{I_{\text{F}}(0)}{1 + \xi^2 q^2} \qquad (1)$$

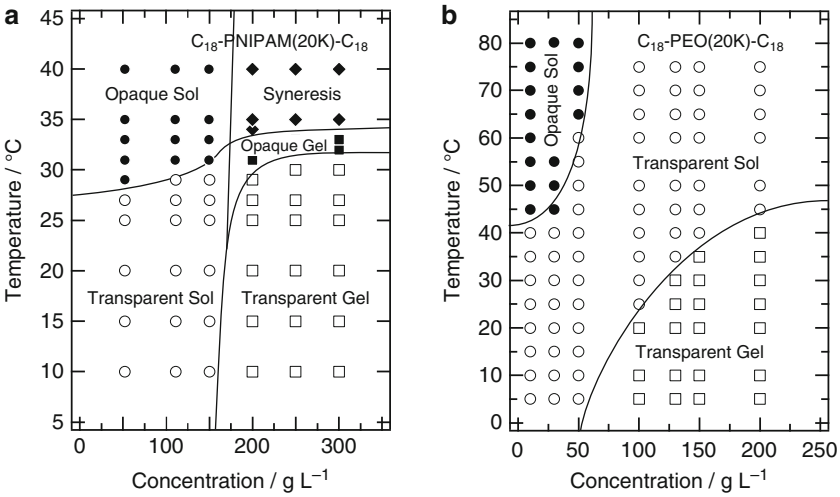


**Fig. 2** Phase diagrams of (a) $C_{18}$-PNIPAM(20K)-$C_{18}$ and (b) $C_{18}$-PEO(20K)-$C_{18}$ in water

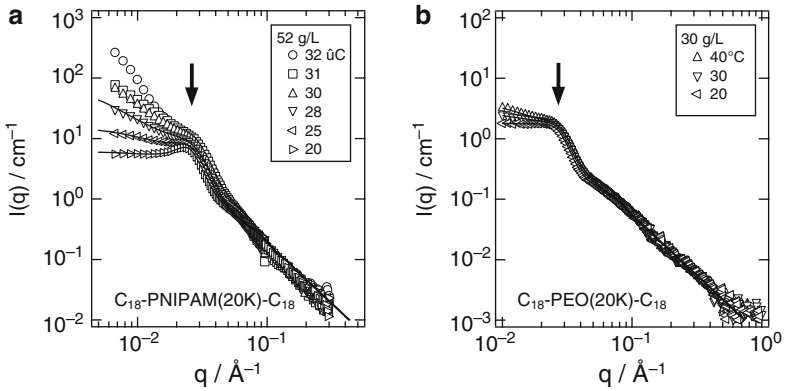


**Fig. 3** SANS profiles for aqueous solutions of (a) 52 g/L $C_{18}$-PNIPAM(20K)-$C_{18}$ and (b) 30 g/L $C_{18}$-PEG(20K)-$C_{18}$. The solid lines are the best-fit curves. The arrows indicate the positions of the scattering peak

$$P_{\text{dilute}}(qR) = \left[\frac{2(1-\cos(qR))}{(qR)^2}\right]^2 \quad (2)$$

Here, the polymers are assumed to be in a Θ solvent, and the polymer concentration in the corona decreases with $C(r) \sim 1/r$ with the distance from the center of micelle, $r$. The polymers form flower micelles with a radius $R$. For simplicity, the Percus-Yevick approximation is applied to the structure factor $S(2qR_{\text{hs}},\Phi)$ with the hard sphere radius, $R_{\text{hs}}$, and its volume fraction, Φ. $I_{\text{F}}(q)$ represents the concentration fluctuations which originate from internal blobs of the micelles with a correlation length, ζ. $I_{\text{p}}(0)$ and $I_{\text{F}}(0)$ correspond to the fraction of the contributions of the micellar particles and blobs to the scattering intensity, respectively. $Ip(0) = (\Delta\rho)^2 C M_{\text{w}} N_{\text{agg}}/N_{\text{A}}$ consists of the difference of the scattering length density between the polymer and the solvent, $\Delta\rho$, Avogadro number, $N_{\text{A}}$, polymer concentration, $C$, molecular weight of the polymer, $M_{\text{w}}$, and the aggregation number of polymers forming a single micelle, $N_{\text{agg}}$. Fig. 3 also contains the best-fit curves. The observed SANS profiles are satisfactorily reproduced by eq. 1.

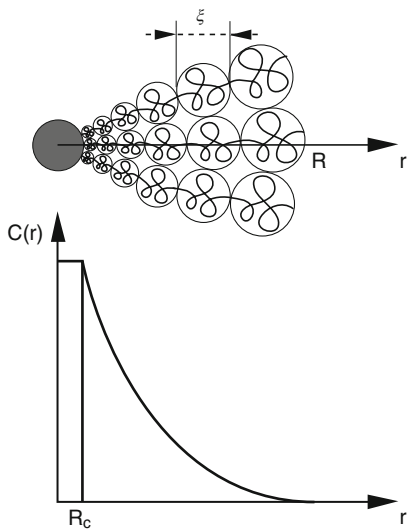


**Fig. 4** Schematic representation of dilute solutions of star-like polymer micelles (Daoud-Cotton model)

Fig. 5 presents the temperature dependence of the micelle radius $R$, hard sphere radius, $R_{\text{hs}}$, and the hard sphere volume fraction Φ. The values of $R$ are consistent with those obtained by dynamic light scattering (DLS) [3, 12]. This means that both DLS and SANS measure the outer radius of micelles in the dilute regime. As shown in Figure 5 the values of $R$, $R_{\text{hs}}$, and Φ all decrease with increasing temperature in $C_{18}$-PNIPAM(20K)-$C_{18}$ system representing the shrinkage of the micelles, but these same values are hardly affected by changes in temperature in the case of the $C_{18}$-PEG(20K)-$C_{18}$ system. These facts clearly indicate that, in the case of the $C_{18}$-PNIPAM(20K)-$C_{18}$ system, the hydrophobic interactions are affected significantly in the temperature range between 20 to 28 °C. The behavior of the correlation length, ζ, will be discussed in the next section, together with that in semi-dilute regime.

From the fitting results, we can estimate the aggregation number, $N_{\text{agg}}$ of the $C_{18}$-PNIPAM(20K)-$C_{18}$ micelle using the relationship $Ip(0) = (\Delta\rho)^2 C M_{\text{w}} N_{\text{agg}}/N_{\text{A}}$. With increasing the temperature, however, PNIPAM corona chains start to collapse due to the dehydration of the chains, and the collapsed PNIPAM corona chains is likely to locate on the surface of the core and is detected as part of the core by SANS. This leads to the temperature dependence of the difference of the scattering length density between the polymer and the solvent $\Delta\rho$. We have to know the temperature dependence of specific mass of polymer to calculate the aggregation number of the micelle. Therefore we do not discuss the aggregation number of the micelle here.

**(ii) Semi-dilute regime.** The temperature dependence of the SANS profiles recorded for aqueous solutions of $C_{18}$-PNIPAM(20K)-$C_{18}$ and $C_{18}$-PEO(20K)-$C_{18}$ with concentrations of 250 g/L and 130 g/L, respectively, are presented in Fig. 6. The scattering peak is much sharper, compared to the case of the dilute regime, in both systems, due to stronger intermicellar interferences caused by the higher volume

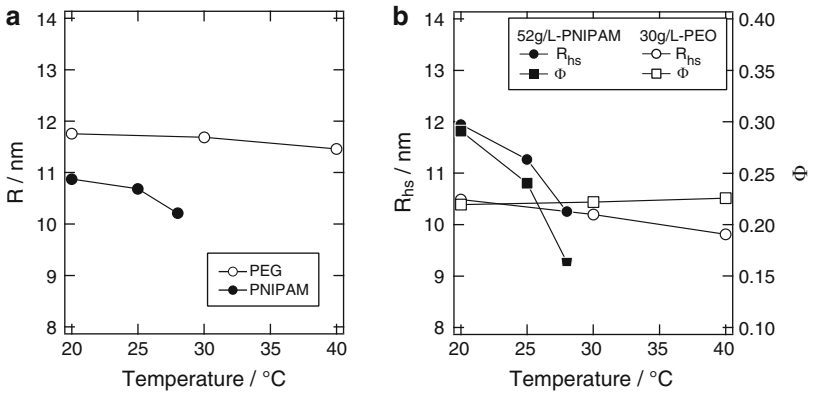


**Fig. 5** Temperature dependence of (a) the micelle radius, $R$, and (b) the interaction radius, $R_{\text{hs}}$, and its volume fraction, Φ for 52 g/L $C_{18}$-PNIPAM(20K)-$C_{18}$ and 30 g/L $C_{18}$-PEG(20K)-$C_{18}$ systems

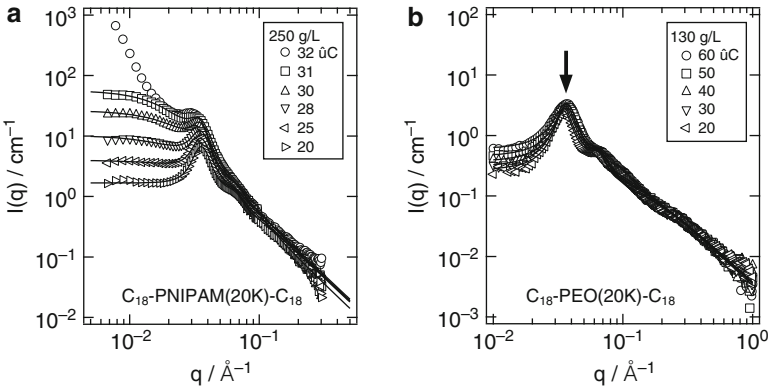


**Fig. 6** SANS profiles for aqueous solutions of (a) 250 g/L $C_{18}$-PNIPAM(20K)-$C_{18}$ and (b) 130 g/L $C_{18}$-PEG(20K)-$C_{18}$. The solid lines are the best-fit curves

fractions in the semi-dilute regime. To quantify the structural parameters of the systems in the semi-dilute regime, we have employed the "sea of blobs" concept[7,12] in addition to the star-like micelles model (eqs. 1 and 2) in order to capture the effect of intermicelle overlapping, which should be significant in flower micelle systems. A semi-dilute solution of star-like micelles is represented schematically in Fig. 7, where the overlapping regions of the coronas constitute a semi-dilute polymer solution, which is considered to be a "sea of blobs" of constant size $\zeta$, while within a radius of $\rho$, the unperturbed structure of the corona equivalent to that in the dilute regime is preserved [8,11]. We shall refer to these unperturbed internal regions as "depleted micelles" which are embedded in the "sea of blobs". The monomer concentration profile is also schematically presented in Fig. 7. The concentration inside the "sea of blobs" is uniform, $C_b$. In the unperturbed internal region of the micellar coronas, the concentration decreases as a function of the distance $r$ from the center of the micelles reaching a value of $C_b$ at the edge of the unperturbed part, i.e., at $r = \rho$. To calculate the form factor of the depleted micelles in the semi-dilute regime, we have to take into account that (i) the central-symmetrical monomer density profile $C(r)$ extends up to $r = \rho$, and (ii) the background concentration $C_b$ has to be subtracted from $C(r)$, which corresponds to the effective reduction of the contrast for the depleted micelles embedded in the semi-dilute polymer solution (the "sea of blobs") of concentration $C_b$ as shown in Fig. 7. Therefore the scattering function is given by

$$I(q) = I_P(0)P_{\text{semi-dilute}}(q)S(2qR_{hs}, \Phi) + \frac{I_F(0)}{1+\xi^2 q^2} \quad (3)$$

$$P_{\text{semi-dilute}}(q\rho) = \left[\frac{6(q\rho - \sin(q\rho))}{(q\rho)^3}\right]^2 \quad (4)$$

where $\rho$ is the radius of non-overlapped region of micelles. In the following, we will refer to this radius as the

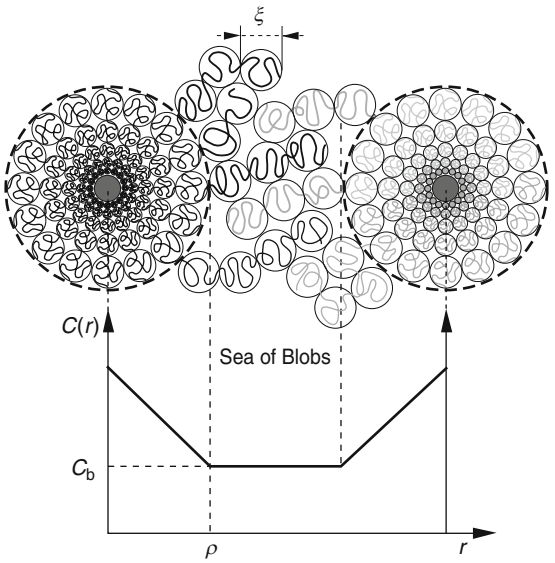


**Fig. 7** Schematic representation of semi-dilute solutions of star-like polymer micelles. The "sea of blobs" and internal unperturbed regions of coronas are depleted

"non-overlapping radius". The correlation length, $\zeta$, may include the contribution of the "sea of blobs" as well as that of internal micelles. The best-fit curves are shown in Fig. 6.

Fig. 8 shows the temperature dependence of $R_{hs}$ and $\Phi$ for aqueous solutions of $C_{18}$-PNIPAM(20K)-$C_{18}$ and $C_{18}$-PEO(20K)-$C_{18}$ with concentrations of 250 g/L and 130 g/L, respectively. As seen already in the dilute regime, $R_{hs}$, and $\Phi$ are decreasing functions of temperature in the $C_{18}$-PNIPAM(20K)-$C_{18}$ system and the temperature dependence is much more pronounced in the $C_{18}$-PNIPAM(20K)-$C_{18}$ system than in $C_{18}$-PEO(20K)-$C_{18}$ system. The values of both $R_{hs}$ and $\Phi$ are smaller in the semi-dilute regime than in the dilute regime, which can be explained by a simple soft micelles packing process. The temperature dependence of the "non-overlapping radius", $\rho$, is shown in Fig. 9. As in the case of the dilute regime, $\rho$ does not vary significantly with

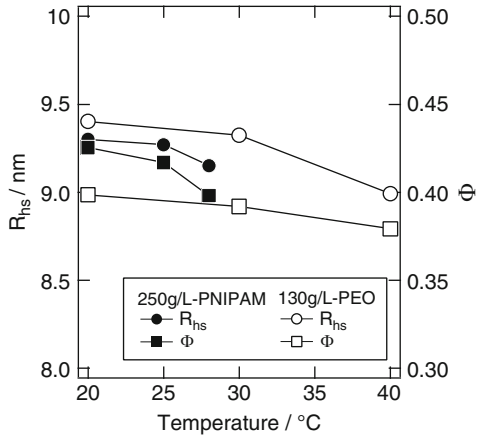


**Fig. 8** Temperature dependence of the interaction radius, $R_{hs}$, and its volume fraction, Φ for 250 g/L $C_{18}$-PNIPAM(20K)-$C_{18}$ and 130 g/L $C_{18}$-PEG(20K)-$C_{18}$ systems

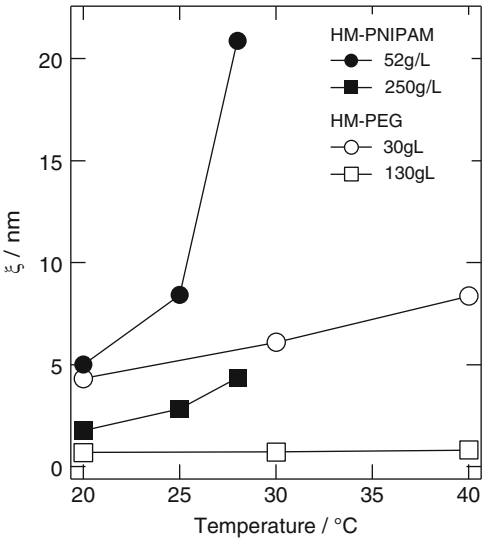


**Fig. 10** Temperature dependence of the correlation length, $\xi$

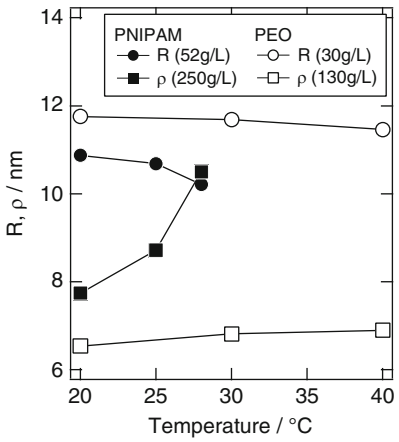


**Fig. 9** Temperature dependence of the micelle radius, $R$, for the dilute systems, and the non-overlapping radius, $\rho$, for the semi-dilute systems

temperature in the $C_{18}$-PEO(20K)-$C_{18}$ system, indicating the stability of the micelles and/or "sea of blobs" structure with respect to temperature. Interestingly, in the semi-dilute $C_{18}$-PNIPAM(20K)-$C_{18}$ system, $\rho$ is an increasing function of temperature, a behavior opposite to that of the micelle radius, $R$, in the same system in dilute conditions and also shown in Fig. 9. Thus, $R$ decreases with increasing temperature in the 52 g/L $C_{18}$-PNIPAM(20K)-$C_{18}$ system whereas $\rho$ increases in the 250 g/L $C_{18}$-PNIPAM(20K)-$C_{18}$ system. The trend exhibited by $R$ indicates shrinkage of micelle coronas. The increase of $\rho$ with temperature may be explained as follows; at high concentrations, the overlap of micelles is so significant that the "non-overlapping radius", in which the density profile has a gradient along the radial direction from the micelle core, is comparable to or smaller than the inter-micelle distance. With increasing temperature, the coronas shrink increasing the density of micelles, and therefore the interaction radius, $R_{hs}$, hardly decreases and the "non-overlapping radius" increases.

Plots of the correlation lengths, ζ's, as function of temperature for all the systems studied are presented in Fig. 10. Regarding the concentration dependence, ζ is smaller in the more concentrated systems, implying densification of the network and suppression of fluctuations in these systems. With increasing temperature, ζ increased steeply in the $C_{18}$-PNIPAM(20K)-$C_{18}$ system, as a result of increased thermal fluctuations upon heating, which may be coupled with the increase of inter-segment correlations caused by the hydrophobically-driven aggregation. These effects cause mesoscopic heterogeneities in the solution, eventually leading to the macroscopic opacity typical of ordinary PNIPAM gels.

**(iii) Scattering from association of micelles or mesoglogule.** For both dilute and semi-dilute solutions, above 20°C, the scattering intensity in low $q$-region ($< 0.02$ Å$^{-1}$) increases with temperature, which indicates association of micelles. At 32°C, for small values of $q$ ($< 0.02$ Å$^{-1}$), the scattering intensity $I(q)$ for dilute regime exhibits a power law behavior $I(q) \sim q^{-\alpha}$ with a slope of $-3 < \alpha < -4$ that can be attributed to scattering from rough interfaces for dilute regime. And $I(q)$ for semi-dilute regime decreases with increasing $q$ according to the -4th power law (Porod scattering) [13], indicating that the surface of the mesoglobule is very smooth. It is worthy to note that the scattering from individual micelles is also observed at $q = 0.02 - 0.05$ Å$^{-1}$, and it becomes less prominent with increasing temperature. These observations indicate that each mesoglobules consist of many micelles, and with increasing temperature the micelles start to merge within each mesoglobule [14].

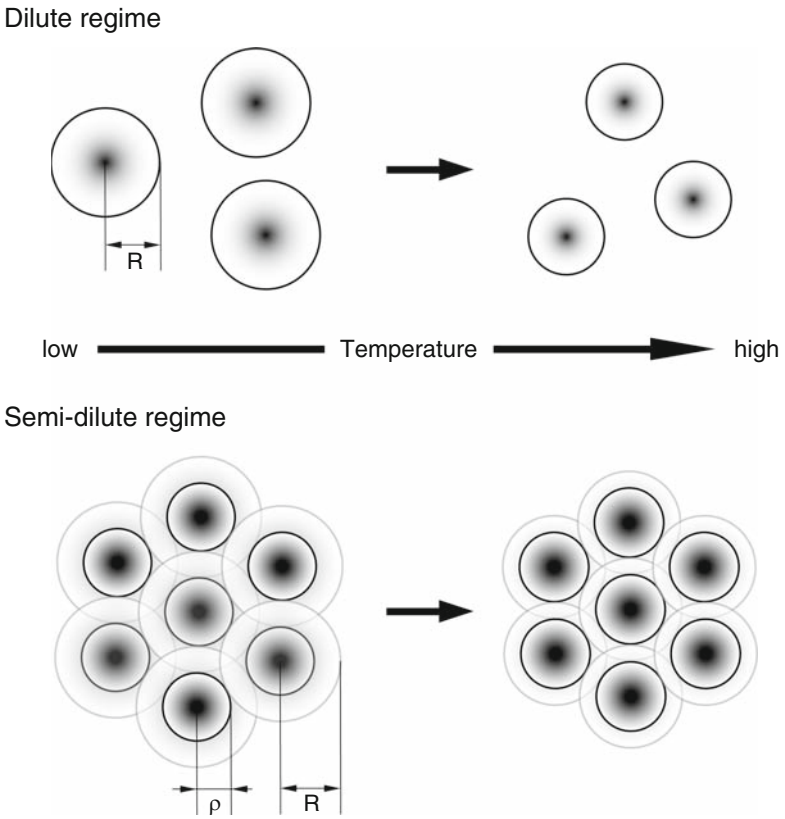


**Fig. 11** Illustrations of overlapping micelles and their responses to heating. (a) In dilute solution, the shrinkage of PNIPAM corona causes only a decrease in the corona size. (b) In semi-dilute solution, the highly overlapping micelle coronas shrink which reduces the extent of the "sea of blobs" region, resulting in an enhancement of the "non-overlapping radius" of the micelles, compared to the situation in solutions of lower temperature

Based on the SANS results, we present in Fig. 11 a schematic illustration of overlapping micelles and their responses to heating in the dilute and semi-dilute regimes, with special emphasis on the $C_{18}$-PNIPAM(20K)-$C_{18}$ systems. At low concentrations, shrinkage of the micelle coronas causes a decrease in the micelle size without further implications. In the semi-dilute regime, however, as the highly overlapping coronas shrink, the "sea of blobs" region is reduced, and, consequently, the "non-overlapping radius" of the micelles becomes larger. The inter-micellar network of $C_{18}$-PNIPAM(20K)-$C_{18}$ in the mesoscale behaves as a typical polymeric gel, although the unit structure is quite different in the two situations. Unlike the case of covalently crosslinked networks, the gel formed by densely packed flower micelles can be unraveled by external stimuli.

## Conclusion

The microscopic structure of aqueous dispersions of hydrophobically modified poly(*N*-isopropylacrylamides) (HM-PNIPAM) and hydrophobically modified poly(ethylene oxide) (HM-PEO), which carry an octadecyl group at each chain end with average molecular weights 20000 g/mol were investigated by SANS. The characteristic feature of HM-PNIPAM and HM-PEO in water is their ability to form flower micelles via attraction of the end groups. When the polymer concentration exceeds the overlap concentration, connectivity through bridging chains takes place, resulting in the formation of a network in which flower micelles act as junctions.

In the dilute regime, the structure factors of the micellar solutions of HM-PNIPAM and HM-PEO reflect repulsive steric interactions between coronas of the micelles. These repulsive interactions can be mimicked by a hard sphere potential with an effective interaction radius, $R_{hs}$, decreases with increasing temperature in the $C_{18}$-PNIPAM(20K)-$C_{18}$ system, implying shrinkage of the micelles, whereas the $R_{hs}$ value exhibits no significant temperature dependence in the case of the $C_{18}$-PEG(20K)-$C_{18}$ system.

In the semi-dilute regime, SANS profiles for both HM-PNIPAM and HM-PEO indicate that (i) micelles are organized in a liquid-like ordered structure, and (ii) the effective interaction radius scales with concentration as the distance between centers of the micelles, which confirms interpenetration of the coronas of micelles. The effective interaction radius, $R_{hs}$ is a weakly decreasing function of temperature in the $C_{18}$-PNIPAM(20K)-$C_{18}$ system and the temperature dependence is much weaker in $C_{18}$-PEO

(20K)-$C_{18}$ system. The fact that the value of $\rho$ increases abruptly with temperature in the semi-dilute regime is taken as evidence of a reduction of the "sea of blobs" region caused by the shrinkage of the highly overlapping coronas and the fact that the interaction radius, $R_{hs}$, is a rather weak function of temperature. This interesting behavior is characteristic of $C_{18}$-PNIPAM(20K)-$C_{18}$ systems, but hardly noticed in the $C_{18}$-PEO(20K)-$C_{18}$ system, an observation that stresses the paramount importance of hydrophobic interactions in controlling the structural stability of flower micelle systems.

**Acknowledgement** The work was partly supported by a Grant-in-Aid for Scientific Research on Priority Areas "Soft Matter Physics" (No. 19031024) and by a Grant-in-Aid for the Global COE Program, "Science for Future Molecular Systems" from the Ministry of Education, Culture, Science, Sports and Technology of Japan. SANS experiments were performed with the approval of the Institute for Solid State Physics, The University of Tokyo (Proposal No. 7404) and the approval of the Neutron Science Laboratory (KENS) at the High Energy Accelerator Research Organization (KEK) (Proposal No. 2005B1-008). Authors acknowledge Prof. Tanaka and Dr. Koga (Kyoto University) for valuable discussion.

## References

1. Kujawa P, Watanabe H, Tanaka F, Winnik FM (2005) Euro. Phys. J. E 17:129
2. Kujawa P, Segui F, Shaban S, Diab C, Okada Y, Tanaka T, Winnik, FM (2006) Macromolecules 39:341
3. Kujawa P, Tanaka F, Winnik FM (2006) Macromolecules 39:3048
4. Pham QT, Russel WB, Thibeault JC, Lau W (1999) Macromolecules 32:2996
5. P Pham QT, Russel WB, Thibeault JC, Lau W (1999) Macromolecules 32:5139
6. Okada Y, Tanaka F, Kujawa P, Winnik FM (2006) J Chem Phys 125:244902
7. Beaudoin E, Borisov O, Lapp A, Billon L, Hiorns R, François J. (2002) Macromolecules 35:7436
8. Daoud M, Cotton JP (1982) J. Phys. (Paris) 43:531
9. Birshtein TM, Zhulina EB (1984) Polymer 25:1453
10. Marques CM, Izzo D, Charitat T, Mendez E (1998) Euro. Phys. J. B 3:353
11. Birshtein TM, Zhulina EB, Borisov OV (1986) Polymer 27:1078
12. Yoshimoto E, Annaka M. unpublished data.
13. Glatter O, Kratky O (1982) Small Angle X-ray Scattering. Academic Press, New York
14. Koga T, Tanaka F, Motokawa R, Koizumi S, Winnik FM (2008) Macromolecules 41:9413

Progr Colloid Polym Sci (2009) 136:87–94
DOI: 10.1007/2882_2009_12

# Some Thoughts on The Definition of a Gel

Katsuyoshi Nishinari

**Abstract** To avoid the confusion of the concept of a gel frequently encountered in daily markets of food, cosmetics, and other industrial products, the definition of a gel is revisited. Recent proposals of the definition of a gel are overviewed, and classifications of various gels from different points of view are described. Discussion is mainly focused on the gel-sol transition and the difference between the structured liquid and the gel, and the classification of gels by temperature dependence of elastic modulus. Finally, the definition of a gel is proposed as a working hypothesis from rheological and structural view points.

**Keywords** Gel-sol transition • Rheology • Structure • Classification2

## Introduction

Since the concept of gels is often understood in different meanings, it causes a confusion and misunderstanding in various areas. Cosmetics for hair treatment sometimes called by a name having "gel" but sometimes it is not a material which should not be called a gel because it flows. Similar examples are found in foods. A commercial name cannot be restricted rigorously, and a namer has sometimes an intention to make it sound attractive and never thinks about the scientific validity of the name, and the name often develops a life of its own. It is necessary to make the definition clear to avoid a further confusion. We try to summarize briefly the history and describe various proposals for the classification of gels, and propose the definition of a gel as a working hypothesis in this manuscript.

K. Nishinari
Department of Food and Health Sciences, Graduate School of Human Life Science
Osaka City University, 3-3-138
Sugimoto, Sumiyoshi, Osaka 558-8585, Japan
e-mail: nisinari@life.osaka-cu.ac.jp

## Definition of a gel

Many definitions to try to answer a question "What is a gel?" have been proposed since the early phrase of Jordan Lloyd "The colloidal condition, the 'gel', is one which it is easier to recognize than to define" [1]. In the review on structure of gels, she classified gels into 1) heat-reversible gels such as gelatin or agar in water, soap in water and organic solvents, azomethine in organic solvents, cellulose acetate in benzoyl alcohol, and 2) heat-irreversible gels such as silica in water, colloidin in chloroform and alcohol, many metallic sulphides and oxides in water. Then, she summarized the contemporary studies on drying, imbibition and displacement of one fluid by another, swelling, contraction of a gel immersed in various solvents, heat evolution accompanying the sol-gel transition, the similarity and the difference between gelation and crystallization, gels and glasses. This review has presented diverse aspects in gel science to be studied, and many of them remain to be clarified.

According to the definition of polymer gels in Dictionary of Polymers [2], "a polymer gel consists of a three dimensional crosslinked network and swells in a solvent to a certain finite extent, but does not dissolve even in a good solvent". This definition is limited to chemically crosslinked gels and excludes physical gels made by secondary molecular forces such as hydrogen bonds and hydrophobic interactions. It was found recently that some molecular chains in a gellan gel release out from the gel when it is immersed in a solvent such as water or salt solutions [3, 4]. After a long time, the gel swells infinitely, and disperses completely in a great amount of water. Therefore, the gellan gel is excluded from an above-mentioned "polymer gel" although gellan is a polysaccharide which is a polymer. The above-mentioned

definition of a polymer gel should be limited to a chemical gel in which the knot of a three dimensional network is formed by covalent bonds. Even a chemical gel may be dissolved completely if it is immersed in a solvent which degrades covalent bonds. If gels of agarose, gelatin or gellan are excluded from the category of gels, a gel is not at all "easy to recognize" contrary to the expression of Jordan Lloyd. Otsuka and Suzuki [5] recently prepared a poly (vinyl alcohol) (PVA) gel by a casting method, and then immersed this gel in water. By exchanging external water, they found that the gel weight decreased and tended to a constant weight, which is different from the behaviour of a gellan gel. The initial decrease of weight of PVA gels seems to have the same origin reported for gellan gels because crosslinking points in PVA gels consist of only hydrogen bonds and not covalent bonds. Whether the difference between gellan gels and PVA gels is only a problem of time scale of observation or not should be studied further.

Gels prepared by casting solutions of flexible polymers such as pullulan or PVA should also be called a gel as long as they do not flow. This depends on the patience of the observer, or if $G'$ and $G''$ follow the criteria proposed by Almdal, Kramer et al [6] which will be mentioned later, it can be called a gel although Winter [7, 8] does not agree with this idea. Winter emphasizes that if it flows after a long time, it should not be called a gel. It may be logically true. However, we can not extend the time scale of the observation to an infinite time, and we cannot observe $G'$ and $G''$ at so low frequencies. Of course, the advance of the technology will extend the time scale of the observation than the present limit, but there will be still a limit. As has been observed for many amorphous polymers, time-temperature superposition principle holds well. As for gels, time-concentration superposition may hold for flexible polymer solutions. For more concentrated gels, both $G'$ and $G''$ show a plateau at lower frequency range than less concentrated gels. Then, the definition of gels is obliged to change with the advance of experimental technique, for instance, a material which we feel a gel may turn out to be a sol (liquid) when a rheometer which can measure at an ultra low frequency is realized in the future. Before an actual measurement, we cannot predict for the moment whether it flows or not based on the rheological data limited within a narrow frequency range.

As Koga and Tanaka [9] showed by computer simulation, the critical concentration for gel formation decreases with increasing persistence length of the polymer. This conclusion is consistent with experimental data for many gelling agents such as agarose, carrageenan, gellan, etc which are stiff molecules and show a very low critical concentration for gelation. However, solutions of schizophyllan which has much longer persistence length ca.180nm do not form a gel but form only a structured liquid, (formerly called a weak gel; this will be mentioned later) [10], which questions the general validity of this conclusion. The critical concentration for gel formation does depend not only on the persistence length but also on other factors such as molar mass, electric charge distribution, degree of branching or other structural features.

Rubber resembles a gel because of its structure consisting of molecular network, but it does not contain solvent, and so it is different from a gel, and should be classified as a solid. Swollen rubber in organic solvents can be called a gel. The lower limit of solvent content is, however, not clearly defined. The situation is similar for hydrophilic polymers such as pullulan and PVA. A dried film of these materials should not be called a gel and it is a solid. Almdal et al [6] say that materials with moduli of the order of $10^8$ Pa are far too rigid to be called a gel. From a metallurgist point of view, almost all the polymeric materials may be classified as soft materials. It seems to be difficult to find the limit of the moduli above which the material should not be called a gel.

A gel can be defined as an intermediate state between a liquid-like rheological behaviour and a solid-like rheological behaviour. It consists of a dispersed phase (polymers or colloids) and a dispersing medium (water or other solvents), and can be very close to a liquid or to a solid. The liquid-like properties originate from the fact that the major constituent is water or other solvents. The solid-like behaviours are due to the network which prevents the system from flowing, and characterized by a finite elastic modulus. Since the gel consists of liquid and solid, its mechanical properties are in between ideal (Hookean) elasticity and ideal (Newtonian) viscosity. In a sol, molecular chains or colloidal particles diffuse, and in a gel this motion is restricted. After these chains or particles are connected to span the whole space, or "percolated", chains or particles constituting a network do not show a macro-Brownian motion; their center of gravity do not show a diffusion. However, this fixed connectivity is limited only in chemical gels. Tanaka and Edwards [11, 12] proposed a transient network theory for physical gels assuming that polymer network chains can interchange each other. This theory explained rheological behaviour of HEUR (hydrophobically modified ethoxylated urethane) gels successfully.

Almdal, Kramer et al [6] proposed the following phenomenological definition of a gel in the first paper in a journal "Polymer Gels and Networks":

1. A gel is a soft, solid or liquid-like material of two or more components, one of which is a liquid, present in substantial quantity.
2. Solid-like gels are characterized by the absence of an equilibrium modulus, by a storage modulus, $G'(\omega)$, which exhibits a pronounced plateau extending to times at least of the order of seconds, and by a loss modulus, $G''(\omega)$, which is considerably smaller than the storage modulus in the plateau region.

Nijenhuis [13] commented that the applicability of this definition depends on the patience of the observer. Raghavan and Cipriano [14] stated that "xanthan gum and carbopol$^{R}$ samples are physical gels that have appreciable yield stresses and hence are able to suspend dense spherical particles for more than a month." Is it possible to limit the patience of the observer up to one month? In the polymer gel community, aqueous dispersion of xanthan gum is classified as a structured liquid, which will be discussed later again. It reminds us the famous saying of a prophetess Deborah: Even the mountains flow before the Lord. Then, Nijenhuis was obliged to propose a more philosophical or cynical definition: A gel is a gel, as long as one cannot prove that it is not a gel [13].

It is surely difficult to propose a final definition for a gel because it might be possible to find some exceptions. Although it is said that there are no rules without exceptions, the scientific definition should not include the exception. In other words, it may be only possible to have a tentative definition and when a new gel, which is not included in a previous definition, is discovered, that difinition should be changed.

## Gelation point

Since the analogy between the gelation and percolation was pointed out by de Gennes [15] and Stauffer [16], many studies on the gelation have been done by using percolation theory. The shear modulus of gels $G_0$ and the zero-shear viscosity of the solution $\eta_0$ are shown to obey a power law near the sol-gel transition point

$$G_0 \sim \varepsilon^t$$

$$\eta_0 \sim \varepsilon^{-k}$$

where $\varepsilon = |p - p_c|/p_c$ represents the relative distance of a percolation probability $p$ from the gel point value $p_c$ (percolation threshold). The parameter $p$ is the probability of the site occupation or of the bond formation in the lattice percolation model, the counterpart of the reactivity in polycondensation. It represents concentration, temperature, degree of crosslinking etc [17].

Later in 1980s, Winter and Chambon proposed a criterion for the linear dynamic-mechanical modulus by which the sol-gel transition can be judged [7, 18]. This can be summarized as follows: the storage and loss moduli, $G'$ and $G''$, of the dispersion should show the same frequency scaling law at the gelation point,

$$G'(\omega) \sim G''(\omega) \sim \omega^n$$

$$\tan\delta = G''(\omega)/G'(\omega) = \tan(n\pi/2)$$

where the relaxation exponent $n$ was first proposed as 0.5, and then later other values between 0.1 and 1 have been reported for various gelation processes [19]. These equations are valid at times longer than a certain characteristic time $t_0$ or at lower frequencies than $1/t_0$.

By using the analogy between the complex modulus and AC conductivity of a random resister network first proposed by de Gennes, Durand et al [20] showed that the critical index $n$ is related to the two fundamental indices $t$ and $k$ through the equation

$$n = t/(k + t).$$

Typical values found by Nemoto and his coworkers for $n, t, k$ are $n = 0.66, k = 1, t = 2$ [21]. The gelation of agarose [22], casein [23], PVC [24] has also been studied successfully by percolation treatment.

The frequency scaling law was first proposed to determine the gelation point of covalently crosslinked systems. This criterion has been shown to work well especially for chemical gelation [7, 18]. This method was extended to thermoreversible gelation by te Nijenhuis and Winter [25]. The gel point (time) was identified successfully as a time at which time evolution curves of $\tan\delta$ at various frequencies intersect for $\alpha,\omega$-dimethyl silyl poly(propylene oxide) [21] and polybutadiene [18].

However, there have been many papers which mention the invalidity of the Winter-Chambon's criteria. Nyström et al [26, 27] found that in the vicinity of sol-gel transition for poly(ethylene oxide)-poly(propylene oxide) -poly(ethylene oxide) (PEO-PPO-PEO) triblock copolymer aqueous solution, the relation $G' \sim G'' \sim \omega^n$ does not hold. In some colloidal suspensions with a non-zero yield stress, such as ovalbumin and BSA solutions [28–32], curdlan suspension [33], $G' > G''$ and both moduli show plateau values even at low frequencies and even well before a gelation point. Tobitani and Ross-Murphy found for BSA solutions $G' > G''$ even well before the gelation point, and they proposed to determine the gelation point as a time at which $G'$ increased rapidly or $G'$ rose above a threshold value, ca. 2~3 Pa [34, 35].

Ross-Murphy classified the rheological behaviour of polymer solutions into four groups according to mechanical spectra, the frequency dependence of storage and loss shear moduli $G'$ and $G''$ in a reasonably accessible frequency range from $10^{-3}$ to $10^{2}$ rad/s [36]:

1. A strong gel (an elastic gel or a true gel) behaviour, i.e., $G'$ is far larger than $G''$ and both moduli are independent of frequency as found for agar gels [37].

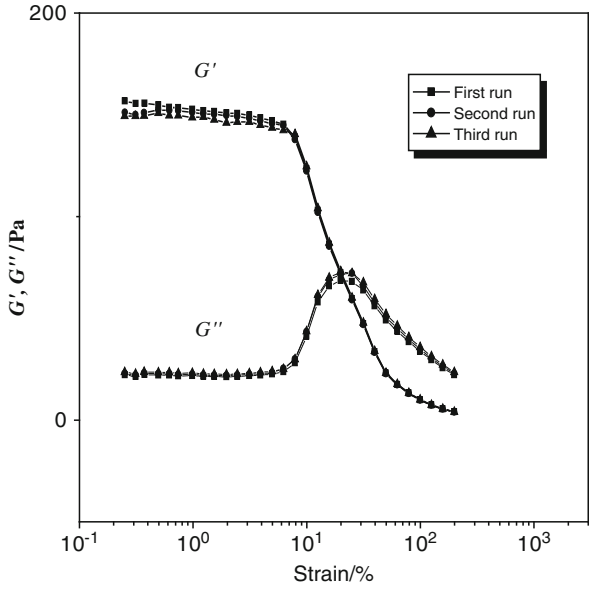


**Fig. 1** Strain dependence of $G'$ and $G''$ determined by dynamic strain sweep measurement at 1 rad/s for SPG-sorbitol aqueous solution at 15 °C [10]. SPG molar mass, $2.5\times10^6$; SPG concentration, 0.8 wt%; sorbitol content, 42 wt%

2. A weak gel behaviour, which should now be called a structured liquid behaviour as mentioned below, i.e., $G'$ is slightly larger than $G''$ and both moduli are only slightly dependent on frequency such as xanthan [38] and bovine serum albumin (BSA) [31] solutions.
3. An entangled polymer solution behaviour in which the concentration $C$ is higher than the critical overlap concentration $C^*$, i.e., $G'$ is smaller than $G''$ at lower frequencies but both moduli increase with increasing frequency and show a crossover, and then $G'$ becomes larger than $G''$ at higher frequencies.
4. A non-entangled polymer solution behaviour ($C < C^*$), i.e., $G'$ is far smaller than $G''$ at all the frequencies and both moduli are strongly dependent on the frequency; at very low frequencies the relations $G' \sim \omega^2$ and $G'' \sim \omega$ have been known for polymer solutions [39].

This definition or a classification of the behaviour is in good agreement with our daily feeling. However, Ross-Murphy regrets the usage of "a weak gel" and it is a terminology to be deplored [40]. "Weak gel" in the above context is not a gel, and it is essentially a liquid. Therefore, it should not be called a gel, and he proposes now another word to describe such a liquid as "a structured liquid". There have been many papers discussing the structure of water [41]. It is well known that even water has also an instantaneous structure, a structure of a very short life time. Therefore, the word "structured liquid" may not be a good term, but we cannot find a better word to describe such a liquid. For the moment, it is not easy to propose a definition more concrete other than the statement "a gel is an intermediate state of matters between liquid-like mechanical behaviour and solid-like mechanical behaviour", which seems to be too broad.

One condition which is necessary to be called a gel is thought to be self-supporting ability of a gel. However, it is evident that it depends on the gravity so that the lower limit of the modulus or fracture stress below which the material should not be called a gel should be different on the earth and on the other planet when we judge whether it maintains its shape against the gravity or not. In this connection, one of the most important parameter which seems to be useful to distinguish a sol from a gel is a yield stress. If we observe a flow curve, stress-strain rate relation, below its yield stress, it may be recognized as a gel because it does not flow. The precise value of the yield stress depends on the sensitivity of the rheological apparatus. It is difficult to distinguish a structured liquid and an elastic gel only by a small deformation rheology. Schizophyllan(SPG)-sorbitol system was claimed as a gel and the structure of junction zones was proposed at first the aggregates of SPG triple helices induced by the reduction of water activity by sorbitol [42] and then the dissociated parts of triple-stranded helices [43] by Kajiwara and Burchard and their coworkers, and no proof from SAXS results could confirm the presence of aggregation of triple helices [43]. Fang et al. [10] showed by ORD, DSC and rheology that this gelation is induced by the transition from SPG triple helix II to I [44], which leads to a three-dimensional network constituted by the extremely entangled and stiff SPG triple helices I. The SPG-sorbitol "gel" (should be called a structured liquid rather than a gel) is structurally like a solution which is unable to flow within a timescale of usual observation [10]. A typical behaviour of this structured liquid is shown in Figure 1.

While the transition temperature was strongly dependent on sorbitol concentration, it was almost independent of SPG concentration [10], which indicated that this transition is caused by intramolecular change and not by intermolecular interactions.

A similar behavior was observed for a kappa-carrageenan-NaI solution [45]. Although 0.15wt% kappa-carrageenan forms a gel in 0.2mol/dm$^3$ KCl, ten times more concentrated 1.5wt% kappa-carrageenan does not form a gel in 0.2mol/dm$^3$ NaI where kappa-carrageenan molecules form helices but these helices donot aggregate to form junction zones.

## Classification of gels

In the Faraday Discussion meeting on Gels and Gelling Processes in 1974, Flory classified four different types of gel on the basis of the structural criteria [46]:

1. Well-ordered lamellar structures, including gel mesophases, such as soap gels and inorganic gels formed from minerals and clays.

2. Covalent polymeric networks; completely disordered, such as vulcanised rubber or polyacrylamide gels in which network is formed by covalent crosslinks.
3. Polymer networks formed through physical aggregation; predominantly disordered, but with regions of local order, including gelatin, agar, carrageenan, methylcellulose gels where the junction zones are believed to be formed by the aggregation of helices or stiff chains.
4. Particulate, disordered structures which may include many gels of globular proteins where the network is formed by clusters of connected spheres.

In the Faraday Discussion meeting on Gels in 1995, Keller discussed various structures in more detail [47]. He illustrated schematically gel morphology obtained by liquid-liquid phase separation intercepted by vitrification:

1. Polymer rich phase connected by isolated solvated chains.
2. Bicontinuously connected phases.
3. Glassy solid phase connected (containing solvent rich phases)
4. Glassy disperse phase connected through adhesive contact.

He also showed two classes of gels arising from liquid to crystalline phase transformation (crystallization):

1. Junctions, bundles or micelles, aggregated rigid chains which are connected by released chains.
2. The network elements are formed by fibrous crystals constituted by rigid or semi-flexible chains that do not fold on crystallization.

Most commonly used classification of gels is based on the nature of the bond involved in crosslinking region, and the classification into chemical gels and physical gels has been widely accepted. In the former gels, the crosslinking region is formed by covalent bond while in the latter gels, that is formed by hydrogen bond, ionic bond, and hydrophobic interaction. For a liquid-like rheological behaviour, entanglement plays a role of temporary crosslinking point, but this leads only to liquid-like rheological behaviour and should not be classified into a gel. With the advent of sliding gels proposed by de Gennes [48] or slide-ring gels of Okumura-Ito [49], it may be natural to extend the concept of physical gels to embrace these gels because the crosslinking point is not composed by covalent bonds but by topological constraints. Although double network gels studied by Hokkaido University Group [50] are interpenetrating networks consisting of double chemical networks, an interpenetrating network can also be called a physical gel if each network alone does not form a gel but the interpenetration leads to a gel formation. Djabourov tried to separate the contribution of physical and chemical bonds to the network elasticity by introducing a reactant, bisvinyl sulfonemethyl (BVSM) [51].

Recently, paying special attention to the structure of crosslinks, Tanaka classified gels into six categories [52, 53]: 1) simple gelation where one single component of a polymer forms a gel by pairwise crosslinking in a solvent, 2) gelation by multiple crosslinking where more than 3 chains are linked in the junction point, 3) gelation from two different polymers, which include interpenetrating networks, alternately crosslinked networks, randomly mixed networks, 4) gelation competing with hydration (solvation), and coexisting with hydration (solvation), where gelation is either blocked or accelerated by hydration, 5) gelation induced by polymer conformational transition such as coil-helix transition, coil-globule transition, coil-rod transition, 6) gelation coupled with liquid-crystallization, where hydrogen bonded mesogens form crosslinks.

Classification of gels according to optical, thermal and mechanical properties is also necessary and useful. The transparency as well as mechanical compatibility are required for contact lenses. Tokita pointed out that agarose solution forms a transparent gel on cooling, and the system became opaque on further cooling [54]. Many food gels are thermoreversible but some are thermoirreversible. Some polymers form a gel on cooling and the others form a gel on heating [13, 19, 36, 55].

## Temperature dependence of elastic modulus

Now, the classification by the temperature dependence of storage modulus of gelling systems will be discussed.

The Figure 2(a) is a typical gelation on cooling observed in gelatin, agarose, kappa-carrageenan, poly(vinyl alcohol), the gelation on heating shown in Figure 2(b) is also observed in other cellulose derivatives such as hydroxypropyl methyl cellulose. A rheological behaviour shown in Figure 2(c) can be also realized by mixing substances showing (a) and (b) type behaviour such as a mixture of gelatin and methyl cellulose [19]. A behaviour shown in Figure 2(d) is also seen in 2-(2-ethoxy) ethoxyethyl vinyl ether and 2-methoxyethyl vinyl ether [60] and aqueous solution of xyloglucan from which some galactose residues are removed [61]. It is noteworthy that these four types are not exhaustive: Hvidt et al [62] showed more than two gel-sol transitions at different temperatures as mentioned below. It seems that the temperature dependence of storage modulus can be controlled by changing molecular forces responsible for network formation.

The old and new problem discussed since long time is whether the elasticity of gels is of entropic or of enthalpic. When longer macromolecular chains form a three dimensional

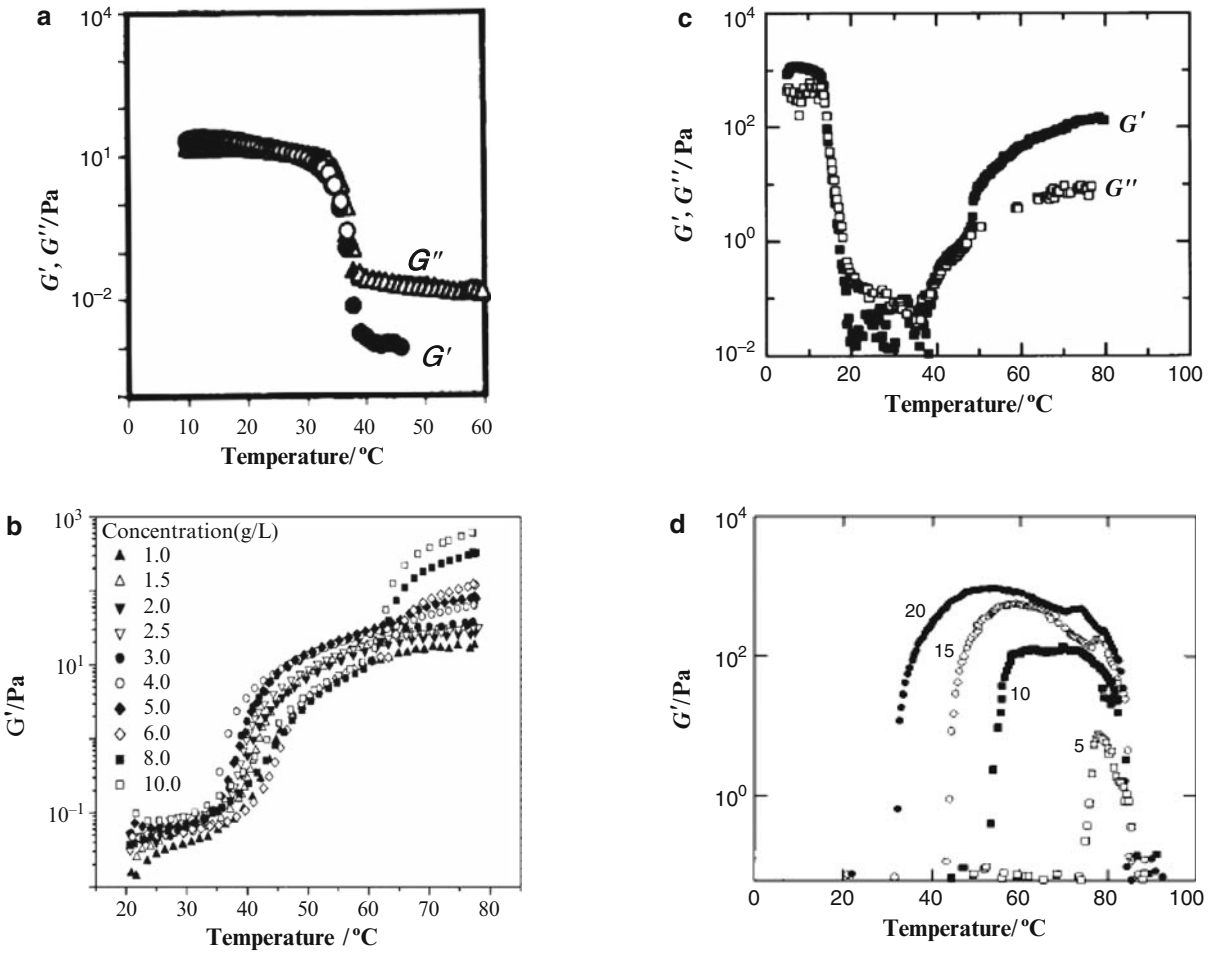


**Fig. 2** Temperature dependence of storage shear modulus $G'$ and loss shear modulus $G''$ of (a) 2.5wt% gellan at 0.1rad/s at scan rate 0.5°C/min, filled, heating; open, cooling [56]; (c) 5wt% $E_{184}B_{18}$ (E = oxyethylene unit, B = oxybutylene unit) at 1Hz and at heating rate 1°C/min [57], and $G'$ of (b) methylcellulose at 1rad/s at heating rate 1°C/min with various concentrations (g/L) indicated in the figure [58], (d) $E_{41}B_8$ at 1Hz and at heating rate 1°C/min with various concentrations (wt%) indicated in the figure [59]

network, the structure of gels resembles that of rubbers and therefore the elasticity should be entropic [63]. However, some groups propose enthalpic elasticity for polymer gels [64] and a fibrous model proposed by AFM seems to support it [65]. However, the following problem should be taken into account: when the sample solution is fixed on mica surface, the conformation of macromolecular chains might be also changed from flexible to stiff chains, and Brownian motion will be also inhibited under the condition of usual AFM observation. The Brownian motion of these long chains confers a totally different feature to polymeric gels which show a large deformation [66] in comparison to low molar mass gelators.

Gelation of low molar mass gelators, amino acid derivatives [67, 68], porphyrin [69], and copoly(oxyalkylene)s [57, 70] have been studied extensively, and they all seem to have a common feature different from polymeric gels, i.e., the gelating fibres are short and the gel is not rheologically robust; the linear viscoelastic regime is very narrow. Hvidt et al [62] found two different gels of 25.5 wt% triblock copolymers of ethylene oxide and propylene oxide $(EO)_{21}(PO)_{47}(EO)_{21}$ at lower temperature range from 30 to 40°C and at higher temperature range from 55 to 75°C. He called a lower temperature gel a "hard gel" and a higher temperature gel a "soft gel" because the former showed the storage modulus $10^4$ Pa which is two orders of magnitude greater than the latter.

Gels with both high elastic modulus and high fracture strain have attracted much attention because they are expected to be used as a new material [50, 71]. In the opposite extremity, soft food gels are also produced to satisfy consumers' preference. To represent the mechanical strength of a gel, usually the fracture stress or gel strength is used. The difference among adjectives such as hard, solid, firm, stiff, rigid, tough, not easily bent, cut or broken may be explained by native English speakers, but it has not been explained

when the fracture or yield stress and the elastic modulus determined at small deformation show the opposite tendency. For example, a 4.4wt% agar gel shows the Young's modulus $2\times10^5$ Pa far larger than that of a 25wt% gelatin gel ($7\times10^4$Pa) while the fracture stress of the 25wt% gelatin gel is 1.5times larger than that of the 4.4 wt% agar gel at 15°C [72]. Therefore, it is not evident which we should use the elastic modulus or fracture stress to judge when we classify the soft and hard gels. Surely, we should take into account both fracture stress and strain as well as elastic modulus which is usually defined at small deformation.

When we discuss the definition of a gel, we should take into consideration the environment in which our gel is placed because evidently it can not be placed in vacuum and without any force field. Physical environment such as force field such as gravity, electromagnetic field, pressure or temperature as well as biochemical environment such as pH, ionic strength, coexistence of various small and large molecules including enzymes affect structure and properties of gels and therefore the substance can be a gel in an environment but it may turn into a sol or a solid in another environment. Gel-sol transition has been attracting much attention in biomedical and pharmaceutical field where the erosion of gels in stomach and intestines is important for drug delivery [73, 74]. The gel formation [75] of tracheobronchial mucin with alginate produced by an opportunistic pathogen inhibits mucociliary transportation leading to a serious problem in cystic fibrosis patients whilst the gel formation of alginate in stomach at low pH has been used beneficially for the treatment of heartburn and gastro-oesophageal reflux disease [76]. Gel erosion has been applied skillfully to drug delivery, biosensors and tissue engineering [77, 78]. The definition of gels is closely related with understanding of these phenomena and is crucial to the development of biomedical applications in gel technology.

## Concluding Remarks

It is indeed difficult to answer to the question "Whai is a gel?". The author tends to agree to the philosophical conclusion of his good friend Nijenhuis : A gel is a gel, as long as one cannot prove that it is not a gel [13] although he is not an agnostic. A working hypothesis is necessary to solidify the definition. Gels can be defined both from a rheological behaviour and from a structural feature.

Rheological definition of a gel is that the system does not flow, and it can be characterized by the presence of a plateau region of storage modulus and the low $\tan\delta$ ($< 0.1$) at an angular frequency range from $10^{-3}$ to $10^2$ rad/s, which is accessible by many commercially available rheometers. This should be called an operational definition and it can not exclude the possibility to find the violation of this definition if a material obeying this definition shows a liquid-like rheological behaviour at further lower frequencies.

Structural definition of a gel is based on the connectivity of the system. Gel is a system consisting of molecules, particles, chains etc, which are partially connected to each other in a fluid medium by crosslinks to the macroscopic dimensions. According to this structural definition, the loss of fluidity is the result of connectivity. Entanglement of long object may be regarded as connected by delocalized crosslinks. The sol-gel transition can be treated by a percolation theory. This is also another operational definition, and it cannot exclude the possibility of finding gels whose constituents are not directly connected.

## Note added in the proof

Rogovina, Vasil′ev and Braudo (2008) recently published a paper on the definition of polymer gels and stated that a physical gel is characterized by the presence of one or two yield points at stresses above which network degradation and gel transition from the solid to the fluid state takes place.

**Acklnowledgement** The author thanks Prof.F.Tanaka for his precious advice.

## References

1. Jordan Lloyd D (1926) The problem of gel structure. In: Alexander J (ed) Colloid chemistry, vol. 1. Chemical Catalogue Co., New York, pp 767–782
2. Gong JP (2005) In: SPSJ (ed) Dictionary of polymers (Kobunshi jiten). Asakura Shoten, Tokyo, p 208
3. Tanaka S, Nishinari K (2007) Polymer J 39:397
4. Hossain KS, Nishinari K (2008) Discussion meeting of research group on polymer gels, SPSJ, pp 101–102 and this issue
5. Otsuka E, Suzuki A (2008) Abstract of Tanaka memorial symposium pp 137–139
6. Almdal K, Dyre J, Hvidt S, Kramer O (1993) Polymer Gels Networks 1:5
7. Winter HH, Mours M (1997) Adv Polym Sci 134:165
8. Winter HH (1999) Private Communications
9. Koga T, Tanaka F (2008) Private communications
10. Fang Y, Nishinari K (2004) Biopolymers 73:44–60
11. Tanaka F, Edwards SF (1992) J Non-Newtonian Fluid Mech 43:247, 272, 289
12. Tanaka F, Edwards SF (1992) Macromolecules 25:1516
13. Nijenhuis Kte (1997) Adv Polym Sci 130:1
14. Raghavan SR, Cipriano BH (2005) Gel formation: phase diagrams using tabletop rheology and calorimetry. In: Weiss RG, Terech P (ed), Molecular gels: materials with self-assembled fibrillar networks. Springer, Dordrecht, pp. 233–244
15. de Gennes P-G (1979) "Scaling concepts in polymer physics", Cornell University Press, New York

16. Stauffer D (1985) "Introduction to percolation theory", Taylor and Francis, London
17. Tokita M (1989) Food Hydrocolloids 3:263
18. Chambon F, Winter HH (1985) Polymer Bulletin 13:499
19. Nishinari K (2000) Rep Prog Polym Phys Japan 43:163
20. Durand D, Delsanti M, Adam M, Luck JM (1987) Europhys Lett 3:297
21. Koike A, Nemoto N, Takahashi M, Osaki K (1994) Polymer 35:3005
22. Tokita M, Hikichi K (1987) Phys Rev A35:4329
23. Tokita M, Niki R, Hikichi K (1985) J Chem Phys 83:2583
24. Li, L.and Aoki Y (1998) Macromolecules 31:740
25. Nijenhuis Kte, Winter HH (1989) Macromolecules 22:411
26. Nyström B, Walderhaug H, Hansen FK (1995) Faraday Discuss 101:335
27. Nyström B, Walderhaug H (1996) J Phys Chem 100:5433
28. Matsumoto T, OkuboT (1991) J Rheol 35:135
29. Matsumoto, T. and Inoue, H., J. Chem. Soc. Faraday Trans, 87, 3385 (1991b)
30. Ikeda S, Nishinari K (2000) Biomacromolecules 1:757
31. Ikeda S, Nishinari K (2001) Int J Biol Macromol 28:315
32. Ikeda S, Nishinari K (2001) Biopolymers 59:87
33. Hirashima M, Takaya T, Nishinari K (1997) Thermochim Acta 306:109
34. Tobitani A, Ross-Murphy SB (1997) Macromolecules 30:4855
35. Ross-Murphy SB, Tobitani A (2000) In Nishinari K (ed) Hydrocolloids, Part 1: Physical Chemistry and Industrial Application of Gels, Polysaccharides, and Proteins. Elsevier, Amsterdam, pp. 379–387
36. Clark AH, Ross-Murphy SB (1987) Adv Polym Sci 83:57
37. Nishinari K (1976) Jpn J Appl Phys 15:1263
38. Ross-Murphy SB, Morris VJ, Morris ER (1983) Faraday Symp Chem Soc 18:115
39. Strobl G (1996) "The Physics of Polymers", Springer, Berlin
40. Ross-Murphy SB (2008) In: Tanaka F (ed) Lecture Note at Kyoto University
41. Grossfield A (2005) J Chem Phys 122:024506
42. Fuchs T, Richtering W, Burchard W, Kajiwara K, Kitamura S (1997) Polym Gels Networks 5:541
43. Maeda H, Yuguchi Y, Kitamura S, Urakawa H, Kajiwara K, Richtering W, Fuchs T, Burchard W (1999) Polym J 31:530
44. Itou T, Teramoto A, Matsuo T, Suga H (1986) Macromolecules 19:1234
45. S Ikeda, Nishinari K (2001) J Agric Food Chem 49:4436
46. Flory PJ (1974) Faraday Discuss Chem Soc 57:7
47. Keller A (1995) Faraday Discuss Chem Soc 101:1
48. de Gennes P-G (1999) Physica A 271:231
49. Okumura Y, Ito K (2001) Adv Mat 13:485
50. Tominaga T, Tirumala VR, Lin EK, Gong JP, Furukawa H, Osada Y, Wu WL (2007) Polymer 48:7449
51. Hellio-Serughetti D, Djabourov M (2006) Langmuir 22:8516
52. Tanaka F (2002) Development of Computer System for Predicting Phase Diagrams of Associating Polymers
53. Tanaka F (2006) Theory of Molecular Association and Thermoreversible Gelation In: Weiss RG, Terech P (ed), Materials with Molecular Gels – Self-Assembled Fibrillar Networks. Springer, Dordrecht
54. Morita T, Narita T, Tokita M (2008) Food & Food Ingredients J Jpn 213:452
55. Nishinari K (1997) Colloid & Polym Sci 275:1093
56. Miyoshi E, Nishinari K (1999) Progr Colloid Polym Sci 114:68
57. Kelarakis A, Mingvanish W, Daniel C, Li H, Haredaki V, Booth C, Hamley IW, Ryan AJ (2000) Phys Chem Chem Phys 2:2755
58. Yin Y, Nishinari K, Zhang H, Funami T (2006) Macromol Rapid Commun 27:971
59. Li H, Yu G-E, Price C, Booth C, Hecht E, Hoffmann H (1997) Macromolecules 30:1347
60. Aoshima S, Sugihara S (2000) J Polym Sci Polym Chem 38:3962
61. Shirakawa M, Yamatoya K, Nishinari K (1998) Food Hydrocolloids 12:25
62. Hvidt S, Joergensen EB, Brown W, Schillen K (1994) J Phys Chem 98:12320
63. Nishinari K, Koide S, Ogino K (1985) J Physique (France) 46:793
64. Jones L, Marques CM (1990) J Physique (France) 51:1113
65. Morris VJ, Kirby AR, Gunning AP (1999) Progr Colloid Polym Sci 114:102
66. Kawai S, Nitta Y, Nishinari K (2008) J Chem Phys 128:134903
67. Menger FM, Caran KL (2000) J Am Chem Soc 122:11679
68. Hanabusa K, Matsumoto M, Kimura M, Kakehi A, Shirai H (2000) J Colloid Interface Sci 224:231
69. Shirakawa M, Fujita N, Shinkai S (2005) J Am Chem Soc 127:4164
70. Booth C, Attwood D, Price C (2006) Phys Chem Chem Phys 8:3612
71. Haraguchi K, Li H-J (2006) Macromolecules 39:1898
72. Nishinari K, Horiuchi H, Ishida K, Ikeda K, Date M, Fukada E (1980) Nippon Shokuhin Kogyo Gakkaishi 27:227
73. Coviello T, Palleschi A, Grassi M, Matricardi P, Bocchinfuso G, Alhaique F (2005) Molecules 10:6
74. Itoh K, Yahaba M, Takahashi A, Tsuruya R, Miyazaki S, Dairaku M, Togashi M, Mikami R, Attwood D (2008) Int J Pharm 356:95
75. Taylor C, Pearson JP, Draget KI, Dettmar PW, Smidsrød O (2004) Carbohydr Polym 59:189
76. http://www.gaviscon.co.uk/
77. Anseth KS, Metters AT, Bryant SJ, Martens PJ, Elisseeff JH, Bowman CN (2002) J Control Rel 78:199
78. Polizzotti BD, Fairbanks BD, Anseth KS (2008) Biomacromolecules 9:1084

Progr Colloid Polym Sci (2009) 136:95–100
DOI: 10.1007/2882_2009_13

# Structural Transition of Non-ionic Poly(acrylamide) Gel

Sada-atsu Mukai, Hirohisa Miki, Vasyl Garamus[2], Regine Willmeit[2], and Masayuki Tokita[1]

**Abstract** We discuss the structure of the opaque poly(acrylamide) gel that is synthesized at higher mole fractions of the cross-linking agent above 0.2. The structure of the opaque gel is analyzed by the small angle neutron scattering technique. The fractal analysis of the scattering function yields that the polymer network of the opaque poly(acrylamide) gel can be seen as a mass fractal of the fractal dimension of about $D_M \sim 2.7$ when the mole fraction of the cross-linker is higher than 0.3. On the other hand, much larger exponents are obtained in the lower concentration region of the cross-linker less than 0.3. It suggests that the polymer network of the gel behaves as a surface fractal of the fractal dimension of $D_S \sim 2.5$. The structure of the polymer network changes from the surface fractal to the mass fractal at the mole fraction of the cross-linker is 0.3 when the mole fraction of the cross-linker is increased from 0.2 to 0.5. The structure of the gel is also observed by using the confocal laser scanning microscope. The fractal analysis of the confocal images indicate that the fractal dimension of the two dimensional distribution of the colloidal particles in the cross section of the colloidal aggregate is found to be about 1.7.

## Introduction

Gel is an important state of matter in which a great deal of fluid is contained in the polymer network. Because of this molecular structure, the gels are soft and elastic. Poly(acrylamide) gel is a typical synthetic polymer gel that is used in a wide variety of separation techniques such as the gel electrophoresis.

It has been reported that poly(acrylamide) gel becomes opaque when the concentration of the cross-linker is increased [1, 2]. In Fig. 1, we show the appearance of poly (acrylamide) gel in a photograph. In this case, the total concentration of the main chain component and the cross-linking agent is fixed at 700 mM, while the mole fraction of the cross-linker is changed as 0.01, 0.03, 0.05, and 0.1 from left to right. It is clear that the opaqueness of the gel increases with the concentration of the cross-linker. The gel becomes completely opaque when the mole fraction of the cross-linker is higher than 0.1. In the case of poly(acrylamide) gel electrophoresis, the mole fraction of the cross-linker is fixed at about 0.01 to obtain the transparent gel in which the substances can be separated clearly. Although the opaqueness of the gel is of importance in the practical use of the gel, the structure and the properties of the opaque gel is still a matter for discussion [3, 4].

Recently, the structure of the opaque poly(acrylamide) gels has been studied by using the optical microscope such as the confocal laser scanning microscope (CLSM) [5]. The real space structure of the gel that is observed by CLSM indicates that the opaque poly(acrylamide) gel consists of the fractal aggregate of the colloidal particles of about few hundred nanometers in diameter. The hydrodynamic friction between the polymer network and the gel fluid has been also studied [6]. The friction of the gel thus determined has been discussed in terms of the structure of the colloidal aggregate that is revealed by the CLSM. The results indicate that the frictional property of the gel is well described by the structural parameters of the colloid gel of poly(acrylamide) that are determined by the real space structural analysis by the CLSM. It is found from these studies of the opaque poly (acrylamide) gel that the formation of the colloidal particles and the drastic decrease of the friction occur at the same concentration of the cross-linking agent, namely, 0.3 in mole fraction of the cross-linker.

M. Tokita (✉)
[1]Department of Physics, Faculty of Science, Kyushu University, 6-10-1 Hakozaki, Fukuoka 812-8581 Japan
e-mail: tokita@phys.kyushu-u.ac.jp
[2]Department of Macromolecular Structure Research Institute for Material Research, GKSS Research Center Geesthacht 21502 GmbH, Germany

Although the structure of the gel is studied by the CLSM, the information on the fine structure of the opaque poly (acrylamide) gel has yet to be obtained because the spatial resolution of the CLSM is limited to about few hundred nanometers. We, therefore, study the fine structure of the gel by the small angle neutron scattering (SANS) and discuss the results with the large scale real space structure of the gel that is obtained by the CLSM.

## Experimental

The opaque poly(acrylamide) gels are obtained by a photo-polymerization method. The procedure of the preparation of gel is described in previous papers [5, 6]. The main chain component (acrylamide) and the cross-linker (N, N'-methylene-bis-acrylamide) are purchased from BioRad Japan and used without further purification. The photo-initiator (VA-086) is kindly supplied from Wako Pure Chemical Co.. The total amount of the polymer network is fixed at 700 mM while the mole fraction of the cross-linker is changed from 0.2 to 0.5. Hereafter, samples are abbreviated by the mole fraction of the cross-linker such as 0.2-Bis, 0.3-Bis, 0.4-Bis, and 0.5-Bis for the mole fraction of the cross-linker at 0.2, 0.3, 0.4, and 0.5. The sample gels for the SANS measurements are prepared at a temperature of 20.0 °C using $D_2O$ as a solvent. The sheet shaped gels thus prepared are soaked in $D_2O$ to remove the un-reacted substances. The sample gel is then transferred into a quartz cell of 1.5 mm in thickness and then the SANS measurements are carried out.

The sample gels used in the SANS measurements are then labeled by fluorescein isothiocyanate (FITC, Isomer I, Sigma), which is a fluorescence dye for the CLSM observation. The CLSM used in this study is constructed by an inverted microscope (Axiovert S100, Carl Zeiss), a confocal unit (CSU 10, Yokogawa), and an Ar-ion laser (type 532-50BS/170, Omnichrome). The confocal images of gels are gained using an image processor (cooled CCD camera C5985H and ARGUS-20 image processing system, Hamamatsu). Whole confocal laser scanning microscope system is controlled by a microcomputer system (Power Macintosh 7600/200) that equipped with an image graver system LG3 and IPLab Spectrum (Scanalytics Inc.). The objective lenses used here is the Plan-APOCHROMAT (Carl Zeiss, 100×, N. A.= 1.4) and the C-APOCHROMAT (Carl Zeiss, 40×, N. A.=1.2 and 10×, N.A. = 0.45). The thickness of the focal plane in this system is 1 μm (100× and 40×) and 15 μm (10×).

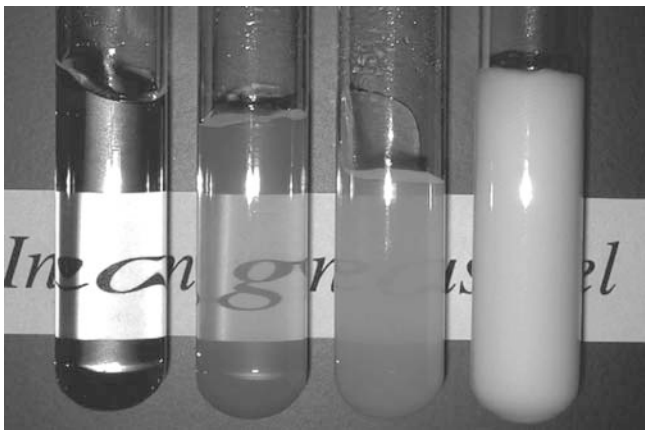

**Fig. 1** The appearance of the opaque poly(acrylamide) gels. The mole fraction of the cross-linker is 0.01, 0.03, 0.05, and 0.1 from left to right

## Results

The angular dependence of the scattering intensity from the opaque gels is shown in Fig. 2 in a double logarithmic manner. The absolute values of the scattering function, $S(q)$, of the higher cross-linker concentrations are shifted along the vertical axis to avoid the overlap of the results. In this figure, the results of $S(q)$ for the 0.5-Bis, 0.4-Bis, and 0.3-Bis are multiplied by a factor of 1000, 100, and 10, respectively.

It is clear from this figure that the scattering function of the gel, $S(q)$, is well described by the straight lines at small scattering vectors. The power law behaviors of the scattering intensity are analyzed by the least square fitting to the following function.

$$S(q) = Aq^{-b} + C \tag{1}$$

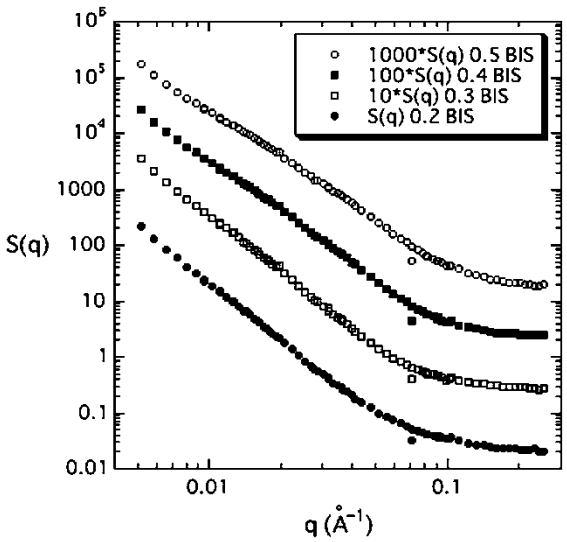


**Fig. 2** The double logarithmic plot of the scattering function. The mole fraction of the cross-linker is 0.5, 0.4, 0.3, and 0.2 from top to bottom. The scattering functions of 0.5-Bis, 0.4-Bis, and 0.3-Bis gels are multiplied by factors of 1000, 100, and 10 to avoid the overlap of the results

| Sample | 0.2-Bis | 0.3-Bis | 0.4-Bis | | 0.5-Bis | |
|---|---|---|---|---|---|---|
| **q range** | **–** | **–** | **$q < 0.02$** | **$q > 0.02$** | **$q < 0.02$** | **$q > 0.02$** |
| **A** | $3.0\times10^{-6}$ | $3.0\times10^{-6}$ | $6.0\times10^{-5}$ | $6.0\times10^{-6}$ | $1.3\times10^{-4}$ | $1.7\times10^{-5}$ |
| **b** | 3.39 | 3.51 | 2.83 | 3.42 | 2.64 | 3.16 |

The results of the fractal analysis of the scattering data

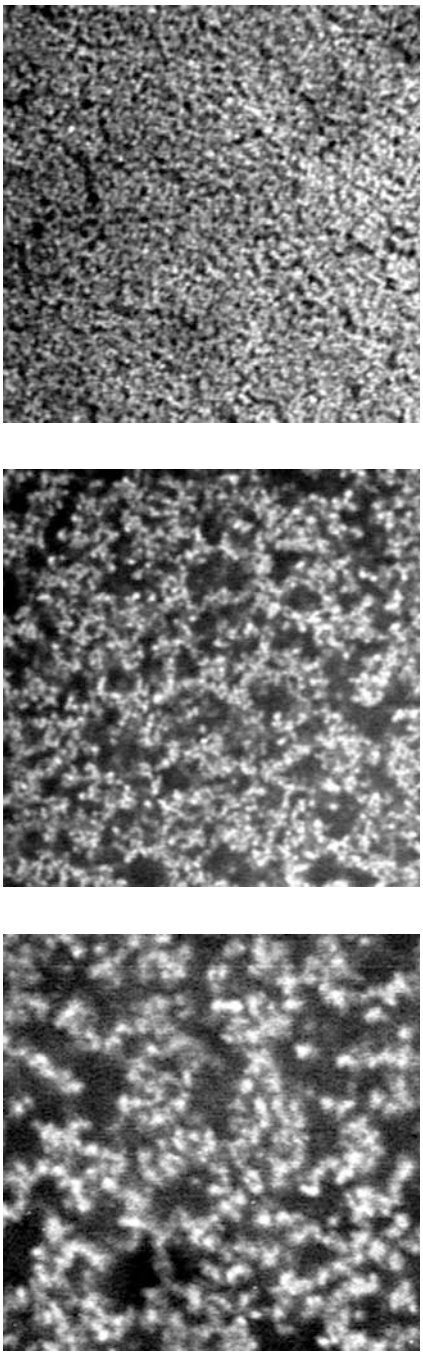

**Fig. 3** The CLSM images of the 0.5-Bis gel. The magnification of the images is 10×, 40×, and 100× from top to bottom. The one side of the images is 200 pixels which correspond to 192, 48.8, and 18.9 μm for 10×, 40×, and 100×, respectively

Best fitting values of A and b are listed in the above Table.

It is find that the $S(q)$'s of 0.2-Bis and 0.3-Bis gels are well explained by the equation 1) with the exponent of about $b \sim 3.5$. On the other hand, we find that the scattering functions of 0.4-Bis and 0.5-Bis gels are expressed by the combination of two limiting functions. The scattering function is explained by a simple power law function with $C = 0$ and $b \sim 2.7$ in the region of $q < 0.02$ ($A^{-1}$) while the scattering function is well explained by the equation 1) where $q > 0.02$ ($A^{-1}$).

In Fig. 3, we show the CLSM images of the 0.5-Bis gel gained at three magnifications. The brighter regions of the images correspond to the region where the density of the FITC is higher. Since the polymer network of the gel is labeled by FITC in our case, the density of the polymer network is higher at the brighter region of the images. The details of the procedure of analysis of the CLSM images are given in the previous papers [5, 6]. It is clearly shown in these images that the polymer network of the opaque poly (acrylamide) gel is the fractal aggregate of the colloidal particles. The two-dimensional distribution of the particles (brighter region of the image) in the CLSM images is analyzed by the box counting method. The results yields that the distribution of the colloidal particles within the two-dimensional cross-section of the bulk polymer network is well described by the fractal dimension of $D_{f\ CLSM} \sim 1.7$.

## Discussion

The scattering function from the opaque gels represents the three dimensional structure of the polymer network. The fractal analysis of the scattering functions of the 0.4- and 0.5-Bis gel suggest that the polymer network of the opaque gels of acrylamide can be seen as a three dimensional mass fractal with the fractal dimension of $D_{f\ SANS} \sim 2.7$ in the length scale larger than 5 nm. On the other hand, the fractal dimension of the same gels that is determined by the CLSM, $D_{f\ CLSM} \sim 1.7$, represents the two dimensional distribution of the colloidal particles in the cross section of the polymer network. In our case, the thickness of the focal plane of the CLSM images is less than one tenth of the length of the one side of the images at each magnification. We can, thus, safely assume that the images shown in Fig. 3 are the two

dimensional cross section of the gel. The fractal dimension obtained from the images reflects the two dimensional distribution of the colloidal particles in the cross section of the gel. Although, there are exceptions, the empirical relationship between the three dimensional fractal dimension and the fractal dimension of the two dimensional cross section has been suggested by Mandelbrot as follows [7].

$$D_{f\,SANS} = D_{f\,CLSM} + 1 \tag{2}$$

The results obtained here are in good agreement with the empirical relationship. These results indicate that the fine structure of the colloidal particles of few hundred nanometers, which observed in the CLSM images, are also the mass fractal of much smaller units.

In contrast, the scattering function of the 0.2- and 0.3-Bis gel shows a typical surface fractal behavior within the present length scale of the measurements. It is also found from the CLSM images of these gels that the diameter of the colloidal particles becomes smaller and the distribution of the colloidal particles in the CLSM image also becomes uniform. The fractal analysis of the CLSM image of 0.2-Bis gel yields to $D_{f\,CLSM} \sim 2$ suggesting the uniform distribution of the colloidal particles in the cross section of the colloidal aggregate [5]. These results suggest that the size of the colloid particle becomes smaller when the mole fraction of the cross-linker is less than 0.3. The slopes of the scattering functions determined by Equation 1) indicate that the polymer networks of these gels are seen as a surface fractal of $D_S \sim 2.5$ according to the following relationship [8].

$$b = 2d - D_s \tag{3}$$

Here, $d$ represents the Euclidean dimension, $d = 3$ in this case. The structure of the polymer network of the opaque gel is a mass fractal of $D_f \sim 2.7$ when the mole fraction of the cross-linker is larger than 0.3 while it becomes a surface fractal of $D_S \sim 2.5$ if the mole fraction of the cross-linker is less than 0.3. By comparing with the previous results of the real space structure and the frictional study of the opaque poly(acrylamide) gels, we again find a "*magic*" mole fraction of the cross-linker of 0.3 at which the structure and the frictional properties of the gel changes drastically.

It may be of importance to understand the transition behaviors of the gel that observed in the real space structure, the frictional property, the SANS data of the opaque poly(acrylamide) gel in terms of the common scientific background. Here, we discuss it on the basis of the chemical reactions between the main chain component and the cross-linker. We focus our attention to the primary structures of polymers that is created in the initial stage of the reaction between acrylamide and N, N'-methylene-bis-acrylamid. A characteristic point of the opaque gel system is the fact that the concentration of the cross-linking agent in the reaction system is much higher than poly(acrylamide) gel system in which one can obtain the transparent gels. When the fraction of the cross-linker is increased, the primary structures of the reaction products may be considerably affected. Let us abbreviate acrylamide and N, N'-methylene-bis-acrylamide as A and B, respectively. According to the rate theory, the reaction rate, $K$, is determined by the following Arrhenius relationship [9].

$$K = \Phi \exp\left(-E/RT\right) \tag{4}$$

Here, $\Phi$ is called as the frequency factor (or the collision factor), $E$ is the energy of activation, $R$ is the gas constant, and $T$ the temperature. The rates of the reactions in the system of A and B are determined by $\Phi$, $E$, and the temperature $T$. Usually, both $\Phi$ and $E$ depend on the temperature and the chemical properties of the reacting substances. However, the temperature is constant during the reaction in the present case. Besides, it has been experimentally shown that the energy of activation is not sensitive to the chemical structures of the reacting substances in the case of acrylamide and its derivatives [10]. Hence, the primary structures of the polymers are mainly determined by the frequency factor alone in our case. The frequency factor may be reasonably assumed to be proportional to the product of the concentrations of the reactants, i.e., $\Phi_{AB} \sim C_A C_B$ for the reaction A + B $\rightarrow$ AB. In the present case, however, each reactant A and B are the polyfunctional units of functionalities of $Z_A$ and $Z_B$. We, thus, should use the concentrations of the functional sites rather than the raw concentrations of A and B to calculate the frequency factor of the reactions [11].

$$\begin{aligned} \Phi_{AA} &= Z_A^2(1 - f_{CL})^2 \\ \Phi_{AB} &= Z_A Z_B(1 - f_{CL}) f_{CL} \\ \Phi_{BB} &= Z_B^2 f_{CL}^2 \end{aligned} \tag{5}$$

Here, $\Phi_{AA}$, $\Phi_{AB}$, and $\Phi_{BB}$ are the frequency factors for the reaction between A-A, A-B, and B-B. The mole fraction of the cross-linker is expressed by $f_{CL}$. Since the temperature and the activation energy are regarded as constants in the present case, the frequency factors, $\Phi_{AA}$, $\Phi_{AB}$, and $\Phi_{BB}$, are proportional to the reaction rates. By solving above equations, one find that all the reactions proceed at the same rate when the mole fraction of the cross-linker becomes $f_{CL} = 1/3$ in the present case, that is, $Z_A = 2$ for acrylamide and $Z_B = 4$ for the cross-linker. The frequency factors are plotted as a function of the mole fraction of the cross-linker, $f_{CL}$, in Fig. 4.

As shown in this figure, the reaction between the cross-linkers, $\Phi_{BB}$, becomes dominant above $f_{CL} = 1/3$. It strongly

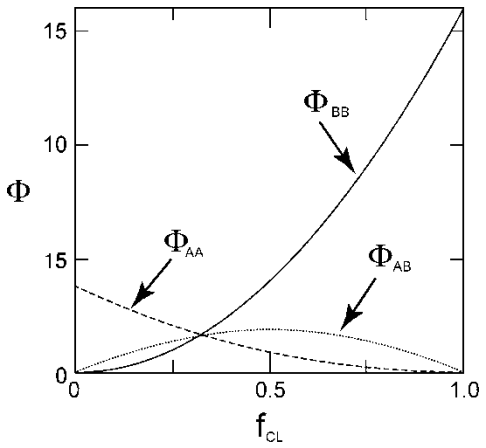


**Fig. 4.** The cross-linker concentration dependence of the frequency factors. $\Phi_{AA}$, $\Phi_{AB}$, and $\Phi_{BB}$ are plotted as a function of the mole fraction of the cross-linker, $f_{CL}$

suggests that the chance of the formation of the units of B-B is much higher than other pairs, A-A and A-B. The dimers of the cross-linker, B-B units, have six un-reacted functional units on it and hence it behaves as a six functional monomers. Once such polyfunctional units of the cross-linker are formed in the system, the reactions between the polyfunctional units of the cross-linker become dominant [12, 13]. The polyfunctional units of the cross-linker also have much chance to react with other units such as A-A and A-B. The larger clusters, thus, adsorb the smaller clusters, and hence, it grows quickly to form larger colloidal particles through the cluster-cluster aggregation mechanism (CCA) [14]. The large colloidal particles, which observed by CLSM, thus may be formed by the aggregation of the clusters of the cross-linkers. It may be worth noting that the calculation of the reaction rates, equations 5), are varied only in the beginning of the gelation reaction because there appear origomers of various types if once the reaction is initiated. It is, however, suggested that the final structure of the system is mainly determined by the presence of large clusters that carry a large number of functional group even though such clusters are formed in the initial stage of the reaction [15].

## Conclusion

We discuss the structure and the formation of the colloidal gel of acrylamide and N,N'-methylene-bis-acrylamide. The real space structure of the gel, the frictional property of the gel, and the small angle neutron scattering data from the gel shows a drastic change when the mole fraction of cross-linker is higher than 1/3. A simple calculation of the reaction rates suggest that the reaction between the cross-linkers becomes dominant when the mole fraction of the cross-liker is higher than 1/3. It, thus, suggests the formation of the particles that is made of the cross-linkers that finally aggregate into a fractal aggregate, which can be observed by the CLSM. All the results suggest that the structure of the polymer network changes from the molecular network to the colloidal gel at the critical composition of the reaction system.

## References

1. Richards EG and Temple CJ (1971) Nature 220:92
2. Bansil Rand Gupta MK (1980) Ferroelectrics 30:63
3. Asnaghi D Giglio M Bossi A and Righetti PG (1997) Macromolecules 30:6194
4. Benguigui L and Boue F (1999) Eur. Phys. J. B11:439
5. Doi Y and Tokita M (2005) Langmuir 21:5285
6. Doi Y and Tokita M (2005) Langmuir 21:9420
7. Mandelbrot BB (1997) The Fractal Geometry of Nature. W. H. Freeman and Company, New York
8. Schmidt PW (1995) Modern Aspects of Small-Angle Scattering. Bumberger H, Eds., Kluwer Academic Publishers, Netherlands. pp. 1–56
9. See for instance, The theory of Rare Processes, The Kinetics of Chemical Reactions, Viscosity, Diffusion and Electrochemical Phenomena. Glasstone S, Laidler KJ and Eyring H, McGRAW-HILL, Inc., New York and London, 1964
10. Nakamura T (1998) Doctoral Thesis, Mie University
11. Flory PJ (1953) Principles of Polymer Chemistry. Cornell University Press, Ithaca and London, Chapter 5
12. Ziff RM (1980) J. Stat. Phys., 23:241
13. Ziff RM and Stell G (1980) J. Chem. Phys. 73:3492
14. Weitz DA and Huang JS (1984) Kinetics of Aggregation and Gelation F, Family and DP Landau, Eds., Elsevier Science Publishers B.V., p. 19
15. Witten TA and Sander LM (1981) Phys. Rev. Lett. 47:1400

Progr Colloid Polym Sci (2009) 136:101–106
DOI: 10.1007/2882_2009_14

# Swelling Equilibrium of a Gel in Binary Mixed Solvents

Hirohisa Miki, Shin Yagihara[1], Sada-atsu Mukai, and Masyuki Tokita[2]

**Abstract** We study the swelling equilibrium of the non-ionic poly(acrylamide) gel in the six binary mixed solvent systems. All the swelling curves of the gel obtained here are superposed onto a single master-swelling curve if the number of water molecule in a unit volume of the mixed solvent is chosen as a variable. The master-swelling curve of the gel is well described by the theoretical swelling curve of the gel.

**Keywords** Volume phase transition • Binary mixed liquids • Poly(acrylamide) gel • Swelling equilibrium

## Introduction

Polymer gels are known to show the phase transition between the swollen and the collapsed states [1]. Many studies have been made after the finding of the phase transition phenomenon. The swelling behaviors of the hydrogels, which is one of the fundamental properties of the gel to be known firstly, have been studied extensively [2]. One of the important reasons of this is the fact that the solvent, that is water, is a common liquid for the biological systems. The information of the swelling behaviors of the hydrogel is of importance when the gels are used in the practical purposes. The swelling behaviors of the hydrogels are studied often in the binary mixed solvent systems of water and the organic liquid. It has been shown that the swelling behavior of the gel depends strongly on the choice of the mixed solvent as well as the number of the ionic group that is polymerized into the polymer network of the gel [3]. The swelling behaviors of hydrogels of various species are studied in many mixed solvent systems. However, the results obtained so far only suggest that any gel shows the volume transition by choosing the appropriate combination of the constituent polymer and the solvent system. Although the diverse data of the volume transition of the gel have been accumulated thus far, the unified aspects of the volume transition of the gel are yet to be obtained.

The polymer gels consist of the polymer network and the gel fluid. One of the important components, and that strongly affect the final properties of the hydrogel, is water. The structure of water and its physical and chemical properties are one of the most interesting subjects in a variety of scientific fields [4]. Several attempts have been made to clarify the structure of water in the liquid state. One of the most important results obtained by X-ray analysis of water indicates that the number of correlated oxygen atoms with one oxygen atom is 4.4 [5]. It suggests that five to six water molecules construct the cluster structure in the liquid water. The microwave dielectric studies of water are also carried out in many systems of the binary mixtures of water and the organic liquids and also in the polymer solutions [6–10]. Among others, the structure of water in the binary mixtures of water and organic liquid is extensively studied in detail. The microwave dielectric studies so far made indicate the formation of the dynamic cluster in the binary mixtures. The life time of such cluster is determined to be around 10 ps. Besides, the formation and the extinction of the dynamic cluster of water occur at a universal mole fraction of water, $X_w \cong 0.8$. The binary mixtures so far studied by the microwave dielectric measurements are simple systems. It is, hence, of interest to study the swelling equilibrium of the hydrogel in the same binary mixed solvent systems in detail.

Here we would like to show a systematic study of the volume transition of poly(acrylamide) gel in the six binary mixed solvent systems that are studied by the microwave dielectric measurements. Since the amount of ionic group in

M. Tokita (✉)
[1]Department of Physics, Faculty of Science, Tokai University, Kanagawa 259-1292, Japan
e-mail: tokita@phys.kyushu-u.c.jp
[2]Department of Physics, Faculty of Science, Kyushu-university, Fukuoka 812-8581, Japan

an active chain of the polymer network has significant effects on the swelling behaviors of the gel, we should be careful to this point. First of all, it may be better to study the swelling behaviors of the non-ionic gel systems because a factor, and it has significant effects on the swelling of the gel, can be neglected. In addition to this, the measurements of the swelling curve should be made using only a single piece of gel sample because the composition and the structure of the polymer network of the gel should be the *same* for all data gained in various solvent systems.

## Experimental

Poly(acrylamide) gel, which is the sample of the present study, is usually prepared by using ammoniumpersulfate and tetraethylmethylenediamine as an initiator and an accelerator. In the case of the radical polymerization method, the initiator molecules are chemically bound to the free ends of the network chain. Since the initiator, ammoniumpersulfate, contains the sulfate groups, the gel that is prepared by this method eventually becomes an ionic gel. We, therefore, should avoid this method here. In this study, we prepare the gel by a photo-polymerization method by using 2,2'-azobis[2-methylene-N-(2-hydroxyethyl)propionamide] as a photo-initiator, which is kindly supplied from Wako Chemicals Co.. The above initiator does not contain the ionic group, and hence the gel prepared here is totally non-ionic poly(acrylamide) gel [11].

The main-chain component, acrylamide, and the cross-linker, N,N'-methylene-bis-acrylamide, are purchased from BioRad Co. and used without further purification. The total molar amount of the gel is 700 mM and the mole fraction of the cross-linker and the photo-initiator are 0.01. The desired amounts of the main-chain component, the cross-linker, and the photo-initiator are dissolved into distilled and de-ionized water that prepared by a Milli-Q system. The pre-gel solution is de-gassed and is then shone by UV light at a wavelength of 360 nm. The gel is polymerized in a capillary of the inner diameter of $d_0 = 141\mu m$. The gel is taken out of the capillary and extensively washed by distilled and de-ionized water. The swelling curves of the gel are measured in six binary mixed solvent systems of water and the organic liquid. The organic liquids chosen here are, methanol, ethanol, 1-propanol, 2-propanol, acetone (Wako Chemicals Co., reagent grade), and 1,4-dioxane (Aldrich, HPLC grade).

The gel is fixed in a capillary of inner diameter of about 1 mm. The gel is continuously flushed with the mixed solvent of a certain composition from the reservoir. The diameter of the rod shape gel in the equilibrium state, $d$, is measured under a microscope. The swelling ratio of the gel, $d/d_0$, is then calculated. After a measurement at a certain composition of the mixed solvent, the composition of the mixed solvent is changed by adding water or the organic solvent to the reservoir. The mole fraction of water in the mixed solvent is determined from the density of the mixed solvent, which is measured in prior to the swelling experiments. The temperature is fixed at $20.00\,^{\circ}C$ to accuracy better than $\pm\, 0.01\,^{\circ}C$. Because of this measurement system, all the swelling curves of the gel in six mixed solvent systems are obtained using only one sample of the gel. The details of the apparatus used here are reported elsewhere [12].

## Results

In Fig. 1, we show two swelling curves of non-ionic poly (acrylamide) gel in the binary mixtures of water and the organic liquids. The one is measured in the mixed solvent of water-methanol and the other is obtained in the mixed solvent of water-acetone. The gel, which is swollen in water, continuously collapses into a compact state as the mole fraction of the organic component in the mixed solvent is increased. The gel shows the typical swelling behaviors of the non-ionic gels. Namely, both swelling curves are entirely reversible and the volume change of the gel is continuous [1]. In addition to this, we find that the swelling ratio of the gel is the same in the pure organic solvents. The volume phase transition point of the gel is determined from the middle point of the swelling curve, $d/d_0 = 0.77$. The volume transition point of the gel is $X_w = 0.78$ for water-methanol

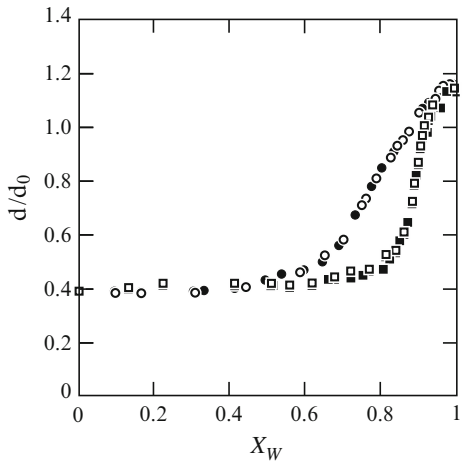


**Fig. 1** Swelling curves of the non-ionic poly(acrylamide) gel in the mixed solvent systems of water-methanol (circles) and water-acetone (squares) measured at a temperature of $20.00\,^{\circ}C$. The mole fraction of water in the mixed solvent systems is expressed by $X_w$. The open symbols and the closed symbols indicate the increasing processes of the organic component and the decreasing processes of the organic component

system and $X_w = 0.89$ for water-acetone system, respectively. The swelling curve of the gel in the mixed solvent of water-methanol system is shifted to lower mole fraction of water than water-acetone system.

The swelling curves of the gel in all mixed solvent systems studied here are shown in Fig. 2. It is found that the swelling curves of the gel are reversible and continuous in all mixed solvent systems studied here. Besides, we find that the swelling ratio of the gel in the pure organic liquids is the same. The results indicate that the quality of the pure organic solvents is almost the same for poly(acrylamide). Since the swelling ratio of the gel in the pure organic solvents is $d/d_0 =$ 0.4, the gel still contains a lot of solvent molecules even in the collapsed state. The organic solvents chosen here are, thus, the poor solvent but not the non-solvent for poly(acrylamide). Although the swelling ratios of the gel in the pure organic solvents are the same, the transition point of the gel slightly varies with the organic component of the mixed solvent. The swelling behavior of the gel depends on the choice of the organic liquid that is mixed with water. The mole fraction of water at the transition point is determined from the middle point of the swelling curves: 0.78; methanol, 0.85; ethanol, 0.91; 1-propanol, 0.88; 2-propanol, 0.89; acetone, and 0.84; dioxane. The transition points of the gel in these mixed solvents fall around $W_w \cong 0.85$.

## Discussion

We firstly discuss the swelling behaviors of the gel in the mixed solvent system of water and methanol in terms of the thermodynamic data of the linear polymer chain of acrylamide. The thermodynamic study of the poly(acrylamide) solution has been made in the mixed solvent system of water and methanol [13]. It has been shown that the Θ conditions are attained at the mole fraction of methanol is 0.24. By the definition, the polymer chain is in the unperturbed state under the Θ conditions [14]. The ideal chain configuration of the polymer chain is realized under the Θ conditions. Since the state of the swollen random coil and that of the collapsed globule is divided at the Θ point, the Θ point is the natural choice for the volume transition point of the gel. If we define the volume transition point by the Θ point, the mole fraction of methanol at the Θ point of the polymer solution coincides with that at the middle point of the swelling curve, which is 0.22. It further suggests that the Θ point of other solvent systems, and hence the volume phase transition point of the gel in the mixed solvent systems, are easily assigned to the middle point of the swelling curves since only one piece of the gel sample is used to determine the swelling curves, and hence, the structure of the polymer network is exactly the same. The mole fractions of water at the transition point of the gel in the mixed solvent system thus determined are given in the previous section.

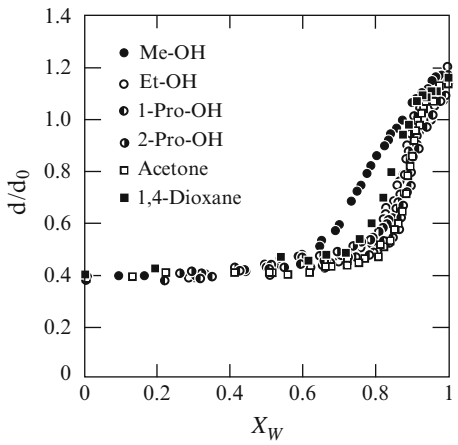


**Fig. 2** Swelling curves of the non-ionic poly(acrylamide) gel in six binary mixed solvent systems measured at a temperature of 20.00 °C

The quality of the mixed solvent is proportional to the product of the electronic polarizabilities of both components of the binary mixture [15, 16]. Since the volume transition occurs at higher mole fractions of water in the mixture, we assume here that the quality of the mixed solvent is determined mainly by the number of water molecule in a unit volume of the mixed solvent.

$$N_W = \frac{m_W}{M_W}\frac{\delta_M}{m_W + m_O}N_A \tag{1}$$

Here, $N_w$ and $N_A$ are the number of water molecule in a unit volume of the mixed solvent and the Avogadro's number. The mass of water and the organic solvent in feed, which is necessary to obtain a mixed solvent at a certain mole fraction, are given by $m_w$ and $m_o$, respectively. The density of the mixed solvent at a mixing ratio of $m_w + m_o$ is expressed by $\delta_M$ and $N_A$ the molecular weight of water. The first term of Equation 1, $(m_W/M_W)$, corresponds to the mole number of water in the mixed solvent of a certain mixing ratio ($m_w + m_o$). The second term $[\delta_M/(m_W + m_O)]$ is the inverse of the total volume of the mixed solvent that is mixed at a mixing ratio of $m_w + m_o$. All the values of $m_w$, $m_o$, and $\delta_M$ are experimentally measured, and hence, the number of water molecule in a unit volume of the mixed solvent $N_w$ can be calculated from them. In Fig. 3, the swelling ratio of the gel that is normalized by the swelling ratio at the Θ point, $(d/d_\Theta)$, is plotted against the number of water molecule in a unit volume of the mixed solvent, $N_w$. It is clear from Fig. 3 that the swelling curves of the gel that measured in six binary mixed solvent systems are superposed onto a master-swelling curve. The results indicate that the number of water molecule in a unit volume of the mixed solvent is a

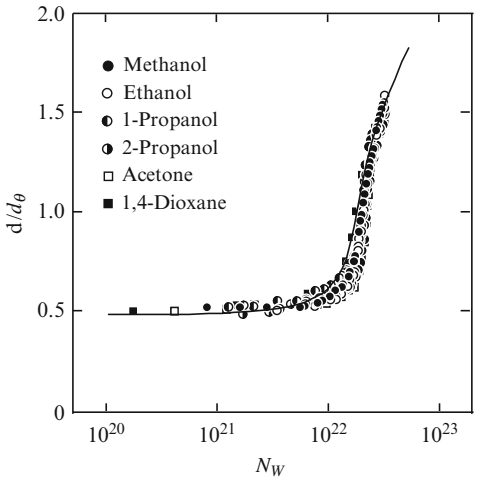


**Fig. 3** Normalized swelling curves of the gel. The swelling ratios of the gel are normalized by the swelling ratio of the gel at the Θ condition, $(d/d_\Theta)$. The horizontal axis represents the number of water molecule in a unit volume of the mixed solvent, $N_w$, calculated from Equation 1. The solid line is the best fitting results to Equation 3

relevant variable to describe the universal swelling behaviors of the gel.

We, thus, obtain a master-swelling curve of poly(acrylamide) gel. It may be of interest to analyze the master-swelling curve in terms of the equation of state of gel [17].

$$1-\frac{\Delta F}{kT}=-\frac{v\upsilon}{N_A\phi^2}\left[(2f+1)\left(\frac{\phi}{\phi_0}\right)-2\left(\frac{\phi}{\phi_0}\right)^{1/3}\right]+1+\frac{2}{\phi}+\frac{2\ln(1-\phi)}{\phi^2} \tag{2}$$

Here, $N_A$, $k$, and $T$ are Avogadro's number, the Boltzmann's constant, and the absolute temperature. The free energy between the solvent and the polymer segment is expressed by $\Delta F$, and $v$ is the molar volume of the solvent. The volume fractions of the network in the equilibrium state in the solvent and at the preparation are expressed by φ and $\varphi_0$. The number of elastically active chain in a unit volume of the gel at $\varphi_0$ is expressed by $v$. The number of ionic group on an elastically active chain is given by $f$. The theoretical swelling curve of the gel given above is known to rewritten as follows.

$$t=S\left(\rho^{-5/3}-\frac{1}{2}\rho^{-1}\right)-\frac{1}{3}\rho \tag{3}$$

Here, $t$, $S$, and ρ are defined as follows.

$$t\equiv\left[\frac{\left(1-\frac{\Delta F}{kT}\right)(2f+1)}{2\phi_0}\right] \tag{4}$$

$$S\equiv\left(\frac{v\upsilon}{N_A\varphi_0^3}\right)(2f+1)^4=S_0(2f+1)^4 \tag{5}$$

$$\rho\equiv\left(\frac{\phi}{\phi_0}\right)(2f+1)^{3/2} \tag{6}$$

Using Equation 3 we fit the results shown in Fig. 3. Here, the number of the ionic group on an active chain is, of course, safely chosen as $f=0$. Practically, we write $t=(N_W/N_\Theta)-1$ to normalize the swelling curves at the Θ point where $N_\Theta$ is the number of water molecules in the unit volume of the mixed solvent at the Θ point. The swelling ratio of the gel is also normalized as $\rho=(d/d_\Theta)^3$. The right hand side of the Equation 3 is multiplied by a numerical factor $C$. Then, the best fitting values of $C$ and $S_0$ are determined. The result of fitting is also given in Fig. 3. The experimental results are well explained by Equation 3 when the fitting parameters are chosen as $C=0.3$ and $S_0=0.3$, respectively. The number of active chain in a unit volume of the gel, $v$, which is an important measure of the structure of the polymer network, can be calculated from the value of $S_0$ using the relationship given in Equation 5. Here, the value $\varphi_0=0.05$ is determined by the measurement. On the other hand, the molar volume of the mixed solvent depends on the mixing ratio of the organic component and water. We, hence, calculate the maximum and the minimum values of $v$ from both the maximum and the minimum values of the molar volume of pure solvents; $\upsilon=0.018(l/mole)$ for water and $\upsilon=0.028(l/mole)$ for dioxane. The number of active chain in a unit volume of the gel thus calculated is ranging from 0.8 to $1.2\times10^{21}(l^{-1})$. The value of $v$ is either estimated from the composition of the gel in feed. The ratio of the main chain component and the cross-linker is 100:1 in this study. The concentration of the network chain is, taking into account that the cross-linker is a four-functional monomer, calculated to be 14 mM, which yields to $v=8\times10^{21}(l^{-1})$. Although the fitting results of $v$ are smaller than the calculated one, we believe that the results obtained here are not too bad because the actual polymer network of the gel contains a lot of defects such as the dangling ends and the loops. The value of $v$ calculated from the composition in feed may corresponds to the maximum number of the active chain in a unit volume of the ideal gel.

The binary mixed solvents used here have been studied in detail by the microwave dielectric measurements [6–10]. The relaxation parameters, such as the relaxation time, the relaxation strength and the relaxation time distribution parameter related to the shape of dispersion and loss curves, show the singular behaviors at a universal mixing ratio of water and the organic liquids. The mole fraction of water at the singular point in the solvent systems studied here is reported to be about 0.8 [6–9]. The results are discussed in

terms of the formation of the dynamic cluster structure of water in the mixture when the mole fraction of water is larger than 0.8. Although it is not exactly the same, the volume phase transition point is close to the universal mixing ratio of water and the organic liquids that determined by the dielectric studies. It strongly suggest that the binary mixtures become the good solvent for poly(acrylamide) gel in the region where water molecules form the dynamic clusters in the mixtures. The quality of the binary mixed solvent of water and the organic liquid for poly(acrylamide) may be related to the presence of the cluster structure of water in the mixed liquids.

## Conclusion

The swelling curves of the gel gained in six binary mixed solvents are superposed onto a master-swelling curve when the swelling ratio of the gel, which is normalized by the swelling ratio of the gel at the $\Theta$ point, is plotted as a function of the number of water molecule in a unit volume of the mixed solvent. The results indicate that the number of water molecule in a unit volume of the mixed solvent is the relevant parameter to describe the swelling behaviors of the hydrogels.

The master-swelling curve of the gel is analyzed in terms of the theoretical swelling curve of the gel. It is found that the master-swelling curve of the gel is well explained by the theoretical swelling curve of the gel. Although the theory is based on the mean field approximation, it is still capable of describing the experimental results fairly well.

**Acknowledgements** The authors thank Dr. Y. Maki and Professor T. Dobashi of Gunma University for their fruitful discussions on the thermodynamic data of poly(acrylamide). We dedicate this wok to the late Professor Toyoichi Tanaka of Massachusetts Institute of Technology on the occasion of the 30$^{th}$ anniversary of the finding of the volume phase transition of the gel.

## References

1. Tanaka T (1978) Phys. Rev. Lett. 40:820
2. See for instance, *Responsive Gels: Volume Transitions 1 and 2, Adv. Polym. Sci. 109 and 110 (1993)*
3. Tanaka T (1981) Sci. Amer. 244:124
4. Eisenberg D and Kauzmann W The structure and Properties of Water, (Oxford Univ., Oxford, 1969)
5. Narten AH, Danford MD and Lavy HA (1967) Disc. Faraday Soc. 43:97
6. Mashimo S, Kuwabara S, Yagihara S and Higasi K (1989) J. Chem. Phys. 90:3292
7. Mashimo S, Umehara T and Redlin H (1991) J. Chem. Phys. 95:6257
8. Mashimo S, Miura N, Umehara T, Yagihara S and Higasi K (1992) J. Chem. Phys. 96:6358
9. Mashimo S and Miura N (1993) J. Chem. Phys. 99:9874
10. Shinyashiki N, Asaka N, Mahimo S and Yagihara S (1990) J. Chem. Phys. 93:760
11. Doi Y and Tokita M (2005) Langmuir 21:5285
12. Kawasaki H, Nakamura T, Miyamoto K, Tokita M and Komai T (1995) J. Chem. Phys. 103:6421
13. Schwartz T, Sabbadin J and Francis J (1981) Polymer 22:609
14. Flory PJ Principle of Polymer Chemistry, (Cornell University Press: Ithaca, NY, 1953)
15. Debye PJW Molecular Forces, (JOHN WILEY & SONS Inc., NY, 1967)
16. de Gennes PG Scaling Concept in Polymer Physics, (Cornell University Press: Ithaca, NY, 1979)
17. Tanaka T, Fillmore D, Sun S, Nishio I, Swislow G and Shah A (1980) Phys. Rev. Lett., 45:1936

Progr Colloid Polym Sci (2009) 136:107–112
DOI: 10.1007/2882_2009_15

# Revisit to Swelling Kinetics of Gels

Kenji Urayama, Naoki Murata, Shoji Nosaka, Masahiro Kojima, and Toshikazu Takigawa

**Abstract** The swelling and shrinking dynamics of the gels with a wide variety of aspect ratios is experimentally investigated. As the aspect ratio becomes sufficiently larger or smaller than unity, the swelling kinetics asymptotically approaches that of infinitely long cylinders or infinitely large disks, respectively. The characteristic times of the infinitely long cylinders and infinitely large disks are compared to the predictions of the classical Li-Tanaka model and its modified models.

**Keywords** Gels • Swelling • Shrinking

## Introduction

Swelling dynamics of polymer gels is a classical issue in polymer physics. Tanaka and Fillmore [1] firstly showed that the characteristic time ($\tau$) for the swelling of spherical gels was proportional to the square of diameter, and that the diffusion constant ($D$) was given by the ratio of the osmotic modulus and friction coefficient between polymer networks and solvents ($f$) on the basis of their "diffusion model". Peters et al. [2] and Tanaka et al. [3] extended the applicability of the diffusion model to the swelling of infinitely long cylinder or infinitely large disk gels. The diffusion model assumes that the polymer networks move (diffuse) in quiscent solvents, i.e., it does not consider the solvent motion during swelling. The diffusion model is apparently successful in interpreting the swelling dynamics, but evidently, we need to consider the relative motion between networks and solvents for the strict description of swelling phenomena. For instance, the diffusion model assuming quiscent solvent cannot explain the solvent-flow induced swelling phenomena: The solvent flow drives a further swelling when the solvent is transmitted through fully swollen gels by imposed pressure [4]. There exist several modified models considering the effect of solvent motion on swelling dynamics [5–7]. The "stress-diffusion coupling model" proposed by Yamaue and Doi among them can treat the solvent-flow induced swelling [8].

For the swelling in solvents without imposed field ("free swelling"), the diffusion model and stress-diffusion coupling model predict the different values of $\tau$. The difference becomes more obvious in the comparision of the $\tau$ values for the gels with various shapes such as long cylinder, sphere and large disk [7]. Unexpectedly, there have been a quite limited number of experimental studies examining systematically the swelling dynamics of the gels with various shapes [3]. In the present study, we investigate the swelling and shrinking kinetics of the cylindrical and disk gels with a wide variety of the aspect ratio ($A$: $A = 0.08 \sim 10$) where $A$ is the ratio of height to diameter. We elucidate the $A$ dependence of $\tau$ which provides an important basis to understand the fundamental aspects of swelling dynamics. We also compare the experimental results with the predictions of the classical diffusion model and the two different modified models. It should be emphasized that we focus on the swelling and shrinking processes where the total volume change is small enough to validate the linear approximation for deformation: The swelling processes accompanied by large volume variations such as volume phase transition phenomena are beyond the scope of present study because the complicated nonlinear effect becomes dominant [9].

## Experimental Section

Poly(N-isopropylacrylamide) (PNIPA) gels were prepared by radical copolymerization of N-isopropylacrylamide (NIPA) and N,N′-methylenebis(acrylamide) (BIS). The

K. Urayama (✉)
Department of Material Chemistry
Kyoto University
Nishikyo-ku, Kyoto, 615-8510, Japan
e-mail: urayama@rheogate.polym.kyoto-u.ac.jp

mixture of NIPA and BIS was dissolved in distilled water under nitrogen atmosphere. The total concentration of NIPA and BIS was 15 wt%, and the molar ratio [NIPA]/[BIS], which is a measure of crosslink density, was 200. After the addition of ammonium peroxodisulfate (initiator) and N,N,N′,N′-tetramethylethylenediamine (accelerator) to the solution, the pregel solution was transferred into glass capillaries with the inner diameter of 6.0 mm. The gelation was performed at 7 °C for 24 h. The resultant cylindrical gel samples were removed from the capillaries and were allowed to swell in distilled water (25 °C) to wash out the unreacted reagents. The water was renewed several times. The cylindrical gel with $A = 10$ was first employed for the swelling experiment. The cylindrical gels with smaller $A$ ($A = 5.0$, 3.8, 2.5 and 1.0) but with the same diameter ($d$: $d = 7.6$ mm in the fully swollen state at 25 °C) were obtained by cutting out the gel with $A = 10$.

The dimensional variation processes were observed during the cooling-induced swelling or heating-induced shrinking. The fully swollen cylindrical gels at 25 °C were transferred to a water bath whose temperature was controlled at 8 °C. The swelling process was observed with the two CCD cameras for evaluating the time courses of diameter ($d$) and height ($h$) each. After the swelling was equilibrated at 8 °C, the gels were transferred to a water bath at 25 °C to observe the shrinking process in the same manner. The cylindrical gel with $A = 1.0$ exhibited the concave (convex) profile in the initial stage of swelling (shrinking), and $d$ in this case was obtained by averaging the widths at the top surface and the position of a half height. For the gels with $A > 2.5$, the profile is sufficiently flat throughout the process, which allows us to measure $d$ at only one position.

For comparison, the similar experiments were conducted under the conditions where the water flow-in and flow-out were prohibited at both ends of the cylindrical gels with $A =$ 10 and 2.5: The end surfaces of the gels were coated with a non-aqueous adhesive.

The disk gels with various $A$ ($A = 1.0$, 0.50, 0.25, 0.13, and 0.083) but with the same $h$ ($h = 3.8$ mm in the fully swollen state at 25 °C) were prepared by the gelation in the molds with various diameters and the same height. The diameter changes of the disk gels during the swelling and shrinking processes were examined. The corresponding thickness change was not evaluated owing to the difficulty in the observation. The observation of only diameter variation provides sufficient information for discussion, because the swelling and shrinking of sufficiently large disks are reasonably expected to proceed with keeping shape similarity, as described later.

It should be noted that all the measurements were conducted within the temperature region corresponding to the swollen phase of the NIPA gels. The experimental temperatures are sufficiently below the volume phase transition temperature of ca. 35 °C. The resultant dimensional variation (less than 15 %) in the total volume change was small enough to avoid the complex nonlinear effect.

## Results and Discussion

Figure 1 shows the time ($t$) dependencies of the strains in the diameter and height directions during swelling and shrinking of the long cylindrical gel with $A = 10$. The strains are given by $\Delta d / d_0$ and $\Delta h / h_0$ where $d_0$ and $h_0$ are the initial dimensions before $T$-jumps, $\Delta d = d(t) - d_0$ and $\Delta h = h(t) - h_0$. Evidently, the time courses of the strains along the two principal axes are identical throughout the volume change processes. This behavior was also reported for a long cylindrical gel in the earlier literature [3]. The result in Fig. 1 obviously indicates that the shape of the sufficiently long gels remains similar throughout the swelling and shrinking processes. The concave or convex profile was observed only in the initial stage of swelling or shrinking for the short gel with $A = 1.0$. Such curvature of the profiles was negligibly small for the long cylindrical gels with $A > 2.5$. The shape similarity during volume changes was first derived theoretically by Li and Tanaka [3] on the basis of the assumption that the shape of the gel in the transient state is determined by minimizing the elastic energy of the shear deformation. Yamaue and Doi [7] also theoretically derived the same conclusion from the condition of no force acting at the ends of long cylinder gels.

Figure 2 displays the semi-logarithmic plots of the quantity $(d - d_0) / (d_\infty - d_0)$ versus time for the swelling process of the cylindrical gel with $A = 10$. The subscript $\infty$ denote the equilibrium state in the long time limit. Almost all data points fall on a straight line excepting the very short time

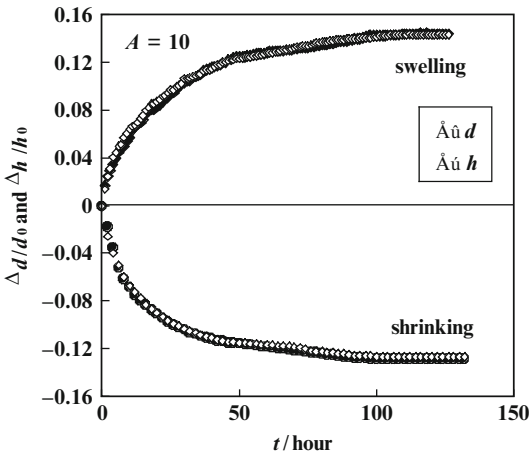


**Fig. 1** Time dependencies of the variations in diameter and height of a cylindrical gel with $A = 10$ during swelling and shrinking

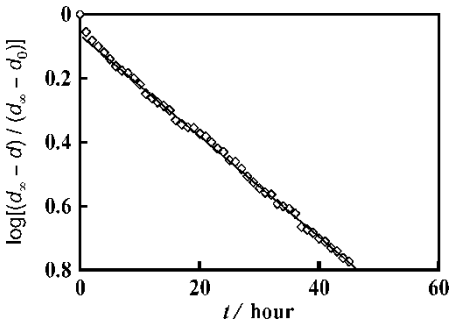


**Fig. 2** Semi-logarithmic plots of the normalized dimensional variation versus time for the swelling of the cylindrical gel with A = 10

**Table 1** The longest relaxation time for the gels with various aspect ratios ($A$)

| | $A$ | swelling $\tau_1\times10^{-4}$/s | shrinking $\tau_1\times10^{-4}$/s |
|---|---|---|---|
| $d = 7.6$ mm | 10 5.0 3.8 2.5 1.0 | 9.9 9.5 9.1 8.1 5.6 | 7.7 7.5 7.0 6.6 4.3 |
| $h = 3.8$ mm | 1.0 0.50 0.25 0.125 0.083 | 1.4 3.3 5.5 6.9 7.0 | 1.0 2.2 4.1 5.3 5.5 |

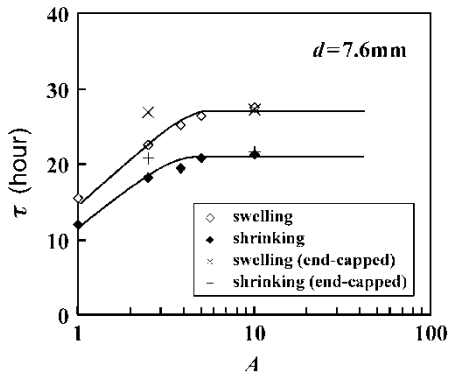


**Fig. 3** Longest characteristic times for swelling and shrinking of cylindrical gels a function of A

region, which was also observed for all other samples. This indicates that the kinetics is well approximated by a single exponential relaxation process. The longest characteristic time ($\tau_1$) is estimated from the inverse of the slope. Table 1 summarizes the values of $\tau_1$ in each process for all samples.

Figure 3 illustrates $\tau_1$ as a function of $A$ for the cylindrical gels. The time $\tau_1$ increases with $A$, but it levels off at sufficiently large $A$ of $A > 5$. The data for the end-capped gels are also shown in the figure. When the water flow-in and flow-out at both ends of the gels are prohibited, $\tau_1$ is independent of $A$ and it agrees with the plateau value of $\tau_1$ in the free swelling without constraint. These results clearly show that the effect in the height direction on swelling dynamics becomes negligibly small for sufficiently long gels. In other words, these results strongly indicate that the gels with $A > 5$ correspond to infinitely long gels whose

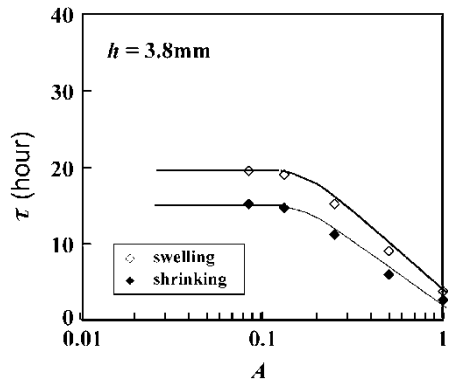


**Fig. 4** Longest characteristic times for swelling and shrinking of disk gels a function of A

effective dimensions for swelling dynamics ($D_{\text{eff}}$) are reduced to two. The ratios of $\tau_1$ for the infinitely long gels and the short gel with $A = 1.0$ are $1.8 \pm 0.1$ for swelling and $1.8 \pm 0.1$ for shrinking.

Figure 4 shows the $A$ dependence of $\tau_1$ for the disk gels. An increase in disk diameter increase $\tau_1$, and $\tau_1$ becomes independent of $A$ for sufficiently large disks with $A < 0.1$. The gels with $A < 0.1$ correspond to infinite large disk gels with $D_{\text{eff}} = 1$, i.e., with no effect in the diameter directions on swelling dynamics. The ratios of $\tau_1$ for the infinitely large disk gels and the short gel with $A = 1.0$ are $5.0 \pm 0.1$ for swelling and $5.5 \pm 0.1$ for shrinking.

There exist several models of swelling kinetics [3, 6, 7]. They provide different solutions of $\tau_1$ for infinitely long cylinder and infinitely large disk gels. The difference in $\tau_1$ of a gel with a given shape between the model predictions is considerably small, but the difference becomes more evident in the ratio of $\tau_1$ between the gels with different shapes [7]. Each theory expects that $\tau_1$ depends on the following modulus ratio $R$ related to the osmotic mechanical property of gels:

$$R = \frac{G}{K_{\text{OS}} + (4/3)G} = \frac{1 - 2\mu_{\text{OS}}}{2(1-\mu_{\text{OS}})} \qquad (1)$$

where $G$, $K_{\text{OS}}$ and $\mu_{\text{OS}}$ are the shear modulus, osmotic bulk modulus and osmotic Poisson's ratio, respectively. Figures 5–7 show the ratios ($\tau_{1,\text{cylinder}}$ / $\tau_{1,\text{sphere}}$), ($\tau_{1,\text{disk}}$ / $\tau_{1,\text{sphere}}$) and ($\tau_{1,\text{disk}}$ / $\tau_{1,\text{cylinder}}$) as a function of $R$ expected by the Li-Tanaka (LT), Wang-Li-Hu (WLH) and Yamaue-Doi (YD) theories, respectively. The theoretical expressions are given in Appendix. The predictions of the WLH and YD models in these figures are almost similar, while the predictions of the LT model are higher than those of the other two models. In addition, the $R$ dependencies of the $\tau_1$ ratios for the LT model are negative while those for the other two models are positive.

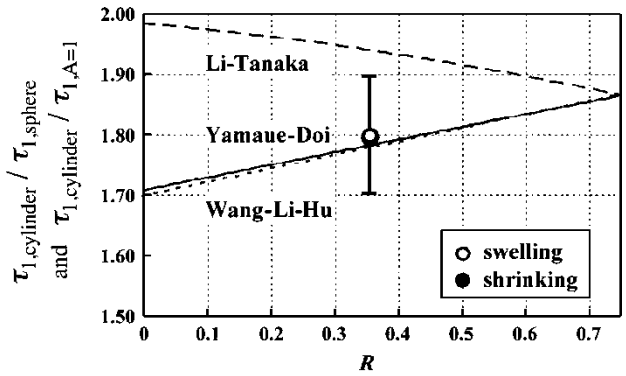


**Fig. 5** Comparison of the theoretical $\tau_1$ ratios of spherical and infinitely long cylindrical gels with the corresponding experimental data

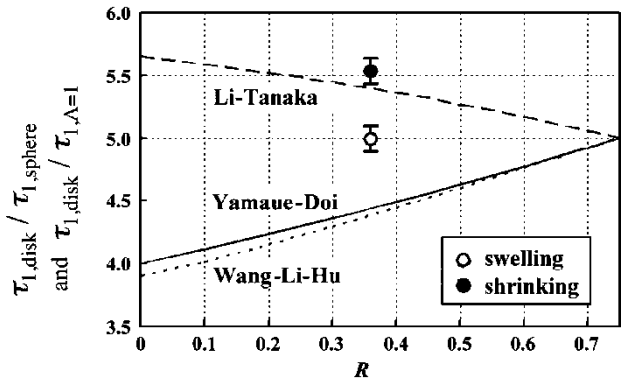


**Fig. 6** Comparison of the theoretical $\tau_1$ ratios of spherical and infinitely large disk gels with the corresponding experimental data

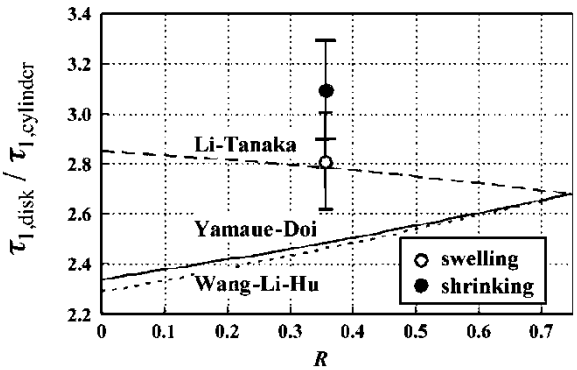


**Fig. 7** Comparison of the theoretical $\tau_1$ ratios of infinitely long cylindrical gels and infinitely large disk gels with the corresponding experimental data

The experimental results in the present study are also shown in the figures. The value of $R$ for the present sample is estimated to be 0.33∼0.38 from the value of $\mu_{OS}$ (1/5 ∼ 1/4) which was obtained by the experiments of stretching-induced swelling for a NIPA gel [10]. In Figs. 5–7, we display the experimental data at $R$ = 0.36 for convenience, because the theoretical $\tau_1$ ratios are not significantly affected by $R$ in the narrow range of $R$, i.e., $0.33 < R < 0.38$. The crosslinking densities in the present study and Ref. 10 are not the same, but $\mu_{OS}$ is insensitive to crosslink density [11]. We assume $\tau_1$ for the short gels with $A$ = 1.0 as that for spherical gels ($\tau_{1,\text{sphere}} = \tau_{1,A=1}$) in Figs. 5 and 6.

In Fig. 5 regarding ($\tau_{1,\text{cylinder}} / \tau_{1,\text{sphere}}$), the experimental data appears to be closer to the predictions of the YD and WLH models than the LT model, but the superiority is not definite in view of the experimental error. As can be seen in Fig. 6, the difference in the model predictions for ($\tau_{1,\text{disk}} / \tau_{1,\text{sphere}}$) is considerably larger than that in ($\tau_{1,\text{cylinder}} / \tau_{1,\text{sphere}}$), although the predictions of the YD and WLH models are still hardly distinguishable. The difference in the theoretical $\tau_1$ ratios becomes greater with increasing the difference in $D_{\text{eff}}$ between two gels under consideration. The experimental results for ($\tau_{1,\text{disk}} / \tau_{1,\text{sphere}}$) appear to be closer to the prediction of the LT model than those of the YD and WLH models.

The assumption of $\tau_{1,\text{sphere}} = \tau_{1,A=1}$ may leave ambiguity in the comparison of the experiments and theories in Figs 5 and 6, because the total surface area and volume of the short gel with $A$ = 1 are larger than those of the spherical gel with the same diameter. The ambiguities originating from the absence of the data of the spherical gels are excluded by employing the ratio ($\tau_{1,\text{disk}} / \tau_{1,\text{cylinder}}$) for comparison (Fig. 7). The ratio ($\tau_{1,\text{disk}} / \tau_{1,\text{cylinder}}$) is calculated from the two ratios ($\tau_{1,\text{disk}} / \tau_{1,A=1}$) and ($\tau_{1,\text{cylinder}} / \tau_{1,A=1}$) for the gels with $d = 7.6$ mm and $h = 3.8$ mm, respectively, for excluding the effects of $\tau_{1,A=1}$ as well as the difference in dimension. The experimental ratios (2.8 ± 0.1 for swelling; 3.1 ± 0.1 for shrinking) more satisfactorily agree with the prediction of the LT model than those of other two models. This result puzzles us because the latter two models apparently consider the effect of solvent motion which is neglected in the LT model.

Table 2 lists the diffusion constants $D$ for the gels corresponding to the infinitely long cylinder and large disk which were evaluated from $\tau_1$ using the equations of each model (see Appendix). No significant difference in $D$ for swelling and shrinking indicates that the total volume change is enough small to satisfy the condition of linear approximation. It is worth mentioning that $D$ must be independent of the shapes of gels because $D$ is a material specific parameter. The YD and WLH models lead to the larger difference in $D$ between cylinder and disk than the LT model as can be seen in Table 2.

The values of $A$ satisfying infinitely long and large gels are roughly estimated to be $A > 5$ and $A < 0.1$, respectively. These asymptotic behaviors remain to be understood quantitatively. Numerical simulations for the swelling dynamics of finitely long and large gels using the governing equations of the diffusion or modified models will contribute to the understanding of this issue. This is a future subject of our study.

**Table 2** The diffusion constants for the gels corresponding to infinitely long cylinder and large disk on the basis of the Li-Tanaka (LT), Wang-Li-Hu (WLH) and Yamaue-Doi(YD) models.

| | | | $D\times10^{10}/\mathrm{m^2s^{-1}}$ | | |
|---|---|---|---|---|---|
| | $A$ | | LT | WLH | YD |
| $d = 7.6$ mm | 10 | (swelling) | 2.4 | 2.2 | 2.2 |
| | | (shrinking) | 2.3 | 2.1 | 2.1 |
| $h = 3.8$ mm | 0.083 | (swelling) | 2.4 | 1.9 | 1.9 |
| | | (shrinking) | 2.3 | 1.8 | 1.9 |

## Summary

The sufficiently long and thin disk gels (roughly $A > 5$ and $A < 0.1$, respectively) can be regarded as infinitely long gels with $D_{\mathrm{eff}} = 2$ and infinitely large gels with $D_{\mathrm{eff}} = 1$, respectively, from viewpoints of swelling dynamics. The classical diffusion model appears to give a better description of the ratio of the characteristic times for the infinitely long and large gels than the existing modified models.

**Acknowledgements** This work was partly supported by a Grant-in-Aid for Scientific Research on Priority Area "Soft Matter Physics" (No. 19031014) from the Ministry of Education, Culture, Sports, Science and Technology (MEXT) of Japan. This research was also supported in part by the Global COE Program "International Center for Integrated Research and Advanced Education in Materials Science" (No. B-09) of MEXT of Japan, administrated by the Japan Society for the Promotion of Science.

## Appendix

We summarize the expressions for $\tau_{1,\mathrm{sphere}}$, $\tau_{1,\mathrm{cylinder}}$ and $\tau_{1,\mathrm{disk}}$ in each model. The expression of $\tau_{1,\mathrm{sphere}}$ is common to all models, and it is given by

$$\tau_1 = \frac{a_\infty^2}{D\upsilon_1^2} \tag{A1}$$

where $a_\infty$ corresponds to the equilibrium diameter and $\upsilon_{1,\mathrm{sphere}}$ satisfies the equation (A2).

$$4R\left[1 - \upsilon_{1,\mathrm{sphere}}\cot(\upsilon_{1,\mathrm{sphere}})\right] - \upsilon_{1,\mathrm{sphere}}^2 = 0 \tag{A2}$$

The quantities ${\upsilon_{1,\mathrm{cylinder}}}^{(\mathrm{YD})}$ and ${\upsilon_{1,\mathrm{disk}}}^{(\mathrm{YD})}$ for the Yamaue-Doi[7] model are the solutions of the equations (A3) and (A4), respectively.

$$\upsilon_{1,\mathrm{cylinder}}^{(\mathrm{YD})} J_1'(\upsilon_{1,\mathrm{cylinder}}^{(\mathrm{YD})}) + \left(1 - \frac{8R}{3}\right) J_1(\upsilon_{1,\mathrm{cylinder}}^{(\mathrm{YD})}) = 0 \tag{A3}$$

$$\upsilon_{1,\mathrm{disk}}^{(\mathrm{YD})}\cos(\upsilon_{1,\mathrm{disk}}^{(\mathrm{YD})}) - \frac{4}{3}R\sin(\upsilon_{1,\mathrm{disk}}^{(\mathrm{YD})}) = 0 \tag{A4}$$

where $J_1(x)$ is the Bessel function. We have derived the equation (A4) on the basis of their governing equations because the solution for large disk gels was not given in the original paper [7]. The values of ${\tau_{1,\mathrm{cylinder}}}^{(\mathrm{YD})}$ and ${\tau_{1,\mathrm{disk}}}^{(\mathrm{YD})}$ are obtained from (A1) assuming $a_\infty$ as the equilibrium diameter of cylinders and the equilibrium height of disks, respectively. The values of ${\tau_{1,\mathrm{cylinder}}}^{(\mathrm{LT})}$ and ${\tau_{1,\mathrm{disk}}}^{(\mathrm{LT})}$ for the Li-Tanaka [3] model are given by the following equations:

$$\tau_{1,\mathrm{cylinder}}^{(\mathrm{LT})} = \frac{3}{2}\frac{a_\infty^2}{D\upsilon_{1,\mathrm{cylinder}}^{(\mathrm{LT})2}} \tag{A5}$$

$$\tau_{1,\mathrm{disk}}^{(\mathrm{LT})} = \frac{3a_\infty^2}{D\upsilon_{1,\mathrm{disk}}^{(\mathrm{LT})2}} \tag{A6}$$

where ${\upsilon_{1,\mathrm{cylinder}}}^{(\mathrm{LT})}$ and ${\upsilon_{1,\mathrm{disk}}}^{(\mathrm{LT})}$ are the solutions of the equations (A7) and (A8), respectively.

$$\upsilon_{1,\mathrm{cylinder}}^{(\mathrm{LT})} J_1'(\upsilon_{1,\mathrm{cylinder}}^{LT}) + 2(1-2R)J_1(\upsilon_{1,\mathit{cylinder}}^{(Lt)}) = 0 \tag{A7}$$

$$4R - 2 - \upsilon_{1,\mathrm{disk}}^{(\mathrm{LT})}\cot(\upsilon_{1,\mathrm{disk}}^{(\mathrm{LT})}) = 0 \tag{A8}$$

The expressions of ${\tau_{1,\mathrm{cylinder}}}^{(\mathrm{WLH})}$ and ${\tau_{1,\mathrm{disk}}}^{(\mathrm{WLH})}$ for the Wang-Li-Hu (WLH) model [6] are given by

$$\tau_{1,\mathrm{cylinder}}^{(\mathrm{WLH})} = \frac{2+B_1}{2}\frac{a^2}{D\upsilon_{1,\mathrm{cylinder}}^{(\mathrm{LT})2}} \tag{A9}$$

$$\tau_{1,\mathrm{disk}}^{(\mathrm{WLH})} = \left(1 + 2B_1'\right)\frac{a^2}{D\upsilon_{1,\mathrm{disk}}^{(\mathrm{LT})2}} \tag{A10}$$

where $B_1$ and $B_1{}'$ are the quantities related to $R$ as

$$B_1 = \frac{2(3-4R)}{\alpha_1^2 - (4R-1)(3-4R)} \tag{A11}$$

$$B_1' = \frac{4}{\alpha_1}\frac{(\sin\alpha_1 - \alpha_1\cos\alpha_1)}{[2\alpha_1 - \sin(2\alpha_1)]}\sin\alpha_1 \tag{A12}$$

## References


1. Tanaka T, Fillmore DJ (1979) J Chem Phys 70:1214
2. Peters A, Candau S (1988) Macromolecules 21:2278
3. Li Y, Tanaka Y (1990) J Chem Phys 92:1365
4. Takigawa T, Uchida K, Takahashi K, Masuda T (1999) J Chem Phys 111:2295
5. Onuki A (1993) Adv Polym Sci 109:97
6. Wang C, Li Y, Hu Z (1997) Macromolecules 30:4727
7. Yamaue T, Doi M (2005) J Chem Phys 122:084703
8. Doi M (2004) Nihon Reoroji Gakkaishi 32:11
9. Matsuo ES, Tanaka T (1992) Nature 358:482
10. Nosaka S, Urayama K, Takigawa T (2005) Polym J 37:694
11. Takigawa T, Morino Y, Urayama K, Masuda T (1996) Polym J 28:1012

Progr Colloid Polym Sci (2009) 136:113–120
DOI: 10.1007/2882_2009_16

# Effect of Residual Swelling Solvent on Nanopore Formation in Replication of Swollen Hydrogel Network

Ken-ichi Kurumada, Atsushi Suzuki, Emiko Otsuka, Susumu Baba, Youhei Seto, Keisuke Morita, and Takanori Nakamura

**Abstract** Hydrogel network of poly N, N′ – isopropyl acrylamide (PNIPAM) was replicated into a silica matrix in the coexistence of PNIPAM hydrogel and solidifying preform sol of silica. During the drying process, the nanoscopic network structure was gradually immobilized in the solidifying silica matrix. The condition for the drying was shown to be highly influential on the total volume of the nanopore and pore size distribution. When the drying was carried out near the saturated vapor pressure of water in order to retard the evaporation of the contained water, the total volume and cross-sectional diameter of the nanopore as the replica of PNIPAM hydrogel were significantly larger than those in the case of normal air-drying open to air. This result indicates that the residual water enveloped PNIPAM polymer chains as a "water robe", and as a result of that, the size and total volume of the nanopore significantly enhanced. The comparison of the formed volume of the nanopore to the water content in the preform revealed that a nonnegligible proportion over the half of the water evaporated during the retarded drying without contributing to the formation of the nanopore. Thus, only the water that remained in the hybrid of PNIPAM and silica at the stage of the entire solidification of the silica matrix could play the role of enhancing the nanopores.

**Keywords** Hydrogel • Nanoscopic network • Replication • Residual water • Pore size distribution • Water robe

## Introduction

Hydrogel generally has a nanoscopic network structure comprised of linear polymer chains. As indicated by the highly deformable appearance, the network of hydrogel is not immobilized as in solid matters. Nevertheless, we should consider that those polymer chains are topologically fixed to each other and the network structure is virtually retained as indicated by the macroscopically lasting elasticity. From this typical speculative viewpoint, a replica which reflects the network structure of the hydrogel can be prepared by a sort of nanoscopic "casting" method. To our interest as follows, we should examine whether the nanoscopic network structure can be really replicated or not.

There have been a number of studies wherein hydrogels were used as media for formation of various solid matters. Those works can be mainly classified into two categories. First, the largest proportion of them report the cases where microparticles with distinctive morphologies could be obtained using hydrogels as the media for the formation of particulate solids [1-16]. Particularly, anisotropic growth of the particle tends to occur [1,3,9,14]. This is probably because of the restricted mass transfer in hydrogel which leads to the highly selective growth of the thermodynamically favored facets. The feature of the particle formation in hydrogel is the retardation in the growth which is occasionally accompanied by the anisotropy in the geometry of the microparticles. The other major category focuses on biomimetic methods for fabricating various bio-compatible materials [17–23]. These trials are rooted from the intuitive idea that hydrogel is apparently quite similar to biological systems where biomaterials are generated. Therefore, the idea of the biomineralization in hydrogel is intriguing from the virepoint of biomimetic engineering. The latter category is also related to the bulk properties of hydrogel.

In the present work, we aim to fabricate a nanoscopic replica of the hydrogel network. There have been quite scant works which reported the results of the trials of replicating the nanoscopic network of hydrogel. Zhao et al tried using polyacrylamide hydrogel for fabricating nanoporous solids [24]. The resultant pore size in the order of decades of nanometer was probably due to some collective mode of the structure formation whose scale was much larger than the unit mesh size of the network forming the hydrogel.

K-i. Kurumada (✉)
[1]School of Environment and Information Sciences,
Yokohama National University,
Yokohama, 240-8501, Japan
e-mail: kurumada@ynu.ac.jp

Sisk et al reported that nanoporous silver was obtained using swollen silica hydrogel as the template [25]. In their case, the resultant pore radius of the nanoporous silver solid was in the order of $10^0$ nm.

We also reported a work of replicating PNIPAM (poly N, N′ – isopropyl acrylamide) hydrogel into silica matrix [26]. Empirically, we had noticed that the drying rate significantly affects the dimension of the sample piece. The retardation in the drying tends to result in larger bulks. Considering that the cracking is normally triggered during the shrinkage in the drying process, the shrinkage can be diminished by retarding the drying process. Since the decrease in the shrinkage is due to the larger volume of the remaining water, the retarded drying can influence the total volume and size of the nanopores formed as the nanoscopic replica of the hydrogel. In the present work, we report the effect of the residual volatile species in the retarded drying on the formation of the nanopores replicated from PNIPAM hydrogel.

## Experimental

### Materials

N, N′- methylenebis acrylamide (BIS), N, N, N′, N′ – tetramethylethylenediamine (TEMED), ammonium persulfate (APS) and hydrochloric acid (HCl) were purchased from Wako Pure Chemical, Japan and used as provided. Tetraorthoethylsilicate (TEOS) as the silica source was provided by Tama Kagaku (Japan) at the analytical grade and used as provided. N, N′ – isopropyl acrylamide (NIPAM) monomer was purchased from Kojin Chemical, Japan, and was used as provided. Water for the sample preparation was purified by ion-exchange followed by distillation.

### Sample preparation

The silica preform was prepared by hydrolyzing TEOS (20.8 g, 0.10 mol) with water (18.0 g, 1.0 mol) and 1 M HCl (0.10 g) under vigorous stirring using a magnetic stirrer. Here, the limiting component was TEOS which were expected to yield 6.0 g of silica. The samples were prepared at various weight ratios ( ε ) of NIPAM to silica ($\varepsilon = 0 \sim 3$). The preform solution of the hydrogel was prepared as follows. NIPAM and BIS were dissolved in water at a weight ratio of 1:4 (NIPAM:water). The molar ratio of BIS to NIPAM was fixed at 1/81. The completion of the dissolution required approximately 2 hours at 200 r.p.m. stirring using a magnetic stirrer. Then, TEMED was added at a weight ratio of 1.0:0.03 (NIPAM:TEMED). TEMED readily dissolved in the above solution. Subsequently, APS was added at a weight ratio of 1:0.125(NIPAM:APS) in the form of 1 wt % aqueous solution. Finally, the above two preform solutions of silica and PNIPAM hydrogel were mixed to obtain a uniform solution, which was subsequently kept at 273 K in a refrigerator for 24 hours in order to complete the polymerization and cross-linking of PNIPAM. The gellation occurred during this period of refrigeration. In the present work, we adopted two different conditions for the drying process. The air-dried sample was desiccated at 323 K for 24 hours being kept open to air. The retarded drying was carried out by keeping the sample at 323 K for a week. The sample was wrapped in a beaker during the above process which was followed by subsequent air-drying in an open state at the same temperature. The desiccated samples were calcined at 873 K for 5 hours to eliminate the combustible organic and volatile moieties.

### Measurement and observations

Nitrogen adsorption / desorption measurements were carried out at 77 K using Belsorp Mini (Nippon Bell, Japan). The saturated adsorption volume was obtained at the relative pressure $P/P_0 = 0.9814$. The pore size distribution was calculated by the Barrett – Joyner – Halenda (BJH) method [27]. The TEM observation was carried out at 175 kV or 200 kV of the acceleration voltage (HITACH H – 800, Hitachi, Japan). The sample was carefully ground, dilutely dispersed in ethanol and placed on a microgrid by dripping a drop of the above dispersion.

### Prediction and evaluation of porosity

The porosity of the sample was evaluated from the maximum adsorbed volume of nitrogen at the limiting relative pressure to unity ( $P/P_0 \rightarrow 1$). The assumption for estimating the adsorbed volume was that the adsorbed layer of nitrogen molecules has the same density as the bulk of liquid nitrogen at 1 atm (808 kg / $m^3$). The true density of the silica matrix was assumed to be 2200 kg / $m^3$ according to the preliminary experiments.

The porosities of the samples prepared by three different drying conditions or preparation conditions were predicted by calculating the expected volume fraction of moieties which were eliminated during the drying or calcination. The volume occupied by each component was estimated by dividing the contained weight by the density of each

component. The porosity of the sample prepared by the normal air-drying was predicted as follows;

$$(predited\ porosity) = \frac{(volume\ of\ PNIPAM)}{(volume\ of\ PNIPAM) + (volume\ of\ silica)}$$

In the case where the sample was prepared by the retarded drying in the vicinity of the saturated vapor pressure of water, all the contained PNIPAM and water were assumed to contribute to the pore volume. Thus, the porosity was estimated by taking into account the volume of water in the above calculation;

$$(predited\ porosity) = \frac{(volume\ of\ PNIPAM) + (volume\ of\ water)}{(volume\ of\ PNIPAM) + (volume\ of\ water) + (volume\ of\ silica)}$$

The porosity of the "green body" (the sample before the calcination) was also predicted by assuming that only the contained water contributed to the formation of the pore. In this case, the porosity was evaluated by taking into account the formed volume of the pore by the elimination of the contained water;

$$(predited\ porosity) = \frac{(volume\ of\ water)}{(volume\ of\ PNIPAM) + (volume\ of\ water) + (volume\ of\ silica)}$$

In the above calcination, the densities of water, PNIPAM, and silica were given as 1000 kg/m$^3$, 1000 kg/m$^3$ and 2200 kg/m$^3$, respectively.

## Results and Discussion

### TEM observation

Figure 1 shows transmission electron microscope (TEM) images of the replica of PNIPAM hydrogel prepared by the air-drying (Fig. 1a) and retarded drying (Fig. 1b). Both of them were prepared at the weight ratio of PNIPAM to silica, $\varepsilon = 5/3$. The mesh-like pattern reflecting the network in PNIPAM hydrogel was observed as reported in our previous work [26]. The darker part in the bottom of Fig. 1a shows that the thickness of the observed particle increases with the separation distance from the end seen at the top of Fig. 1a. The appended photographs show that the retarded drying is advantageous to obtain bulk samples of replica. The tendency of the formation of larger bulks in the retarded drying is probably because of the reduction in shrinkage caused by the

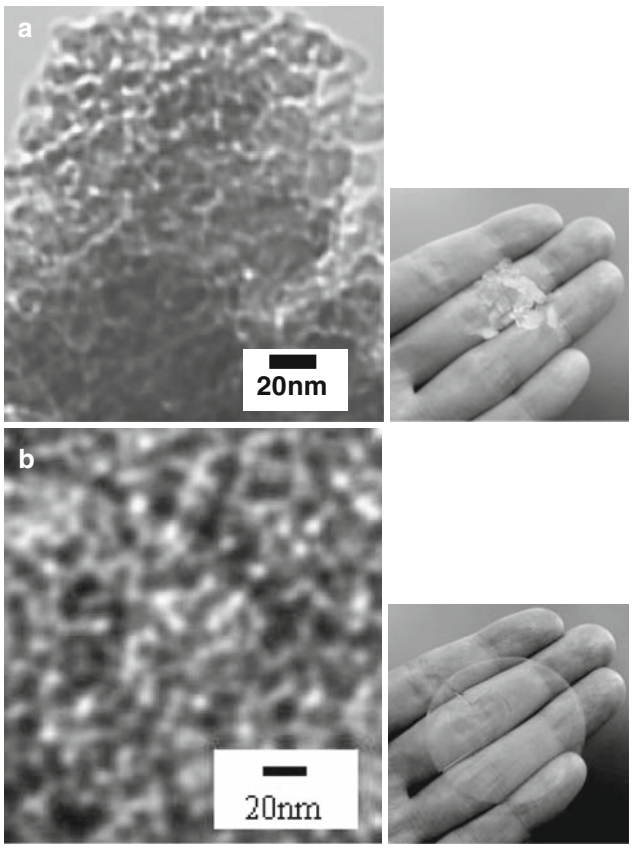


**Fig. 1** Transmission electron microscope (TEM) images and photographs of the prepared replica of PNIPAM (poly N, N′ – isopropyl acrylamide) hydrogel. **a** normal air-drying, $\varepsilon = 5/3$; **b** retarded drying, $\varepsilon = 5/3$

evaporation of volatile species like water. When the shrinkage is prominent, the delay in the drying inside the solidifying bulk brings about lateral tensile stress on the surface of the sample. The other feature due to the retardation in the drying is that the cross-sectional diameter of the tubular nanopores was larger when the drying was retarded. This "thickening" of the tubular nanopore indicates nonnegligible effect of the residual water on the total volume and size of those tubular nanopores.

### Nitrogen adsorption / desorption

Figure 2 shows the nitrogen adsorption / desorption isotherms of the samples prepared by the air-drying and retarded drying. Here, the weight ratio of PNIPAM was set at $\varepsilon = 1/2$. The predicted and measured porosities of both samples are shown beside the isotherm in Figure 2. Since both isotherms show hysterysis behavior typical of nanoporous solids, the hydrogel is considered to work as a template for the formation of those nanopores. In the case of the

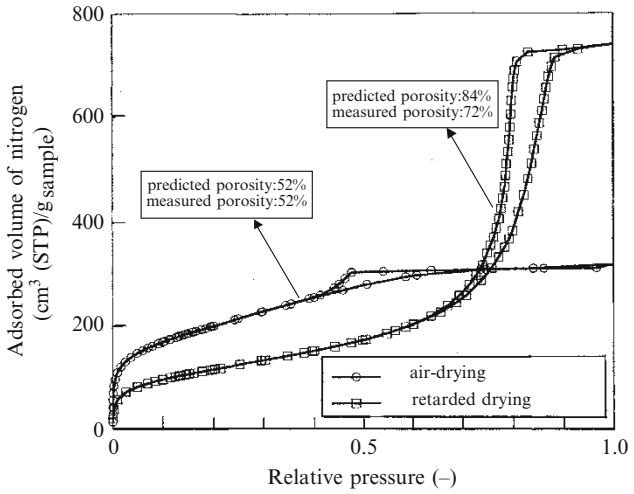


**Fig. 2** Nitrogen adsorption / desorption isotherms at 77 K. *Open circle*, normal air-drying, ε = 1/2; *Open square*, retarded drying, ε = 1/2; The predicted and measured porosities are shown beside the corresponding isotherm

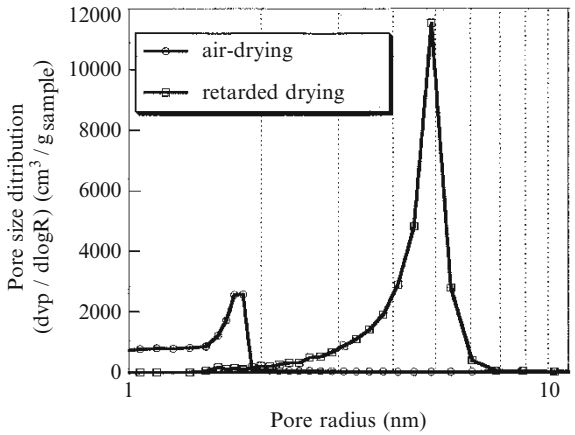


**Fig. 3** Pore size distribution estimated from the nitrogen desorption isotherm by the Barrett – Joyner – Halenda (BJH) method at 77 K. *Open circle*, normal air-drying, ε = 1/2; *Open square*, retarded drying, ε = 1/2

air-dried sample, the actually measured porosity agreed with the predicted value (52 %). This result shows that the space which was occupied by PNIPAM polymer chains was converted to the tubular nanopores by the calculation in air. The effect of the retarded drying in enhancing the nanopore formation is clearly seen in Figure 2. The porosity of the sample prepared by the retarded drying was predicted assuming that all the water that existed at the stage of mixing the preform NIPAM gel solution and preform silica sol contributed to the nanopore formation. Since the actual porosity (72 %) was nonnegligibly smaller than the predicted value (84 %), the replica of the hydrogel underwent partial shrinkage. Since the constituent PNIPAM polymer is completely nonvolatile, this partial shrinkage of the nanopore was due to the partial evaporation of the residual water which occurred even in the vicinity of the saturated vapor pressure of water. Assuming that the decrease in the porosity from 84 % (predicted) to 72 % (measured) was entirely due to the gradual evaporation of the water during the retarded drying, the lost fraction of the water can be estimated as follows; Let the total volume of the sample be 100 as the reference value in the case of the "predicted porosity" of the "retarded drying". Then, the predicted volume of the water which can contribute to the nanopore formation is given by 100-16-(16)(52/48). On the other hand, the volume of the actually formed nanopore was (16)(72/28). Therefore, the actual contribution by the residual water to the formation of the nanopore can be estimated as the difference of (16)(72/28) from the volume formed by the replication of the constituent polymer chains, (16)(52/28). In conclusion, the volume fraction of the residual water which was lost during the retarded drying process could be estimated as

$$1 - \frac{(16)\left(\frac{72}{28}\right) - (16)\left(\frac{52}{48}\right)}{100 - 16 - (16)\left(\frac{52}{48}\right)} \cong 0.64.$$

Therefore, more than 60 % of the water contained in the preform evaporated and did not contribute to the formation of the nanopore even in the case where the retarded drying near the saturated vapor condition was applied.

Figure 3 shows the corresponding pore size distributions calculated by the BJH method, which normally applies to open-pore type nanoporous solids. The cross-sectional diameter of the nanopore obviously increased by the retarded drying. Since the water can exist only in the space between the polymer chain and silica matrix after the polycondensation of the silica matrix completes, the result shown in Figure 3 indicates that the residual water envelopes the PNIPAM polymer chain as a "water robe". At the same time, the surrounding silica matrix undergoes gradual solidification. Eventually, the nanoscale morphology of the hydrogel including the water robe is replicated in the completely solidified silica matrix. After the complete removal of the combustible and volatile species, the nanopores with the increased cross-sectional diameter are formed.

Figure 4 shows the dependence of the measured porosity on the weight ratio ε of PNIPAM to silica in both cases of the air-drying and retarded drying. Quite naturally, the porosity monotonously increased with the weight ratio ε of PNIPAM. At any value of ε, the porosity was larger when the sample was prepared by the retarded drying than when the normal air-drying was employed. Therefore, the water robe enveloping the polymer chain is formed when a part of volatile species is forced to remain under a certain condition at which the evaporation of the volatiles is suppressed.

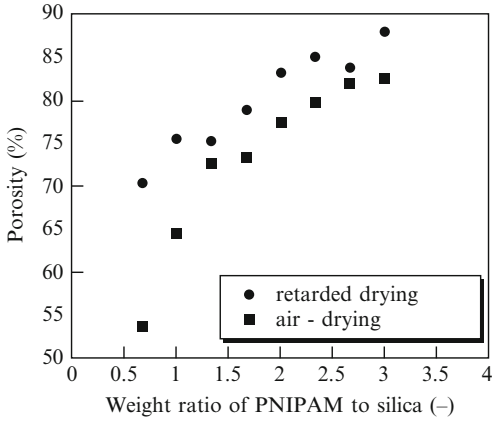


**Fig. 4** Dependence of porosity on weight ratio ε of PNIPAM to silica. *Filled square*, normal air-drying; *Filled circle*, retarded drying

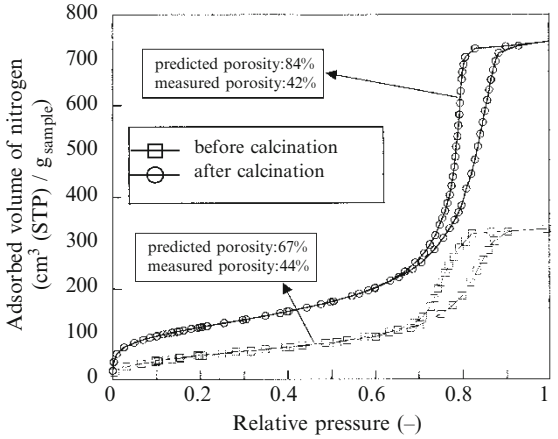


**Fig. 5** Nitrogen adsorption / desorption isotherms at 77 K. *Open square*, before calcination (green body), ε = 1/2; *Open circle*, after calcination, ε = 1/2; The predicted and measured porosities are shown beside the corresponding isotherm

## *Supplementary supporting results*

Figure 5 shows a comparison of the nitrogen adsorption / desorption isotherms between (a) the finally obtained replica of PNIPAM hydrogel and (b) its "green body" before the calcination in air (b). Here, both of them were prepared by the retarded drying at the weight ratio ε = 1/2. The isotherm of the latter (b) clearly shows that the green body in the hybridized state of PNIPAM gel and silica matrix had already had the nanopores before the organic moiety was eliminated by the calcination in air. This result can be considered as an evidence for the formation of the water robe which enveloped the PNIPAM polymer chains. The water robe converted to the nanopore when the residual water evaporated. The predicted and measured porosities of both samples are shown beside the isotherm. Here, we can discuss the porosity of the green body as we did in the preceding section; The predicted porosity of the green body can be estimated as 100-16-(16)(52/46) since it is smaller than the predicted porosity by the volume of the hydrogel ((16)(52/48)). Thus, the porosity of the green body was estimated to be approximately 67 %. Similarly, the actual porosity of the green body can be estimated by considering that the total pore volume was smaller than that of the calcined sample of the "retarded drying" by the volume of the hydrogel, (16)(52/48). Consequently, the actual porosity of the green body was estimated to be [(16)(72/28-52/48)]/[16+(16)(72/28)] ≈ 0.42. This value is noticeably close to the measured porosity of the green body (44 %). These consistencies in the volumes of the silica matrix, PNIPAM and water support the speculative view that the residual water (water robe) plays a significant role in the determination of the resultant porosity.

Figure 6 shows the corresponding BJH pore size distribution. The peak radius of the formed nanopore increased from approximately 4 nm to 5 nm, which roughly corresponds to

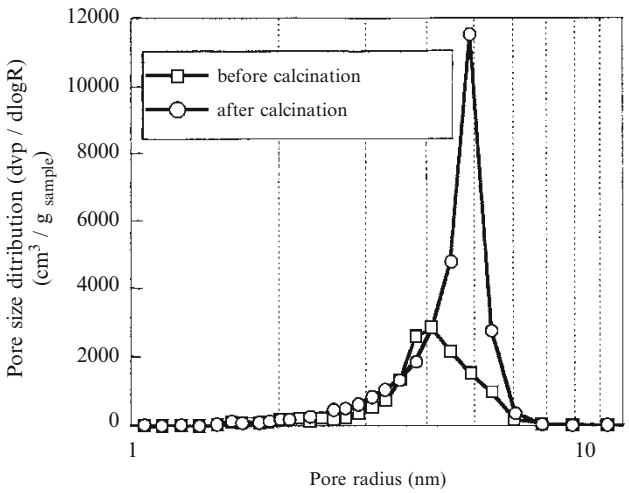


**Fig. 6** Pore size distribution estimated from the nitrogen desorption isotherm by the Barrett – Joyner – Halenda (BJH) method at 77 K. *Open circle*, before calcination (green body), ε = 1/2; *Open square*, after calcination, ε = 1/2

$5^2 / 4^2 \approx 1.6$ fold enhancement in the cross-sectional area of the nanopore. On the other hand, the total volume of the nanopore increased to [(16)(72/28)]/[(16)(72/28-52/48)] ≈ 1.7 times. From this satisfactory agreement of the above two ratios representing the nanopore enhancement, the result of the comparison shown in Figure 5 indicates that the increase in the total volume of the nanopore was mostly due to the elimination of the remaining PNIPAM hydrogel by the calcination.

Figure 7 shows schemes of the formation of the nanopore in the silica matrix as the result of the replication of the hydrogel network structure; (a) When the normal air-drying was carried out, the surrounding silica matrix was squeezed

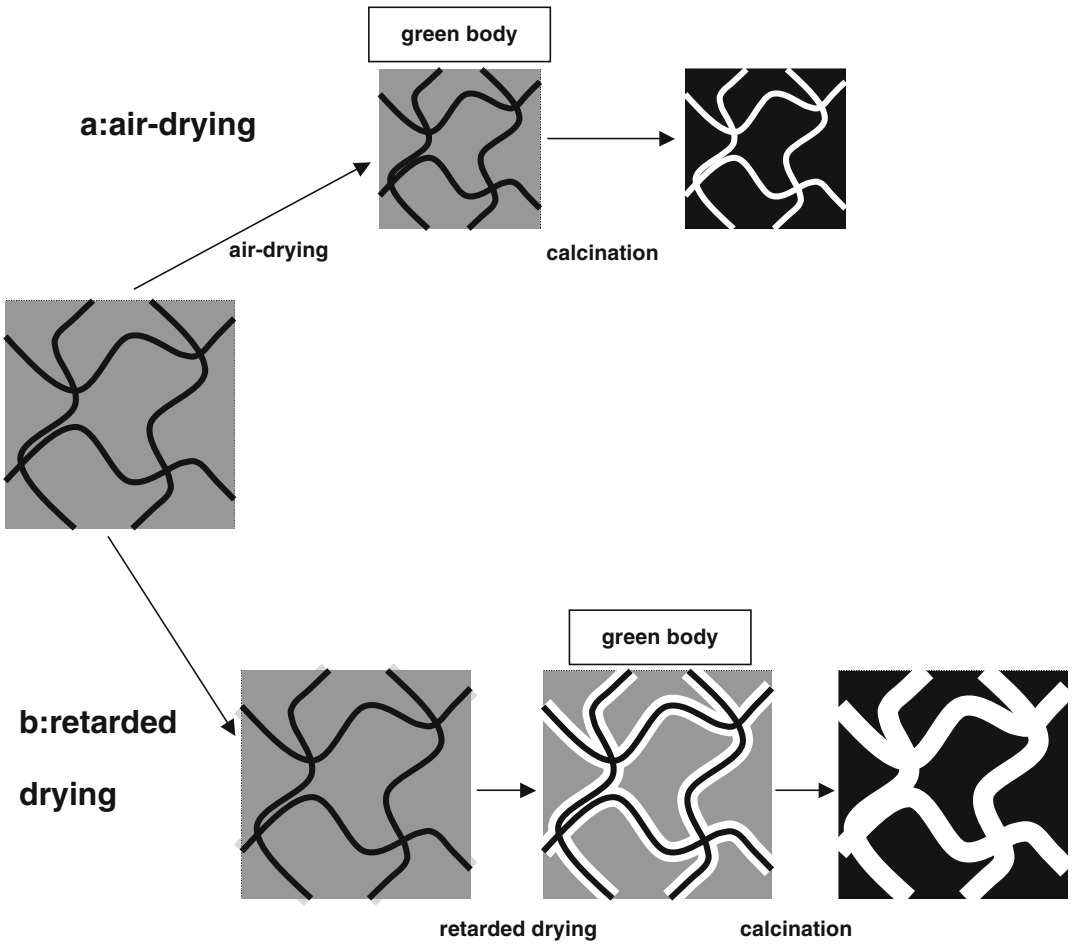


**Fig. 7** Schematic representation of the formation of the nanopore. **a** In the case of air-drying, the water robe is not formed. **b** The retarded drying allows the residual water to form the water robe around the polymer. As a result of that, the pore size and total pore volume enhance

while the water was evaporating. Thus, the total volume of the nanopore matched that of the hydrogel. (b) When the retarded drying was carried out, a part of the water remained and formed the water robe which enveloped the constituent polymer chain of the hydrogel. Before the retarded drying was completed, the silica matrix solidified and stopped being squeezed by the evaporating water. When the drying process terminated, only the hydrogel remained in the network of the tubular nanopores. After the calcination, the network of the nanopores became empty having obtained the inner volume corresponding to that occupied by the remaining hydrogel.

## Conclusion

1. A negative replica of PNIPAM (poly N, N′ – isopropyl acrylamide) hydrogel was fabricated by polycondensation of preform silica sol in the coexistence of PNIPAM hydrogel followed by the air-drying and calcination in air.

2. The residual swelling solvent (water) was revealed to contribute to the formation of the network of nanopores. The residual water remained between the PNIPAM chain and surrounding silica matrix and formed a water robe. As a result of that, a larger cross-sectional diameter of the tubular nanopore was obtained than in the case of the normal air-drying.

3. Even in the case where the retarded drying was carried out in the vicinity of the saturated vapor condition of water, a nonnegligible proportion of the residual water evaporated without contributing to enhancing the total volume of the nanopore. This is probably because the residual water started to contribute only after the surrounding silica matrix sufficiently solidified to stop being squeezed by the diminishing water.

4. The nanopore was already formed even before the thermal elimination of the template hydrogel. The “water robe” converted to the nanopore itself. The subsequent calcination enhanced the total volume of the nanopore. The enhanced volume of the nanopore corresponded to the net

volume of the PNIPAM hydrogel which remained after the completion of the drying.

**Acknowledgment** The authors gratefully acknowledge the continuous financial support and many useful suggestions by Hitachi Chemical Co. Ltd.

## References

1. Tan C, Lu R, Xue P, Bao C, Zhao Y (2008) Mater Chem Phys in press
2. Lopez-Ureta LC, Orozco-Guareño E, Cruz-Barba LE, Gonzalez-Alvarez A, Bautista-Rico F (2008) J Polym Sci, Part A: Polym Chem 46:2667
3. Fu XJ, Wang NX, Zhang SZ, Wang H, Yang YJ (2008) Wuji Cailiao Xuebao (Journal of Inorganic Materials) 23:393
4. Ford J, Yang S (2007) Chem. Mater. 19:5570
5. Nelson K, Deng Y (2007) Macromol Mater Eng 292:1158
6. Zhao J, Li Y, Cheng G (2007) Chin Sci Bull 52:1796
7. Shen Z, Duan H, Frey H (2007) Adv Mater 19:349
8. Sahiner N (2006) Colloid Polym Sci 285:283
9. Bao C, Lu R, Xue P, Jin M, Tan C, Liu G, Zhao Y (2006) Journal of Nanoscience and Nanotechnology 6:807
10. Zhao J, Li Y, Kuang Q, Cheng G (2005) Colloid Polym Sci 284:175
11. Firestone MA, Dietz ML, Seifen S, Trasobares S, Miller DJ, Zaluzec NJ (2005) Small 1:754
12. Marty JD, Mauzac M (2005) Adv Polym Sci 172:1
13. Aburto J, Mendez-Orozco A, Le Borgne S (2004) Chem Eng Process 43:1587
14. Bao C, Lu R, Jin M, Xue P, Tan C, Zhao Y, Liu G (2004) Journal of Nanoscience and Nanotechnology 4:1045
15. Jung JH, Lee SS, Shinkai S, Iwaura R, Shimizu T (2004) Bull Korean Chem Soc 25:63
16. Wang H, Holmberg BA, Yan Y (2003) J Am Chem Soc 125:9928
17. Shen X, Tong H, Jiang T, Zhu Z, Wan P, Hu J (2007) Compos Sci Technol 67:2238
18. Matsusaki M, Yoshida H, Akashi M (2007) Biomaterials 28:2729
19. Hutchens SA, Benson RS, Evans BR, O'Neill HM, Rawn CJ (2006) Biomaterials 27:4661
20. Sugawara A, Yamane S, Akiyoshi K (2006) Macromol Rapid Commun 27:441
21. Hawkins DM, Stevenson D, Reddy SM (2005) Anal Chim Acta 542:61
22. Alexandre E, Cinqualbre J, Jaeck D, Richert L, Isel F, Lutz PJ (2004) Macromol Symp 210:475
23. Bellamkonda R, Ranieri JP, Bouche N, Aebischer P (1995) J Biomed Mater Res 29:663
24. Zhao QC, Chen WM, Zhu QR (2003) Mater Lett 57:3606
25. Sisk CN, Gill SK. Hope-Weeks LJ (2006) Chem Lett 35:814
26. Kurumada K, Nakamura T, Suzuki A, Umeda N, Kishimoto N, Hiro, M (2007) J Non-Cryst Solids 353:4839
27. Barrett EP, Joyner LJ, Halenda PP (1951) J Am Chem Soc 73:373

Progr Colloid Polym Sci (2009) 136:121–126
DOI: 10.1007/2882_2009_17

# Swelling Properties of Physically Cross-linked PVA Gels Prepared by a Cast-drying Method

Emiko Otsuka and Atsushi Suzuki

**Abstract** We report the swelling properties of physically cross-linked polyvinyl alcohol (PVA) hydrogels prepared by a cast-drying method. The swelling ratio of PVA cast gel in its swollen state decreased after repeated processes of water exchange with drying. The measurements using a Fourier Transform Infrared Spectroscopy and X-ray diffraction suggested that the hydrogen bonds were additionally formed during the process of water exchange with drying. We concluded that non-cross-linked polymers with low molecular weight eluted into the solvent by water exchange and additional hydrogen bonds were formed during the dehydration, which resulted in the decrement of the water content in the swollen state.

**Keywords** PVA hydrogel • Cast-drying method • Swelling ratio • Water exchange • Hydrogen bond

## Introduction

Polyvinyl alcohol (PVA) is a water-soluble polymer and has been widely used in practical applications in a variety of fields because of its excellent chemical resistance and physical properties, low toxicity, and high biocompatibility. For the same reasons, PVA or PVA-based hydrogels are also used in a variety of pharmaceutical and biomedical applications as biomaterials, including wound dressing, implants, cell encapsulation, drug-delivery systems, soft contact lenses, and dental applications. For the preparation of PVA gels [1], various methods have been reported until now. Among them, an aqueous solution of PVA can form hydrogels through a freezing and thawing process first reported by Nambu [2,3]; PVA solutions are frozen at −5 to −20 °C and allowed to thaw to around room temperature, and this method results in the formation of micro-crystals that serve as physical cross-links to render the material insoluble in water.

Recently, we developed a new gelation technique of PVA, called a cast-drying method, in an attempt to address a simple process at room temperature starting from an aqueous PVA solution without using additional chemical reagents [4]. Briefly, this new method produces a physically cross-linked transparent polymer network from water and PVA powders, i.e., a swollen PVA cast gel in water.

In this paper, we report the equilibrium swelling characteristics in pure water of the thin plate of physically cross-linked PVA gels prepared by a cast-drying method, especially to obtain information about various factors to affect the swelling properties. The static swelling ratio was measured whenever the dehydrated PVA cast gel was re-swelled after the exchange of solvent water was exchanged with or without drying. The molecular interaction and the network structure were analyzed using Fourier Transform Infrared Spectroscopy (FT-IR) and X-ray diffraction (XRD) measurements as well as the measurements of the swelling ratio. The swelling behavior is discussed in terms of the elution of polymers and the formation of hydrogen bonds by the exchange of solvent with drying.

## Experimental

### *Materials*

The PVA powder (the degrees of polymerization and hydrolysis were 1500 ∼ 1800 and 98 ∼ 100 mol%, respectively) was purchased from Wako Pure Chemical Industries, Ltd., and used without further purification. An aqueous PVA solution was obtained by dissolving 15.0 wt% of the PVA powder into deionized and distilled water at 90 °C for more than 2 hrs.

E. Otsuka (✉)
Graduate School of Environment and Information Sciences
Yokohama National University
79-7 Tokiwadai, Hodogaya-ku, Yokohama, 240-8501 Japan

The PVA solution (3.0 g) was poured into a plastic dish of polyethylene with an inner diameter of 33 mm and left in air at room temperature (ca. 25 °C). The solution became very viscous within a few days and solidified (thin disk) within a week or more. The sample was prepared by a single process of dehydration of the PVA aqueous solution at room temperature.

### Measurements of the water content

The change in the weight of the PVA solution, $W_s$, during the dehydration was measured against time, and the respective water content, $w$, was calculated. In this paper, $w$ is defined as the ratio of the weight of water to the nominal weight of PVA powder (the manufacturing product without any pre-treatment), $W_p$: $w = (W_s - W_p)/W_p \times 100$ (%). In the case of the dehydration of the PVA solution, the initial $W_s$ was the weight of the PVA solution (= 3.0 g), and $W_p$ was the nominal weight, 0.45 g.

### Measurement of the swelling ratio

Figure 1 shows the schematic diagram of the measurements of the weights of the swollen PVA cast gel and dehydrated PVA cast gel. The sample of 6 × 4 mm cut from the dehydrated thin disk was put into 100 g of pure water and kept for 24 hrs to reach the equilibrium state. After the sample was taken out from the solvent water, the drops of water on the surface were wiped off with Kimwipes, and the weight of the sample, $W_t$, was measured at room temperature (I in Fig. 1). After the sample was dried at room temperature for 72 hrs, the dehydrated weight, $W_d$, was measured (II in Fig. 1), and the swelling ratio, which is defined here as $W_t/W_d$, was obtained. The elution ratio of the polymer, $r$, defined as $r = (1 - W_d/W_p) \times 100$ (%), was also calculated. This process of water exchange with drying was repeated 9 times (the number of the repeated times, $N = 9$). For comparison, the swelling ratio without drying was also measured as follows: another sample of 6 × 4 mm cut from the same dehydrated thin disk was put into 100 g of pure water and kept for 24 hrs. Hereafter, the solvent water was exchanged repeatedly by keeping the swollen condition without drying. After $N = 9$, the sample was dried at room temperature for 72 hrs, the dehydrated weight, $W_d$, was measured, and the swelling ratio, $W_t/W_d$, was calculated.

### ATR FT-IR and XRD measurements

To study the change in molecular structures (e.g., the formation of hydrogen bonds) of the PVA cast gel during the water exchange with drying, the measurements of FT-IR with an Attenuated Total Reflection (ATR) method were carried out at room temperature. The ATR FT-IR spectra were recorded on an FT-IR spectrophotometer (Jasco FTIR 610) equipped with an ATR attachment with a horizontal ZnSe crystal (Jasco PRO 400S). The resolution of the spectra was 4 $cm^{-1}$, and the scans were repeated 100 times. The IR absorbance spectra were normalized by the peak height of the C-H bending vibration at 1427 $cm^{-1}$ [5], which was obtained by the deconvolution of the spectra. The components of the absorption band, consisting of multiple peaks, were deduced from the second-derivative of spectra and resolved by applying the curve-fitting method. The measurements were conducted on samples whenever the process of water exchange with drying was repeated from $N = 0$ to 5.

To confirm the structural details in the different length scales, XRD measurements were performed at room temperature using a SAXSess camera (Anton Paar, PANalytical) with a $K_\alpha$ wavelength of 0.1542 nm operated at 40 kV and 50 mA. This apparatus combines both small-angle scattering (SAXS) and wide-angle X-ray scattering (WAXS) techniques, which allows the measurements of structures with scattering features down to 0.25 nm in a single scan.

## Results and Discussion

### Network structure of PVA cast gel prepared by a cast-drying method

Figure 2 shows the change in $w$ during a dehydration process of the PVA aqueous solution over time in a semi-logarithmic

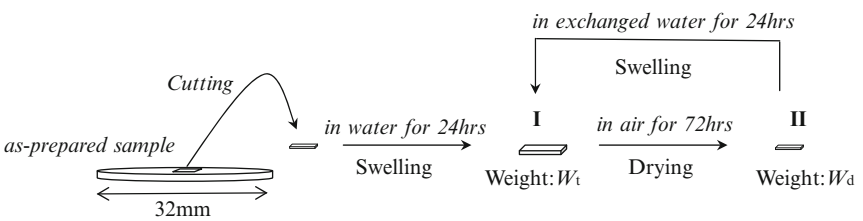


**Fig. 1** The measurement of swelling ratio of PVA cast gel during repeated water exchange with drying

plot. In this plot, there are three characteristic points shown in No. 1, 2 (inflection point), and 3. The normalized $W_s$ is also plotted against time in the inset of this figure, where the change between No. 1 to 3 is more rectilinear and more gradual after No. 3. The time evolution of $w$ or $W_s$ was classified into three different regions characterized by initial slow (before point No. 1), rapid (between points No. 1 and 3), and very slow (after point No. 3) decrements. The first region corresponds to the evaporation of excess water from the solution. The second and third ones seem to correspond, respectively, to the results of the dehydration experiments for chemically cross-linked hydrogels [6,7]; $W_s$ decreased rapidly due to the evaporation of free water molecules and gradually due to the evaporation of bound water molecules. During this dehydration process, the sample changed from a liquid to a solid, i.e., from a PVA aqueous solution to a dehydrated PVA cast gel. The dehydrated PVA cast gel remained transparent and firm, like soft plastic. The diameter was 32 mm (slightly shrunk from the size of the mold), and the thickness was about 0.5 mm at the center and about 1 mm at the edge; the edge became thicker due to the surface tension between the PVA solution and the inside wall of the dish. The measurements using ATR FT-IR and XRD, which were consistent with those in our preliminary work [4], suggested that cross-links due to the hydrogen bonds and micro-crystals were formed during the dehydration process of the PVA solution. Figure 3 shows the schematic illustration of the network structure of the dehydrated PVA cast gel: hydrogen bonds with an average distance, $d$ formed a micro-crystal with an average crystallite size, $D$. The micro-crystals were distributed with an average distance, $L$. This picture is similar to the physically cross-linked PVA gel in a DMSO/water mixed solvent [8]. The dehydrated PVA cast gel was swollen in water without dissolution and remained transparent.

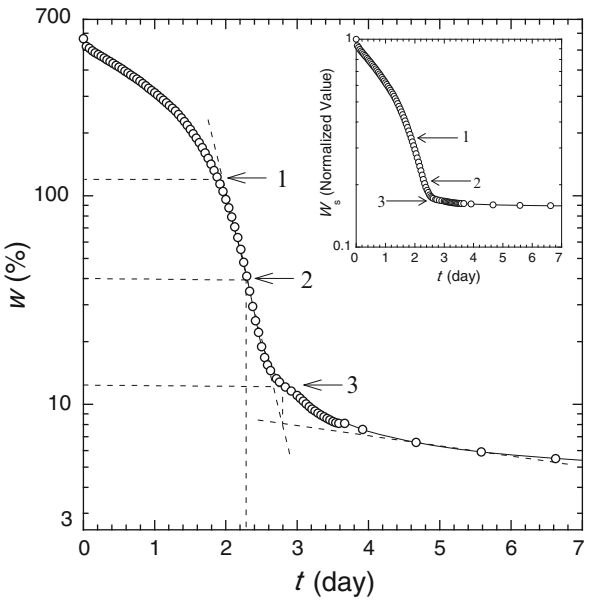


**Fig. 2** Time evolutions of water content and normalized $W_s$ (small figure) of PVA solution during the dehydration process. The numbers are characteristic points (see text)

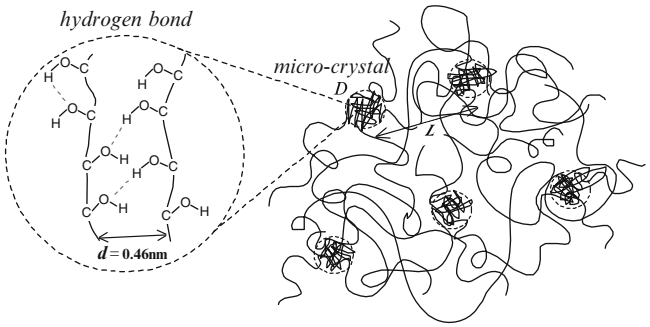


**Fig. 3** Schematic representation of the network structure of PVA cast gel cross-linked by micro-crystals

## Effects of w on the swelling ratio

Figure 4 shows the swelling ratio, $W_t/W_d$, and the elution ratio, $r$, as functions of the initial $w$ at preparation. With decreasing $w$, $W_t/W_d$ exhibited a rapid decrease and showed a gradual decrease after a characteristic $w$ around No. 2. Although there are scatterings in the data points to some extent, $r$ also decreased with decreasing $w$, which roughly correlates with the change in $W_t/W_d$. This observation should be attributed to the fact that the dehydration of free water brought the polymer

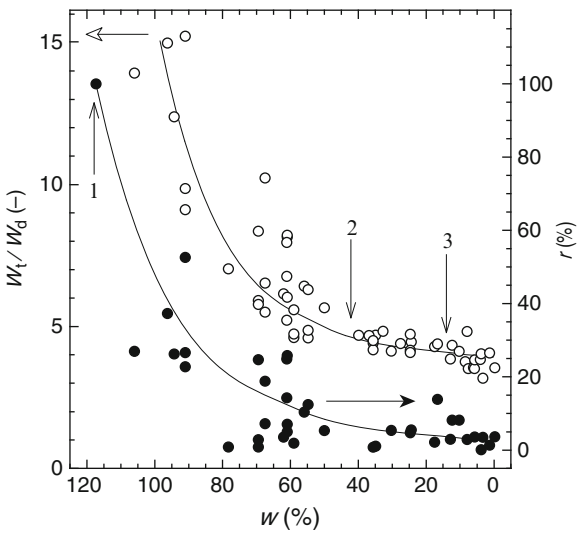


**Fig. 4** $w$ dependence of $W_t/W_d$. The numbers corresponds to the same numbers in Fig. 2. The solid lines are to guide the eye

chain physically closer, which contributed to the formation of hydrogen bonds and cross-link points. On the other hand, the samples with $w$ around No. 1 dissolved completely in the solvent water, i.e., $r = 100$. This evidence should be attributed to the fact that the insufficient dehydration could not make enough cross-link points to form the networks. In the following experiments, samples with low $w$ at preparation were used to study the effects of the water exchange with or without drying on the swelling behavior and the network structure. It should be noted that the results shown in Fig. 4 were the elution against $w$ on the first water exchange process and not on the sufficient water exchange. However, the total elution amount was finite, which was confirmed in our preliminary work [4].

## Swelling ratio during water exchange with or without drying

Figure 5 shows $W_t/W_d$ of the sample with $w = 5.5$ at preparation (sufficient dehydration after No. 3 in Fig. 4) as a function of $N$ with or without drying. In the case of the water exchange with drying, $W_t/W_d$ decreased rapidly in $N$ from 0 to 5. After $N = 6$, $W_t/W_d$ became constant, and $r$ was 1.0 at $N = 9$. In the case of the water exchange without drying, on the other hand, $W_t$ decreased very slowly with increasing $N$. Assuming that $W_d$ is constant and equal to that of the dehydrated weight at $N = 9$, $W_t/W_d$ will decrease, as shown in Fig. 5. However, this assumption

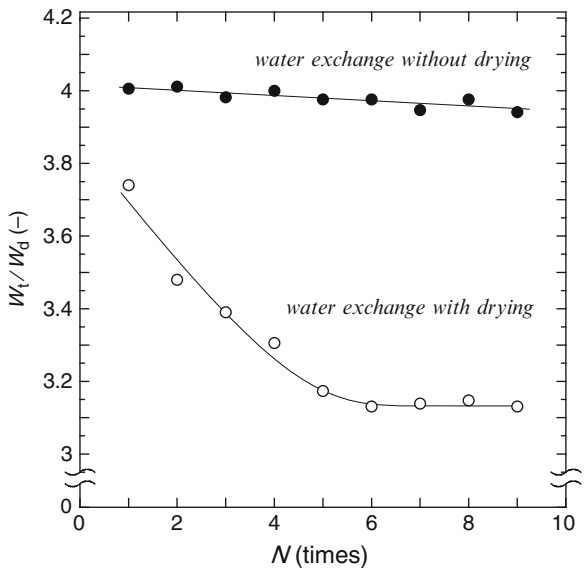


**Fig. 5** $W_t/W_d$ of PVA cast gels during water exchange with or without drying. The solid lines are to guide the eye

is not correct at all because of elution during the water exchange. The dehydrated weight should be measured separately whenever the water is exchanged. According to our preliminary work [4], the real $W_t/W_d$ at $N = 1$ is expected to be smaller than that at $N = 9$. It is noteworthy that $r$ was 3.6 at $N = 9$ in the water exchange without drying, i.e., clearly larger than $r$ (= 1) in the water exchange with drying.

Figure 6(a) shows the ATR FT-IR spectra of the dehydrated PVA cast gels during the water exchange with drying, where the typical local maxima are indicated. The vertical axis of each spectrum is shifted for clarity. The large peak at around 3300 $cm^{-1}$ due to the O–H stretching of the hydrogen bonds [9] was analyzed; its peak height increased slightly and decreased with increasing $N$ and became almost constant after $N = 5$. This non-monotonic change might be related with the formation and the destruction of hydrogen bonds during water exchange with drying.

Two peaks at 2940 and 2910 $cm^{-1}$ can be seen in the range of 2900 – 2950 $cm^{-1}$ and their overall shape changed with increasing $N$. Moreover, a shoulder at 2855 $cm^{-1}$ became evident with increasing $N$. In order to deconvolute the spectra, the second-derivative was calculated in the range of 2800 – 3000 $cm^{-1}$, and the results of $N = 0$, 3, and 5 are shown in Fig. 6(b). The components of the absorption band at 2900 – 2950 $cm^{-1}$ were deduced from these second-derivatives; the initial components at $N = 0$ were two peaks at 2946 and 2905 $cm^{-1}$, which could be assigned to the $CH_2$ stretching [5] and the C–H stretching [10], respectively. The peak intensity of the former remained constant, while that of the latter tended to increase with increasing $N$. In addition, the third component appeared at 2917 $cm^{-1}$ with increasing $N$. Although we could not assign the peak at 2917 $cm^{-1}$ at present time, it could be related to the formation of hydrogen bonds by the repeated processes. As for the shoulder, the second-derivative at 2851 $cm^{-1}$ changed clearly with increasing $N$. This peak could be assigned to the C-H stretching [11], and the change in its intensity by the repeated processes suggested that the formation of additional hydrogen bonds between –OH groups might affect the movements of the –CH groups.

The C–O stretching at 1143 $cm^{-1}$ in Fig. 6(a) due to the formation of micro-crystals [12] did not change with increasing $N$. This result suggested that the micro-crystal regions were not affected by the repeated processes.

The XRD spectra of the dehydrated PVA cast gels during the water exchange with drying were obtained, and the results of $N = 0$, 3, and 5 are shown in Fig. 7. The vertical axis of each spectrum is shifted for clarity. A sharp peak at $q = 13.7$ $nm^{-1}$ ($d = 0.46$ nm), which was assigned to the micro-crystals (cross-linked region) [4], was not affected by

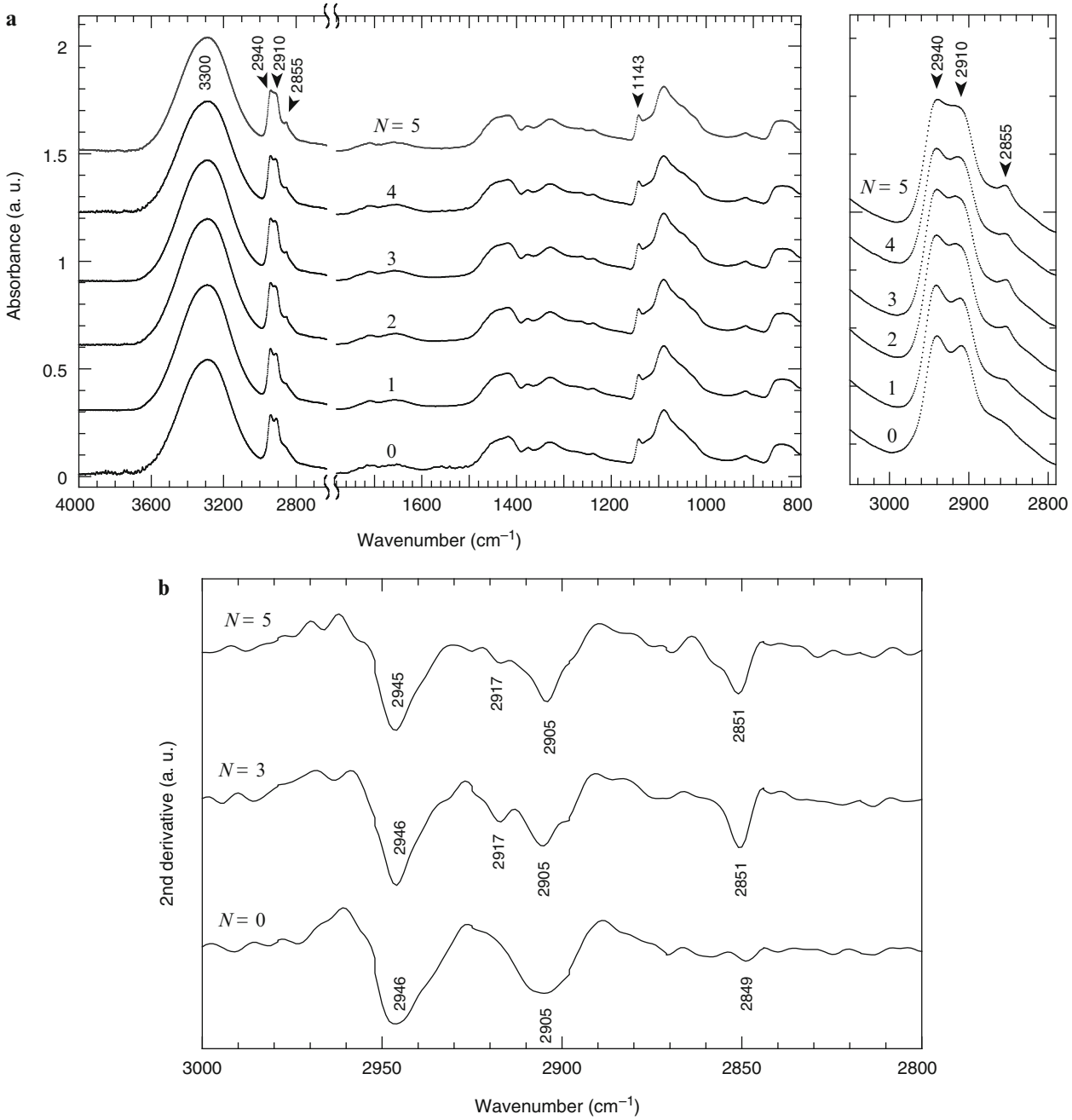


**Fig. 6** (a) ATR FT-IR spectra of the dehydrated PVA cast gels during water exchange with drying. (b) Second-derivative spectra in the 3000 – 2800 cm$^{-1}$ region of PVA cast gels at $N = 0$, 3 and 5

the repeated processes. In order to estimate the size of micro-crystals with different *N*s, the average crystallite size, $D$, was calculated from the half-width of the diffraction peak using Scherrer's formula [4, 9]. As a result, $D$ did not change and kept constant around 2.5 nm. On the other hand, a broad peak below around $q = 1$ nm$^{-1}$, which was assigned to the distance between the micro-crystals, $L$ in the dehydrated gels [4], was observed after the repeated water exchange with drying. The peak intensity of $N = 0$ was much smaller than the others, and the peak-top position was in the range between $q = 0.58$ nm$^{-1}$ and 0.66 nm$^{-1}$, i.e., $L = 10.8$ nm and 9.6 nm. If it is possible to measure the XRD spectra of the swollen gels, L is expected to change with different Ns due to the elution of polymers and the formation of hydrogen bonds by the water exchange with drying. This is an important subject in the future investigations.

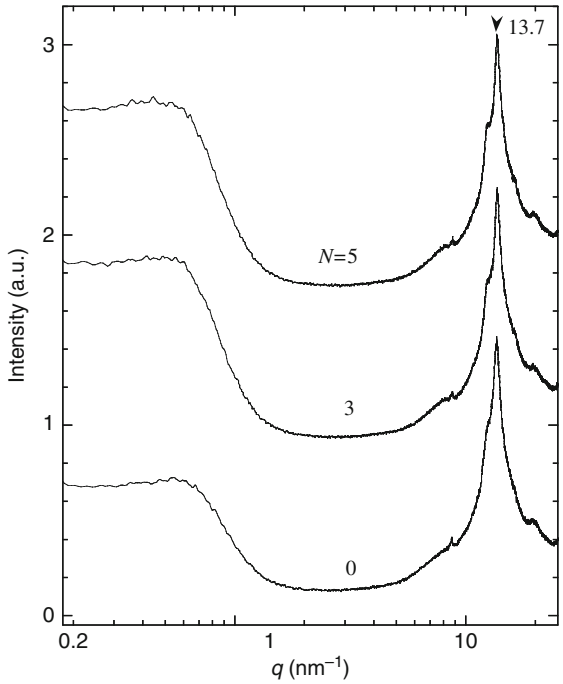


**Fig. 7** XRD spectra of the dehydrated PVA cast gels during water exchange with drying ($N = 0$, 3, and 5)

## Conclusion

We have studied the effects of water exchange with or without drying on the swelling properties of PVA cast gel prepared by a cast-drying method. In the case of the water exchange with drying, the swelling ratio decreased at first and became constant after several water exchanges. The decrement of the swelling ratio resulted mainly from the formation of additional hydrogen bonds. The ATR FT-IR spectrum changed during the water exchange with drying due to the elution of non-cross-linked polymers from the network and the formation of additional hydrogen bonds between -OH groups of PVA. The present results of IR and XRD spectra indicated that the repeated water exchange with drying might result in the formation of hydrogen bonds in the amorphous regions of the network without strongly disturbing the hydrogen bonds in the micro-crystal regions. From these results, we can conclude that the polymers were not eluted, and hydrogen bonds in the network structure of PVA cast gel were not formed after sufficient water exchange with drying.

## References

1. Hassan CM, Peppas NA (2000) Adv Polym Sci 153:37
2. An Y, Koyama T, Hanabusa K, Shirai H, Ikeda J, Yoneno H, Itoh T (1995) Polymer 36:2297
3. Praptowidodo VS (2005) J Mol Struct 739:207
4. Otsuka E, Suzuki A (2009) J Appl Poym Sci, 114:10
5. Kumar GNH, Rao JL, Gopal NO, Narasimhulu KV, Chakradhar RPS, Rajilu AV (2004) Polymer 45:5407
6. Takushi E, Asato L, Nakada T (1990) Nature 345:298
7. Masuike T, Taki S, Hara K, Kai S (1995) Jpn J Appl Phys 34:4997
8. Kanaya T, Takeshita H, Nishikoji Y, Ohkura M, Nishida K, Kaji K (1998) Supramol Sci 5:215
9. Miya M, Iwamoto R, Mima S (1984) Poly Phys Ed 22:1149
10. Mitsumata T, Hasegawa C, Kawada H, Kaneko T, Takimoto J (2008) React Funct Polym 68:133
11. Bhajantri RF, Ravindrachary V, Harisha A, Crasta V, Nayak SP, Poojary B (2006) Polymer 47:3591
12. Lee J, Lee KJ, Jang J (2008) Polym Test 27:360

Progr Colloid Polym Sci (2009) 136:127–134
DOI: 10.1007/2882_2009_18

# Influence of Heating Temperature on Cooking Curve of Rice

Kunio Nakamura, Atsuko Akutsu, Ayumi Otake, and Hatsue Moritaka

**Abstract** The swelling behavior of a rice grain in water and an aqueous NaCl and acetic acid solution was investigated as a function of temperature. We observed that the rice grain in water shows an abrupt change in shape and size at 61 °C. The transition temperature Tv became higher in an order: sodium chloride aqueous solution > water > acetic acid aqueous solution. In order to clarify Tv, we also investigated kinetics on cooking of rice grains by the rheological measurement. The time development of compliance of rice grains in compression (cooking curve) from 5 to 1440 min was measured in the range of cooking temperatures from 61 to 80°C. We found that Tv is the onset temperature to complete the cooking of rice. The cooking curve at the cooking temperature neighborhood Tv was approximated by the first order reaction with the two different rate constants. The faster and slower reactions were explained as indicating the plasticizing effect of water on rice grains, and mainly the gelatinization of the starch in rice grains, respectively.

**Keywords** Rice • Cooking curve • Rheology • Kinetics • Cooking temperature • Phase transition

## Introduction

The physicochemical properties of rice, especially the cooking mechanism of rice have been discussed extensively in Japan [1–3]. The cooking method of rice is only heating rice grains in water. It is well known that during usual cooking of rice, grains absorb water in the concentration range from ca.14 to 65% and undergo gelatinization of starch. Recently, Kasai et al [4] and Horigane et al [5–7] have reported the water content and its distribution in the cooking process of rice in a study of NMR imaging investigation. There are many studies on the relation between the water and the gelatinization of rice starch, and the swelling behavior of rice [8–11]. We have reported previously that the quality of cooked rice depended not only on a rice species but also on used water containing sodium or calcium ions [12]. There are recently many packages of rice cooked using various sauces. It is important to investigate the effects of the additives in water used for cooking rice. The objective of this study is to clarify the swelling behavior of rice on the mechanical properties of boiled rice grains.

K. Nakamura (✉)
Graduate School of Dairy Science
Rakuno Gakuen University
Ebetsu, Hokkaido 069-8501, Japan
e-mail: nakamura@rakuno.ac.jp

## Materials and Methods

### *Observation of swelling for a rice grain*

Rice used is a commercial polished rice of japonica rice, Akitakomachi. The broken and cracked grains were removed out of the sample rice, and the grains of similar size were collected as much as possible. Acetic acid and NaCl were purchased from Wako Industries Ltd Tokyo, Japan, and these were used without further purification.

One rice grain was put in a test tube ($\phi$10mm, H 60mm) with distilled water of 5ml and then put on a tight fitting lid. The profile of a rice grain was observed by the microscope (SMZ-2T, Nikon). The grain was soaked in the test tube for 1 hour at 40°C and heated in the glass jacket which was connected with the outlet of water bath (NCB-2200, EYELA, Japan) to 80°C at the increasing speed of 0.025°C /min. With increasing temperature, the shape of a rice grain changed as follows (Fig. 1). 1. Both shape and size did not change in the temperature range from 40 to 59°C (a). 2. The rice broke at the center of a grain at 60°C (b). 3. Both shape and size changed abruptly like flower blooming at 61°C (c). 4. The increase in size of rice extended to whole grain

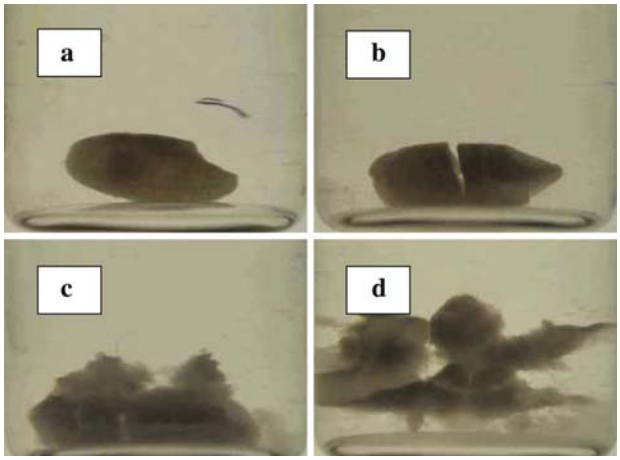


**Fig. 1** Photographs of a rice grain in water at different temperatures during heating. a: room temperature, b: 60°C, c: 61°C, d: 70°C

in the temperature range from 62 to 80°C (d). The observations were performed with 6 grains and the temperature of the abrupt change in shape and size as shown in (c) varied from 59 to 62°C. The obtained temperature as (c) expressed with the average of 6 grains was 61°C in distilled water. We defined 61°C as the transition temperature Tv. The same observation experiments were performed to the system of rice in sodium chloride solutions and acetic acid solutions.

### *Measurements of absorbed water and elastance of rice grains during cooking*

Six g (ca. 300 grains) of uncooked rice was put in a 50ml beaker. After the addition of 9g distilled water to the rice, a beaker was put on a tight fitting lid. The suspensions of uncooked rice in the beaker were kept at room temperature ca. 25°C for 1 hour, heated in the water bath (NCB-2200, EYELA, Japan) to a given temperature, and the beaker was taken out at time intervals of 5 to 1440 min, and then soaked in another water bath at 25°C for 5 min to prevent further reaction. Then, the mass of excess water in a 50 ml beaker was weighed using an electric balance (PB303-S, Mettler Toledo, USA) after separating water by decantation from the beaker. Absorbed water (%) in a rice was calculated by the next equation, $(W_R + W_S - W_{RS})/(W_R + W_S)100$, where $W_R$ is the mass of rice grains before heating, $W_S$ the mass of water, and $W_{RS}$ the mass of excess water which remains in a 50ml beaker.

After the measurement of absorbed water in rice grains, a grain taken from the center portion of a 50ml beaker was compressed between two disks at a cross head speed of 5 mm/min by a tensile tester (mini 55 type, Instron, USA) at the room temperature, as shown in Fig. 2. Apparent elastance,

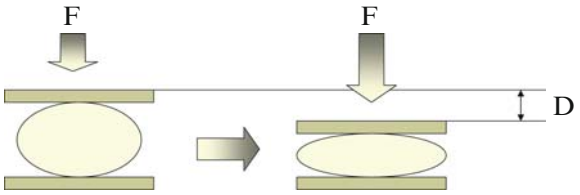


**Fig. 2** Schematic diagram of Load - Compression Test

G of rice grains were calculated from a load versus indentation curve using the equation based on Hertz's theory [13]:

$$F = G\,D^{3/2}$$

$$G = E\,(2R/1.13)^{1/2}(1-\mu^2)$$

where R is the radius of the rice grain, F is the load, D is indentation of the rice grain, μ is Poisson's ratio, and E is apparent elasticity. Compression measurements of 8 rice grains were carried out for each sample and the results were evaluated with the average of 8 measurements. The same experiments of absorbed water and elastance of rice grains during cooking were performed to a rice grain cooked with a 0.5 M sodium chloride solution and a 0.5 M acetic acid solution.

## Results and Discussions

### *Effect of additives on swelling of rice grain*

We observed a discontinuous change in shape at 61°C, gradually heating a raw rice grain under the existence of a large amount of water. This kind of the transition is also observed in various external solutions, that is, 1 M aqueous solution of halides, organic acids, and sugars in the preliminary experiment. The transition temperature Tv for salts became higher in the order:

$$\text{water} < \text{KCl} < \text{CsCl} < \text{LiCl} < \text{NaCl}$$

Tv for organic acids:

$$\begin{aligned}\text{Malonic acid} < \text{Tartaric acid} < \text{Acetic acid} < \text{Citrate}\\ < \text{Succinic acid} < \text{Malic acid} < \text{water}\end{aligned}$$

Tv for sugars:

$$\begin{aligned}\text{water} < \text{fructose} \sim \text{sorbitol} < \text{glucose} < \text{sucrose}\\ < \text{trehalose}\end{aligned}$$

The concentration dependence of Tv is shown in Fig. 3 for aqueous NaCl solution, aqueous acetic acid solution and sucrose solution. $T_v$ for acetic acid solution is lower than that for water. On the other hand, $T_v$'s for NaCl and sugar solution are higher than that for water. These tendencies increased with increasing concentration. Tv values of a 0.5 M sodium chloride solution and 0.5 M acetic acid solution used for measurements of absorbed water and elastance of rice grains during cooking were 68 and 55°C, respectively. These solvent effects on raw rice were parallel to the results reported in a study of gelatinization of starch [14, 15].

## *Absorbing curve of rice grains*

The cooking time dependence of the absorbed distilled water in a rice grain at various temperatures is shown in Fig. 4. Fig. 4 shows the progress of the cooking process of rice. A heating time 0 means 1 hour of soaking. At this time the rice grains did not contain a large amount of water. At the 400 min cooking time below 63°C, the quantity of the absorbed water inside the rice grains increased to 100%. In order to evaluate the absorbing rate, we define the time at which the absorbed water attains to 100% as the absorbing time $t_{ab}$. The absorbing time $t_{ab}$ at cooking temperatures 80, 70, and 65°C are 20, 70, 200 min, respectively. On the other hand, the absorbed water remains to ca. 80% within 1440 min at 61°C (Tv). Figs. 5 and 6 show the absorbing curves for the rice grain-0.5M acetic acid system and the rice grain-0.5M NaCl system, respectively. The $t_{ab}$ was observed for the 0.5M acetic acid solution at all measured cooking temperatures and for the 0.5M NaCl solution only at cooking temperatures 80°C and 70°C within 1440 min. But the $t_{ab}$ was

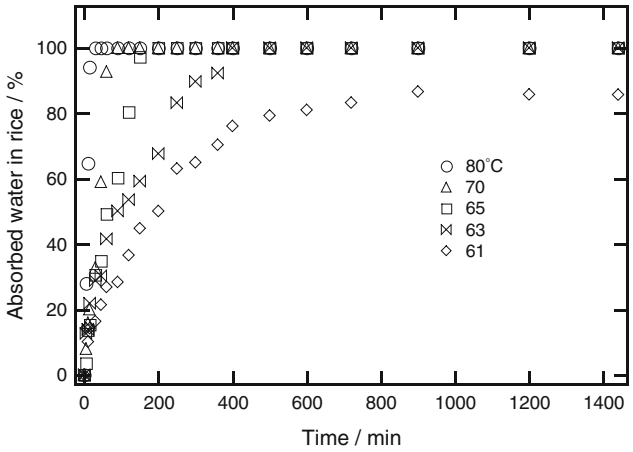


**Fig. 4** Absorbed water in a rice grain cooked with water plotted against time at various cooking temperatures

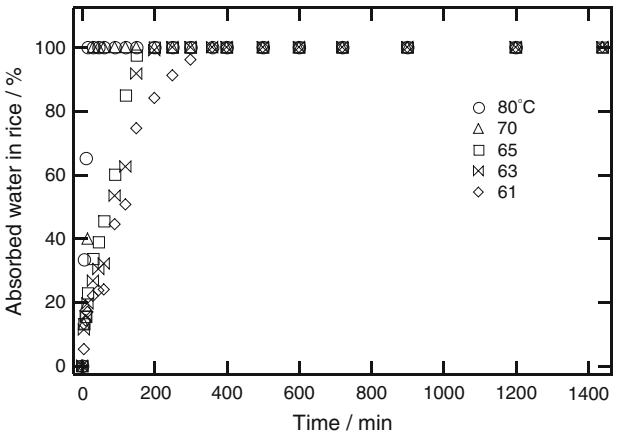


**Fig. 5** Absorbed water in a rice grain cooked with 0.5M acetic acid solutions plotted against time at various cooking temperatures

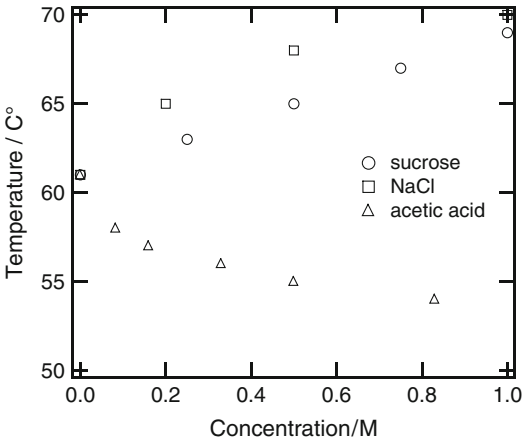


**Fig. 3** Concentration dependence of transition temperature of rice grain for aqueous NaCl, sucrose, and acetic acid solutions

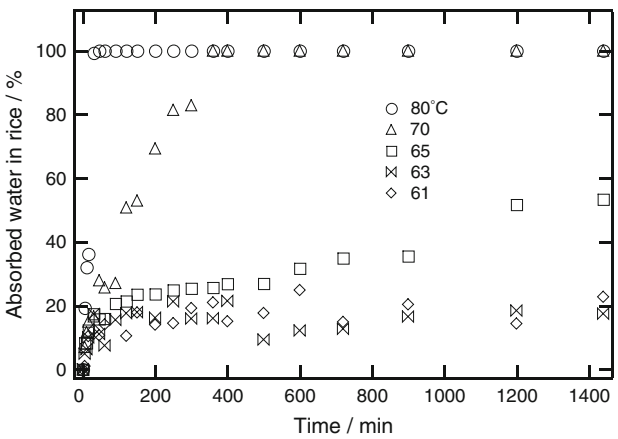


**Fig. 6** Absorbed water in a rice grain cooked with 0.5M NaCl solutions plotted against time at various cooking temperatures

not observed for the 0.5M NaCl solution at 65°C, 63°C and 61°C (<Tv). Fig. 7 illustrates how the $t_{ab}$ changes with increasing cooking temperature. While cooking temperature approaches Tv, the water absorption time increases rapidly. Such a tendency was clearly seen also in 0.5M acetic acid solution or 0.5M NaCl solution. The ratio of water to rice in this experiment was 1.5 (w/w)(=$W_S/W_R$), which is the standard value for Japonica rice. Accordingly, Tv could be used as the indication of the minimum temperature required for water absorption.

## Cooking curve of rice grains

The heating time dependence of compliance J for a rice grain in distilled water at various temperatures is shown in Fig. 8, where compliance J was defined as the reciprocal of elastance G. We call later the plot of compliance versus cooking time as cooking curve.

At the 61°C cooking temperature, J clearly began to increase with cooking time, and this tendency of the increase in J was not remarkable around 200 min. J on further cooking time again increased notably at the 300 min cooking time and then asymptotically approached a steady value. Although cooking curve was expressed by 2-step reaction at lower cooking temperatures, J at 80°C monotonously increased during cooking rice. Cooking curves shifted to shorter times with increase of cooking temperature, and simultaneously showed the change from 2-step reaction to 1-step reaction. The steady values of J at each cooking temperature were similar. Figs. 9 and 10 show the cooking curves for the rice grain-0.5M acetic acid and the rice grain-

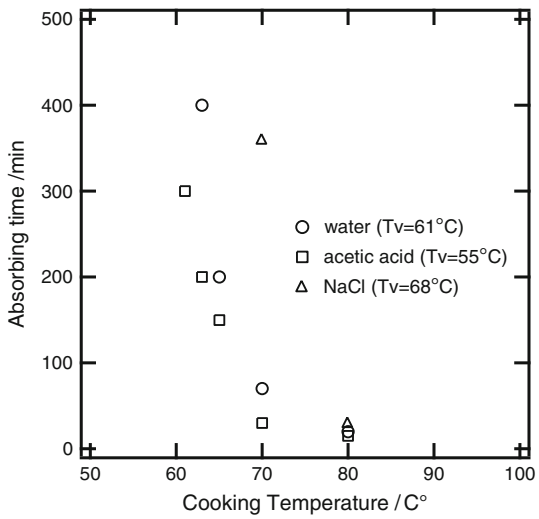


**Fig. 7** Absorbing time in rice grain with water, 0.5M acetic acid solutions, and 0.5M NaCl solutions plotted against cooking temperature

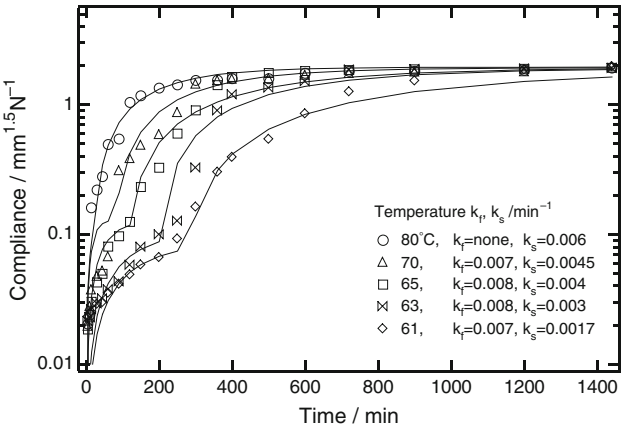


**Fig. 8** Compliance of a rice grain cooked with distilled water plotted against time at different cooking temperatures. The lines in figure denote the fitting curves by the equation 1

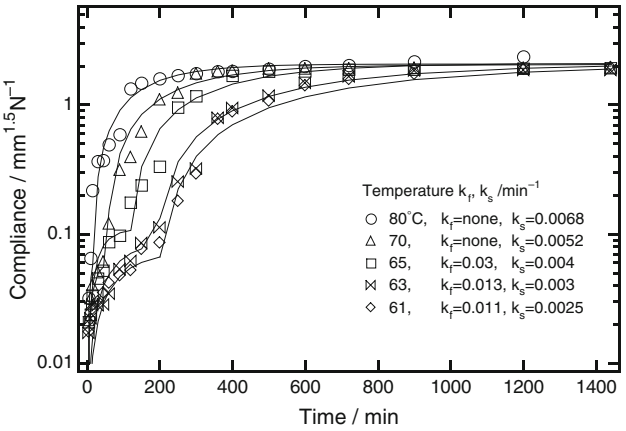


**Fig. 9** Compliance of a rice grain cooked with 0.5M acetic acid solutions plotted against time at different cooking temperatures. Lines in the figure denote the fitting curves by the equation 1

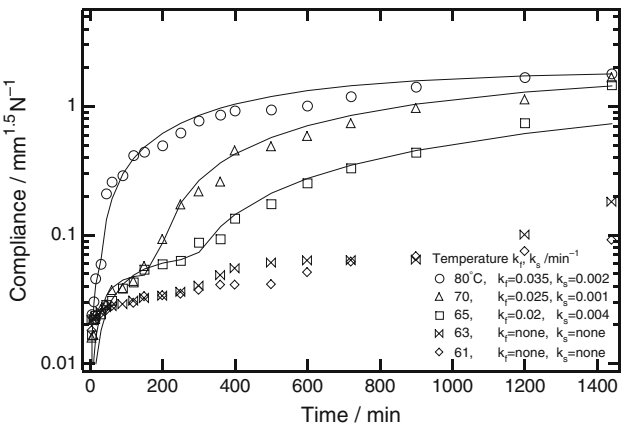


**Fig. 10** Compliance of a rice grain cooked with 0.5M NaCl solutions plotted against time at different cooking temperatures. Lines in the figure denote the fitting curves by the equation 1

0.5M NaCl solutions, respectively. The behaviors of cooking curves for a 0.5 M acetic acid solution were similar to those for water, except that the addition of acetic acid to water considerably increased cooking speed (Fig. 9). Fig. 10 shows the influence of the addition of NaCl to water on cooking curves. The behavior of cooking curve for a 0.5 M sodium chloride solution at the cooking temperature of 80°C or 70°C, which was higher than Tv of 68°C, was similar to those for water, and the steady value of J was ca. 2 $mm^{1.5}N^{-1}$. But, at the cooking temperature of 65°C, which was lower than Tv, J value reduced to 0.7 $mm^{1.5}N^{-1}$ at the 1440 min cooking time.

The relation between the cooking curve and the water absorption curve is now examined. The absorbed water (%) for a 0.5M NaCl solution is shown in Fig. 6. At the 65°C which was slightly lower than Tv, the absorbed water started to increase with the cooking time, and this tendency of the increase in the absorbed water was not obvious around 200 min. The absorbed water on further cooking time again increased considerably at 500 min, and then asymptotically approached 50 %. Although the inflection point at 500 min of the absorbed water was larger than that of J, as shown in Fig. 10, both curve of the absorbed water and J was described by a 2-step reaction. On the other hand, in comparison with the water absorption curve (Fig. 4) and a cooking curve (Fig. 8) for water at the cooking temperature of 61°C and 63°C, which was slightly higher than Tv, the cooking curve described by a 2-step reaction in the case of water, but the absorbed water showed the monotonous increase with the cooking time.

## Kinetics of cooking rice

The cooking curve of rice was approximated by the first order equation composed of two reactions with different rate constants, $k_f$ and $k_s$:

$$J = J_i + J_{f,0}\left(1 - \exp\left(-k_f t\right)\right) + J_{s,0}\left(1 - \exp\left(-k_s\left(t - t_{L,s}\right)\right)\right) \quad (1)$$

where $J_i$, $J_{f,0}$ represent J of the raw rice grain, and the steady value of J for a faster reaction component, respectively. $J_{s,0}$ and $t_{L,s}$ represent the steady value of J, and the latent time for the slower reaction component, respectively. t is the cooking time. The term of $J_i$ in the equation 1 was ignored, taking into account that $J_i$ of the raw rice grain is small enough compared with J.

The rate constants $k_f$ and $k_s$, the steady compliances $J_{f,0}$ and $J_{s,0}$, and the latent time $t_{L,s}$ were determined by the method of curve fitting based on the equation 1 to data of the measured cooking curve as shown in Figs. 8–10 using a personal computer. Fig. 11 shows the Arrhenius plot of the values of $k_f$ and $k_s$ for rice cooked using water, 0.5M acetic acid, and 0.5M NaCl. The activation energy $E_{af}$ of 1st (faster) reaction for water was 220 kJ/mol. The $E_{as}$ for 0.5M acetic acid was close to that for water, but the $E_{as}$ for 0.5M NaCl is remarkably lower than that for water. The $k_s$ data for water at Tv of 61°C deviated from the linear relation of the Arrhenius plot in the higher temperature. The activation energy $E_{a,s}$ of 2nd (slower) reaction for water was 43.2 kJ/mol. The $E_a$ for 0.5M acetic acid is slightly larger than that for water. The $E_{a,s}$ for 0.5M NaCl was not shown, because we have not enough $k_s$ points of cooking temperatures above Tv.

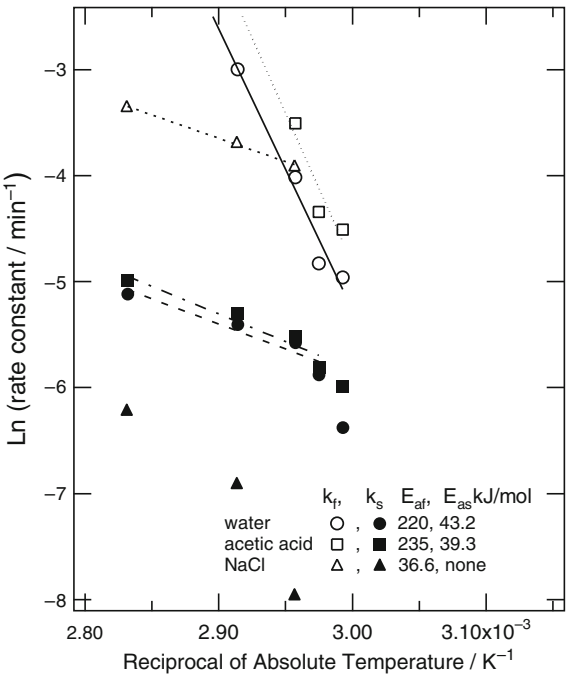


**Fig. 11** Rate constant $k_f$ and $k_s$ plotted against the reciprocal of absolute temperature for rice cooked with water, 0.5M acetic acid and 0.5M NaCl

We found that the cooking curve at the cooking temperature neighborhood of Tv was reduced to the first-order kinetic equation composed of two reactions with different rate constants. Tokita presented the equation,

$$G = G_\infty(1 - \exp\left(-k\left(t - t_L\right)\right)) \quad (2)$$

with respect to the time-dependent modulus in the gelation process using percolation theory [16]. Here, the reaction rate constant k was related to the reciprocal of latent time $t_L$. namely

$$k = A\left(1/t_L\right)^n, \; n = 1 \quad (3)$$

where A is a numerical constant. Assume that the cooking curve may relate the process of the transition from the raw

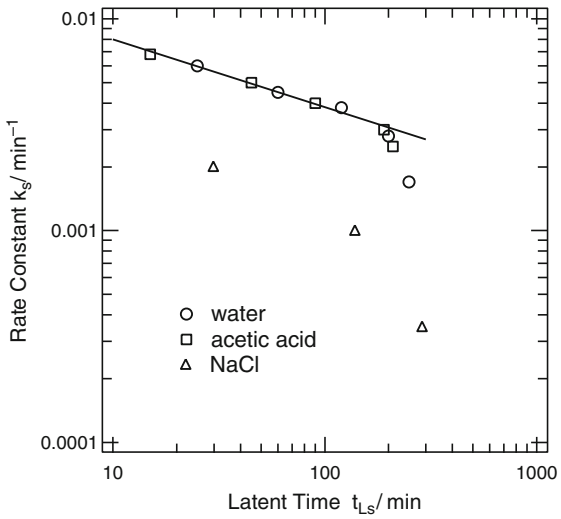


**Fig.12** Rate constant $k_s$ plotted against latent time $t_{Ls}$ at different cooking temperatures for rice cooked with water, 0.5M acetic acid and 0.5M NaCl

grains of rice in the glass state to the cooked rice in the gel state, the second term of the equation 1 with respect to compliance by analogy with the equation 2 can describe the cooking curve at the various cooking temperatures. In this process the water content increases from ca.15 to 65%. Fig. 12 shows the relation with the rate constant and the latent time of 2nd process. $K_s$ and $t_{Ls}$ data for water and 0.5M acetic acid were expressed by the equation 3 with the power law index as $n = 0.32$. Rate constants $k_f$ and $k_s$ for rice grains cooked with water at the 100°C cooking temperature were calculated from the Arrhenius equation as 24 $min^{-1}$ and 0.15 $min^{-1}$, respectively. The higher the cooking temperature, the smaller the ratio of $k_s/k_f$. Therefore, the cooking curve at higher cooking temperatures may be expressed by the 2nd term of equation 1. The latent time which was evaluated by equation 3 as $k_s$=0.15 $min^{-1}$ was 2 min (see Fig.12). The latent time at higher cooking temperatures is so short that the cooking curve was practically approximated by the first order equation without the latent time. Suzuki et al have already reported that the cooking rate in the temperature range 75 to 150°C followed the equation of a first order chemical reaction [17].

## Relationship between Tv and cooking temperature

It is of interest that we compare the cooking temperature with the transition temperature. $J_{s,0}$ value for the rice cooked with water at the cooking temperature, as a transition temperature Tv was1.8 $mm^{1.5}N^{-1}$. This value was not different from $J_{s,0}$ values of the rice cooked at a temperature higher than Tv (Fig. 8). The 2nd reaction was not observed in the cooking curve (Fig. 10) cooked with a 0.5M NaCl solution at cooking temperatures, 61 and 63°C which are sufficiently lower than Tv of 68°C and the $J_{f,0}$ value of the1st reaction remained below 0.1 $mm^{1.5}N^{-1}$ over the measured cooking time. At the same time the absorbed water (Fig. 6) was kept around 20%. At the 65°C cooking, the absorbed water increases to 25% over 300 min and at the same time 2nd reaction begins gradually to start, where $J_{s,0}$ value was 1.6 $mm^{1.5}N^{-1}$. On the other hand, the $J_{s,0}$ value obtained from the cooking curve during 70 and 80°C cooking was 2 $mm^{1.5}N^{-1}$. The depression of $J_{s,0}$ at the 65°C cooking may reflect the existence of the uncooked portion in the rice grain. All $J_{s,0}$ values obtained from the cooking curves for a rice-0.5M acetic acid system (Fig. 9) at 61, 63, 70, and 80°C (>Tv) were 2 $mm^{1.5}N^{-1}$. Consequently, Tv was considered to be the minimum temperature required to the transition temperature required to complete cooking rice. In this cooking rice experiment, two reaction mechanisms exist near the transition temperature. Water absorption of rice grains arises as the 1st reaction below the transition temperature. Rice grains began to absorb slightly water, resulting in softening from glass-like to gel-like. This process can be interpreted as the plasticizing effect in a glass state macromolecule [18,19]. That is, the glass transition temperature decreased by the increase of the additional free volume by addition of water. The second reaction was mainly dominated by the reaction of gelatinization.

## Effect of acetic acid and sodium chloride on cooking curve

The reactions of rice cooking are known to be the absorption of water into the rice and the gelatinization of the starch. These reactions were performed only by adding water and heat to rice. In order to investigate the cooking conditions for rice [20, 21], there have been many reports on water content of rice and the gelatinization during cooking. The acetic acid causes to decrease the gelatinization temperature of starch [22]. As hydrogen bonds between starch and water molecules are replaced by bonds between the starch and acetic acid molecule, hydrophobic side chain is introduced to starch, resulting in the decrease of the hydrophobic interaction between starches and the decrease in the gelatinization temperature. Acetic acid causes the increase of cooking speed, indicating the depression of Tv. The increase in the gelatinization temperature by NaCl may be attributed to the effect of the so-called salting out, indicating that the aqueous NaCl solution acts as the poor solvent to starch. NaCl causes abruptly the decrease of cooking speed in the1st reaction (Fig. 11). The cooking rate of the1st reaction was limited by the rate of diffusion of water toward the interface of

uncooked portion where the gelatinization occurs. The permeation of water to rice grains is prevented and the gelatinization is inhibited under the presence of sodium ions [12].

## Conclusion

Finally, we observed change in a discontinuous shape at 61°C, gradually heating a raw rice grain under the existence of the large amount of water. This kind of the transition is also observed in various external solutions. The transition temperature is considered to be the minimum temperature required to complete cooking rice. In the cooking rice experiment, two reaction mechanisms exist near the transition temperature. Water absorption of rice grains arises as the 1st reaction below the transition temperature. Rice grains begin to absorb slightly water, resulting in softening from glass-like to gel-like rice. The second reaction was mainly dominated by the reaction of gelatinization.

## References


1. Matsuo M, Takaya T, Miwa A, Moritaka H, Nishinari K (2002) Nihon Soshaku Gakukaishi 12:11
2. Moritaka H, Hasegawa M, Imai Y (2005) J Cookery Sci Jpn 38:30
3. Okadome H, Toyoshima H, Sudo M, Ando I, Numaguchi K, Ohtsubo K (1998) Nippon Shokuhin Kagaku Kogaku Kaishi 45:398
4. Kasai M, Lewis A, Marica F, Ayabe S, Hatae K, Fyfe CA (2005) Food Research Int 38:403
5. Horigane AK, Toyoshima H, Hemmi H, Engelaar WMHG, Okubo A, Nagata T (1999) J Food Science 64:1
6. Horigane AK, Engelaar WMHG, Maruyama S, Yoshida M, Okubo A, Nagata T (2001) J Cereal Science 33:105
7. Horigane AK, Takahashi H, Maruyama S, Ohtsubo K, Yoshida M (2006) J Cereal Science 44:307
8. Lelievre J (1976) Polymer 17:854
9. Donovan JW (1979) Biopolymer 18:263
10. Biliaderis CG, Page CM, Maurice TJ, Juliano BO (1986) J Agr Food Chem 34:6
11. Slade L, Levine H (1988) Carbohydr Polym 8:183
12. Moritaka H, Nakamura K (2005) J Soc Rheology Jpn 33:75
13. Shpolyanskaya AL (1952) Colloid Journal (USSR) 14:137
14. Kohyama K, Nishinari K (1991) J Agr Food chem 39:1406
15. Oosten BJ (1982) Starch/Stärke, 34:233
16. Tokita M (1989) Food Hydrocolloids 3:263
17. Suzuki U, Kubota K, Omichi M, Hosaka H (1976) J Food Sci 41:1180
18. Fujita H, Kishimoto A (1958) J Polym Sci A-2 28:547
19. Nakamura K, Nakagawa T (1975) J Polym Sci Polym Phys Ed, 13:2299
20. Honma N, Sato E, Shibuya U, Ishihara K (1983) J Home Economics Japan 34:698
21. Kohyama K, Yamaguchi M, Kobori C, Nakayama Y, Hayakawa F, Sasaki T (2005) Biosci Biotechnol Biochem 69:1669
22. Ohishia K, Kasai M, Shimada A, Hatae K (2007) Food Research International 40:224

Progr Colloid Polym Sci (2009) 136:135–142
DOI: 10.1007/2882_2009_19

# Effects of Thickness and Curvature on the Adhesion Properties of Cylindrical Soft Materials by a Point Contact Method

D. Sakasegawa, M. Goto, and A. Suzuki

**Abstract** The effects of the sample thickness, $h$, and the curvature, $R$, on the adhesion properties between two viscoelastic materials were investigated with the use of a point contact method. Poly (sodium acrylate) (PSA) hydrogels and cross-linked polydimethylsiloxane (PDMS) were used in this study, where $h$ and $R$ were independently changed. The $W$ (normal load)-dependences of the apparent contact area, $S_0$, and the displacement of the bulk deformation, $\Delta h$, were measured simultaneously by a point contact in a crossed-cylinder geometry. With decreasing $h/R$, the slope of $\Delta h$ vs. $W$ was found to decrease and to deviate largely from the prediction of the Hertz contact ($= 2/3$). An equation between $S_0$ and $\Delta h$ in the range of $2 < W < 100$gf was obtained, by which $S_0$ can be empirically estimated using the obtained $\Delta h$ if $h$ and $R$ are given. The effects of $h/R$ on the separation energy, $E_A$, were discussed on the basis of the changes in the density of molecular-to-molecular contacts between polymer chains at the surface and in the degree of deformation of the bulk.

**Keywords** Point contact • Thickness • Curvature • Contact area

## Introduction

Recently, we developed a new technique for measuring the adhesion properties between two cylindrical soft materials by a point contact in a crossed-cylinder geometry [1]. This technique is simple and reproducible under a wide variety of experimental conditions to explore the adhesion of soft materials, especially thick materials; it was found that the easiness to separate (rank of adhesion force and the separation energy) of seven anti-inflammatory analgesic cataplasms on the market by the use of this apparatus was consistent with the results of those obtained by organoleptic evaluations [1]. The adhesion properties of swollen poly (sodium acrylate) hydrogels physically cross-linked by aluminum ions were evaluated by this point-contact method; the adhesion force, $F_A$, increased with increasing the experimental conditions (the normal load, $W$, the waiting period, $t_W$, and the separation velocity, $v$) and obeyed the power laws. In the point contact method, the stress at the center of the circle is the largest in the contact area and decreases along the radius direction to the edge. Therefore, the contact surface separates from the edge of the circle and the contact area decreases continuously during the separation. These characteristics result in the above unique properties of the present system. In order to qualitatively compare $F_A$ and the separation energy, $E_A$, of different kinds of viscoelastic materials, it is very important to evaluate the apparent contact area, $S_0$ since $S_0$ depends strongly on the materials constant, e.g., the density of network and the degrees of cross-linker.

As for the evaluation of adhesion properties of the viscoelastic materials by the point contact, many studies have been reported on the basis of the Hertz contact theory [2–13]. For example, Johnson, Kendal and Roberts modified the Hertz contact theory by taking into account the effects of the surface energy on the contact surface [3], and Archard studied the effects of the asperities on the surface force [4]. In order to estimate $S_0$, Shull et al. empirically obtained the equation between the radius of the contact circle, $a_0$, and the displacement of the bulk deformation, $\Delta h$, in the point contact between the rigid hemisphere and the elastic plate with a thickness of $h$ [5]. However, the study on a crossed-cylinder geometry between two cylindrical viscoelastic materials has not been extensively studied so far. In this paper, the effects of the sample shape (the sample thickness, $h$, and the radius of curvature, $R$) on the adhesion properties in a point contact by a crossed-cylinder geometry between viscoelastic materials

D. Sakasegawa (✉)
Graduate School of Environment and Information Sciences
Yokohama National University, NIPRO PATCH Co., Ltd.
Yokohama, 240–8501, Japan
e-mail: d07tb002@ynu.ac.jp

have been investigated in detail and an empirical equation to estimate $S_0$ has been obtained. Moreover, the effects of $h/R$ on the adhesion properties were examined in detail.

## Experimental

### *Sample preparation*

The viscoelastic materials used here were poly (sodium acrylate) (PSA) hydrogels physically cross-linked by aluminum ions and cross-linked polydimethylsiloxane (PDMS), which were prepared by the following methods.

The pregel solution was obtained by mixing PSA aqueous solution (for the main constituent, Wako Pure Chemical Industries; 18.1wt% aqueous solution; average degree of polymerization ranging from 2,700 to 7,500) with aluminum hydroxide $Al(OH)_3$ (for the cross-linker, Kyowa Chemical Industry) under an acidic condition, and 3wt% of $Al(OH)_3$ for PSA solution was added into the solution and mixed completely. The pregel solution was poured into a space between a cylindrical glass stick and a cylindrical glass tube, which were both centered, and it was left at room temperature for 7 days. The radius of curvature, $R$, and the thickness, $h$, were changed by changing the glass diameters; the outer radius of glass stick was ($R$ - $h$), and the inner radius of glass tube was $R$. After the gelation, the hydrogel with $R$ mm-curvature and $h$ mm-thickness clamped on the glass stick was obtained (Fig. 1(a)), which was designated here as PSA (4, 8) in the case of $h = 4$mm and $R = 8$mm.

In order to prepare the cross-linked polydimethylsiloxane (PDMS), SILPOT 184 (Dow Corning) and CATALYST SILPOT (curing agent, Dow Corning) were used without further purification; SILPOT 184 was mixed with the curing agent of 3wt% or 5wt% to SILPOT 184 and stirred for 30 minutes. The mixture was poured into the same mold of cylindrical glass stick and tube (by the similar method used in the preparation of PSA gel, see above), and it was left at 50 °C for 24 hours. Thus, two types of cross-linked PDMS with $R$ and $h$ clamped on the glass stick were obtained, which was designated here as PDMS3 ($h$, $R$) or PDMS5 ($h$, $R$), e.g., PDMS3 (4, 8) denotes the cross-linked PDMS of 3wt%-curing agent with $h = 4$mm and $R = 8$mm.

### *Measurement of the separation energy*

The process of a point contact and separation between two cylindrical samples are schematically illustrated in Fig. 1(a). Two glass sticks with the PSA gel or the cross-linked PDMS

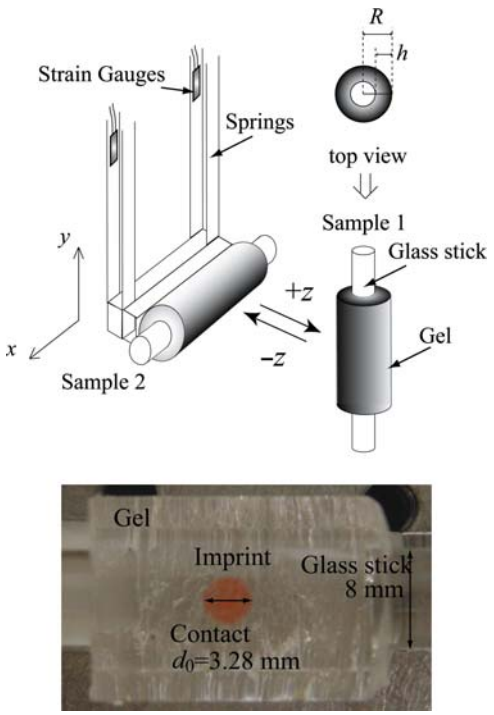


**Fig. 1** (a) Schematic illustration of an experimental set-up. Two samples were placed in crossed cylinder geometry, where the contact area was circular. One of the samples (Sample 1) was fixed to the position-controlled stage by the stepping motor and moved to the $\pm z$-direction. The other sample (Sample 2) was fixed to the spring with four strain gauges. Adhesion force, $F$, was measured in air at room temperature. In the stamp experiment, vermilion was put on the surface of Sample 1. (b) An example of a surface photograph of sample 2 (PDMS3 (4, 8)) with a circular imprint. The diameter of the contact circle, $d_0$, was measured

were placed in a crossed-cylinder geometry, where the contact area was circular. One of the sticks (Sample 1) was fixed to the position-controlled stage by the stepping motor and moved to the $\pm z$-directions. The other stick (Sample 2) was fixed to the spring, which consisted of four phosphor-bronze thin springs with dimensions of $0.3\times5\times50$mm$^3$, with four strain gauges (Kyowa Electronic Instruments, KFG-2-120-C1-16 L1M2R). The spring constant, $k$, used here was 108gf/mm. Four active gauges were used to maintain the accuracy of the measurements. Sample 1 was moved to the -$z$-direction with a constant advancing velocity, $v_0$, and contacted Sample 2. After the position-controlled stage stopped (at the appropriate position, $z_0$, from the initial contact position) and was maintained for the waiting period, $t_w$, Sample 1 was moved to the $+z$-direction with a constant receding velocity, $v$, and separated from Sample 2. The present measurements were conducted in air at room temperature. The force, $F$, was calculated using the strain of the spring and $k$. Here, $W$ and $E_A$ were defined as the normal load and the separation energy. The measurement conditions were $v = v_0 = 1$mm/s, $t_w = 60$s (constant), and $W$ was changed.

The deformation by a contact along the $z$-direction, $\Delta h$, was calculated as follows; since $z_0$ is the sum of $\Delta h$ and the displacement of the spring after standing for $t_w = 60$s at the position, $z_0$, $\Delta h$ was calculated by subtracting the displacement of the spring estimated by the strain from $z_0$.

### *Estimation of the apparent contact area by a stamp experiment*

The stamp experiment was conducted as follows. Vermilion ink (made of vegetable oil, synthetic resin, and pigment) was put on the surface of Sample 1 before contact. Sample 1 was moved a constant distance $z_0$ to $-z$-direction with 1mm/s. After 60s, it was moved to $+z$-direction with 1mm/s. As is shown in Fig. 1(b), the circular imprint was obtained on the surface of Sample 2. We measured the diameter of the circle, and determined the apparent contact area, $S_0$. This experiment should be conducted separately from the $E_A$-measurement; the stamp experiment could not be conducted using the same sample after the $E_A$-measurement since the surface after the separation was damaged. The $E_A$-measurement vice versa since the vermilion ink could not be removed completely.

## Results and Discussions

### *Relation between $S_0$ and $\pi R\Delta h$*

Figure 2(a) shows the $W$-dependences of $S_0$ and $\Delta h$ for the PSA gels ($h = 4, 6, 7$, $R = 8$). Both $S_0$ and $\Delta h$ were found to increase by power laws with increasing $W$ (> ca. 2gf). Both slopes of the PSA gel with the same $h$ were almost same, which increased with increasing $h$.

Fig. 2(b) shows the $W$-dependences of $S_0/\pi R\Delta h$ calculated from the data in Fig. 2(a). The absolute values of $S_0/(\pi R\Delta h)$ were almost constant ($= \alpha$) for $W >$ ca. 2gf, therefore $S_0$ is expressed as follows;

$$S_0 = \alpha(\pi R\Delta h), \tag{1}$$

where the constant $\alpha$ decreased with increasing $h$. In the case of a small $W$ (< 2gf), $S_0/\pi R\Delta h$ was apparently larger than $\alpha$ because of the attractive force on the contact area along the normal direction to the surface; even if $\Delta h$ would decrease to zero by decreasing $W$, the attractive force should result in a finite $S_0$. It should be noteworthy that $S_0$ and $\Delta h$ obtained

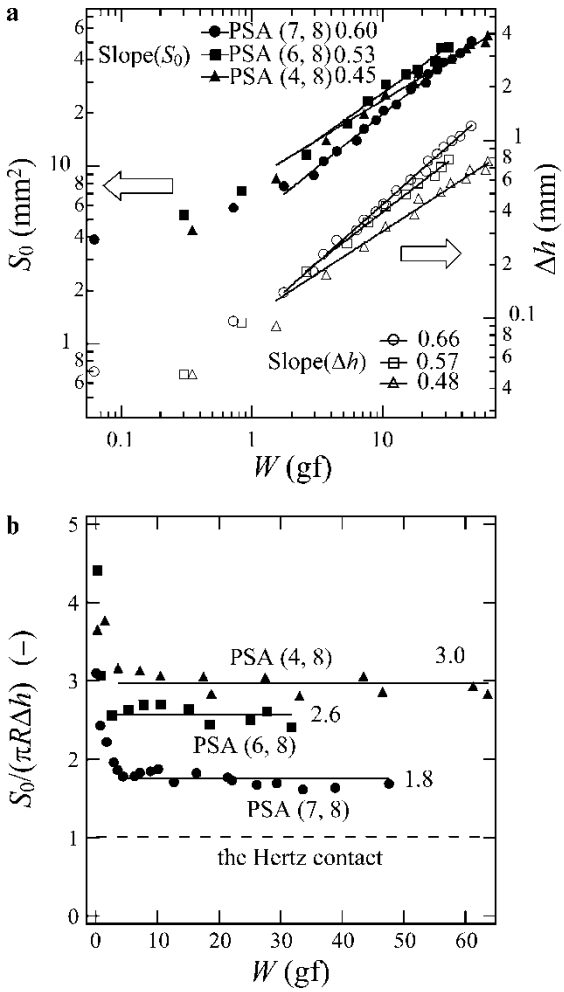


**Fig. 2** $W$-dependences of $S_0$ and $\Delta h$ (a), and $S_0/(\pi R\Delta h)$ (b) of PSA (7, 8) (●, ○), PSA (6, 8) (■, □), PSA (4, 8) (▲, Δ). (a) The closed and open symbols denote $S_0$ and $\Delta h$, respectively. The solid lines were obtained by the least-square method. The values of Slope($S_0$) and Slope($\Delta h$) in the figure denote the powers obtained from $W$-$S_0$ plot and $W$-$\Delta h$ plots in the respective sample. (b) Solid line and the number denote the average of the respective $S_0/(\pi R\Delta h)$ (when $W >$ ca. 2gf)

here for all samples of PSA and PDMS satisfied this equation for $W >$ ca. 2gf, and $\alpha$ was larger than 1 that depended on $h$ and $R$. This observation indicates that $S_0$ can be estimated if a set of $h$ and $R$ is given.

According to the Hertz contact theory, i.e., a contact model between two bodies filled with uniform isotropic linearly elastic media, the relation between $S_0$ and $\Delta h$ can be written as $S_0 = \pi R\Delta h$ [2], which corresponds to eq. (1) in the case of $\alpha = 1$. Therefore, $\alpha = 1$ for the Hertz theory is the minimum limit for the point contact by the crossed-cylinder geometry. From these results, the deviation from the Hertz theory depends strongly and uniquely on the sample dimensions, i.e., $h$ and $R$.

## h, R and h/R-dependences of α and the estimation of $S_0$

Figure 3(a) shows the $h$- and $R$-dependences of α, where all data of PSA, PDMS3, and PDMS5 were plotted. As for the $h$-dependence, three different $R$s were tested. For a technical reason, $h$ could not be kept constant for the $R$-dependence; the multiple points of the same symbol at the same horizontal axis, $h$ (or $R$) in Fig. 3(a) indicate the different $h$ (or $R$) values. Although α tended to decrease with increasing $R$ in this figure, the scattering in the data points seems large, because α depends on $h$ and $R$ independently. In Fig 3(b), α is plotted against $h/R$ for selected samples, which have $R = 4$, 6.25, or 8. It can be seen that α decreases linearly with increasing $h/R$; the relation between α and $h/R$ is expressed by the following master line for all samples used here,

$$\alpha = a(\mathrm{h}/R) + b. \tag{2}$$

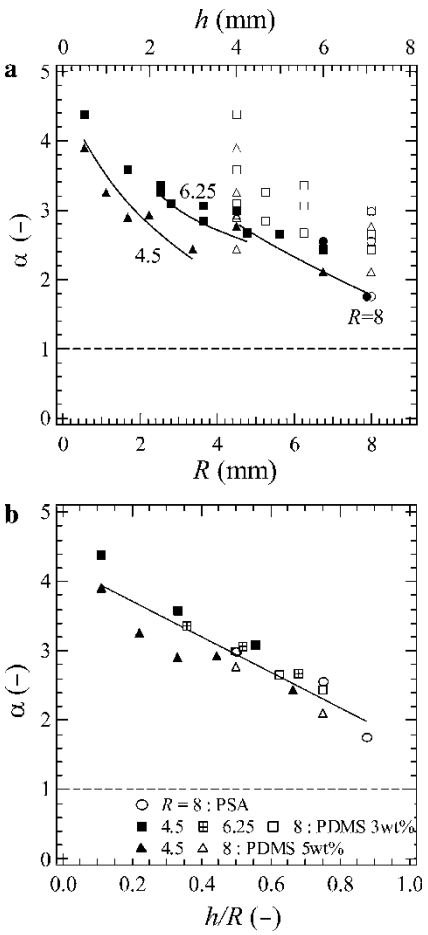


**Fig. 3** (a) $h$ and $R$-dependences of α of PSA (●, ○), PDMS3 (■, □), and PDMS5 (▲, Δ). The closed symbols were $h$-dependence and the open symbols were $R$-dependence. (b) $h/R$-dependence of α of PSA, PDMS3, and PDMS5. The respective broken line at $\alpha = 1$ indicates the prediction of the Hertz theory. The solid line in (b) was obtained by the least-square method

In the present experiments, $a = -2.6$ and $b = 4.2$, which was obtained from Fig. 3(b) by the least-square method. This observation indicates that eq. (2) is applicable to the samples with different kinds of polymers and different degrees of cross-linker. In other words, α is determined by $h/R$, and not by the network properties of materials, such as molecular interactions and the bulk stiffness. Form the eqs. (1) and (2), $S_0$ can be rewritten as follows,

$$S_0 = \pi \Delta h(ah + bR). \tag{3}$$

Using this empirical equation, we can estimate $S_0$ from the measurement of $\Delta h$ when $h$ and $R$ are given.

Figure 4 shows the examples of the relationships between $S_0/R$ and $\Delta h$ of the samples (with $R = 5.25$, 6, and 10.5), which were not used in the estimation of α in Fig. 3(a). The data points obtained by the experiments agree with the estimated ones by substituting $\Delta h$ into eq. (3) in spite of the different kinds of samples. These results confirmed the validity of the method to estimate $S_0$ of a point contact in a crossed-cylinder geometry; eq. (3) is useful to simply estimate $S_0$ for the present samples with a given set of $h$ and $R$ using the measured $\Delta h$.

## h, R and h/R-dependences of slope(Δh)

Figure 5(a) shows the $h$- and $R$-dependences of slope($\Delta h$), where all data of PSA, PDMS3, and PDMS5 were plotted. In this figure, slope($\Delta h$) tended to increase with increasing $h$ (or $R$). As discussed in the above section, the scattering seems large, because α depends on $h$ and $R$ independently. In Fig. 5(b),

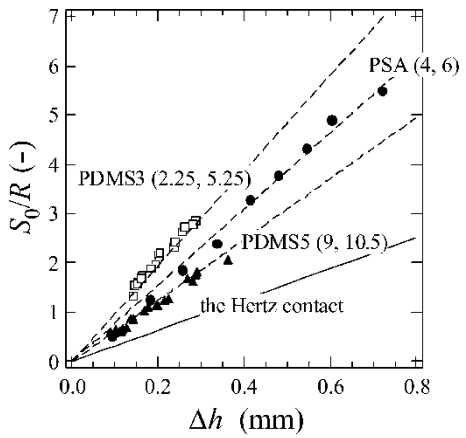


**Fig. 4** The relationships between $S_0/R$ and $\Delta h$ obtained by the experiments (PSA, PDMS3 (4, 8) and PDMS5 (1, 4.5)) (symbols) and those of the estimation by substituting $\Delta h$ into eq. (3) (broken lines). The solid line indicates the prediction by the Hertz contact theory

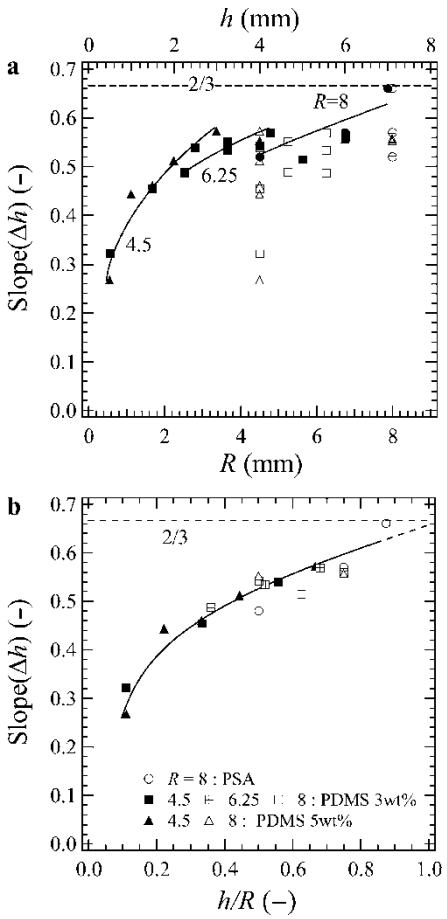


**Fig. 5** (a) $h$ and $R$-dependences of slope($\Delta h$) of PSA (●, ○), PDMS3 (■, □), and PDMS5 (▲, Δ). The closed symbols were $h$-dependence and the open symbols were $R$-dependence. (b) $h/R$-dependence of slope ($\Delta h$) of PSA, PDMS3, and PDMS5. The respective broken line at slope ($\Delta h$)=2/3 indicates the prediction of the Hertz theory (eq. (4))

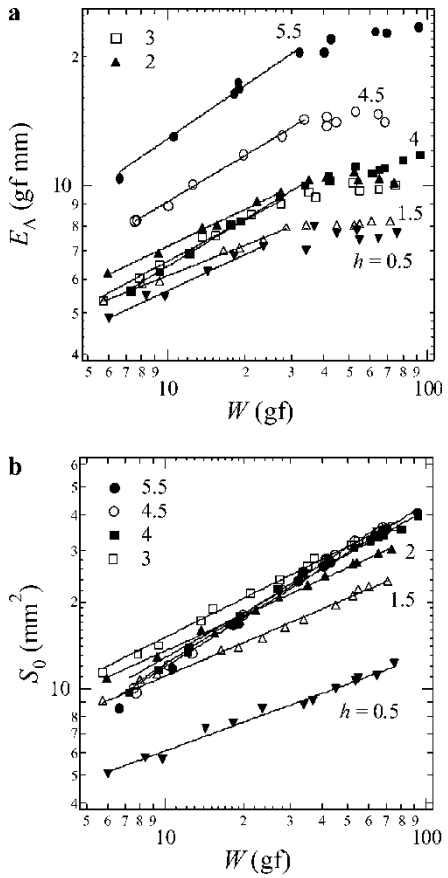


**Fig. 6** $W$-dependences of (a) $E_A$ and (b) $S_0$ of PDMS3; PDMS3 (5.5, 8) (●), PDMS3 (4.5, 8) (○), PDMS3 (4, 8) (■), PDMS3 (3, 8) (□), PDMS3 (2, 8) (▲), PDMS3 (1.5, 8) (Δ) and PDMS3 (0.5, 8) (▼). $S_0$ was calculated from $\Delta h$, which was measured simultaneously, using eq. (3).The respective solid line was obtained by the least-square method

slope($\Delta h$) is plotted against $h/R$, which indicates that, slope ($\Delta h$) follows a master curve with increasing $h/R$. According to the Hertz theory, the slope of $\Delta h$ vs. $W$ in the log-log scale is 2/3;

$$\Delta h \propto W^{2/3}. \tag{4}$$

As is shown in this figure, slope($\Delta h$) seems to approach 2/3 with increasing $h/R$. The observation indicates that the slope($\Delta h$) would approach 2/3 when the effect of the substrate on the deformation of the bulk becomes negligibly small. According to the literature [14, 15], the slope($\Delta h$) deviates from 2/3 due to the effects of the lateral extension and to the non-linear Young's modulus on the bulk deformation when the elastic sphere is largely deformed. If $h/R$ is relatively small and/or $W$ is relatively large in the present experiment, the slope($\Delta h$) should deviate from 2/3. In other words, the slope($\Delta h$) might approach 2/3 for all samples when $W$ is negligibly small when $h/R$ is not extremely small. Therefore, the approach to 2/3 of the slope($\Delta h$) with increasing $h/R$ to 1 in the present experiment (Fig. 5(b)) should result from the experimental conditions used here; $R$ (= 4.5, 6.25, and 8mm) was relatively large and $W$ (in the range of 2gf < $W$ < 100gf) was relatively small.

## Effects of h on the separation energy

Fig. 6(a) shows the $W$-dependences of $E_A$ of PDMS3 ($h$ = 0.5, 1.5, 2, 3, 4, 4.5, 5.5) samples with a constant $R$ = 8. With increasing $W$, $E_A$ increased by power laws in the range of $W$ < 30gf, while it exhibited a slight increase in the range of $W$ > 30gf. The overall value of $E_A$ tended to increase with increasing $h$. In order to understand the unique $W$-dependence of $E_A$, $S_0$ was calculated by eq. (3) with the use of $\Delta h$, which was measured simultaneously at the measurement of $E_A$.

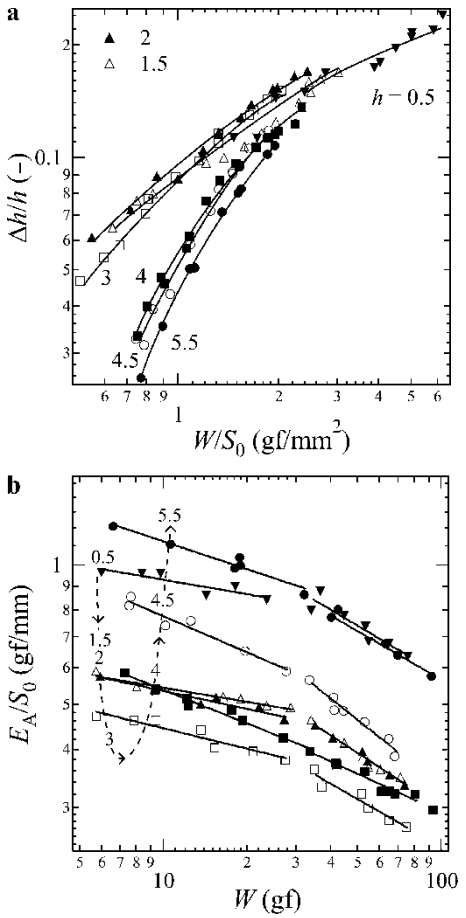


**Fig. 7** (a) $W/S_0$-dependences of $\Delta h/h$ and (b) $W$-dependences of $E_A/S_0$ of PDMS3; PDMS3 (5.5, 8) (●), PDMS3 (4.5, 8) (○), PDMS3 (4, 8) (■), PDMS3 (3, 8) (□), PDMS3 (2, 8) (▲), PDMS3 (1.5, 8) (Δ) and PDMS3 (0.5, 8) (▼). The respective solid line was obtained by the least-square method

As a result (Fig. 6(b)), $S_0$ increased by power laws with increasing $W$ in the whole range used here and its slope gradually increased with increasing $h$. The absolute value of $S_0$ increased ($h \leq 3$) and decreased ($h \geq 4$) with increasing $h$ in the range of $W < 30$gf, while it increased and became almost constant in the range of $W > 30$gf. On the other hand, the absolute value of $\Delta h$ increased with increasing $h$ in the whole range of $W$. This difference between $\Delta h$ and $S_0$ could be attributed to the fact that $\alpha$ decreased with increasing $h$ in eq. (2); $S_0$ at the same $\Delta h$ decreased with increasing $h$ since the deformation occurred not only in the vicinity of the contact surface but also in the bulk far from the surface due to the decrement of the restriction by the substrate to deform. From these results, we can summarize the unique $W$-dependence of $E_A$ in the range of $W > 30$gf as follows; the number of the molecular-to-molecular contacts, which dominantly determined $E_A$, increased with increasing $W$ below 30gf and saturated above 30gf. The slight increase of $E_A$ above 30gf could be attributed to the increment of the bulk deformation with increasing $W$.

In order to understand the $h$-dependence of $E_A$, $\Delta h/h$ was plotted against $W/S_0$ in Fig. 7(a). The values of $\Delta h/h$ and $W/S_0$ indicate the contraction ratio at the center of the contact area and the average stress at the contact area, respectively. In this figure, $\Delta h/h$ becomes smaller at the same $W/S_0$ with increasing $h$; the stiffness of the bulk just before the measurement of separation (i.e, after standing for $t_W$) decreased with increasing $h$, and the large difference to the absolute values of $\Delta h/h$ was seen between $h = 3$ and 4. These observations indicate that the energy to recover the deformation of the bulk with $h \leq 3$ by the measurement of separation is relatively smaller than that of the bulk with $h \geq 4$, which affects the value of $E_A$. In order to take into account the effects of the bulk deformation at the separation, $E_A$ was normalized by the calculated $S_0$, which is shown in Fig. 7(b). With increasing $W$, $E_A/S_0$ decreased, and each curve consisted of two power laws below and above 30gf. With increasing $h$, the overall value of $E_A/S_0$ decreased ($h \leq 3$) and increased ($h \geq 4$). Furthermore, the slope($E_A/S_0$) in the range of $W < 30$gf changed between $h = 3$ and 4, while it remained almost constant in the range of $W > 30$gf. These observations indicate that there is a specific value of $h$ between $h = 3$ and 4 for $R = 8$, where the minimum separation energy to remove in a unit apparent contact area should exist. With increasing $h$ under the same $R$, the increment of the number of the molecular-to-molecular contacts in polymer chains in a unit apparent area should be dominant due to the increase of $S_0$ in the range of $h \leq 3$. On the other hand, the increment of the deformation of bulk during the separation process could be dominant in the range of $h \geq 4$. In other words, with increasing $h$ and $W$, $E_A/S_0$ decreases due to the increment of $S_0$, while it increases due to the increment of the energy to recover the deformation of bulk. That is, there is a specific $h/R$, which results in the minimum $E_A/S_0$. Further experiments are required to clarify the suitability of eq. (3) for other experimental conditions to understand the adhesion properties by a point contact.

## Conclusion

We investigated the effects of the sample thickness, $h$, and the radius of curvature, $R$, on the adhesion properties between two viscoelastic materials in a point contact. From the $W$ (normal load)-dependences of the contact area, $S_0$, and the displacement of the bulk deformation, $\Delta h$, of PSA gel and

PDMS, we successfully obtained an empirical equation to estimate $S_0$ in the range of $2\text{gf} < W < 100\text{gf}$. With decreasing the relative thickness, $h/R$, the slopes of $\Delta h$ for $W$ were found to decrease and largely deviate from the prediction of the Hertz contact. After the initial decrement, the separation energy in a unit apparent contact area, $E_A/S_0$, increased with increasing $h$. That is, $E_A/S_0$ was found to take a minimum with changing $h$ at a given $R$. The experimental results were consistently explained on the basis of the changes of the number of molecular-to-molecular contacts in polymer chains and of the deformation of the bulk with increasing $h$.

We believe that the present results are crucial to understand the adhesion properties between two cylindrical viscoelastic materials in a point contact. Moreover, the equation between $S_0$ and $\Delta h$ obtained here is also important for the practical uses since the deviation of the relation between $S_0$ and $\Delta h$ from the prediction of the Hertz contact theory becomes evident for the thin sample, i.e., $h/R << 1$.

## References


1. Sato T, Goto M, Nakano K, Suzuki A (2005) Jpn J Appl Phys 44:8168
2. Hertz H (1882) J Reine Angew Math 92:156
3. Johnson KL, Kendall K, Roberts AD (1971) Proc R Soc London Ser A 324:301
4. Archard JF (1957) Proc R Soc London Ser A 243:190
5. Shull KR, Ahn D, Chen W-L, Flanigan CM, Crosby AJ (1998) Macromol Chem Phys 199:489
6. Shull KR (2002) Mater Sci Eng R 36:1
7. Mowery CL, Crosby AJ, Ahn D, Shull KR (1997) Langmuir 13:6101
8. Derjaguin BV, Muller VM, Toprov YP (1975) J Colloid Interface Sci 53:314
9. Flanigan CM, Shull KR Langmuir 15:4966
10. Greenwood JA, Johnson KL (1981) Phil Mag A 43:697
11. Greenwood JA (1997) Proc R Soc London Ser A 453:1277
12. Johnson KL (1998) Tribology International Vol. 31 No. 8:413
13. Hui C-Y, Baney JM (1998) Langmuir 14:6570
14. Tatara Y (1991) J Eng Mater Tech 113:285
15. Tatara Y, Shima S, Lucero JC (1991) J Eng Mater Tech 113:295

Progr Colloid Polym Sci (2009) 136:143–148
DOI: 10.1007/2882_2009_20

# Electrophoresis of Dyes and Proteins in Poly(Acrylamide) Gel Containing Immobilized Bilayer Membranes

Hiroki Ishihara[1,2], Goh Matsuo[1], Takanori Sasaki[3], Yuko Saito[3], Makoto Demura[3], and Kaoru Tsujii[1]

**Abstract** Electrophoresis of dye stuffs and proteins in poly (acrylamide) gel containing immobilized bilayer membranes have been studied. Bilayer membranes of a polymerizable surfactant, dodecylglyceryl itaconate (DGI), can be immobilized in poly(acrylamide) gels, and the hybrid gels are first applied to a substrate of the poly(acrylamide) gel electrophoresis (PAGE). The bilayer-membranes-immobilized-gel (abbreviated as BM-gel) showed different separation behaviors from those by the conventional PAGE. The separation behavior of dye stuffs suggests that the bilayer membranes in the BM-gel work as a separator of the test molecules due to their hydrophilic/hydrophobic nature. Water-soluble proteins migrated faster in the BM-gels than in the simple poly(acrylamide) gels. Membrane proteins, on the other hand, did not move at all in the BM-gels probably because the protein molecules were entrapped firmly inside the bilayer membranes.

**Keywords** Electrophoresis • Bilayer mambranes • Gel • Poly(acrylamide) • Proteins

## Introduction

A polymerizable surfactant, dodecylglyceryl itaconate (DGI), forms an iridescent lamellar liquid crystalline phase in water in the presence of small amount of ionic surfactant, and can be polymerized in the bilayer membrane system [1–3]. Furthermore, this iridescent liquid crystalline structure can be immobilized in hydrogels by means of polymerization of DGI together with gel-forming monomers such as acrylamide and methylenebis(acrylamide) [1–3]. The gels thus synthesized contain a number of bilayer membranes inside, and are quite unique soft materials showing iridescent color [2,3], anisotropic [3] and super rapid shrinking [4] properties, stabilization of myelin structures [5] and so on. As an application of this unique hydrogel, we have tried in this work to use it for a substrate of the poly(acrylamide) gel electrophoresis.

The poly(acrylamide) gel electrophoresis (PAGE) is a powerful analytical technique for biological substances such as proteins and DNA, and is now utilized quite frequently for genome analysis. This technique separates the biological substances in terms of their molecular size utilizing the mesh size distribution of the polymer hydrogel. Our new poly(acrylamide) gel contains a number of bilayer membranes inside, and the membranes may work to separate the compounds due to their hydrophilic and hydrophobic property. This novel PAGE method can be a powerful tool in future for the analysis in the field of biological sciences.

## Experimental Section

**Materials.** Dodecylglyceryl itaconate (DGI; *n*-$C_{12}H_{25}OCOCH_2C(=CH_2)COO–CH_2CH(OH)\ CH_2OH$) was synthesized by essentially the same procedures described in the previous work [3]. The crude product was applied twice to a silica-gel column (Wacosil C-200; Wako Pure Chemical Co.), and eluted with a hexane/ethyl acetate mixture (4/6 in weight). The final product (m.p. = 62–63°C ) was proven to be more than 99% pure by NMR and HPLC analysis. Itaconic anhydride and pyridinium *p*-toluene sulfonate were purchased from Aldrich Chem. Co. 1-Dodecanol was

K. Tsujii[1] (✉)
[1]Nanotechnology Research Center,
Research Institute for Electronic Science, Hokkaido University
(CRIS Building) N-21, W-10, Kita-ku, Sapporo 001-0021
e-mail: tsujik@gc4.so-net.ne.jp
[2]Graduate School of Science,
Hokkaido University,
N-10, W-8, Kita-ku, Sapporo 060-0810
[3]Faculty of Advanced Life Science,
Hokkaido University,
Sapporo 060-0810

purchased from Tokyo Chemical Industry Co. Ltd. Monomers and a reaction accelerator for preparation of gel samples were acrylamide (AAm; Wako Pure Chemical Industries Ltd.), *N*,*N*′-methylenebis(acrylamide) (a cross-linker; Wako Pure Chemical Industries Ltd.), and *N*,*N*,*N*′,*N*′-tetramethylethylenediamine (an accelerator of polymerization reaction; Wako Pure Chemical Industries Ltd.). All the samples used in this work were in guaranteed reagent grade, and used without further purification.

Test samples to be applied to PAGE were dye stuffs and proteins. Three anionic dyes (sulforhodamine 640, sulforhodamine B and disodium fluorescein) were purchased from Tokyo Instruments Co. and the bromophenol blue from Wako Pure Chemicals Industries Ltd. They were used without further purification. Their molecular structures are shown in Fig. 1. Water-soluble proteins (trypsin inhibitor from soybean, pepsin from pig gastric mucosa, egg albumin, bovine serum albumin, human serum γ-globulin, catalase from bovine liver) were purchased from Wako Pure Chemical Industries Ltd. Some of the samples contained some other protein impurities.

Membrane proteins used were bacteriorhodopsin and *Natronomonas pharaonis* halorhodopsins. The bacteriorhodopsin was a kind gift from Prof. Naoki Kamo of Hokkaido University, and the *Natronomonas pharaonis* halorhodopsins were prepared as follows. The expression of the recombinant NpHR (wild-type, E234Q-mutant, F150A-mutant) in *E. coli* (strain BL21 (DE3)) and purification procedures have been described elsewhere [6,7]. Fractions of the proteins separated with Ni-NTA-agarose (Qiagen, Hilden, Germany) were collected by elution (flow rate, 56 mL/h) with a buffer [50 mM Tris-HCl (pH 7.0), 300 mM NaCl, 150 mM imidazole, 0.1% *n*-dodecyl *β*-D-maltopyranoside (dodecyl maltoside, DM) (Dojindo Lab, Kumamoto, Japan)]. The samples were stored at 4°C for one month, and then the supernatant (DM- NpHR complex) was collected by centrifugation (18,000g, 20 min). After the buffer exchange, the protein concentration was estimated using an excitation coefficient $\varepsilon_{600}$ of 50,000 $M^{-1}\,cm^{-1}$. The monomeric proteins were obtained by desalting the trimeric protein solutions at 40°C for 3 h followed by adding 0.5 M NaCl at 25°C for 12h. The number of monomer unit of trimer was confirmed by chemical cross-linking of proteins, gel filtration chromatography and mass spectrometry.

**Polymerization procedures and gel preparations.** As mentioned previously, DGI monomer molecules form an iridescent lamellar liquid crystalline phase in water in the concentration range of 1 ∼ 2 wt % of DGI in the presence of small amount of ionic surfactant (0.2 ∼ 2.0 wt % with respect to DGI) [1–3]. In this work, we use sodium dodecyl

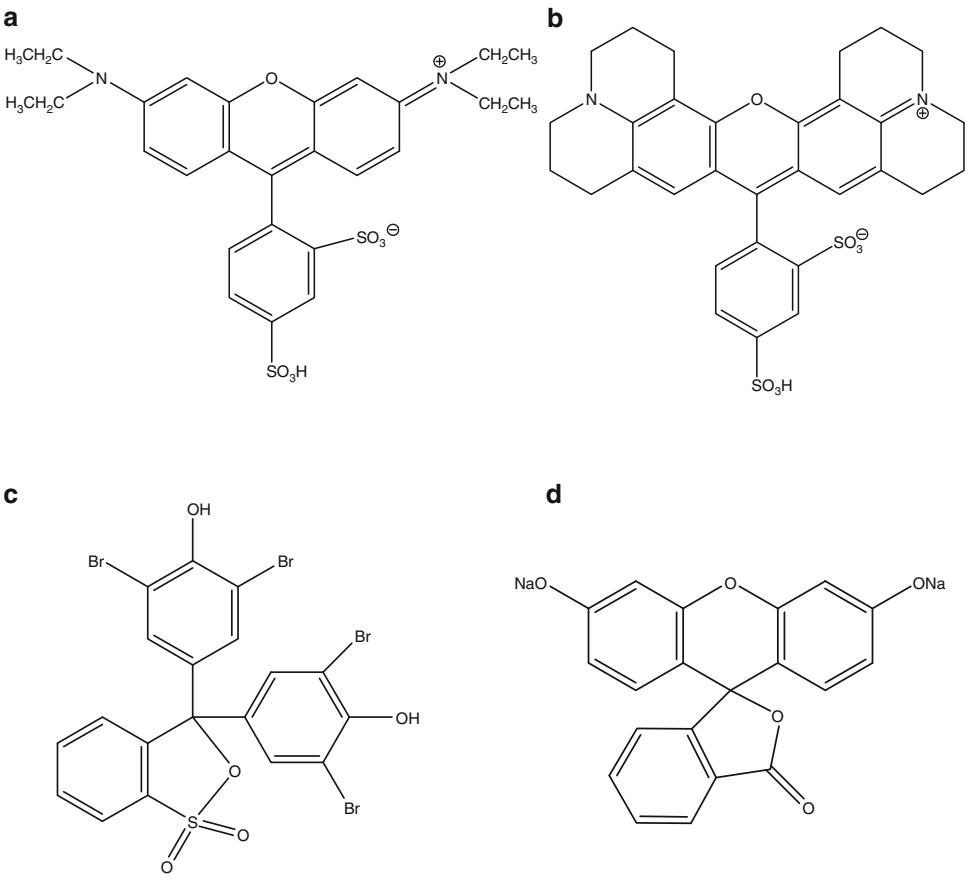


**Fig. 1** Molecular structure of dye stuffs used in this work as the test samples: (a) Sulforhodamine 640, (b) Sulforhodamine B, (c) Bromophenol blue and (d) Disodium fluorescein

sulfate (SDS) as an ionic surfactant. This iridescent structure of DGI is maintained even in the aqueous solution of the monomers of AAm and *N*,*N*′-methylenebis(acrylamide). The iridescent solution of DGI containing AAm and the cross linker was photo-polymerized by UV light using Irgacure 2959 (Ciba Geigi Co. Ltd.) as an initiator, and the lamellar structure of the polymeric DGI was immobilized inside the network of AAm gel [1–3]. Since the surface area of the bilayer membranes decreases due to the bond-formation between the DGI molecules, the iridescent color shifts to red side due to the increase of the inter-membrane distance during the above polymerization process [1]. The wavelength shift during polymerization is almost the same for every concentration of the samples, and the final color after polymerization still depends on the concentration of DGI. Molecular weight of the DGI polymer was estimated by gel permeation chromatography to be about 100,000 when the DGI was polymerized alone (homo-polymerization) [1]. The network density, i.e., the mesh size of the gel between the bilayer membranes can be assumed to be the same as that of a simple gel, since the initial swelling degree of poly(*N*-isopropylacrylamide) gel containing the bilayer membranes is almost the same as that of the simple gel [3].

For the substrate of PAGE a mixed stock solution of 29.2 wt % of AAm and 0.8 wt % of *N*,*N*′-methylenebis(acrylamide) was prepared. A part of the above 30 wt % stock solution was mixed to be 10 - 14 wt % for the final monomer solution with 1.0 – 2.0 wt % DGI containing 0.5 mol % SDS with respect to DGI, 4.5 wt % tris(hydroxymethyl)aminomethane (Tris) as a buffer, 0.1 wt % Irgacure 2959. The pH of the mixed monomer solutions was adjusted to be 8.8 or 11.0 with an HCl solution. A mixed monomer solution of above was bubbled with Ar gas, and then poured between two glass or quartz plates (8.0 cm × 8.4 cm) having a spacing distance of 1 mm. Photo-polymerization was carried out with a high pressure mercury lamp, SEN LIGHTS Co. Model HLR1000F-29, at 1000 w for 25 min. Simple AAm gels were also synthesized with no DGI for reference experiments. In this polymerization procedure, ammonium peroxodisulfate (0.06 wt %) as an initiator and *N*,*N*,*N*′,*N*′-tetramethylethylenediamine (0.2 wt %) were put in the monomer solution.

**Gel electrophoresis.** A substrate gel was set in an electrophoresis trough in which a buffer solution [0.3 wt % Tris and 0.146 wt % glycine] was filled. Electrophoresis was carried out with a commercial apparatus (BIO CRAFT, BE-230) at a constant voltage of 280 V, and was stopped when the marker dye (bromophenol blue: BPB) migrated to the position of 1 cm from the gel terminal. $R_f$ values were defined to be the ratio of the migrated distance of the sample to the total length of the gel. The pH value in the gel was adjusted at 8.8 or 11.0 with an HCl solution.

The test samples of the dyes were prepared as follows: 1 mg of dye stuff and 2 mL of glycerol were dissolved in 1.5 M Tris-HCl buffer (pH = 8.8), and the total volume of the solution was adjusted to be 10 mL. The 20 μL of sample solution was applied to the AAm and the BM-gel. In the experiments of dye stuffs, the concentrations of DGI and AAm in the BM-gels were kept constant at 1.9 and 12.0 wt %, respectively.

A water-soluble protein sample was dissolved in 10 mM phosphate buffer (pH = 7.0) at the concentration of 1 mg/mL. This sample solution was diluted twice with a sample buffer [62.5 mM Tris-HCl at pH = 8.8, 40 wt % glycerol, 0.01 wt % BPB], and mixed with a Vortex mixer. The 20 μL of sample solution was applied to the AAm and the BM-gel. The concentrations of DGI and AAm in the BM-gels were changed in the range of 0 ∼ 2.0 wt % and 10.0 ∼ 14.0 wt %, respectively. The pH value in the gels was adjusted at 8.8.

The bacteriorhodopsin was dissolved in 10 mM phosphate buffer (pH = 7.0) at the concentration of 0.5 mg/mL, and was diluted twice with the sample buffer [62.5 mM Tris-HCl at pH = 8.8, 40 wt % glycerol, 0.01 wt % BPB] containing 0.1, 0.5, 1.0, 1.5 wt % Triton X-100 (a nonionic surfactant). The *Natronomonas pharaonis* halorhodopsins were dissolved in the solution of 150 mM NaCl, 0.1 wt % DM, 10 mM phosphate buffer (pH = 7.0). The 10 μL of the membrane protein sample solutions of above was applied to the AAm and the BM-gel. The concentration of DGI was changed from 0 to 0.5 wt % and that of AAm was kept constant at 10.0 wt % in the BM-gels. The pH value in the gels was adjusted at 8.8.

## Results and Discussion

**Electrophoresis of dye stuffs.** Fig. 2 shows the electrophoretic patterns of 4 kinds of dyes in an acrylamide gel (a, b) and in a BM-gel (c, d) at pH = 8.8. The $R_f$ values at pH = 11.0 were plotted against time in Fig. 3. One can see from these figures that the BM-gel shows the good electrophoretic performance enough to be used as a substrate gel of PAGE. It is also interesting to note that the dye molecules migrate more slowly in the BM-gel than in the AAm gel. This may result from the hydrophobic interaction between the dye molecules and the bilayer membranes in the BM-gel. All the data for the electrophoretic mobilities ($R_f$ / min) were listed in Table I. The smaller electrophoretic mobility in the BM-gel is shown more clearly at pH = 8.8 than at 11.0, probably because of the stronger hydrophobic interaction owing to the reduction of the ionic nature in the dye molecules. No advantage was found in the BM-gel electrophoresis unfortunately, although some different electrophoretic behaviors from those in the conventional PAGE were observed.

**Electrophoresis of water-soluble proteins.** Electrophoresis of water-soluble proteins were investigated in details

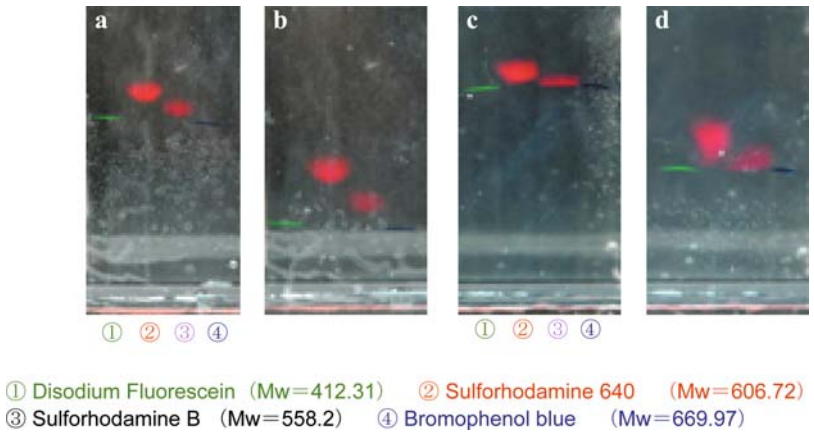


**Fig. 2** Gel-electrophoretic patterns of the dye stuffs in polyacrylamide gel (a, b) and bilayer-membranes-immobilized gel (c, d) at pH = 8.8. The patterns of a and c are obtained at 5 min after electrophoresis starts, and ones of b and d are done at 15 min. Acrylamide and DGI concentration are 12.0 wt % and 1.9 wt %, respectively

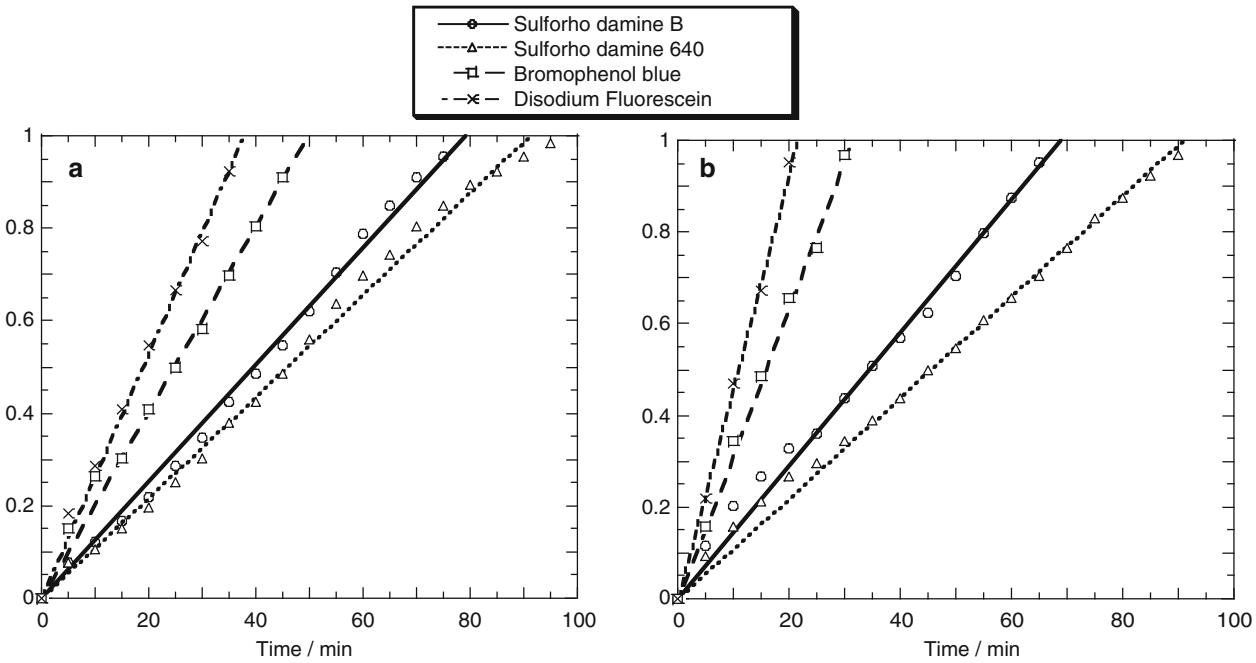


**Fig. 3** The plot of $R_f$ values against time at pH = 11.0 in the BM-gel (a) and the AAm gel (b)

**Table I** Electrophoretic mobility of the dye stuffs in the bilayer-membranes-immobilized gel and the polyacrylamide gel

| Dye stuff | Electrophoretic mobility/$R_f$ $min^{-1}$ | | | |
|---|---|---|---|---|
| | pH = 8.8 | | pH = 11.0 | |
| | Bilayers- immobilized gel | Polyacrylamide gel | Bilayers- immobilized gel | Polyacrylamide gel |
| Sulforhodamine B | 0.006 | 0.010 | 0.013 | 0.015 |
| Sulforhodamine 640 | 0.006 | 0.008 | 0.011 | 0.011 |
| Bromophenol blue | 0.007 | 0.014 | 0.020 | 0.032 |
| Disodium fluorescein | 0.007 | 0.014 | 0.027 | 0.047 |

by changing the concentrations of DGI and AAm in the BM-gels. Fig. 4 shows an example of the electrophoretic patterns of 7 kinds of proteins in the BM-gel containing 12.0 wt % AAm. There appear several bands in some samples, since the samples contain several protein impurities. It can be seen from the figure that (i) the mobility of the water-soluble proteins increases with increasing concentration of the bi-layer mambranes (DGI) in the gel, (ii) the BM-gel cannot be used as a substrate gel for PAGE at higher concentrations of DGI than 2.0 wt % since the protein bands are smeared.

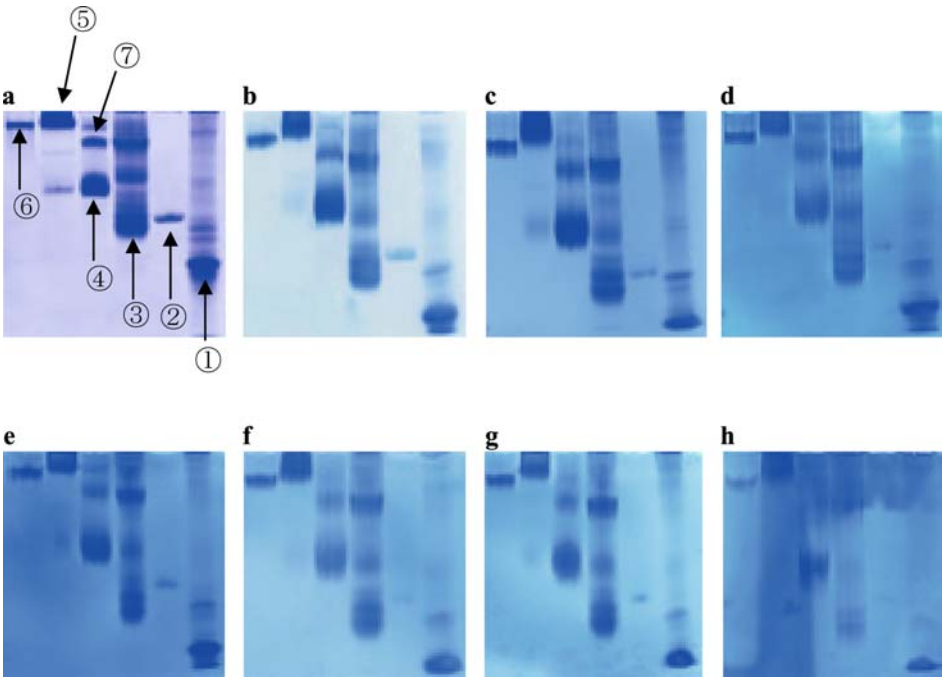


**Fig. 4** Gel-electrophoretic patterns of water-soluble proteins in polyacrylamide and bilayer-membranes-immobilized gels. Acrylamide concentration in the gels is constant at 12.0 wt %, and the DGI concentrations are 0 (a), 1.0 (b), 1.2 (c), 1.4 (d), 1.5 (e), 1.6 (f), 1.8 (g) and 2.0 wt % (h). Protein samples are ① trypsin inhibitor from soybean, ② pepsin from pig gastric mucosa, ③ egg albumin, ④ bovine serum albumin, ⑤ catalase from bovine liver, ⑥ human serum γ-globulin, ⑦ bovine serum albumin, dimer

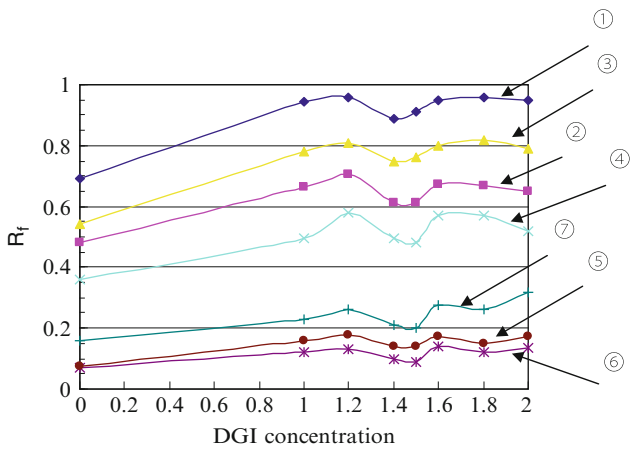


**Fig. 5** Gel-electrophoretic mobility of various water-soluble proteins plotted against the bilayer membrane (DGI) concentration. AAm concentration and sample protein numbers are the same as those in Fig. 4

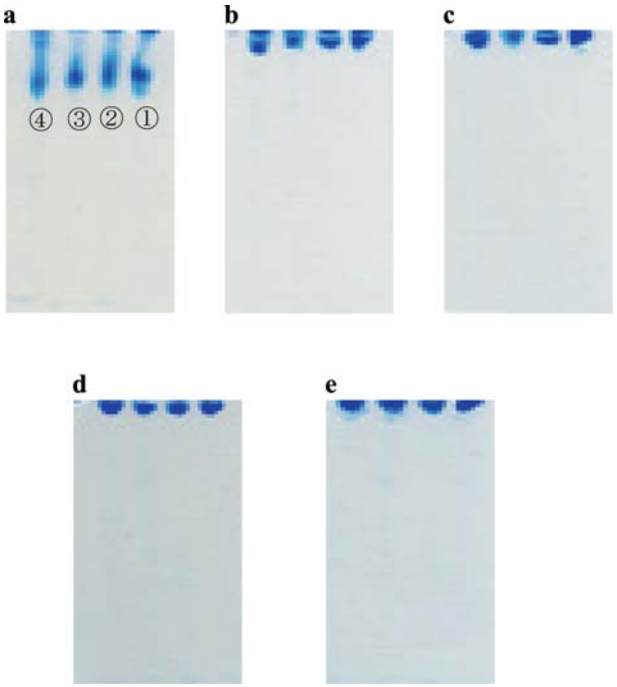


**Fig. 6** Gel-electrophoretic patterns of membrane proteins, *Natronomonas pharaonis* halorhodopsin. AAm concentration: 10 wt %, DGI concentration: 0 (a), 0.01 (b), 0.05 (c), 0.1 (d) and 0.5 wt % (e). Protein samples are ① wild-type, ② E234Q-mutant, trimer, ③ E234Q-mutant, monomer, ④ F150A-mutant, monomer

The mobility of each protein was plotted against the concentration of DGI in Fig. 5. The same results shown in Fig. 4 are quantitatively seen from the figure. The faster mobility in the BM-gels could be understood if the hydrophilic water-soluble proteins would migrate in water phase passing over the hydrophobic bilayer membranes. It is not clear at present why there is a small minimun in the mobility at about 1.5 wt % DGI.

The concentrations of AAm in the BM-gels were changed from 10.0 to 14.0 wt %. The mobilities of the proteins become larger reasonably when the AAm concentration decreases. The dependence of the protein mobility on the DGI concentration was basically the same in all the BM-gels of various AAm concentrations. A small minimum at about 1.5 wt %, however, was the most prominent in the BM-gel of 12 wt % AAm. In some experimental conditions the separation between the protein bands in the BM-gels is larger than that in the simple AAm gels (the conventional PAGE).

**Electrophoresis of membrane proteins.** Figure 6 shows the electrophoretic patterns of the membrane proteins, *Natronomonas pharaonis* halorhodopsin, in the BM-gels containing various concentrations of DGI. One can see clearly that the membrane proteins do not migrate at all in the BM-gels even when only a small amount of DGI is introduced to the gel. The proteins move a little when no DGI is present in the gel, since the protein molecules are solubilized in the solution by nonionic surfactant. Quite similar results were also obtained for another membrane protein sample, bacteriorhodopsin. The nonionic surfactant which solubilizes the membrane proteins may adsorb the bilayer membranes, and the proteins become insoluble in water. The membrane protein molecules may then be entrapped firmly, and immobilized in the bilayer membranes.

As mentioned before, water-soluble proteins migrate faster in the BM-gels than in the AAm gels. Membrane proteins, on the other hand, do not move in the BM-gels. These results mean that the BM-gels are powerful as the separation tool for the water-soluble and membrane proteins. The BM-gels may also be useful to make an immobilized enzymes of membrane proteins.

## Conclusions

We conclude that 1) the BM-gels can be used as a substrate gel for PAGE, 2) the electrophoretic mobility of water-soluble proteins increases wth increasing concentration of the bilayer membranes in the gel indicating that the water-soluble proteins would migrate passing over the hydrophobic bilayer membranes, 3) the membrane proteins do not migrate at all in the BM-gels probably because of the firm entrapping of the protein molecules by the bilayer membranes, and 4) the BM-gels are powerful as the separation tool for the water-soluble and membrane proteins.

**Acknowlegdements** The authors thank the financial support of the Grant-in-Aid for Scientific Research (No. 17655071) from Ministry of Education, Culture, Sports, Science, and Technology, Japan. G. M. acknowledges also to Shimadzu Science Foundation, and Shiseido Science Foundation, Japan for their financial support. We also appreciate Professor Naoki Kamo of Hokkaido University for his kind gift of the sample of bacteriorhodopsin.

## References

1. K. Naitoh, Y. Ishii, K. Tsujii (1991) J Phys Chem 95:7915
2. M. Hayakawa, T. Onda, T. Tanaka, K. Tsujii (1997) Langmuir 13:3595
3. K. Tsujii, M. Hayakawa, T. Onda, T. Tanaka (1997) Macromolecules 30:7397
4. X. Chen, K. Tsujii (2006) Macromolecules 39:8550
5. X. Chen, K. Tsujii (2007) Soft Matter 3:852
6. M. Sato, M. Kubo, T. Aizawa, N. Kamo, T. Kikukawa, K. Nitta, M. Demura (2005) Biochemistry 44:4775
7. M. Kubo, M. Sato, T. Aizawa, C. Kojima, N. Kamo, M. Mizuguchi, K. Kawano, M. Demura (2005) Biochemistry 44:12923

Progr Colloid Polym Sci (2009) 136:149–154
DOI: 10.1007/2882_2009_21

# An Application of Microcapsules Having Enzyme-degradable Gel Membrane to Cell Culture

Toshiaki Dobashi[1], Michiru Koike[1], Kentaro Kobayashi[1], Yasuyuki Maki[1], Takao Yamamoto[1], and Susumu Tanaka[2]

**Abstract** Newly developed microcapsules having gelatin wall membrane was applied as a scaffold for suspension cell culture. The optimum preparation condition was determined, and the stability of the cultured human fibroblast cells using the microcapsules was examined at both protein and gene levels.

**Keywords** Cell culture scaffold • Microcapsule • Fibroblast cell • Gelatin gel membrane

## Introduction

Recent widespread and increasing use of regenerative therapies including the emerging stem cell therapy depends upon the availability of validated methods for rapid and large-scale cell culture, storage and distribution, which stimulates further research development of cell culture [1]. It is well known that most cells necessitate an appropriate scaffold to be cultured regularly. Therefore, to increase the surface area is necessary to enhance the cell yield in a short time. Suspension cell culture is one of the sophisticated methods to solve this problem [2]. Cytodex is a well known commercial scaffold consisted of dextran core covered with degenerated collagen for suspension culture [3]. Serial sub-cultivation by means of suspension culture consists of three steps: (1) cell culture on the surface of microparticles in the medium, (2) cytodetachment from the microparticles with peptidase such as trypsin, and (3) separation of cells from microparticles. However, the cell yield is often significantly reduced at the second and the third step. Our idea to improve the efficiency is to simplify the procedure by using enzyme-degradable microcapsules as the scaffold. Since the present method can skip the third step, it is hoped to enhance the cell yields. Required characteristics of the microcapsule scaffold for the purpose are (1) diameters of 100–500mm, (2) nontoxicity, (3) high cell adhesion, (4) stability at cell culture condition, (5) appropriate degradability and (6) autoclavability. Microcapsules with thin gelatin gel wall membranes satisfy the requirements (2), (3) and (6). To meet the other requirements (1), (4) and (5), preparation need to be properly designed, especially the melting point $T_m$ of the gelatin wall membrane must be raised to above the physiological temperature. In the preceding paper [4], we studied the UV cross-linking effect on the melting point of gelatin gel microcapsules with the diameter ~30 μm and showed that microcapsules with desired $T_m$ can be prepared by controlling the UV irradiation time. In the course of the experiment it was suggested that $T_m$ strongly depends on the size of microcapsules. Therefore, for practical use, it is required to examine the melting point behavior of microcapsules with larger diameters that are applicable to the cell culture scaffold. In this paper, we studied the stability of gelatin microcapsules with the average diameter of 300 μm, examined its applicability as a cell culture scaffold, and assessed the cell function of the cultured cells both at the protein level and the gene level.

T. Dobashi (✉)
[1]Department of Chemistry and Chemical Biology
Graduate School of Engineering, Gunma University
Kiryu, Gunma 376-8515, Japan
e-mail: dobashi@chem-bio.gunma-u.ac.jp
[2]Department of Health and Nutrition
Faculty of Health and Welfare, Takasaki University
of Health and Welfare
37-1, Nakaorui-machi, Takasaki, Gunma 370-0033, Japan

## Experimental

### *Preparation of gelatin microcapsules*

Porcine gelatin (type:APH-250, Nitta Gelatin Inc) was dissolved in MilliQ water at 40°C at 10wt% to make gelatin solutions. Aliquot of surface-active agent, tetra glycerin fatty

acid ester (SYglyster CR-310, Sakamoto Yakuhin Kogyo Co. Ltd), was added to reagent-grade isooctane (Wako Pure Chemical Industries Ltd) at 5wt% to make a dispersing medium. A 0.5 ml of the 10wt% gelatin solution was added to 30 ml of the dispersing medium. The suspension was simply stirred at 40°C at the stirring rate of 500 rpm to emulsify the solution. The emulsions were then incubated at 15°C for 10 min to turn the droplets into physical gel particles, which were collected as precipitates. The gelatin gel particles were washed in hexane (Wako Pure Chemical Industries Ltd) for three times. Then we put 0.5 g of the gelatin particles in 10ml of hexane in a beaker with the diameter of 3.5 cm. The suspension was irradiated with UV ray at 3400 μW/cm$^2$ of 254 nm (CSL-100C, Cosmo Bio Co. Ltd) under stirring for 0–15 h at 15°C. The distance between the light source and the surface of the suspension was 5.5 cm. The obtained chemically cross-linked gelatin gel particles were washed in ethanol three times. Finally, they were dispersed in MilliQ water or phosphate-buffered physiological saline solution (PBS). Microscopic observation showed that the particles are of core-shell type, i.e., microcapsules, which is attributed to low penetration of UV ray in gelatin solution. All the organic solvents were reagent grade ones purchased from Wako Pure Chemicals Co. Ltd.

## Measurements

The gelatin microcapsules were observed with an inverted microscope equipped with a water bath, and the data for the image were taken with a digital camera. An aliquot of microcapsule suspension was used for determining the melting point of microcapsules. The average size and size distribution were obtained by measuring diameters of 200 microcapsules. Then the temperature of the suspension was raised from 25°C to 75°C at the rate of 0.1 K/min, and the number of microcapsules and the average cross-sectional area of microcapsules that remains insoluble at each temperature was measured. The melting point of the microcapsules was determined as the temperature when half of the microcapsules were dissolved in water. An aliquot of microcapsule suspension was incubated in PBS at 37°C for 5 days and the number of microcapsules that remains insoluble was measured. Then trypsin was added to find the time for complete melting of microcapsules.

## Cell culture and assessment of cultured cell

Cell culture was performed using gelatin microcapsules prepared by UV irradiation for 3h. Human fibroblast cells (WI-38) and the cancer cells (WI-38-VA-13) were purchased from DS Pharma Biomedical. The cell culture medium was Minimum Essential Medium Eagle containing 10 v/v% fetal bovine serum, 50 units/ml of penicillin, 50 mg/ml of streptomycine, vitamine solution and amino acid solution. Commercial microparticles (Cytodex 1, GE healthcare) was used as a control. After an appropriate amount of medium was poured in a petri dish for floating cells, each kind of cells was added at a concentration of $5 \times 10^4$ ml$^{-1}$. 0.5 g of the gelatin microcapsules or Cytodex were further added into the medium. The total volume of the suspension was 10 ml. The cells were cultured at 37°C for 5 days. After the cell culture, cells were observed by means of the Giemza staining. The supernatant was removed from the remaining suspension, and 1.5 ml of trypsin-EDTA (0.25% Trypsin with EDTA-4Na, Invitrogen Corporation) was added. 7.5 ml of the medium was further added and centrifuged at 1200 rpm for 5 min. After the supernatant was removed, 2 ml of the medium was added to disperse the cells. The number of cells in 50 μl suspension was counted by the tripan blue staining method. The cells collected from the remaining suspension were transferred to petri dishes for adhesion cells. 8 ml medium was further added to them to make 10 ml suspension. The cells were recultured at 37°C for 5 days. The cell function was examined based on both IL-6 protein production and IL-6 mRNA expression by stimulating with IL-1β on human fibroblast cells WI-38 [5]. Cells were cultured in a common method in a petri dish for two days with and without 5 ng/ml of IL-1β (Lot No. AD144101; R&D Systems) were prepared. Then each cell was cultured continuously for 3 h. One ml of the supernatant was extracted from each petri dish and IL-6 production was examined by ELISA Kit (BD Biosciences). For the examination of IL-6 mRNA expression, total RNA was isolated from them with ISOGEN (Nippon Gene). One μg of total RNA was used to synthesize the first-strand cDNA according to the manufacturer's instructions (GE healthcare). RT-PCR (34 cycles) was performed using primers for IL-6 and for glyceraldehyde-3-phosphate dehydrogenase (GAPDH) used as a control of housekeeping gene [6]. PCR products were then separated by means of 1% agarose gel electrophoresis and stained with ethidium bromide.

## Theoretical expression for melting temperature of gelatin gel

UV irradiation yields cross-linking of gelatin intermolecularly and increases the molecular weight. Gel is regarded as three-dimensionally homogeneous. For simplicity if we assume radicals be yielded proportionally to UV dose and no loops are produced by cross-linking, the degree of polymerization is

linearly proportional to UV irradiation time [4]. If we also assume harmonic potential for interaction of gelatin molecules and gels melt by thermal motion according to the Lindeman's law [7], the UV irradiation time dependence of melting temperature $T_m$ is derived as

$$T_m/T_0 = (1 + \beta t_{UV})^{2/3} \quad (1)$$

where $T_0$, $t_{UV}$ and $\beta$ are the melting temperature of gelatin gel without irradiation (physical gel), UV irradiation time and a constant related with reactivity of radicals.

## Results and Discussion

According to the microscopic observation, the average diameter of the microcapsules is 355 μm. The size distribution is fairly narrow [8], but the melting temperatures of microcapsules have a slight scatter, resulting in gradual decrease of the number of insoluble microcapsules with increasing temperature, as shown in Fig. 1. This tendency is clearer for larger UV irradiation time. We could not observe the melting point of the microcapsules prepared with $t_{UV} > 2$h in the experimental range of temperature less than 75°C. The melting temperature was determined by the temperature when half of the microcapsules were melted (dashed line). Figure 2 shows the melting temperature as a function of UV irradiation time. As expected from Eq. (1), the 3/2 power of melting temperature is linear to UV irradiation time. This result suggests that we can estimate the appropriate irradiation time for preparing microcapsules with a desired melting temperature based on the theory. For the cell culture performed at 37°C, typically 5 days incubation is necessary. Figure 3 shows the relative number of microcapsules insoluble after the incubation at 37°C for 5 days (120 h) which is the time for the standard cell culture. The microcapsules prepared with both short irradiation time less than 1 h and long irradiation time more than 10h are dissolved in the medium gradually. The microcapsules prepared with irradiation time in the range between 3h and 8h remained insoluble after 5 days incubation required for cell culture. Generally, UV irradiation results in both scission and cross-linking of polymers. For cross-linking, enough amount of radicals and mobility of them to react with other chains are necessary. Therefore, at too large dose, disintegration of network (scission) dominates because of low mobility of chains in the highly cross-linked network. Ethanol treatment of the microcapsules did not deteriorate them significantly, which guarantees the stability against sterilization of the microcapsules with ethanol. Figure 4 shows a typical time course after trypsin treatment of microscopic images of gelatin microcapsules prepared by 3h UV irradiation. The time required for complete melting was 6, 13 and 14 min for UV irradiation time 3, 5 and 8 h, respectively. From these

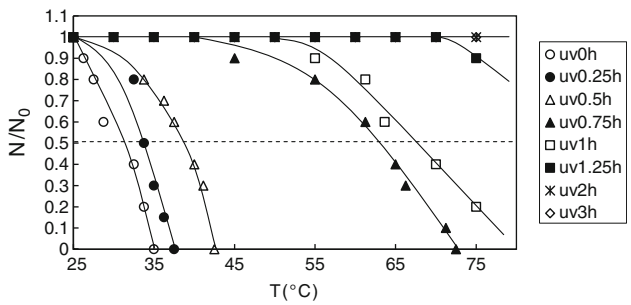


**Fig. 1** The number of microcapsules that remains insoluble as a function of temperature. $N_0$ is the number of microcapsules at 25°C. The melting point was determined as the temperature when the half of the microcapsules was dissolved in water. The microcapsules were prepared with the indicated UV irradiation time

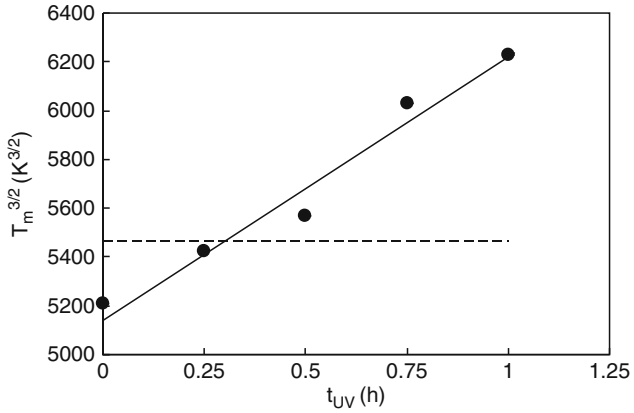


**Fig. 2** Melting temperature of gelatin microcapsules prepared with different UV irradiation times. The solid line represents Eq. (1). The dashed line indicates the incubation temperature for cell culture of 37 °C

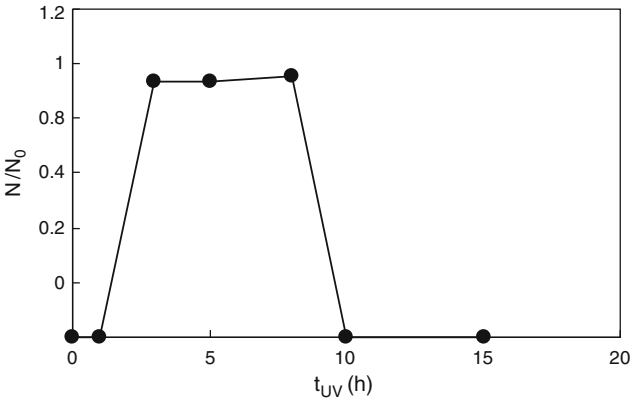


**Fig. 3** The number $N$ of microcapsules insoluble after the incubation at 37°C for 5 days divided by the initial one $N_0$ plotted as a function of UV incubation time

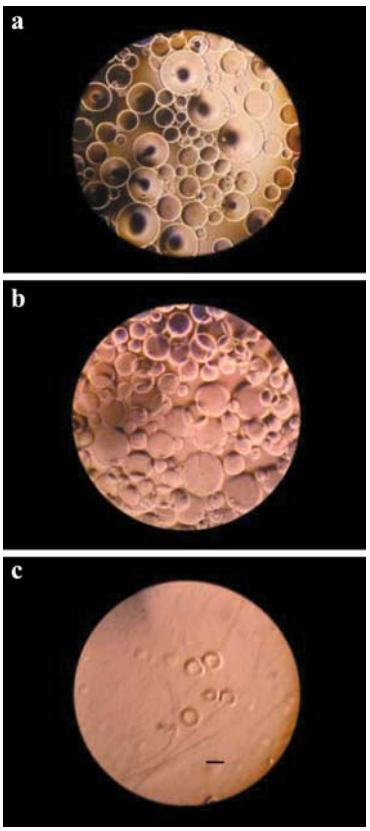


**Fig. 4** Microscopic images of gelatin microcapsules prepared by 3h UV irradiation before trypsin treatment (a), 1 min after trypsin treatment (b), and 3 min after trypsin treatment (c). Scale bar shown in (c) denotes 200 μm

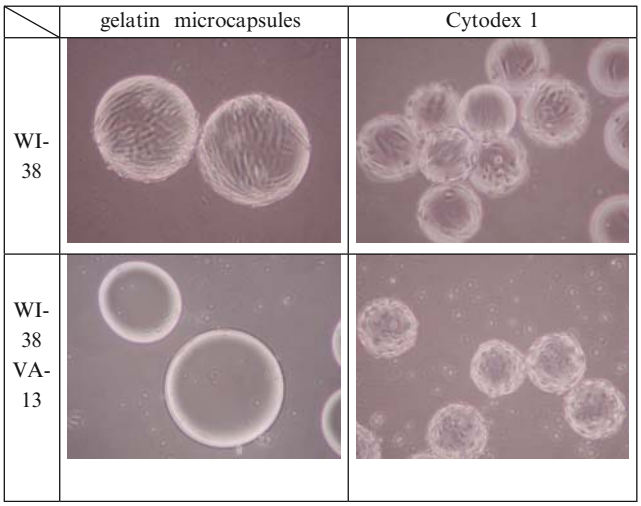


**Fig. 5** Microscopic images of cultured fibroblasts WI-38 or WI-38-VA-13 on gelatin microcapsule scaffolds prepared with UV irradiation to gelatin emulsions for 3h or Cytodex 1

experimental results UV irradiation time was fixed at 3 h in the real cell culture. Figure 5 shows microcapsules and Cytodex after 5 days culture of WI-38 and WI-38-VA-13.

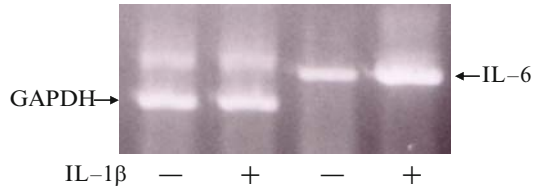


**Fig. 6** IL-6 mRNA expression of fibroblast cells cultured on gelatin microcapsules in the presence or absence of IL-1β. GAPDH was used as an internal control

Comparable degree of cell adhesion and growth of cells were observed on gelatin microcapsules and Cytodex 1 for WI-38, whereas no cell growth of WI-38-VA-13 was observed on gelatin microcapsules, in contrast that cell growth of WI-38-VA-13 was comparable to WI-38 on Cytodex 1. This could be attributed to weaker adhesion capability of cancer cells. It is interesting to utilize the cell selectivity of gelatin microcapsules in application of real cell culture. The Giemza staining of the cells cultured on gelatin microcapsules showed a clear image of cell nucleus, cytoplasma and nuleic body that indicates no apotosis and cell shape stability on gelatin microcapsules. The suspension after cell culture for 5 days followed by trypsin treatment was transparent for gelatin microcapsule scaffold because of their melting, whereas it was turbid for Cytodex 1 scaffold because of light scattering from them. The reculture of the cells on both gelatin microcapsules and Cytodex 1 for 4 days showed normal cell growth and cell number increase, indicating no damage by trypsin treatment. The number of collected cells after the culture for 5 days obtained using gelatin microcapsules was 5 times that obtained using the same weight of Cytodex 1. Since the size distributions are not exactly the same for gelatin microcapsules and Cytodex 1, we cannot conclude gelatin microcapsules are better than Cytodex 1, but at least we could not find any disadvantage of gelatin microcapsules. The cell function stability of fibroblast cells cultured on the microcapsules were clarified by the response (IL-1β) to the stimulation of IL-6, as conventionally used for assessment. The ratio of IL-6 production of fibroblast cells cultured on gelatin microcapsules with and without stimulating with IL-1β was 3, which is comparable with the value 8 by common cell culture in a petri dish. This suggests that the cell function is normal at the protein level. Furthermore, IL-6 mRNA expression of the cultured cells on gelatin microcapsules was induced twice with IL-1β, which was determined from the analysis of the electrophoresis image as shown in Figure 6. On the other hand, mRNA expression of control GAPDH used as a housekeeping gene was not changed in the presence or absence of IL-1β. This suggests that the cell function is normal at the gene level. These results of morphology of

cells and cell functions suggest no damage of the cells cultured on gelatin microcapsules.

## Conclusion

Microcapsule scaffold made from gelatin was designed for cell culture by means of suspension culture. Fibroblast cell culture using the microcapsules was successfully performed, and no damage of the cell function was observed.

**Acknowledgements** This work was partly supported by Grant-in-Aid for Science Research from The Ministry of Education, Culture, Sports, Science and Technology in Japan (grant no. 16540366) and (grand no. 20656129).

## References

1. van Wezel AL (1976) Dev. Biol. Standard 37:143–147
2. Katayama H, Itami S, Koizumi H and Tsutsumi M (1987) J. Invest. Dermatol. 38:33–36
3. Microcarrier cell culture principle & method, Amersham Biosciences
4. Yamamoto T, Koike M and Dobashi T (2007) Langmuir 23: 8531–8537
5. Kawada M, Ishizuka M and Takeuchi T (1999) Jpn. J. Cancer. Res. 90:546–554
6. Yoshida Y, Maruyama M, Fujita T, Arai N, Hayashi R, Araya J, Matsui S, Yamashita N, Sugiyama E and Kobayashi M (1999) Am. J. Physiol. 276:L900–L908
7. Lindemann FA, Physik Z (1910) 11:609
8. Koike M, Kobayashi K, Tanaka S, Harano A, Yamamoto T and Dobashi T (2006) Trans. MRS-J 31:823–825

Progr Colloid Polym Sci (2009) 136:155–162
DOI: 10.1007/2882_2009_22

# Development of a Novel Hydrogel to Prevent Bacterial Infectious Diseases

Norihiro Kato[1], Azumi Kobayashi[1], Hiroshi Motohashi[1], Yu Ozonoe[1], Tomohiro Morohoshi[2], and Tsukasa Ikeda[2]

**Abstract** Temperature-induced phase separation (TIPS) technique was applied to create cyclodextrin (CD) immobilized 2-hydroxypropyl cellulose (HPC) gel sheets. A heterogeneous polymer network could be fixed when the reaction temperature was stepwise increased above a lower critical solution temperature (LCST) of the HPC polymer at approximately 40°C during the cross-linking reaction. Dynamics of polymer network formation was characterized by measuring the viscosity change of the pre-gel solution with or without the TIPS process. A temperature increase is responsible for drastic increase of the viscosity of which change was translated as the acceleration of the cross-linking reaction rates. The immobilized α-CD or hydroxypropyl-β-CD (HP-β-CD) onto the TIPS-generated polymer network effectively decreased the production of red pigment prodigiosin that was one of the second metabolites through the cell-population-density dependent quorum sensing (QS) system in *Serratia marcescens* AS-1. Since virulence expression in some opportunistic pathogens was regulated by diffusible acylhomoserine lactone (AHL) mediated QS system, trapping AHLs onto the host matrices could make the CD-immobilized gels interrupt the hierarchical QS system from outside of cells. The AHL-mediated prodigiosin production could be drastically decreased to approximately 10% using the CD-AHL inclusion complex formation when the TIPS process was applied to HPC/α-CD gel synthesis with optimized condition of the phase separation.

N. Kato (✉)
[1]Department of Advanced Interdisciplinary Sciences
Graduate School of Engineering, Utsunomiya University
7-1-2 Yoto, Utsunomiya 321-8585, Japan
e-mail: katon@cc.utsunomiya-u.ac.jp
[2]Department of Material and Environmental Chemistry
Graduate School of Engineering, Utsunomiya University
7-1-2 Yoto, Utsunomiya 321-8585, Japan

**Keywords** Cell-to-cell communication • Quorum sensing • Cyclodextrin • Gene expression control • *N*-Acylhomoserine lactone

## Introduction

Molecular recognition is one of the indispensable systems in nature to coordinate a living system. Biological systems often utilize bioaffinity such as combination of enzyme-substrate, antigen-antibody, saccharide-lectin, and receptor protein-ligands. Application of such biomolecules has been developed to biosensors as well as the biomimetic systems [1–3]. Gel technology could be successfully applied to biomolecule-sensitive hydrogels that respond to the specific molecules [4–7]. However, no report yet to appear in relation to biomolecule-sensitive gel that could operate through remote-control system on the cell functions especially for the desired gene expression from outside of cells. In our previous papers, a novel biomolecule-sensitive gel was successfully applied directly to control the target-gene transcription in bacterial cells [8–12]. In the present study, we focused on an induced system with small signal molecules for the target gene expression.

Several bacteria perceive and respond to cell density, relying on the local concentration of the diffusible signal molecules. A quorum sensing (QS) is one of the cell-to-cell communication systems in bacteria to regulate multiple cell functions which were derived from the cell density dependent gene expression [13]. Different classes of secreted signal molecules termed as autoinducer are involved in the different major QS classes. The QS in gram-negative bacteria produces and utilizes acylated homoserine lactone (AHL) consists of a homoserine lactone ring joined to a fatty acid chain to communicate within or sometimes across species [14]. Gram-positive bacteria utilize some small peptides as autoinducer [15]. The third class of the QS is regulated by

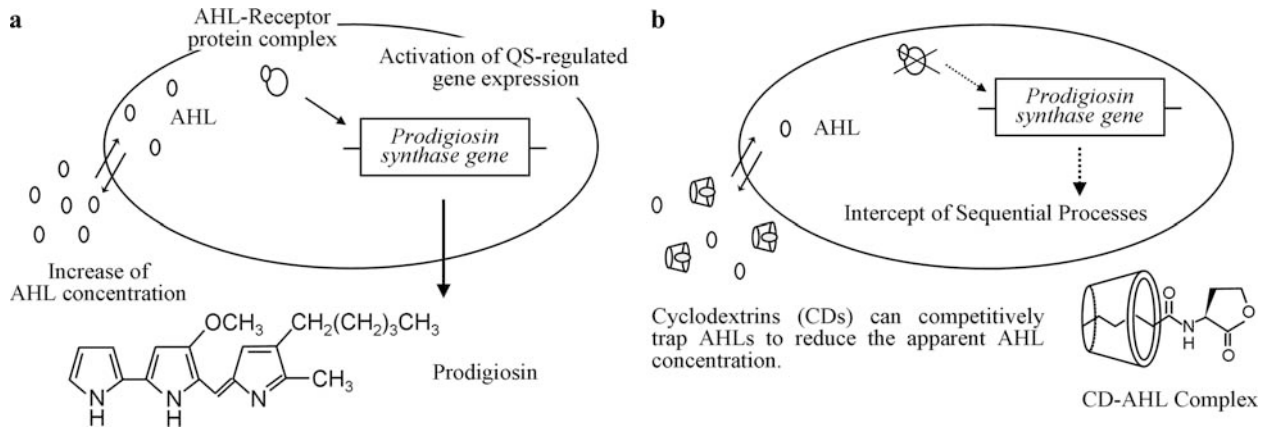


**Fig. 1** Schematic illustration of AHL-mediated quorum sensing system in *S. marcescens*. (a) Production of red pigment prodigiosin is enhanced by increment of the AHL concentration through the cell growth. (b) The inclusion complex formation between AHLs and additive CDs was responsible for the intercept of the sequential quorum sensing.

furanosyl borate diester autoinducer 2, abbreviated as AI-2, in both gram negative and positive bacteria [16]. Among them, AHL-mediated QS system is exclusively studied to artificially repress virulence in opportunistic pathogens including *Pseudomonas aeruginosa* and *Serratia marcescens* because it was known that some infectious bacteria can regulate their virulence factor expression by QS system. Antibiotic resistance of infectious bacteria becomes an issue of public concern due to the widespread use of antibiotics. Therefore, it is necessary to develop a novel method for prevention of the infectious diseases without applying antibiotics. From such viewpoints, we focused on the AHL-mediated QS system as one of the highly probable feasible methods to solve the problem.

In this report, artificial QS control in *S. marcescens* AS-1 was investigated using hydrogel sheets which possess the affinity with AHLs. *Serratia* sp. is an opportunistic human pathogen, and sometimes causes infections in immunocompromised hosts. The AHL-mediated QS system is briefly described as follows (Fig. 1a). Each bacterial cell synthesizes AHLs at a low basal concentration. It is considered that the diffusible AHLs can move to outside of cells according to their concentration gradient. Thus increase of local AHL concentration is linked to increase of the cell population density. The AHL forms complex with a transcription factor and then the transcription factor activates expression of the QS-regulated genes at a threshold level of the AHL. In our previous papers, the inclusion complex formation was reported between acyl-chains of AHLs and cyclic oligosaccharide cyclodextrins (CDs) in aqueous solution. Some CD analogues can be utilized to some commercial products due to its safety for human, including food additives, deodorizer, and carriers for hydrophobic drugs. Now CD is one of the suitable host materials to trap autoinducer AHLs because the use of CDs is approved in many biomedical fields. Previously, QS control in *P. aeruginosa* and *S. marcescens* was reported using soluble or immobilized CD onto the cross-linked polymer gel as shown in Fig. 1b [8–12]. Production of red pigment prodigiosin was effectively reduced by adding CDs in liquid medium during shake culture [9]. The prodigiosin is a linear tripyrrole, produced in the stationary phase of the growth in *Serratia* sp. or in some actinomycetes. It was reported that the prodigiosin production was regulated by many factors, involving SmaI and SmaR QS systems as homologues of LusI and LuxR in *Vibrio fischeri*. The AHLs allow the cell population to up-regulate expression of the prodigiosin biosynthetic gene (*pig*) clusters in *Serratia* sp [17, 18].

Trapping AHLs onto the immobilized CDs probably reduce the apparent autoinducer concentration irrespective to the intensity of cell population density to trigger the hierarchical QS (Fig. 1b). The rate of the AHL secretion from cells and also the rate of the AHL movement inside gel sheets should limit the extent of the QS inhibition. If the AHL concentration increases exponentially or drastically at the given time, it becomes more difficult to capture all AHL molecules even when excess amount of immobilized CDs were existed on the gel. Thus improvement of the molecular transfer rate inside gels and maximization of the inner surface area of gels play an important role to enhance the inhibitory effects on the QS.

To create microporous hydrogel, a variety of protocols are proposed including γ-irradiation, template of gas bubbles, leaching of embedded particles, ice crystal template due to freezing, and phase separation of polymer solution [19–26]. Diffusion-limited kinetics of the volume change on stimuli-responsive gel can be overcome by porous structure formation because network diffusion occurs over the scale of the microstructure rather than in macroscopic dimensions when the microstructure allows the fluid to be absorbed or desorbed by convection though the pores [19]. A temperature-induced phase separation (TIPS) method is one of the most

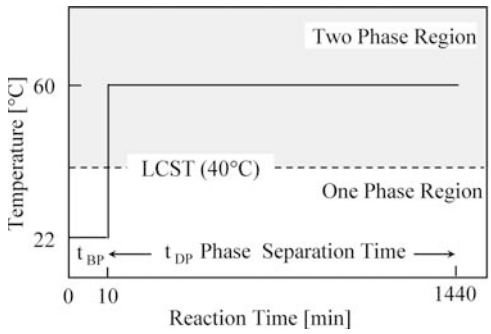


**Fig. 2** Temperature-induced phase separation method. The reaction process was carried out by two different time/temperature intervals. After addition of the divinylsulfone, the temperature is stepwise increased above the LCST of the polymer into the two-phase region of the phase diagram. Cross-linking can continue during the phase separation time.

readily suited techniques to generate microporous networks on a thermosensitive gel [27, 28]. In this technique, a chemical cross-linking reaction is carried out concurrent with the phase separation. Gehrke and coworkers reported that the technique allowed a great degree of control over porosity, pore size and type of gel microstructure [27]. Therefore, the technique was applied to the gel synthesis of CD-immobilized 2-hydroxypropyl cellulose (HPC) gel to control the porous properties of the gel. Schematic illustration of the TIPS process is shown in Fig. 2. Two different time and temperature intervals were controlled by immersing the mold filled with the pre-gel solution in temperature-controlled water bath at 22 or 60°C because a lower critical solution temperature (LCST) of the aqueous HPC solution was observed at approximately 40°C. In the first period as the time before phase separation ($t_{BP}$), an embryonic network forms at 22°C. The timing for changing temperature sensitively determines the final structure of polymer networks. Then the temperature was stepwise increased above the LCST to induce phase separation. During the phase separation time ($t_{DP}$), induced heterogeneous polymer network was determined by combined effects of phase separation kinetics and cross-linking reaction kinetics. The temperature was kept at 60°C until completion of the reaction. Application of the TIPS process onto the HPC gel was generally conducted through the three different periods when the thermally triggered shrinking properties of gels were important to serve the purpose [27]. In the case, temperature was decreased to the original temperature below the LCST to remix the phases as the final period after phase separation ($t_{AP}$). The degree of the volume change drastically reduced when the sufficiently phase-separated polymer network was locked-in by cross-linking when the third interval ($t_{AP}$) was omitted and then the cross-linking reaction was completed at 60°C. However, this research aims to optimize preparing gel properties as the artificial autoinducer receptor under the isothermal adsorption process. The TIPS process could be simplified as two time/temperature periods to investigate the relationship between the generated microporous properties and inhibitory effects on the AHL-mediated prodigiosin production in *S. marcescens* AS-1.

The purpose of this research is to investigate one-pot synthesis of microporous CD-immobilized HPC gels using the TIPS process and their effects onto inhibitory control of the prodigiosin production in *S. marcescens* AS-1. The optimum condition of introducing the phase-separated structure would be analyzed to maximize performance of the AHL trapping method with immobilized CDs.

## Experimental section

### *Materials*

Hydroxypropyl-β-CD (HP-β-CD) and HPC (Mw: 100,000) were purchased from Acros Organics. Divinyl sulfone (DVS) and α-cyclodextrin (α-CD) were purchased from Wako Pure Chemical.

### *Preparation of CD-immobilized gel sheets*

Desired amount of α-CD or HP-β-CD was dissolved in aqueous HPC solution and pH was adjusted to 12 with NaOH. DVS was then added to the pre-gel solution at room temperature. The solution was stirred for about 20 s and then poured into the glass mold separated by silicone rubber gasket (1.5 mm thick). Cross-linking of the HPC polymer and immobilization of the CD onto the HPC polymer network simultaneously occurred to synthesize a CD-immobilized gel sheets. The assembly of the mold was clamped with spring clips and immersed in a temperature-controlled water bath at 22°C to proceed a cross-linking reaction at homogeneous condition. During the period, viscosity of the solution could gradually increase due to the polymer network formation. After approximately 10 min, the temperature was stepwise increased up to 60°C by transferring the assembly of the mold into the different water bath. Phase separation could be induced at the period ($t_{DP}$) to give a heterogeneous polymer network. The chemical reaction of the DVS continued to fix the ever-changing polymer network during phase separation. Total reaction time was set as 24 h to complete the reaction. After the reaction, the gel sheets were separated from the mold and then immediately cut into pieces of 10×10×1.5 mm before washing and

re-swelling in water. The NaOH catalyst was neutralized by immersing gel sheets in dilute HCl solution. The unreacted cross-linker and sol fraction were leached away from the gel sheets by immersing in distilled water. Then the gel sheets were equilibrated in water at 22°C to characterize the fundamental properties.

## Characterization of the gel sheets

The equilibrium swelling degree ($Q = M_s/M_{dry}$) was determined as the weight ratio of swollen mass at 22°C ($M_s$) to dry mass ($M_{dry}$) of the gel sheet. To observe the temperature-induced macroscopic structure, scanning electron microscopy (SEM) was performed (JSM-5610LV, JOEL). The swollen gel sheet at 22°C was soaked in ethanol to substitute the solvent for 24 h. The gel sheet was picked up and wiped to remove excess droplets at the surface of the gel sheet. Then the gel sheet was transferred into heptane as the representative solvent for low surface tension to minimize the deformation of gels during drying. The heptane in the gel sheet was evaporated by natural drying.

Open pores with sufficient dimension could allow convective flow of solvent. In this research, an effective porosity ε was defined as the fraction of total gel volume occupied by interconnected pores through which water can flow. The effective porosity is more suitable for the useful index of the pore interconnectivity rather than the conventional porosity as total void volume per gel volume [29]. The gel sheet equilibrated at 22°C was placed between 10 layers of lint-free tissue papers and then approximately 10 kPa of mechanical pressure was applied to the assembly of sandwich between two glass plates for 1 min. The expelled water could be immediately absorbed into the tissue papers. The mass of the expelled water ($M_c$) was determined by measuring the gel weight before ($M_i$) and after applying the external mechanical pressure. The relationship between the effective porosity ($\varepsilon = M_c/M_i$) and the time before phase separation ($t_{BP}$) was discussed to optimize the phase separation condition.

## Quorum sensing control in S. marcescens AS-1

*S. marcescens* AS-1 was cultured in Luria-Bertani (LB) medium at 25°C for 10 h. Red pigment prodigiosin was accumulated inside cells when the sequential QS system was normally activated by AHL accumulation. After the desired period of the shaking culture, the cell population density was measured by $OD_{600}$ as the turbidity of the culture broth at 600 nm (V-550DS, JASCO). The prodigiosin amount was determined as follows [18]. The cell pellet was collected by centrifugation and then suspended in acidified ethanol (2% 2 mol $dm^{-3}$ HCl in ethanol) to extract prodigiosin from cells. The cell debris was removed by centrifugation and the prodigiosin amount was evaluated by measuring absorbance at 534 nm ($A_{534}$). The prodigiosin production was calculated as $A_{534}$ per $OD_{600}$. Six pieces of CD-immobilized gel sheets ($10 \times 10 \times 1.5$ mm) were added to the liquid medium from the beginning of the cell growth. The inhibitory effect of the CDs on prodigiosin production was compared after the normalization with $A_{534}/OD_{600}$ of control in the absence of CD and gel sheets.

## Time evolution of the viscosity during the TIPS process

Microporous structure of the polymer network was fixed by cross-linking reaction when the temperature was stepwise increased up to 60°C. Dynamics of polymer network generation was examined by measuring viscosity change with sine-wave vibro viscometer (SV10, A&D). The pre-gel solution was filled in a sample cup equipped with a water jacket in conjunction with a water circulating system (UC-55N, Tokyo Rikakikai). The pre-gel solution could be gently stirred with a magnetic stirrer during the measurement (Variomag micro, H+P Labortechnik AG). Time evolution of the viscosity was determined under the isothermal and TIPS conditions by importing the measurements of viscosity and temperature to a PC.

## Stability constant of CD complex

Just after synthesis CD-immobilized gel sheets were immersed in the distilled water to expel the remained CD molecules. After thorough washing process of the gel, the amount of the diffused CDs was determined by HPLC system equipped with refractive index detector (RID-6A, Shimadzu). Immobilized CD amounts onto the gel sheets could be calculated from the difference between the initial weight and weight loss through leakage in washing solution. Previously described method was followed to measure the stability constant for the inclusion complex between CD and *N*-hexanoyl-$_L$-homoserine lactone (C6-HSL) as the representative autoinducer produced in *S. marcescens*, C6-HSL was chemically synthesized [29–31]. Desired numbers of HPC/α-CD or HPC/HP-β-CD gels sheets (approximately 1.5 mm thick) were immersed in aqueous C6-HSL solution at 22°C for 24h. The stability constant ($K$) between immobilized CD and C6-HSL was determined from the concentration of immobilized CDs and equilibrated C6-HSL concentration determined by refractive index.

## Results and discussion

### *Key properties of microporous gels*

The α-CD and HP-β-CD could be immobilized onto the polymer network even when the microporous structure was formed by applying TIPS. The TIPS made gels clouded while the conventional CD-immobilized HPC gels (HPC/α-CD or HPC/HP-β-CD gel) were translucent. The thermosensitive properties of gels remained after immobilization of CDs and also applying TIPS; any CD-immobilized gels with or without applying TIPS possess thermosensitive properties and shrinking profiles gave nearly same LCSTs around 40°C (data not shown). Figure 3 showed SEM images of gel surfaces of which macroscopic morphologies could be altered by controlling periods during ($t_{DP}$) and before phase separation ($t_{BP}$). The TIPS process could lead macroscopically heterogeneous, porous structure as shown in Fig. 3C.

Fundamental properties of gels prepared by TIPS were summarized in Table 1. As compared with equilibrium swelling degree of the HPC gel (Q = 20.3), the Qs drastically decreased to Q = 8.4–9.0 when the $t_{BP}$ was set around 11–12.5 min. It was also clear that the amounts of immobilized α-CD or HP-β-CD decreased with decreasing $t_{BP}$. Under the one-pot synthesis condition, greater amounts of DVS were needed to form gels in the presence of CDs because some of the additive DVS should be consumed to fix CDs instead of cross-linking between polymers. These syntheses were carried out in the presence of sufficient amounts of crosslinker DVS. Moreover, the TIPS condition crucially determined the effective porosities as well as the Qs. The shorter periods of the embryonic polymer network formation made the equilibrium swelling degrees (Qs) reduce, while their effective porosities sufficiently increased to improve the water flow through the convection. These results clearly indicated that generated interconnected channels suited to expel pore water by simply applying a small mechanical pressure. Figure 3 showed that the macroscopic morphology of the gel ever-changed by increasing the phase separation time, while the effective porosities at $t_{BP}$ = 11 and 20 min were sufficiently large for the convective flow. It was possible that the longer $t_{DP}$ reduced the Qs due to the crosslinking reaction in the polymer-rich regions and also kept the sufficiently large ε. In this study, the initial CD concentration for all gel samples was set as 3.5 wt% in aqueous pre-gel solution. Immobilized α-CD amounts decreased from 0.55 to 0.13 mmol/g-dry gel with decreasing the $t_{BP}$. These results showed that the sufficient period of the

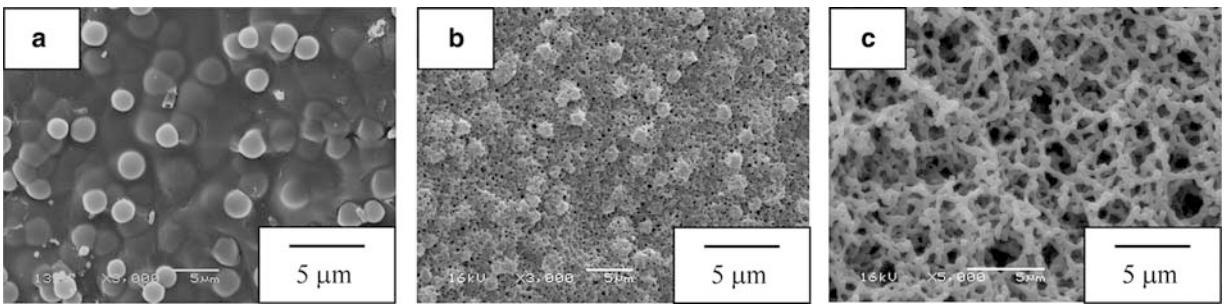


**Fig. 3** SEM microphotographs of the HPC/HP-β-CD hydrogel prepared by TIPS. (a) $t_{BP}$ = 24 h, (b) $t_{BP}$ = 20 min, (c) $t_{BP}$ = 11 min.

**Table 1** Properties of HPC gel and CD-immobilized gels prepared by TIPS. The temperature of the pre-gel solution was heated to 60°C after the embryonic network began to form.

| | | Immobilized CD mmol/g-dry gel | Equilibrium Swelling Degree (Q)[1] | Effective Porosity (ε)[1] |
|---|---|---|---|---|
| HPC gel | | 0 | 20.3 | 0.054 |
| HPC/α-CD gel | $t_{BP}$ = 12.5 min | 0.13 | 9.0 | 0.53 |
| | 22 min | 0.27 | 19.9 | 0.65 |
| | 24 h | 0.55 | 17.6 | 0.088 |
| HPC/HP-β-CD gel | $t_{BP}$ = 11 min | 0.052 | 8.4 | 0.52 |
| | 20 min | 0.15 | 19.1 | 0.58 |
| | 24 h | 0.30 | 14.7 | 0.15 |

[1] 22°C.

embryonic network formation gave relatively homogeneous polymer network, of which effective porosity was small, and also improved amounts of immobilized CDs.

The initial processes for isothermal and temperature-induced embryonic network formation were detected by *in situ* analysis of viscosity. Vibro viscometer possesses sensor plates that can vibrate with a frequency of about 30 Hz. The viscosity was converted from the electric current for keeping a constant frequency in viscous sample solution. Under the isothermal gelation process without TIPS, the viscosity of the pre-gel solution gradually increased with time (Fig. 4a). Abrupt increment of the viscosity was observed when the temperature was stepwise increased to above the LCST at 12.5 (Fig. 4b) and 22 min (Fig. 4c). Since the temperature-induced phase separation of aqueous HPC solution without DVS made the solution viscosity decrease due to the temperature jump above the LCST (data not shown), the abrupt increase of the viscosity observed in Figs. 4b and 4c was derived from not the induced-phase separation but probably increase in molecular mass due to acceleration of the DVS reaction.

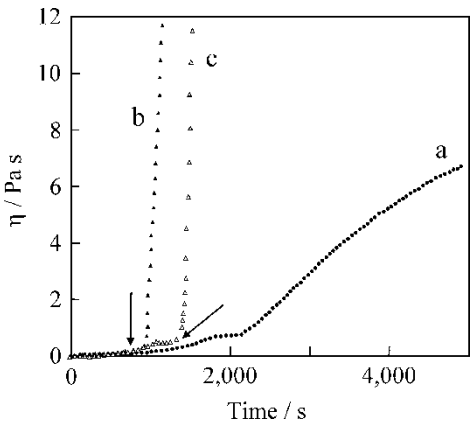


**Fig. 4** Time evolution of the viscosity during gelation process. The solution temperature was stepwise increased to 60°C. (a) conventional HPC/α-CD gel without TIPS ($t_{BP} = 24$ h). (b) $t_{BP} = 12.5$ min. (c) $t_{BP} = 22$ min. The arrows are the guide for eyes at 12.5 and 22 min.

## *Control of prodigiosin production in* S. marcescens *AS-1*

*S. marcescens* is one of the human pathogens of which virulence is regulated by AHL-mediated QS system. As shown in Fig. 5, four different AHL signals were known to produce in *S. marcescens*: *N*-hexanoyl (C6-), *N*-heptanoyl (C7-), *N*-octanoyl- (C8-) and *N*-(3-oxo-hexanoyl)-homoserine lactone (3-oxo-C6-HSL). The AHL production in *S. marcescens* AS-1 was examined using the AHL reporter *Chromobacterium violaceum* CV026 [32]. The reporter can produce a purple pigment violacein in response to the QS activation in the presence of sufficient amounts of short-chained AHLs, while the reporter can not produce any AHLs by itself. The AHLs and other materials were extracted from the culture broth of *S. marcescens* AS-1 by ethylacetate. The AHL sample could be concentrated into dimethyl sulfoxide (DMSO). The sample solution and the chemically synthesized AHL standards were spot on the C18 reverse-phase thin-layer chromatography (TLC) plate, and then developed with 20 vol% methanol aqueous solution. The dried TLC plate was overlaid with agar gel plate containing CV026 cells. After incubation at 28°C for the desired period, C6-HSL and 3-oxo-C6-HSL were clearly detected as the purple spots at the same Rf values of control samples. Consequently, these results suggested the AHL-mediated signaling system in *S. marcescens* AS-1.

Prodigiosin biosynthesis gene cluster is activated by AHL-mediated QS system in the strain [17]. Prodigiosin is one of the secondary metabolites, possessing no essential function for the cell growth. It is convenient to investigate additive effects of free or immobilized CDs using production of the red pigment prodigiosin. In our previous reports, conventional, nonporous CD-immobilized gel sheets could reduce the prodigiosin production when the gel sheets were immersed in the liquid medium throughout the shake culture [9]. However, improvement of the AHL trapping system was expected to maximize the effects on the QS interruption. Figure 6 showed the results of controlling relative

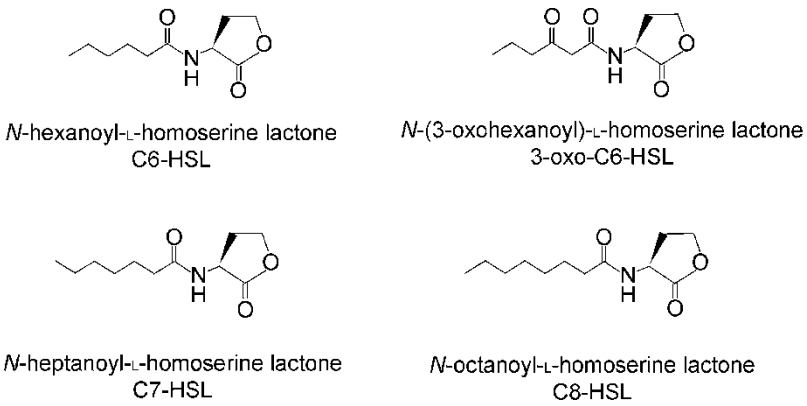


**Fig. 5** Acyl homoserine lactones (AHLs) produced in *Serratia marcescens*.

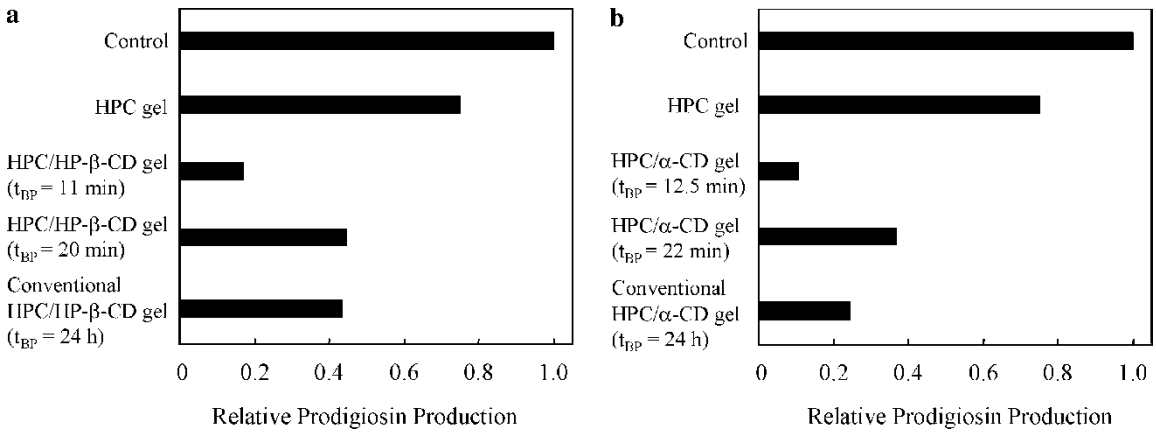


**Fig. 6** Control of relative prodigiosin production with addition of CD-immobilized gel sheets. *S. marcescens* was grown in LB medium at 25°C for 10 h. Six pieces of the gel sheets (10×10×1.5 mm) were immersed in 4 ml of liquid medium.

prodigiosin production using microporous CD-immobilized gel sheets. As compared with the HPC gel sheets without any CDs, HPC/α-CD and HPC/HP-β-CD gel sheets effectively reduced the relative prodigiosin production. Interestingly, the interrupted effects of the QS depended upon the TIPS conditions. For both α-CD and HP-β-CD, higher effects on the QS inhibition were caused by microporous gel (approx. $t_{BP}$ = 10 min). SEM images and effective porosity measurements showed macroscopically heterogeneous polymer network could be created through the TIPS process. The structure was suitable for easier AHL transfer and also reduced the sterific hindrance of immobilized CDs. The prodigiosin production was possible to reduce to approximately 10% using the HPC/α-CD gel sheets prepared by TIPS ($t_{BP}$ = 12.5 min). We previously reported the cavity size dependence of CDs onto the control of prodigiosin production in *S. marcescens* AS-1 [9] and also green pigment pyocyanin production in *P. aeruginosa* AS-3 [33]. The $^1$H-NMR analysis clearly showed the α-CD and β-CD cavities, of which sizes respectively are 0.45 and 0.70 nm, suited to form the inclusion complex with acyl-chains of AHLs. The inhibitory effects on the QS was probably determined by the total amounts of additive CDs, their stability constants of the complex, amounts of the competitive inhibitors derived from LB medium including polypeptone and yeast extract, and the local environmental condition of the immobilized CDs. As shown in Table 1 and Fig. 6, the HPC/α-CD gel prepared as $t_{BP}$ = 12.5 min contained minimum CD amounts (0.13 mmol/g-dry gel) and also had highest effects of the QS interruption.

Chemically synthesized C6-HSL was dissolved in distilled water and then the desired amounts of gel sheets were immersed to determine the AHL uptake into the gel sheets. Equilibrated AHL concentration measured by refractive index gave the stability constant $K$ ($M^{-1}$) for the CD-AHL inclusion complex, while soluble AHLs in the pore water were omitted according to the water content of gels. The $K$ for immobilized α-CD increased with increasing the phase separation time ($t_{DP}$); namely, shorter $t_{BP}$ gave the highest $K$ values (Table 2). These results clearly showed the sterific hindrance could not be negligible when the CD molecules were immobilized onto the polymer using the excess amounts of DVS under conditions of this research. Applying TIPS on CD immobilized gel preparation could avoid the problem of sterific hindrance to improve the CD-AHL complex formation and then enhance effects of the QS control. Above mentioned results clearly indicated that the inhibitory effects of the QS were closely connected with the TIPS control. The CD molecules could easily react with DVS because of possessing lots of OH groups, and then the colloidal HPC/CD particles were formed during $t_{BP}$. It was reported that the residual hydroxyl groups on the surfaces of neighboring HPC particles could be bonded to form a network when the DVS was added at the temperature above the LCST [34]. The CD molecules could be easily immobilized onto the HPC network during $t_{BP}$ (22°C), although CD cavities probably were covered by polymer

**Table 2** Stability constants for inclusion complex between *N*-hexanoyl-L-homoserine lactone and immobilized CDs[1]

| | | | K |
|---|---|---|---|
| | | | $M^{-1}$ |
| HPC/α -CD gel | $t_{BP}$ = 12.5 | min | $5.0 \times 10^2$ |
| | 22 | min | $3.7 \times 10^2$ |
| | 24 | h | $1.2 \times 10^2$ |
| HPC/HP-β-CD gel | $t_{BP}$ = 11 | min | $2.5 \times 10^2$ |
| | 20 | min | $2.8 \times 10^2$ |
| | 24 | h | $0.11 \times 10^2$ |

[1] 22 °C.

network. The timing to increase temperature during the TIPS process was sensitive to avoid formation of dense cross-linked polymer network around CDs.

Reduction of the local AHL concentration is responsible for interruption of the QS cascade in cells. By using CV026 bioassay, we could easily confirm the decrement of the AHL concentration in the culture broth after immersing CD-immobilized gel sheets besides the AHL uptake onto gel sheets. The AHL detection through the violacein production clearly showed that the CD was essentially needed to capture AHLs because of the color difference from a purple shade. In our previous reports, the AHL trapping methods effectively interrupt the QS in *P. aeruginosa* as another opportunistic pathogen. Reporter *P. aeruginosa* PAO1 (pQF50-*lasB*) contains *lasB*-*lacZ* transcriptional fusion where *lacZ* codes the reporter enzyme β–galacosidase [11]. Since the addition of CD-immobilized gel could make the β–galacosidase activity reduce after the cell growth, CD-AHL complex could reduce the AHL concentration and then interrupt the expression of QS-controlled genes. Judging from such experimental results, decrement of the prodigiosin production observed in this research was probably caused by inhibiting expression of the prodigiosin synthetic gene clusters (*pig*). More improvement is to be needed for the AHL trapping efficiency which is important to realize the QS control system using CDs. By applying TIPS technique, the immobilized CD molecules were adequately dispersed to minimize the sterific hindrance of polymer chains and cross-linkers.

## Conclusion

The TIPS process effectively gave the microporous CD-immobilized gel that could be suited for inhibitory control the QS system in *S. marcescens* AS-1. Time evolution of the viscosity change in the initial period of gel preparation revealed the temperature increment during the TIPS drastically increased the cross-linking reaction rates. Therefore, the porous structure was determined by temperature-dependent complicated interactions including phase separation kinetics and cross-linking kinetics after increasing temperature above the LCST of the HPC polymer. Introducing the TIPS structure made the immobilized CDs easier to interact with the diffusible AHLs. The CDs are the safe materials that can be approved for medical use. The host-guest chemistry of CDs and controlled structure of hydrogel matrices can put forward fresh interdisciplinary fields to create versatile materials for infectious disease prevention.

**Acknowledgements** This research was partially supported by the Japan Society for the Promotion Science, a Grant-in-Aid for Scientific Research (C), 19560775, 19510081, 2008.

## References

1. Ikariyama Y, Suzuki S, Aizawa M (1982) Anal Chem 54:1126
2. Ikariyama Y, Furuki M, Aizawa M (1985) Anal Chem 57:496
3. Kokufuta E (1992) Prog Polym Sci 17:647
4. Momji N, Hoffman AS (1987) Appl Biochem Biotech 14:107
5. Chang L, Hoffman AS (1991) J Controlled Rel 15:141
6. Miyata T, Uragami T, Nakamae K (2002) Adv Drug Del Rev 54:79
7. Kokufuta E, Zhang YQ, Tanaka T (1991) Nature 351:302
8. Kato N, Matsumoto H, Nozawa T, Morohoshi T, Ikeda T (2005) Trans Mater Res Soc Jpn 30:827
9. Kato N, Morohoshi T, Matsumoto H, Tanaka T, Ikeda T (2005) Trans Mater Res Soc Jpn 30:815
10. Kato N, Morohoshi T, Nozawa T, Matsumoto H, Ikeda T (2006) J Incl Phenom Macro Chem 56:55
11. Kato N, Tanaka T, Nakagawa S, Morohoshi T, Hiratani K, Ikeda T (2007) J Incl Phenom Macro Chem 57:419
12. Kato N, Ozonoe Y, Umebayashi E, Morohoshi T, Ikeda T (2008) Adv Sci Tech 57:94
13. Greenberg EP (1997) ASM News 63:371
14. Fuqua C, Parsek MR, Greenberg EP (2001) Annu Rev Genet 35:439
15. Kleerebezem M, Quadri LEN, Kulpers OP, de Vos WM (1997) Mol Microbiol 24:895
16. Stover CK et al (2000) Nature 406:959
17. Harris AKP, Williamson NR, Slater H, Cox A, Abbasi S, Foulds I, Simonsen HT, Leeper FJ, Salmond GPC (2004) Microbiol 150:3547
18. Slater H, Crow M, Everson L, Salmond GPC (2003) Mol Microbiol 47:303
19. Kato N, Gehrke SH (2004) Reflexive Polymers and Hydrogels. CRC Press, USA, pp 189–215
20. Huang X, Unno H, Akehata T, Hirasa O (1987) J Chem Eng Jpn 20:123
21. Serizawa T, Wakita K, Akashi M (2002) Macromolecules 35:10
22. Kato N, Takahashi F (1997) Bull Chem Soc Jpn 70:1289
23. Suzuki M, Hirasa O (1993) Adv Polym Sci 110:241
24. Kato N, Sakai Y, Shibata S (2003) Macromolecules 36:961
25. Kato N, Gehrke SH (2004) Colloid Surf B Biointerfaces 38:191
26. Kabra BG, Gehrke SH (1991) Polym Commun 32:322
27. Kabra BG, Gehrke SH, Spontak RJ (1998) Macromolecules 31:2166
28. Kabra BG, Gehrke SH (1994) ACS Symp Ser 573:76
29. Chhabra SR, Sread S, Bainton NJ, Salmond GPC, Stewart GSAB, Williams P, Bycroft BW (1993) J Antibiot 46:441
30. Winson MK, Camara M, Latifi A, Foglino M, Chhabra SR, Daykin M, Bally M, Chapon V, Salmond GPC, Bycroft BW, Lazdunski A, Stewart GSAB, Williams P (1995) Proc Natl Acad Sci USA 92:9427
31. Schaefer AL, Hanzelka BL, Eberhand A, Greenberg EP (1996) J Bacteriol 178:2897
32. Ravin L, Christensen AB, Molin S, Givskov M, Gram L (2001) J Microbiol Methods 44:239
33. Kato N, Nakagawa S, Ozonoe Y, Tanaka T, Morohoshi T, Ikeda T (2007) Proc Fourth Asian Cyclodextrin Conference pp 28–33
34. Hu Z, Lu X, Gao J, Wang C (2000) Adv Mater 12:1173

Progr Colloid Polym Sci (2009) 136:163–170
DOI: 10.1007/2882_2009_23

# Effect of Particles Alignment on Giant Reduction in Dynamic Modulus of Hydrogels Containing Needle-Shaped Magnetic Particles

Tetsu Mitsumata, Yuhei Kosugi, and Shunsuke Ouchi

**Abstract** We investigated the giant reduction in the dynamic modulus of magnetic gels with aligned particles. The magnetic gel is consisting of a κ-carrageenan gel loaded with $\gamma$-$Fe_2O_3$ particles with an aspect ratio of ~8. The magnetic particles were aligned by a weak magnetic field of 50 mT during gelation. The gels with aligned particles demonstrated giant reductions in the storage Young's modulus on the order of $10^6$ Pa due to magnetization; however, no reductions in the storage modulus were observed for the gels with random particles. The storage modulus of gels with aligned particles did not follow the Halpin-Tsai equation above volume fractions of 0.01, indicating the heterogeneous dispersion of the magnetic particles; however, the modulus of the gels with random particles satisfied the equation at all volume fractions, suggesting the random dispersion of the particles. It was noted that the gels with aligned particles demonstrated enhanced nonlinear viscoelasticity and a large value of the loss tangent, while the gels with random particles exhibited weak nonlinear viscoelasticity and a small value of the loss tangent. This indicates that the magnetic particles form a particle network in the gel with aligned particles. It was also found that the magnetic gel with aligned particles did not undergo a marked reduction in the storage modulus when the magnetic field was applied in parallel with the alignment of magnetic particles. This strongly indicates that the giant reduction in dynamic modulus is caused by breaking the particle network developed in the magnetic gel.

**Keywords** Magnetic gels • Magnetorheology • Composite gels • Rheology • Stimuli-responsive gels

T. Mitsumata (✉)
Department of Polymer Science and Engineering,
Graduate School of Engineering, Yamagata University,
Yonezawa, 992-8510, Japan
Email: tetsu@yz.yamagata-.ac.jp

## Introduction

The viscoelastic property of soft materials containing magnetic particles can be modulated by magnetic fields, and the materials are called magnetorheological (MR) materials. For example, a poly(vinyl alcohol) (PVA) gel containing magnetic fluids exhibited a change in Young's modulus of 31 Pa under a magnetic field of $B = 0.5$ T [1]. A silicone gel in which iron particles were aligned demonstrated an increase in storage modulus of 18 kPa at $B = 43$ kA/m when the volume fraction of the iron particles was $\phi = 0.28$. The increase in the modulus decreased under large strains of $\gamma > 0.1$ [2]. An elastomer containing aligned carbonyl iron particles exhibited an increase in shear modulus of 0.6 MPa at $B = 0.8$ T and $\phi = 0.3$ [3]. An elastomer made of natural rubber and carbonyl iron particles underwent an increase in shear modulus of 2 MPa at $B = 0.6$ T and $\phi = 0.27$ [4]. The storage modulus of a silicone elastomer containing carbonyl iron particles increased by 4 MPa upon curing under a magnetic field at $B = 42$ kA/m and $\phi = 0.3$ [5]. An MR rubber with carbonyl iron powder underwent dynamic modulus changes of 2.5 MPa at $B = 170$ kA/m and $\phi \sim 0.5$ [6] and 3.5 MPa at $B = 525$ kA/m and $\phi \sim 0.38$ [7]. It was also revealed using a poly(dimethyl siloxane) elastomer with aligned magnetic particles that the MR effect strongly depends on the direction of the magnetic field [8]. The positive change in the elastic modulus for these materials can be understood by considering the magnetic energy acting between magnetized particles. In contrast, a material has been used to demonstrate the negative change in the elastic modulus due to magnetization.

Our previous studies revealed that a natural polymer gel containing barium ferrite particles demonstrated significant negative changes in the dynamic modulus upon magnetization [9, 10]. The magnetic gel with a volume fraction of magnetic particles 0.39 exhibited reductions in the storage Young's modulus of $\sim 10^7$ Pa and in the loss modulus of $\sim 10^6$ Pa upon magnetization at $B = 1$ T. Magnetic gels demonstrating such a giant reduction in the dynamic

modulus had enhanced nonlinear viscoelasticity, which is called the Payne effect [11]. This originates from the temporal destruction of particle networks, which were made of many fragile (physical) contacts between the magnetic particles. The nonlinear viscoelasticity is dominated by the particle dispersibility in the gel matrix, and the magnetic gels exhibiting the giant MR effect indicates the heterogeneous dispersion such as large agglomeration of magnetic particles. The giant reduction in the dynamic modulus is probably caused by the permanent destruction of the particle network induced upon magnetization, however the mechanism is not well understood.

In the present study, we synthesized a magnetic gel in which the magnetic particle is intensively aligned by a weak magnetic field. The magnetic particle in the gel makes contacts among particles and forms columnar structure at low particle concentrations. Accordingly, the magnetic gel with aligned particles probably undergoes the giant reduction in dynamic modulus at low volume fraction of magnetic particles. The purpose of this study is to obtain the magnetic gel in light weight demonstrating the giant MR effect. The magnetic gel exhibiting the giant reduction in the modulus is heavy because the gel contains large amount of magnetic particles of barium ferrite (>45 wt%) with a density of 5.1 g/cm$^3$. Another purpose is to elucidate the mechanism of the giant MR effect observed in carrageenan magnetic gels. The iron oxide particle ($\gamma$-$Fe_2O_3$) with high aspect ratio was used as a magnetic particle because the particle is easy to be aligned by magnetic fields. We synthesized the magnetic gel with aligned particles and measured the dynamic modulus before and after magnetization at 1 T. In this paper, the rheological properties and particle dispersibility are described and the mechanism of the giant MR effect is discussed.

## Experimental Procedures

### *Synthesis of Magnetic Gel*

Magnetic gels consisting of fine magnetic particles and κ-carrageenan, a natural polymer, were synthesized. The carrageenan is a sodium type one with a molecular weight of 857 kDa, and the sodium content was 0.57 wt%. A pre-gel solution of the magnetic gel was prepared by mixing a 3 wt.% k-carrageenan (CS-530, San-Ei Gen F.F.I., Osaka) aqueous solution and iron oxides ($\gamma$-$Fe_2O_3$, Titankogyo, Tokyo) at 90°C using a mechanical stirrer for 30 min. Scanning electron microscope (SEM) image of these particles in a dry state is shown in Fig. 1(a). The magnetic particle, primary particle, has an anisotropic shape with 0.1 μm in diameter and 0.8 μm in long. The size distribution of the magnetic particles in deionised water was obtained using a particle size analyzer (Mastersizer 2000, Malvern Instruments, Malvern) and is shown in Fig. 1(b). In pure water, the agglomerate of iron oxide had a large mean volume diameter of 0.71 μm, which corresponds to the diameter in the dry state. For gels with random particles, the pre-gel solution was poured into a glass mold of 10 mm thickness and was cooled to 20°C without exposing magnetic fields. For gels with aligned particles, the pre-gel solution was cooled to room temperature under uniform magnetic field of 50 mT for 20 min (Fig. 2). The densities of carrageenan gel and magnetic gel were measured

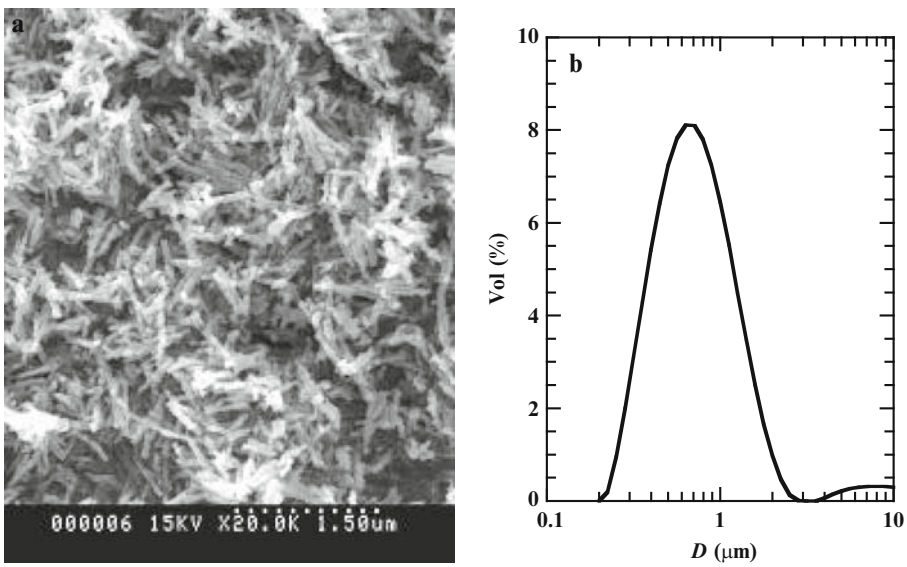


**Fig. 1** (a) SEM photograph and (b) particle size distribution of $\gamma$-$Fe_2O_3$ magnetic particles in deionized water

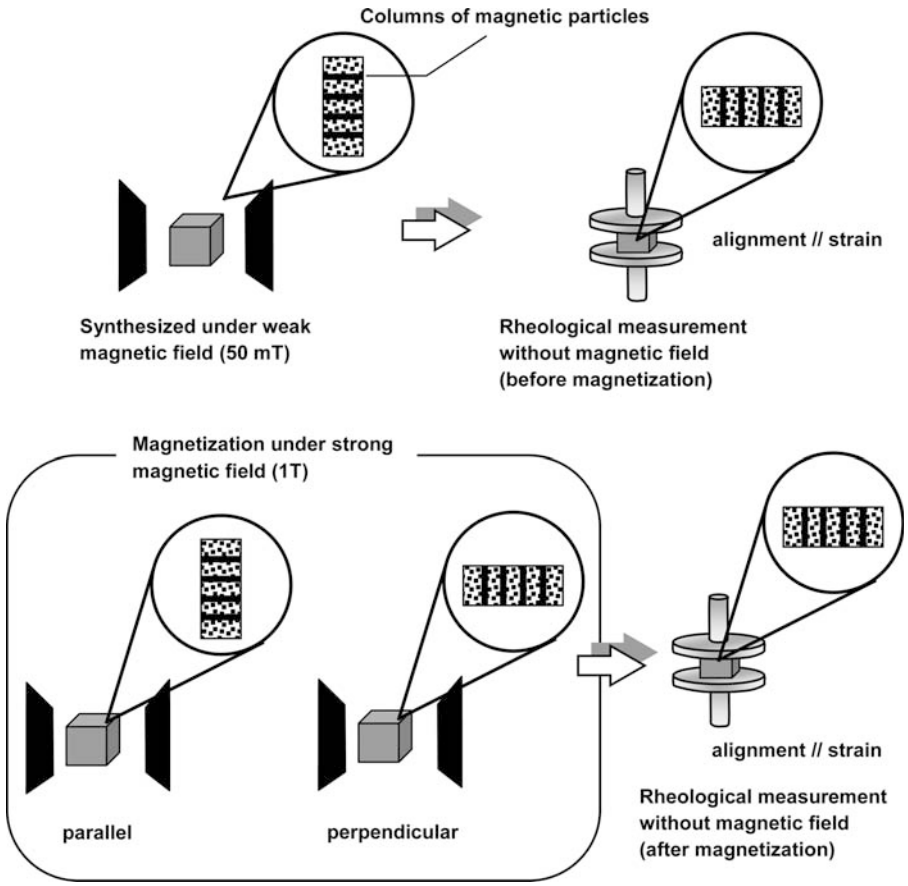


**Fig. 2** Schematic illustration representing synthesis and rheological measurements in the present study

using an electric densimeter (Mirage MD-300S, Osaka), and the density of magnetic particles was measured using a pycnometer.

## Rheological measurements

Dynamic viscoelastic measurements were carried out using a rheometer (Dve-V4, Rheology, Kyoto). Oscillatory compressional strain was applied to the magnetic gel and the stress response was measured; hence, the elastic modulus obtained is Young's modulus. The frequency was 1 Hz, and the oscillation amplitude was varied from approximately $10^{-5}$ to $10^{-2}$. The offset strain with respect to the sample thickness was kept at 3 %. The temperature was maintained at $23.0 \pm 1.0$°C during viscoelastic measurement. The shape of samples for the mechanical measurement was cubic with dimensions of approximately $10 \times 10 \times 10$ mm. A schematic illustration representing the rheological measurement studied here is shown in Fig. 2. First, we placed a sample in the rheometer and measured its complex modulus before magnetization; then the sample was placed in an electromagnet to magnetize it at a field strength of 1 T at room temperature. Afterwards, the modulus was measured again. Note that the viscoelastic measurement was carried out in the absence of magnetic fields. Each modulus was determined from an average of three measurements using different samples.

## Magnetic measurements

Magnetization measurements in fields up to 1 T were carried out using a vibrating sample magnetometer (VSM-P7, Toei Industrial, Tokyo) at room temperature. The samples were disks with dimensions of 2 mm diameter and 1 mm thickness. Each sample was wrapped in a thin film of poly(vinyl chloride) to prevent the evaporation of water from the sample.

## Microscope and SEM observations

Observations were carried out using an upright microscope (Axio Imager M1m, Carl Zeiss, Gttingen) with transmitted light illumination at room temperature. Magnetic gels with volume fraction of 0.01 were prepared on a glass by mixing small amounts of magnetic particles and 3 wt.%

κ-carrageenan aqueous solutions (total weight was ∼0.1 g), while heating by a hot stage at 90°C. When the samples with high volume fractions of magnetic particles such as the samples used in the rheological measurement, the light transmitted from a microscope was completely blocked by the samples. The shape and size of the magnetic particles were observed using a SEM with an accelerating voltage of 15 kV (S-800, Hitachi High-Technologies, Tokyo).

## Results and Discussion

The volume fraction of magnetic particles was determined using the following equation:

$$\phi = \frac{d_{MG} - d_{CG}}{d_{MP} - d_{CG}} \quad (1)$$

Here, $d_{MG}$ denotes the density of the magnetic gel, $d_{CG}$ is the density of the carrageenan gel matrix, and $d_{MP}$ is the density of the magnetic particles. The density of 3 wt.% carrageenan gel was measured to be 1.033 g/cm$^3$. The measured density of $Fe_2O_3$ particles used in this study was 4.387 g/cm$^3$, respectively, by Archimedes' principle.

### *Rheology of magnetic gels before magnetization*

The strain dependence of the storage modulus of magnetic gels with various volume fractions of magnetic particles is shown in Figs. 3(a) and (b). The storage modulus of the carrageenan gel without particles was $\sim 3.9 \times 10^5$ Pa and exhibited little sensitivity to strain. For both magnetic gels with random and aligned particles, the storage modulus at low strains increased with the volume fraction. However, the storage modulus at high strains had the same value for all magnetic gels, independent of the volume fraction or the alignment of particle. This means that the enhanced nonlinear viscoelastic response is caused by the contact between magnetic particles; this phenomenon has been called the Payne effect [11]. This originates from the temporary destruction of the contacts between magnetic particles which starts to occur from extremely small strains. In the linear viscoelastic regime, the increase in the storage modulus for gels with aligned particles was much higher than that for gels with random particles. The storage modulus in parallel to the particle alignment was 1.3 times larger than that in perpendicular to the alignmentm. These results suggest that the gels with aligned particles have a fragile structure that is easily broken by small strains, in contrast to the gels with random particles.

Fig. 4 displays the storage modulus of magnetic gels as a function of the volume fraction of magnetic particles. The solid line in the figure represents the modulus $E'$, calculated

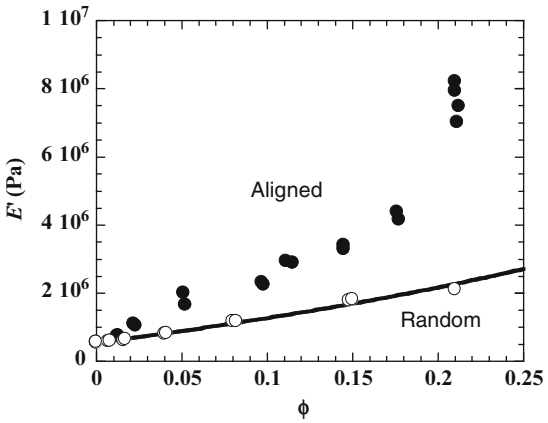


**Fig. 4** Volume fraction dependence of the storage modulus for magnetic gels with (○) random and (●) aligned particles

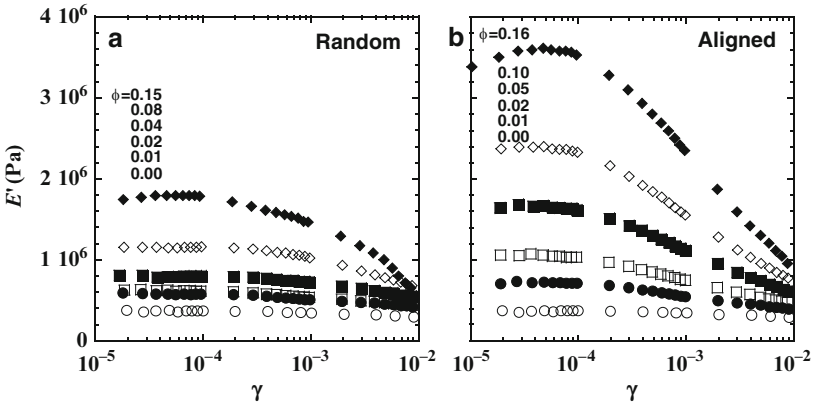


**Fig. 3** Strain dependence of the storage modulus for magnetic gels with various volume fractions of magnetic particles at 1 Hz, (a) random particle, (b) aligned particle.

by the following Halpin-Tsai equation, for a random dispersion of particles with anisotropic shape [12]:

$$E' = E'_0 \frac{1 + \zeta\eta\phi}{1 - \eta\phi}$$
$$\eta = \frac{E'_f/E'_0 - 1}{E'_f/E'_0 + \zeta} \quad (2)$$

where $E'$, $E'_o$, and $E'_f$ are the storage moduli of the magnetic gel, carrageenan gel, and the magnetic particle, respectively. The value of $\eta$ can be approximated to $\eta \approx 1$ because the Young's modulus of the magnetic particle is much higher than that of carrageenan gel. $\zeta$ is the aspect ratio of the particle, i.e. $\zeta = 2(l/t)$ where $l$ and $t$ are the length and thickenss of the particle. For magnetic gels with aligned particles, the storage modulus obeyed eq. (2) only below a volume fraction of ~0.01, but had a higher value than the theoretical values above this volume fraction. We consider that the $Fe_2O_3$ particles come in contact with each other and form a structure with a high modulus. At the volume fractions above approximately 0.18 the relative storage modulus increased dramatically with the volume fraction, indicating the 3-dimentional percolation of magnetic particles. The relative storage modulus above the percolation threshold can be explained by the following equation,

$$E'/E'_0 \propto (\phi - \phi_c)^n \quad (3)$$

Here, $\phi_c$ stands for the percolation threshold. Least mean squares fitting was carried out hypothesizing the percolation threshold of $\phi_c = 0.17$. The exponent in the eq.(3) was determined to be 1.3, which was in good agreement with the theoretical value of percolation $(1.2 < n < 1.4)$ [13]. Also, this coincides with the percolation threshold of PVA gels containing non magnetic aluminum hydroxide particles ($\phi \sim 0.18$) [14]. On the other hand, the storage modulus of magnetic gels with random particles followed eq. (2) over the whole range of volume fractions. Thus, the $Fe_2O_3$ particles were dispersed randomly in the carrageenan gel, and the particles aligned and make a columnar structure by the weak magnetic field which was applied during the gelation. According to the fitting by eq.(2), the fitting value of $\zeta$ was determined to be 11 which is in aggreement with the twice of the aspect ratio (=16).

Figure 5 shows the volume fraction dependence of the value of $E'/E'_m$ showing the degree of nonlinear viscoelasticity. $E'/E'_m$ is the storage modulus divided by maximum storage modulus $E'_m$ in the linear viscoelastic regime shown in Fig. 3. $E'/E'_m$ for carrageenan gel without magnetic particles had a value of approximately 0.7. For random particles, the $E'/E'_m$ took high values compared to the gels with aligned particles, and linearly decreased with the volume fraction. The magnetic gels with aligned particles underwent low values of $E'/E'_m$ even at low volume fractions. The lowest values of $E'/E'_m$ for gels with random and aligned particles at $\phi \sim 0.21$ were 0.28 and 0.16, respectively.

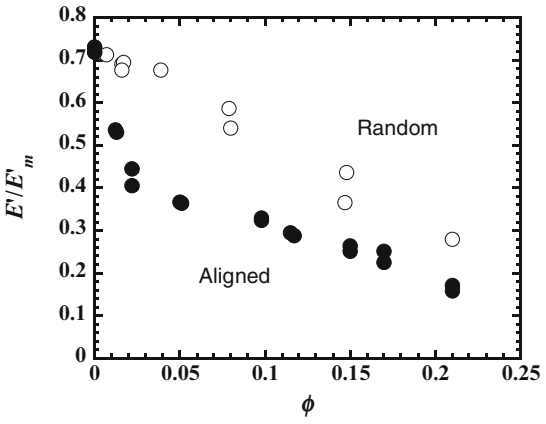


**Fig. 5** Storage modulus normalized by the modulus at low strains as a function of the volume fraction of magnetic particles, (○): random particle, (●): aligned particle

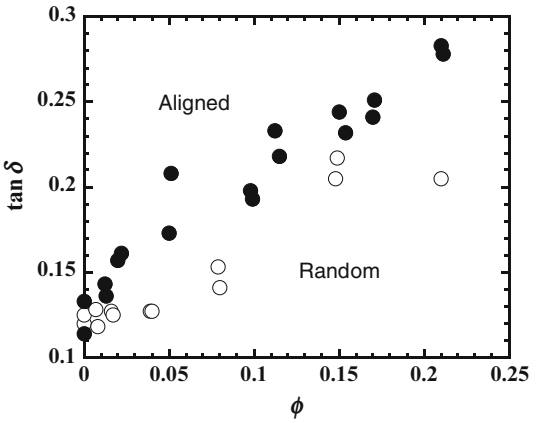


**Fig. 6** Loss tangent at $\gamma = 0.1$ vs volume fraction of magnetic particles, (○): random particle, (●): aligned particle

The relationship between the loss tangent at $\gamma = 10^{-2}$ and the volume fraction of magnetic particles is presented in Fig. 6. However, the strain is in the nonlinear viscoelastic region, the value of loss tangent is considered to indicate the energy loss originating from the destruction of the particle network. The loss tangent in the linear viscoelastic region is dominated by the friction energy among magnetic particles. Contrary to this, the loss tangent in the nonlinear region is attributed to the destruction energy of the particle network; therefore, the loss tangent in the nonlinear region gives us the information relating to the brittleness or the number of contact of the particle network. The loss tangent for carrageenan gel without magnetic particles was approximately 0.12. For the magnetic gels with aligned particles, the loss tangent increased rapidly and then gradually increased with

volume fraction. On the other hand, magnetic gels with random particles, the loss tangent linearly increased with the volume fraction.

## Magnetization effect on rheology

Figure 7 shows the strain dependence of the storage modulus for magnetic gels with random and aligned particles. Closed symbols represent the storage modulus after magnetization. For the magnetic gel with aligned particles, the modulus apparently decreased upon magnetization. It is worth to mention that the modulus change with ~0.1 MPa occurred at only $\phi = 0.01$. However, no change in the modulus was observed for the magnetic gel with random particles.

Figure 8 shows the relationship between the change in the storage modulus before and after magnetization at 1 T as a function of the volume fraction of the magnetic particles. For magnetic gels with random particles, no clear change in the modulus was observed at $\phi < 0.1$, however positive changes in the modulus were observed above the volume fraction; that is normal MR effect. This originates from the magnetic interaction between $Fe_2O_3$ particles which were dispersed randomly in the carrageenan gel. The changes in the modulus for magnetic gels with aligned particles were insensitive to the volume fraction at $\phi < 0.17$, and exhibited a sudden increase over 1.0 MPa at $\phi = 0.21$ that is in the percolated regime. The magnetically induced modulus can be written as the following equation [10],

$$\Delta E' \sim \mu_0 (M_r \phi)^2 \tag{4}$$

Here, $\triangle E'$ is the change in the storage modulus due to magnetization, $\mu_0$ represents the magnetic susceptibility in vacuum, $M_r$ is the remanent magnetization of the magnetic particles, and $\phi$ is the volume fraction of the magnetic particles. The change in the storage modulus for gels with barium ferrite at $\phi = 0.21$ was estimated to be 42 Pa using a value of $M_r = 0.29 \times 10^5$ A/m. Therefore, the modulus change observed here in MPa order cannot be explained by the magnetic interaction between magnetic particles.

The magnetic gels demonstrating the giant MR effect have enhanced nonlinear viscoelasticity ($E'/E'_m < 0.2$) and large values of the loss tangent ($\tan\delta > 0.25$), which coincides with the result for magnetic gels with barium ferrite [15]. This strongly indicates that the giant reduction in the storage modulus is caused by the destruction of the local network of magnetic particles. Figure 9 shows the relationship between the change in the storage modulus before and after magnetization at 1 T as a function of the volume

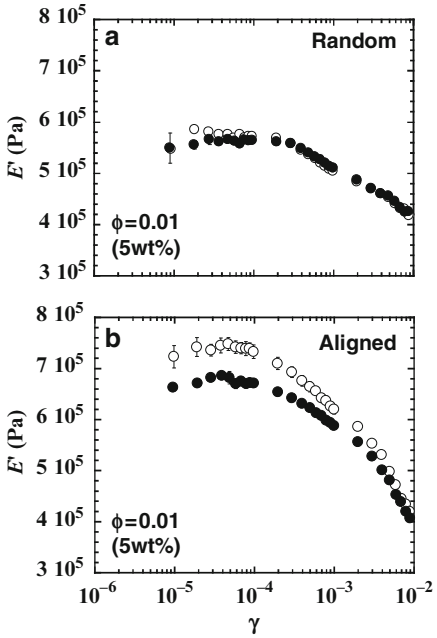


**Fig. 7** Strain dependence of the storage modulus for magnetic gels with (a) random and (b) aligned particles, (○): before magnetization, (●): after magnetization

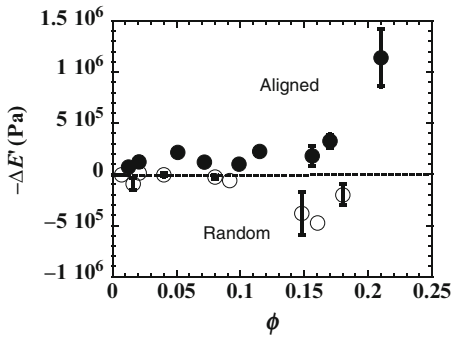


**Fig. 8** Change in storage modulus due to magnetization vs volume fraction of magnetic particles, (○) random particles, (●) aligned particles

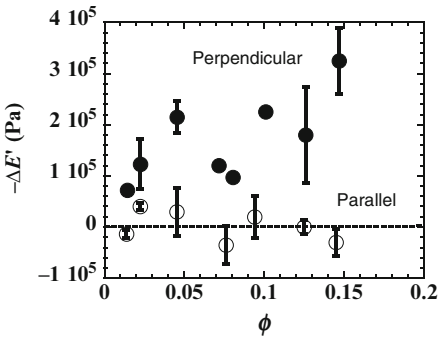


**Fig. 9** Change in storage modulus due to magnetization vs volume fraction of magnetic particles for (○) parallel and (●) perpendicular geometries

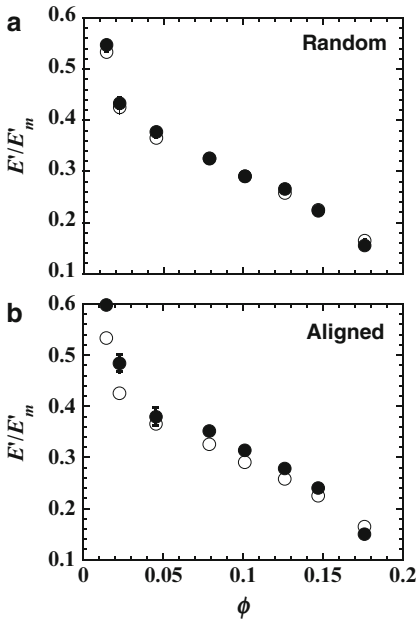


**Fig. 10** Degree of nonlinear viscoelasticity vs volume fraction of magnetic particles for (a) random and (b) aligned particles; (○): before magnetization, (●): after magnetization

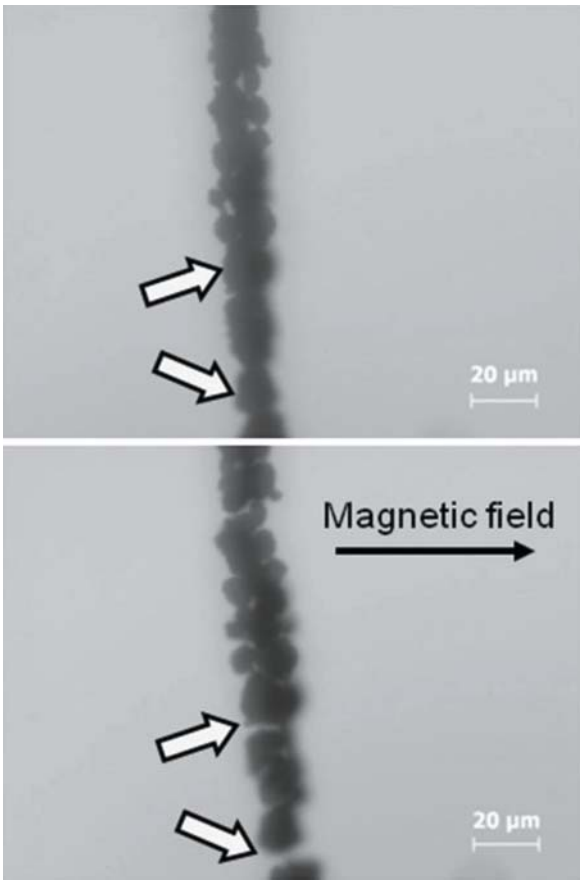


**Fig. 11** Microphotographs of magnetic gels with aligned particles before (top) and after (bottom) magnetization

fraction of the magnetic particles. The change in the storage modulus increased with the volume fraction when the particle alignment was perpendicular to the magnetic field. However, no clear change in the modulus was observed when the particle alignment was parallel to the field. This evidence suggests that the giant MR effect is caused by the destruction of particle contacts in the particle network, i.e. the columnar structure is cut microscopically by the magnetic field, although the gel keeps its macroscopic shpae. Actually, for magnetic gels with aligned particles, the magnetization effect was seen in only low strains; the storage modulus at $\gamma = 0.01$ was invariable upon magnetization.

As described in Figure 5, the degree of nonlinear viscoelasticity gives us the information about the degree of contact between magnetic particles. We investigated the difference in the degree of nonlinear viscoelasticity before and after magnetization. Figure 10 shows the volume fraction dependence of the degree of nonlinear viscoelasticity, $E'/E'_{\mathrm{m}}$. For magnetic gels with random particles, the degree of nonlinearity did not change upon magnetization. The degree of nonlinearity for magnetic gels with aligned particles exhibited obvious decrease after magnetization; that is, the nonlinearity became weaker after magnetization. This means the number of particle contact in the columnar structure decreased due to magnetization.

Figure 11 shows microphotographs of magnetic gels with aligned particles before and after magnetization. The concentration of carrageenan was 0.5 wt% and the volume fraction of magnetic particles was $\phi = 0.01$. The column consists of agglomerations of magnetic particles with a diameter of approximately 10 μm, and aligns in parallel with a weak magnetic field which is applied during synthesis of the gel. After exposing the gel to strong magnetic fields, the agglomeration elongated to the direction of the magnetic field, while maintaining the contour of the columnar structure. This may be caused by a magnetic effect that the deformation forces to decrease the demagnetizing field within the agglomeration. The direct microscopic observation supports the idea that the giant MR effect is caused by breaking the particle network due to magnetization; although its mechanism is now unclear.

## Conclusion

We investigated the giant reduction in the dynamic modulus of κ-carrageenan magnetic gels in which γ-$Fe_2O_3$ particles were aligned by a weak magnetic field of 50 mT during the gelation. The gels with aligned particles demonstrated giant reductions in the storage Young's modulus on the order of $10^6$ Pa due to magnetization; however, no reductions in the storage modulus were observed for the gels with

random particles. The storage modulus of gels with aligned particles did not follow the Halpin-Tsai equation above volume fractions of 0.01, indicating the heterogeneous dispersion of the magnetic particles; however, the modulus of the gels with random particles satisfied the equation at all volume fractions, suggesting the random dispersion of the particles. It was noted that the gels with aligned particles demonstrated enhanced nonlinear viscoelasticity and a large value of the loss tangent, while the gels with random particles exhibited weak nonlinear viscoelasticity and a small value of the loss tangent. This indicates that the magnetic particles form a particle network in the gel with aligned particles. It was also found that the magnetic gel with aligned particles did not undergo a marked reduction in the Young's modulus when the magnetic field was applied in parallel with the alignment of magnetic particles. This strongly indicates that the giant reduction in dynamic modulus is caused by breaking the particle network developed in the magnetic gel. This investigation reveals that the giant MR effect is caused by breaking the particle network due to magnetization although its mechanism is now unclear.

**Acknowledgements** We are grateful to San-Ei Gen F.F.I., Inc. for the offer of k-carrageenan. This research is partially supported by the SUZUKI foundation. We also thank to Dr. T. Okazaki of Bando chemicals for taking SEM photographs and valuable discussions.

## References

1. Mitsumata T, Ikeda K, Gong JP, Osada Y, Szabo D, Zrinyi M (1999) J App Phys 85:8451
2. Shiga T, Okada A, Kurauchi T (1995) J Appl Polym Sci 58:787
3. Jolly MR, Carlson JD, Munoz BC, Bullions TA (1996) J Int Mat Sys Struct 7:613
4. Ginder JM, Clark SM, Schlotter WF, Nichols ME (2002) Int J Modern Phys B 16:2412
5. Bossis G, Bellan C (2002) Int J Modern Phys B 16:2447
6. Lokander M, Stenberg B (2003) Polym Test 22:245
7. Lokander M, Stenberg B (2003) Polym Test 22:677
8. Varga Z, Filipcsei G, Zrinyi M (2006) Polymer 47:227
9. Mitsumata T, Nagata A, Sakai K, Takimoto J (2005) Macromol Rapid Commun 26:1538
10. Mitsumata T, Sakai K, Takimoto J (2006) J Phys Chem 110:20217
11. Payne AR (1960) J Appl Polym Sci 3:127
12. Halpin JC, Kardos JL (1976) Polym Eng Sci 16:344
13. Onoda GY, Liniger ER (1990) Phys Rev Lett 64:2727
14. Mitsumata T, Hachiya T, Nitta K (2008) Euro Polym J 44:2574
15. Mitsumata T, Wakabayashi T, Okazaki T (2008) J Phys Chem 112:14132

Progr Colloid Polym Sci (2009) 136:171–176
DOI: 10.1007/2882_2009_24

# Molecular Diffusion in Polysaccharide Gel Systems as Observed by NMR

Shingo Matsukawa, Daisuke Sagae, and Akiko Mogi

**Abstract** The diffusion coefficients $D$ of dendrimers in agar gel and pullulan in gellan gel were determined by pulsed field gradient spin-echo (PFGSE) NMR measurements. The ratio of $D$ to $D_0$ (diffusion coefficient in dilute solution) was used to estimate mesh size. The mesh size increased as the temperature fell below the gelling temperature, suggesting that the solute polysaccharides are involved in aggregation. Changes in mesh size explain the experimental results of water exudation from a stored agar gel under compression and the heat resistance of gellan gel in the presence of divalent cations.

**Keywords** Molecular diffusion • Pulsed field gradient spin-echo NMR • Gel mesh size • Aggregation of polysaccharide

## Introduction

The diffusion of molecules in gel depends on intermolecular interaction between the diffusant molecule and the network chains. The diffusion coefficient $D$ of the diffusant decreases significantly when intermolecular interaction occurs via hydrogen bonding [1] or hydrophobic interaction [2] (Fig. 1a). When no direct intermolecular interaction occurs, $D$ of the diffusant decreases because of hydrodynamic interaction via solvent movement [3] (Fig. 1b). When the diffusant has a large molecular weight and is entangled with the network chains, topological interaction becomes the dominant controlling factor in its diffusion within gel (Fig. 1c).

In synthetic gel, the network size is dependent on concentration [3,4], which affects hydrodynamic interaction. Many polysaccharides form network structures via the aggregation of polysaccharide chains. When the diffusant is involved in the aggregation, its mobility is restricted, resulting in a marked decrease in $D$; otherwise, the diffusant diffuses in the network interspace. In this latter case, $D$ is affected by hydrodynamic interaction with the network and the change in polymer concentration caused by the inclusion of solute polymers into the aggregates. As a consequence, $D$ varies even if the polymer concentration remains constant when the network structure is altered by the aggregation.

NMR measurements provide information about the mobility of molecules in gel. The spin-lattice relaxation time ($T_1$) and the spin-spin relaxation time ($T_2$) reflect the local mobility and flexibility of the molecules, respectively,

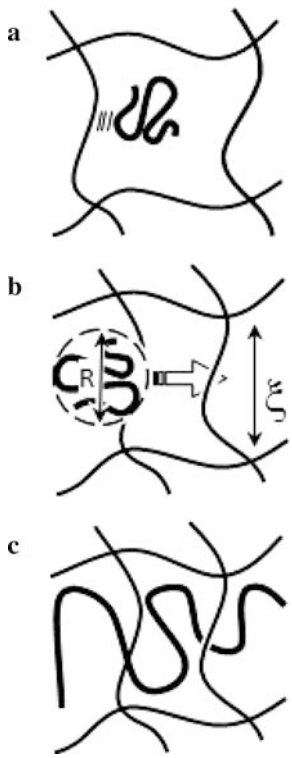


**Fig. 1** Schematic representation of molecular diffusion in gel with intermolecular interaction (a), hydrodynamic interaction (b), and topological interaction (c)

S. Matsukawa (✉)
Department of Food Science and Technology,
Tokyo University of Marine Science and Technology,
4-5-7 Konan, Minato-ku, Tokyo, 108-8477, Japan
Email: matsukaw@kaiyodai.ac.jp

and D measured by field gradient NMR reflects the displacement of a molecule by self-diffusion. In this paper, the diffusion behavior of molecules and the network structures of polysaccharide gels are elucidated based on the results of field gradient NMR measurements. Two systems were employed: a 1.3 wt% agar solution containing 0.1 wt% dendrimer, which is a highly branched spherical molecule, and a 1 wt% gellan solution containing 5 mM $CaCl_2$ and 0.1 wt% pullulan. The principle of the diffusion measurement is also provided in Appendix for a better understanding of the experimental results.

## Materials and Methods

A 5% methanol solution of dendrimer (poly(amidoamine) dendrimer, ethylenediamine core, generation 4.5, COONa terminal groups) was purchased from Sigma-Aldrich Ltd.

The solution was repeatedly diluted with distilled water and evaporated to exchange the methanol solution with the distilled water. Yamato, agar powder, was supplied by Ina Food Industry Co., Ltd. (Nagano, Japan). The dendrimer solution was mixed with a 1.5 wt% agar solution at 60°C to give a 1.3 wt% agar solution containing 0.1 wt% dendrimer.

Gellan gum was supplied by San-Ei Gen FFI Co. (Osaka, Japan) and ion-exchanged from K type to Na type by dialyzing against NaCl solution [6]. The gellan solutions were prepared in the same manner as that previously reported [7]. Briefly, powdered gellan gum was stirred in distilled water to afford a concentration of 2 wt%, and then allowed to swell and disperse homogeneously at 40°C overnight. The resulting solution was then stirred at 70°C for 2 h and at 90°C for 30 min to allow for complete dissolution, and then mixed with 10 mM $CaCl_2$ solution containing 0.2 wt% pullulan (Mw = 112,000) at 90°C, and stirred at 90°C for 30 min to produce a 1 wt% gellan solution containing 5 mM $CaCl_2$ and 0.1 wt% pullulan. The obtained solution was immediately poured into each sample cell of a plate preheated at 85°C for thermal scanning rheological measurements.

Thermal scanning rheological measurements were performed in the linear viscoelastic regime at a frequency of 0.07 Hz with a RheoStress RS50 rheometer (HAAKE Co., Ltd., Germany), using a parallel-plate geometry of 35 mm diameter and 1 mm gap. The plates were kept at 85°C before sample loading and covered with a glass cover to avoid sample drying during measurements. After sample loading, the temperature was decreased to 5°C at a rate of 0.5°C/min.

High-resolution $^1$H NMR spectra were measured with a Bruker Avance II 400WB spectrometer operating at 400.13 MHz. The temperature was controlled from 60°C to 20°C with a variable temperature unit (Bruker BVT-3200) and was continuously monitored with an optical fiber thermometer (Takaoka Electric Manufacturing Co., Tokyo, Japan) placed in the sample tube. Each measurement was carried out while confirming that the sample had reached equilibrium after setting the temperature (approximately 20 min). The pulsed field gradient stimulated spin-echo sequence was used, where two field gradients (max strength = 5.0 T/m, duration = 1 ms) were applied with a separation of 10 ms.

## Results and Discussion

**Network size in agar gels**. The gelation of polysaccharides is induced by the aggregation of polysaccharide chains. Polysaccharide chains that aggregate to form a network have a strongly restricted molecular motion, commonly resulting in very short $^1$H $T_2$; consequently, the echo signal for the polysaccharide chains of the aggregates disappears because of $T_2$ decay. Figure 2 shows changes in the $^1$H NMR spectra of the 1.3 wt% agar gel containing 0.1 wt% dendrimer as the temperature was decreased from 58°C to 20°C. The peak intensities of the agar chains started to decrease at around 40°C, indicating that a portion of the agar chains aggregated at the gelling temperature, $T_{gel}$, to form the network and that another portion of the agar chains remained as solute within the network at $T_{gel}$; these chains gradually aggregated to form the network as the temperature decreased further.

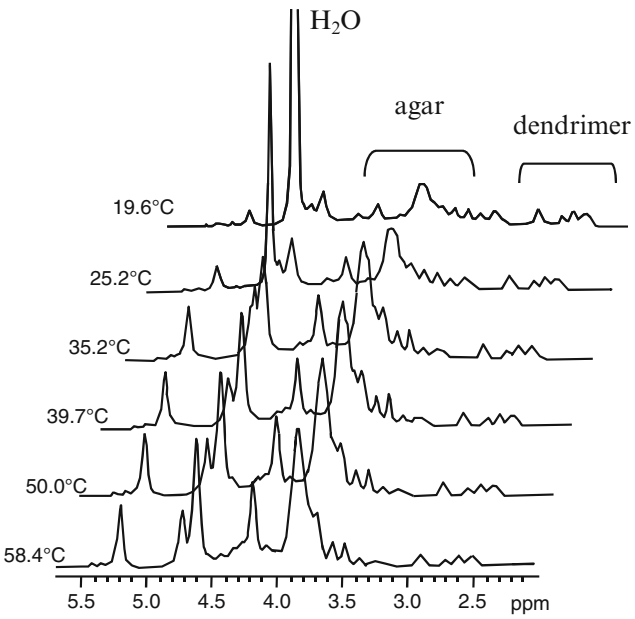


**Fig. 2** Progressive changes in $^1$H NMR spectra of a 1.3 wt% agar gel containing 0.1 wt% dendrimer with decreasing temperature

The peaks of the dendrimer did not decrease with decreasing temperature, indicating that the dendrimer was not involved in the aggregation of agar chains. We therefore interpret that the dendrimer has no intermolecular interaction with agar chains other than hydrodynamic interaction.

Hydrodynamic interaction would be reflected by the diffusion coefficient of the dendrimer, $D_{\mathrm{dend}}$, in the agar solution. Figure 3 shows the temperature dependence of $D_{\mathrm{dend}}$ in the agar solution. $D_{\mathrm{dend}}$ in dilute solution, $D_{\mathrm{dend,0}}$, was also measured at various temperatures. $D_{\mathrm{dend,0}}$ showed a dependence on diffusion time, $\Delta$, at each temperature, probably related to convection in the dilute solution. This dependence was pronounced at high temperatures (data not shown). When the directions of convection at each part in the sample solution negligibly change during $\Delta$, the mean square of displacement by convection in the z direction (field gradient direction), $\langle z^2 \rangle_{\mathrm{conv}}$, is given by the square of $\langle v_z \rangle \Delta$, where $\langle v_z \rangle$ is the average velocity of the convection in the z direction. The apparent $D$ observed at $\Delta$, $D_{\mathrm{app}}(\Delta)$, is therefore expressed as

$$\mathrm{D_{app}}(\Delta) = \frac{(\mathrm{z}^2)_{\mathrm{diff}^+}(z^2)_{\mathrm{conv}}}{\Delta} = \frac{D_0\Delta + ((v_z)\Delta)^2}{\Delta} = D_0 + \langle v_z \rangle^2 \Delta \tag{1}$$

where $\langle z^2 \rangle_{\mathrm{diff}}$ is the mean square of displacement by diffusion. At lower temperatures, $D_{\mathrm{app}}(\Delta)$ shows a linear dependence on $\Delta$; therefore, $D_{\mathrm{dend,0}}$ at 30°C was obtained using Eq. (1). From $D_{\mathrm{dend,0}}$ at 30°C, the hydrodynamic radius $R_H$ of the dendrimer at 30°C was calculated by

$$D_{\mathrm{dend,0}} = \mathrm{k_B}T/(6\mathrm{p}\pi\eta_{\mathrm{s}}R_{\mathrm{H}}), \tag{2}$$

where $\mathrm{k_{B,}}$ $T$, and $\eta_s$ are the Boltzmann constant, absolute temperature, and viscosity of the solvent, respectively. Because $R_{\mathrm{H}}$ of the dendrimer is thought to be constant with changing temperature, $D_{\mathrm{dend,0}}$ at various temperatures was calculated using Eq. (2) (see Fig. 3).

As seen in Fig. 3, $D_{\mathrm{dend}}$ is smaller than $D_{\mathrm{dend,0}}$ and was observed to decrease with decreasing temperature. As a parameter that describes the restriction of diffusion in gel, $D/D_0$ is plotted against temperature in Fig. 4. $D/D_0$ decreased with decreasing temperature above $T_{\mathrm{gel}}$ (ca. 40°C). The agar used in this study is a mixture of agarose and agaropectin with variable chemical structure and molecular weight. Therefore, it is considered that a portion of the agar chains forms micro-aggregates that do not induce gelation, but restrict diffusion of the dendrimer. Below $T_{\mathrm{gel}}$, $D/D_0$ increases with decreasing temperature. When $D/D_0$ is changed by hydrodynamic interaction with the agar network, $D/D_0$ is expressed as follows [4,5]:

$$D/D_0 = \exp(-R_H/\xi), \tag{3}$$

where $\xi$ is the dynamic shielding length, considered to represent the hydrodynamic mesh size. The values of $\xi$ corresponding to the $D/D_0$ values calculated using Eq. (3) are indicated on the right-hand axis in Fig. 4, where an increase in $D/D_0$ indicates an increase in mesh size. As shown in Fig. 2, solute agar chains are involved in aggregation below $T_{\mathrm{gel}}$, thereby accounting for the decrease in peak intensity. This inclusion into the aggregation is considered to reduce the local agar concentration and enlarge the mesh size (Fig. 5).

The rate of water exudation from the agar gel under compression increased after storage for 3 days, suggesting an increase in mesh size during storage (data not shown). Figure 6 shows the dependence on storage time of $D/D_0$ values for the dendrimer in 1.3 wt% agar gel after sudden cooling from 58°C to 25°C. The values of $\xi$ corresponding to the $D/D_0$ values calculated using Eq. (3) are indicated on the right-hand axis. The initial value of $\xi$ is smaller than that at 25°C (see Fig. 4), suggesting that sudden cooling creates a network structure with a smaller mesh size than that achieved by

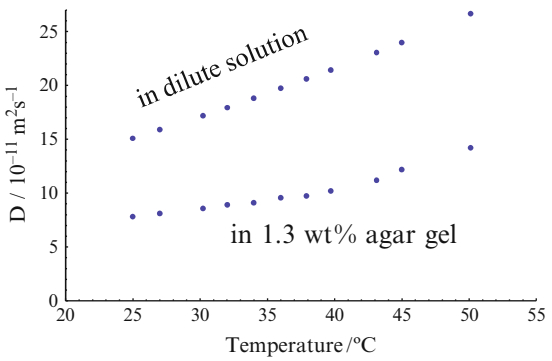


**Fig. 3** Temperature dependence of the diffusion coefficient ($D$) of a dendrimer. $D$ in solution was calculated from the theoretical temperature dependence of the dilute solution

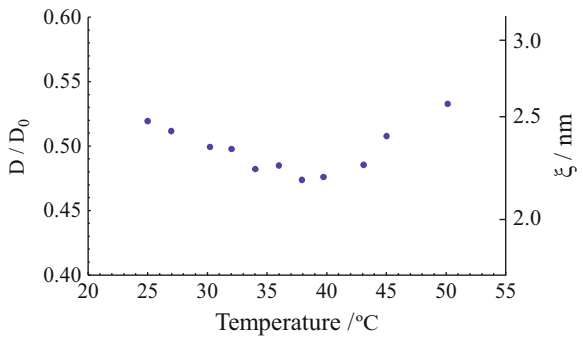


**Fig. 4** Temperature dependence of the $D/D_0$ of a dendrimer in 1.3 wt% agar gel. The corresponding $\xi$, calculated using $D/D_0 = \exp(-Rh/\xi)$, is indicated on the right-hand axis

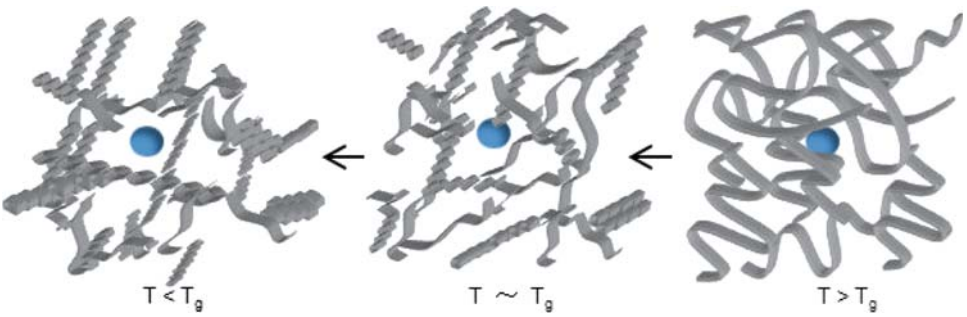


**Fig. 5** Schematic of the structural changes that occur in agar gel during the cooling process

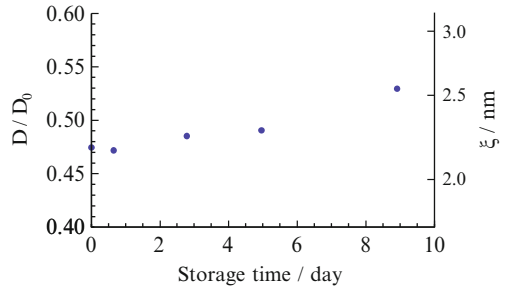


**Fig. 6** Storage-time dependence of the $D/D_0$ value of dendrimer in 1.3 wt% agar gel. The corresponding $\xi$ is indicated on the right-hand axis

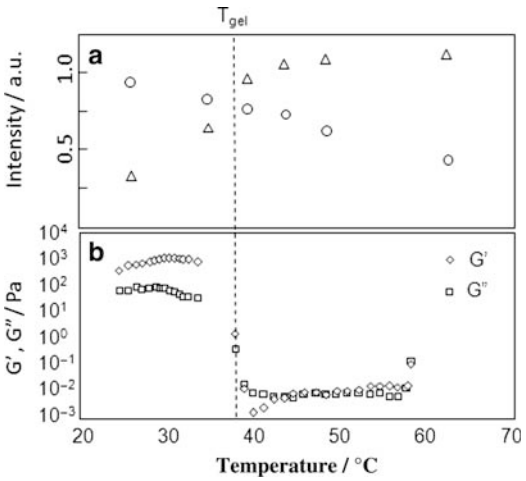


**Fig. 7** Temperature dependence of NMR signal intensity for gellan (triangles) and pullulan (circles) (a), and $G'$ and $G''$ on cooling (b) for a 1 wt% gellan gel containing 5 mM $CaCl_2$

slow cooling. However, $\xi$ became large (exceeding 2.5 nm) on Day 9 of the experiment, suggesting that during storage the mesh size gradually increases and the solute agar chains become progressively involved in the aggregation.

**Network size in gellan gels**. We investigated the network size in 1 wt% gellan solution with 5 mM $CaCl_2$. Pullulan was used as the high-molecular-weight probe molecule as it has high solubility in water and no ionic groups. In the $^1$H NMR spectra of the 1 wt% gellan gel containing 0.1 wt% pullulan, the peak of the methyl proton in gellan gum at 1.3 ppm and the peaks of the anomer proton in pullulan from 5.2 to 5.3 ppm appeared separately from the other peaks; consequently, they were used in the analysis of the $^1$H NMR results.

The temperature dependence of the signal intensity at $g = 0$ $I(0)$ was calculated from the signal decay in the gradient NMR measurements using Eq. A9 (see Appendix), and is shown in Fig. 7 together with the thermal scanning rheological measurements. $I(0)$ of the peak of gellan gum began to decrease at around 40°C, which is higher than $T_{gel}$ and corresponds to the temperature at which $G'$ and $G''$ started to increase. This finding suggests that the gellan gum chains began to form aggregates above $T_{gel}$ and that the proportion of chains involved in the aggregation increased over time to form the network structure at $T_{gel}$. Below $T_{gel}$, a portion of the gellan chains remained as solute within the network; these chains decreased in number with progressive involvement in network formation during decreasing temperature.

The peak intensities of pullulan increased gradually with decreasing temperature, probably in response to increasing magnetization recovery (during the repetition interval of 1 s) with decreasing $T_1$. This finding indicates that pullulan was not involved in the aggregation of gellan chains; consequently, pullulan is interpreted to have no intermolecular interactions with gellan chains other than hydrodynamic interaction, which reflects the diffusion coefficient, $D$, of pullulan.

Figure 8 shows the temperature dependence of $\xi$ of the 1 wt % gellan gum containing 5 mM $CaCl_2$ and 0.1 wt% pullulan. $\xi$ was calculated from the $D_{pul}/D_{pul,0}$ value of pullulan using Eq. 3, where $D_{pul}$ was measured by pulsed field-gradient spin-echo (PFGSE) NMR with $\Delta$ of 10 ms, and $D_{pul,0}$ was calculated using Eq. 2 and the following equation [8]

$$R_H = 2.96\ 10^{-9} Mw^{0.49}, \tag{4}$$

where Mw is the molecular weight of pullulan. It is clear that $\xi$ increased with decreasing temperature below a $T_{gel}$ value of approximately 42°C. From this result, it is considered that the solute gellan is involved in aggregation at temperatures below $T_{gel}$ to enlarge the interspaces among the network chains, in the same manner as that observed for agar gel. Here, $\xi$ was largely constant during the heating

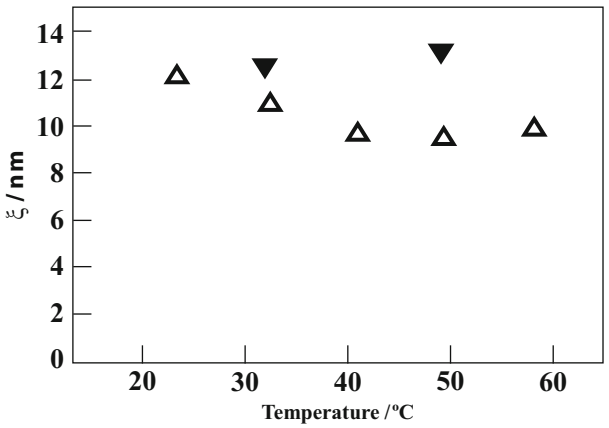


**Fig. 8** Temperature dependence of the $\xi$ value of a 1 wt% gellan gel containing 5 mM $CaCl_2$ on cooling (open triangles) and heating (filled triangles)

process. The 1 wt% gellan gel containing 5 mM $CaCl_2$ showed a high level of stress and retained its highly ordered structure during reheating after setting at low temperature [7]. The result shown in Fig. 8 indicates that the microscopic structure of the gel network is retained during reheating [6].

## Conclusions

The $D/D_0$ value of probe molecules in polysaccharide gels was used to estimate the hydrodynamic shielding length, $\xi$, which corresponds to the mesh size of the network. $\xi$ increased with decreasing temperature below $T_{gel}$, suggesting that the solute polysaccharides are involved in aggregation and are diluted to increase $\xi$. After sudden cooling, $\xi$ of the 1.3 wt% agar gel increased with storage time, consistent with the experimental result that the exudation rate of water under compression increased after storage for 3 days. After setting at low temperature, it was observed that $\xi$ of the 1 wt % gellan gel with 5 mM $CaCl_2$ did not decrease as a result of reheating; this indicates that the network structure does not change on reheating. This finding is consistent with the results of rheological measurements and circular dichroism (CD) spectroscopy measurements.

## Appendix. Diffusion Measurement by Pulsed Field Gradient Spin-Echo (PFGSE) NMR Method

The spatially dependent Larmor frequency, $\omega(\mathbf{r})$, at position $\mathbf{r}$ under a spatially linear field gradient, $\mathbf{g}$, is expressed as follows:

$$\omega(\mathbf{r}) = \gamma(H_0 + \mathbf{g}\,\mathbf{r}) = \omega_0 + \gamma\mathbf{g}\,\mathbf{r}, \tag{A1}$$

where $H_0$ is the externally applied magnetic field and $\mathbf{g}\,\mathbf{r} = 0$ at position $\mathbf{r} = 0$. When the duration of the field gradient is $\delta$, the difference between the phase angle at $\mathbf{r}$ ($\phi(r)$) and that at r = 0 is

$$\phi(\mathrm{r}) = \gamma\ \mathbf{g}\,\mathbf{r}\ \delta. \tag{A2}$$

The distance in the $\mathbf{g}$ direction where $\phi(r) = 2\pi$ is

$$q^{-1} = 2\pi/\gamma\ g\,\delta \tag{A3}$$

$q^{-1}$ is the length scale with the field gradient. For example, $q^{-1}$ is 235 μm when $g = 10$ G/cm and $\delta = 1$ ms. When the sample size or the size of the detection area is several times larger than $q^{-1}$, the total signal intensity vanishes because of dephasing.

For measurements of $D$, a second field gradient is applied to rephase the dephased magnetization. Figure A1 shows a typical pulse sequence with two pulsed field gradients (PFGs) having a rectangular shape along the z axis and the dephasing and rephasing behaviors of the magnetization when the individual spins do not change their positions at interval Δ between the two PFGs [9,10]. In Fig. A1, vectors on the z axis represent the isochromats, which are the sums of spin moments under the same magnetic fields, corresponding to individual positions. In Fig. A1(a), the isochromats are aligned along the y axis by an r.f. π/2 pulse. Under the first PFG, the isochromats precess at an angular velocity of γ**gr**, corresponding to individual positions in the rotating frame (Fig. A1(b)). At the end of the first PFG, the isochromats are spirally twisted by a pitch of $q^{-1}$ (Fig. A1(c)). The application of an r.f. π pulse along the y axis rotates the individual isochromats along the y axis by 180°, creating a mirror-symmetric arrangement of the isochromats with respect to the y-z plane (Fig. A1(d)). Under the second PFG, the individual isochromats precess at the same angular velocity as that under the first (Fig. A1(e)). At the end of the second PFG, the isochromats are aligned along the y axis (Fig. A1(f)). When the nucleus has displacement Δz in the z direction during Δ, it has a phase angular shift of

$$\phi(\Delta z) = 2\pi\frac{\Delta z}{q^{-1}} = \gamma g\delta\Delta z. \tag{A4}$$

The echo signal intensity, $I(2\tau,g\delta)$, at $2\tau$ is proportional to the vector sum of the isochromats in the sample, and is therefore expressed as follows:

$$I(2\tau, g\delta) = I(2\tau, 0)\int\int \cos\ (\phi(\Delta z))\rho(r)p(r,\Delta z)drd\Delta z, \tag{A5}$$

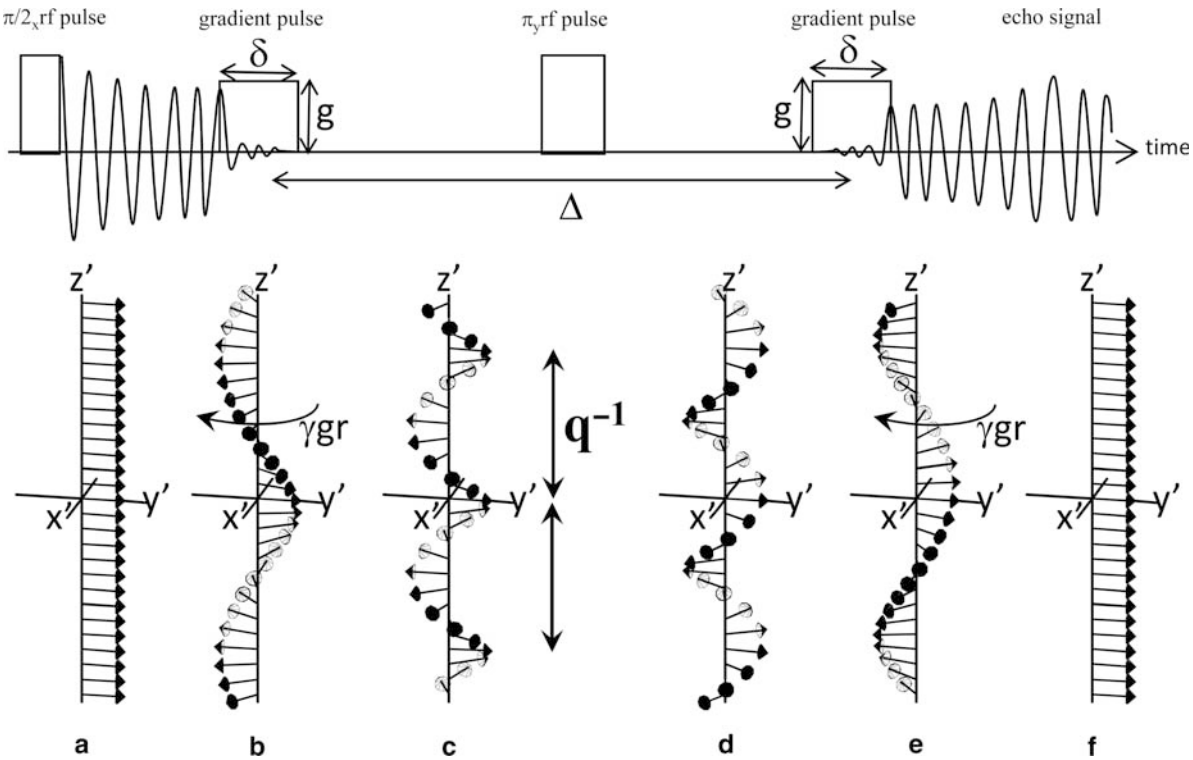


**Fig. A1** Pulse sequence of pulsed field gradient spin-echo (PFGSE) NMR, and dephasing and rephasing behavior of the magnetization

where $\rho(\mathbf{r})$ is the density of the nucleus (constant for a homogeneous sample), $p(\mathbf{r},\Delta z)$ is the probability of displacement during $\Delta$ for the nucleus at $\mathbf{r}$, and $I(2\tau,0)$ is the total signal intensity without PFG, expressed as

$$I(2\tau,0) = I(0,0)\exp(-2\tau/T_2), \tag{A6}$$

where $I(0,0)$ is the initial signal intensity immediately after the r.f. $\pi/2$ pulse. For free diffusion in an isotropic medium, $p(\mathbf{r},\Delta z)$ has a Gaussian distribution:

$$p(r,\Delta z) = (4\pi D\Delta)^{-1/2}\exp\left(-\frac{\Delta z^2}{4D\Delta}\right), \tag{A7}$$

where $D$ is the diffusion coefficient. Taking the diffusion during $\delta$ into account, $I(2\tau,g\delta)$ is rewritten as follows:

$$I(2\tau,g\delta) = I(0,0)\exp\left(-\frac{2\tau}{T_2} - (rg\delta)^2 D\left(\Delta - \frac{\delta}{3}\right)\right). \tag{A8}$$

In common measurements, $g\delta$ is varied under constant $\Delta$, where $\tau$ is also constant. In this case, Eq. (A8) can be rewritten as follows:

$$I(2\tau,g\delta) = I(0)\exp\left(-(rg\delta)^2 D\left(\Delta - \frac{\delta}{3}\right)\right), \tag{A9}$$

where $I(0)$ is $I(2\tau,g\delta)$ with constant $\tau$ and $g\delta = 0$. It should be noted that $I(0)$ decays on $T_2$ relaxation.

## References

1. Matsukawa S, Ando I (1997) Macromolecules 30:8310
2. Matsukawa S, Ando I (1999) Macromolecules 32:1865
3. Matsukawa S, Ando I (1996) Macromolecules 29:7136
4. de Gennes PG (1976) Macromolecules 9:594–598
5. Cukier R (1984) Macromolecules 17:252
6. Matsukawa S, Tang Z, Watanabe T (1999) Progress in Colloid & Polymer Science 114:15–24
7. Miyoshi E, Nishinari K (1999) Progress in Colloid & Polymer Science 114:68–82
8. Nishinari K, Kohyama K, Williams PA, Phillips GO, Burchard W, Ogino K (1991) Macromolecules 24:5590–5593
9. Stejskal EO, Tanner JE (1965) J. Chem. Phys. 42:288
10. Karger J, Pfeifer H, Heink W (1988) Adv. Magn. Reson. 12:1

Progr Colloid Polym Sci (2009) 136:177–186
DOI: 10.1007/2882_2009_25

# Chain Release Behavior of Gellan Gels

Khandker S. Hossain[1] and Katsuyoshi Nishinari[2]

**Abstract** The chain release behavior from gellan gels was studied by immersing the gel into water and monitoring the mass loss as a function of time. Concentration of released gellan in the external solution was determined for gels of different sizes using phenol-sulfuric acid method. The chain release process became faster with increasing total surface area and volume. However the concentration of released chain normalized by surface area and volume suggests that the chain release itself is governed not only by the ionic effect and the amount of unassociated chains in gel but other factors such as osmotic pressure may play an important role on the chain release from the gels. The diffusion coefficient was estimated from the chain release process which is in the same order of magnitude reported for an isolated gellan chain by light scattering. Rheological measurements also suggest that the unassociated gellan chains are released out when immersed in pure water while unassociated chains are restricted to release out when immersed in salt solution due to the intrusion of cations which is responsible for further association of the unassociated gellan chains being in agreement with the previously published results. The elastic modulus of gels was increased by immersion of gels in water and in salt solutions, which can be attributed as the stiffening of network chains due to gel swelling and the conversion from free and unassociated chains into network chains, respectively, leading to an increase in elastic modulus with time.

**Keywords** Chain release • Gel erosion • Gellan • Rheology • Diffusion

K. Nishinari (✉)
[1]Department of Physics
University of Dhaka
Dhaka-1000, Bangladesh
e-mail: k.s.hossain@gmail.com
[2]Graduate School of Human Life Science
Osaka City University
3-3-138, Sugimoto, Sumiyoshi, Osaka 558-8585, Japan
e-mail: nisinari@life.osaka-cu.ac.jp

## Introduction

Gellan gum is a bacterial exopolysaccharide, discovered through the screening of thousands of bacteria and prepared commercially by aerobic submerged fermentation from *Sphingomonas elodea* (previously called *Pseudomonas elodea*), in a manner similar to xanthan [1].

The characteristic feature of gellan gum is that it can produce thermoreversible transparent gels in aqueous solution even at a very low concentration, which depends on the kind and concentration of metallic ions. Thus it is widely used as a gelling agent, viscosity builder and texture modifier in food and pharmaceutical industry [2–5].

The most readily available gellan is a deacyled form with a tetrasaccharide repeating unit. As gellan molecules possess carboxyl groups in the repeating unit, the gelation of gellan is remarkably enhanced by the addition of cations in aqueous solutions [6,7]. Monovalent counter ions are responsible for the screening of the electrostatic repulsion between adjacent molecules and promote coil-helix transition and association between gellan molecules while divalent ions form the ionic bonding between two carboxyl groups.

It is widely believed that gellan takes random coil conformation at high temperature. On cooling, salt induced coil to double helix conformational change occurs, which is followed by a cation mediated side by side helix-helix aggregation, leading to a three dimensional network [8]. In a physically crosslinked gellan gel, there are crosslinking regions called junction zones composed of aggregated helices which are interconnected by chains called network chains. However during gel formation, it is highly probable that some fraction of polymer chains remains uncrosslinked to the network and exists as free chains and dangling chains. They do not contribute effectively to the formation of the gel network and thus to the elasticity. If it is really the case, it is not unreasonable to think that these free chains release from the gel and diffuse out to water when gellan gel is immersed in water as solvent, which motivated us to start a thorough study on this problem. We observed the presence of gellan

molecules in the external solvent when a gel was immersed in it. Quite recently the first paper on chain release was published by Tanaka and Nishinari [9] and it has been reported that free (un-crosslinked) chains exist in physical gellan gels in addition to the network chains, and these gellan chains release out into an external solution as a function of time when it was immersed in water. The release of free chains from the gel was suppressed by adding KCl while it was promoted by adding TMAC (tetramethylammonium chloride) to the external solution.

However, there are some other important issues regarding the chain release problem which requires a further clarification. For example, the previous study [9] reported the chain release behavior only from one size of the gel. There is no information of how the release of chain is influenced with the change in size of the gels i.e. with the change in surface area and volume of the gel. Simultaneously it is also important to study the diffusion behavior of the released chain. Moreover, if the chain release behavior occurs solely due to the presence of uncrosslinked chains, the rheological behavior more precisely the modulus of the gel should be independent with time during the chain release.

To scrutinize those issues, in this study, investigations have been made to clarify the chain release behavior and to characterize the rheological change of gellan gels during chain release by immersing the gel into water and various salt solutions and monitoring the change in Young's modulus with time during the chain release process.

## Experimental

### Materials and Sample Preparation

Gellan gum was supplied by San-Ei-Gen FFI Ltd., Osaka, Japan. In this study, we used potassium type gellan sample. The sample was used without further purification. The metal content of dry gellan was analyzed as Na = 0.42%, K = 5.03%, Ca = 0.37%, and Mg = 0.09% by a LIBERTY inductively coupled plasma optical emission spectrometry (ICP-OES) system (Varian Inc., Palo Alto, CA, USA).

Powdered gellan gum was mixed with distilled water, and the solution was stirred for 2 hours at 90°C. The solution was poured into three types of cylindrical moulds with the constant length of 15mm and with the diameter of 3mm, 5mm and 10mm and cooled at 10°C inside a refrigerator for 24 hours to obtain the cylindrical gellan gels samples to examine the amount of gellan released from the gel when it is immersed in solution. The same solution was poured into Teflon moulds (30mm height and 20mm diameter) in order to prepare the gel sample for the rheological measurement.

### Method

To examine the release of gellan molecular chains from the gels, one cylindrical gel was immersed in distilled water or a salt solution. The weight of the external solution was 50g and the weight of the cylindrical gels with diameters 10mm, 5mm and 3mm were 1g, 0.25g and 0.10g, respectively. External solution containing released gellan chains was collected at appropriate intervals and it is done separately for each interval.

#### Concentration Measurements

The gellan concentration in the external solution was determined using a phenol-sulfuric acid method [10]. In this method, the solution is mixed with phenol and sulfuric acid with this mixing ratio of sample : phenol : $H_2SO_4 = 1$: 1:5. The UV shows an absorption maximum at 483 nm. The gellan concentration in the external solution, $C_{release}$, was estimated from the calibration curve of absorbance vs concentration.

#### Rheological Measurements

The storage Young's modulus $E'$ and the loss Young's modulus $E''$ were determined by the observation of longitudinal vibrations of cylindrically moulded gels. The apparatus used [11,12] was a Rheolograph Gel (Toyo Seiki Seisakusyo Ltd, Tokyo). $E'$ and $E''$ were measured in the equilibrium state. The advantage of this method is that it is completely free from the problem of slippage which affects quite often the viscoelastic measurement in shear oscillation mode. Since it is well known that the storage modulus of a gel does not depend so much on the frequency [13], the frequency is fixed as 3Hz and the amplitude was also fixed as 100 μm (strain 0.03) for this apparatus.

#### NMR Measurements

$^1$H NMR spectra were obtained with Unity-Plus500 ($B_0 = 11.7$ T) (Varian, U.S.A.) to elucidate the molecular motion of gellan in gellan gel and solution in 99.9% $D_2O$. The NMR spectra were measured at a constant temperature of 20°C and 50°C on gellan solution with $C = 0.1$wt% and on gellan gel with $C = 1.0$wt%.

#### SEC-MALLS Measurements:

The size exclusion chromatography system used consisted of a HPLC pump, a guard column, and a main column, which is coupled to a DAWN-DSP multiangle laser light scattering

detector (Wyatt Technologies, Santa Barbara, CA) and a Shimadzu refractometer used for light scattering intensity and concentration detection, respectively. The mobile phase was 0.02 wt % sodium azide in distilled deionized water. Samples of the dilute gellan solutions were injected into the size exclusion system after filtering through 0.45 μm filters (Millipore). Data were captured and analyzed using the software package ASTRA.

## Results and Discussion

### *Characterization of gellan gel by NMR*

So far we have assumed that the probability of presence of free or uncrosslinked chain in gellan network, however, in the previous work on chain release there was no experimental results or even a qualitative result which demonstrates that free chains are indeed present in the gellan gel. Here is an attempt to demonstrate such a result by using NMR on two gellan aqueous solutions with $C = 0.1$wt% and 1.0wt% at $T = 50$ and 20°C.

The probe temperatures are chosen taking into consideration of the coil-helix transition temperature of gellan which is near 30°C. At $T = 20$°C, 0.1wt% gellan is a solution but 1.0wt % gellan is a gel. Whereas at $T = 50$°C, both $C = 0.1$wt% and 1.0wt% gellan are solutions. The Fig. 1 shows the NMR spectra of $C = 0.1$wt% and 1.0wt% gellan gel at $T = 50$ and 20°C. At $T = 50$°C, we observe approximately a 10-fold increase in peak area with 10 fold increase in the concentration which is reasonable. However this is not the case at $T = 20$°C but almost comparable. Therefore network formation through coil helix transition occurs and thus the proton peaks are suppressed. Since the peak is still observed in the case of $C = 1.0$wt% gellan gel at $T = 20$°C, it can be considered qualitatively that not all chains participate to the network formation but some fraction of polymer chains remains uncrosslinked to the network and exists as free chains and dangling chains. By a rough calculation from the peak area at 1.3 ppm it can be estimated that 1.0wt% gel contains approximately 90% of helix and 10% of random coil because the peak at $T = 50$°C (gellan molecules are in coil state) is suppressed aprox. 90% when the temperature is reduced to 20°C which is far below the coil-helix transition temperature $T_C = 30$°C.

### *Characterization of released chain solution by SEC-MALLS*

In our previous report of chain release problem [9], an effort was made to clarify whether the released chains are shorter than network chain. An Ubbelohde-type viscometer was used for this purpose to measure the intrinsic viscosities which allow an estimation of viscosity averaged molecular weight of released and unreleased gellan chains (network chains).

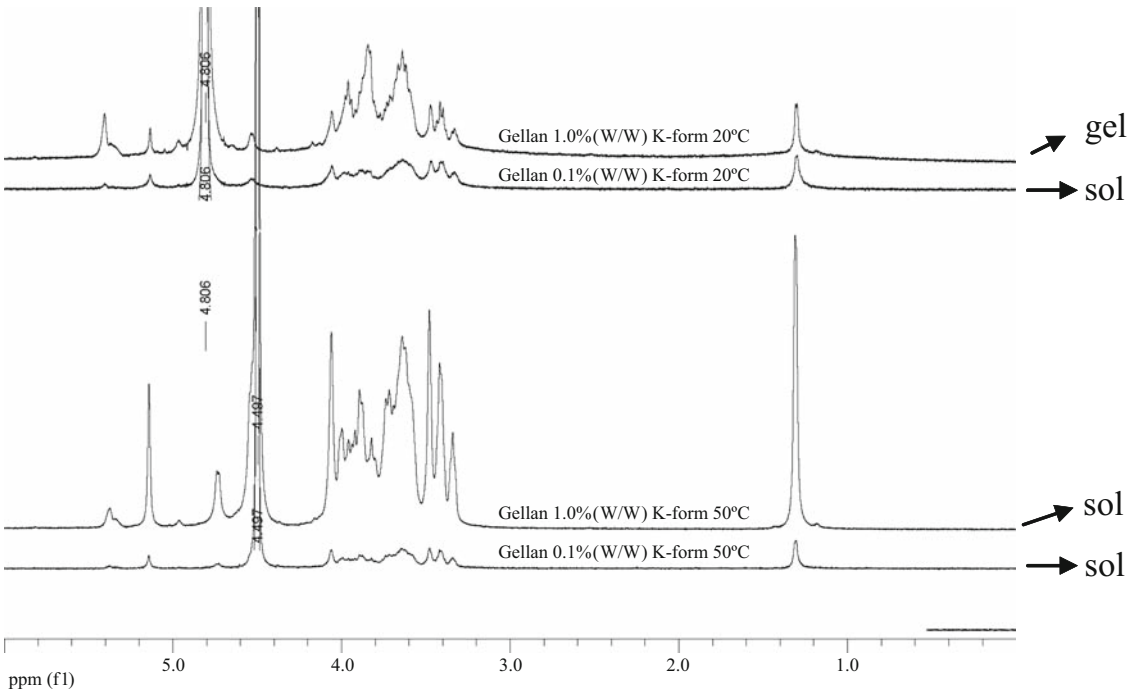


**Fig. 1** NMR spectra of K-type gellan gels with $C = 0.1$wt% and 1.0wt% at $T = 20$°C (upper) and $T = 50$°C (lower)

Results suggested that the molar mass ratio of unreleased and released gellan chains = 3.5, i.e. molar mass of the released gellan chains is lower than that of the unreleased gellan chains or network chains. However, during the intrinsic viscosity measurement of this kind of polyelectrolytes, potassium chloride was used in order to neutralize the strongly concave upturn of $\eta_{sp}/C$ vs. $C$ plot at lower $C$ which is a typical polyelectrolyte behavior in aqueous solution. But since monovalent cation potassium is believed to promote coil-helix transition and further association between gellan double helices, the released gellan chains may further be associated by the addition of KCl and the estimation of the molar mass ratio of released and unreleased gellan chains might not be so reliable.

To see the difference in molar mass of released and unreleased gellan chains, SEC-MALLS experiment was done on the released and original gellan solution.

Figure 2 shows a typical example of the SEC-MALLS chromatograms obtained, in terms of differential weight fraction vs. measured weight average molar mass, $M_w$ for released fraction and original sample. The chromatogram for released chain solution is relatively narrower than that of the original gellan solution and shifts towards the lower molecular weight values. This result suggests that comparatively shorter chains are releasing out to the external water.

## Chain release behavior from gels of different sizes

The release of chains might be influenced by the surface area of the gel which is exposed to external solvent (water in this case) and the volume of the gel. The possibility can be checked by observing the chain release behavior using cylindrical gels with different sizes at gel concentration $C_g = 2.0$wt% and $T = 10°C$. In our case the length of the gel was fixed to 15mm and the diameter of the gel was changed.

Figure 3 shows the concentration of gellan chains in the external solution, $C_{release}$, as a function of time for initial gellan concentrations, of the gel $C_g = 2.0$ wt%. Measurement of $C_{release}$ was carried out at 10°C, a temperature much lower than the helix-coil transition temperature of gellan (above 30°C). As the Fig. 3 shows the $C_{release}$ values increased with time and reached a plateau after ca. 500 min. for the cylindrical gel with the diameter of 3mm. Almost similar trend of $C_{release}$ as a function of time is observed for the cylindrical gel with a diameter of 5mm but the concentration of released chain is much higher than that of the thinnest gel. As for a cylindrical gel with a diameter of 10mm the behavior of $C_{release}$ with time is completely different from that of the other two, because in this case $C_{release}$ shows a linearly increasing function of time within the measurement time of our study and the respective values of the $C_{release}$ at respective times are the highest. The leveling-off of curves for two gels of smaller sizes indicates that the release of chains is suppressed possibly due to the unavailability of the free chains which are already released out to the external solution. However no leveling-off of the curve is seen for the largest sized gel which means that there are still enough free or unreleased chains in the gel which may be released out gradually if the measurement is further continued.

Results suggest that chain release becomes faster with increasing size of the cylindrical gel i.e. with increasing the diameter of the cylindrical gel as the length is constant for all cases. The increase in diameter of the cylindrical gel means increase in the total surface area, the volume and the weight

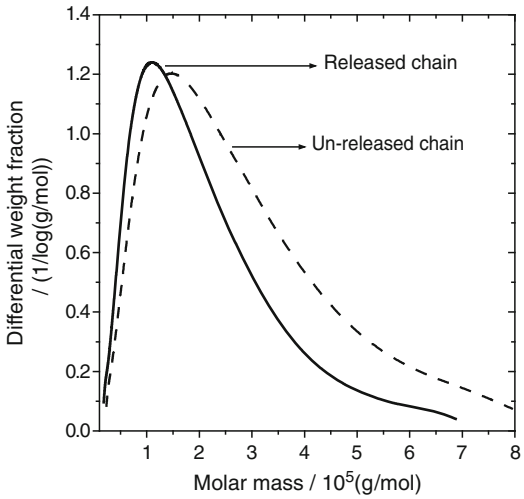


**Fig. 2** Molecular weight distributions of released gellan and original gellan samples measured by SEC-MALLS

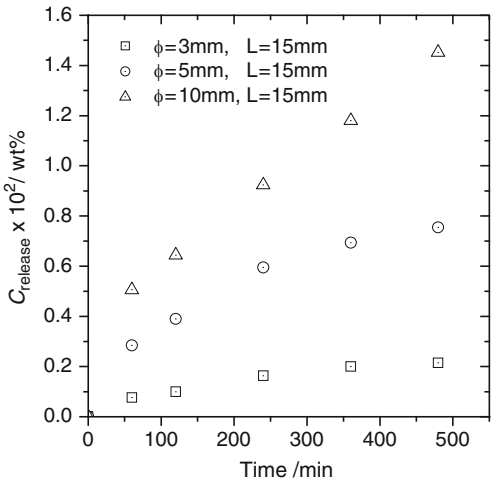


**Fig. 3** Concentration of released chain from gels as a function of time for different cylindrical gel sizes with gel concentration $C = 2.0$wt%

of the gel. So it is expected that when larger surface area of the gel are in contact with the surrounding water, the release of chain will be faster. If the release of chains from the gel is the only function of the surface area and volume, the concentration of the released chain divided by the total surface area and volume should be independent of the gel sizes considered in this study. However, the $C_{release}$ values normalized by the surface area and volume are different with different gel sizes even at the shortest measurement time and the differences are further increased with increasing measurement time as shown in Figs. 4 and 5.

Both Figs. 4 and 5 suggest that chain release from the medium sized gel (5mm diameter) are faster than the other two (3mm and 10mm diameter). Chain release from the large sized gel is faster than the small sized gel when $C_{release}$ is normalized by gel surface area while it is slower when $C_{release}$ is normalized by the gel volume.

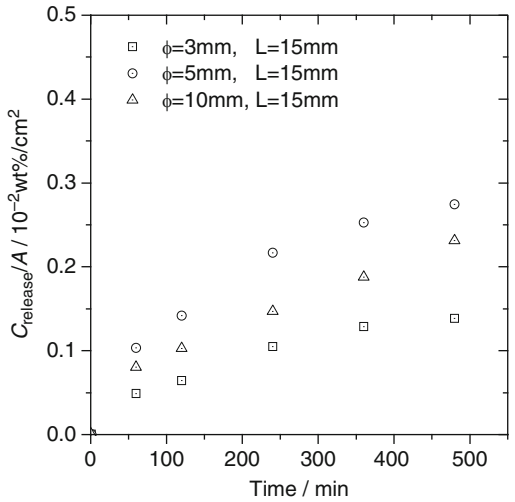


**Fig. 4** Plot of concentration of released chain from gels normalized by gel surface area, $A$, as a function of time for gels of different sizes with gel concentration $C = 2.0$wt%

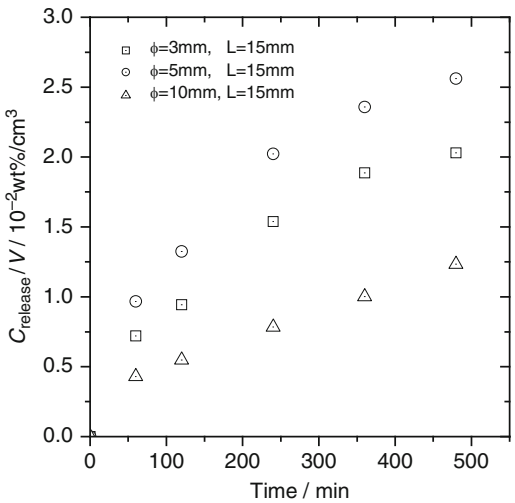


**Fig. 5** Plot of concentration of released chain from gels normalized by gel volume, $V$, as a function of time for gels of different sizes with gel concentration $C = 2.0$wt%

These results reveal that chain release from gels to the surrounding water is governed not only by the changing of the gel sizes but there are some other factors involved in this process besides the ionic effect and the amount of unassociated chains in the gel. Among these factors, osmotic pressure and chemical potential seem to play important roles. When gellan gel is immersed in surrounding water, gellan chains along with the metallic ions diffuse out to the surrounding water which may restrict the release of chains to some extent. This effect may be more applicable when large sized gel is taken into consideration and therefore, shows a slower release of gellan chains when $C_{release}$ is normalized.

It should be kept in mind that the weight of the cylindrical gels with diameters 10mm, 5mm and 3mm were 1g, 0.25g and 0.1g, respectively. Therefore such a comparison of chain release from gels with different gel sizes may not be realized in strict sense because the ratio of the volume of a gel to that of the external solvent is not constant in these three different cases. This effect can be neglected by use of large quantity of external solution; however, in the presence of large amount of external solvent, the $C_{release}$ will be too low to be measured precisely. Therefore an attempt is made to calculate the concentration of the released chain by keeping the ratio of the volume of a gel to that of the external solvent constant i.e. considering for gels of the same weight (1g) as summarized in Table 1. Experimentally we should immerse one gel with diameter 10 mm, 4 gels with diameter 5 mm, and 10 gels with diameter 3 mm if we wish to compare $C_{release}$ or we should multiply the $C_{release}$ for one gel with diameter 10mm, 5mm, or 3mm by 1, 4 or 10, respectively as shown in Table 1. The release was found in the order $C_{release}$ (4 cylindrical gels with $\phi = 5$mm) $>C_{release}$ (10 cylindrical gels with $\phi = 3$mm) $> C_{release}$ (one cylindrical gel with $\phi =$ 10mm) for the immersing time of the gel of 480 minutes.

The total surface area A of these gels is evidently, in the order $A(\phi = 3\text{mm}) > A(\phi = 5\text{mm}) > A(\phi = 10\text{mm})$ when the gel weight is kept at a constant value of 1g. The reason why the $C_{release}$ was not the largest in the smallest cylindrical gel (the largest total surface area) is uncertain for the moment: the shape of cylinders used was not similar.

However, the experimentally found order $C_{release}$ (4 cylindrical gels with $\phi = 5$mm) $> C_{release}$(10 cylindrical gels with $\phi = 3$mm) $>C_{release}$(one cylindrical gel with $\phi =$ 10mm) may not hold true after a very long immersion time and the amount of released chain may become the same for all cases after a very long time because the shorter chains can release out rapidly from the surfaces of many (4 or 10) small cylinders than from one large cylinder. Moreover, comparatively longer uncrosslinked or free chains in the

**Table 1** Concentration of released gellan chains in water from 2.0wt% gellan gels with different sizes and various calculations at 10°C.

| Diameter of the Cylindrical gel /mm | Volume of one gel $V$ /cm$^3$ | Surface area of one gel $A$ /cm$^2$ | Weight of the gel $W$ /g | $C_{release}$ for one gel ($10^{-2}$ wt%) (approx.) After 480 min | $C_{release}/A$ $10^{-2}$ wt%/cm$^2$ | Multiplication factor for the same gel weight (**MF**) | $C_{release}$ × (**MF**) $10^{-2}$wt% |
|---|---|---|---|---|---|---|---|
| 3 | 0.106 | 1.55 | 0.1 | 0.215 | 0.138 | 10 | 2.15 |
| 5 | 0.294 | 2.75 | 0.25 | 0.75 | 0.273 | 4 | 3.0 |
| 10 | 1.18 | 6.28 | 1.0 | 1.45 | 0.231 | 1 | 1.45 |

gel need much longer time to diffuse out to the external water.

## Estimation of diffusion constant, *D*, of released gellan chains

Diffusion behavior of small molecules like sucrose and aspartame has been studied in kappa-carrageenan and gellan gels of different rheological properties by immersing cylindrical gels containing diffusants (sucrose and aspartame) in deionised water [14]. After predetermined time intervals gels were withdrawn and sucrose and aspartame concentration in surrounding water was determined.

The following equation has been used for this purpose which was proposed by Vergnaud [15] to study diffusion from cylinders under nonsteady state conditions and in short time experiences. When a cylindrical gel is immersed in a solvent and if a mass flow from the cylindrical gel to the solvent occurs, the diffusion equation can be written as

$$\frac{M_t}{M_\infty} = 4\left(\frac{Dt}{\pi}\right)^{0.5}\left(\frac{1}{R}+\frac{1}{2L}\right) \qquad (1)$$

Where $M_t$ and $M_\infty$ are the amount of substance transported at time $t$ and $t=\infty$, respectively. Here $2L$ = length of the cylindrical gel and $R$ = radius of the cylindrical gel. A plot of $M_t / M_\infty$ vs $t^{0.5}$ yields a straight line and the slope allows a direct determination of $D$ according to eq. (1). As an example, the mean diffusion constants $D$ of sucrose in kappa carrageenan gel is (5.9–7.3)×$10^{-10}$ m$^2$ s$^{-1}$ which are in broad agreement with some of the data reported in literature for different diffusing media.

Using the results of released gellan concentration in the external solution for different gel size as discussed in the previous section and in Fig. 3, an attempt has been made to check whether it is possible to estimate the diffusion constant of uncrosslinked gellan chains in gels i.e. in the diffusing media considering the same procedure stated above. Results are shown in Fig. 6 which is the plot of $M_t / M_\infty$ as a function of root time for three cylindrical gel sizes. Although the equilibrium values of $C_{release}$ are not clearly seen for cylindrical gels with diameter of 5mm and 10mm as shown in Fig. 3, a curve fitting was done to make a rough estimate of $M_\infty$ using a Weibull equation [16]. Only the values of $M_t / M_\infty$ are considered which were linear functions of root time and in short time experiments.

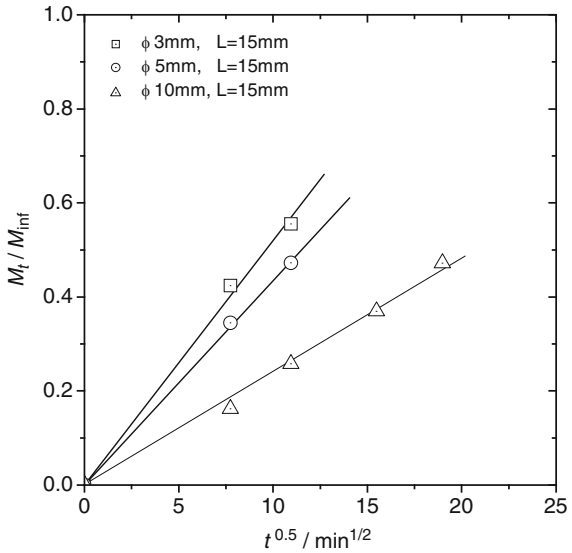


**Fig. 6** Estimation of diffusion constant, $D$, of released gellan chains for 3 different sizes of gels of diameters 3mm, 5mm and 10mm (length 15mm was fixed)

The diffusion constants of gellan were estimated from the slope of the respective curve and equation 1 as 1.61×$10^{-11}$ m$^2$s$^{-1}$, 2.89×$10^{-11}$ m$^2$s$^{-1}$, and 2.86×$10^{-11}$ m$^2$s$^{-1}$ for the gel with the diameter of 3mm, 5mm and 10mm, respectively. The diffusion coefficient of pullulan in water was determined and reported as (1 ~ 12) × $10^{-11}$ m$^2$ s$^{-1}$ for molar mass range from 1.01 × $10^6$ to 5 × $10^3$ [17]. Matsukawa et al. [private communication] determined the diffusion constant of pullulan in gellan gels by using NMR, and got the value ca. 70 ~ 80% of the value observed in water, which seems to be reasonable because the molecular motion is restricted in gels in comparison with that in pure water. The diffusion constant of gellan determined by Takahashi et al [18] ranges from 0.6×$10^{-11}$m$^2$ s$^{-1}$ to 1.0×$10^{-11}$m$^2$ s$^{-1}$ at 25°C in 25mM NaCl for molar mass range from 2.2× $10^5$ to 1.3 × $10^5$. Taking into consideration of the order of magnitudes of the diffusion constant of gellan in water, pullulan in water and gel stated above and the value of the diffusion constant (1.6 ~ 2.8)×$10^{-11}$m$^2$ s$^{-1}$ which we obtained for the released chain diffusion, it is indeed very difficult to consider our experimental values as a diffusion constant of gellan chains in gels or in other words, this

method might be inappropriate for the estimation of diffusion constant of high molecular weight polymer. These experimental values of diffusion constants are rather in agreement with the diffusion coefficients of gellan chains in water measured by light scattering. If it is really the case, a bit larger values of diffusion constant than that determined by light scattering in water by Takahashi et al. can be realized as being due to the fact that released chains are shorter than un-released chain as obtained from SEC-MALLS data shown in earlier section. Exact meaning of the diffusion coefficient estimated in this study is still unclear. Further study on the diffusion of gellan free chains in gellan gel using the NMR technique like pullulan is necessary to conclude.

## *Rheological behavior of gels immersed in aqueous solution*

In order to make a relation between chain release and the elasticity of gels during the process we have attempted to measure the complex Young's modulus of the gellan gel as a function of time using a Rheolograph Gel by immersing the gellan gel in pure water and various solutions such as KCl and TMAC solution at various molar concentrations. Storage Young's modulus, $E'$, of 2.0% gellan gels immersed in various solutions (pure water, TMAC, and KCl) has been obtained as a function of time. Each result was checked several times whether they were reproducible or not. Although the starting values of the $E'$ (the value of $E'$ before immersion) in each case were a little bit different, however, the trends of variation of $E'$ with time in respective cases were found similar.

### Gel immersed in pure water

The storage Young's modulus $E'(t)$ of gellan gels with different concentrations is plotted as a function of time. $E'(t)$ was constant with time when the gel was immersed in silicon oil as found previously [12]. According to Fig. 7, for a 2% gel, storage Young's modulus $E'(t)$ increased with time and took a constant value, then started to decrease slowly and eventually after a certain time, a rapid decrease in the value of $E'(t)$ was observed i.e. the erosion of gel took place as identified in the sample chamber as shown in Fig. 8. However for 2.5 and 3 wt% gel, $E'(t)$ increased with time and took a constant value and almost independent of time and eventually after 400 min started to decrease very slowly. The massive erosion of the gel was not observed for 2.5 and 3 wt% gel. It is interesting to note that without any mono- or di-valent cations, the storage modulus of the gel was

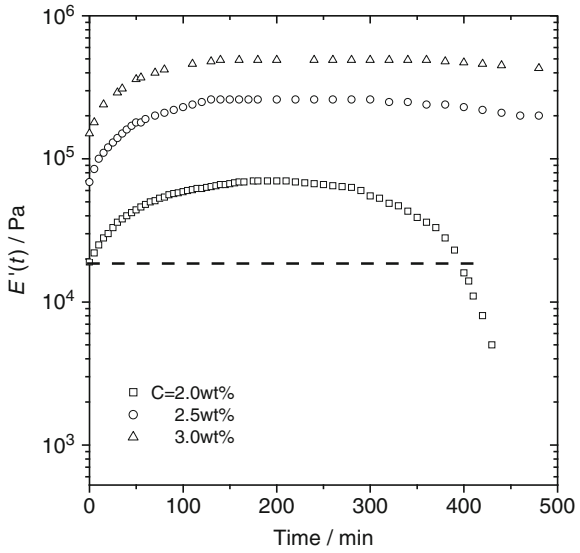


**Fig. 7** The storage Young's modulus $E'(t)$ of gellan gels immersed in pure water with different concentrations is plotted as a function of time. The dotted line represents $E'(t)$ of gellan gels immersed in silicon oil

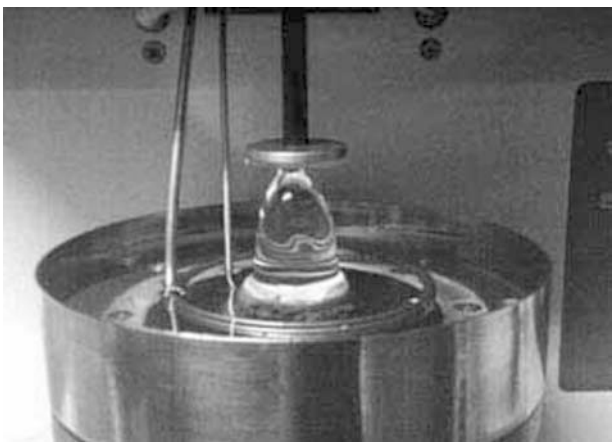

**Fig. 8** Photograph of the erosion of a gel with $C = 2.0$wt% took place after 400 min. identified in the sample chamber

increased when immersed in only distilled water. In order to interpret this result we have studied the swelling behavior of the gels as a function of time considering the similar time scales of the rheological measurement. The weight swelling ratio of 2.0 wt% gellan gel was determined after 8 Hours at $T = 20°$C and the percent weight swelling ratio was 19% as shown in Table 2 which suggests that immersion of gels in pure water made the gel swell. If it is really the case, the increase in elastic modulus of gels by immersion of gels in water can be attributed as the stiffening of network chains due to gel swelling leading to an increase in elastic modulus with time. Simultaneously, gellan chains started to release after immersion of the gel in pure water as identified from the value of concentration of gellan in the external solution.

**Table 2** Weight swelling ratio of 2.0 wt% gellan gels in water and various salt solutions after elapsed time, $t = 8$ hours and at temperature, $T = 20°C$

| Solvent | Swelling ratio | Shrinking ratio |
|---|---|---|
| Water | 19% | – |
| 0.2M TMAC | 6.9% | – |
| 0.1M TMAC | 4.3% | – |
| 0.2M KCl | – | 2.1% |
| 0.1M KCl | – | 0.8% |

In this case, erosion of gellan gel might have started with the release of free chains in initial stage.

However, after a considerable period of time (~400min) a rapid decrease in $E'$ suggests a rapid mass loss within a short period of time as was identified as the collapse of the gel sample from the sample chamber as shown in Fig. 8. In order to interpret this result the amount of potassium ions in ppm in the external water which was collected at different interval was determined by ICP- mass analysis and plotted as a function of collection time as shown in Fig. 9 which suggests that potassium ions are releasing out to the external water with time.

Since potassium ions are mainly responsible for the network formation of gellan gels, releasing out of potassium ions to the external solution due to the intrusion of water inside the gel may lead to the dissociation of the network structure and therefore such a massive erosion of the gel network observed for 2.0wt% gellan gel as shown in Figs. 7 and 8. Such massive erosion is not observed for 2.5wt% and 3.0wt% gellan gels within our experimental time range, however, may experience similar type of behavior if measured for an extended period of time. From the discussions stated above it can be concluded that, free chains are released in the short time region and the network chains are released in longer time region.

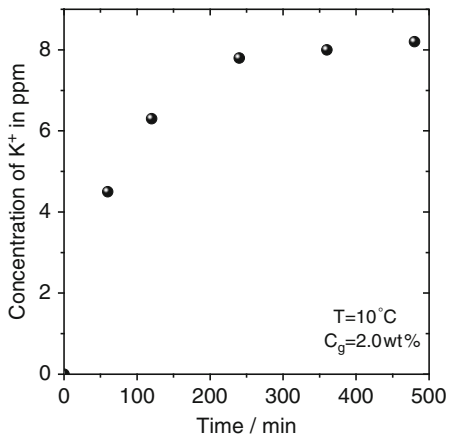


**Fig. 9** Amount of potassium ions ($K^+$) in external water measured by ICP-mass analysis at different time when a 2.0wt% cylindrical gellan gel with 10mm diameter and 15 mm height was immersed in 50g of distilled water

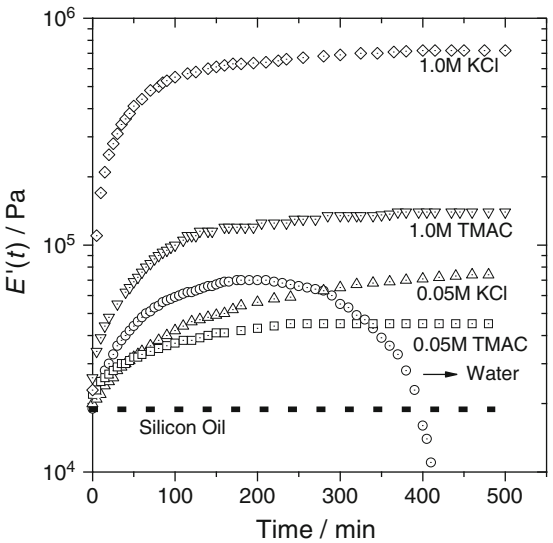


**Fig. 10** Plot of the storage Young's modulus $E'(t)$ as a function of time of 2.0wt% gellan gel immersed in various salt solutions. The dotted line represents $E'(t)$of gellan gels immersed in silicon oil

## Gels immersed in various salt solutions

Fig. 10 shows the storage Young's modulus $E'$ as a function of time for 2.0wt% gellan gels immersed in various salt solutions such as KCl and tetramethylammonium chloride (TMAC) with different salt concentrations. As stated before, gellan gel immersed in pure water showed massive erosion which is not observed when the gel is immersed in 0.05 M of KCl and TMAC solution. The $E'$ values are less than that of gel immersed in water.

When the gel was immersed in 1 M KCl solution a rapid increase in $E'$ is observed within a short period of time and then stays constant to a value of $E'$ which is a 10-fold increase from the initial value. Such an observation indicates that before immersion of the gel in the solution, a considerable amount of free chains are present in gellan gels which do not usually contribute effectively to the network and thus to the elasticity of the gels. The intrusion of metallic ions ($K^+$) facilitates the association of unassociated/partly associated gellan helical chains leading to the increase of the number of junction zones thus the elastically active chains. It is plausible that increase in KCl concentration in the external solution will surely have an effect on the chain release behavior simply because the mobility of molecular chains towards the surface of the cylindrical gel will probably be restricted due to increase in the network density and also due to the decrease in the number of available free chains. It may be interesting to measure the concentration of released chains (by phenol-sulphuric acid method) in

various concentration of $K^+$ ion environment and simultaneously measure the modulus of the gel which may give some information among the relation between chain releases, ionic concentration and gel modulus. Gels immersed in KCl solution showed no swelling behavior as shown in Table 2, therefore, the increase of $E'$ with time is solely because of the intrusion of potassium ions into gellan gel which induce the formation and aggregation of gellan helices resulting in reinforcement of the gel network.

As we have mentioned in this paper that, during the immersion, cations such as $K^+$ and $Ca^{2+}$ in salt solutions penetrate into gels to enhance the aggregation of free chains or gellan helices in gels, leading to the decrease of released out chains in the external solution. In this connection, it might be interesting to make an attempt to monitor the chain release behavior of gellan gels by immersing the gel in the TMAC salt solution because TMA ions are known to be a network disrupting agent. Morris et al. found that the TMA salt form of gellan by converting $K^+$ type gellan allows the inhibition of the network formation which led to AFM images of heterogeneous populations of gellan aggregates [19]. It has been revealed from atomic force microscopy measurement that $TMA^+$ prevents lateral association of double helices. The AFM images show a dispersion of complex branched fibrous structure and suggest that the majority of the branched structures are aggregates rather than individual gellan molecules. They also reported that TMA gellan at 1.2wt% concentration shows a characteristic behavior of fluid in contrast to $K^+$ salt form of gellan which shows the gel-like behavior [19]. As discussed in the previous paper [9] that the amount of released gellan chains decreased with increasing concentration of KCl and $CaCl_2$ in the external solution while the situation is completely opposite in the case of TMAC. This result suggests that the increase in the amount of released gellan chains is induced by diffusion of $TMA^+$ into the gels. It can be considered that a fraction of the unreleased gellan chains which were unassociated with the crosslinking domains composed of the associated double helices in the gels, are converted into released out chains by disruption of the lateral association of double helical gellan chains following diffusion of $TMA^+$.

Rheological measurement indicated that when the gel is immersed in 0.05M TMAC solution, the value of $E'(t)$ increases gradually and stays constant and again decreases very slowly which is in contrast to the behavior observed in pure water within the measurement time and the value of $E'$ is relatively lower than that obtained when immersed in distilled water. Taking into account that TMAC is known to be responsible for the disruption of the lateral association of double helices of gellan, the result suggests that the associated gellan chains might be converted into released gellan chains, which is in agreement to the results depicted in the previous paper [9]. However, decreasing tendency of the value of storage modulus $E'$ with time from the initial stage was not observed simply because increase of the elasticity due to gel swelling was effective. As for gel immersed in TMAC swelled with 5% increase of the gel weight after 8 hours, therefore, the increase in $E'$ with time can be explained in terms of the stiffening of network chains.

On the other hand, when considering higher TMAC concentration of 1M in external solution, a 3-fold increase of $E'$ after 100 min is observed and after a certain period of time the modulus stays constant and its value is much higher than that of the gel immersed in 0.05 M TMAC solution and to that of water. The behavior is completely different and somewhat like the role of KCl i.e. enhances further association. The intrusion of TMA ions facilitates the association of unassociated/partly associated gellan chains leading to a stronger gel. The high concentration of TMAC in the external solution might have an effect on the chain release behavior which inhibits the mobility of molecular chains from the gel to the external solution.

These results suggest that TMA cations may have some possibility to shield the electrostatic repulsion between carboxylic ions in gellan molecules, and therefore the effect of TMAC may be different at lower and higher concentrations. This type of complex behavior was also reported by Kobayashi et al. in the effects of NaCl on storage and loss moduli of hyaluronic acid solutions, however, the behavior was opposite at lower and higher salt concentrations, i.e. $G'$ and $G''$ showed a higher value at $C_s = 0.01$M whilst $G'$ and $G''$ were decreased at all frequencies with increasing NaCl higher than 0.05M [20]. The molecular size of the hyaluronan is decreased by the addition of cations leading to the decrease in $G'$ and $G''$ of hyaluronan solution whilst in gel forming polysaccharide gellan, added cations promote the helix formation and aggregation leading to the increase in $G'$ and $G''$. Moreover, the comparison of the rheological data of the 0.05M and 1 M TMAC system with the pure water system made us clear that TMA ions gave the gellan gel system a more stable structure and prevents such massive erosion within the measurement time in our study.

## Conclusion

The chain release behavior of gellan gels has been characterized by several methods and can be concluded as follows:

Free or un-crosslinked chains exist in physically crosslinked gellan gels in addition to the network chains as revealed by NMR study, and these chains release out into an external solution.

The SEC-MALLS chromatogram for released chain solution is relatively narrower than that of the original gellan solution and shifts towards the lower molecular weight values. This result suggests that comparatively shorter chains are releasing out to the external water.

Results suggest that chain release become faster with increasing dimensions of the gel, however the concentration of released chain normalized by surface area and volume suggests that some additional factors are responsible to control the chain release behavior.

The network chains of the gellan gel become stiffer due to gel swelling leading to an increase in elastic modulus with time. Results suggests that the free chains release in shorter immersion time region and network chains release in longer time region when the gel is immersed in water.

The unassociated gellan chains along with $K^+$ ions released out into pure water leading to gel erosion. The intrusion of K and TMA ions into the gel facilitates the association of unassociated/partly associated gellan chains and give the gellan gel system a more stable structure and prevents such gel erosion within the measurement time of our study.

**Acknowledgement** We thank Dr. M. Takemasa for his help in NMR and GPC-MALLS measurements, and Dr. T. Funami and Ms. S. Noda of San-Ei-Gen FFI for their help in ICP-mass measurement. We also acknowledge the funding of Osaka City University Priority Research Project and the encouragement and precious advice of P. G. de Gennes.

## References

1. Jansson PE, Lindberg B, Sandford PA (1983) Carbohydr Res 124:135
2. Graham HD (1993) J Food Sci 58:539
3. Papageorgiou M, Kasapis S, Richardson RK (1994) Carbohydr Polym 25:101
4. Duran E, Costell E, Izquierdo L, Duran L (1994) Food Hydrocolloids 8:373
5. Sworn G, in: Phillips GO, Williams PA (Eds.) (2000) Handbook of Hydrocolloids, Woodhead Publishing Ltd., Cambridge, p. 117
6. Miyoshi E, Takaya T, Nishinari K (1994) Food Hydrocolloids 8:505
7. Miyoshi E, Takaya T, Nishinari K (1994) Food Hydrocolloids 8:529
8. Nishinari K, in: Phillips GO, Williams PA, Wedlock DJ (Eds.), (1996) Gums and Stabilisers for the Food Industry 8, IRL Press, Oxford, p. 371
9. Tanaka S, Nishinari K (2007) Polymer J. 39:397–403
10. DuBois M, Gilles KA, Hamilton JK, Rebers PA, Smith F (1956) Anal Chem 28:350
11. Nishinari K, Horiuchi H, Ishida K, Ikeda K, Date M, Fukada E (1980) Jap J Food Sci Tech 27:227–233
12. Nitta Y, Ikeda S, Nishinari K (2006) Int J Biol Macromol 38:145–147
13. Clark AH, Ross-Murphy SB (1987) Adv Polym Sci 83:122–249
14. Bayarri S, Rivas I, Costell E, Durán L (2001) Food Hydrocolloids 15:67–73
15. Vergnaud JM (1991) Liquid transport processes in polymeric materials, Prentice Hall, New Jersey
16. Papadopoulou V, Kosmidis K, Vlachou M, Macheras P (2006) Int J Pharm 309:44–50
17. Nishinari K, Kohyama K, Williams PA, Phillips GO, Burchard W, Ogino K (1991) Macromolecules 24:5590–5593
18. Takahashi, R, Tokunou H, Kubota K, Ogawa E, Oida T, Kawase T, Nishinari K (2004) Biomacromolecules 5:516–523
19. Gunning AP, Kirby AR, Ridout KJ, Brownsey GJ, Morris VJ (1996) Macromolecules 29:6791–6796
20. Kobayashi Y, Okamoto, A, Nishinari K (1994) Biorheology, 31:235–244

Progr Colloid Polym Sci (2009) 136:187–194
DOI: 10.1007/2882_2009_26

# Gel Formation of Recombinant Fibrinogen Lacking αC Termini

Kenji Kuboa[1], Yuka Masuda[1], Yoshiharu Toyama[1], Nobukazu Nameki[1], Nobuo Okumura[2], and Masanori Ochiai[3]

**Abstract** In order to examine the role of αC domains, especially the terminal region of it, of fibrinogen Aα chain in the fibrin gel formation, we prepared a recombinant fibrinogen, Aα570 fibrinogen. Aα570 fibrinogen is the fibrinogen that is truncated at Aα570 and lacks 40 amino acids at the terminus of the αC domain. We examined the thrombin-catalyzed polymerization by transmission spectroscopy and confocal laser scanning microscopy (CLSM). We found that Aα570 fibrinogen exhibited a significantly delayed aggregation showing the importance of the terminal region of the αC domain in the polymerization process. Contrary to the fact that the addition of glucose to the mixture of fibrinogen and thrombin results in a substantial delay of the lateral aggregation of protofibrils for the native fibrinogen, delaying effect due to the addition of glucose disappeared thoroughly in the case of Aα570 fibrinogen. Turbidity measurements dependent upon the wavelength in the time course of gelation showed that mass per unit fiber length of Aα570 fibrinogen decreased significantly compared to the native fibrinogen, and the lateral aggregation of protofibrils was hindered significantly. Those results are consistent with the CLSM measurements that the bundles of protofibrils of Aα570 fibrinogen are thinner and denser with more branching than those of the native one. It was confirmed that C-terminal region of the αC domain plays an important role in the lateral aggregation and glucose interferes the interacting process between the αC domains.

**Keywords** Fibrinogen • Truncation • αC domain • Gelation • Saccharides

K. Kuboa (✉)
[1]Department of Chemistry and Chemical Biology,
Graduate School of Engineering, Gunma University,
Kiryu, Gunma 376-8515, Japan
e-mail: kkubota@chem-bio.gunma-u.ac.jp
[2]Department of Bimedical Laboratory Sciences,
School of Medicine, Shinsyu University,
Matsumoto, Nagano 390-8621, Japan
[3]Institute of Low Temperature Science, Hokkaido University,
Sapporo, Hokkaido 060-0819, Japan

## Introduction

Fibrinogen is a rod-shaped glycoprotein, 340 KDa in molecular weight and 45 nm in length, and plays essential roles in hemostasis and wound healing. Fibrinogen molecule is composed of six polypeptide chains, heterodimer of tripeptides that Aα, Bβ, and γ chains are adjoined at the N-terminals of them with each other by S–S bonds. The central domain of fibrinogen molecule is composed of N-termini of six chains named as E domain. C-termini of each set of three polypeptide chains extend in opposite directions, and respective chain terminates forming domains. Globular domains of the Bβ chain (β module) and γ chain (γ module) associate adjacently together forming D domain. Aα chains pass through the distal D domains and fold backward the E domain. C-terminal two-thirds of Aα chain is called αC domain, and interacts with each other and associates with the E domain [1].

Fibrin clot formation, gelation of fibrinogen molecules by the enzymatic reaction of thrombin, proceeds in a stepwise manner, protofibril formation of fibrin monomer and lateral aggregation resulting in a network formation [1,2]. Protofibril formation is triggered by the specific cleavage of fibrinopeptides A and B from the E domain by thrombin, which is called fibrin, and the exposed N-terminal sites (A-knob) of α chains interact with the complementary sites (a-pocket) at the D domain of γ chain of other fibrin molecules [1,3]. The spontaneous association of fibrin molecules induced by this interaction results in fibrin oligomers with half-staggered overlapping, and the resultant double-stranded oligomers are called protofibrils. During the protofibril formation and its growth, fibrinopeptide B is cleaved effectively and conformational change of αC domains occurs in a large scale simultaneously [4]. That is, αC domains dissociate from the E domain and the intramolecular association between αC domains breaks allowing to interact intermolecularly [5,6]. As a result, protofibrils aggregate laterally to form networking fibers through the αC-αC intermolecular interaction.

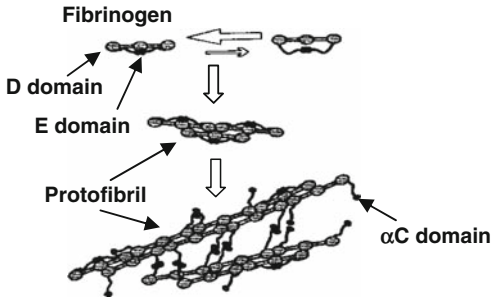


**Fig. 1** Schematic illustration of fibrin gel network formation and fiber structure [1]

Finally, fibrin clot, fibrin gel, is constructed. The schematic illustration of this process is shown in Fig. 1. The interaction between αC domains is the critical step in the fibrin gel formation. In fact, it has been reported that fragment of the αC domain functions to inhibit (delay) the lateral aggregation by interfering the αC domains dissociated from the E domain [6,7,8]. Furthermore, the NMR study on bovine fibrinogen showed that there is a structured region restricted by S-S bond in the αC fragment and αC domain is intrinsically unstable [9]. Although it has been expected that the αC domain participates essentially in the process of lateral aggregation, the detailed interacting mechanism has not been clarified yet.

Addition of various saccharides to the mixture of fibrinogen and thrombin affects on the fibrin gel formation depending upon the steric structure of saccharides without affecting enzymatic activity of thrombin. For example, the addition of glucose delays the thrombin-catalyzed polymerization significantly [10]. This effect is not due to the Maillard reaction, because the delay of polymerization has been observed even for nonreducing saccharides, e.g. trehalose. On the other hand, N-linked carbohydrate chains to Bb at N364 and γ chains at N52 also affect on the gelation: deglycosylated fibrinogen being cleaved of N-linked carbohydrates exhibits more enhanced polymerization than the intact one [11]. The addition of saccharides does not affect on the protofibril formation, but does on the lateral aggregation of protofibrils: that is, more delayed or enhanced switchover to the step of lateral aggregation occurs. Similarly, deglycosylation affects neither on the fibrinopeptide release nor on the protofibril formation, but affects on the lateral aggregation of protofibril. Therefore, it is expected that saccharides and N-linked carbohydrates interact with the αC domain interfering the lateral aggregation process, although the interacting mechanism could be different.

Those effects are observed both in human and bovine fibrinogen. Because no essential differences in the thrombin-catalyzed polymerization process are recognized between the species, the interacting site(s) in the αC domain may locate in the region with high homology in the sequence of amino acid residues. One of the possible candidates is the C-terminal region of the αC domain. Then, we designed to synthesize a truncated fibrinogen that lacks 40 amino acids at the C-terminus of Aα chain by using bioengineering technique. Simultaneously, recombinant normal fibrinogen, amino acid sequences of which are the same as the native one, was also synthesized to assure the validity of synthesizing procedure [12]. Recombinant normal fibrinogen has homogeneous peptide chains between two tripeptides, in contrast that the native fibrinogen may contain heterogeneity in the sequence of amino acid residues of them. In fact, the studies about the fibrin gel formation mechanism at the molecular level have become to utilize the synthesized variant fibrinogens, not by using the congenital dysfibrinogens [13,14]. Related to this point, it is interesting that congenitally hereditary dysfibrinogens of Aα truncation (truncation of αC domain, Fibrinogen-Marburg) and addition of extra carbohydrate (Fibrinogen-Caracas II) shows severely impaired lateral aggregation [15,16].

The synthesized fibrinogens were examined about the thrombin-catalyzed polymerization by the transmission spectroscopic measurement in the course of fibrin gel formation and the network structure by the real space observation employing the confocal laser scanning microscopy [17].

## Experimental

*Materials*. Human fibrinogen as a native control was obtained from Sigma-Aldrich with >95% clottability. Fibrinogen was dissolved in PBS buffer (pH 7.4) and dialyzed thoroughly against PBS buffer. The concentration was determined from the absorption at 280 nm using an extinction coefficient of 1.51 mL/mg·cm. Bovine thrombin was purchased from Wako Pure Chemical Industries, and was prepared in PBS or HEPES buffer (20 mM HEPES and 120 mM NaCl, pH 7.4). Special care was paid to avoid unnecessary adsorption and loss of activity. In the sample preparation, final concentrations of fibrinogen and thrombin were adjusted as 2 mg/mL and 0.01 or 0.005 units/mL, respectively. Glucose (Wako Pure Chemical Industries) and dextran (M.W. = 77 KDa, Sigma-Aldrich) were used without further purification. The final concentration in the measurements was 10 mg/mL for both saccharides.

*Preparation of variant fibrinogen*. Preparation of truncated fibrinogen, Aα570 fibrinogen, was carried out as follows. The plasmid that encodes 1–570 amino acid residues of human fibrinogen Aα chain was constructed from the expression vector encoding Aα1-610. The oligonucleotide CGAGTTACTAGAGAGGAGACTC was used as the primer

to induce the mutation at the Aα571 AAC (Asn) to TAG (stop codon). Transformation was done using Transformer Site-Directed Mutagenesis Kit (BD Biosciences Clontech). Mutated plasmid was proliferated in *E. coli* BMH71-18*mut*S. The obtained variant plasmid DNA was checked for the DNA sequence by Genetic Analyzer (ABI), and was used for the expression of recombinant fibrinogen in CHO (Chinese Hamster Ovary) cell culture. Firstly, CHO cells were transfected simultaneously by the plasmids that encode normal human Bβ and γ chains. Variant plasmid of Aα 1–570 (571 stop) was further transfected to these CHO cells. Glycerol shock was used for the effective transfection. Selection of colonies was done by neomycin and histidinol. Selected colonies were cultivated on DMEM/F12 medium in the roller bottle, and the recombinant fibrinogen secreted in the medium was harvested by the ammonium sulfate precipitation and purified by the affinity chromatography on IF-1 MoAb conjugated column. Purified fibrinogen was dialyzed against HEPES buffer and concentrated by the ultrafiltration using Vivaspin2 (MWCO 3000, Vivascience). Removal of $Ca^{2+}$ ion was achieved simultaneously. Sample solution was kept in the deep freezer (−80°C) after determination of the concentration. Recombinant normal fibrinogen was prepared in the same procedure as the above. Fibrinogen thus prepared was confirmed by SDS-PAGE.

*Analyses of thrombin-catalyzed polymerization*. Polymerization of intact and variant human fibrinogen was monitored by measuring turbidity change with time at 450 nm using Hitachi U-0080D spectrophotometer at 37°C. Wavelength dependence of turbidity over 400 to 800 nm was also obtained in a time-resolving manner to evaluate the mass per unit length ratio in the time course of gelation. Concentrations of fibrinogen and thrombin were 2.0 mg/mL and 0.005 U/mL, respectively. Analyses of the wave length dependence of turbidity were carried out according to the Carr's method [18,19]. For long rigid rods with fiber radius r with no absorption, the relation

$$C/\tau\lambda^3 = A/\mu + B\left(r^2/\mu\right)/\lambda^2 \qquad (1)$$

is obtained by integrating the scattering function of rods. C, μ, and λ denote the concentration, mass per unit length ratio, and the wavelength, respectively. A and B are the constants relating with refractive index. No absorption means that turbidity comes from the scattering only.

*Confocal laser scanning microscopy*. Confocal laser scanning microscope observations were carried out at the Nikon imaging center of Hokkaido University using the real-space imaging confocal laser microscope system Clsi (Nikon). Gels formed on the glass-bottom dishes were treated by fluorescent isothiocyanate (FITC) and the fluorescent images of fibrin fibers were observed.

## Results

*Preparation of Aα570 fibrinogen*. Figure 2 shows the SDS-PAGE image of synthesized recombinant Aα570 fibrinogen compared with the native one under the reducing condition. Three bands of the native one are Aα (66 KDa), Bβ (56 KDa), and γ (48 KDa) chains from the top to the bottom, respectively. Variant Aα chain of Aα570 fibrinogen should be 62 KDa. As expected, the corresponding band appeared a little lower position than that of Aα chain of the native one.

*Time course of the polymerization of Aα570 fibrinogen*. Time course of the polymerization monitored by transmission at 450 nm is shown in Fig. 3 as a function of the elapsed time after the addition of thrombin with and without glucose and dextran. The left panel (A) shows the comparison between the results of recombinant normal and native fibrinogens, and the right panel (B) for the Aα570 fibrinogen and normal one. Native and normal fibrinogens without glucose or dextran, control ones, showed essentially the same transmission behavior suggesting that the recombinant normal fibrinogen was synthesized properly, proper folding and glycosylation. Delay and enhancement of gelation by the addition of glucose and dextran were clearly observed, respectively. A little wiggling appeared in the native control sample may be due to the heterogeneity in the preparation from plasma. On the other hand, the result of control sample (without glucose or dextran) of Aα570 fibrinogen showed clearly impaired and delayed polymerization. Furthermore, the effect of addition of glucose disappeared completely, although the addition of dextran brought about almost the same enhancing effect on the polymerization as the normal one [20]. It should be noted that almost superposed behaviors of the normal fibrinogen with glucose and Aα570 fibrinogen (without and with glucose) are only accidental, because the

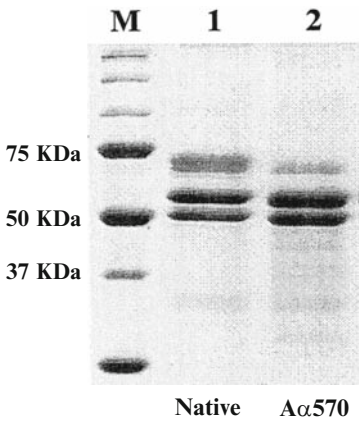


**Fig. 2** Preparation of Aα570 fibrinogen characterized by SDS polyacrylamide gel electrophoresis. M means the marker. The bands of native fibrinogen are Aα, Bβ, and γ chains respectively from the top to the bottom, respectively

extent of delayed polymerization by glucose for the normal fibrinogen depends on the concentration of glucose.

*Lateral aggregation of fibrin fibers*. Figure 4 depicts the results of wavelength dependence of turbidity analyzed by the equation 1. Increase in μ values means the progress of lateral aggregation. In case of the native fibrinogen, addition of glucose resulted in the impaired lateral aggregation, delayed increase and lower saturated value of μ. Those features are essentially the same as the previous results obtained for the bovine fibrinogen [10]. However, as expected from the results in Fig. 2, μ values of Aα570 fibrinogen, control and with glucose, showed no difference between them, and the delayed increase and lower saturation were clearly observed compared with the native one.

*Network structure of fibrin clots*. The results of CLSM observations were illustrated in Fig. 5. Scale bar means 20 μm. Similar to the results in Fig. 4, Aα570 fibrinogen without glucose or dextran showed thinner fibers (more number of fibers) and denser network with more branching than those of the native one, and the results were quite similar to those obtained for the native fibrinogen with the addition of glucose. Almost no changes were observed between the sample of Aα570 fibrinogen with glucose and the control one of Aα570 fibrinogen. Addition of dextran to Aα570 fibrinogen brought about almost the same results as the native and normal ones with dextran. These results are consistent enough with the results derived from the wavelength dependence of turbidity.

## Discussion

*Critical role of C-terminal region revealed by truncation*. The recombinant Aα570 fibrinogen provides interesting and useful tool to examine the functional significance of αC domains in the fibrin polymerization (gel formation). Aα570 fibrinogen is homogeneous different from the preparation by the lyses or degradation of native fibrinogen, for example by plasmin [21]. Present results clearly showed that the αC domains play an essential role in the fibrin polymerization. Especially, C-terminal 40 amino acid residues participate significantly in the process of lateral aggregation. The addition of glucose affects inhibitingly on the interaction between the αC termini. Therefore, the effect of glucose to Aα570 fibrinogen was depleted because of the deletion of interfering region in αC domain. On the contrary, the addition of dextran was not affected by the deletion of C-termini of the αC domains. That is, dextran may interact with other region(s) than C-terminal region.

*Choice of the mutation site based on the homology*. Aα 570 fibrinogen was determined as a candidate to examine the role of αC domain. According to the sequences of amino acid residues between human and bovine fibrinogen, high homology of more than 70% is conserved in the N-terminal one-third of Aα chain (also in E domain, coiled-coil, and D domain) and the region restricted by C442-C472, where β-hairpin structure is constructed in bovine fibrinogen C423-C453, is also highly conserved [9]. The region of αC

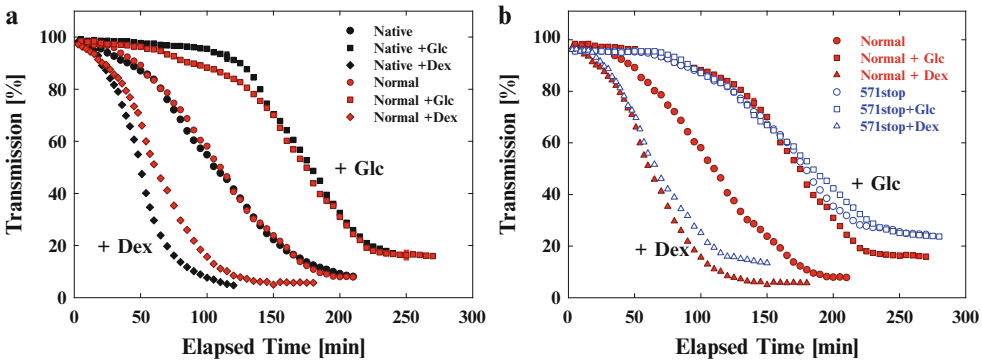


**Fig. 3** Time course of transmission in the fibrin polymerization. Panel A: Native and normal (recombinant) fibrinogen without and with glucose and dextran. Panel B: Comparison of Aα570 fibrinogen with normal fibrinogen

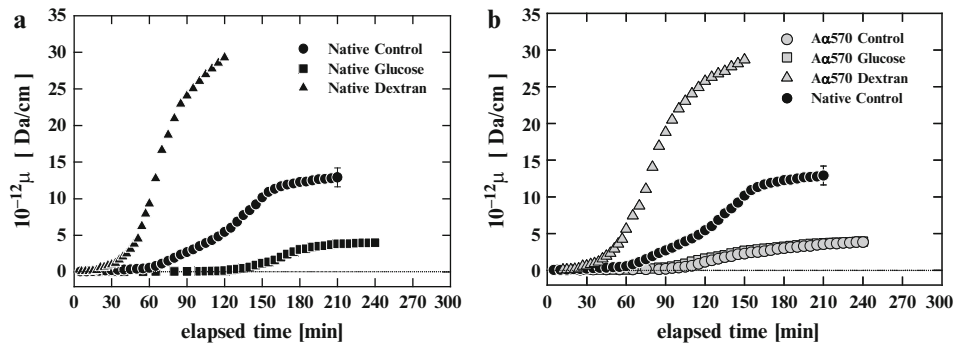


**Fig. 4** Increase in the mass per unit fiber length (μ) of native (A) and Aα570 (B) fibrinogens in the process of fibrin polymerization

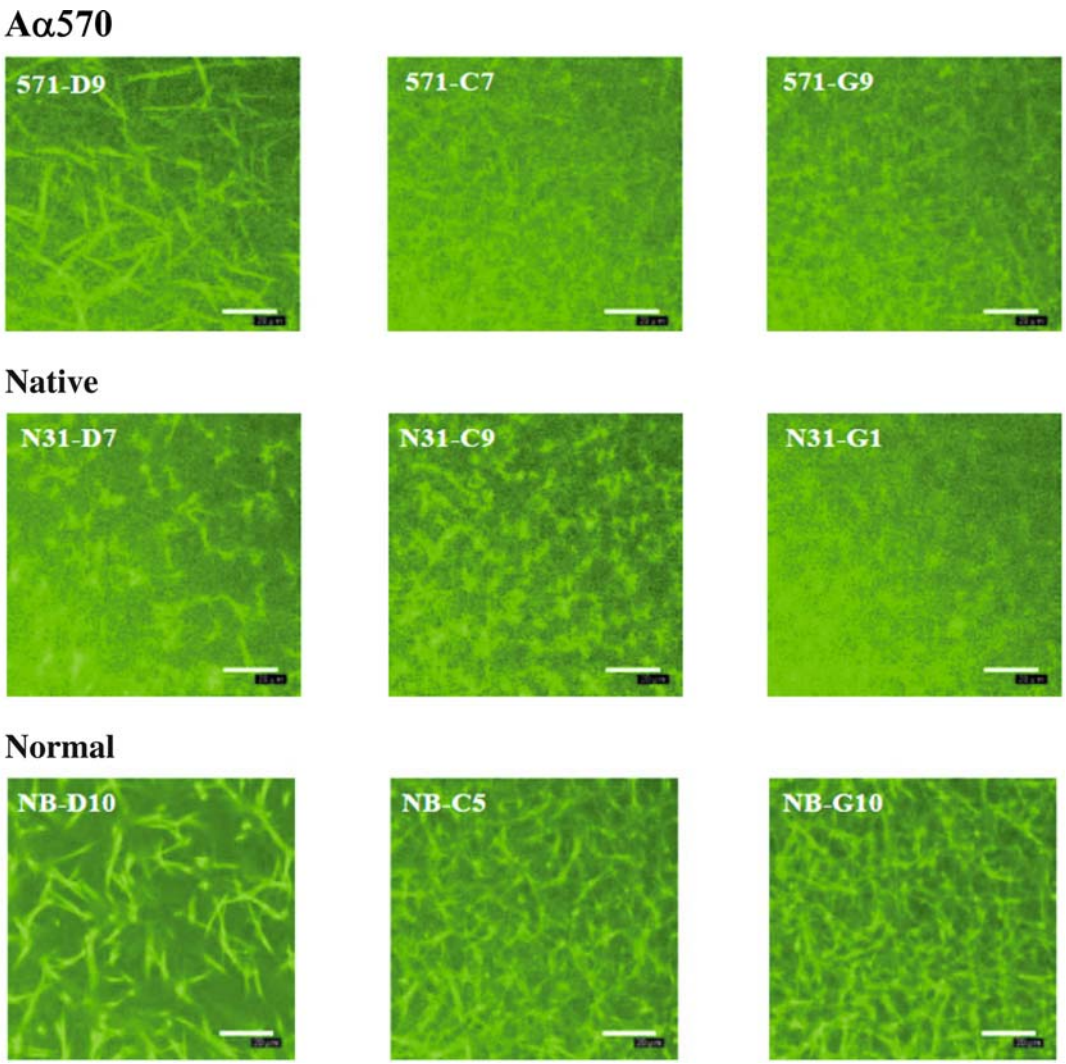


**Fig. 5** Fluorescent images of fibrin gels constituted of Aα570, native, and normal (recombinant) fibrinogen. D, C, and G denote fibrinogen with dextran, control (without glucose nor dextran), and with glucose, respectively. For the native and normal fibrinogens, both the number of fibers and the branching increase compared to those of control with the addition of glucose. On the contrary, both the control and the sample with glucose are almost the same in those characteristics

domain preceding C442 contains 13-residue tandem repeats, and it has been reported that this region interacts with fibrinogen to inhibit the lateral aggregation, although the homology is worse (less than 60%) [6]. On the other hand, in the region of C-terminal 40 residues of αC domain about 60% homology is retained and cell adhesion motif of RGD sequence is also contained. Additionally, positive and negative charged amino acid residues locate separated well. This feature suggests the likeliness of electrostatic interaction between those regions and fibrinopeptides, which are rich of acidic residues. In fact, the difference of the fibrin monomer polymerization between the native and truncated fibrinogen is known to decrease substantially at high salt concentration [22].

*Effect of $Ca^{2+}$ion*. In the present study, $Ca^{2+}$ was not contained in the sample. Generally, human plasma contains several mM of $Ca^{2+}$. $Ca^{2+}$ is the factor IV in the blood coagulation, and enhances the fibrin gel formation [1]. According to the CLSM observations of Aα570 fibrin clots with 1mM $CaCl_2$, the network structure became fairly similar to that of the native one (data not shown). The interaction between protofibrils through the Ca-binding site at the D domain of γ chain may result in the enhancement of lateral aggregation, and make vague the effect of truncation of the C-terminal region of αC domain. In order to clarify the role of αC domain and the addition of saccharides, we intended to simplify the sample condition and did not contain $Ca^{2+}$. In fact, impaired polymerization was more markedly observed for Fibrinogen-Marburg without $Ca^{2+}$ [15,23].

*Unstable and flexible characteristics of αC domain*. In contrast to the structural stability of the D and E domains, the αC domains are highly movable and easily degraded into

smaller fragments. The αC domains might be flexible enough. In fact, only two structural regions were identified for the αC domain, the β-hairpin restricted by C442-C472 and the collapsed hydrophobic region (about 30 residues) next to the hairpin. It has been suggested that those two regions cooperate with each other to form a single folded unit [9]. It is probable that this unit is attributable as the origin of αC-αC interaction, although the necessity of detailed clarification still remains. C-terminal region including the truncated region examined in the present report might work cooperatively with that unit.

*Predictions form the results of Fragment-X*. Experiments of fragment-X, one of the fibrinogen degradation products isolated from plasmin digests that were the product being cleaved of αC domains, have shown that the defects in the αC domain results in the impaired fibrin polymerization [24]. Although the αC domains are not necessary for the protofibril formation, they participate in the lateral aggregation of protofibrils critically. When the isolated αC fragments of 40 KDa of bovine fibrinogen spanning S220 and/or M240 to K581 was added to the fibrin monomers, a decrease in the rate of polymerization resulted in a dose-dependent manner [5]. 24 KDa fragment successive to M240 of human Aα chain also showed anticoagulant function [6]. Recombinant αC domain was very likely to form inclusion body in agreement with the result that the αC domain is intrinsically unstable [9]. That is, the αC-αC interaction must play an essential role in the lateral aggregation process. Although the importance of αC domains in the polymerization process has been well certified, Aα251 fibrinogen, which is truncated at Aα251 and lacks almost the whole αC domain, showed fairly similar behaviors to that of the native one in the thrombin-catalyzed polymerization [13]. However, the viscoelastic properties of Aα251 fibrin clots are markedly different (weakened) compared to the native one [25]. The reason of the subtle influence of truncation is not clear yet, but several regions might work cooperatively.

*Role of saccharides and N-linked carbohydrates*. Addition of saccharides affects on the fibrin polymerization. Time course of scattered light intensity from the mixture of bovine fibrinogen with various saccharides has been examined previously. The increasing behaviors of the scattered light intensity at the early stage after the start of reaction by thrombin are almost the same for all the samples examined [20]. This fact means that the addition of saccharides does not affect on the protofibril formation, but does on the lateral aggregation. Similarly, deglycosylation of fibrinogen, where N-linked carbohydrate chains were cleaved by PNGF, accelerates the polymerization and enhances the lateral aggregation without affecting the protofibril formation. It has been reported that additional N-linked carbohydrate to Bβ chain affects to delay the fibrin polymerization [26]. Although the relation of N-linked carbohydrate chains with the αC domains has not been examined explicitly and the reason of deglycosylating effect has not been clarified enough [1,3,11], those results mean that N-linked carbohydrate chains may interact with αC domains. And, it is suggested that the carbohydrate chains participate in the release of the αC chain from the central E domain after the protofibril formation and function to regulate the switchover from the protofibril aggregation step to the lateral aggregation step. Additionally, since the delaying effect by the addition of glucose is observed for the partially deglycosylated fibrinogen and this effect becomes less with the deglycosylation (unpublished results), the interactions of glucose and N-linked carbohydrates with the αC domain might work in a correlated manner. This scheme is still open to the questions and the experimental confirmations to specify the interacting mechanism in more microscopic level are necessary. In order to clarify these points further, direct interaction analyses between the αC chains and N-linked carbohydrates by SPR or QCM should be important [27].

## Conclusion

Truncated fibrinogen Aα570 lacking C-terminal 40 residues of the αC domain was prepared successfully. The truncation resulted in a significantly impaired thrombin-catalyzed fibrin polymerization, delayed switchover to lateral aggregation, and substantial change in the network structure. Addition of glucose does not affect the polymerization process and network structure at all, in contrast that it results to delay the polymerization significantly in case of the native fibrinogen. It was ascertained that the C-terminal region of the αC domain plays an important role in the lateral aggregation and glucose molecules influence the interacting process between the αC domains. It was suggested that N-linked carbohydrate chains interact with αC domains and such an interaction works to regulate the polymerization process.

**Acknowledgments** Authors, K. Kubota and N. Okumura, thank Prof. S. T. Lord for providing the plasmid vector that encodes the fibrinogen Aa chain. This work was partly supported by the Grant for Joint Research Program of the Institute of Low Temperature Science, Hokkaido Univ. and by the Ministry of Education, Japan.

## References

1 Weisel JW (2005) Adv Protein Chem 70:247
2 Kita R, Takahashi A, Kaibara M, Kubota K (2002) Biomacromolecules 3:1013
3 Sugo T, Sakata Y, Matsuda M (2002) Current Protein and Peptide Sci 3:239
4 Veklich YI, Gorkun OV, Medved LV, Nieuwenhuizent W, Weisel JW (1993) J Biol Chem 268:13577

5 Rudchenko S, Trakht I, Sobel JH (1996) J Biol Chem 271:2523
6 Lau HK (1993) Blood 81:3277
7 Tsurupa G, Tsonev L, Medved L (2002) Biochemistry 41:6449
8 Pechik I, Madrazo J, Mosesson MW, Hernadez I, Gilliland GL, Medved L (2004) Proc Natl Acad Sci USA 101:2718
9 Burton RA, Tsurupa G, Medved L, Tjandra N (2006) Biochemistry 45:2257
10 Masuda Y, Toyama Y, Kogure H, Kubota K, Ochiai M (2004) Trans MRS-J 29:3331
11 Langer BG, Weisel JW, Dinauer PA, Nagaswami C, Bell WR (1988) J Biol Chem 263:15056
12 Lord ST, Strickland E, Jayjock E (1996) Biochemistry 35:2342
13 Rooney MM, Mullin JL, Lord ST (1998) Biochemistry 37:13704
14 Gorkun OV, Veklich YI, Weisel JW, Lord ST (1997) Blood 89:4407
15 Koopman J, Haverkate F, Grimbergen J, Egbring R, Lord ST (1992) Blood 80:1972
16 Maekawa H, Yamazumi K, Muramatsu S, Kaneko M, Hirata H, Takahashi N, de Bosch NB, Carvajal Z, Ojeda A, Arocha-Pinango CL, Matsuda M (1991) J Biol Chem 266:11575
17 Kubota K, Kogure H, Masuda Y, Toyama Y, Kita R, Takahashi A, Kaibara M (2004) Colloid Surf 38:103
18 Carr Jr ME, Gabriel DA (1980) Macromolecules 13:1473
19 Carr Jr ME, Gabriel DA, McDonagh J (1986) Biochem J 239:513
20 Kogure H, Kitazawa M, Toyama Y, Kubota K, Ochiai M (2003) Trans MRS-J 28:949
21 Walker JB, Nesheim ME (1999) J Biol Chem 274:5201
22 Gorkun OV, Henschen-Edman AH, Ping LF, Lord ST (1998) Biochemistry 37:15434
23 Hogan KA, Gorkun OV, Lounes KC, Coates AI, Weisel JW, Hantgan RR, Lord ST (2000) J Biol Chem 275:17778
24 Gorkun OV, Veklich YI, Medved L, Henschen AH, Weisel JW (1994) Biochemistry 33:6986
25 Collet JP, Moen JL, Veklich YI, Gorkun OV, Lord ST, Montalescot G, Weisel JW (2005) Blood 106:3824
26 Sugo T, Nakamikawa C, Takano H, Mimuro J, Yamaguchi S, Mosesson MW, Meh DA, DiOrio JP,Takahashi N, Takahashi H, Nagai K, Matsuda M (1999) Blood 94:3806
27 Chtcheglova LA, Vogel M, Gruber H, Dietler G, Haeverli A (2006) Biopolymers 83:69

Progr Colloid Polym Sci (2009) 136:195–204
DOI: 10.1007/2882_2009_27

# Dynamic Light Scattering Study of Pig Vitreous Body

Toyoaki Matsuura[1], Naokazu Idota[2], Yoshiaki Hara[1], and Masahiko Annaka[2]

**Abstract** The phase behaviors and dynamical properties of pig vitreous body were studied by macroscopic observation of swelling behavior and dynamic light scattering under various conditions. From the observations of the dynamics of light scattered by the pig vitreous body under physiological condition, intensity autocorrelation functions that revealed two diffusion coefficients, $D_{fast}$ and $D_{slow}$ were obtained. We developed the theory for describing the density fluctuation of the entities in the vitreous gel system with sodium hyaluronate filled in the meshes of collagen fiber network. The dynamics of collagen and sodium hyaluronate explains two relaxation modes of the fluctuation. The diffusion coefficient of collagen obtained from $D_{fast}$ and $D_{slow}$ is very close to that in aqueous solution, which suggests the vitreous body is in the swollen state. Divergent behavior in the measured total scattered light intensities and diffusion coefficients upon varying the concentration of salt (NaCl and $CaCl_2$) was observed. Namely, a slowing down of the dynamic modes accompanied by increased "static" scattered intensities was observed. This is indicative of the occurrence of a phase transition upon salt concentration.

**Keywords** Vitreous body • Sodium hyaluronate • Collagen • Phase transition • Critical phenomenon • Dynamic light scattering

## Introduction

The vitreous body is a tenuous gel that contains collagen and sodium hyaluronate [1]. The volume fraction of the polymer network is only about 1-2%, and the remaining is water. The vitreous body is located between the lens and the retina, and comprises 80% of the overall volume of eye. The functions of the vitreous body are supposed to keep the shape of the eyeball, to absorb the external mechanical shock, to maintain the homoeostasis of the eye, and to regulate the position of the lens. The appearance of fresh vitreous body is transparent, and hence, the vitreous body is considered a uniform tissue. Many studies performed to date have suggested that sodium hyaluronate, which has a coil shape, is uniformly distributed throughout the three-dimensional network of collagen fibers that form the triple helix in the vitreous body [2]. Essentially no investigations on the structural, dynamics, and phase equilibrium properties of the vitreous body, however, have been performed to verify indisputably that the vitreous body is indeed a gel network. Some diseases affect changes in the complex structure of the vitreous body. The collapse of the vitreous body in the eye may cause many diseases such as posterior vitreous detachment, vitreous bleeding, and retinal detachment [3, 4]. In the search for the underlying principle of the functions of the vitreous body, it is crucial to understand its physical properties, which leads to promote better understanding of the mechanism of diseases of the vitreous body. In this study, the microscope laser light scattering spectroscopy is applied to investigate the structural and dynamical properties of the gel network in the pig vitreous body. It is natural to consider the collagen motion is the coupled with the dynamics of sodium hyaluronate, therefore we develop the equation for the mode coupling of flexible sodium hyaluronate and semi-rigid network of collagen. The unique physical properties of a gel arise from its structure. The gel is characterized by two kinds of bulk coefficients: (1) the elastic constants of the gel network and (2) the friction coefficients between gel network and the fluid [5]. We determine the friction coefficients between vitreous gel network and gel fluid using a specially designed apparatus. Together with experimental and theoretical results of dynamic light scattering (DLS), we discuss the elastic properties of the pig vitreous body.

M. Annaka (✉)
[1]Department of Ophthalmology
Nara Medical University 840
Shijyo-choKashihara-shi, Nara 634-8522, Japan
e-mail: annaka@chem.kyushu-univ.jp
[2]Department of Chemistry, Faculty of Sciences
Kyushu University 6-10-1
Hakozaki, Higashi-ku Fukuoka 812-8581, Japan

## Theory for the density fluctuation of complex system of polymers filling in the network meshes

The situation that sodium hyaluronate fill in the meshes of collagen fiber network to prevent them from collapsing can be modeled as a complex system of polymers interacting with the network meshes. The dynamic light scattering (DLS) measures the time correlation of density fluctuation of the scattering entities, which are the segments of the sodium hyaluronate and the collagen mesh. The concentration fluctuation of the sodium hyaluronate segment, $\delta C_{HA}(\mathbf{r},t)$ $(= C_{HA}(\mathbf{r},t) - C^0_{HA})$, where $C_{HA}(\mathbf{r},t)$ and $C^0_{HA}$, respectively, are the local and the averaged concentrations of the segment can be described by the following diffusion equation [6].

$$\frac{\partial \delta C_{HA}(\mathbf{r},t)}{\partial t} = D_{HA}\nabla^2 \delta C_{HA}(\mathbf{r},t) + L_{HA-Col} D_{HA} \frac{C^0_{HA}}{C^0_{Col}} \nabla^2 \delta C_{Col}(\mathbf{r},t) \tag{1}$$

where $D_{HA}$ and $L_{HA\text{-}Col}$, respectively, are a diffusion coefficient defined in the inter-particle interaction free condition and a phenomenological coefficient, which is significant in the case that the acting force of collagen matrix on the sodium hyaluronate is large. The subscripts, HA and Col, denote sodium hyaluronate and collagen, respectively. Here, $C^0_{Col}$ and $\delta C_{Col}(\mathbf{r},t)$, respectively, are the averaged concentration and the concentration fluctuation of the collagen segment. The collagen network can be regard as an elastic body. According to the linear theory for the elastic body, a force balance among elastic and the external forces can be described by the following Newton equation.

$$\rho \frac{\partial^2}{\partial t^2}\mathbf{u} = \mu \nabla^2 \mathbf{u} + \left(K + \frac{1}{3}\mu\right)\nabla(\nabla \cdot \mathbf{u}) - f\frac{\partial}{\partial t}\mathbf{u} + \mathbf{F}_{Col} \tag{2}$$

where $\boldsymbol{\rho}$, $\mathbf{u}$, $\boldsymbol{\mu}$, $K, f$, and $\mathbf{F}_{Col}$, respectively, are the density of the network, a displacement vector of the collagen segment, a shear modulus, a bulk modulus, a friction coefficient of an unit volume and the force acted by the sodium hyaluronate, which is given by

$$\mathbf{F}_{Col} = -L_{Col-HA} T C_{Col}(\mathbf{r},t) \nabla \ln C_{HA}(\mathbf{r},t) \tag{3}$$

$T$ is the Boltzmann temperature. Here we use units where Boltzmann constant $k_B$ is unity to use energy units for temperature. We should mention here the relation $f = C^0_{Col}\varsigma_{Col}$, where $\varsigma_{Col}$ is a friction coefficient of the collagen segment. The inertia term is negligibly small in the fluctuation, that is, $\rho\partial^2\mathbf{u}/\partial t^2 = 0$. Using Eq. 3, and the relations $\overrightarrow{\nabla} \cdot \mathbf{u}(\mathbf{r}) = \delta C_{Col}(\mathbf{r},t)/C^0_{Col}$, Eq. 2 can be rewritten as

$$\frac{\partial \delta C_{Col}(\mathbf{r},t)}{\partial t} = D_S \nabla^2 \delta C_{Col}(\mathbf{r},t) + L_{Col-HA} D_{Col} \frac{C^0_{Col}}{C^0_H} \nabla^2 \delta C_{HA}(\mathbf{r},t) \tag{4}$$

where

$$D_S = (K + 4\mu/3)/f \tag{4-1}$$

$$D_{Col} = (\mathbf{T}/f) C^0_{Col} \tag{4-2}$$

where $L_{Col\text{-}HA}$ is a phenomenological coefficient related to the acting force of sodium hyaluronate on collagen matrix. Eqs. 1 and 4 can be rewritten in the form of Fourier transform of the concentrations as:

$$\frac{\partial C_{HA}(q,t)}{\partial t} = -q^2 \left\{ D_{HA} C_{HA}(\boldsymbol{q},\boldsymbol{t}) + L_{HA-Col} D_{HA} \frac{C^0_{HA}}{C^0_{Col}} C_{Col}(\boldsymbol{q},\boldsymbol{t}) \right\} \tag{5}$$

$$\frac{\partial C_{Col}(q,t)}{\partial t} = -q^2 \left\{ D_S C_{Col}(\boldsymbol{q},\boldsymbol{t}) + L_{Col-HA} D_{Col} \frac{C^0_{Col}}{C^0_{HA}} C_{HA}(\boldsymbol{q},\boldsymbol{t}) \right\} \tag{6}$$

where

$$\delta C_{HA}(\mathbf{r},t) = \left(\frac{1}{2\pi}\right)^3 \iiint d\mathbf{r}^3 C_{HA}(\mathbf{q},t) \exp(i\mathbf{q}\cdot\mathbf{r})$$

and

$$\delta C_{Col}(\mathbf{r},t) = \left(\frac{1}{2\pi}\right)^3 \iiint d\mathbf{r}^3 C_{Col}(\mathbf{q},t) \exp(i\mathbf{q}\cdot\mathbf{r})$$

Eqs. 5 and 6 can be converted into matrix form as

$$\frac{\partial}{\partial t}\mathbf{C}(\mathbf{q}) = -q^2 \tilde{A}\mathbf{C}(\mathbf{q}) \tag{7}$$

where

$$\mathbf{C}(\mathbf{q}) = \begin{pmatrix} C_{HA}(\mathbf{q},t) \\ C_{Col}(\mathbf{q},t) \end{pmatrix} \quad \text{and}$$

$$\tilde{A} = \begin{pmatrix} D_{HA} & L_{HA\text{-}Col} D_{HA} \frac{C^0_{HA}}{C^0_{Col}} \\ L_{Col-H} D_{Col} \frac{C^0_{Col}}{C^0_{HA}} & D_S \end{pmatrix}$$

The solution of Eq. 7 is given as

$$\begin{pmatrix} C_{HA}(\mathbf{q},t) \\ C_{Col}(\mathbf{q},t) \end{pmatrix} = B(\mathbf{q}) \begin{pmatrix} D_1(\mathbf{q})\exp(-q^2\lambda_1 t) \\ D_2(\mathbf{q})\exp(-q^2\lambda_2 t) \end{pmatrix}$$

where

$$\tilde{B}^{-1}(\mathbf{q})\tilde{A}(\mathbf{q})\tilde{B}(\mathbf{q}) = \begin{pmatrix} \lambda_1 & 0 \\ 0 & \lambda_2 \end{pmatrix}$$

with

$$2\lambda_{1or2} = D_{HA} + D_S \pm \left[(D_{HA} - D_S)^2 + 4D_{HA}L_{Col-H}AD_{Col}L_{HA-Col}\right]^{1/2} \quad (\lambda_1 \geq \lambda_2) \tag{8}$$

and

$$\tilde{B} \approx \frac{1}{\sqrt{D_{HA}L_{Col-HA}D_{Col}L_{HA-Col} + \Delta D^2}} \begin{pmatrix} L_{Col-HA}D_{Col}\frac{C^0_{Col}}{C^0_{HA}} & \Delta D \\ -\Delta D & L_{HA-Col}D_{HA}\frac{C^0_{HA}}{C^0_{Col}} \end{pmatrix}$$

$$\tilde{B}^{-1} \approx \frac{1}{\sqrt{D_{HA}L_{Col-HA}D_{Col}L_{HA-Col} + \Delta D^2}} \begin{pmatrix} L_{HA-Col}D_H\frac{C^0_{HA}}{C^0_{Col}} & -\Delta D \\ \Delta D & L_{Col-HA}D_{Col}\frac{C^0_{Col}}{C^0_{HA}} \end{pmatrix}$$

$$\Delta D = \frac{|D_S - D_{HA}|}{2}\left\{1 - \sqrt{1 + 4D_{HA}L_{Col-HA}D_{Col}L_{HA-Col}(D_{HA} - D_S)^{-2}}\right\} \tag{9}$$

Thus concentration fluctuation can be given by

$$C_{HA}(\mathbf{q},t) \propto L_{Col-HA}D_{Col}\frac{C^0_{Col}}{C^0_{HA}}\exp(-q^2\lambda_1 t) + \Delta D\exp(-q^2\lambda_2 t) \tag{10}$$

$$C_{Col}(\mathbf{q},t) \propto -\Delta D\exp(-q^2\lambda_1 t) + L_{HA-Col}D_{HA}\frac{C^0_{HA}}{C^0_{Col}}\exp(-q^2\lambda_2 t) \tag{11}$$

Finally Eq. 11 yields a double exponentially decaying function for the time correlation of the electric field of scattering light as follows.

$$g^{(1)}(q,\tau) \propto A_{fast}\exp(-q^2\lambda_1 t) + A_{slow}\exp(-q^2\lambda_2 t) \tag{12}$$

where $A_{fast}$ and $A_{slow}$ are constants.

## Experimental

### Materials

Pig vitreous bodies were isolated from sclera of the eyeball. The choroid membrane was also carefully removed by the standard method [6]. The samples were excised within eight hours after extraction of the eye at a local slaughterhouse. The appropriate age of the pigs was 1 year. NaCl, and $CaCl_2$ (Wako Pure Chemicals) are used as received.

### Swelling Experiments

The effects of salts on the swelling ratio of the vitreous body were studied. The salt concentrations were changed from $1.0\times10^{-7}$ to 1 mol/L using NaCl and $CaCl_2$. Since the size of the pig vitreous body was of the order of 4 $cm^3$ in volume, the time required to attain the equilibrium state was three weeks. Each solvent of sufficient volume was, therefore, changed every two days, and then the equilibrium-swelling ratio was determined. To avoid the growth of bacteria, we used the solvent containing 0.02% sodium azide especially for swelling experiments. This amount of sodium azide had no effect on the swelling ratio of the vitreous body. The swelling ratio of the vitreous body was determined by weighing in a gel in the equilibrium state. Both the weight of the sample at equilibrium state in water, $W_{\text{water}}$ and the weight of sample at equilibrium state in aqueous salt solution, $W_{\text{salt}}$ (salt = NaCl, $CaCl_2$), were measured. Then the swelling ratio was calculated from the ratio, $W_{\text{water}}/W_{\text{salt}}$. The solvent attached to the gel was carefully wiped to minimize the error.

### Measurement of Friction Coefficient

The principle of the measurement of the friction coefficient of a vitreous body is schematically shown in Fig. 1. The apparatus originally designed by Tokita and Tanaka, by which they determined the friction coefficients of poly(acrylamide) gel and poly(N-isopropylacrylamide) gel accurately under various conditions [8, 9]. A vitreous body of thickness $d$ is fixed to the

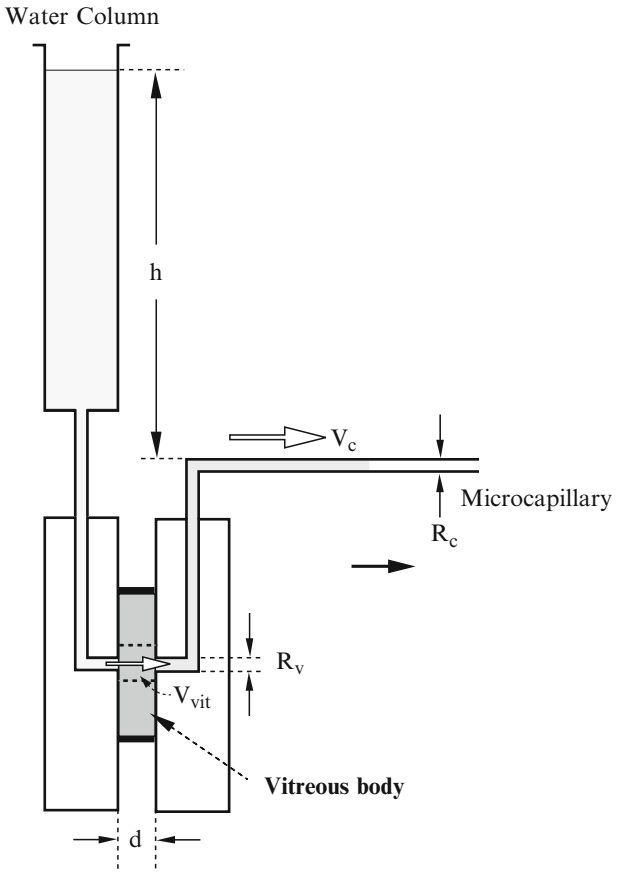


**Fig. 1** Schematic diagram of the apparatus for the measurement of friction coefficient between the gel network and water. The sample mold is tightly held between two plexiglass plates. The velocity of the fluid flow in the micropipette is measured by a movable microscope with an accuracy of 0.001 mm

wall by silicon glue, and water is pushed through the vitreous body with a small pressure $P$. The average velocity of the water flow through the openings inside the vitreous gel, $v$, is determined by measuring the rate at which water flows out of the vitreous body in a steady state. The friction coefficient, $f$, is defined as:

$$f = \frac{P}{d \cdot v} \tag{13}$$

The chromatography column is used as a reservoir of water to generate the hydrostatic pressure. The range of the height of the water column can be changed from 20 to 60 cm, which corresponds to the pressure from $2.0\times10^2$ to $6.0\times10^2$ N/m$^2$. The temperature of the sample is controlled within $\pm$ 0.1°C. The apparatus is set on the vibration-free table to avoid any external mechanical disturbances. The rate of water flow through the gel was determined by measuring the movement of the water meniscus in a micropipette under a microscope.

### Dynamic Light Scattering

Dynamic light scattering (DLS) measurements on pig vitreous body were carried out using a DLS/SLS-5000 (ALV, Langen, Germany). A 22mW He-Ne laser (Uniphase, USA) operating at 632.8 nm was used. In the DLS experiments, the full homodyne intensity autocorrelation function was determined with ALV-5000 multiple-τ-digital correlator. Data were obtained using a scattering angle ranging from 30° to 150° at a temperature of 37°C unless stated.

The Siegert relation relates the normalized intensity autocorrelation function $g^{(2)}(q,t)$ to the normalized electric field autocorrelation function $g^{(1)}(q,t)$, assuming the scattered field has Gaussian statistics.

$$g^{(2)}(q,t) = 1 + B\left|g^{(1)}(q,t)\right|^2 \tag{14}$$

where $B$ ($\leq$1) is an instrumental parameter.

As we shall see later and as shown in Fig. 5, a time autocorrelation function have a distinct double-exponential feature associated with cooperative diffusion ($\Gamma = Dq^2$, where $\Gamma$ is the relaxation rate and $D$ is the cooperative diffusion coefficient). This indicates the presence of two different diffusive modes within the gel. In this work, therefore, all the correlation data were analyzed using the following relationship:

$$g^{(1)}(t) = A_{fast}\exp\left(-D_{fast}q^2t\right) + A_{slow}\exp\left(-D_{slow}q^2t\right) \tag{15}$$

with $A_{fast} + A_{slow} = 1$ where $A_{fast}$ and $A_{slow}$ are the amplitudes and $D_{fast}$ and $D_{slow}$ the diffusion coefficients of the fast and slow components in the bimodal distribution, respectively, and $q = (4\pi n/\lambda)\sin(\theta/2)$ ($n$: refractive index, θ scattering angle, λ:wavelength of the incident beam) is the magnitude of the scattering vector.

## Results

### Swelling Behavior

The swelling behavior of a gel is determined by the osmotic pressure of the gel. The osmotic pressure of the gel consists of four contributions, that is, the rubber elasticity of the polymer network, the effects of the counter ion of the ionic group on the polymer network, the interaction free energy between the polymer and the solvent, and the mixing entropy. The balance of these four factors determines the equilibrium-swelling ratio of the gel [10]. The vitreous body is

a typical biological gel that consists of collagen and sodium hyaluronate. The collagen is a main protein component of the vitreous body [1]. Hyaluronic acid is a typical acidic mucopolysaccharide carrying carboxyl groups as the ionic side chain. These components form a complex in the vitreous gel and built-up the three-dimensional polymer networks of the gel. The vitreous body is, therefore, one of the multi-component ionic gels.

Fig. 2 shows the swelling ratios of vitreous body as a function of the concentrations of aqueous solutions of NaCl and $CaCl_2$ at 37°C. A marked decrease in swelling ratio is observed when the salt concentration in the external solution is increased. This is in accordance with the Donnan equilibrium theory, which predicts that the difference in ionic concentration between the inside and the outside of a gel decreases when the concentration of salt in the surrounding liquid is increased. It is worthy to mention that the vitreous body swells in aqueous solutions of NaCl of the concentration of saline (0.153 mol/L).

Due to its network structure, the gel acts as if it provides its own semipermiable membrane. To allow for changes in swelling caused by altering the concentration of salts outside the gel, it is necessary to treat the ionic term, $\Pi_{ion}$, as the effective difference in chemical potential of the solvent due to mobile ions inside the gel. The osmotic pressure generated by the Donnan potential is then given by [11]

$$\Pi_{ion} = -\frac{\Delta\mu}{V_s} \approx RT\Delta C_{mobile} \tag{16}$$

where $V_s$ is the molar volume of the solvent and Δμ is the chemical potential change caused by gel swelling. The effective osmolarity of the mobile ions, $\Delta C_{mobile}$ (i.e., the concentration difference of mobile ions between the inside and outside of the gel), is given by

$$\Delta C_{mobile} = (C_+ + C_-) - \left(C'_+ + C'_-\right) \tag{17}$$

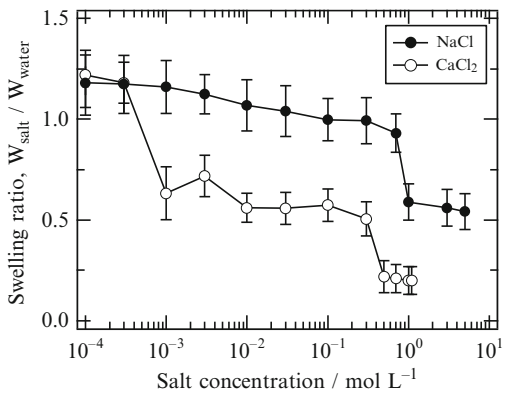


**Fig. 2** The swelling ratio of pig vitreous body in different concentrations of NaCl, $MgCl_2$, and $CaCl_2$ aqueous solutions at 37°C ($n = 5$ for each concentration)

where $C_+$ and $C$-, and $C'_+$ and $C'$- are the concentrations of positive and negative mobile ions inside and outside the gel, respectively. The ion concentrations are determined by the Donnan equilibrium [11, 12], which for anionic polymers in 1: 1 (NaCl) and 2: 1 ($CaCl_2$) electrolytes are described by the following equations:

$$z_+C_+ = z_-C_- + z_pC_p \qquad \text{(inside the gel)} \qquad (18\text{-}1)$$

$$z_+C'_+ = z_-C'_- \qquad \text{(outside the gel)} \qquad (18\text{-}2)$$

$$\gamma_\pm^2 C_+^{z_-} C_-^{z_+} = \gamma'^{\,2}_\pm C'^{\,z_-}_+ C'^{\,z_+}_- \qquad (18\text{-}3)$$

where $C_+$ and $C_-$ are the absolute values of the valences of the mobile ions, $Z_v$ is the number of non-condensed charges per monomer residue, $C_v$ is the concentration of polymer in the gel expressed as the molar concentration of monomer residues $\gamma_\pm$ and $\gamma'_\pm$ are the mean activity coefficients of the salt inside and outside the gel, respectively. The fraction of non-condensed ions per monomer residue $Z_v$ can be calculated from the Manning theory of counter ion condensation [13]. The chain may be characterized by a dimensionless parameter ζ,

$$\xi = \frac{e^2Q}{Dk_BTL} \tag{19}$$

where $e$ is the electron charge, $Q$ is the number of (electron) charges in length $L$, $D$ is the bulk solvent dielectric constant, $k_B$ is the Boltzmann constant, and $T$ is the absolute temperature. For monovalent counter ions the value ζ = 1 regarded as a critical value, above which counter ion condensation occurs in some fraction near the polyion and below which the polyion may be regarded as fully ionized. The value of ζ for the hyaluronate polyion was taken to be 0.70 [14. 15], which is below the critical value. Here we assume that the polymer is fully ionized in the Debye-Hückel sense.

The vitreous gel swells in $10^{-7}$–$10^{-4}$ mol/L of the salt solution due to the charge repulsion force of the carboxylate group on hyaluronic acid, resulting in expansion of the gel networks. When the salt concentration of the external solution increased from $10^{-4}$–$10^{-3}$ mol/L, the negative charges in hyaluronic acid were neutralized by the cations and the swelling ratio rapidly decreased, that is, the gel show deswelling behavior. Almost all the negative charges on the polymer chains were neutralized by the external cations in this concentration range. This results from the Donnan effect. But the salt concentration further increased over $10^{-3}$ mol/L, the vitreous gel became nonionic-type hydrogel, therefore the swelling curve reflected nearly a horizontal line in the range of $10^{-3}$–$10^{-1}$ mol/L. When the salt concentration was raised to 1 mol/L, the salting-out effect was

enhanced, due to the high external ionic concentration, and the swelling ratio of the vitreous gel sharply decreased.

## Friction coefficient

The velocity of the water in the micropipette at the stationary state, $V_c$, is obtained by measuring the shift of water meniscus for a given period of time using a movable microscope with an accuracy of 0.001 mm. The velocity thus obtained is plotted as a function of the pressure in Fig. 3. At relatively high pressures, the water flow in the vitreous body is high. Presumably, the network structure of the vitreous body is broken under high pressure; therefore we chose five points measured at lower pressure to calculate the friction coefficients. The relationship between the applied pressure and the velocity is linear at lower pressures as predicted. The friction coefficient between vitreous body and water, $f = 6.4 \times 10^{11}$ N s/m$^4$, was obtained from the slope of the straight line in Fig. 3 using the following equation:

$$f = \left(\frac{dV_C}{dp}\right)^{-1} \cdot \frac{1}{d} \cdot \left(\frac{R_V}{R_C}\right)^2 \tag{20}$$

where, $dV_C/dp = 3.1 \times 10^{-8}$ m/N.s is determined from the slope of the straight line as given in Fig. 4. The thickness of the sample $d$, is $d = 0.005$ m. The factor $(R_V/R_C)^2$ is the ratio of the area of the micropipette of radius $R_c = 3.4 \times 10^{-4}$ m and the area of the hole in the vitreous body with radius $R_v = 3.3 \times 10^{-3}$ m, which is necessary to convert $V_c$ to $V_{vit}$. The value of $f$ measured here is from the total water flow along the orbital axis in the vitreous body. More precise measurements at difference positions are needed, but it is very difficult to measure water flow in a high-water-content vitreous body without destruction of its network structure. Therefore we use this friction coefficient in the following discussions.

## Dynamic Light Scattering

Pig vitreous bodies were investigated by DLS in aqueous solutions of NaCl and $CaCl_2$. Intensity correlation functions were recorded at five different scattering angles between 30° and 150°. For each scattering angle, the measurements were repeated five times and the values for relaxation times given below are averaged of these five measurements.

Fig. 4 shows the scattering angle dependence of (a) normalized electric field autocorrelation function, $g^{(1)}(\tau)/g^{(1)}(0)$

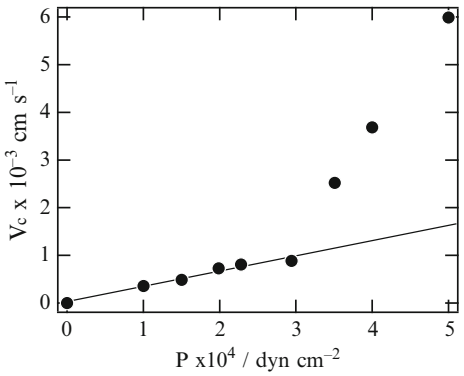


**Fig. 3** The velocity of water in the micropipette is plotted as a function of the water pressure. The solid line in this figure is obtained by the least square fit

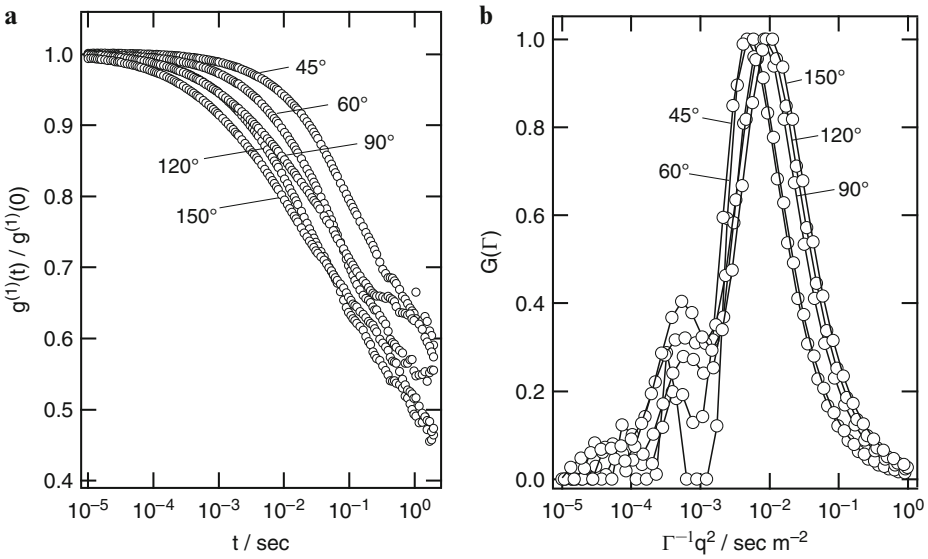


**Fig. 4** (a) The scattering angle dependence of normalized electric field autocorrelation function, $g^{(1)}(\tau)/g^{(1)}(0)$ vs. $t$, and (b) the relaxation time distribution for the pig vitreous body in saline at 37°C

vs $t$, and (b) the decay rate distribution functions, $G(\tau)$ vs $\tau^{-1}q^2$ for the pig vitreous body immersed in 0.16 mol/L aqueous solutions of NaCl (saline). For a diffusive mode, one expects that $\tau$ is proportional to $q^2$. For all scattering angles, the $\tau q^{-2}$ for both fast and slow modes are almost $q$-independent as shown in Fig. 4b. This indicates that the observed two modes are diffusive. It should be mentioned that the apparent $q^2$-dependence of the $\tau q^{-2}$ is within experimental error. Very slow relaxation with decay time ranging from 1 to 10 sec is observed as shown in Fig. 4a. The vitreous gel has a very dilute network-like structure of collagen whose interstices are filled with sodium hyaluronate. There seems to exist a very slow accordion-like movement of semi-rigid network of collagen threads in the vitreous gel. This could originate in the observed very slow relaxation. It is important to note that this slow relaxation, not yet well understood, is possibly generated by a different physical mechanism, and is independent of the other faster modes. Therefore for the CONTIN analysis we introduced a cut-off at 0.1sec and subtracted the non-zero baseline.[20] It was verified for the correlation curves that the cut-off did not influence the decay rates and amplitudes of the faster modes. But no satisfactory explanation for this slow relaxation is given here. The detail study on the pig vitreous body is in progress now. The essential parameters for the diffusion coefficients $D_{fast}$ and $D_{slow}$ that represents the two apparent, collective diffusion motions of the vitreous gel, designated as fast and slow motions, respectively, were derived. The results of the fits yielded for $D_{fast} = 5.9 \pm 0.83 \times 10^{-12}\,\mathrm{m^2/s}$ and $D_{slow} = 1.9 \pm 0.78 \times 10^{-13}\,\mathrm{m^2/s}$ for vitreous gel in saline (data shown in Fig. 4).

Other significant parameters of the fit include the relative contributions of the fast and slow components to overall dynamic scattered light intensity $I_D$, designated as $f(A_{fast})$ and $f(A_{slow})$, respectively, where $f(A_{fast}) = A_{fast}/(A_{fast}+A_{slow})$. The static $f(I_S)$ and dynamic $f(I_D)$ components of scattered light intensities, where $f(I_D) = I_D/(I_S + I_D)$, to the total scattered light intensity $I_{total}$ observed at a particular wave vector, were also determined. The temporal fluctuations of the scattered light intensity $I(t)$ were analyzed in terms of intensity autocorrelation functions [16],

$$G^{(2)}(\tau) = \langle I(t) \cdot I(t+\tau) \rangle \tag{16}$$

where $\langle \mathrm{L} \rangle$ stands for the time average over $t$. The rate of the fluctuations of the scattered light intensity, that represent the density fluctuations of the vitreous gel, is proportional to the rate of local swelling and shrinking of the gel via molecular Brownian motions. There are also permanent and static inhomogeneities within the vitreous that also contribute to light scattering. The static inhomogeneities are characteristic of polymer gels and arise from topological constrains of the network chain molecules. The light intensity scattered by these inhomogeneities does not fluctuate with time. The scattered light intensity is, thus, the superposition of contributions from scattering elements that are static from those that dynamically fluctuate [17]:

$$I(t) = I_S + I_D(t) \tag{17}$$

In dynamic light scattering the time correlation of the intensity of scattered light is recorded. Assuming the Gaussian nature of the scattered light photons, the correlation function of the intensity of scattered light is rewritten in terms of the autocorrelation function $G^{(1)}(\tau)$ of the scattered electric field $E(t)$, that is related to the scattered light intensity: $I(t) = E(t)E^*(t)$ [16],

$$G^{(1)}(\tau) \equiv \frac{\langle E(t) \cdot E^*(t+\tau) \rangle}{\langle E(t) \cdot E^*(t) \rangle} \tag{18}$$

Then $G^{(2)}(\tau)$ is written as

$$G^{(2)}(\tau) = (I_S + I_D)^2 + A \left\{ I_D^2 \cdot G^{(1)^{(2)}}(\tau) + 2 I_S \cdot I_D\, G^{(1)}(\tau) \right\} \tag{19}$$

where $A$ is the efficiency parameter of the apparatus, which is uniquely determined by the optical configuration of the set-up, the value, $I$ and the average intensities scattered by the gel fluctuations and the static inhomogeneities [17]. Base on the Eqs. 16–19, for the data shown in Fig. 4, $f(A_{slow}) \approx 61 \pm 5$ and $f(I_D) \approx 22 \pm 3$ for vitreous gel in saline at 37°C.

## Discussion

The vitreous body can be regarded as a gel composed of the highly flexible sodium hyaluronate polymers. The fluid gel is interwoven by semi-rigid network of collagen threads which serve the mechanical stabilization of the body. As mentioned in the theoretical section, the DLS measures the time correlation of density fluctuation of the scattering entities, which are the segments of the hyaluronate polymers and the collagen mesh. The vitreous body is found to show two different diffusion coefficient modes, one relatively fast and the other relatively slow mode. This may due to the complex structure of the vitreous body, in which the highly flexible sodium hyaluronate is interwoven by semi-rigid collagen threads. In this case, it is natural to consider the coupling of the collagen motion with the dynamics of sodium hyaluronate can explain the fast mode. According to Eqs. 8 and 12, $D_{fast}(=\lambda_1)$ and $D_{slow}(=\lambda_2)$ and are given by $D_{fast} = D_{HA} - \Delta D$ and

$D_{slow} = D_S + \Delta D (D_{HA} > D_S)$ and $D_{fast} = D_S - \Delta D$ and $D_{slow} = D_{HA} + \Delta D (D_{HA} < D_S)$

Takahashi et al. [18] measured the diffusion coefficient of sodium hyaluronate diluted in the 0.2M NaCl aqueous solution, molecular weight of which is similar to that $(M_w \sim 1.4 \times 10^6)$ in the pig vitreous body by DLS, and found to be $D_{HA} \approx 2.4 \times 10^{-12}$ m$^2$/s. Using this result, the values of $D_S$, $\Delta D$ and $D_{Col} L_{Col-HA} L_{HA-Col}$ are evaluated from the obtained $D_{\text{fast}}$- and $D_{\text{slow}}$-values and found to be $D_S = 3.7 \times 10^{-12}$ m$^2$/s, $\Delta D = -2.2 \times 10^{-12}$ m$^2$/s, and $D_{Col} L_{Col\text{-}HA} L_{HA\text{-}Col} = 11 \times 10^{-12}$ m$^2$/s. It should be mentioned that the value of $D_{Col} L_{Col-HA} L_{HA-Col}$ is very close to the reported diffusion constant of collagen with a contour length 280 nm in 0.1N HCl aqueous solution ($D_{Col} \sim 9 \times 10^{-12}$ m$^2$/s) [19]. It is plausible that the $L_{Col-HA} L_{HA-Col}$-value for the collagen strongly coupled to sodium hyaluronate in the vitreous body is an order of magnitude 1. It can be inferred, therefore, that the collective diffusion coefficient of collagen in the vitreous body is very close to that in the aqueous solution. This can be realized in the highly swollen vitreous body, which have enough space for the polymer segments to move freely.

The longitudinal elastic modulus of the vitreous network $G$ $(= K + 4\mu/3)$, estimated from the $D_S$ $(= 3.7 \times 10^{-12}$ m$^2$/s) and $f$ $(= 6.4 \times 10^9$ N s/m$^4$) using Eq. 4-1 is 2.4 N/m$^2$. Assuming Poisson's ratio of the network is zero, the longitudinal elastic modulus is readily $G = 2$ μ [5]. Therefore, the shear modulus of the vitreous network is calculated to be $\mu = 0.012$ N/m$^2$. Tokita et al. determined the share modulus μ of calf vitreous body to be in the order of 0.05 N/m$^2$ by using torsion pendulum apparatus [20]. Although this value is in the same order of our result, there still remain several factors we have to consider. The shear modulus of the vitreous gel may be variable between species. And it is worthy to mention that Nickerson et al. recently reported the time-dependent modulus change of the Bovine vitreous body [21]. The drop in the shear modulus indicates a molecular-level change from a relatively rigid *in-oculo* state, which is not stable outside of the constraints of the eye, to a measurably softer state *ex-oculo*. The viscoelastic properties of the vitreous body is still under controversy, however, we could determine the elastic constant m from the independently obtained values; the time correlation of the scattered light intensity and the friction coefficient between polymer network and solvent, $f$ from macroscopic method.

The dynamics of vitreous gels were observed with respect to externally increased NaCl and $CaCl_2$ concentrations. Fig. 5 shows the averaged fast and slow diffusion coefficients, $D_{fast}$ and $D_{slow}$, and the measured scattered light intensity $I_{total}$ in aqueous solutions of (a) NaCl and (b) $CaCl_2$ in the concentration range between $1.0 \times 10^{-4}$ and 3.0 mol/L (1.0 mol/L for $CaCl_2$). The diffusion coefficients

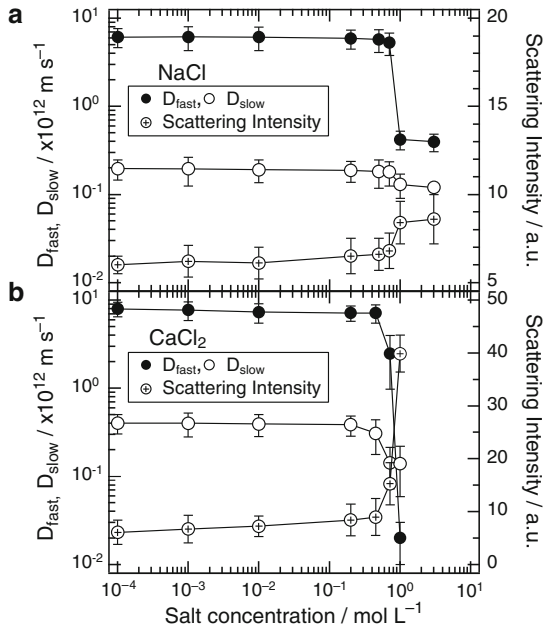


**Fig. 5** Diffusion coefficient, $D_{fast}$ (○) and $D_{slow}$ (●) and scattered light intensity ( ⊕ ) as a function of (a) NaCl and (b) $CaCl_2$ concentration at 37°C ($n = 5$ for each concentration). The solid lines are guide for the eyes

gradually decreased with the concentration of salt. It is remarkable that the diffusion coefficient diminished at 1 mol/L of $CaCl_2$. It is worthy to mention that the vitreous body became slightly opaque as a threshold for $CaCl_2$ concentration was approached in the range of 1 mol/L.

Parallel to the diminishment of the diffusion coefficients, the measured intensity $I_{total}$ from the vitreous body in $CaCl_2$ solution observed at 90° increased and appeared to diverge as the concentration approached the critical threshold, 1mol/L (Fig. 6). No remarkable change was observed for $I_{total}$ from the vitreous body in NaCl solution. The changes in $I_{total}$ can be attributed to the increased compressibility of the vitreous gel as it approached the critical point of concentration. The divergent behavior in the observed diffusion coefficients and total scattered light intensities is indicative of the occurrence of a phase transition upon calcium ion concentration. These changes were reversible.

Under condition of increased $CaCl_2$ concentration, the vitreous body approached a critical point where it became opaque. Critical opalescence occurs as a result of large-scale temporal fluctuations in the local densities of the collagen gel, where regions of high and low collagen densities form. Therefore, as a phase transition is approached, the magnitude of intensity fluctuations is increased while they become slowed down. This behavior was readily evidenced by a divergent behavior in the observed scattered light intensities ($I_{total}$) and diffusion coefficients ($D_{fast}$ and $D_{slow}$). Moreover, the dramatic increase in the observed scattered light

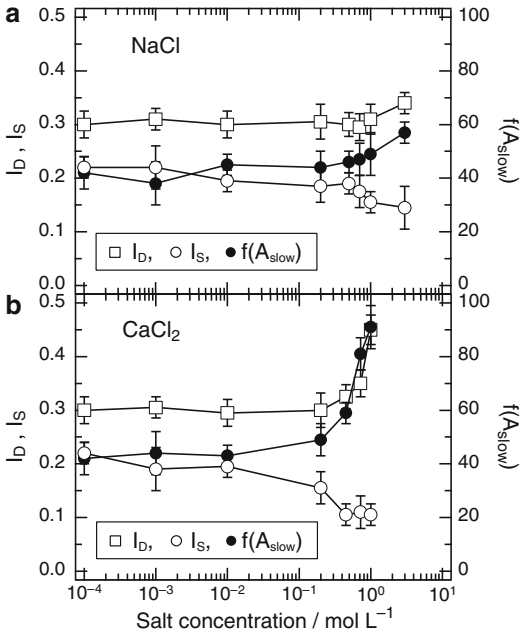


**Figure 6** Changes in the static and dynamic components, $I_S$ (□) and $I_D$, (○), contributed to the total scattered intensity $I_{total}$ (●) as a function of (a) NaCl and (b) $CaCl_2$ concentration at 37°C ($n = 5$ for each concentration). The corresponding contribution of the "slow" scatterer $\%A_s$ to the overall increase in $I_D$ is also shown ($n = 5$ for each concentration). The solid lines are guide for the eyes.

intensities $I_{total}$ is associated directly with an increase in the dynamic component of the scattered light $I_D$ rather than the static component $I_S$ (Fig. 6). The primary contributor to the increase in $I_D$ is the "slow" mode, where an increase in $\%A_s$ is also observed as the calcium concentration was increased. This behavior is indicative of a gel undergoing a phase transition.

## Conclusion

Dynamic light scattering spectroscopy was applied to investigate the structural and dynamical properties of pig vitreous body. From the observations of the dynamics of scattered light scattered by the pig vitreous body, two different diffusive modes, one relatively fast and the other relatively slow mode, were observed. We developed the coupling theory in vitreous gel system describing the coupling of the collagen motion with the dynamics of sodium hyaluronate under the assumption that sodium hyaluronate was filled in the meshes of collagen fiber network. The calculated value of diffusion coefficient of collagen is very close to that in aqueous solution, which suggests the vitreous body is in the swollen state, and the validity of our model. The diffusion coefficients from the intensity correlation function decreased with the concentration of $CaCl_2$, and diminished at 1 mol/L. Parallel to the diminishment of the diffusion coefficients, the measured intensity increased and appeared to diverge as the concentration approached at 1mol/L. The divergent behavior in the observed diffusion coefficients and total scattered light intensities is indicative of the occurrence of a phase transition upon calcium ion concentration. This study represents new structural and dynamic properties of the vitreous body. The simple consideration presented here may be helpful toward understanding of physicochemical aspects of diseases.

**Acknowledgments** The work was partly supported by a Grant-in-Aid for Scientific Research on Priority Areas "Soft Matter Physics" (No. 19031024) and by a Grant-in-Aid for the Global COE Program, "Science for Future Molecular Systems" from the Ministry of Education, Culture, Science, Sports and Technology of Japan. Authors acknowledge Prof. Tokita for valuable discussion.

## References

1. Berman ER, Voaden M (1970) In: Smelser GK (ed) Biochemistry of the Eye, Academic Press, London, p 373
2. Balazs EA (1968) In: McPherson A (ed) New and Controversial Aspects of Retinal Detachment, Academic Press: Philadelphia, vol 1, p 3
3. William ST (1968) Tras Amer Acad Opthalmol Otolaryngol 72:217
4. Norman SJ (1968) Arch Ophthal 79:568.
5. Tanaka T, Hocker LO, Benedek GB (1973) J Chem Phys 59:5151
6. Sasaki S, Schipper FMJ (2001) J Chem Phys 115:4349
7. Worst JGF, Los LI (1995) Cisternal Anatomy of the Vitreous. Kugler Publications, Amsterdam
8. Tokita M, Tanaka T (1991) J Chem Phys 95:4613
9. Tokita M, Tanaka T (1991) Science 253:1121
10. T Tanaka (1978) Phys Rev Lett 40:820
11. Tanaka T, Fillmore D, Nishio I, Sun, ST, Shah A, Swislow G (1980) Phys Rev Lett 45:1636
12. Flory PJ (1953) In:Principle of Polymer Chemistry, Cornell Univ. Press, Ithaca, pp 541–593
13. Manning GS (1969) J Chem Phys 51:924
14. Cleland RL, Wang JL, Detweiler DM (1982) Macromolecules 15:386
15. Cleland RL (1982) Macromolecules 15:382
16. Berne BJ, Pecora R (1976) Dynamic Light Scattering, Plenum Press, New York
17. Peeterman J, Nishio I, Onishi S, Tanaka T (1986) Proc Natl Acad Sci USA, 83:352
18. Takahashi R, Kubota K, Kawada M, Okamoto A (1999) Biopolymers 50:87
19. Claire K, Pecora R (1997) J Phys Chem B 101:746
20. Tokita T, Fujita Y, Hikichi K (1984) Biorheology 21:751
21. Nickerson CS, Park J, Kornfield JA, Karageozian H (2008) J. Biomechanics 41:1823

Progr Colloid Polym Sci (2009) 136:205–210
DOI: 10.1007/2882_2009_28

# The Relationship Between the Changes in Local Stiffness of Chicken Myofibril and the Tenderness of Muscle During Postmortem Aging

T. Iwasaki, Y. Hasegawa, K. Yamamoto, and K. Nakamura

**Abstract** We have investigated that the relationship between the stiffness of myofibrils and the tenderness of muscle during postmortem aging. The stiffness (elasticity) of A and I bands as well as Z-line of chicken myofibrils during postmortem aging were measured by atomic force microscope. The stiffness of all regions increased till 12 hr of postmortem, then it decreased to 96 hr. This tendency was the same as the changes of shear force value of whole muscle during postmortem aging. The elasticity of the Z-line of chicken myofibrils treated with calcium ions in the presence of protease inhibitor decreased with treating time. This indicates that the nonenzymatic structural changes of myofibrils is one of the causes of meat tenderization.

## Introduction

Meat is a tissue of skeletal muscle which is made up of bundles of muscle fiber. The muscle fiber is composed of myofibrils, which consist of a series of sarcomere.The sarcomere contains two types of filaments, that is, thick and thin filaments. Muscle contraction is induced by the interaction between these two filaments. Each sarcomere in a myofibril is divided by Z-line.

The tenderness of meat is determined by the properties of myofibrils and the intramuscular connective tissue [1]. The muscle contracts and becomes tough after death, and this is called rigor mortis. Riogr mortis is then resolved and this is called as rigor off. In rigor off state, myofibril weakening occurs by proteolytic degradation of muscle protein and resulting structural change of myofibrils [2–4]. The tenderization of meat occurs in two steps: a rapid first phase and a slow phase thereafter [5]. The rapid increases in tenderness are mainly due to the structural weakening of myofibrils, and the slow process is chiefly caused by the structural weakening of connective tissue.

We used myofibrils prepared from chicken in this study. Since aging progresses fast in chicken muscle, there may be little influence of weakening connective tissue to tenderness. Therefore, we expected that the relationship between the changes in local stiffness of myofibrils and tenderization of meat becomes clear.

The local stiffness of myofibril was measured using atomic force microscope (AFM). The AFM has some advantages over electron microscopy; that is, it makes possible rheological measurement as well as morphological observation in a solvent under atmospheric pressure. From such characteristics, AFM were used in many fields [6–10]. This study is aimed to clarify the relationship among morphology, local stiffness, biochemical changes of myofibrils, and tenderness of meat during postmortem aging.

## Materials and methods

### Sample preparation

*Preparation of myofibrils having rest length.* Myofibrils were prepared from breast (pectoralis superficialis) muscle of Rhode Island Red chicken at 0–96 hr of postmortem. The ground skeletal muscle was homogenized with 0.1 M NaCl, 5 mM ethlene glycol bis (2-aminoethyl ether) tetraacetic acid (EGTA), 1% Triton X-100, 10 mM Tris-maleate (pH 7.0), then centrifuged at room temperature to prepare myofibrils of resting length. These myofibrils were washed with a solution containing 0.1 M NaCl, and 10 mM Tris-maleate (pH7.0) at 4°C. This washing was repeated five times.

*Preparation of cold shortened myofibrils.* The carcass just after the slaughter was inrmersed in iced water for 10 min to induce cold shortening. Myofibrils were prepared by the same methods described above. All operations were performed at 4°C

T. Iwasaki (✉)
Department of Food Science, Faculty of Science, Rakuno Gakuen, 069–8501, Evetsu, Hokkaido, Japan
e-mail: iwasaki@rakuno.ac.jp

*Preparation of relaxed myofibrils*. The ground breast muscle was homogenized with 0.1 M NaCl, 5 mM EGTA, 2 mM $Na_4P_2O_7$, 10 mM Tris-maleate, (pH 7.0) at room temperature [11]. The homogenate was washed with 0.1 M NaCl, 10 mM Tris-maleate, (pH 7.0) at 4°C. This washing was repeated five times.

*$Ca^{2+}$-treatment of myofibrils* [12]. Freshly prepared myofibrils were washed three times with 0.1 M NaCl, and 10 mM Tris-maleate (pH 7.0) at 4°C to remove EGTA. After the washing, $CaCl_2$ was added to the myofibrils to give a final concentration of 0.1 mM with protease inhibitor cocktail consiting of aprotinin, bestatin, E-64, leupeptin, and pspstatin (Sigma-Aldrich Inc.). The incubation was done up to 96 hr at 4°C.

Atomic force microscopy (AFM)

The isolated myofibrils were absorbed on a (3-aminopropyl) trithoxy silane coated glass slide by dropping myofibril suspension (0.25 mg/ml, 0.1 M NaCl, 20 mM K phosphate, pH 7.0) onto a slide and incubated for 5 min at room temperature. The sample was rinsed with PBS, and fixed with 2.5 % glutaraldehyde for 2 hr, then flushed with PBS. It was immediately immersed in on AFM glass cell filled with PBS.

AFM observation was made with a commercial atomic force microscope (SPA-300HV microscope unit controlled by SPI-4000 probe station, SII Nano Techonology, Japan). "Dynamic force mode" (equivalent to AC mode) was applied for imaging. The maximum scan range of the piezo scanner used in the present study was about 100 × 100 μm (x–y) and 15 μm in height. The used cantilever has spring constant 0.6 N/m, tip height 20 μm, half-opening angle of tip at 15° (Mikro Masch, Estonia). The scanning was done at relatively low frequencies (0.2–0.5 Hz) to obtain high quality images, and the images were captured at 256 pixels × 256 lines.

Measurement of local stiffness of chicken myofibrils

Measurement of local stiffness (elasticity) of myofibrils at various conditions was performed with an AFM. A $Si_3N_4$ cantilever with a half-opening angle of tip at 45° was used. A cantilever with spring constant of 0.08 N/m was used for myofibrils 0, 24, 48 and 96hr, and that with a spring constant of 0.38 N/m was used for myofibrils at 6 and 12hr postmortem.

The force estimated from the cantilever deflection was plotted against the distance between the cantilever tip and the sample surface. This relation is referred as force curve. The Hertz model gives the following relation between the loading force, $F$, and height of the cantilever tip, $Z$ [13],

$$Z - Z_0 = \frac{F}{k}\sqrt{\frac{F}{\frac{2}{\pi}\frac{E}{1-\nu^2}\tan\theta}} \quad (1)$$

where $E$ is elastic modulus of the sample, $Z_0$ is the sample height without loading force, $k$ is the spring constant of the cantilever, $\nu$ is the Poisson's ration of the sample, $\theta$ is tip half-opening angle. Assuming that the sample volume is constant during compression, $\nu$ is regarded as 0.5. $E$ and $Z_0$ were estimated using Eq. (1). The cantilever deflection was calibrated using a stiff glass slide surface before measurement. The measurements were performed at room temperature.

Shear-force of chicken breast muscle

Chicken breast muscle (10×10×40 mm) was dissected from carcass at designated postmortem times stored at 4°C. The shear-force perpendicular to the axis of muscle fibers was measured for 5 samples using a rheometer (RE-33055, Yamaden, Japan) with shearing blade (0.5 mm, thickness) and crosshead speed of 1 mm/sec.

Statistical analyses

The data were analyzed using Kaleida Graph ver. 3.6 for Macintosh (Synergy Software, USA). Statistical analysis was performed by analysis of variance (ANOVA) and Tukey HSD test. The results are expressed as mean ± S.D. and the differences were considered to be statistically significant at $P < 0.05$.

## Results and discussion

Changes in the shear-force and microstructure of chicken breast muscle during postmortem aging

The shear-force value of raw muscle tissue during postmortem aging was shown in Figure 1. The shear-force increased rapidly and reached to 127% of the initial value

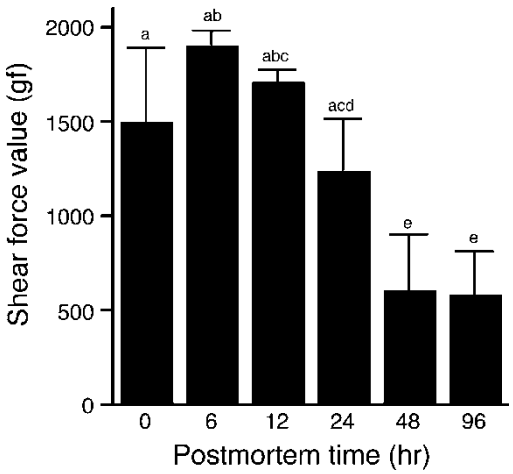


**Fig. 1** Postmortem changes in shear-force value of raw chicken meat. The shear-force value perpendicular to the axis of muscle fibers was measured. Results represented the means ± SD of 5 separate experiments. Value lacking a common letter differed ($P < 0.05$). SD indicates standard deviation

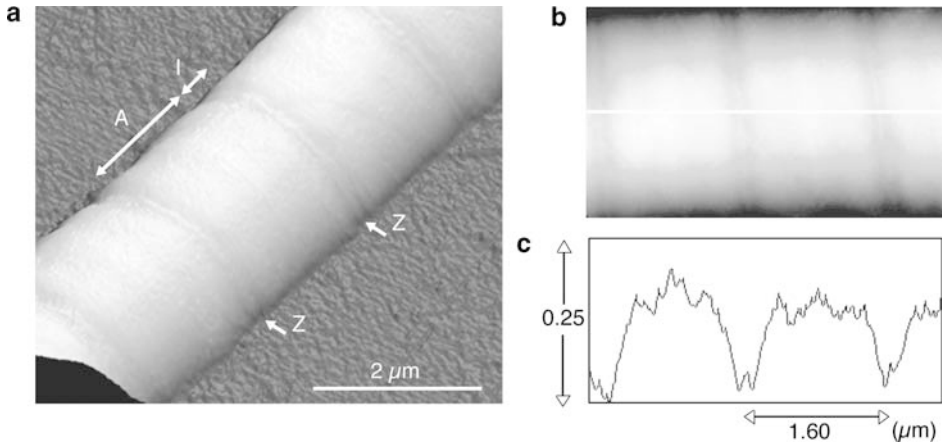


**Fig. 2** Atomic force micrographs of cold shortened chicken myofibril. (a); AFM image, (c); surface profile of myofibril (white line in (b)). Z, A, and I indicate Z-line, A-band, and I-band, respectively

after 6 hr of postomortem. Then it decreased gradually, and reached to 38 % of initial value at 96 hr. The shear-force at 24 hr was 86% of the initial value, and 39 % at 48 hr. The structures of myofibrils and intramuscular connective tissue at the same time were investigated by electron microscope (data not shown). Fragmentation of myofibrils was observed at 48 and 96 hr postmortem, indicating that the weakening of Z-line occured. On the other hand, the structures of the intramuscular connective tissue remained unchanged up to 24 hr postmortem, but the structure clearly changed at 96 hr postmortem, namely, the honeycomb structure of endmysium remained while the perimysial sheets disintegrated into ribbon-like structure.

The decline of shear-force of the whole muscle may be caused by weakening of myofibril and connective tissue during postmortem aging. Nishimura et al [14] showed that the shear-force value of intramuscular connective tissue of beef decreased at 10 days of postmortem. Furthermore, biochemical changes such as fragmentation of skeletal muscle nebulin filaments [15] and connectin [16], weakening of actomyosin rigor complex [17], proteolytic degradation of myofibrilar proteins [18, 19], and liberation of phospholipids from Z-lines [12] were observed in myofibrils during postmortem aging.

There is no report on the changes in stiffness of myofibril itself during postmortem aging so far. This may be due to technical difficulties of the measurement. To measure the local stiffness and morphology of myofibril during postmortem aging, we used the atomic force microscope.

## Changes in morphology and local stiffness of myofibrils during postmortem aging

The myofibrils remain relax just after slaughter, but then they contract by the formation of actomyosin complex, which is caused by ATPase activity of myosin and $Ca^{2+}$ leaked from sarcoplasmic reticulum. Decrease of ATP contents and pH in muscle tissue occurred consequently. After rigor mortis, the muscle became tender. We observed the form of myofibril during postmortem by atomic force microscope.

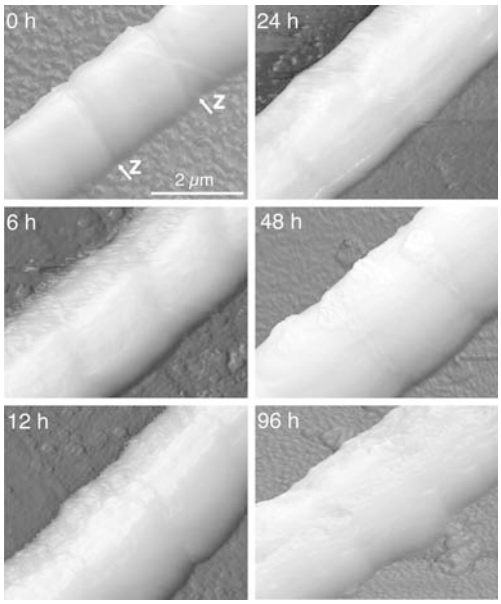


**Fig. 3** Atomic force micrographs of chicken myofibril at various postmortem time. Z indicates Z-line. Images were acquired in Tapping Mode

Figure 2 shows an atomic force micrograph of the cold shortened myofibril. A silicon etched tip was used to obtain the image (Figure 2a). The length of sarcomere, which is the distance between two adjacent Z-lines, was 1.6 μm (Figure 2c). Narrow I-band (thin filament region) with hollowing Z-line in the middle are clearly distinguished from A-band (thick filament region). The aged myofibrils are virtually indistinguishable from those of cold shortnening.

Figure 3 shows the atomic force micrographs of the myofibrils prepared from aged muscle at 4°C. The sarcomere length of fresh myofibril was 1.9 μm (Figure 3a). That of 6 hr was 1.68 μm (Figure 3b), and 1.79 μm at 12 hr (Figure 3c). The sarcomere lengths were 1.83, 1.90, and 1.96 μm at 24, 48 and 96 hr postmortem, respectively. The surface of myofibril was wrinkled, and the Z-line structure of myofibril became indistinct with the progress of postmortem.

The proteolytic, such as calpatic or catheptic, degradation of myofibril and connective tissue was reported during postmotrtem aging [20–22]. It was speculated that the loss of smoothness of the surface and Z-line structure of myofibril was caused by those proteolytic enzymes attached on the surface of myofibril during postmortem.

We observed fragmentation of myofibrils during postmortem aging (data not shown). The results suggested the changes in stiffness of myofibril during postmortem, so that we measured local stiffness (elasticity) of myofibril by AFM.

Figure 4 represents force curve of myofibril. The measurements were done at glass surface (curve 1), and A-band (curve 2) and Z-line (curve 3). Each position is indicated in Figure 4(b). The nonlinear curve fitting was performed for the force curves ranges from 50 to 300 nm in the sample indentation.

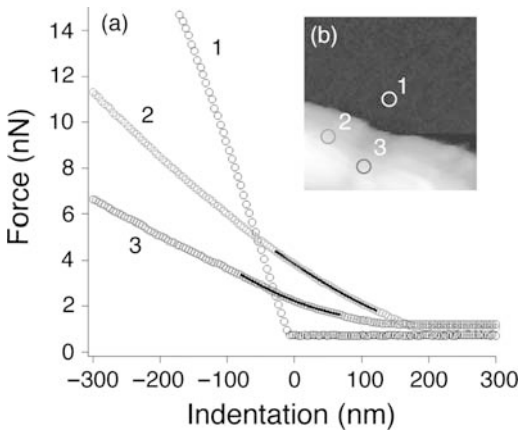


**Fig. 4** Force curve of a myofibril. (a) 1 indicates the force curve of glass, 2 and 3 indicate myofibril. The solid lines in the force curve indicate the regions used for calculation of elasticity. (b) shows the positions where the force curve was obtained. 1, 2, and 3 indicate glass surface, A-band, and Z-line, respectively

Figure 5 shows elasticity of myofibrils at various loci during postmortem aging. The elasticities of fresh myofibrils were 101.6 ± 35.6, 61.3 ± 21.5 and 66.5 ± 18.5 kPa at Z-line, I- and A-bands, respectively. The elasticity of Z-line was the highest. The elasticities of the myofibrils at 6 hr were 166.8 ± 59, 207.3 ± 92.3 and 148.0 ± 67.2 kPa at Z-line, I- and A-bands, respectively. The value of the all loci gradually decreased thereafter. In the previous studies [23, 24], the elasticity of A-band in rigor and relaxed myofibrils was 84–94 kPa and 12–40 kPa, respectively. These values were lower than the value in the present study. This means that the myofibrils of glycerinated rabbit muscle or *Drosophila* are less elastic than chicken myofibrils.

## Stiffness of Z-line at rigor

It is known that the muscle contraction is caused by the interaction of a thin and thick filament, but there is no report about the structural change of Z-line. The elasticities of Z-line at 6 and 12 hr postmortem were higher than fresh myofibril. Two hypotheses can be proposed from this result. The first is the changes in the composition of the Z-line protein, such as α-actinin, at rigor. The second is the increased elasticity of Z-line, because interaction of thin and thick filament becomes firm, the myofibril structure was stable.

To cofirm the first hypothesis, we performed two dimensional gel electrophoresis of I-Z-I brushes prepared from muscle at 0, 6 and 12 hr postmortem time; nevertheless the changes of the protein composition in I-Z-I brushes were not observed during these period (data not shown). For the second hypothesis, the structural stability of sarcomere containing Z-line was investigated by the following methods (11); the myofibril, in which interfilamentous interaction is weak, was prepared from muscle at 0, 6 and 12 hr postmortem

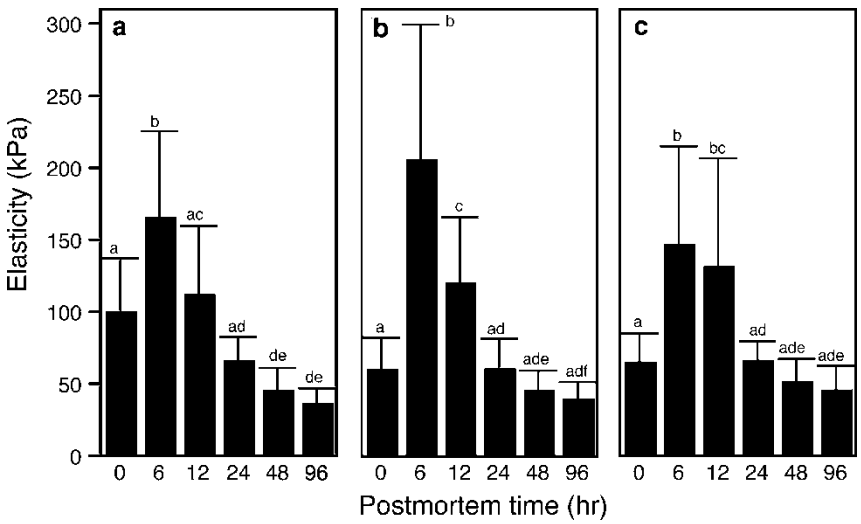


**Fig. 5** Postmortem changes in elasticities of myofibrils. (a); Z-line, (b); I-band, (c); A-band. Results represented the means ± SD of 50 separate experiments. Values not sharing a letter differed; $P < 0.05$

with relaxing buffer containing pyrophosphate. The sarcomere lengths were 1.87 and 2.04 μm at 6 and 12 hr postomortem, respectively (Figure 6). Since the lengths were 0.2 μm longer than that of myofibrils prepared from muscle without pyrophosphate, those myofibril was relaxed. In addition, the elasticity of Z-line region of relaxed myofibrils at 0–12 hr postmortem was 77.38 ± 15.83 kPa in the fresh myofibril, and decreased gradually (Figure 7). The value at 12 hr was 42% of fresh myofibrils, while at 6 and 12 hr postmortem using solution without pyrophosphate increased approximately 1.7 and 1.2 times than the fresh myofibrils (shown in Figure 5a). These results indicate that the increase of elasticity of Z-line is correlative with interaction of thin and thick filaments in myofibrils. Yoshizawa et al [23] showed that the Z-line in rigor myofibrils is stiffer than the other loci, and discussed this as follows. The Z-line network is connected to one end of the thin filament in its adjacent half sarcomeres. Futhermore, the thin filaments interact with myosin heads projected from thick filament to form cross-bridges. These assemblies of the filament lattices mechanically support the Z-line network. The present result supports the view of Yoshizawa et al.

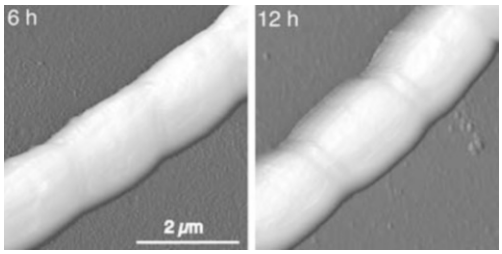


**Fig. 6** Atomic force micrographs of myofibril prepared from chicken pectoralis superficialis muscle at 6 and 12 hours postmortem with addition of 2 mM $Na_4P_2O_7$

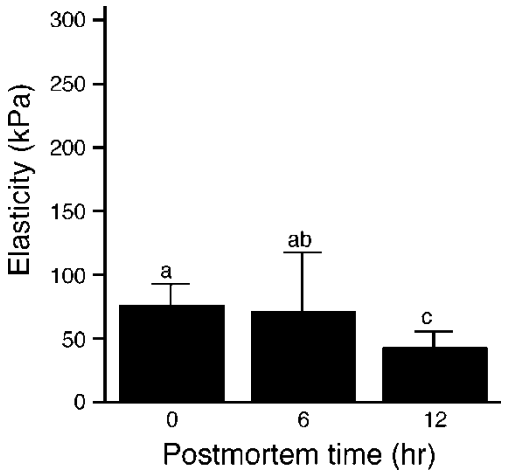


**Fig. 7** Elasticities of Z-line region of myofibrils prepared from chicken muscle 0–12 hours postmortem with addition of 2 mM $Na_4P_2O_7$. Results represented the means ± SD of 50 separate experiments. Values not sharing a letter differed; $P < 0.05$

## Changes of myofibrillar stiffness after the rigor mortis

The tenderization of meat occur in two steps; a rapid first phase and the following slow phase [5]. The first rapid increase in tenderness is mainly due to the structural weakening of myofibrils. The structural changes of myofibrils at postmortem aging include splitting of connectine (titin) and nebulin filaments, depolymerization of desmin filaments, and fragmentation of myofibrils. Those changes are nonenzymatically induced by increase of calcium ions in muscle tissue.

To detemine the influence of calcium ions for elasticity of myofibrils, we measured local stiffness of myofibrils treated with calcium ions in the presence of protease inhibitor (Figure 8). The elasticities of A and I-bands unchanged till 96 hr, but those of Z-lines decreased linearly until 48 hr.

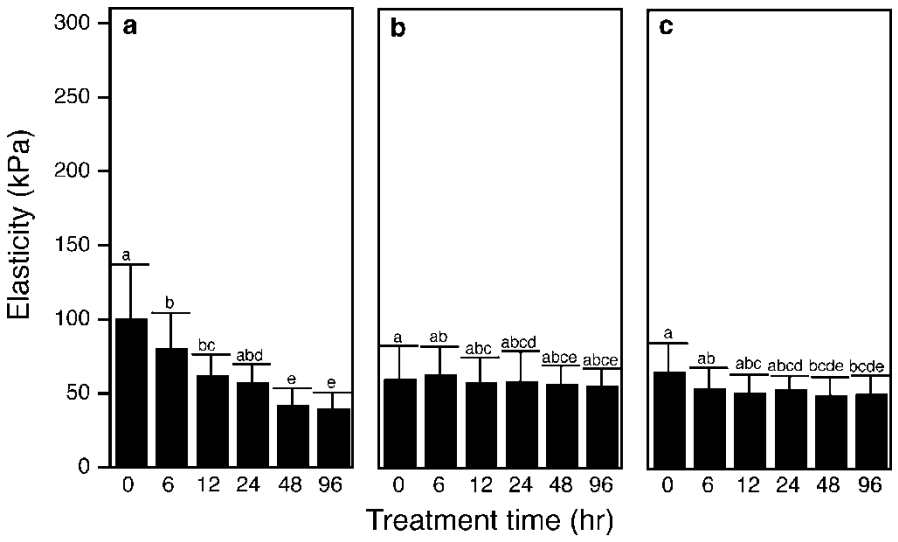


**Fig. 8** The elasticities of the $Ca^{2+}$ -treated isolated chicken myofibril. (a); Z-line, (b); I-band, (c); A-band. Myofibrils were incubated at 4°C for 0–96 hours in 0.1 M NaCl, 0.1 mM $CaCl_2$, 1 mM DTT, protease inhibitor cocktail and 10 mM Tris-maleate (pH 7.0). Results represented the means ± SD of 50 separate experiments. Values not sharing a letter differed; $P < 0.05$

The value at 48 hr was 50% of the initial value. The Z-line of vertebrate skeletal muscle myofibrils is constructed from Z-filament, which is composed of α-actinin and amorphous matrix composed of lipids [25]. Shimada et al reported that the liberation of phospholipids by the binding of calcium ions was the main cause for Z-line weakening during the postmortem aging [12]. The liberation of phospholipids reached a maximum at 48 hr postomortem, and the decrease of the elasticity of Z-lines correlated well with the liberation of phospholipids (Figure 8a). The sarcoplasmic calcium ion concentration increases to 0.2 mM ultimately, which are due to loss of the ability of sarcoplasmic reticulum after death. Those calcium ions bind to phospholipids in Z-line, then the liberation of phospholipid occurs so that Z-line structure becomes weak. The degradation of connectin and nebulin during aging seems to have no substantial effect on stiffness of myofibrils (date not shown).

This work indicates that the tenderness of meat corresponds to local stiffness of myofibrils. The nonenzymatic weakening of Z-lines in myofibrils is the main cause of the meat tenderization.

## References


1. Bailey AJ (1972) J Sci Food Agric 23:995
2. Takahashi K (1992) Biochimie 74:247
3. Wheeler TL, Koohmaraie, M (1994) J Anim Sci 72:12232
4. Merin L, Boehm TLK, Thompson VF, Goll DE (1998) J Anim Sci 76:2415
5. Takahashi K (1999) Anim Sci J 70:1
6. Iwasaki T, Washio M, Yamamoto K (2005) J Agric Food Chem 53:4589
7. Iwasaki T, Washio M, Yamamoto K, Nakamura K (2005) J Food Sci 70:E432
8. Discher DE, Carl P (2001) Cell Mol Biol Lett 6:593
9. Haga H, Sasaki S, Kawabata K, Ito E, Ushiki T, Sambongi T (2000) Ultramicroscopy 82:253
10. Ikai A, Afrin R, Sekiguchi H, Okajima T, Alam MT, Nishida S (2003) Curr Protein Pept Sci 4:181
11. Tatsumi R, Hattori A, Takahashi K (1993) J Biochem 113:797
12. Shimada K, Ahn DH, Takahashi K (1998) Biosci Biotech Biochem 62:919
13. Seneddon IN (1965) Int J Eng Sci 3:47
14. Nishimura T, Liu A, Hattori A, Takahashi K (1998) J Anim Sci 76:528
15. Tatsumi R, Takahashi K (1992) J Biochem 112:775
16. Takahashi K, Hattori A, Tatsumi R, Takai K (1992) J Biochem 111:778
17. Takahashi K, Fukazawa, T, Yasui, T (1967) J Food Sci 32:409
18. Kulesza-Lipla D, Jakubiec-Puka A (1985) FEBS Letters 187:354
19. Sargianos N, Gaitanaki C, Dimitriadis B, Beis I (1996) J Exptl Zool 276:30
20. Geesink GH, Koohmaraie M (1999) J Anim Sci 77:1490
21. Sancho R, Jaime I, Beltran JA, Poncales P (1996) J Muscle Food 8:137
22. Romuald Chéret, Christine Delbarre-Ladrat, Marie de Lamballerie-Anton, Véronique Verrez-Bagnis (2007) Food Chem 101:1474
23. Yoshikawa Y, Yasuike T, Yagi A, Yamada T (1999) Biochem Biophy Res Commun 256:13
24. Nyland LR, Maughan DW (2000) Biophys J 78:1490
25. Takahashi K, Shimada K, Ahn, DH, Ji, JR (2001) J Mus Res Cell Motil 22:353

# Index